PRESSURE AND RATE-TRANSIENT PERFORMANCE BEHAVIORS OF A HORIZONTAL WELL INTERCEPTING MULTIPLE HYDRAULIC FRACTURES WITHIN A SHALE RESERVOIR

A Dissertation

by

ALEX RODRIGO VALDES-PEREZ

Submitted to the Office of Graduate and Professional Studies of
Texas A&M University
in partial fulfillment of the requirements for the degree of

DOCTOR OF PHILOSOPHY

Chair of Committee,	Thomas A. Blasingame
Committee Members,	Maria A. Barrufet
	Jean-Luc Guermond
	Peter Valkó
Head of Department,	Jeff Spath

August 2018

Major Subject: Petroleum Engineering

ABSTRACT

The primary goal of this work is to develop semi-analytical models to predict the pressure and rate performance behaviors of unconventional reservoirs — specifically, shale reservoirs. In these types of reservoirs, there are multi-scale heterogeneities that can hinder the modeling and the diagnostic analyses. Additionally, the use of large stimulation treatments can further complicate the modeling of these heterogeneous reservoir systems. Our approach is to extend the existing models for a multi-fractured horizontal well (MFHW) in a homogenous reservoir to consider the fractal reservoir scenario.

This work presents the detailed derivation of the model of a horizontal well intercepting a single finite-conductivity fracture within a fractal reservoir. The solution of this model is semi-analytical. This is developed by discretizing the hydraulic fracture, which defines a system of equations, the solution of which provides the pressure at any position inside the fracture. The shape of the imposed hydraulic fracture can be either circular or rectangular. By modifying the solution in the Laplace domain of the diffusivity equation for the reservoir, we have investigated different reservoir conditions, such as single porosity fractal reservoirs with typical or anomalous diffusions and double porosity reservoirs with typical diffusion.

We have extended the semi-analytical solution for a horizontal well intercepting a single finite-conductivity fracture to the MFHW case. For this purpose, we have used the principle of superposition in space. We show that the pressure transient response of a MFHW within a fractal reservoir can exhibit a maximum of four (4) distinct periods of flow — (1) fracture (dominated)

flow, (2) early fracture-reservoir interaction, (3) late fracture-reservoir interaction, and (4) reservoir-dominated flow.

To provide an alternative explanation to the anomalous diffusion phenomenon in petroleum reservoirs, we have also developed a double porosity model considering matrix blocks with fractal geometry and a fractal fracture network. We assumed transient interporosity transfer conditions and we modeled it using the classical convolution scheme given in the literature. Under particular conditions, the resulting model acquires a similar mathematical shape to the so-called anomalous diffusion equation.

DEDICATION

To my parents, Marta and Ismael.

ACKNOWLEDGEMENTS

I would like to express my gratitude to:

Prof. Tom Blasingame who has distinguished me with his mentorship and friendship. A friendship based on hard work and high standards of ethics and values…always with a great sense of humor.

Prof. Maria Barrufet, Prof. Peter Valkó and Prof. Jean-Luc Guermond, for serving as my committee members and for their excellent teachings in each one of the courses I took with them.

Prof. Leif Larsen, for his recommendation to this program, his contributions for this work, and his willingness to answer questions.

Dr. Dilhan Ilk, for giving me the opportunity to collaborate in projects related to unconventional reservoirs.

Dr. Andres Moctezuma for his support in the matters related to my scholarship.

Prof. Heber Cinco, Prof. Fernando Samaniego and Mr. Frode Hveding, for their recommendation to this program and their support earlier in my career.

My sibilings (Ivan and Karina) and uncles (Raul and Javier), for their support in each one of the periods of my life.

My colleagues (who turned out to be fantastic friends), for their support, the knowledge I acquired from them and their company in this journey. Nefeli Moridis, Basayir al-Lawati, Jorge Garcia-P, Pedro Sanchez-L, Erick Martinez-A, Nick Wiewiorowski, Adaiyibo Kio, Matias Brolli, Chulhwan Song, Hefdhi Abdennadher and Rui Kou.

The friends I met in College Station, Mariana Valdez, Carla Isnaldi, Husniye Kantarci, and Miguel Ortiz. Thank you for your friendship…

My friends living around the Globe, who were close to me during these years, regardless of the distance. Thank you…

Texas A&M University for the education I received in this institution.

Mr. Hector Pulido, for his mentoring and teachings at the beginning of my career. Without his influence, I would not have achieved this goal.

CONTRIBUTORS AND FUNDING SOURCES

This work was supported by a dissertation committee consisting of Professors Thomas A. Blasingame (chair), Maria Barrufet, Peter Valko of the Department of Petroleum Engineering, and Professor Jean-Luc Guermond of the Department of Mathematics.

The modeling of finite conductivity hydraulic fractures (Chapters III and IV) was additionally supervised by Professor Leif Larsen from the University of Stavanger (retired). The algorithm for numerical inversion used in Chapter V was provided by Professor Peter Valko.

I would like to thank to the High Performance Research Computing (HPRC) group at Texas A&M University for access to its computational resources to generate some of the results presented in this work.

All other work conducted for the dissertation was completed by the student independently.

This graduate study was supported by a scholarship from *Instituto Mexicano del Petróleo* (IMP).

TABLE OF CONTENTS

Page

LIST OF FIGURES

LIST OF TABLES

CHAPTER I

INTRODUCTION

In this chapter, we present the general overview of this dissertation. We divided this chapter into three sections. In the first section, we state the motivation of this research problem and define the strategy that we followed to find a solution. Finally, we define the basic, and recurrent, concepts used in this work in the third section.

1.1. Research Problem

To produce the hydrocarbons contained in highly heterogeneous formations with low/ultralow permeability, such as shale oil and shale gas reservoirs, two main strategies have been implemented: (1) drill horizontal wells to maximize the flowing area and to minimize the number of wells, and (2) stimulate the horizontal well by large hydraulic fracturing treatments that creates multiple hydraulic fractures along the wellbore.

The system created by a horizontal well intercepting multiple hydraulic fractures within a shale gas/oil reservoir becomes a challenging system to model for flow diagnosis purposes given three factors: (1) the heterogeneous and low/ultralow permeability nature of the reservoir, (2) the geometry of the well and fractures, and (3) the properties of the petroleum fluids. In this work, we will address the first two factors to develop diffusivity models and semi-analytical solutions to be used for flow diagnosis.

Some authors have suggested the use of fractal models as the best practice to depict the transient performance behavior of highly heterogeneous reservoirs (*e.g.*, Naturally Fractured Reservoir and

shale reservoirs). Therefore, we modeled the flow of petroleum fluids within a shale reservoir as a fractal object (Chang *et al.*, 1990). In Chapter II, we introduce the classic models related to this topic.

To model the flow towards the horizontal well intercepting multiple hydraulic fractures, we will use the approach proposed by Larsen *et al.* (1994), which applies the principle of superposition in space to extend the models developed for a horizontal well intercepting a single finite-conductivity hydraulic fracture to the multifractured horizontal well case (MFHW).

In Chapter III, we present the pressure and rate transient analyses for a horizontal well intercepting a single finite-conductivity fracture. We investigated two conditions for the geometry of the hydraulic fractures and three conditions of the reservoir. For the geometry of the hydraulic fractures, we assumed them to be either (1) circular transverse or (2) rectangular longitudinal. For the reservoir, we consider the three cases: (1) single porosity fractal reservoir with typical diffusion, (2) double porosity reservoir with typical diffusion, and (3) single porosity fractal reservoir with anomalous diffusion.

In Chapter IV, we apply the principle of superposition in space to extend the finite-conductivity fracture models presented in Chapter III to horizontal wells intercepting multiple hydraulic fractures. We restricted our pressure and rate transient analyses to single porosity fractal reservoirs with typical diffusion.

As an attempt to provide a physical explanation to the anomalous diffusion phenomenon in shale reservoirs, we introduce the double fractal model in Chapter V. This model considers a double

porosity reservoir with transient interporosity transfer, where both the fracture network and the matrix blocks are fractal objects.

We summarize our conclusion and recommendations in Chapter VI. Additionally, we provide an outline for the future work related to the modeling of wells intercepting hydraulic fractures in fractal reservoirs.

1.2. Research Objectives

The main objectives of this dissertation are:

- To *develop* semi-analytical reservoir models to predict the pressure and rate-transient performance behaviors of a horizontal well intercepting multiple hydraulic fractures within an unconventional reservoir— specifically, shale reservoirs.
- To *investigate* the combined effect of the parameters of an unconventional reservoir (*i.e.*, fractal dimension, conductivity index and/or anomalous diffusivity exponent) and the characteristics of the hydraulic fracture (fracture geometry and conductivity) on the flow periods of a horizontal well intercepting multiple hydraulic fractures within a fractal reservoir.
- To *derive* diagnostic interpretation relations to estimate the parameters of the hydraulic fractures for the evaluation of hydraulic fracturing treatments.

1.3. Basic Concepts

In this section, we define the fundamental concepts used in this work. It is not our objective to discuss these concepts in depth (which can be very abstract), but to provide a review and references

that are helpful to understand the fundamental theory behind this dissertation and some of the methods used in it.

Unconventional reservoirs

These are hydrocarbon reservoirs that must be stimulated to be able to produce at commercially viable flowrates. This classification is comprehensive and includes resources such as shale oil/gas reservoirs, heavy oil reservoirs, tight sands reservoirs, etc. In this work, we delimitated our research to shale reservoirs.

Shale reservoirs are highly heterogeneous media that need massive hydraulic fracturing treatments, due to their low porosity and permeability, to produce at economic flowrates. To model the transient performance behavior in these types of reservoirs, some authors have suggested that the use of fractal models is the most appropriate practice given their highly heterogeneous nature.

Fractals

Mandelbrot (1977) defined a fractal as a family of shapes with irregular and fragmented patterns. These irregularities are statistical and identical at all scales. The number of shapes (n) approaches to infinity as their size (l) approaches to zero. This relation is defined as:

$$n \sim l^{-D}, \quad \text{(1.1)}$$

where D is the fractal dimension.

Fractals in Petroleum Reservoir Engineering

The application of the fractal theory in petroleum reservoir engineering became popular in the 1990s, but the mathematical models with similar definition to Eq. 1.1 have been used for over fifty

years. Sahimi *et al.* (1990) presented a review of the applications of the fractal geometry theory in reservoir engineering.

Based on the definition of fractals proposed by Mandelbrot, we can extend such a concept to petroleum reservoirs as follows: a fractal reservoir can be defined as the family of *permeable sites* (*e.g.* lithofacies with hydrocarbon content) with irregular shapes and fragmented patterns which are identical at all scales (sizes). Therefore, the number of the permeable sites is related to a characteristic length (*e.g.* pore radius), R, using a power-law function:

$$N(R) = \sigma R^{D_f - 1}, \quad (1.2)$$

where σ is the density of the permeable sites and D_f is the fractal dimension of the reservoir. A log-log plot of Eq. 1.2 will yield a straight line with a D_f-1 slope. Based on the expression given by Eq. 1.2, the porosity and the permeability for a fractal reservoir can also be modeled as power-law functions (see Appendix B for details). The *porosity of a fractal reservoir* has been defined as space-dependent by:

$$\phi(R) = \phi_0 R^{D_f - d}, \quad (1.3)$$

where ϕ_0 is a reference porosity and d is the Euclidean dimension of the reservoir. Given that there is relation between the permeability and the porosity of a reservoir, the fundamental Darcy's law should also be modified to a power-law expression. This is given by:

$$q_R = \frac{\sigma V_s}{\phi_0} \frac{R^{\beta} k_0}{\mu} \frac{\partial p}{\partial R}, \quad (1.4)$$

where V_s is the volume of the permeable sites and k_0 is a reference permeability. The parameter β in Eq., 1.4 deserves special attention. It is defined as:

$$\beta = D_f - \theta - 1, \quad (1.5)$$

where θ is the *conductivity index*, which depicts the connectivity between the permeable sites. It can acquire values equal or greater than zero. A value of zero represents that the permeable sites are perfectly connected, whereas a high value represents poorly connected permeable sites.

Doe (1991) defined the *spatial dimension* of the reservoir as a manner to describe irregular patterns of flow (*e.g.*, sublinear or hyperspherical flow). Although the author pointed out that this parameter is not necessarily related to the possible fractal nature of the reservoir, we believe that the spatial dimension can be related to β, given that these parameters have similar influence in the pressure and pressure derivative functions of their corresponding models (fractal and fractional models).

Anomalous Diffusion

This concept is related to the random walk theory. It is defined as a process where the mean-square displacement of a random walker is given by a power law function. This is mathematically defined as (Metzler *et al.*, 1994):

$$\left\langle r^2(t) \right\rangle \sim t^{2/d_w}, \quad (1.6)$$

where d_w is the anomalous diffusion exponent.

Fracture Conductivity

This parameter is used for the evaluation of hydraulic fracturing treatments. It is defined by the product of the permeability, k_f, and the width, w, of the hydraulic fracture. In this sense, the fracture conductivity is a concept analogous to the flow capacity of a homogenous reservoir. The dimensionless form of the fracture conductivity can be defined by:

$$F_{cD} = \frac{k_f w}{k l_r}, \quad \text{..... (1.7)}$$

where l_r is a reference length and k is the permeability of the reservoir. In general, a hydraulic fracture with a large F_{cD}-value (*e.g.*, 300 for a fracture in a cylindrical reservoir) is classified as an infinite-conductivity fracture, which is the desired outcome.

Laplace Transform

The Laplace transform is the standard method in petroleum engineering to obtain the analytical solutions of reservoir models. For a function $f(t)$ defined in the real domain, the Laplace transform is defined as:

$$\bar{f}(u) = \int_0^\infty f(t) e^{-ut} dt \quad \text{..... (1.8)}$$

Duhamel's Principle

Using this principle, the dimensionless wellbore pressure, $p_{wD,cr}(t_D)$, can be related with the dimensionless flowrate, $q_{wD}(t_D)$, in the Laplace domain as follows:

$$\bar{q}_{wD}(u) = \frac{1}{u^2 \bar{p}_{wD,cr}(u)}. \quad (1.9)$$

This principle permits to obtain the constant-pressure solution of a reservoir model by using the constant-rate solution and vice-versa.

Wellbore Storage

This effect depicts the capability of a wellbore to store or unload a volume of fluids, when it is subjected to a change in the pressure. It can be included using the relation in the Laplace domain:

$$\bar{p}_{wD}(u,s,C_D) = \frac{\bar{p}_{wD}(u)+s}{1+C_D u^2[\bar{p}_{wD}(u)+s]}, \quad (1.10)$$

where C_D is the dimensionless wellbore storage coefficient, s is the skin (additional drop of pressure) around the wellbore and $p_{wD}(u)$ is the constant-rate solution of a reservoir model.

Numerical Inversion of the Laplace Transform

Most of the reservoir models are solved analytically in the Laplace domain due to the fact that it allows the use of Duhamel's principle (Eq. 1.6) and/or the inclusion of the wellbore storage effects (Eq. 1.7). However, the resulting equations become problematic when inverting from the Laplace domain to the real domain. Therefore, a numerical method to express the solution in the real domain should be applied. The standard methods in petroleum industry are the ones based on Gaver's algorithm (Gaver, 1965).

Based on the probability theory, Gaver (1965) developed an algorithm that estimate the inverse Laplace transform. Later, Stehfest (1970) modified Gaver's work by utilizing the Salzer

summation as an accelerator of convergence. This resulted in the algorithm for numerical inversion of the Laplace transform defined by:

$$f(t) = \frac{\ln[2]}{t} \sum_{i=1}^{N} V_i \bar{f}\left[\frac{\ln[2]}{t} i\right], \quad (1.11)$$

where N is an even number of terms to be used and the coefficients V_i are calculated using the expression:

$$V_i = [-1]^{N/2+i} \sum_{k=[i+1]/2}^{\min[i,N/2]} \frac{k^{n/2}(2k)!}{[N/2-k]!k![k-1]![i-k]![2k-i]!} \quad (1.12)$$

The use of a large number of terms, N, can cause numerical instability in the algorithm due to the limitations of the programming software. In **Fig. 1.1**, we present an example of this numerical instability by comparing the exponential integral function in the real domain:

$$f(t) = -\frac{1}{2} Ei\left[-\frac{a^2}{4t}\right] \text{ (where } a \text{ is a positive constant)}, \quad (1.13)$$

and the numerical inversion of its Laplace transform is given by:

$$\bar{f}(s) = \frac{K_0\left[au^{1/2}\right]}{u}, \quad (1.14)$$

for different values of N.

In the example presented in **Fig. 1.1**, we can see that the Stehfest algorithm can show divergence when using a high number of approximation terms, N.

In general, the numerical instability, or divergence, of the Stehfest algorithm is the result of truncation errors. This can be exacerbated by the type of the function to be inverted, *e.g.*, equations that involve very high or very low arguments of the exponential function, power-law functions, special functions, etc.

As an alternative to the Stehfest algorithm, Valko *et al.* (2004) investigated non-linear methods to accelerate the convergence of the Gaver algorithm. They implemented the Wynn-Rho algorithm as a convergence accelerator in *Mathematica* and concluded that the use of this approach provides accurate results in the numerical inversion of a function in the Laplace domain by reducing the propagation of truncation errors.

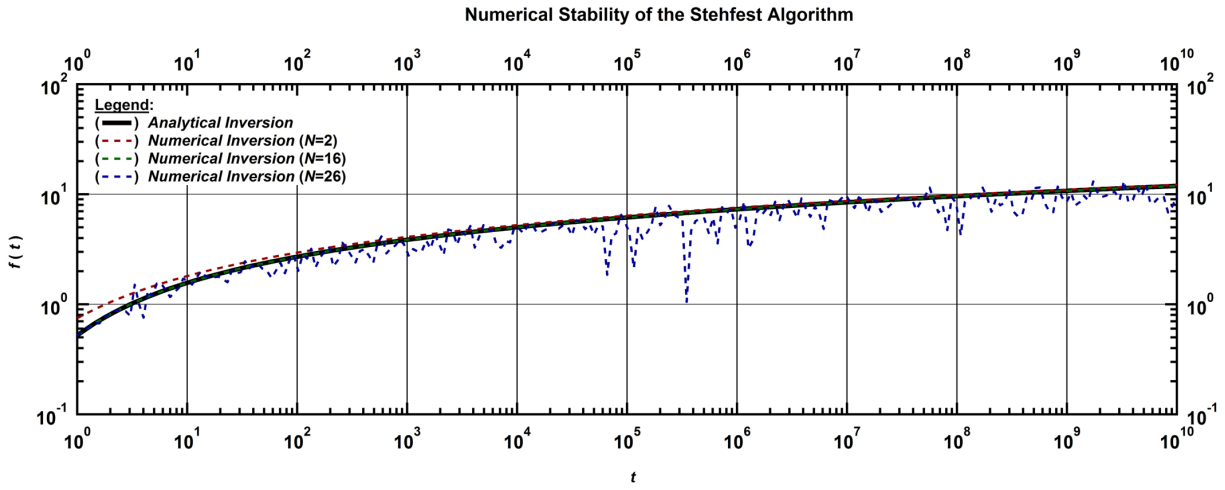

Figure 1.1 — Example of the Numerical Stability of the Stehfest algorithm.

CHAPTER II

LITERATURE REVIEW

The analysis of pressure-transient data as a method to evaluate fracturing jobs has been topic of research for over forty years. During the 1970s decade, the attention was focused on the problem of vertical wells intercepting vertical fractures and the techniques to analyze the pressure-transient data from these type of wells were presented. In the 1990s decade, these techniques were extended to horizontal wells intercepting multiple vertical fractures within homogeneous reservoirs. Given the development and increase in production of shale oil and shale gas reservoirs in the last decade, some authors have extended the methods and techniques used in conventional reservoirs to unconventional reservoirs.

In this chapter, we have summarized the classic works related to the analysis of pressure-transient data of wells intercepting hydraulic fractures and the models used to depict the performance behavior of unconventional reservoirs — specifically, fractal reservoirs and reservoirs with anomalous diffusion.

2.1. Vertical Wells Intercepting Hydraulic Fractures

Gringarten *et al*. (1974) applied Green and Source Functions to develop solutions for the problem of a well intercepting a vertical fracture within a homogeneous reservoir. The authors considered two cases: (1) infinite conductivity and (2) uniform flux fractures. The solution for the first case was obtained semi-analytically by discretizing the fracture into segments and establishing a system of equations whose solution provides the pressure-transient behavior anywhere in the fracture. For

the second case, the solution was derived by superimposing the line-source solution along the fracture length.

The uniform flux solution provides an exact solution at early times and it implicitly assumes that pressure will vary along the fracture. Gringarten *et al*. (1974) found that the infinite conductivity pressure-transient behavior at the wellbore can be reproduced by evaluating the uniform flux solution at a dimensionless position in the fracture, x_D, equal to 0.732. Houze *et al* (1988) extended these ideas to double porosity reservoirs considering both, transient and pseudosteady-state interporosity transfers.

Cinco-Ley *et al*. (1978) presented a general semi-analytical solution for the pressure-transient response of a vertical well intersecting a vertical finite conductivity hydraulic fracture within a homogenous reservoir. This model can reproduce several flow periods observed in wells intercepting a hydraulic fracture by varying the dimensionless fracture conductivity. The authors concluded that the assumption of infinite conductivity applies only when the dimensionless fracture conductivity is equal to or greater than 300. This contribution improved the diagnosis of fracturing jobs, allowing the identification long and/or low permeability fractures.

Cinco-Ley *et al*. (1981a) identified the flow periods generated by the finite conductivity fracture model and introduced the concepts of fracture linear flow and bilinear flow, which were used as a diagnostic technique of pressure-transient data. The flow periods that can be observed in a vertical hydraulic fracture are:

1. Fracture Linear flow: At "very early transient" times the pressure derivative signature shows a half-slope straight line that corresponds to a linear flow occurring in the hydraulic fracture. This period is theoretical and is not observed in practice.

2. Bilinear flow: For low values of the dimensionless conductivity of the fracture, at "early transient" times the pressure derivative signature shows a quarter-slope straight line that corresponds to two linear flows acting simultaneously: a linear flow in the hydraulic fracture and a linear flow from the formation to the fracture.

3. Pseudo-Linear flow: For intermediate and high values of the dimensionless conductivity of the fracture, at "intermediate transient" times the linear flow from the formation to the fracture dominates and the pressure derivative signature shows a half-slope straight line.

4. Pseudo-Radial flow: At "late transient" times the pressure derivative signature exhibits a zero-slope that corresponds to a flow dominated by the reservoir.

Cinco-Ley *et al*. (1981b) included the effects of damage for a vertical well intercepting a hydraulic fracture. The authors considered two types of damage conditions: (1) damaged zone around fracture caused by loss of fluid in the formation (fracture skin), and (2) damaged zone around wellbore caused by crushing, embedding or loss of proppant within the fracture (chocked fracture skin).

Cinco-Ley *et al*. (1981b) pointed out the differences between the pressure-transient response at early times of a finite conductivity fracture and a hydraulic fracture affected by any of the two types of damage mentioned before. They found that for small values of the fracture skin, the pressure-transient response approximates to the infinite conductivity fracture case, whereas for

large values the response converges to the uniform flux case. Additionally, Wong *et al*. (1986) and Valdes-Perez *et al*. (2011) studied the impact of the fracture skin in the pressure-transient and pressure derivative behaviors of the bilinear model and presented techniques to analyze pressure-transient data.

Lee *et al.* (1986) developed a trilinear flow model to provide an analytical approach to the finite conductivity fracture model. In their paper, Lee *et al*. (1986) found the solutions for both constant-pressure and constant-rate cases, including the effects of fracture skin, wellbore storage and fracture storage. This approximate model can match the "early time" period of the finite conductivity fracture model for two logarithmic cycles.

Cinco-Ley *et al*. (1988) extended the finite conductivity fracture model to double porosity reservoirs. In their development, the authors considered both transient and pseudosteady-state interporosity transfers. Based on a fully analytical model for "early times," Cinco-Ley *et al*. (1988) found that under certain circumstances this type of system can yield a one-eight-slope (trilinear flow) in the log-log pressure-transient and pressure derivative plot and not one-quarter (bilinear flow) as in the homogeneous case. Similarly for "intermediate times," a quarter-slope (bilinear flow) could be shown instead a one-half-slope (pseudo-linear flow).

To provide an expression simpler to compute than the semi-analytical solution to the finite conductivity fracture model, Blasingame *et al.* (1993) combined the trilinear solution developed by Lee *et al.* (1986) and the alternative uniform flux solution obtained by Ozkan *et al.* (1991) to develop an equivalent solution in the Laplace domain valid for values of the dimensionless fracture conductivity greater than 0.5.

Cossio *et al.* (2013) presented an application of the fractal theory to provide an improved semi-analytical solution for the flow of a single fluid within a single vertical fracture that fully penetrates a homogeneous infinite-acting reservoir. The authors modified the trilinear flow model (Lee *et al.*, 1986) to introduce fractal parameters in each one of the three regions. The essence of this work is the modification of the diffusivity equation for linear flow to include both permeability and porosity as distance-dependent properties using power-law models. This diffusivity equation was analytically solved for a closed system and validated with a 1D finite-volume black-oil reservoir simulator. The authors verified their fractal-based trilinear solution with the solution developed by Cinco-Ley *et al.* (1988).

2.2. Horizontal Wells Intercepting Hydraulic Fractures

Larsen *et al.* (1991) developed a semi-analytical model of a horizontal well intersecting a finite conductivity vertical fracture within a 3D homogenous reservoir (see the detailed derivation of these models in Appendix A). The authors considered two geometries for the fracture: (1) circular fracture perpendicular to the axis of the wellbore (**Fig. 2.1**) and (2) rectangular fracture parallel to the axis of the wellbore (**Fig. 2.2**).

Fig. 2.3 and **Fig 2.4** show the pressure-transient behavior of the radial and rectangular fractures, respectively. Based on these models, the authors investigated the flow periods that can exist in the pressure-transient response of horizontal wells with multiple vertical fractures (Larsen *et al.* 1994). They found that at early flow periods (before pressure interference between fractures occur), the pressure-transient behavior of a multi-fractured horizontal well can be appropriately analyzed using the single fracture models.

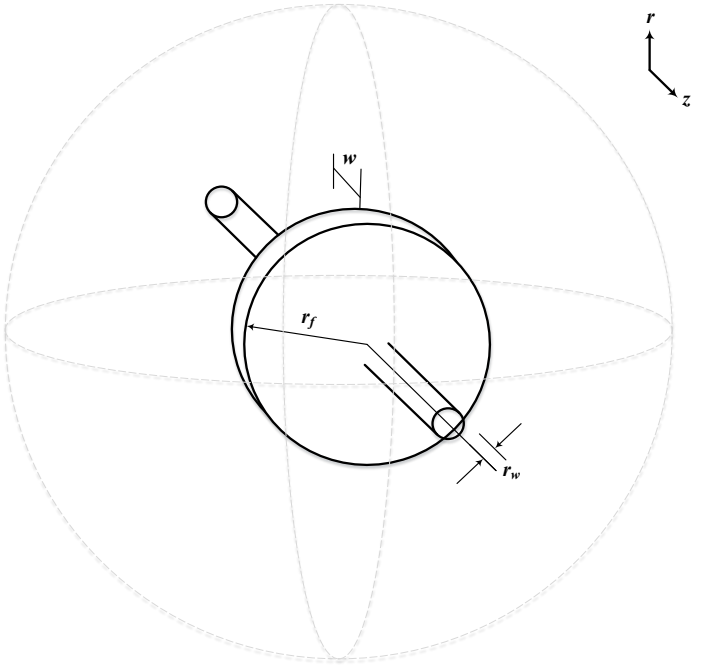

Figure 2.1 — Vertical circular hydraulic fracture transverse to the axis of a horizontal well within an infinite 3D reservoir.

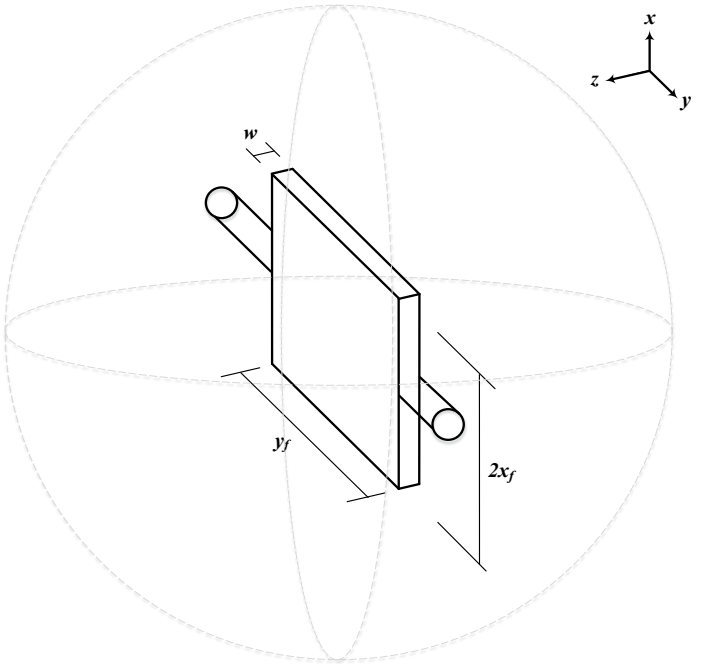

Figure 2.2 — Vertical rectangular hydraulic fracture longitudinal to the axis of a horizontal well within an infinite 3D reservoir.

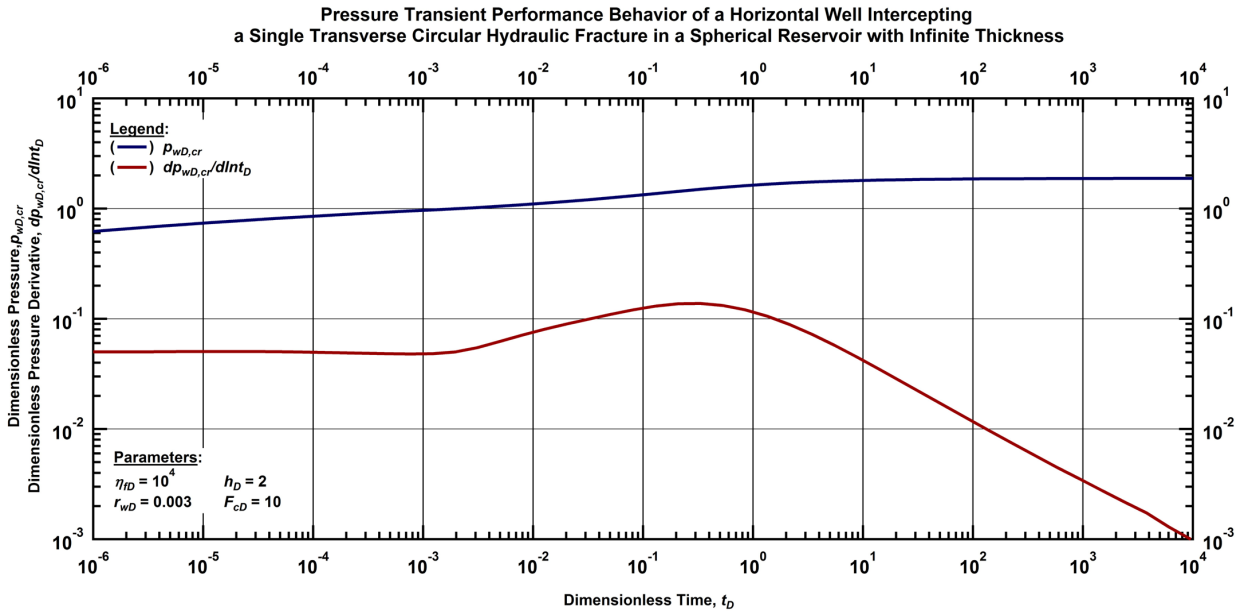

Figure 2.3 — Schematic example of the pressure and pressure derivative of a horizontal well intercepting a single circular transverse finite conductivity fracture within a 3D reservoir.

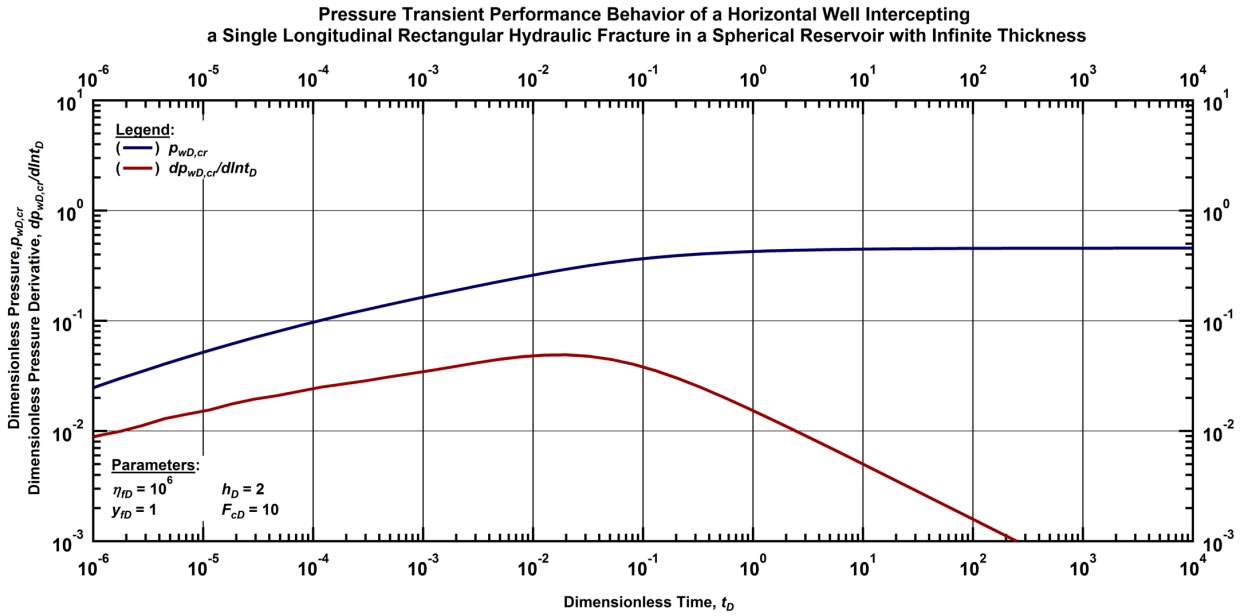

Figure 2.4 — Schematic example of the pressure and pressure derivative of a horizontal well intercepting a single rectangular longitudinal finite conductivity fracture within a 3D reservoir.

Raghavan *et al.* (1997) applied the commingled-reservoir concepts to single fracture solutions and developed a model to analyze the pressure-transient response of a multi-fractured horizontal well in a homogeneous reservoir. Using this approach, the authors concluded (similar to Larsen *et al.* 1994) that a multi-fractured well behaves as an equivalent well intercepting a single fracture with an equivalent conductivity and fracture length equal to the distance between the hydraulic fractures at the edges, where the lowest rate towards the wellbore comes from the hydraulic fractures at the center of the well, whereas the highest production is observed in the outermost fractures.

Based on the point source solution developed by Ozkan *et al.* (1991), Chen *et al.* (1997) derived expressions for pressure distribution caused by a multi-fractured horizontal wells in reservoirs with rectangular shape. A discussion of the flow geometries and regimes that may appear (depending on the properties/characteristics of the hydraulic fractures) in these sort of well completion-reservoir configurations was presented. According to the authors, the main objective of this work was the development of an algorithm capable of incorporating boundary effects without relying on approximations or the use of image wells.

Similar to the developments made by Lee *et al.* (1986), Brown *et al.* (2011) derived a trilinear flow solution for the pressure-transient analysis of multi-fractured horizontal wells in unconventional shale reservoirs. The authors divided the reservoir into three subsystems (hydraulic fracture, inner and outer reservoir zones) with the following characteristics:

- Each hydraulic fracture is considered to be a finite conductivity porous medium
- Double porosity behavior in the inner reservoir zone (zone between hydraulic fractures) with transient interporosity transfer

- Linear flow in a homogenous reservoir in the outer reservoir zone.

This approach was verified with more rigorous analytical (Chen *et al.* 1997 and Raghavan *et al.* 1997) and numerical (Medeiros *et al.* 2008) solutions. One application of this model was presented by Ozkan *et al.* (2011), who studied the impact of reservoir properties such as permeability in the transient performance of a fractured horizontal-well drilled in an unconventional reservoir.

Ozcan *et al.* (2014) modified the inner reservoir zone of the trilinear model proposed by Brown *et al*. (2011) to include the effects of a nano-porous media by using an anomalous diffusivity model, based on the fractional derivative in time.

2.3. Vertical Wells within Fractal Reservoirs

Barker (1988) presented a generalized diffusivity model for hydraulic tests. The author presented the constant flow rate and constant head (constant pressure) solutions for this model. The solutions are given in terms of Modified Bessel Functions. This model and its solutions are able to represent the transient performance (pressure and flow rate) of the flow of a Newtonian fluid in linear, radial or spherical systems. This work is helpful as background to understand the solutions of the diffusivity models for fractal reservoirs.

Based on the work of O'Shaughnessy *et al*. (1985), Chang *et al.* (1990) developed a diffusivity equation to represent the flow of a single phase fluid within a fractal reservoir **(Fig. 2.5).** The system was idealized as a Naturally Fractured Reservoir (NFR) and two cases were studied: (1) without matrix participation, and (2) with pseudosteady-state interporosity transfer. The authors presented the analytical solution for the first case, whereas for the second case the solution was numerical. Appendix D shows the development of this model (case 1) and its procedure of solution

using the Laplace transform. **Fig. 2.6** shows the pressure-transient and pressure derivative for a vertical well within a fractal reservoir for selected values of the fractal dimension, D_f, and the conductivity index, θ.

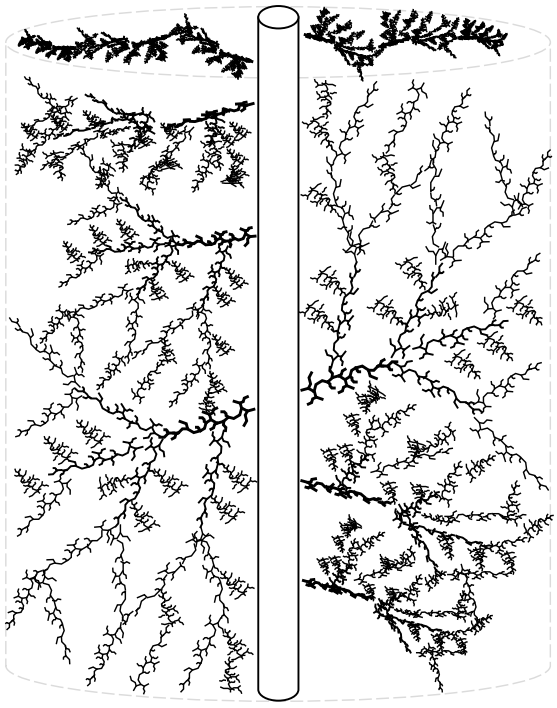

Figure 2.5 — Schematic of a vertical well within a reservoir with fractal fracture network.

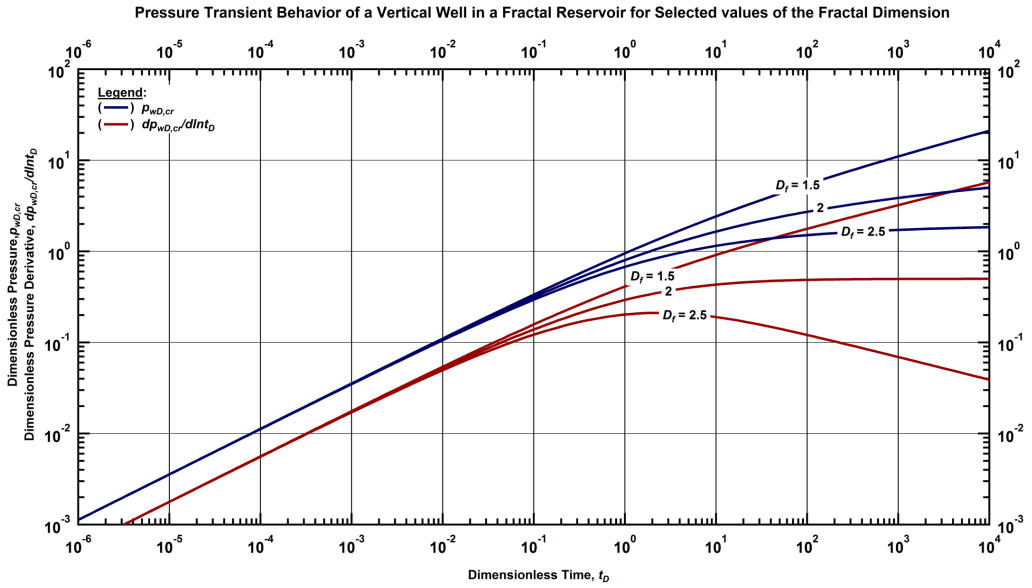

Figure 2.6 — Schematic example of the pressure and pressure derivative of a vertical well within a fractal reservoir for selected values of the fractal dimension (D_f) and fixed conductivity index (θ=0).

Doe (1991) analyzed the impact of the spatial dimension on constant-pressure tests. The spatial dimension describes the variation in the exposed to flow area with distance from the well and the reservoir properties (heterogeneities). Defining r as the distance from the well, the area exposed to flow for linear flow varies proportionally to r^0 (*i.e.*, the area remains unchanged). For radial flow, the area exposed to flow changes linearly (*i.e.*, proportionally to r^1). For spherical flow, the area exposed to flow changes proportionally to r^2. The author pointed out that fractional dimension may or may not indicate fractal reservoir geometries and can be classified as sublinear flow when the exponent of the distance from the well is less than zero and as hyperspherical if it is greater than two.

Acuna *et al.* (1991) proposed a numerical method to represent natural fracturing processes with fractal geometry. The authors used the "Iteration Function System" technique (Barnsley, 1988)

and concepts from the theory of fragmentation to create "numerical fractal fracture networks." The authors created several cases of 2D synthetic fractal fracture networks. For each case, they simulated the pressure-transient response of a well intercepting one of these networks assuming single phase flow of a slightly compressible fluid.

Abbaszadeh (1995) developed a three region composite model divided into three regions. The inner and the outer regions were considered to be radial and the middle region was considered to be fractal. This model attempted to represent phenomena such as precipitation of solids, chemical dissolution processes, matrix acidizing, etc., in the pressure-transient response of a vertical well. The author presented an example of the application of the solution to this model using real data from the Prudhoe Bay reservoir, where laboratory studies of the reservoir indicate precipitation of scales and organic material in the vicinity of producer wells.

Acuna *et al.* (1995) presented analyses of real well tests from NFRs located in western Venezuela, Monterey formation and Geyser geothermal field, applying the model developed by Chang *et al.* (1990). Based on the power-law response of the real pressure-transient data, the authors determined the range of fractal parameters (mass fractal dimension and conductivity index). Subsequently, they used the fractal parameters determined from the analyses to generate fracture networks of the reservoirs, using techniques previously presented by Acuna *et al.* (1991).

Olarewaju (1996) proposed a method to build a heterogeneous reservoir permeability field with stochastic fractal functions. The author used the Weiestrass Mandelbrot fractal unconditional simulation method to generate the permeability field. Such a method is based on the fractional Brownian motion (fBm), given that the processes that follow fBm are selfisimilar. The input parameters to generate such field are obtained from pressure-transient data (effective permeability,

fractal dimension and conductivity index). To estimate the input parameters, Olarewaju (1996) developed a double porosity model, considering transient interporosity transfer. He obtained an analytical solution in Laplace domain that is able to reproduce the three flow periods of an infinite double porosity reservoir (flow in fracture network, interaction between porous media, and single system behavior).

Based on the works of Chang *et al.* (1990) and Olarewaju (1996), Flamenco-Lopez *et al*. (2001) deduced approximate analytical solutions for late transient times for a double porosity system (*i.e.*, when the double porosity reservoir behaves as a single system) and for pseudosteady-state flow period (boundary dominated). One of the conclusions of this work was the necessity of analyzing transient and pseudosteady state flow periods to properly characterize a fractal reservoir. In a revised version of this paper (Flamenco-Lopez *et al.* 2003), the authors included a trial and error methodology to estimate the fractal parameters during transient regime.

To investigate the production decline behavior in fractal reservoirs, Camacho-Velazquez *et al.* (2008) obtained the constant pressure analytical solutions for the models proposed by Chang *et al*. (1990). The authors developed approximate analytical solutions for the single and double porosity models for both, transient and pseudosteady-state flow periods.

2.4. Wells Intercepting Hydraulic Fractures within Fractal Reservoirs

The first work related to wells intercepting a hydraulic fracture in fractal reservoirs was developed by Beier (1994). Motivated by the fractal behavior observed in the pressure-transient response in wells from the San Andres formation, Beier (1994) derived the infinite conductivity and the

uniform flux solutions for a vertical well using a similar approach as the one used by Gringarten *et al*. (1974) and the fractal model presented by Chang *et al.* (1990).

Beier (1994) found that this well-reservoir configuration exhibits two power-law flowing periods. The first one corresponds to a distortion in the formation linear flow due to the superimposed flow of the reservoir towards the plane of the fracture, whereas the second one corresponds to the flow dominated by the fractal reservoir. **Fig. 2.7** shows an example of the two power-law flowing periods generated by a vertical well intercepted by a hydraulic fracture within a fractal reservoir. At early times (formation linear flow), the pressure and pressure derivative exhibit a three-quarters-slope, whereas at late times (infinite-fractal reservoir) a half-slope is observed.

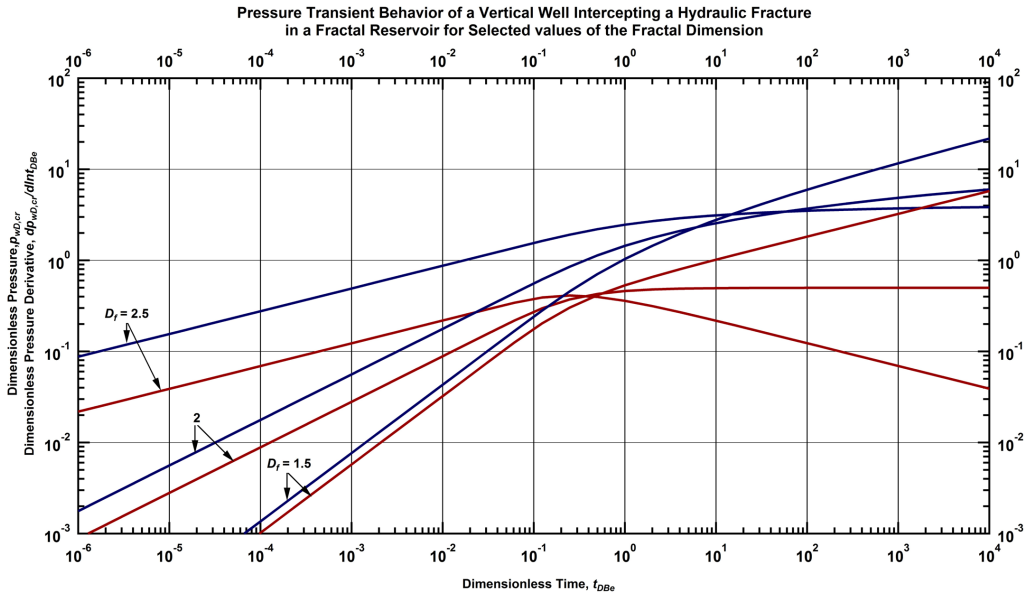

Figure 2.7 — Schematic example of the pressure and pressure derivative of a vertical well intercepting a uniform flux hydraulic fracture within a fractal reservoir for selected values of the fractal dimension (D_f) and fixed conductivity index (θ=0).

2.5. Reservoir Models considering Anomalous Diffusion

In 1994, Metzler *et al*. presented a generalization of the diffusion model of a fractal structure developed by O'Shaugnessy *et al*. (1985). Such a generalization consists in the inclusion of the "anomalous diffusion" concept in the diffusion equation for fractal media. The anomalous diffusivity phenomenon is modeled by a fractional derivative of a probability density function. The authors showed that the solution to their anomalous diffusion model considering an infinite fractal object is given by Fox's H-functions, of which asymptotic case when the time tends to infinite is given by an stretched exponential.

Camacho-Velazquez *et al*. (2008) introduced the concept of anomalous diffusion in the petroleum reservoir engineering, and derived constant-pressure and constant-rate solutions for the analysis of pressure-rate performance behavior in fractal reservoirs. The authors presented complete solutions in Laplace domain in terms of Modified Bessel Functions and developed asymptotic solutions in the real domain, defined by power-law functions. **Fig. 2.8** and **Fig 2.9** show the pressure and rate-transient behaviors, respectively, of a vertical well within a fractal reservoir with anomalous diffusion.

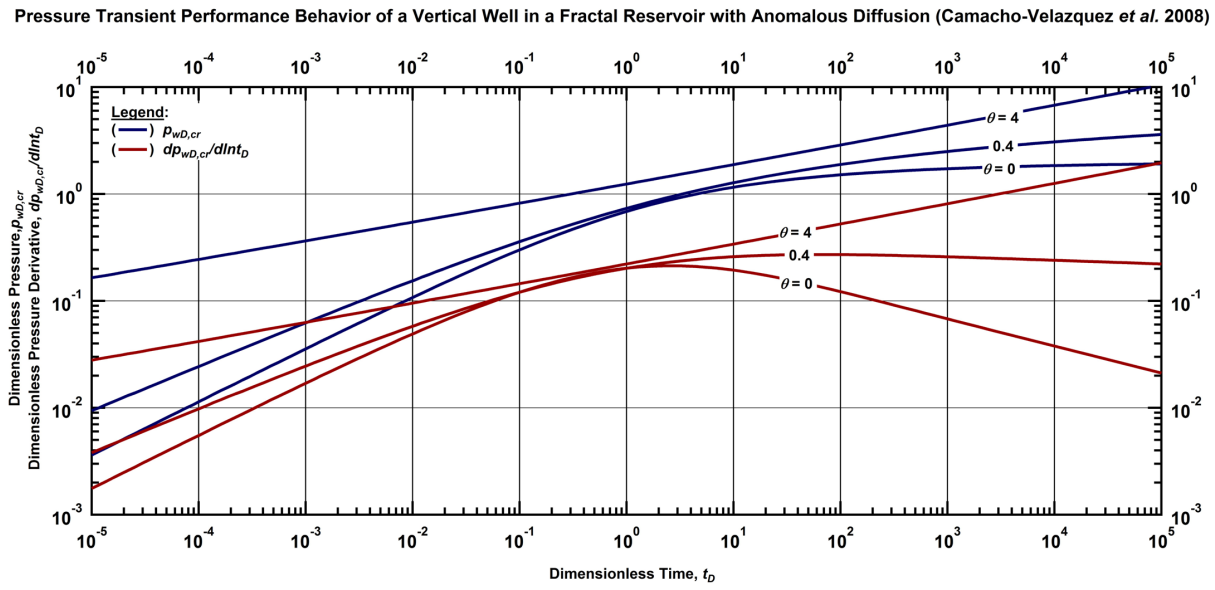

Figure 2.8 — Schematic example of the pressure and pressure derivative of a vertical well within a fractal reservoir with anomalous diffusion for selected values of the conductivity index (θ) and fixed fractal dimension (D_f=2.5).

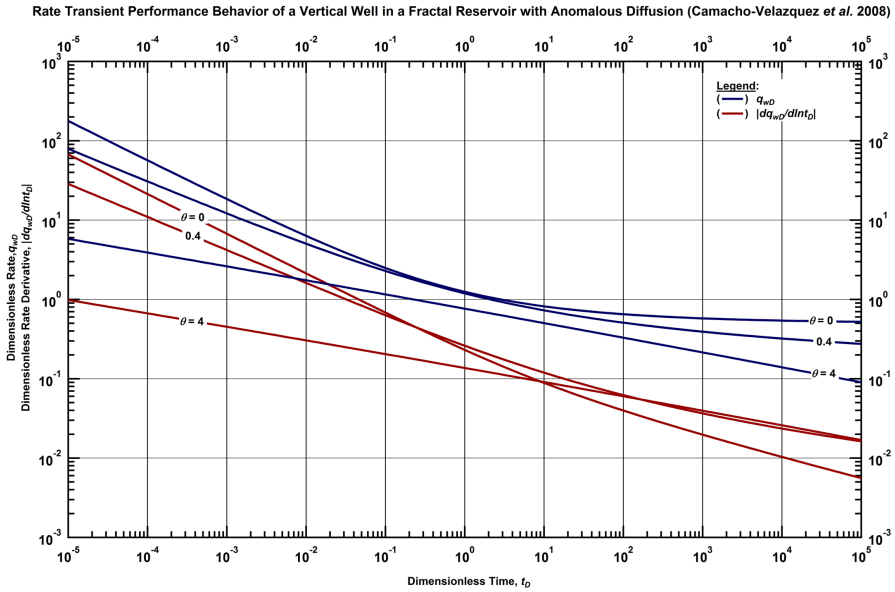

Figure 2.9 — Schematic example of the rate and rate derivative of a vertical well within a fractal reservoir with anomalous diffusion for selected values of the conductivity index (θ) and fixed fractal dimension (D_f=2.5).

Razminia *et al*. (2014) extended the model presented by Camacho-Velazquez *et al*. (2008) to double porosity reservoirs with pseudosteady interporosity transfer, to composite radial systems (Razminia *et al*. 2015a), and to vertical wells intercepting a uniform flux fracture (Razminia *et al*. 2015b).

Raghavan (2012a) modeled a 2D diffusivity equation considering anomalous diffusion phenomenon assuming a time-dependent version of Darcy's Law. Such a variation of the Darcy's Law is modeled by a convolution integral of the gradient of the pressure weighted by a power-law function of the time. Raghavan (2012a) presented the "constant-rate" solution for the proposed diffusivity model, considering an infinite reservoir. The "constant-rate" solution for this type of models implies a time-dependent inner boundary condition that creates a power-law behavior of the pressure and pressure derivative functions (see **Fig. 2.10**). The development of this model and its solution is shown in Appendix F. Raghavan (2012b) and Raghavan *et al*. (2013) applied this approach to the fractured well and multi-fractured –horizontal well cases, respectively.

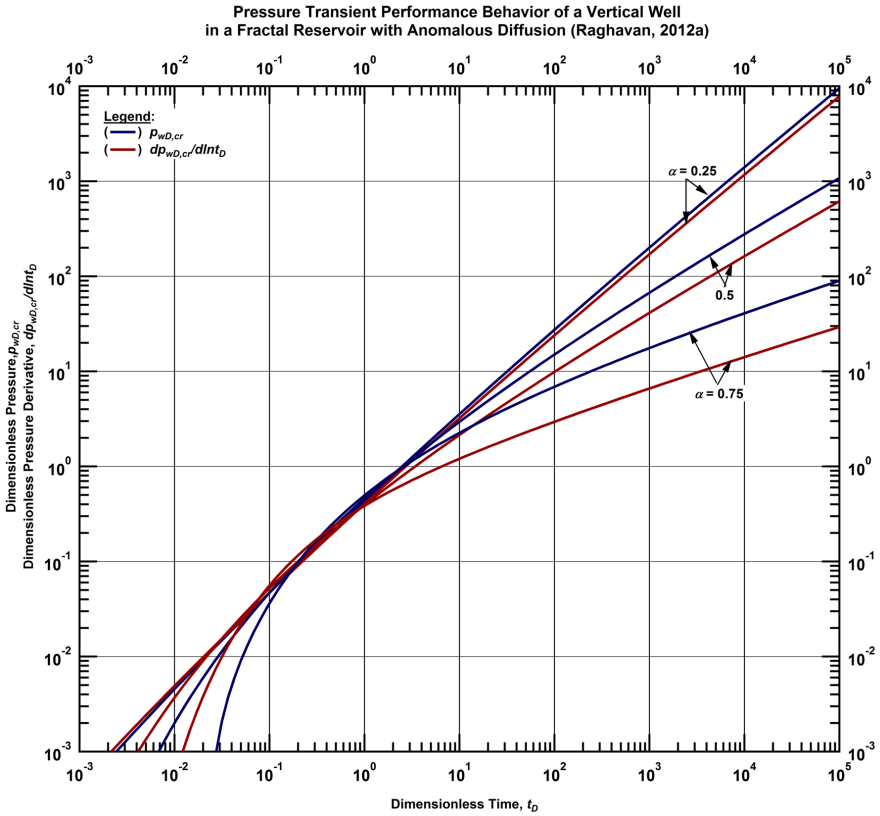

Figure 2.10 — Schematic example of the pressure and pressure derivative of a vertical well within a 2D reservoir with anomalous diffusion for selected values of the anomalous diffusion index (α).

CHAPTER III

PRESSURE AND RATE-TRANSIENT BEHAVIOR OF A HORIZONTAL WELL INTERCEPTING A SINGLE HYDRAULIC FRACTURE WITHIN A FRACTAL RESERVOIR[1]

In this chapter, we present a summary of the semi-analytical solution for the pressure and rate transient behaviors of a horizontal well intercepting a single finite-conductivity hydraulic fracture (either circular or rectangular fracture) within a fractal reservoir considering either single or naturally-fractured/dual porosity reservoir conditions. Naturally-fractured/dual porosity and anomalous diffusion effects are included by modifying the solution of the diffusivity equation for the reservoir in the Laplace domain. The detailed derivations of these models are presented in Appendix D.

3.1. Model Assumptions

Similar to Larsen *et al*. (1991), we have considered two geometries for the hydraulic fractures. **Fig. 3.1a** shows the schematics of a horizontal well intercepting a circular transverse hydraulic fracture within a fractal reservoir and **Fig. 3.1b** shows the rectangular longitudinal hydraulic fracture case. The assumptions of the systems are summarized in **Table 3.1**.

[1] Reprinted with permission from "Pressure-Transient Behavior of a Horizontal Well with a Finite-Conductivity Fracture within a Fractal Reservoir" by Valdes-Perez, A. R., Larsen, L., and Blasingame, T.A., 2018. *SPE Canada Unconventional Resources Conference Proceedings*, SPE-189814-MS. Copyright [2018] by Society of Petroleum Engineers, Inc.

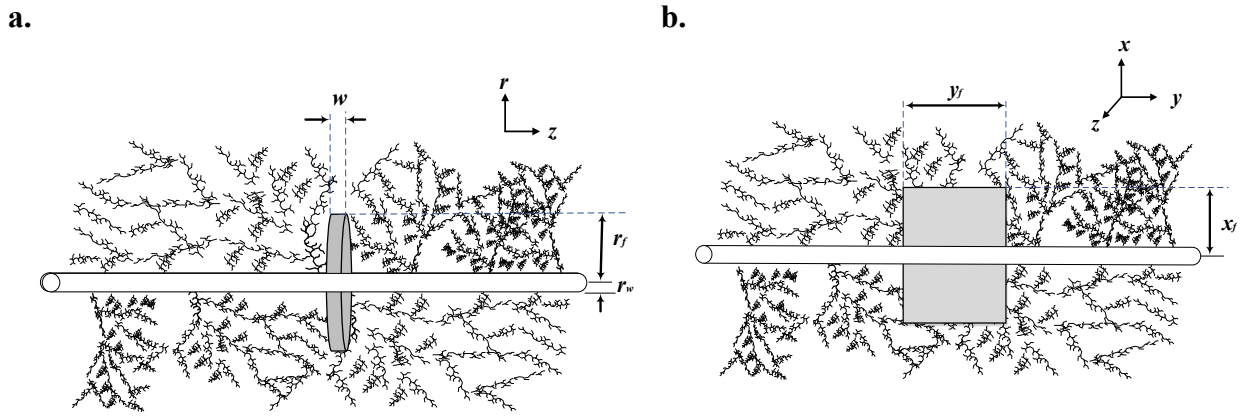

Figure 3.1 — **a.** Vertical circular hydraulic fracture transverse to the axis of a horizontal well within an infinite fractal reservoir, and **b.** Vertical rectangular hydraulic fracture longitudinal to the axis of a horizontal well within an infinite fractal reservoir.

Table 3.1 — Assumptions used to develop the proposed reservoir models

Medium	Assumptions
All	● Flow to the wellbore occurs only through the hydraulic fracture. ● Pressure-squared gradients are negligible. ● The well produces at constant flowrate, q_w. ● Uniform initial pressure, p_i. ● Single slightly-compressible fluid flow with constant compressibility, c_o, and constant viscosity, μ.
Hydraulic Fracture	● Closed facture of constant half-length (r_f for the circular fracture or x_f for the rectangular fracture). ● Flow obeys Darcy's Law. ● The fracture has constant properties: compressibility, c_f, permeability, k_f, porosity, ϕ_f, width, w.
Reservoir	● Unbounded fractal reservoir of D_f-dimension. ● Flow obeys modified Darcy's Law for fractal systems of θ-conductivity index. ● Both porosity and permeability vary according to power law functions. ● The reservoir has constant formation compressibility, c.
Matrix blocks (naturally-fractured/dual porosity reservoir case)	● Finite and single size Euclidean matrix block (either slabs or spheres). ● Flow obeys Darcy's Law. ● The matrix blocks have constant properties: compressibility, c_{ma}, permeability, k_{ma}, porosity, ϕ_{ma}.

The flow of fluids in the hydraulic fracture and in the fractal reservoir is governed by its corresponding diffusivity equation. For a circular fracture, the flow is modeled by the diffusivity equation in radial coordinates with a source term. This equation in its dimensionless form is:

$$\frac{1}{r_D}\frac{\partial}{\partial r_D}\left[r_D\frac{\partial p_{fD,cr}}{\partial r_D}\right]+\frac{2}{F_{cD}}\left[\frac{\partial p_{D,cr}}{\partial z_D}\right]_{z_D=0}=\frac{1}{\eta_{fD}}\frac{\partial p_{fD,cr}}{\partial t_D}. \quad (3.1)$$

For the rectangular fracture case, the flow is modeled by the diffusivity equation for a linear system with a source term, written in dimensionless form, our starting point is given as:

$$\frac{\partial^2 p_{fD,cr}}{\partial x_D^2}+\frac{2}{F_{cD}}\left[\frac{\partial p_{D,cr}}{\partial z_D}\right]_{z_D=0}=\frac{1}{\eta_{fD}}\frac{\partial p_{fD,cr}}{\partial t_D} \quad (3.2)$$

The flow within the fractal reservoir considering typical diffusion (Chang *et al.*, 1990) is modeled by:

$$\frac{1}{R_D^{Df-1}}\frac{\partial}{\partial R_D}\left[R_D^{\beta}\frac{\partial p_{D,cr}}{\partial R_D}\right]=\frac{\partial p_{D,cr}}{\partial t_D}. \quad (3.3)$$

For the case of a fractal reservoir considering anomalous diffusion (Camacho-Velazquez *et al.*, 2008), the flow model is:

$$\frac{1}{R_D^{Df-1}}\frac{\partial}{\partial R_D}\left[R_D^{\beta}\frac{\partial p_{D,cr}}{\partial R_D}\right]=\frac{\partial^{\gamma} p_{D,cr}}{\partial t_D^{\gamma}}, \quad (3.4)$$

where $\gamma=2/[\theta+2]$. The definitions of the dimensionless variables are summarized in **Table 3.2**.

3.2. Development of the Models and Solution Procedure

Given that the source term in the left hand side of Eq. 3.1 and Eq. 3.2 is variable, the solution for this "coupled" model has to be semi-analytical. The procedure we have used is the same applied by Larsen *et al*. (1991). The workflow of this procedure is:

1. Discretize the fracture into *N*-segments. The discretization permits us to approximate the source term to a constant value for each segment. For a *j*-segment of a circular fracture, the diffusivity equation is approximated as

$$\frac{1}{r_D}\frac{\partial}{\partial r_D}\left[r_D\frac{\partial p_{fD,cr}}{\partial r_D}\right]-\frac{2\pi h_D}{F_{cD}}\delta q_{Dj}=\frac{1}{\eta_{fD}}\frac{\partial p_{fD,cr}}{\partial t_D}, \quad \text{(3.5)}$$

whereas for a *j*-segment of a rectangular fracture, the diffusivity equation is approximated as

$$\frac{\partial^2 p_{fD,cr}}{\partial x_D^2}-\frac{2\pi h_D}{F_{cD}}\delta q_{Dj}=\frac{1}{\eta_{fD}}\frac{\partial p_{fD,cr}}{\partial t_D}, \quad \text{(3.6)}$$

2. Obtain the analytical general solutions in the Laplace domain for each one of the segments of the hydraulic fracture. Given that the source term is approximated to a constant value, Eqs. 3.5 and 3.6 can be solved using the Laplace transform. The general solution for a *j*-segment of the circular fracture is:

$$\bar{p}_{fD,cr,j}(r_D,u)=A_jK_0\left[r_D\sqrt{\frac{u}{\eta_{fD}}}\right]+B_jI_0\left[r_D\sqrt{\frac{u}{\eta_{fD}}}\right]-\frac{2\pi h_D\eta_{fD}}{uF_{cD}}\delta\bar{q}_{Dj}. \quad \text{(3.7)}$$

Table 3.2 — Dimensionless variables for the model of a horizontal well intercepting a single finite conductivity fracture within a fractal reservoir.

Dimensionless Variable	Definition
Pressure in the fractal reservoir	$p_{D,cr}(R_D,t_D)=\dfrac{2\pi k_0 h[p_i-p(R,t)]}{q_w B\mu L_r^{\theta}}$
Pressure in the hydraulic fracture	$p_{fD,cr}(\psi_D,t_D)=\dfrac{2\pi k_0 h[p_i-p(\psi,t)]}{q_w B\mu L_r^{\theta}}$
Fractal reservoir rate	$\delta q_D=\dfrac{4\pi}{\alpha_{Df}}\left[\dfrac{b}{L_r}\right]^{Df-3}\dfrac{\delta q_r}{q_w}$
Time	$t_D=\dfrac{k_0}{\phi_0\mu c_t L_r^{2+\theta}}t$
Position in the circular fracture	$r_D=r/r_f$
Position in the z-direction	$z_D=z/L_r$
Position in the x-direction	$x_D=x/L_r$
Position in the fractal reservoir	$R_D=R/L_r$
Fracture length along the wellbore	$y_D=y/x_f$
Height	$h_D=h/L_r$
Fracture conductivity	$F_{cD}=\dfrac{k_f w}{kL_r}$
Fracture fractal conductivity	$F_{fhcD}=\dfrac{k_f w L_r^{\theta}}{kh}$
Fractal hydraulic diffusivity of the hydraulic fracture	$\eta_{fD}=\dfrac{\phi_0 c_t k_f L_r^{\theta}}{\phi_f c_{tf} k_0}$
Hydraulic diffusivity of the matrix blocks	$\eta_{maD}=\dfrac{k_{ma}[\phi c_t]_t L_r^{\theta}}{k_{0fb}\phi_{ma}c_{tma}}$
Storativity ratio	$\omega=\dfrac{\phi_{0fb}c_{tfb}}{\phi_{0fb}c_{tfb}+\phi_{ma}c_{tma}}$
Fracture area	$A_{fD}=A_{fma}h_{ma}$
Matrix block size	$h_{maD}=h_{ma}/L_r$
Interporosity skin	$S_{\text{int}}=\dfrac{k_{ma}l_d}{k_d h_{ma}}$

Where L_r is the reference length. For the circular fracture it is equal to r_f, whereas for a rectangular fracture it is x_f.

For a *j*-segment of a rectangular fracture, the general solution is:

$$\bar{p}_{fD,cr,j}(x_D,u) = A_j \exp\left[-x_D\sqrt{\frac{u}{\eta_{fD}}}\right] + B_j \exp\left[x_D\sqrt{\frac{u}{\eta_{fD}}}\right] - \frac{2\pi h_D \eta_{fD}}{uF_{cD}}\delta\bar{q}_{Dj} \quad \text{..... (3.8)}$$

3. Define a system of equations for 3*N*-unknowns. Since constants A_j, B_j and δq_{Dj} are unknowns for each *j*-segment, a system of 3*N* equations must be defined and solved to determine such constants. The system of equations is defined by:

● Applying the inner boundary condition (constant-rate) to the general solution governing segment 1. For a circular fracture:

$$\left[r_D \frac{\partial p_{fD,cr,1}}{\partial r_D}\right]_{r_D=r_{wD}} = -\frac{1}{F_{fhcD}} \quad \text{..... (3.9)}$$

For a rectangular fracture:

$$\left[\frac{\partial p_{fD,cr,1}}{\partial x_D}\right]_{x_D=0} = -\frac{\pi}{2F_{fhcD}y_{fD}} \quad \text{..... (3.10)}$$

● Applying the outer boundary condition (closed fracture) to the general solution governing segment *N*:

$$\left[\frac{\partial p_{fD,cr,N}}{\partial \xi_D}\right]_{\xi_D=1} = 0 \quad \text{..... (3.11)}$$

Where $\xi_D=r_D$ for a circular fracture and $\xi_D=x_D$ for a rectangular fracture:

● Establishing pressure continuity at each of the interfaces:

$$\bar{p}_{fD,cr,j-1}(\xi_{Dj-1},u) = \bar{p}_{fD,cr,j}(\xi_{Dj-1},u) \quad \text{..... (3.12)}$$

● Establishing the flowrate continuity at each of the interfaces:

$$\left[\frac{\partial p_{fD,cr,j-1}}{\partial \xi_D}\right]_{\xi_D=\xi_{Dj-1}} = \left[\frac{\partial p_{fD,cr,j}}{\partial \xi_D}\right]_{\xi_D=\xi_{Dj-1}} \quad \text{..... (3.13)}$$

● Establishing pressure continuity between each segment of the fracture and the fractal reservoir.

$$\bar{p}_{fD,cr,j}(\xi^*_{Dj},u) = \bar{p}_{D,cr,j}(\xi^*_{Dj},u), \quad \text{..... (3.14)}$$

where ξ_D^* is the middle point in the segment. The pressure in the fractal reservoir is the result of superimposing the constant rate solution of the diffusivity equation for fractal reservoirs over the area, A, of the segment (see Appendix D for more details).

For a fractal reservoir considering typical diffusivity, the pressure behavior is given by:

$$\bar{p}_{D,cr}(R_D,u) = \frac{\delta \bar{q}_D h_D}{[\theta+2]\Gamma[1-v]}\left[\frac{\theta+2}{\sqrt{u}}\right]^v \int_A R_D^{[1-\beta]/2} K_v\left[R_D^{[\theta+2]/2}\frac{2\sqrt{u}}{\theta+2}\right]dA \text{ (where } v=[1-\beta]/[\theta+2]). \text{... (3.15)}$$

Similarly, for a fractal reservoir considering anomalous diffusion:

$$\bar{p}_{D,cr}(R_D,u) = \frac{\delta \bar{q}_D h_D}{[\theta+2]\Gamma[1-v]}\left[\frac{\theta+2}{u^{\gamma/2}}\right]^v \int_A R_D^{[1-\beta]/2} K_v\left[R_D^{[\theta+2]/2}\frac{2u^{\gamma/2}}{\theta+2}\right]dA. \quad \text{..... (3.16)}$$

These models can be extended to the naturally-fractured/dual porosity reservoir case as:

$$\bar{p}_{D,cr}(R_D,u) = \frac{\delta \bar{q}_D h_D}{[\theta+2]\Gamma[1-v]}\left[\frac{\theta+2}{\sqrt{uf(u)}}\right]^v \int_A R_D^{[1-\beta]/2} K_v\left[R_D^{[\theta+2]/2}\frac{2\sqrt{uf(u)}}{\theta+2}\right]dA, \quad \text{..... (3.17)}$$

where the interporosity transfer function is defined by:

$$f(u) = \omega u^{\gamma-1} + \frac{[1-\omega]A_{fD}\,\bar{g}(\eta_{maD}, h_{maD}, u)}{1 + \frac{h_{maD}^2 S_{\text{int}}}{\eta_{maD}}\,\bar{g}(\eta_{maD}, h_{maD}, u)} \quad \text{..... (3.18)}$$

For slab matrix blocks:

$$\bar{g}(\eta_{maD}, h_{maD}, u) = \frac{1}{h_{maD}}\sqrt{\frac{\eta_{maD}}{u}}\tanh\left[\frac{h_{maD}}{2}\sqrt{\frac{u}{\eta_{maD}}}\right], \quad \text{..... (3.19)}$$

and for spherical matrix blocks:

$$\bar{g}(\eta_{maD}, h_{maD}, u) = \frac{1}{h_{maD}}\sqrt{\frac{\eta_{maD}}{u}}\left[\coth\left[\frac{h_{maD}}{2}\sqrt{\frac{u}{\eta_{maD}}}\right] - \frac{2}{h_{maD}}\sqrt{\frac{\eta_{maD}}{u}}\right]. \quad \text{..... (3.20)}$$

Eq. 3.18 considers the anomalous diffusion phenomenon. To restrict it to the typical diffusion case, γ should be equal to unity and considered to be independent of the conductivity index, θ.

4. Solve the system of equations and evaluate the solution at the wellbore. For the results presented in this dissertation, we have used the "mldivide" function of MATLAB. Once the constants A_j, B_j and δq_{Dj} (j=1,…,N) are determined, the solution is evaluated at the wellbore. For a circular fracture, the pressure at the wellbore is determined by:

$$\bar{p}_{fD,cr,1}(r_{wD}, u) = A_1 K_0\left[r_{wD}\sqrt{\frac{u}{\eta_{fD}}}\right] + B_1 I_0\left[r_{wD}\sqrt{\frac{u}{\eta_{fD}}}\right] - \frac{2\pi h_D \eta_{fD}}{u F_{cD}}\delta\bar{q}_{D1} \quad \text{..... (3.21)}$$

Similarly, for a rectangular fracture:

$$\bar{p}_{fD,cr,1}(0, u) = A_1 + B_1 - \frac{2\pi h_D}{u F_{cD}}\delta\bar{q}_{D1} \quad \text{..... (3.22)}$$

The wellbore storage effects can be included using the classic (constant) wellbore storage relation in the Laplace domain presented in Chapter I. To include the skin effect (*i.e.*, using a choked fracture) for the circular fracture case, the effective wellbore radius should be used. For the rectangular fracture case, the skin factor should be added to the dimensionless drop of pressure without wellbore storage:

$$\bar{p}_{wD}(u,s,C_{fD}=0)=\bar{p}_{wD}(u,C_{fD}=0)+s \quad \text{..... (3.23)}$$

5. Apply the Stehfest algorithm to numerically invert the Laplace domain solution.

The Stehfest algorithm is implemented in MATLAB and has been tested for consistency and accuracy. In addition to the dimensionless pressure and rate solutions, we can also use the Stehfest algorithm to provide both the cumulative and the derivative of any given formulation in the Laplace domain.

Constant-Pressure Solution

As defined in Chapter I, Duhamel's principle is used to obtain the models for rate-transient analysis (constant pressure solution) from the models for pressure-transient analysis (constant rate solution). The dimensionless cumulative production at a given time is computed by integrating the dimensionless rate profile as presented in Chapter I.

3.3. Results and Discussion

Single Porosity Fractal Reservoirs

In this section we present the results of our sensitivity analyses which consider the influence of key parameters for the fractal reservoir and the hydraulic fracture in terms of the pressure and rate transient performance behaviors. Based on the configuration of the system, the expected diagnostic signatures for our proposed semi-analytical solution are:

- Period 1 (Fracture flow): Radial or linear flow (depending on the geometry of the fracture) at very early times. As in classic studies for the case of a single finite-conductivity fracture, this period will never be observed in practice.
- Period 2 (Fracture-reservoir interaction): "Radial-Fractal" or "Linear-Fractal" at intermediate-transient times. This period can be subdivided into two sub-periods: (1) early-intermediate and (2) late-intermediate. The early-intermediate period is analogous to the bilinear flow regime for a finite-conductivity vertical fracture in an infinite-acting homogeneous reservoir, whereas the late-intermediate is analogous to the formation-linear flow regime observed at most times for a case with a very high conductivity vertical fracture and at later times for cases with a medium to high conductivity vertical fracture.
- Period 3 (Reservoir dominated flow): "Pseudo-Fractal" flow. This flow period is dominated by the reservoir and yields power-law behavior (*i.e.*, a straight line in the pressure drop and pressure derivative functions versus time on a log-log plot).

The schematics for the expected diagnostic signatures (*i.e.*, the dimensionless pressure and dimensionless pressure derivative functions for the constant rate case) for the circular and rectangular fracture cases are shown in **Fig 3.2** and **Fig 3.3**, respectively.

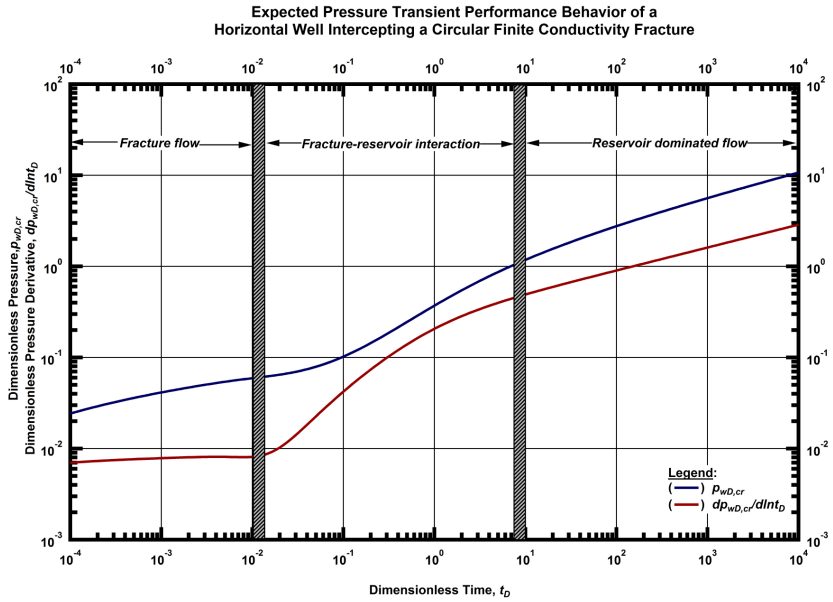

Figure 3.2 — Schematic example of the dimensionless pressure and dimensionless pressure derivative functions for a horizontal well intercepting a single circular hydraulic fracture of finite conductivity within a single porosity fractal reservoir (constant rate case).

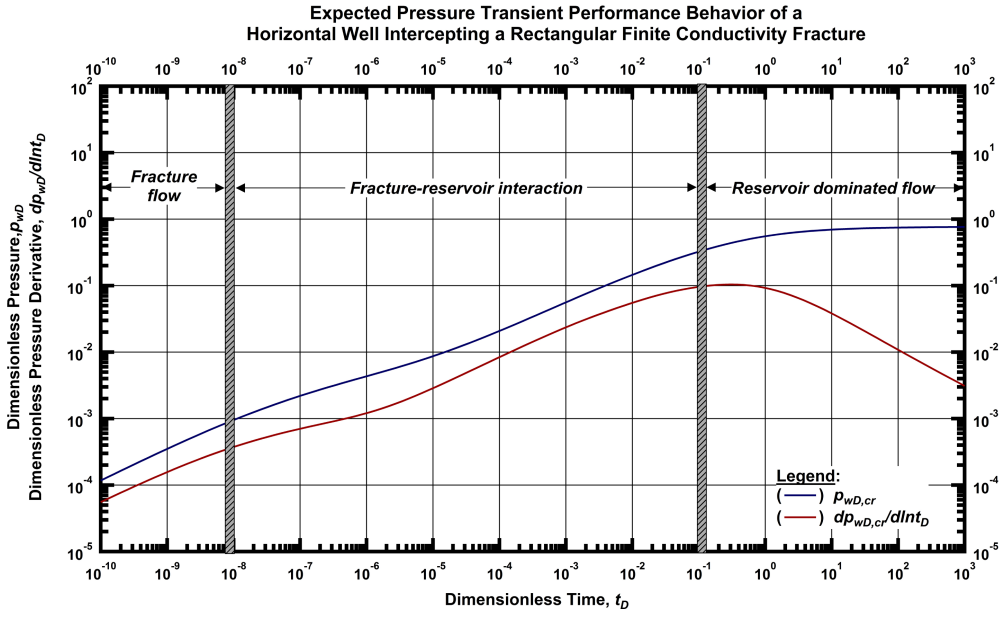

Figure 3.3 — Schematic example of the dimensionless pressure and dimensionless pressure derivative functions for a horizontal well intercepting a single rectangular hydraulic fracture of finite conductivity within a single porosity fractal reservoir (constant rate case).

In **Fig. 3.4**, we show the impact of the fractal dimension of the reservoir (D_f) on the behavior of the dimensionless pressure and dimensionless pressure derivative functions (constant rate case) for the circular fracture case, considering a "low" dimensionless conductivity. Based on the pressure derivative response, we observe that at late-transient times (dimensionless times greater than 1), pseudo-fractal flow is exhibited for all cases. However; at early-transient times (dimensionless times < 10^{-2}), for a fractal dimension of 1.5, a power-law response is observed, instead of the expected radial fracture flow regime. For each of the cases shown in **Fig. 3.4** only one sub-period of flow is observed at intermediate-transient times. These "sub-periods" exhibit a power-law behavior that is the result of the interaction between the fractal reservoir and the circular fracture.

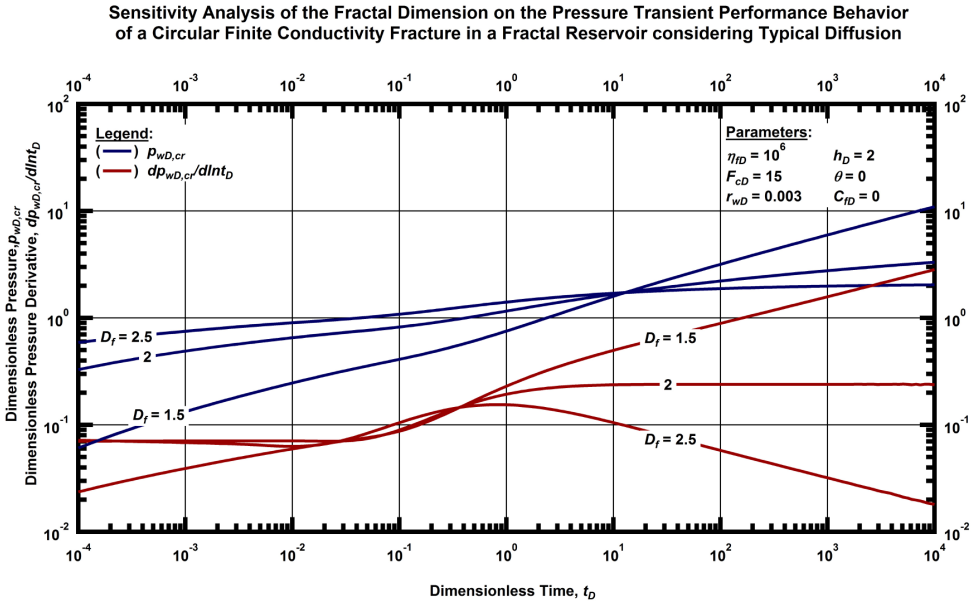

Figure 3.4 — Log-log plot of the dimensionless pressure and dimensionless pressure derivative functions for a horizontal well intercepting a single circular hydraulic fracture of finite conductivity in a fractal reservoir considering typical (constant) diffusion, for selected values of the fractal dimension (D_f) (constant rate case).

Fig. 3.5 shows the (constant pressure) rate-transient case for the example presented in **Fig. 3.4**. At late-transient times (*i.e.*, dimensionless times > 7), this case exhibits higher flowrates at higher values of the fractal dimension. However; at early and intermediate-transient times (dimensionless times < 7), the well exhibits higher flowrates at lower values of the fractal dimension. This behavior implies that the cumulative production of the well is higher for low values of the fractal dimension until a certain point in time, after which the cumulative production is higher for high values of the fractal dimension (see **Fig. 3.6** for the cumulative production behavior).

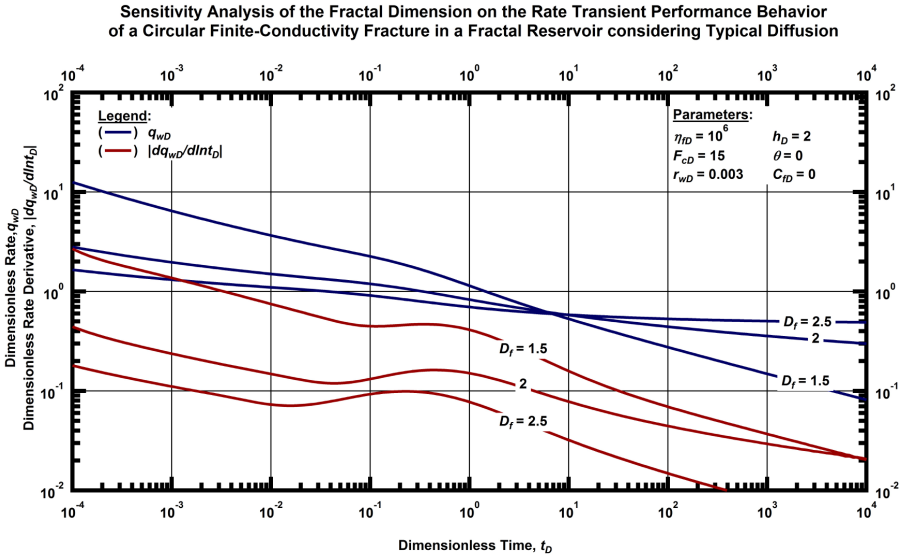

Figure 3.5 — Log-log plot of the dimensionless rate and dimensionless rate derivative functions for a horizontal well intercepting a single circular hydraulic fracture of finite conductivity in a fractal reservoir considering typical (constant) diffusion, for selected values of the fractal dimension (D_f) (constant pressure case).

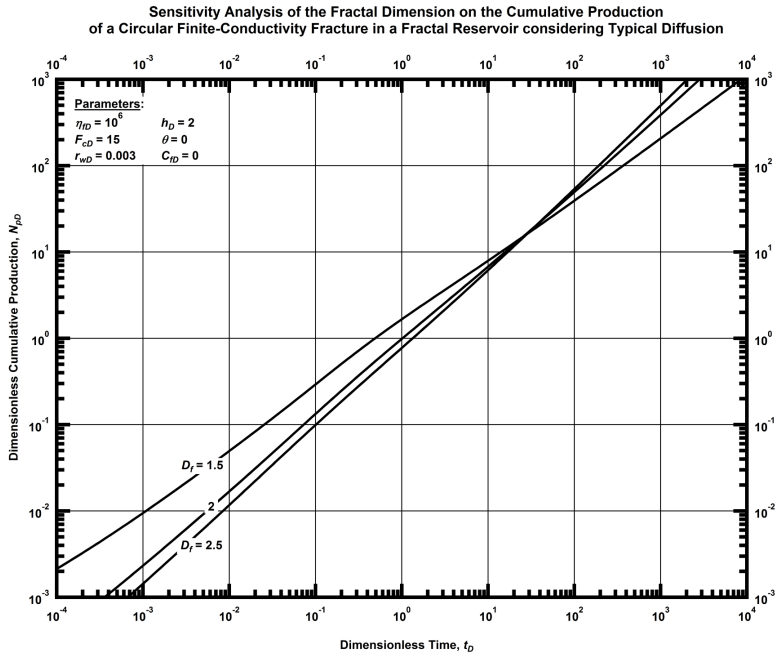

Figure 3.6 — Log-log plot of the dimensionless cumulative production function for a horizontal well intercepting a single circular hydraulic fracture of finite conductivity in a fractal reservoir considering typical (constant) diffusion, for selected values of the fractal dimension (D_f). (constant pressure case)

Similar to our previous comparisons for the circular fracture case, we now consider the rectangular fracture case — and we begin with the constant rate solution for the rectangular fracture case (as shown in **Fig. 3.7**) where we plot the dimensionless pressure and dimensionless pressure derivative functions. We do note a "spectra" of solutions based on the given fractal dimension (D_f) — in particular, the fractal dimension case of 2.5 shows the most "aggressive" behavior, where the D_f = 1.5 case is the most "conservative." We present the constant pressure cases (*i.e.*, the dimensionless rate and dimensionless rate derivative profiles) in **Fig. 3.8** and the dimensionless cumulative production profile is shown in **Fig. 3.9** — and we also note the "aggressive" and "conservative" behaviors as caused by the fractal dimension parameter (D_f) for these cases.

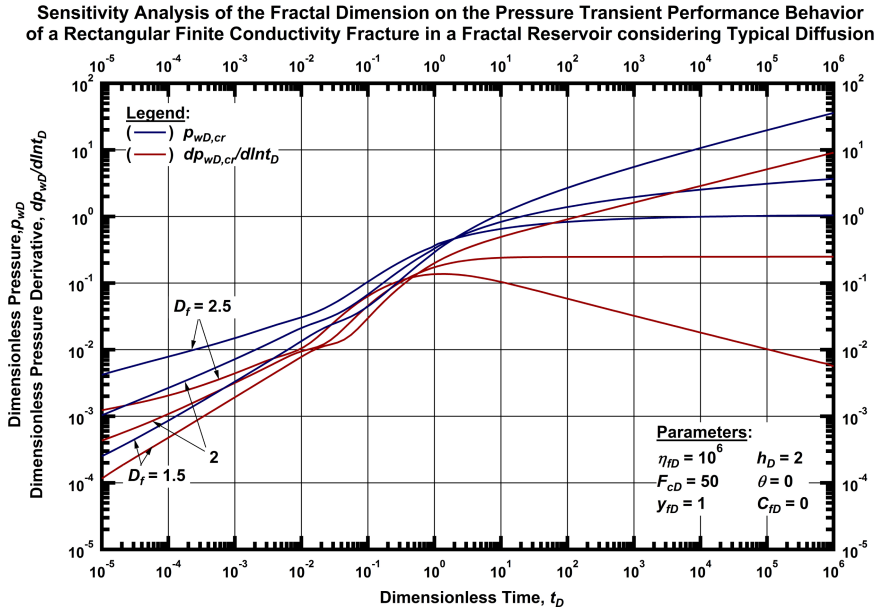

Figure 3.7 — Log-log plot of the dimensionless pressure and dimensionless pressure derivative functions for a horizontal well intercepting a single rectangular hydraulic fracture of finite conductivity in a fractal reservoir considering typical (constant) diffusion, for selected values of the fractal dimension (D_f). (constant rate case).

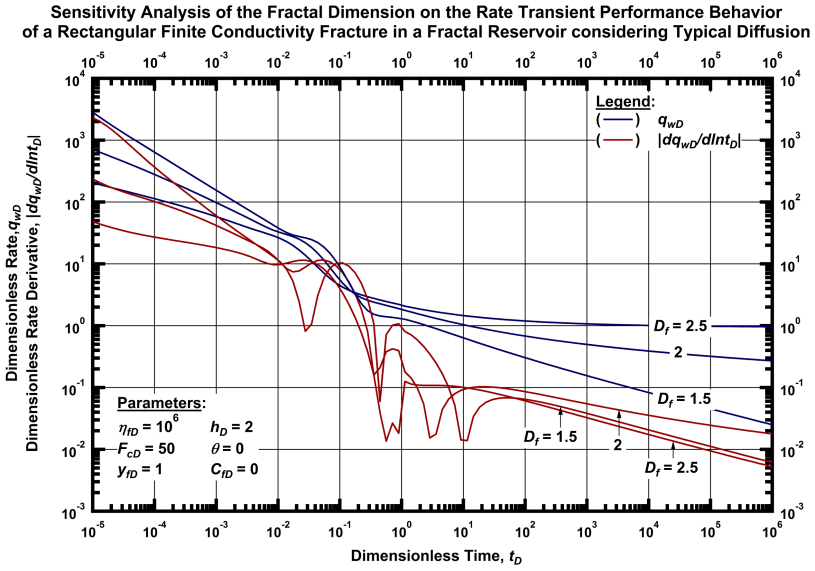

Figure 3.8 — Log-log plot of the dimensionless rate and dimensionless rate derivative functions for a horizontal well intercepting a single rectangular hydraulic fracture of finite conductivity in a fractal reservoir considering typical (constant) diffusion, for selected values of the fractal dimension (D_f). (constant pressure case).

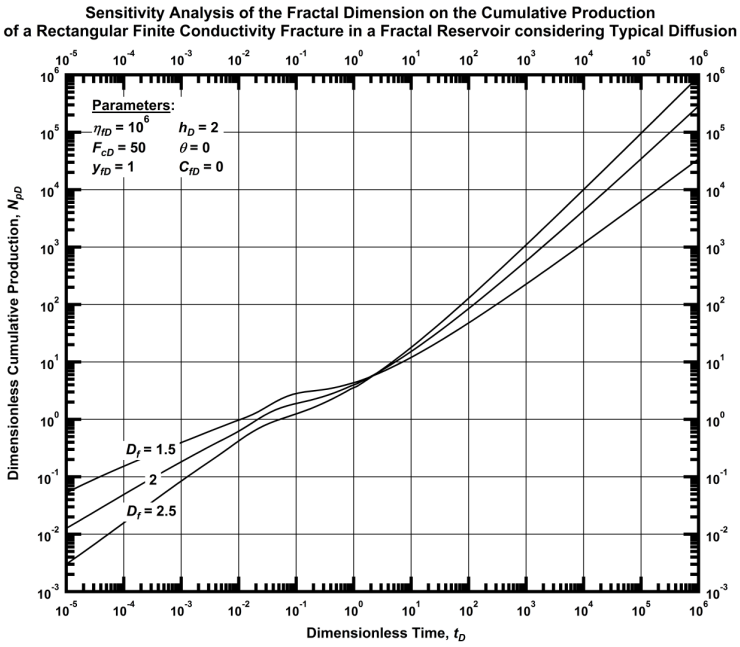

Figure 3.9 — Log-log plot of the dimensionless cumulative production for a horizontal well intercepting a single rectangular hydraulic fracture of finite conductivity in a fractal reservoir consider-ing typical (constant) diffusion, for selected values of the fractal dimension (D_f). (constant pressure case).

We next consider the impact of the (fractal) conductivity index (θ) on the proposed constant rate and constant pressure solutions — and we begin with the constant rate, circular fracture case where the dimensionless pressure and dimensionless pressure derivative functions are shown in **Fig. 3.10**. The influence of the conductivity index (θ) is similar to that for the fractal dimension case (D_f) — however; in the case of the conductivity index the features are much more "subtle" compared to the fractal dimension cases. The constant pressure cases are shown in **Fig. 3.11** (*i.e.*, the dimensionless rate and dimensionless rate derivative functions) and Fig. **3.12** (the dimensionless cumulative production functions) — and much like the constant rate cases, the influence of the conductivity index (θ) tends to be very precise, as in the case of the dimensionless rate derivative functions (**Fig. 3.11**), which are essentially parallel over the entire time scale. Lastly, the dimensionless cumulative production profiles shown in **Fig. 3.12** have very little independent character (*i.e.*, the trends are almost indistinguishable over time).

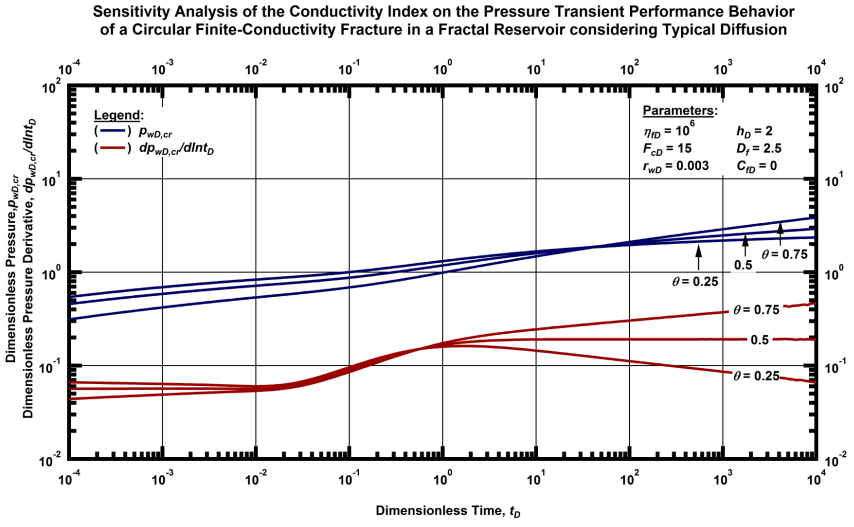

Figure 3.10 — Log-log plot of the dimensionless pressure and dimensionless pressure derivative functions for a horizontal well intercepting a single circular hydraulic fracture of finite conductivity in a fractal reservoir considering typical (constant) diffusion, for selected values of the conductivity index (θ). (constant rate case)

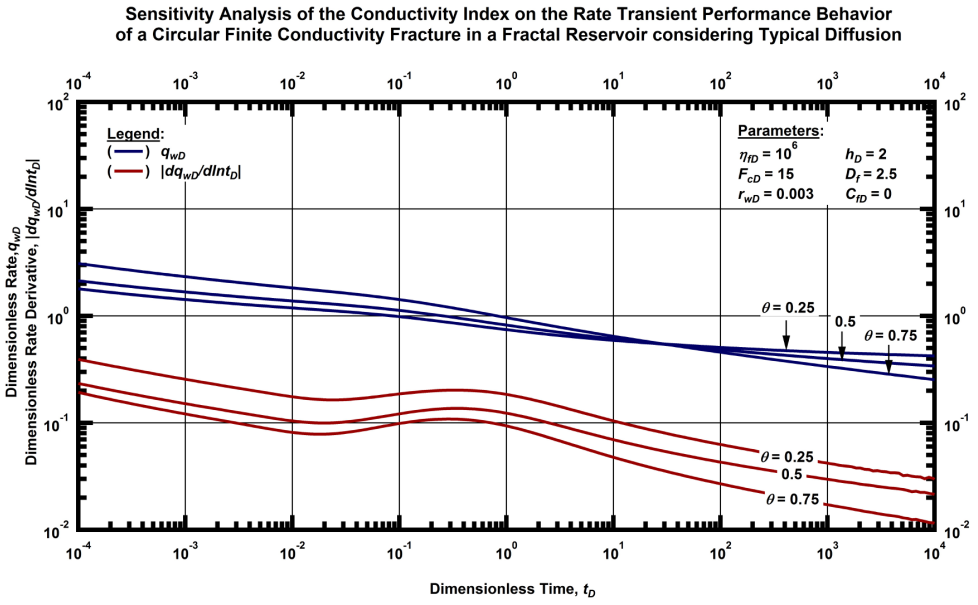

Figure 3.11 — Log-log plot of the dimensionless rate and dimensionless rate derivative functions for a horizontal well intercepting a single circular hydraulic fracture of finite conductivity in a fractal reservoir considering typical (constant) diffusion, for selected values of the conductivity index (θ). (constant pressure case).

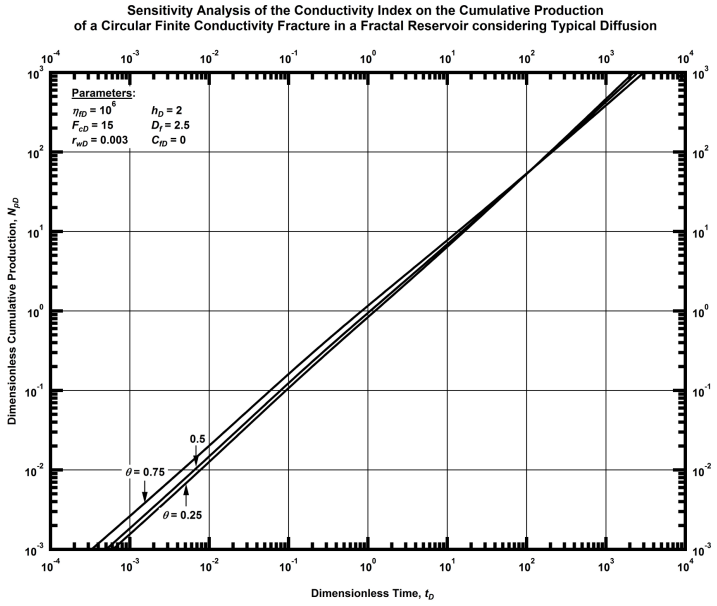

Figure 3.12 — Log-log plot of the dimensionless cumulative production for a horizontal well intercepting a single circular hydraulic fracture of finite conductivity in a fractal reservoir considering typical (constant) diffusion, for selected values of the conductivity index (θ). (constant pressure case).

Finally, we consider the influence of the conductivity index (θ) for the constant rate and constant pressure cases for the case of a rectangular fracture of finite conductivity (see **Figs. 3.13 and 3.14**, respectively). In **Fig. 3.13** we note that both the dimensionless pressure and the dimensionless pressure derivative functions are dominated by the "linear flow" feature (1:2 slope) at early times (*i.e.*, for $t_D < 10^{-2}$), then by the fracture-reservoir transient regime, followed by the fractal-influenced reservoir behavior.

We next present the constant pressure solution in **Fig. 3.14** (*i.e.*, the dimensionless rate and dimensionless rate derivative functions) and we immediately note that these cases are essentially "mirror images" of their corresponding constant rate cases. This behavior is probably due to the uniqueness of this selection of parameters for this particular model. To finish this suite of comparisons, we present the dimensionless cumulative production profile for our selected cases (**Fig. 3.15**) and we find that all of the proposed flow regimes are observed — in particular, the early-time "linear flow" feature (1:2 slope) for $t_D < 10^{-2}$, then the fracture-reservoir transient regime, then the fractal-influenced reservoir behavior.

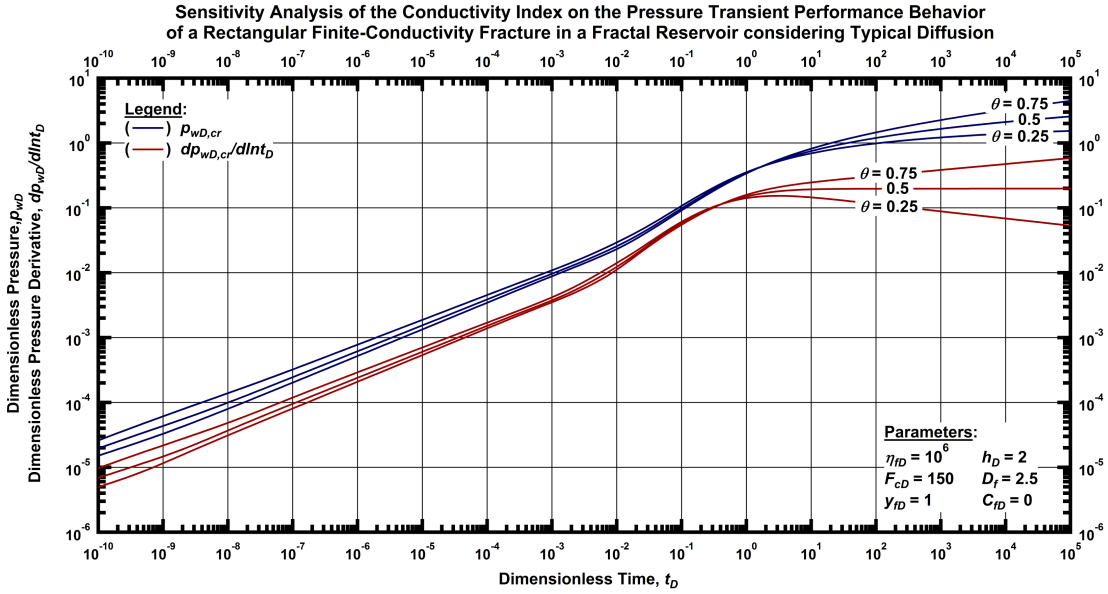

Figure 3.13 — Log-log plot of the dimensionless pressure and dimensionless pressure derivative functions for a horizontal well intercepting a single rectangular hydraulic fracture of finite conductivity in a fractal reservoir considering typical (constant) diffusion, for selected values of the conductivity index (θ). (constant rate case)

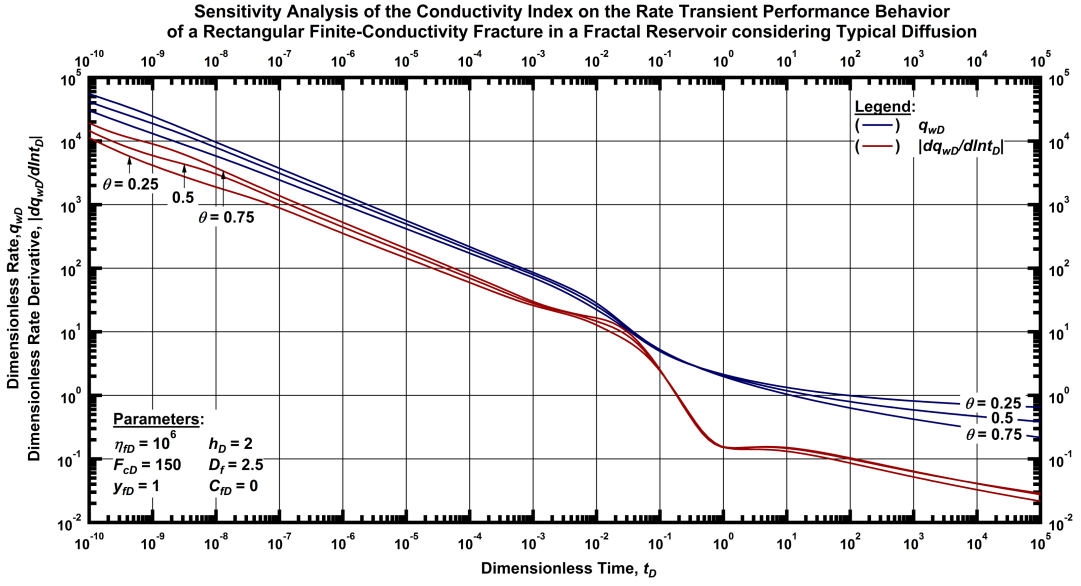

Figure 3.14 — Log-log plot of the dimensionless rate and dimensionless rate derivative functions for a horizontal well intercepting a single rectangular hydraulic fracture of finite conductivity in a fractal reservoir considering typical (constant) diffusion, for selected values of the conductivity index (θ). (constant pressure case).

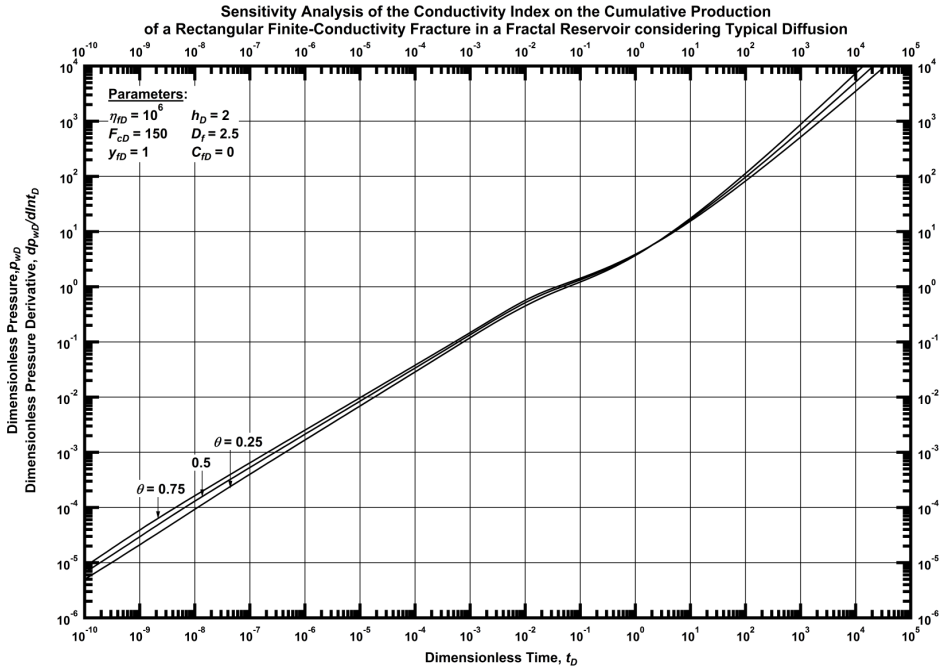

Figure 3.15 — Log-log plot of the dimensionless cumulative production for a horizontal well intercepting a single rectangular hydraulic fracture of finite conductivity in a fractal reservoir considering typical (constant) diffusion, for selected values of the conductivity index (θ). (con-stant pressure case).

In **Fig. 3.16**, we illustrate the effect of the dimensionless fracture conductivity on our proposed solutions, in particular for the dimensionless pressure and dimensionless pressure derivative functions for the circular fracture case (constant rate case). Analogous to the non-fractal models, we have observed that the flow within the fractal reservoir dominates during all periods of flow at very low values of the dimensionless fracture conductivity (F_{cD}=1 in **Fig. 3.16**). At high values of conductivity (*e.g.*, F_{cD}=150), the three expected periods of flow are well defined: (1) fracture flow for dimensionless time < 10^{-2}, (2) fracture-reservoir interaction period for dimensionless times between 10^{-2} and 10, and (3) pseudo-fractal flow for dimensionless times > 10. For intermediate values of dimensionless fracture conductivity (e.g., F_{cD}=10), the fracture flow and the interaction periods yield the expected power-law signatures, where this is a result of a narrower (or perhaps, shorter) fracture.

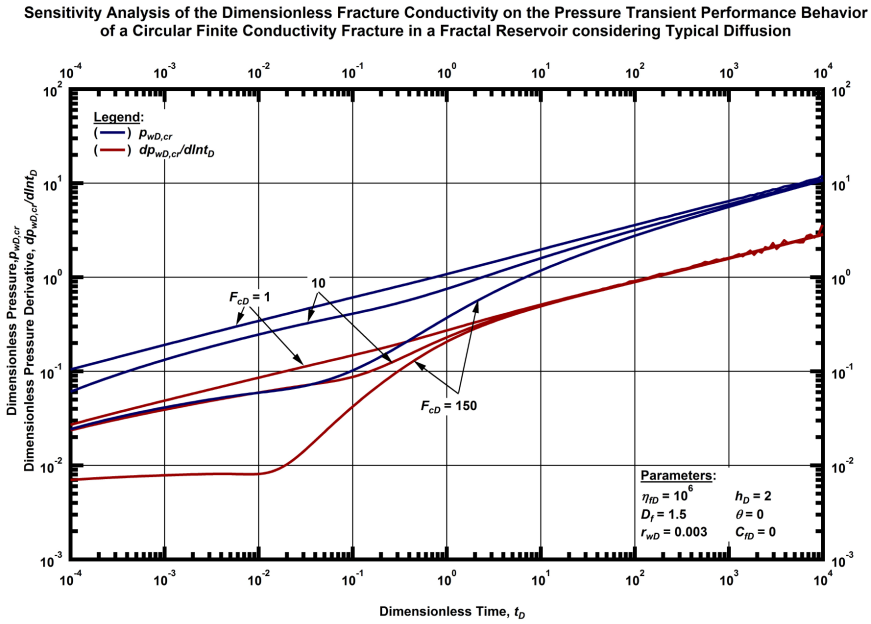

Figure 3.16 — Log-log plot of the dimensionless pressure and dimensionless pressure derivative functions for a horizontal well intercepting a single circular hydraulic fracture of finite conductivity in a fractal reservoir considering typical (constant) diffusion, for selected values of the dimensionless fracture conductivity (F_{cD}). (constant rate case)

Fig. 3.17 shows the influence of the dimensionless fracture conductivity on the rate-transient performance behavior for the circular fracture case — specifically the dimensionless rate and dimensionless rate derivative functions (constant pressure case). As expected, the highest dimensionless flowrate and dimensionless cumulative production profiles (see **Fig. 3.18** for the dimensionless cumulative production profiles) are given by the higher values of the dimensionless fracture conductivity. We believe that the dispersions observed in the dimensionless rate derivative functions for dimensionless times > 30 as shown in **Fig. 3.17** for the lowest dimensionless fracture conductivity case (*i.e.*, F_{cD}=1) are the result of numerical instabilities for small arguments of the modified Bessel functions in the solution for this particular case. The Stehfest algorithm (for numerical inversion) will amplify small scale instabilities, particularly for any derivative functions.

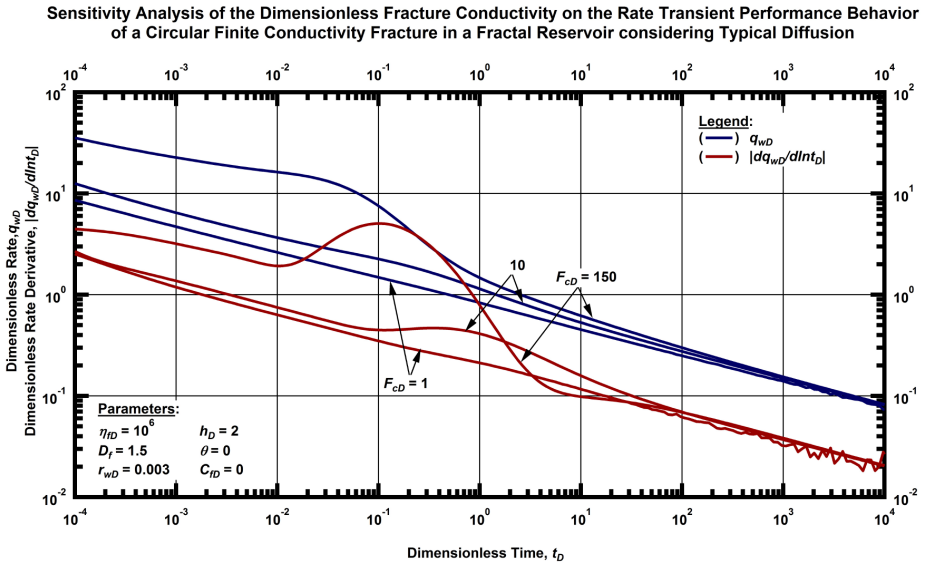

Figure 3.17 — Log-log plot of the dimensionless rate and dimensionless rate derivative functions for a horizontal well intercepting a single circular hydraulic fracture of finite conductivity in a fractal reservoir considering typical (constant) diffusion, for selected values of the dimensionless fracture conductivity (F_{cD}). (constant pressure case).

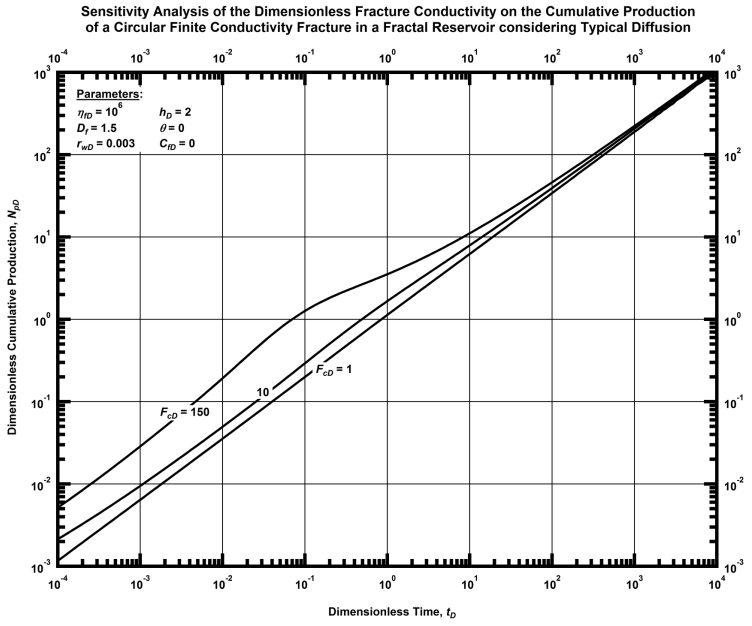

Figure 3.18 — Log-log plot of the dimensionless cumulative production for a horizontal well intercepting a single circular hydraulic fracture of finite conductivity in a fractal reservoir considering typical (constant) diffusion, for selected values of the dimensionless fracture conductivity (F_{cD}). (constant pressure case)

The sensitivity analyses considering variations in the dimensionless fracture conductivity on our proposed solutions for the rectangular fracture case are shown in **Fig. 3.19** and **Fig. 3.20**, respectively. Again we use the dimensionless pressure (constant rate case) and dimensionless rate (constant pressure) solutions as appropriate. Using these plots we observe that the rectangular fracture cases have a very unusual "late-time" effect in that, for the constant rate case, the dimensionless pressure function appears to flatten, but the dimensionless pressure derivative function exhibits an approximate 1/4 slope that is decreasing (see **Fig. 3.19**). A similar feature is observed for the constant pressure case in **Fig. 3.20**.

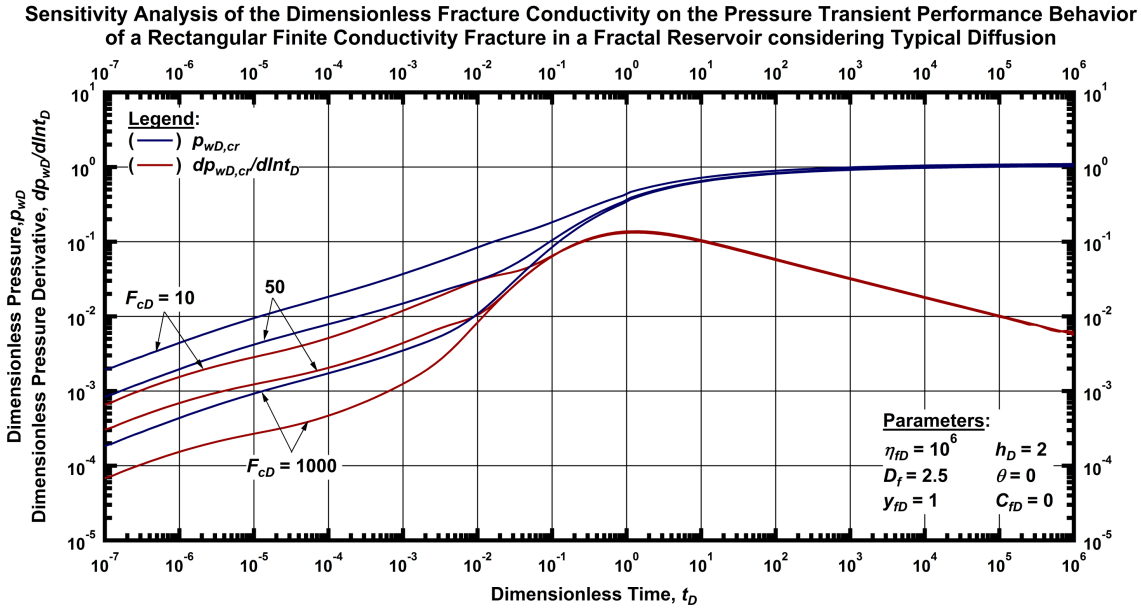

Figure 3.19 — Log-log plot of the dimensionless pressure and dimensionless pressure derivative functions for a horizontal well intercepting a single rectangular hydraulic fracture of finite conductivity in a fractal reservoir considering typical (constant) diffusion, for selected values of the dimensionless fracture conductivity (F_{cD}). (constant rate case)

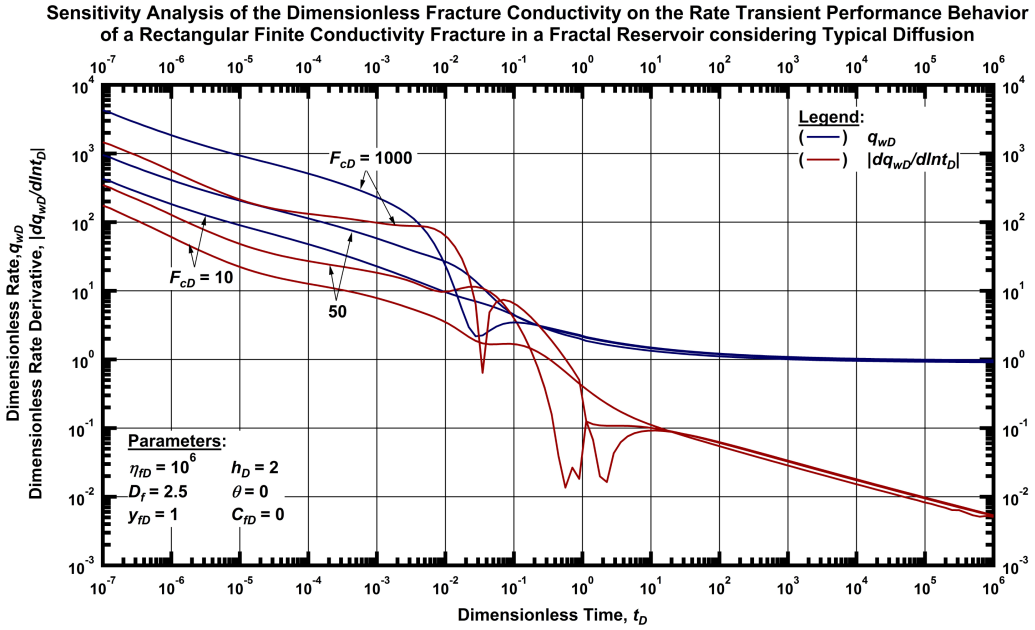

Figure 3.20 — Log-log plot of the dimensionless rate and dimensionless rate derivative functions for a horizontal well intercepting a single rectangular hydraulic fracture of finite conductivity in a fractal reservoir considering typical (constant) diffusion, for selected values of the dimensionless fracture conductivity (F_{cD}). (constant pressure case).

The characteristic signature (*i.e.*, unit-slope in the dimensionless pressure derivative function) of the "transition to reservoir" effect is observed over the dimensionless time period from 10^{-2} to 10^{-1} in **Fig. 3.19**. We also note abrupt changes in the dimensionless rate derivative function over the dimensionless time period from 10^{-2} to 10^{1} (see **Fig. 3.20**) we believe that this is also a consequence of the "transition to reservoir" effect. The dimensionless cumulative production profile is shown in **Fig. 3.21**, where we note that the early transient flow is dominated by the F_{cD}-value (*i.e.*, the higher the F_{cD} value the higher the production during this period), we also not that the unit slope in the dimensionless cumulative production profile for dimensionless times > 10 reflect an essentially constant flowrate at late times.

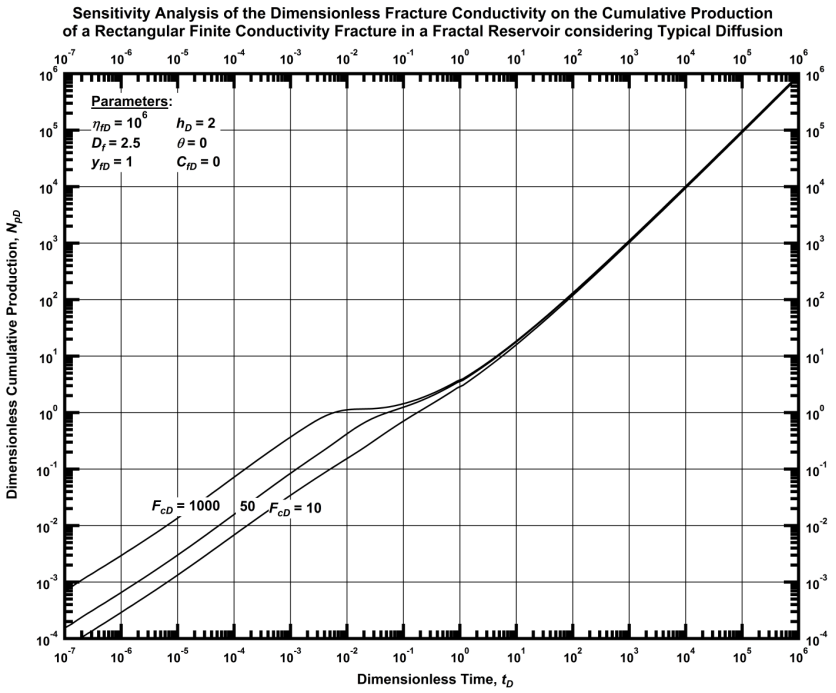

Figure 3.21 — Log-log plot of the dimensionless cumulative production for a horizontal well intercepting a single rectangular hydraulic fracture of finite conductivity in a fractal reservoir considering typical (constant) diffusion, for selected values of the dimensionless fracture conductivity (F_{cD}). (constant pressure case)

Naturally Fractured Porosity/Dual Porosity Fractal Reservoir with Typical Diffusion

To extend these models to naturally-fractured/dual porosity reservoirs, we have used the reservoir model presented by Valdes-Perez (2013), considering the "slab" model for the fracture-matrix systems of all of the cases considered in this work. This model considers transient interporosity transfer and can reproduce pseudosteady-state interporosity transfer conditions at high values of interporosity skin. Regardless of the interporosity transfer conditions, the model solution (as represented by the dimensionless pressure and dimensionless pressure derivative signatures) yields three distinct flow periods, as governed by the model parameters. A schematic log-log plot of the dimensionless pressure and dimensionless pressure derivative functions is shown in **Fig. 3.22**.

The following flow periods are evident for these case:

- Period 1 — (fractal fracture network flow): Early-fractal flow — this period of flow is dominated by the properties of the fractal network and exhibits a power-law signature in both the dimensionless pressure and dimensionless pressure derivative functions (see **Fig. 3.22**).
- Period 2 — (interaction between the fractal fracture network and the matrix blocks): The matrix blocks contribute fluid to the fractal fracture network. The dimensionless pressure and dimensionless pressure derivative functions exhibit a "combined" power-law behavior, different from the behavior observed in Period 1.
- Period 3 — (single porosity fractal reservoir flow): Both porous media (*i.e.*, the fractal fracture network and the matrix blocks) behave as a (total) single porosity fractal system. The dimensionless pressure and dimensionless pressure derivative functions should exhibit the same power-law behavior as that observed in Period 1.

As presented by Cinco-Ley *et al.* (1988), a finite conductivity hydraulic fracture within a naturally-fractured/dual porosity reservoir can exhibit a maximum of twelve (12) sub-periods of flow. The number of sub-periods of flow that may be observed depends on the properties of the hydraulic fracture and the reservoir.

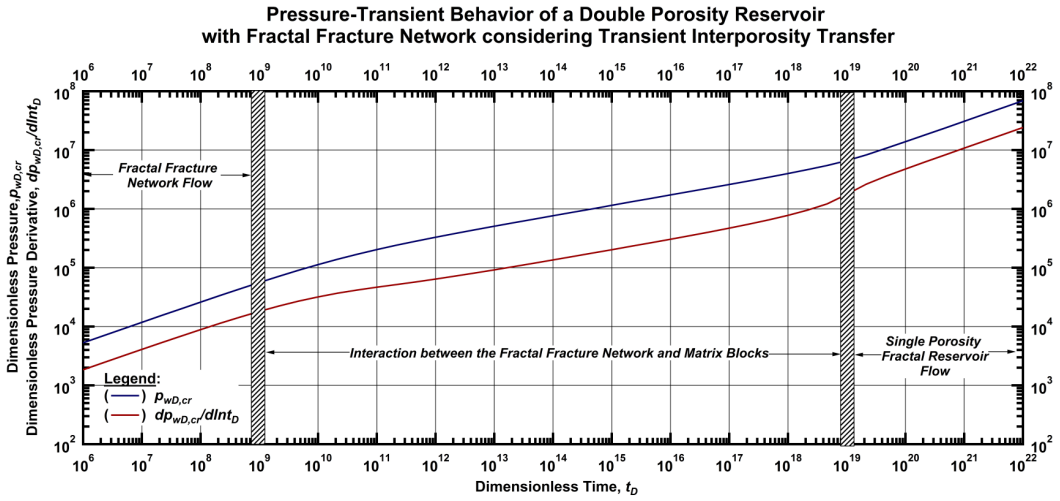

Figure 3.22 — Schematic example — Naturally fractured/dual porosity reservoir with a fractal fracture network, dimensionless pressure and dimensionless pressure derivative functions (various characteristic flow regimes are highlighted). (constant rate case)

In this section, we present selected cases that show the influence of the naturally-fractured/dual porosity effects on the transient performance of a horizontal well intercepting a single finite conductivity fracture.

Sensitivity to the η_{maD}-Parameter: Circular Fracture Case

The plot shown in **Fig. 3.23** presents three (constant rate) cases of the dimensionless hydraulic diffusivity of the matrix (η_{maD}): (1) high (η_{maD} =10^{-4}), (2) intermediate (10^{-10}), and (3) low (10^{-16}). These three cases exhibit radial flow (in the fracture) at early times (dimensionless times < 10^{-5}). At intermediate-transient times (dimensionless times within the range 10^{-5} to 10^{-3}), the dimensionless pressure derivative signatures exhibit a power-law behavior, and we note that the slope is less steep for low η_{maD} -values. At late-transient times (dimensionless times > 10^{-3}), the naturally-fractured/dual porosity reservoir component dominates the flow behavior.

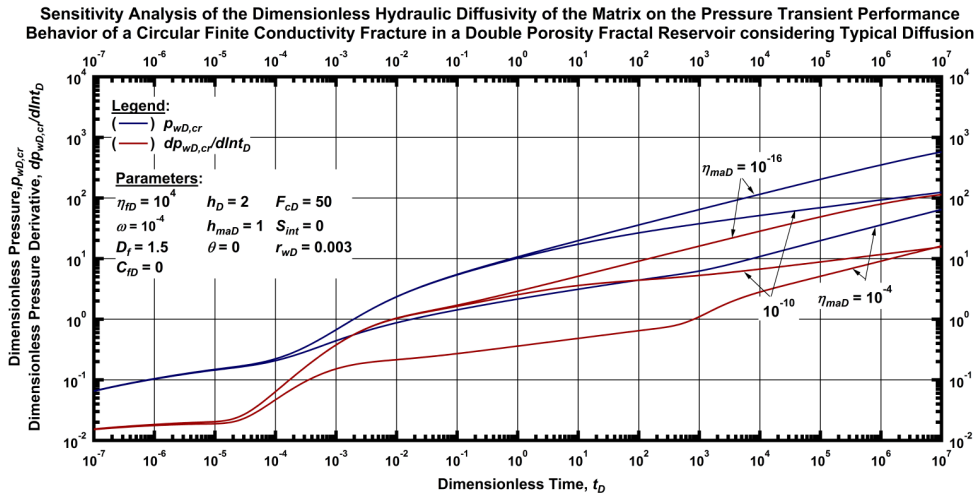

Figure 3.23 — Log-log plot of the dimensionless pressure and dimensionless pressure derivative functions for a horizontal well intercepting a single circular hydraulic fracture of finite conductivity in a dual porosity fractal reservoir considering typical (constant) diffusion, for selected values of the dimensionless hydraulic diffusivity of the matrix (η_{maD}). (constant rate case)

The constant pressure cases are shown in **Figs. 3.24 and 3.25**. In **Fig. 3.24** we present the dimensionless rate and dimensionless rate derivative functions for the constant rate example cases presented in **Fig. 3.23**. As expected, the trends in **Fig. 3.24** confirm that the influence of the dimensionless hydraulic diffusivity of the matrix (η_{maD}) in the sense that the lower the value of the η_{maD}-parameter, the lower the rate performance of these cases. The dimensionless cumulative production cases are presented in **Fig. 3.25** and although there is little character in these curves, it is clear that the highest production corresponds to the highest value of the η_{maD} -parameter.

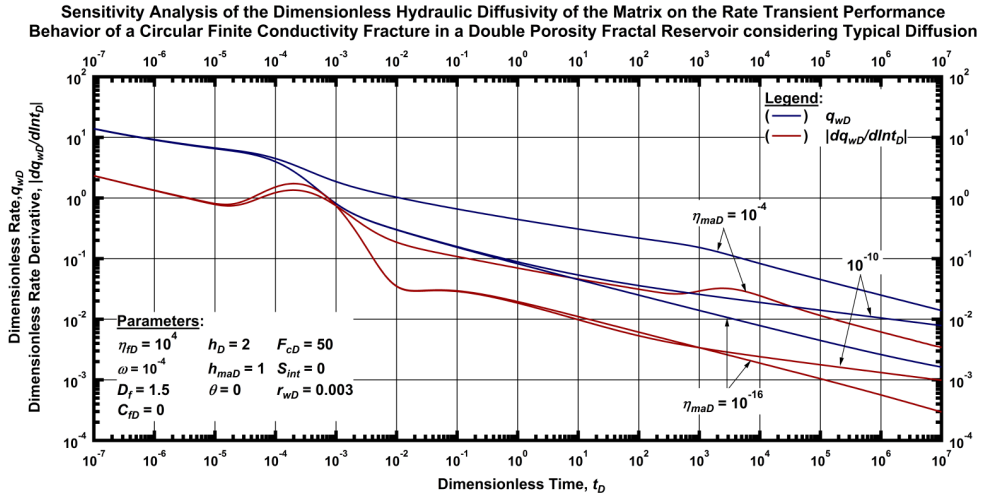

Figure 3.24 — Log-log plot of the dimensionless rate and dimensionless rate derivative functions for a horizontal well intercepting a single circular hydraulic fracture of finite conductivity in a dual porosity fractal reservoir considering typical (constant) diffusion, for selected values of the dimensionless hydraulic diffusivity of the matrix (η_{maD}). (constant pressure case)

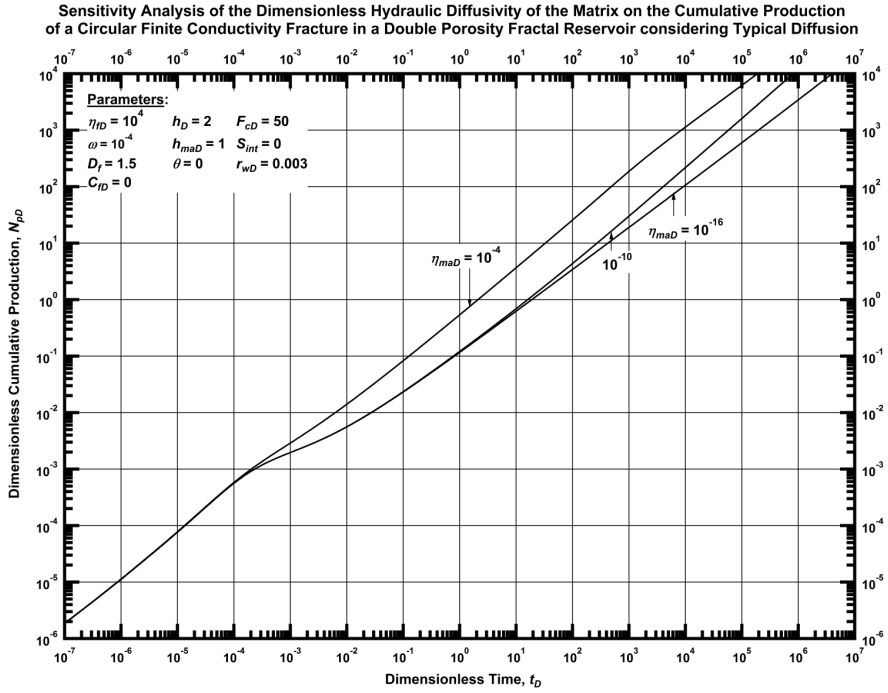

Figure 3.25 — Log-log plot of the dimensionless cumulative production function for a horizontal well intercepting a single circular hydraulic fracture of finite conductivity in a dual porosity fractal reservoir considering typical (constant) diffusion, for selected values of the dimensionless hydraulic diffusivity of the matrix (η_{maD}). (constant pressure case).

Sensitivity to the η_{maD}-Parameter: Rectangular Fracture Case

In **Fig. 3.26** we present three (constant rate) cases for the rectangular fracture case where we have varied the dimensionless hydraulic diffusivity of the matrix (η_{maD}) as follows: (1) high (η_{maD} =10^{-4}), (2) intermediate (10^{-12}), and (3) low (10^{-20}). These three cases exhibit linear flow (in the fracture) at very early times (dimensionless times < 10^{-5}). At intermediate-transient times (dimensionless times within the range 10^{-3} to 10^{2}), the dimensionless pressure derivative signatures exhibit an apparent "transient radial flow" behavior, but we understand that this could also be interpreted as a very shallow power-law behavior. Lastly, we observe the influence of the naturally-fractured/dual porosity reservoir component, which manifests a late-time radial flow regime for dimensionless times > 10^{4}. We acknowledge that these behaviors are uniquely dependent on the selection of the input parameters, and we can clearly see the evidence of the dimensionless hydraulic diffusivity of the matrix parameter (η_{maD}) during the intermediate and late times.

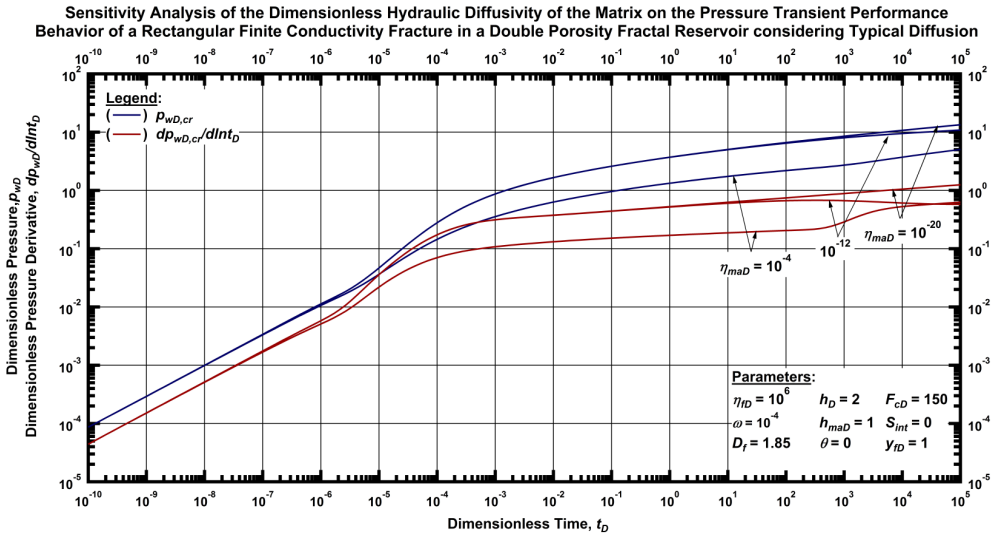

Figure 3.26 — Log-log plot of the dimensionless pressure and dimensionless pressure derivative functions for a horizontal well intercepting a single rectangular hydraulic fracture of finite conductivity in a dual porosity fractal reservoir considering typical (constant) diffusion, for selected values of the dimensionless hydraulic diffusivity of the matrix (η_{maD}). (constant rate case)

The constant pressure cases are shown in **Figs. 3.27 and 3.28**. The dimensionless rate and dimensionless rate derivative functions reflect very closely the behaviors exhibited for the constant rate example cases presented in **Fig. 3.26** (with the anomalies in the dimensionless rate derivative functions for the η_{maD}-parameter values of 10^{-12} and 10^{-20} duly noted — these are artifacts of the character of the dimensionless rate for these cases). In **Fig. 3.28** we present the dimensionless cumulative production and we clearly note that the $\eta_{maD} = 10^{-12}$ and 10^{-20} cases are quite similar across the entire time-scale, but that these cases differ significantly from the $\eta_{maD} = 10^{-4}$ case.

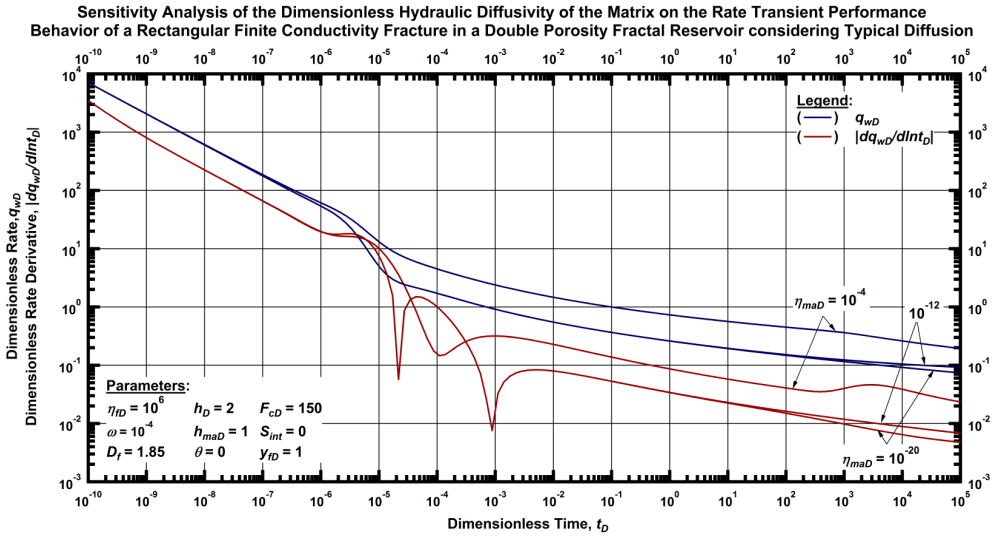

Figure 3.27 — Log-log plot of the dimensionless rate and dimensionless rate derivative functions for a horizontal well intercepting a single rectangular hydraulic fracture of finite conductivity in a dual porosity fractal reservoir considering typical (constant) diffusion, for selected values of the dimensionless hydraulic diffusivity of the matrix (η_{maD}). (constant pressure case)

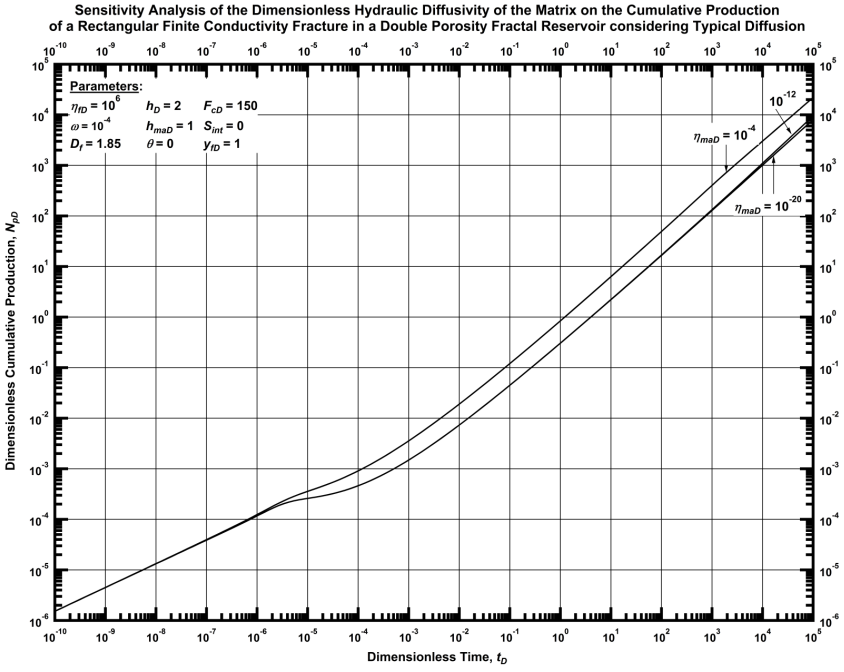

Figure 3.28 — Log-log plot of the dimensionless cumulative production function for a horizontal well intercepting a single circular hydraulic fracture of finite conductivity in a dual porosity fractal reservoir considering typical (constant) diffusion, for selected values of the dimensionless hydraulic diffusivity of the matrix (η_{maD}). (constant pressure case)

Sensitivity to the ω-Parameter: Circular Fracture Case

In this section we consider the influence of the storativity ratio (ω) for the naturally-fractured/dual porosity reservoir component of the solution. We first consider the constant rate cases for a single circular fracture of finite conductivity where we have varied the storativity ratio (ω) as follows: $\omega = 1$ (high/homogeneous), $\omega = 10^{-2}$ (intermediate), and $\omega = 10^{-16}$ (very low) as shown in **Fig.3. 29**. As expected, each case exhibits radial flow (in the fracture) at early times (dimensionless times $< 10^{-4}$). At intermediate-transient times (dimensionless times within the range 10^{-4} to 10^{0}), the dimensionless pressure derivative signatures exhibit a near-unity power-law behavior which reflects the transition to the fractal solution component. At late-transient times (dimensionless times $> 10^{1}$) we observe an approximate slope of 1:4 in the dimensionless pressure derivative profiles, which suggests that the response is now dominated by the fractal reservoir solution component.

We next present the constant pressure cases in **Figs. 3.30 and 3.31** (*i.e.*, the dimensionless rate and dimensionless rate derivative functions are shown in **Fig. 3.30** and the dimensionless cumulative production is shown in **Fig. 3.31**). In relative terms, the dimensionless rate profiles in **Fig. 3.30** roughly reflect the same features we observed for the dimensionless pressure solutions in **Fig. 3.29**. However; the dimensionless rate derivative profiles shown in **Fig. 3.30** are significantly affected by the "transition" features observed in the dimensionless rate profiles — in short, the dimensionless rate derivative profiles exhibit numerous artifacts that could make interpretation of these trends non-unique.

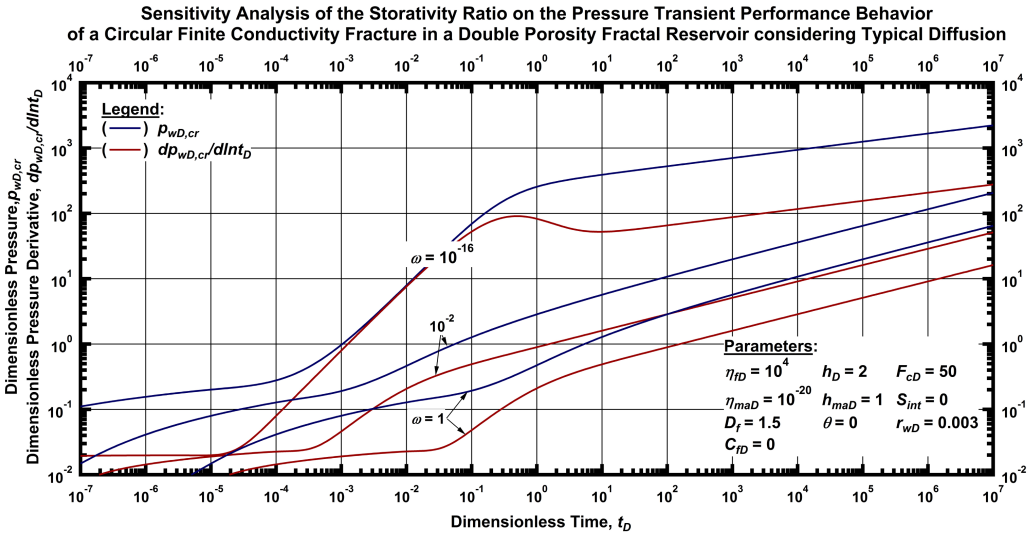

Figure 3.29 — Log-log plot of the dimensionless pressure and dimensionless pressure derivative functions for a horizontal well intercepting a single circular hydraulic fracture of finite conductivity in a dual porosity fractal reservoir considering typical (constant) diffusion, for selected values of the storativity ratio (ω). (constant rate case)

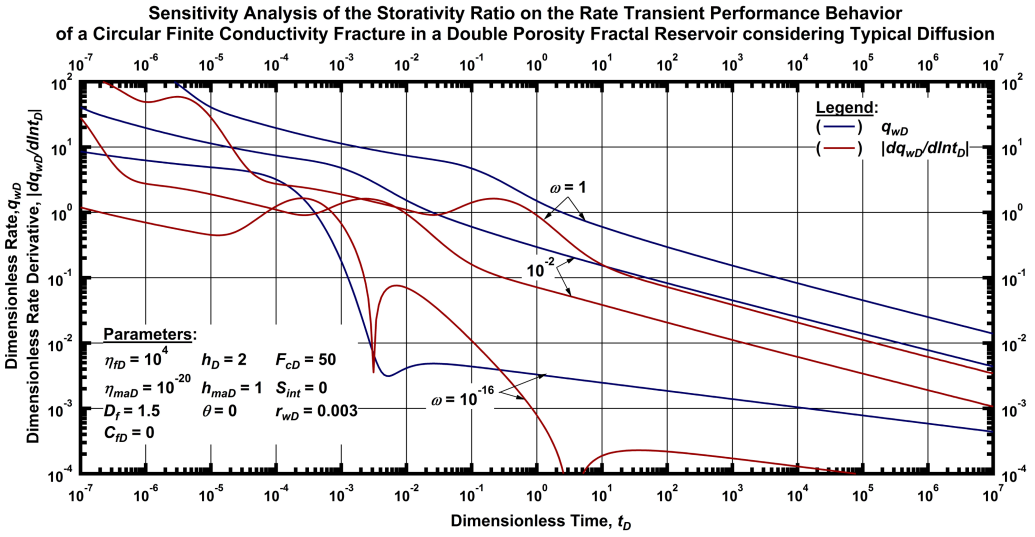

Figure 3.30 — Log-log plot of the dimensionless rate and dimensionless rate derivative functions for a horizontal well intercepting a single circular hydraulic fracture of finite conductivity in a dual porosity fractal reservoir considering typical (constant) diffusion, for selected values of the storativity ratio (ω). (constant pressure case)

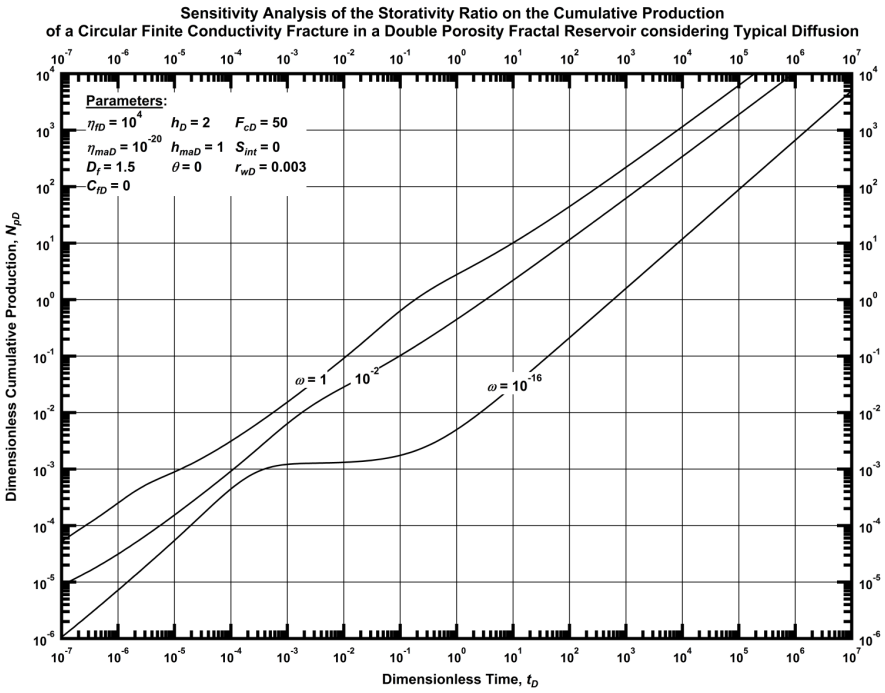

Figure 3.31 — Log-log plot of the dimensionless cumulative production function for a horizontal well intercepting a single circular hydraulic fracture of finite conductivity in a dual porosity fractal reservoir considering typical (constant) diffusion, for selected values of the storativity ratio (ω). (constant pressure case)

In **Fig. 3.31**, we present the dimensionless cumulative production for these cases and we note that each case is strongly distinctive and that the behavior of these functions is uniquely related to the storativity ratio (ω) for the naturally-fractured/dual porosity reservoir component of the solution.

Sensitivity to the ω-Parameter: Rectangular Fracture Case

We continue to consider the influence of the storativity ratio (ω) on the naturally-fractured/dual porosity reservoir component of the solution, but now we move to the constant rate cases for a single rectangular fracture of finite conductivity. We use the following cases for the storativity ratio (ω): $\omega = 1$ (high/homogeneous), $\omega = 10^{-4}$ (intermediate), and $\omega = 10^{-10}$ (very low), where the dimensionless pressure and dimensionless pressure derivative profiles for these cases are shown

in **Fig. 3.32**. At very early times (dimensionless times < 10^{-5} to 10^{-2}, depending on the ω-parameter), we observe linear flow (in the fracture). Similar to the circular fracture case, for intermediate-transient times (dimensionless times within the range 10^{-6} to 10^{-3} for the $\omega = 10^{-4}$ and 10^{-10} cases, and dimensionless times within the range 10^{-1} to 10^{2} for the $\omega = 10^{0}$ case) we observe a near-unity power-law behavior in the dimensionless pressure derivative signatures, which reflects the transition to the fractal solution component. At late-transient times (dimensionless times depending on the ω-parameter) we observe a very low power-law slope of 1:10 in the dimensionless pressure derivative profiles for the $\omega = 10^{0}$ and 10^{-4} cases.

The constant pressure cases are presented in **Figs. 3.33 and 3.34** (*i.e.*, the dimensionless rate and dimensionless rate derivative functions are shown in **Fig. 3.33** and the dimensionless cumulative production is shown in **Fig. 3.34**). As with the circular fracture case, the dimensionless rate profiles in **Fig. 3.33** roughly reflect the same features we observed for the dimensionless pressure solutions in **Fig. 3.32** — and again (as in the circular fracture case), the dimensionless rate derivative profiles shown in **Fig. 3.33** are significantly affected by the "transition" features observed in the dimensionless rate profiles. The dimensionless cumulative production profiles for these cases are shown in **Fig. 3.34**, and as with the circular fracture cases, we note that each trend is quite unique and we believe that the behavior of these functions is exceptionally related to the storativity ratio (ω) for the naturally-fractured/dual porosity reservoir component of the solution.

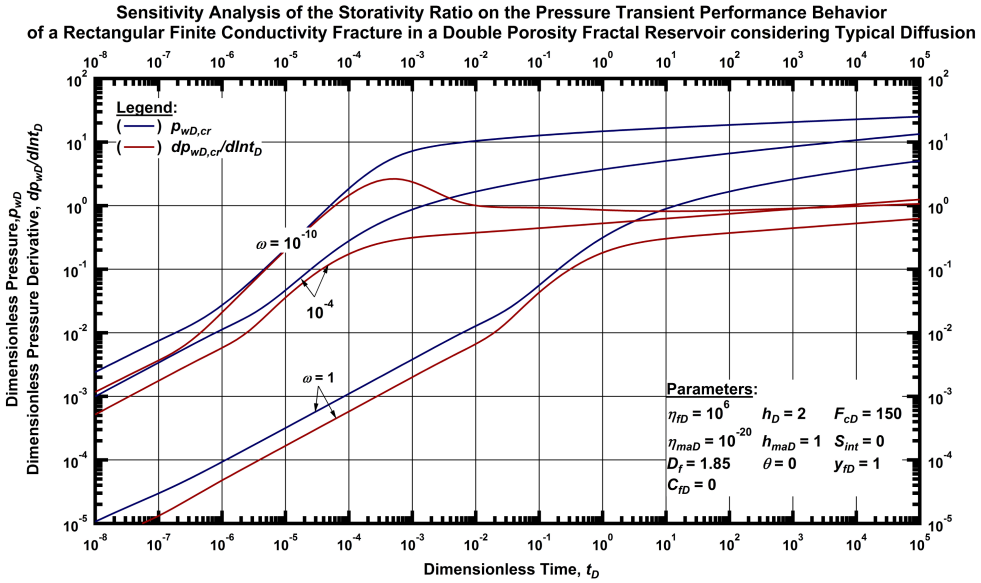

Figure 3.32 — Log-log plot of the dimensionless pressure and dimensionless pressure derivative functions for a horizontal well intercepting a single rectangular hydraulic fracture of finite conductivity in a dual porosity fractal reservoir considering typical (constant) diffusion, for selected values of the for selected values of the storativity ratio (ω). (constant rate case)

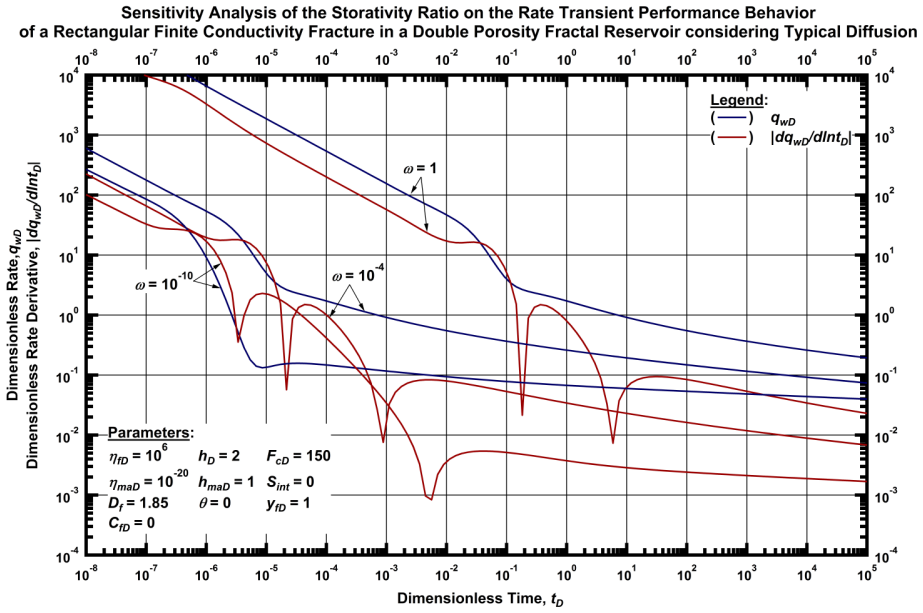

Figure 3.33 — Log-log plot of the dimensionless rate and dimensionless rate derivative functions for a horizontal well intercepting a single rectangular hydraulic fracture of finite conductivity in a dual porosity fractal reservoir considering typical (constant) diffusion, for selected values of the storativity ratio (ω). (constant pressure case).

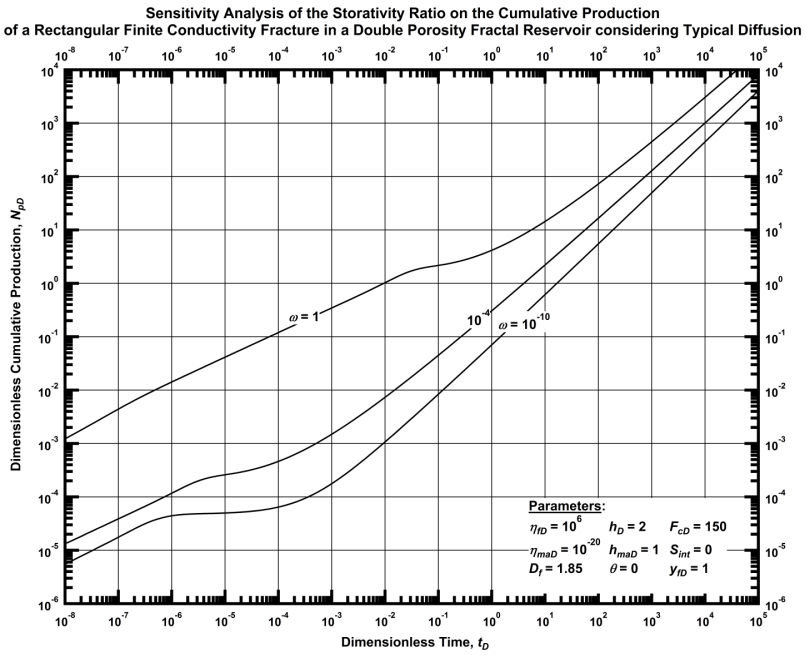

Figure 3.34 — Log-log plot of the dimensionless cumulative production function for a horizontal well intercepting a single rectangular hydraulic fracture of finite conductivity in a dual porosity fractal reservoir considering typical (constant) diffusion, for selected values of the storativity ratio (ω). (constant pressure case).

Sensitivity to the S_{int}-Parameter: Circular Fracture Case

In this section we consider the influence of the interporosity skin (S_{int}) on the naturally-fractured/dual porosity reservoir component of the solution. This is a fairly straightforward exercise, but it is important to recognize that the interporosity skin (S_{int}) *is not an actual reservoir parameter*, but is instead, an "additional/imposed" dimensionless pressure drop. For the constant rate case of a single circular fracture of finite conductivity, we will test the solution behavior for $S_{int} = 0$ (no "additional/ imposed" dimensionless pressure drop) and $S_{int} = 0.1$, which for this solution is a fairly large "additional/imposed" dimension-less pressure drop.

We present the (constant rate) dimensionless pressure and dimensions less pressure derivative profiles for the $S_{int} = 0$ and $S_{int} = 0.1$ cases in **Fig. 3.35**. As with all of our other sensitivity cases,

we observe radial flow (in the fracture) at early times (dimensionless times < 10^{-4}). At intermediate-transient times (dimensionless times within the range 10^{-4} to 10^{3}), the dimension-less pressure and dimensionless pressure derivative profiles exhibit a sharp response that reflects the transition to the fractal solution component. For the case of $S_{int} = 0$, it appears that the solution simply "shifts" to an approximate power-law flow regime. For the case of $S_{int} = 0.1$, we note a very strong response, particularly in the dimensionless pressure derivative profile where a "hump" feature appears (where such features are typically associated with wellbore storage distortion). We believe this behavior is a characteristic of the (relatively) large S_{int} -parameter. At late-transient times (dimensionless times > 10^{3}) we observe an approximate slope of 1:4 in the dimensionless pressure derivative profiles, which suggests that the response is now dominated by the fractal reservoir solution component.

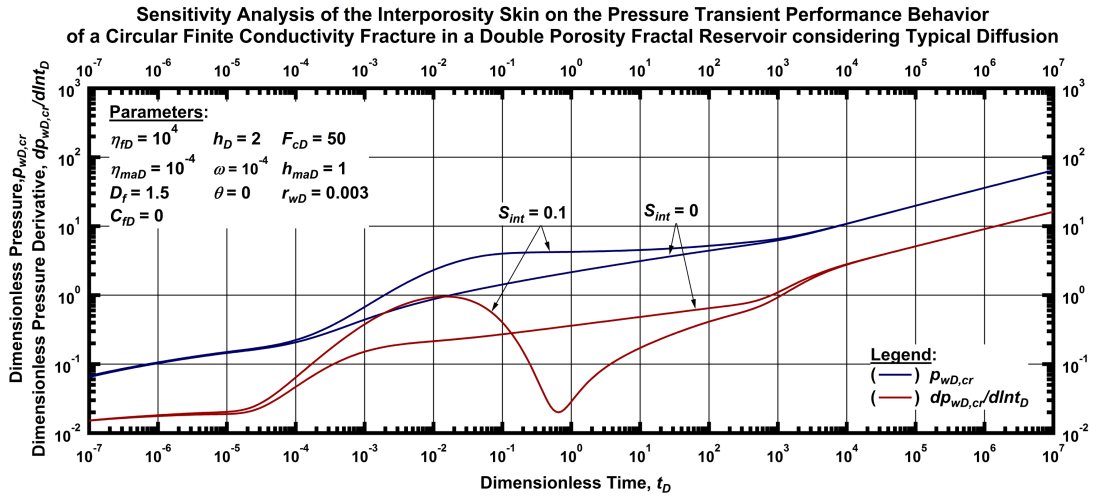

Figure 3.35 — Log-log plot of the dimensionless pressure and dimensionless pressure derivative func-tions for a horizontal well intercepting a single circular hydraulic fracture of finite conductivity in a dual porosity fractal reservoir considering typical (constant) diffusion, for selected values of the interporosity skin (S_{int}). (constant rate case)

The constant pressure cases are presented in **Figs. 3.36 and 3.37** (*i.e.*, the dimensionless rate and dimensionless rate derivative functions are shown in **Fig. 3.36** and the dimensionless cumulative production is shown in **Fig. 3.37**). As has become a common observation, the dimensionless rate profiles in **Fig. 3.36** roughly reflect the same features we observed for the dimensionless pressure solutions in **Fig. 3.35** — and as has also been observed, the dimensionless rate derivative profiles shown in **Fig. 3.36** are dramatically affected by the sharp features observed in the dimensionless rate profiles, which yield artifacts in the dimensionless rate derivative profiles (particularly so for the S_{int} = 0.1 case). We present the dimensionless cumulative production for these interporosity skin (S_{int}) cases in **Fig. 3.37**, we note (somewhat surprisingly) that the S_{int} -parameter only affects the intermediate time behavior of the dimensionless cumulative production profiles.

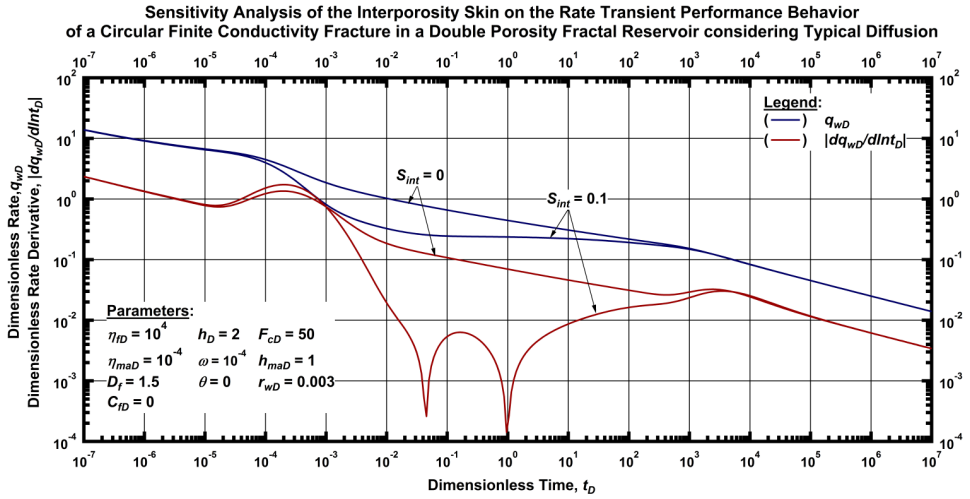

Figure 3.36 — Log-log plot of the dimensionless rate and dimensionless rate derivative functions for a horizontal well intercepting a single rectangular hydraulic fracture of finite conductivity in a dual porosity fractal reservoir considering typical (constant) diffusion, for selected values of the interporosity skin (S_{int}). (constant pressure case).

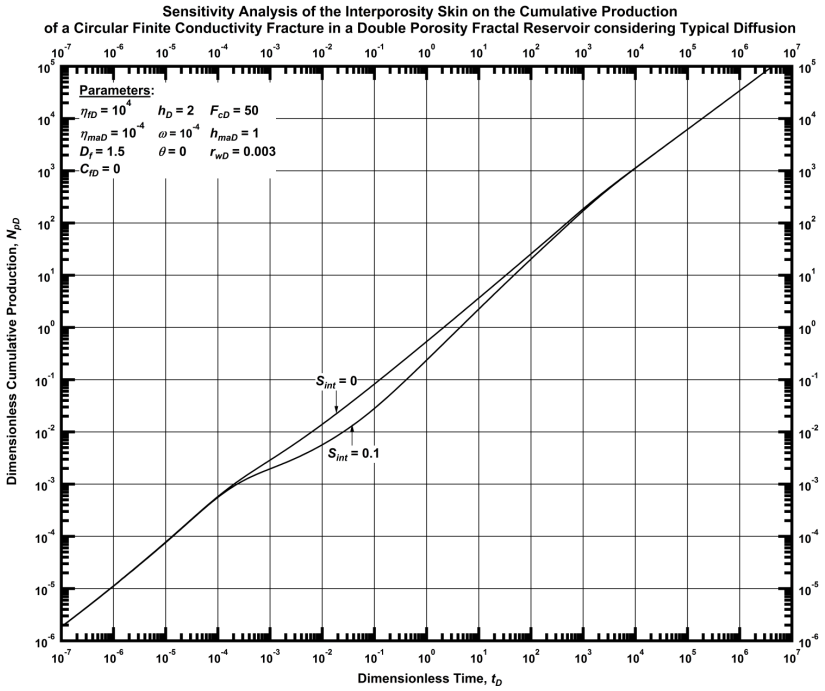

Figure 3.37 — Log-log plot of the dimensionless cumulative production function for a horizontal well intercepting a single circular hydraulic fracture of finite conductivity in a dual porosity fractal reservoir considering typical (constant) diffusion, for selected values of the interporosity skin (S_{int}). (constant pressure case).

Sensitivity to the S_{int}-Parameter: Rectangular Fracture Case

We now consider the effect of the interporosity skin (S_{int}) on the naturally-fractured/dual porosity reservoir component of the solution for the constant rate case of a single rectangular fracture of finite conductivity. Similar to our efforts for the circular fracture cases, we will test the solution behavior for $S_{int} = 0$ (no "additional/ imposed" dimensionless pressure drop), but because of the nature of the rectangular fracture, we will use $S_{int} = 0.01$ for these cases (where we noted that $S_{int} = 0.01$ is still a relatively large "additional/ imposed" dimensionless pressure drop, particularly for the rectangular fracture cases).

We present the (constant rate) dimensionless pressure and dimensions less pressure derivative profiles for the $S_{int} = 0$ and $S_{int} = 0.1$ cases in Fig. **3.38** and we immediately note the existence of a very strong linear flow (in the fracture) signature at very early times (dimensionless times < 10^{-5}). At intermediate-transient times (dimensionless times within the range 10^{-5} to 10^{3}), the dimensionless pressure and dimensionless pressure derivative profiles exhibit a sharp response that reflects the transition to the fractal solution component. As with the circular fracture example, for the case of Sint = 0, it appears that the solution simply "shifts" to an approximate power-law flow regime and for the case of $S_{int} = 0.01$, we note a very strong feature in the dimensionless pressure derivative profile where a "hump" appears. We believe this behavior is a characteristic of the (relatively) large S_{int} -parameter. At late-transient times (dimensionless times > 10^{3}) we observe what appears to be slope of approximately 1:4 in the dimensionless pressure derivative profiles, which suggests that the response is now dominated by the fractal reservoir solution component.

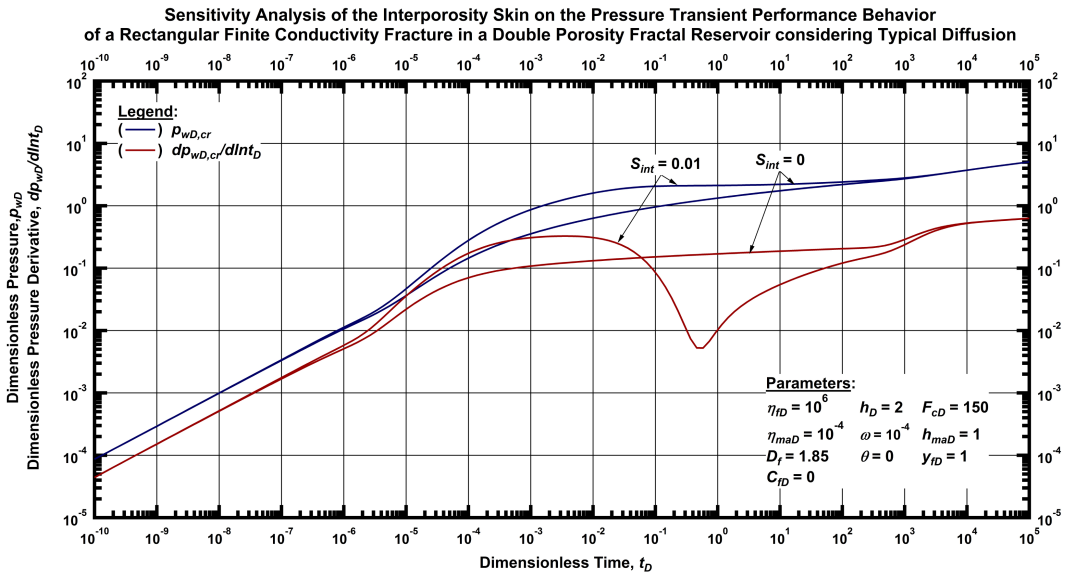

Figure 3.38 — Log-log plot of the dimensionless pressure and dimensionless pressure derivative functions for a horizontal well intercepting a single rectangular hydraulic fracture of finite conductivity in a dual porosity fractal reservoir considering typical (constant) diffusion, for selected values of the interporosity skin (S_{int}). (constant rate case).

The dimensionless rate and dimensionless rate derivative functions for the constant pressure rate cases are presented in **Fig. 3.39** and it appears that the dimensionless rate profiles in **Fig. 3.39** roughly reflect the same features we observed for the dimensionless pressure solutions in **Fig. 3.38** (in fact, these profiles are almost "mirror" images). As has been the observation throughout this work, the dimensionless rate derivative profiles shown in **Fig. 3.39** are dramatically affected by the sharp features observed in the dimensionless rate profiles, which yields significant artifacts in the dimensionless rate derivative profiles for the S_{int} = 0.01 case. In **Fig. 3.40** we present the dimensionless cumulative production for these interporosity skin (S_{int}) cases and we note that, for the rectangular fracture case, the S_{int} -parameter significantly affects the character of the dimensionless cumulative production profiles.

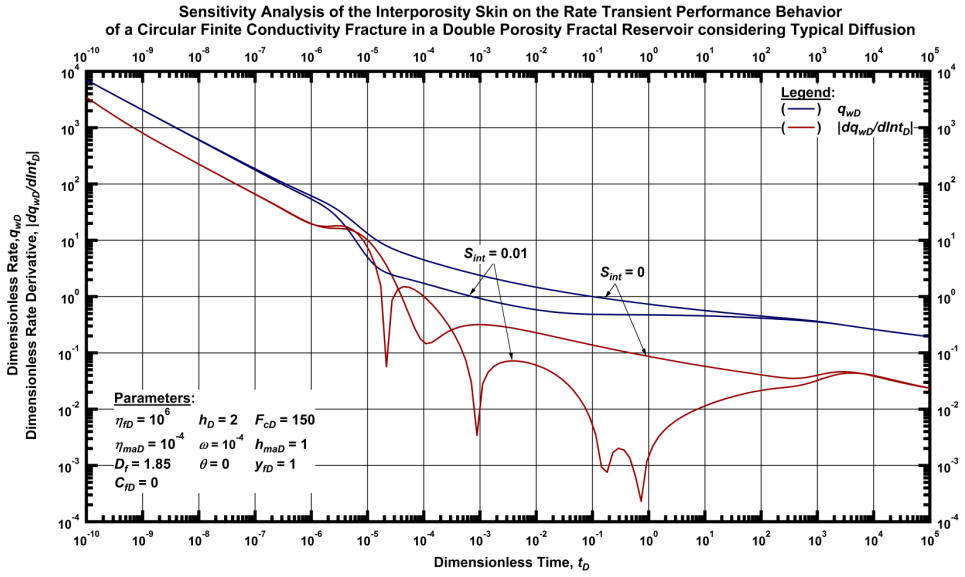

Figure 3.39 — Log-log plot of the dimensionless rate and dimensionless rate derivative functions for a horizontal well intercepting a single rectangular hydraulic fracture of finite conductivity in a dual porosity fractal reservoir considering typical (constant) diffusion, for selected values of the interporosity skin (S_{int}). (constant pressure case).

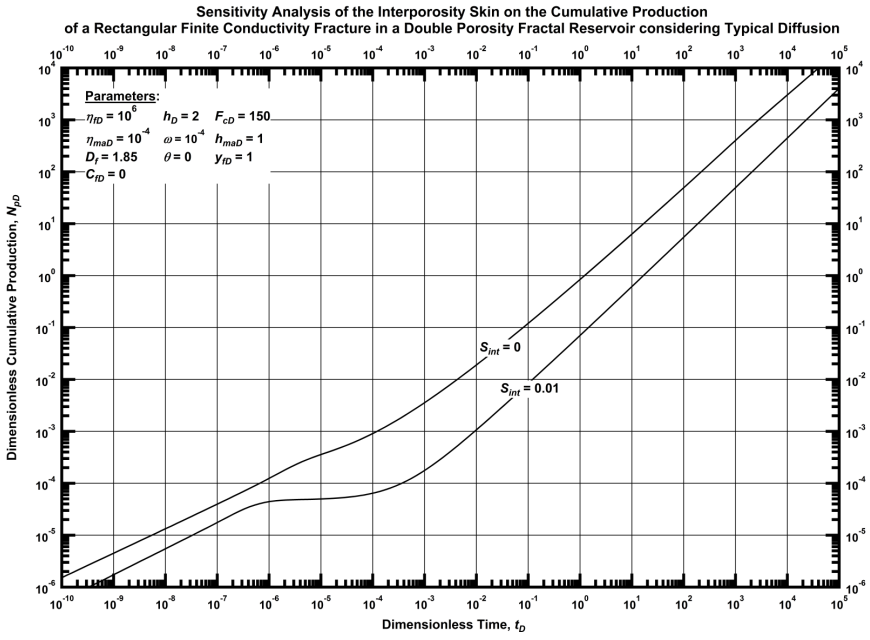

Figure 3.40 — Log-log plot of the dimensionless cumulative production function for a horizontal well intercepting a single rectangular hydraulic fracture of finite conductivity in a dual porosity fractal reservoir considering typical (constant) diffusion, for selected values of the interporosity skin (S_{int}). (constant pressure case)

Single Porosity Fractal Reservoirs with Anomalous Diffusion

In **Figs. 3.41 and 3.42** we present the comparisons of the constant rate solutions (dimensionless pressure and dimensionless pressure drop derivative) for the typical (constant) and anomalous diffusion models, for both the circular and rectangular fracture cases, respectively. We observed that the anomalous diffusion phenomena creates an additional pressure drop at early and intermediate-transient times, but the anomalous diffusion cases also exhibit a lower pressure drop at late times.

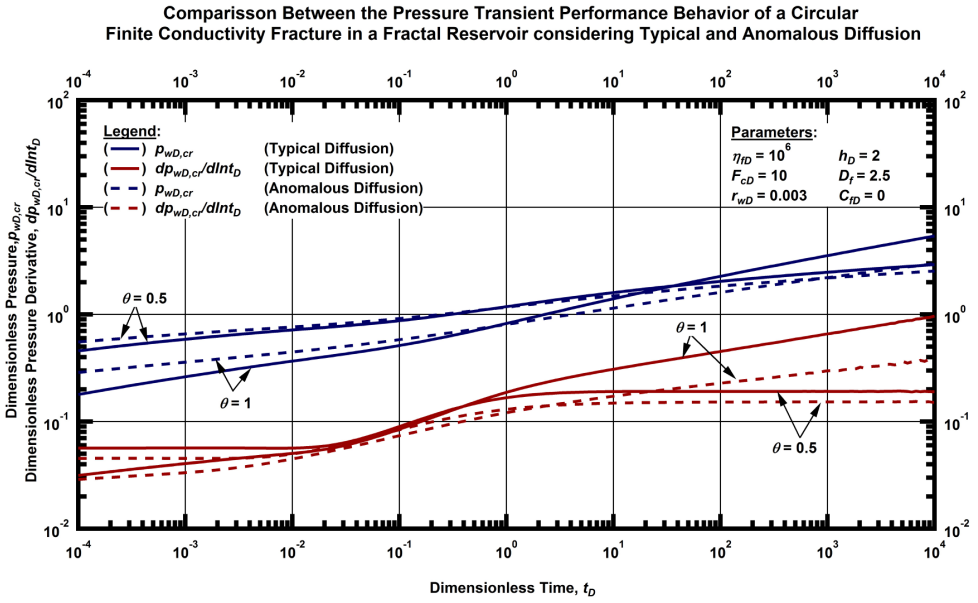

Figure 3.41 — Log-log plot of the dimensionless pressure and dimensionless pressure derivative profiles for a horizontal well intercepting a circular fracture of finite conductivity in a fractal reservoir considering typical (constant) and anomalous diffusions, for selected values of the (fractal) conductivity index (θ). (constant rate case)

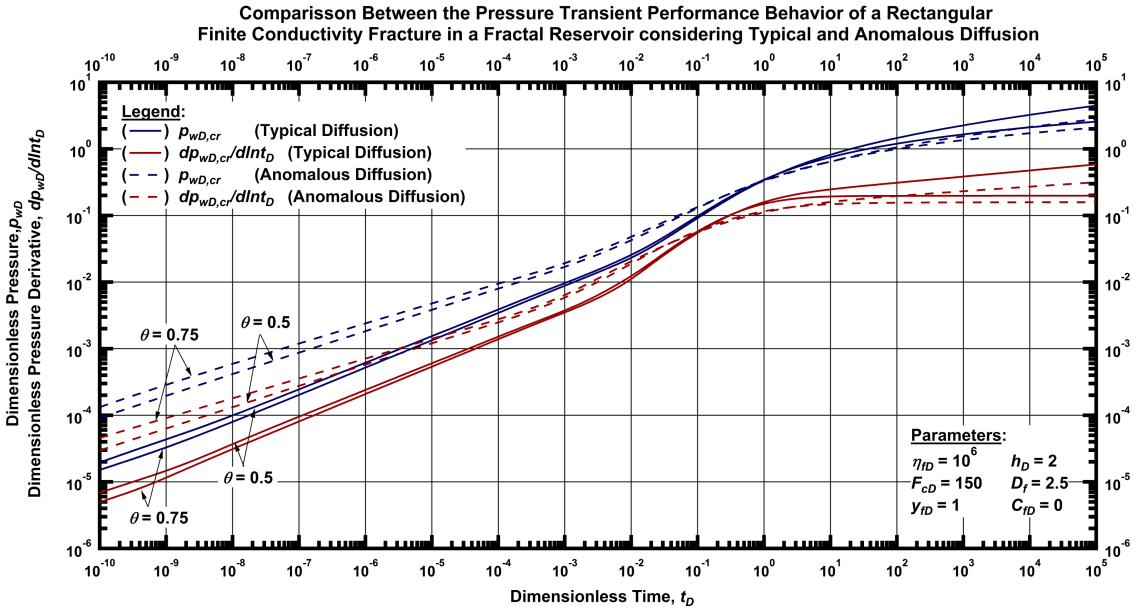

Figure 3.42 — Log-log plot of the dimensionless pressure and dimensionless pressure derivative profiles for a horizontal well intercepting a rectangular fracture of finite conductivity in a fractal reservoir considering typical (constant) and anomalous diffusions, for selected values of the (fractal) conductivity index (θ). (constant rate case)

The constant rate behaviors shown in **Figs. 3.41 and 3.42** imply by induction that at early and intermediate-transient times the typical (constant) diffusion cases yield higher flowrates and have lower flowrates at late-intermediate times (see **Figs. 3.43 and 3.44**). This behavior is confirmed as shown in **Figs. 3.43 and 3.44**, respectively — and it is important to note that the reservoir-transition features (occurring from $10^{-2} < t_D < 10^{1}$) are less salient in all of the anomalous diffusion cases.

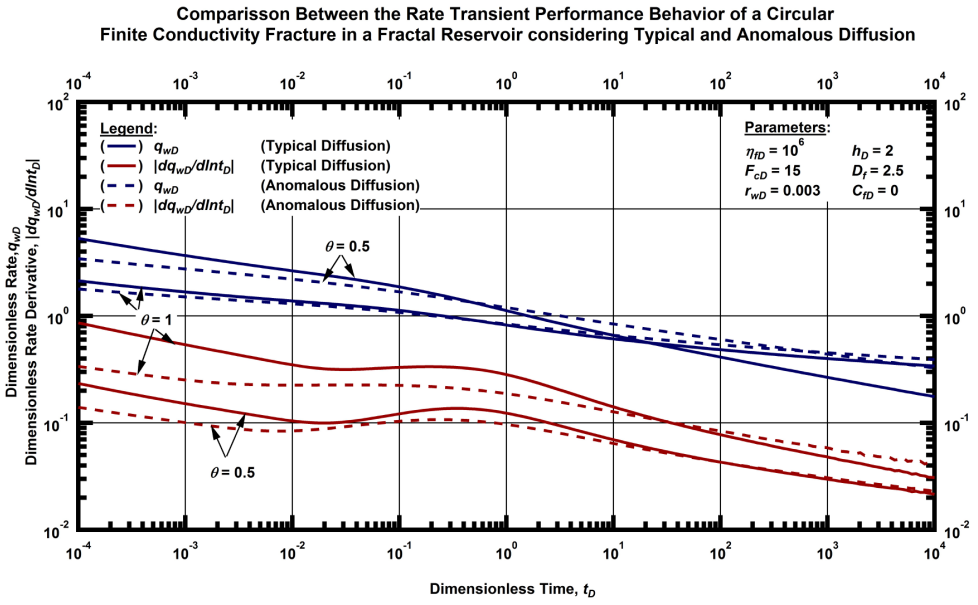

Figure 3.43 — Log-log plot of the dimensionless rate and dimensionless rate derivative profiles for a horizontal well intercepting a circular fracture of finite conductivity in a fractal reservoir considering typical (constant) and anomalous diffusions, for selected values of the (fractal) conductivity index (θ). (constant pressure case)

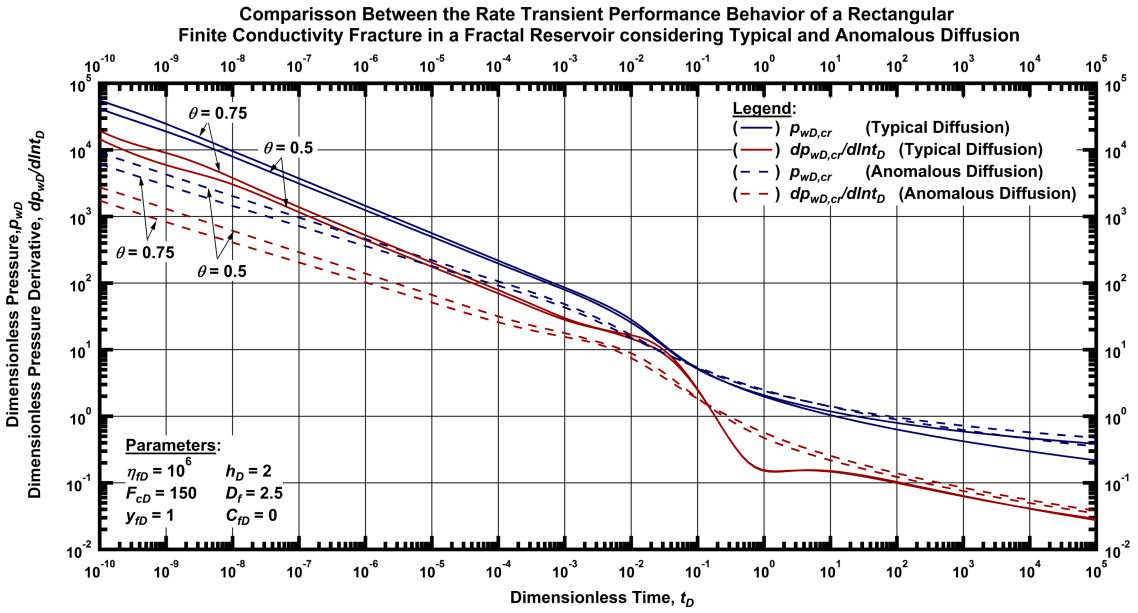

Figure 3.44 — Log-log plot of the dimensionless rate and dimensionless rate derivative profiles for a horizontal well intercepting a rectangular fracture of finite conductivity in a fractal reservoir considering typical (constant) and anomalous diffusions, for selected values of the (fractal) conductivity index (θ). (constant pressure case)

In our final comparison of dimensionless cumulative production profiles (see **Figs. 3.45 and 3.46**), we note that in terms of the ultimate cumulative production, the anomalous diffusion phenomenon does "improve" the hydrocarbon "recovery" in a fractal reservoir — however; this observation may not be general and should only be considered as "guidance." Obviously, the selection of a model (any model) must be validated based on diagnostic comparison with the actual performance data and all geological, completion, and reservoir data should also be incorporated into the model selection process.

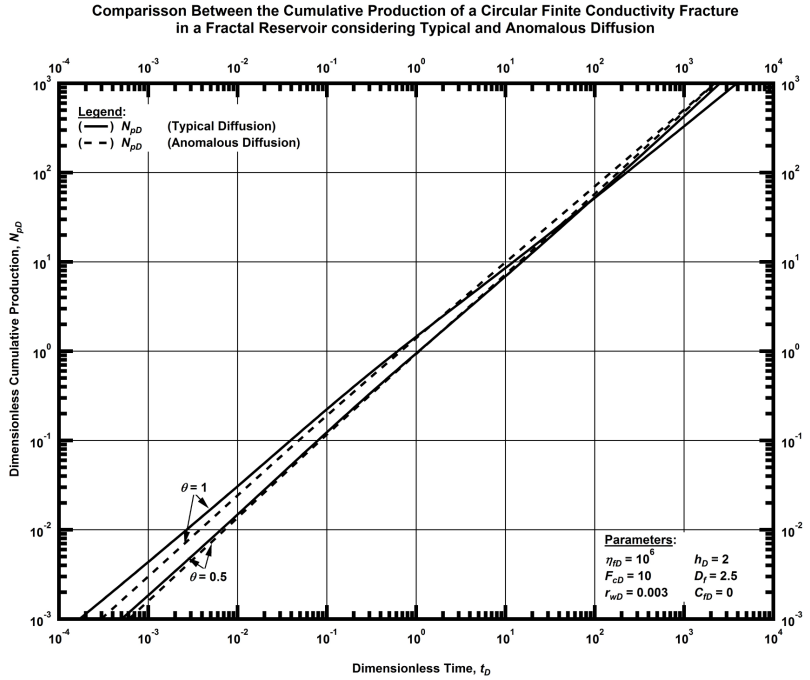

Figure 3.45 — Log-log plot of the dimensionless cumulative production profiles for a horizontal well intercepting a circular fracture of finite conductivity in a fractal reservoir considering typical (constant) and anomalous diffusions, for selected values of the (fractal) conductivity index (θ). (constant pressure case)

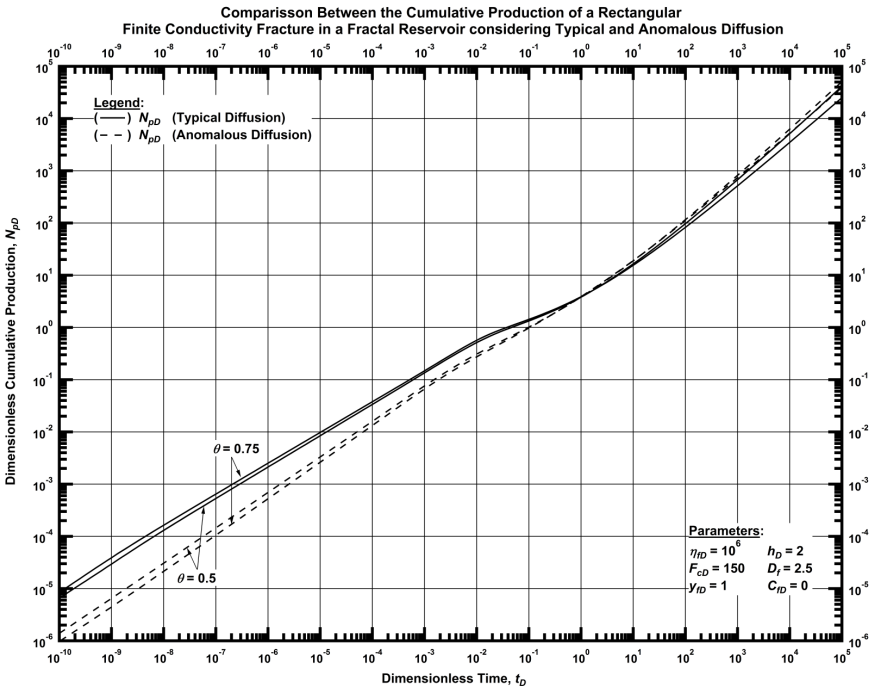

Figure 3.46 — Log-log plot of the dimensionless cumulative production profiles for a horizontal well intercepting a rectangular fracture of finite conductivity in a fractal reservoir considering typical (constant) and anomalous diffusions, for selected values of the (fractal) conductivity index (θ). (constant pressure case).

3.4. Summary

Ultimately, our goal is to demonstrate the viability of the fractal reservoir concept for the transient pressure and rate behavior of unconventional reservoirs. In this chapter we presented a simplified case considers a horizontal well intersecting a single hydraulic fracture, and while this concept can be generalized to consider an arbitrary number of fractures, the purpose of this simplified case is to establish the basis and feasibility of the concept from the standpoint of comparative behavior and diagnostic analysis functions. The extension to horizontal wells intercepting multiple hydraulic fractures is presented in Chapter IV.

CHAPTER IV

PRESSURE AND RATE-TRANSIENT ANALYSIS OF HORIZONTAL WELLS INTERCEPTING MULTIPLE HYDRAULIC FRACTURES WITHIN A FRACTAL RESERVOIR[2]

In this chapter, we present the procedure to apply the principle of superposition in space to extend the models presented in Chapter III to the case of a "multi-fractured horizontal well" (or MFHW) within a fractal reservoir. Additionally, we use the technique of image wells to create vertical boundaries that represent a fractal reservoir with finite thickness.

4.1. Development of the Model

Analogous to Larsen *et al.* (1994), we have used the principle of superposition in space to model the transient performance behavior of a MFHW in a fractal reservoir. We have considered two scenarios: (1) an unbounded fractal reservoir (infinite thickness) and (2) a fractal reservoir vertically bounded by two parallel boundaries (*i.e.*, a finite thickness reser-voir).

The principle of superposition in space takes into account the pressure effects of the individual elements (*i.e.*, the hydraulic fractures and boundaries) which define a system — specifically a MFHW within a fractal reservoir with infinite or finite thickness. In general, the pressure at the

[2] Reprinted with permission from "Pressure and Rate Transient Behavior of a Horizontal Well Intercepting Multiple Hydraulic Fractures within a Fractal Reservoir " by Valdes-Perez, A. R., Larsen, L., and Blasingame, T.A., 2018. *Unconventional Resources Technology Conference* (*URTeC*) *Proceedings*, URTeC-2902854. Copyright [2018] by Society of Petroleum Engineers, Inc.

wellbore for a system defined by a horizontal well intercepting multiple vertical fractures, along a length L_D, in a reservoir with boundaries can be defined by:

$$p_{wD,cr}(t_D) = p_{HF} + p_{BOU}, \quad (4.1)$$

where p_{HF} is the sum of the dimensionless drop of pressure of the hydraulic fractures and p_{BOU} is the sum of the dimensionless drop of pressure of the N_B boundaries. The sum of the dimensionless drop of pressure of the hydraulic fractures (p_{HF}) is mathematically defined as:

$$p_{HF} = \sum_{i=1}^{N_f} p_{fD,cr}(d_i, t_D), \quad (4.2)$$

where N_f is the number of hydraulic fractures and d_i is the distance from a defined observation point to the *i*-hydraulic fracture. In this work, we have assumed evenly spaced hydraulic fractures by a distance F_s between fractures (see **Fig. 4.1a**). The shape and orientation of the hydraulic fractures can be either circular and transverse or rectangular and longitudinal along the wellbore.

The dimensionless drop of pressure of each hydraulic fracture is computed using the models presented in Chapter III (Eq. 3.21 for circular fractures and Eq. 3.22 for rectangular fractures). Therefore, all the assumptions and dimensionless variables established in Chapter III are applicable in this chapter. To use such models in the case of a MFHW, we consider that the well produces only through the hydraulic fractures at a rate equal to:

$$q_i = \frac{q_t}{N_f}, \quad (4.3)$$

where q_t is the total flowrate (production) of the well. Eq. 4.3 implies that the inner boundary condition (*i.e.*, the "rate per fracture") is defined as the total flowrate (q_t) divided by the number

of fractures (N_f). For the case of a reservoir with infinite thickness, the dimensionless drop of pressure of the boundaries (p_{BOU}) is zero. For the finite thickness case, we have assumed that the horizontal well is drilled along the center of the formation, which is vertically delimitated by two parallel and impermeable boundaries (see **Fig. 4.1b**). Using the method of image wells, the dimensionless pressure drop at the boundaries (p_{BOU}) is:

$$p_{BOU} = 2\sum_{i=1}^{\infty} p_{D,cr}(l_{Di}, t_D), \quad \text{(4.4)}$$

where l_{Di} is the distance from the wellbore to the vertical axis of the i-image well. Given that the well is placed in a fractal reservoir, the dimensionless pressure of the image wells is:

$$p_{D,cr}(l_D, t_D) = \frac{h_D l_D^{[1-\beta]/2}}{2[\theta+2]\Gamma[1-v]}\Gamma\left[-v, \frac{l_D^{[\theta+2]}}{[\theta+2]^2 t_D}\right] \text{ (where } v=[1-\beta]/[\theta+2]). \quad \text{(4.5)}$$

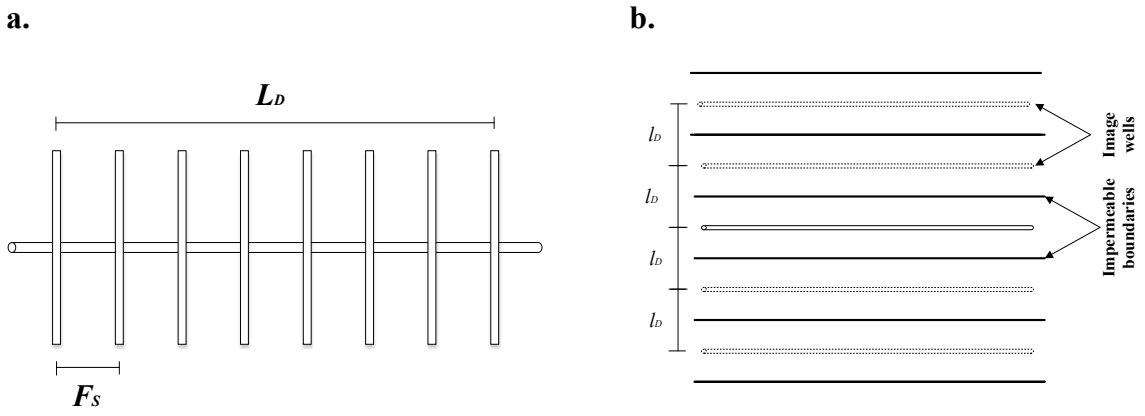

Figure 4.1 — **a.** Schematics of a horizontal well intercepting evenly spaced multiple fractures, and **b.** Schematics of the use of image wells to model a horizontal well placed in the center of a formation vertically bounded by two impermeable boundaries.

For these models, the wellbore storage effects can be included by applying the Laplace transform to Eq. 4.1 and subsequently, using the scheme defined in Chapter I. The inverse Laplace transform for the cases presented in this chapter is numerically made using the Stehfest algorithm.

4.2. Results and Discussion

Larsen *et al.* (1994) and Raghavan (1997) showed that a MFHW behaves as an equivalent system of a well intercepting a single hydraulic fracture. We have constructed cases similar to those presented by Larsen *et al.* (1994) and generated type curves for the resulting pressure and rate-transient performance behaviors. We developed these type curves by varying the number of fractures (N_f) for fixed values of the conductivity of the fractures (F_{cD}) and the fractal parameters (D_f and θ). We present these type curves in Appendix G.

We analyzed the influence of the number of fractures (N_f) in the pressure and rate transient performance behaviors of a MFHW in a fractal reservoir and we concluded that: (1) the pressure and rate-transient signatures of a horizontal well intercepting multiple hydraulic fractures in a fractal reservoir can behave as an equivalent system created by a horizontal well intercepting a single hydraulic fracture, and (2) the spacing of the fractures can create a flow period that corresponds to the interference of flow between hydraulic fractures. In short, the influence of the number of fractures (N_f) and the spacing between the fractures (F_s) in the pressure transient performance behavior of a horizontal well intercepting multiple hydraulic fractures in a fractal reservoir is analogous to the one studied by Larsen *et al*. (1994) for a 3*D* (spherical) reservoir.

Periods of Flow of Horizontal Wells Intercepting Multiple Hydraulic Fractures in a Fractal Reservoir

For the analyses presented in this section, we selected cases with a short spacing between the hydraulic fractures (F_s =5/8) and considered that all the fractures in the system have the same characteristics, *i.e.*, they have the same dimensionless fracture conductivity (F_{cD}) and geometry.

We studied three scenarios of the dimensionless conductivity and hydraulic diffusivity of the fractures: (1) high (F_{cD} =1000 and η_{fD}=10^6), (2) intermediate (F_{cD} =10 and η_{fD}=10^5), and (3) low (F_{cD} =1 and η_{fD}=10^4).

In **Fig. 4.3** we present the pressure transient behavior of a horizontal well intercepting multiple *circular transverse vertical* fractures in a fractal reservoir for selected values of the conductivity of the fractures (F_{cD}), considering infinite or finite thickness. We present the analogous case for *rectangular longitudinal* fractures in **Fig. 4.4**. In these plots, we have identified the characteristic three period of flows for a well intercepting hydraulic fractures: (1) fracture flow at early times, (2) fracture-reservoir interaction flow at intermediate times, and (3) pseudo-fractal flow at late-times. The fracture-reservoir interaction flow is divided into two sub-periods: Early Radial-Fractal (*ERF*) and Late Radial-Fractal (*LRF*) occur for circular fractures and Early Linear-Fractal (*ELF*) and Late Linear-Fractal (*LLF*) occur for rectangular fractures. The *ERF* and *ELF* sub-periods are analogous "bilinear flow" which exists for the case of finite-conductivity fractures in a homogenous, infinite-acting reservoir.

We observed that the effect of interference between fractures is more significant for wells intercepting multiple *low* conductivity fractures. We conclude from the cases with hydraulic fractures having low F_{cD}-values (presented in **Figs. 4.3 and 4.4**) that these cases exhibit additional sub-periods of flow during intermediate times compared to cases with *high* F_{cD}-values. This behavior is clear for the case with circular fractures in a reservoir with infinite thickness (*i.e.*, **Fig. 4.3**), where the pressure derivative signature of the *ERF* sub-period flow is followed by a power-law (straight-line with slope approximately of 1:3) in the range $10^{-2} < t_D < 10^0$. We also observed this phenomenon for the case with rectangular fractures case (*i.e.*, **Fig. 4.4**) — however; we noted

that the interference between fractures for this case is more subtle, exhibiting a smooth transition from the *ELF* sub-period into the pseudo-fractal flow period.

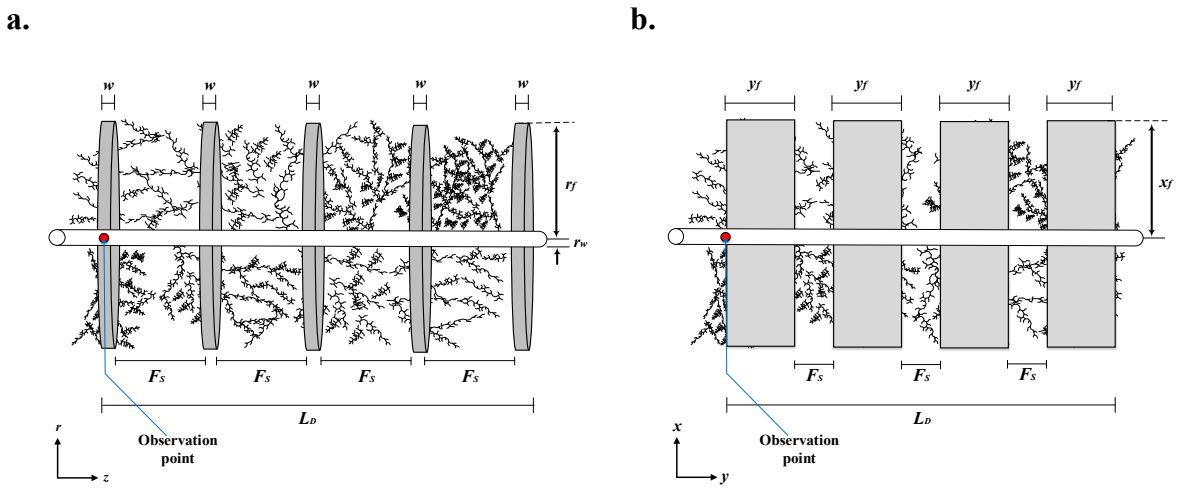

Figure 4.2 — Schematics of a horizontal well intercepting multiple hydraulic fractures in a fractal reservoir with infinite thickness: **a.** circular transverse, and **b.** rectangular longitudinal hydraulic fractures.

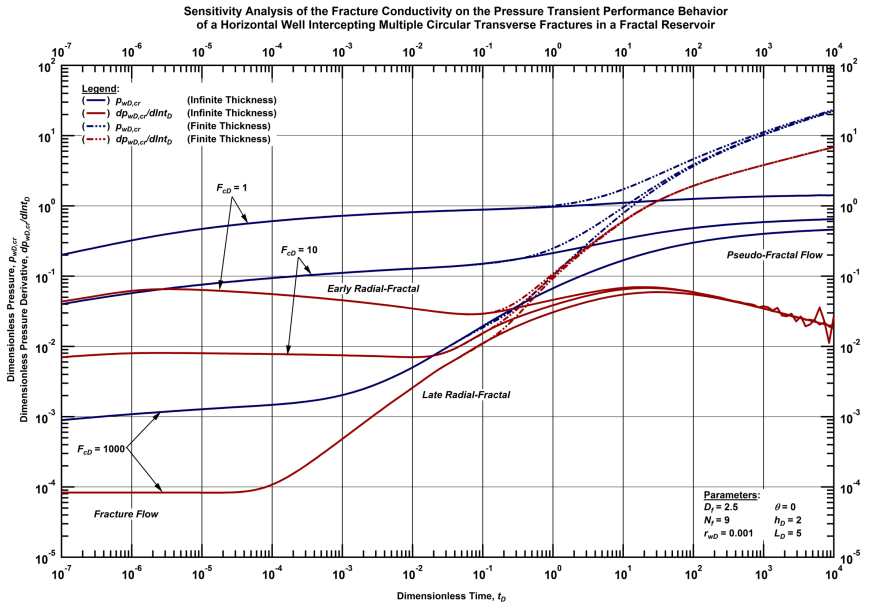

Figure 4.3 — Log-log plot of the dimensionless pressure and dimensionless pressure derivative functions for a horizontal well intercepting multiple circular transverse hydraulic fractures in a fractal reservoir with D_f =2.5 and θ=0 for selected values of the Fracture Conductivity (F_{cD}).

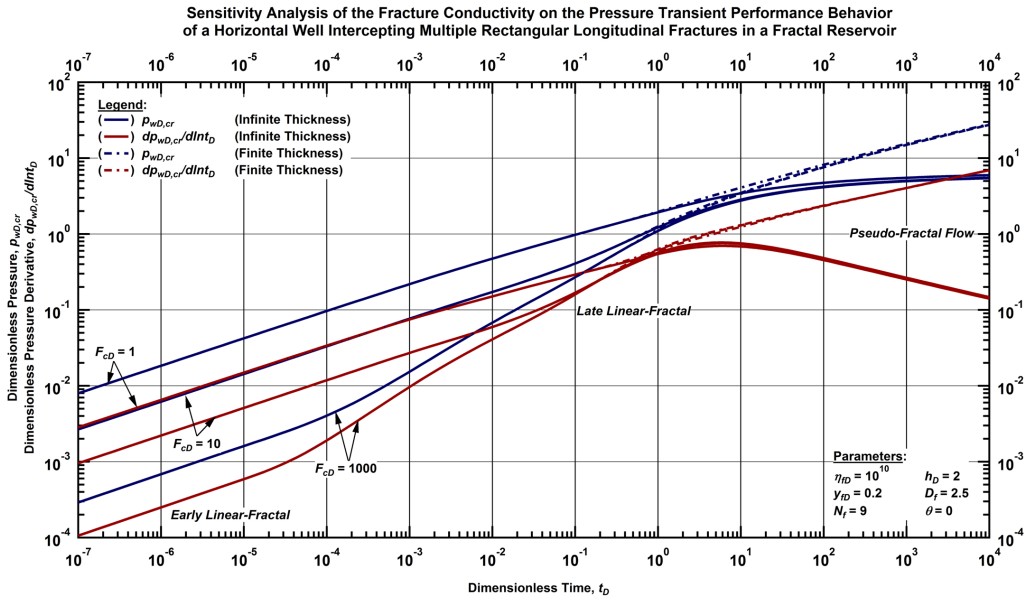

Figure 4.4 — Log-log plot of the dimensionless pressure and dimensionless pressure derivative functions for a horizontal well intercepting multiple rectangular longitudinal hydraulic fractures in a fractal reservoir with D_f =2.5 and θ=0 for selected values of the Fracture Conductivity (F_{cD}).

The pressure derivative function for the F_{cD}=1 case given in **Fig. 4.3** shows numerical instability at t_D>10^3, which is caused by the computation of extremely small arguments of the Modified Bessel Functions in the analytical solution for the circular fracture, and the subsequent numerical solution of the system of equations. This computational instability is systematic, and we have also observed it in the constant-pressure solutions — there may be a mechanism to eliminate/mitigate this instability, but for the purpose of the present work we will note this as an anomaly.

At late-times (pseudo-fractal flow), we noted that the inclusion of parallel impermeable boundaries in a fractal reservoir creates power-law signatures in the pressure and pressure derivative functions (**Figs. 4.3 and 4.4**). As might be expected, the slopes of these power-law signatures are related to the fractal parameters of the reservoir (v and D_f) used in Eq. 4.5. Although different combinations of the D_f and θ-values can yield the same value of v, the power-law behavior (specifically, the

slope of the straight-line in the log-log plot) for the pseudo-fractal flow period depends on the combination of these parameters. We ran several combinations of these parameters and found linear correlations between the fractal parameters and the slope of the pressure derivative function for a fractal reservoir bounded by two parallel impermeable boundaries and present these correlations in **Fig. 4.5**. Except for the upper end of the trend for the D_f=3 case shown in **Fig. 4.5**, the slope of the pressure derivative function for a fractal reservoir vertically bounded by parallel impermeable boundaries can be generated by the equation:

$$v' = v + \frac{1-v}{D_f}, \quad \text{..... (4.6)}$$

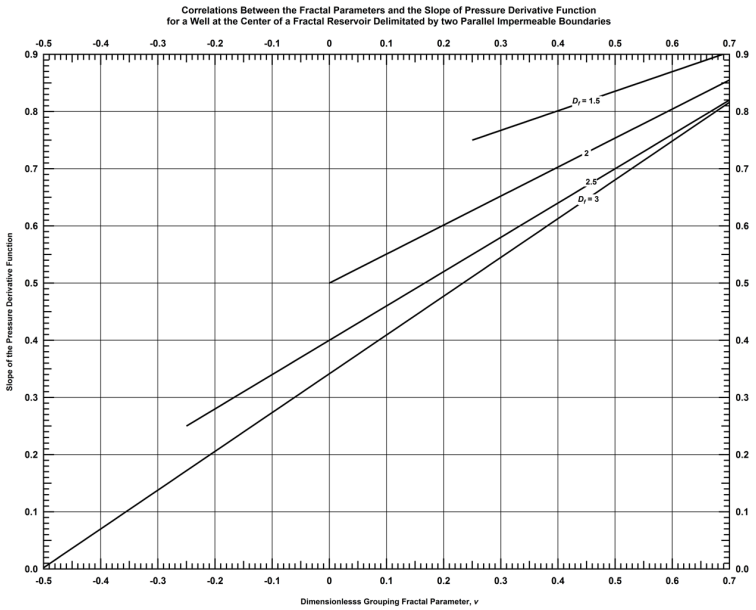

Figure 4.5 — Correlation between the grouping parameter (v) and the slope of the pressure derivative of a fractal reservoir delimitated by two impermeable boundaries.

Influence of the Fractal Parameters in the Pressure and Rate Transient Performance Behaviors

In Chapter III, we showed that a horizontal well intercepting a single hydraulic fracture in a fractal reservoir with low fractal dimension (D_f) and/or higher conductivity index (θ) yields lower values of the dimensionless pressure drop during early and intermediate times, compared to a well with the same conditions but placed in a reservoir with higher D_f and/or low θ-values. This trend is reversed at late times, *i.e.*, the drop of pressure is lower in a well intercepting a hydraulic fracture in a fractal reservoir with high D_f and/or low θ-values. Consequently, the higher flow rates at early and intermediate times are observed in wells intercepting a single hydraulic fracture in a fractal reservoir with a low fractal dimension (D_f) and/or a high conductivity index (θ) the trend is also reversed at late times. As a summary statement, we expect to observe similar behavior for the multi-fracture horizontal well (MHFW) cases considered in this Chapter.

Sensitivity to the Fractal Dimension (D_f) — Circular Hydraulic Fractures

Figure 4.6 shows the impact of the fractal dimension (D_f) on the pressure and pressure transient derivative functions for a horizontal well intercepting multiple (9) hydraulic circular transverse fractures with high-conductivity. In this plot, we observe that the higher D_f-values yield a higher dimensionless pressure drop during early and intermediate times, whereas at late times the pressure drop is lower for high D_f-values. Consequently, lower D_f-values yield higher flowrates (and cumulative production) at early and intermediate times and lower flowrates (and cumulative production) at late times (see **Figs. 4.7 and 4.8**). The change in these trends is defined by an intersection/inflection point of all the dimensionless pressure curves located at $t_D \approx 2$ in **Fig. 4.6**. We have also observed intersection points in the pressure derivative ($t_D \approx 0.5$), in the dimensionless

rate ($t_D \approx 0.07$ of **Fig. 4.7**), and in the dimensionless cumulative production curves ($t_D \approx 1.5$ of **Fig. 4 8**).

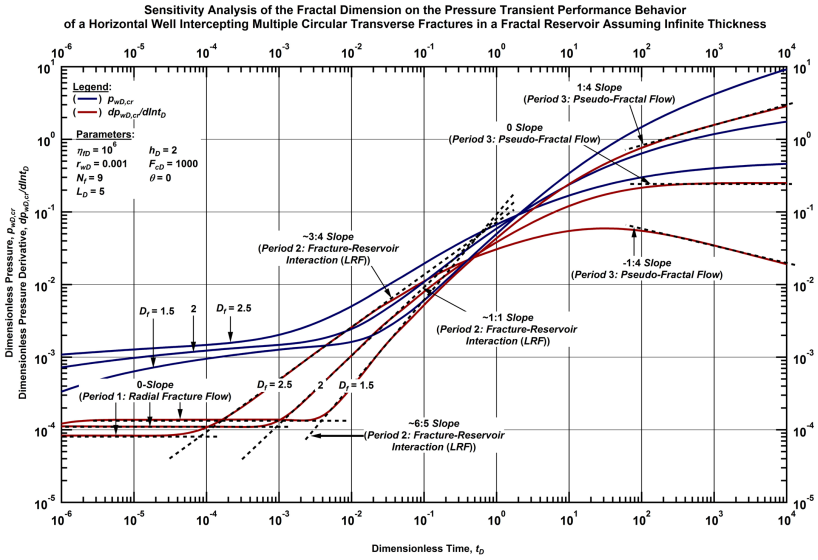

Figure 4.6 — Log-log plot of the dimensionless pressure and dimensionless pressure derivative functions for a horizontal well intercepting multiple circular transverse hydraulic fractures with high conductivity in a fractal reservoir for selected values of the fractal dimension (D_f), assuming infinite thickness. (constant-rate case)

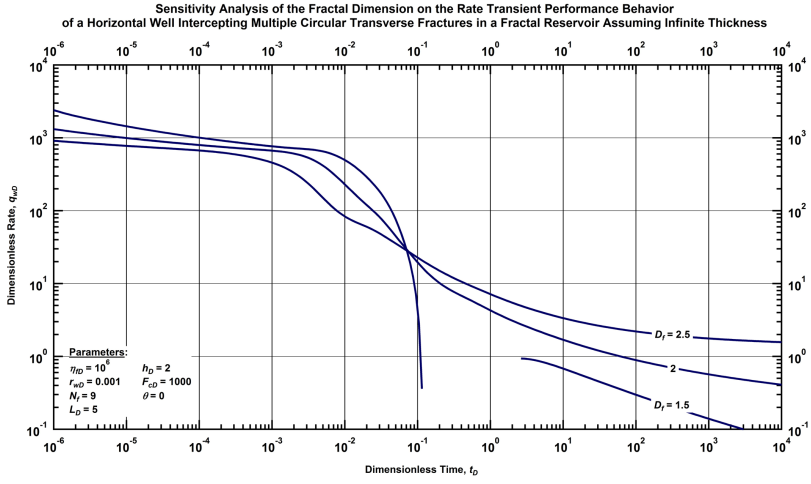

Figure 4.7 — Log-log plot of the dimensionless rate and dimensionless rate derivative functions for a horizontal well intercepting multiple transverse hydraulic fractures with high conductivity in a fractal reservoir for selected values of the fractal dimension (D_f), assuming infinite thickness. (constant-pressure case)

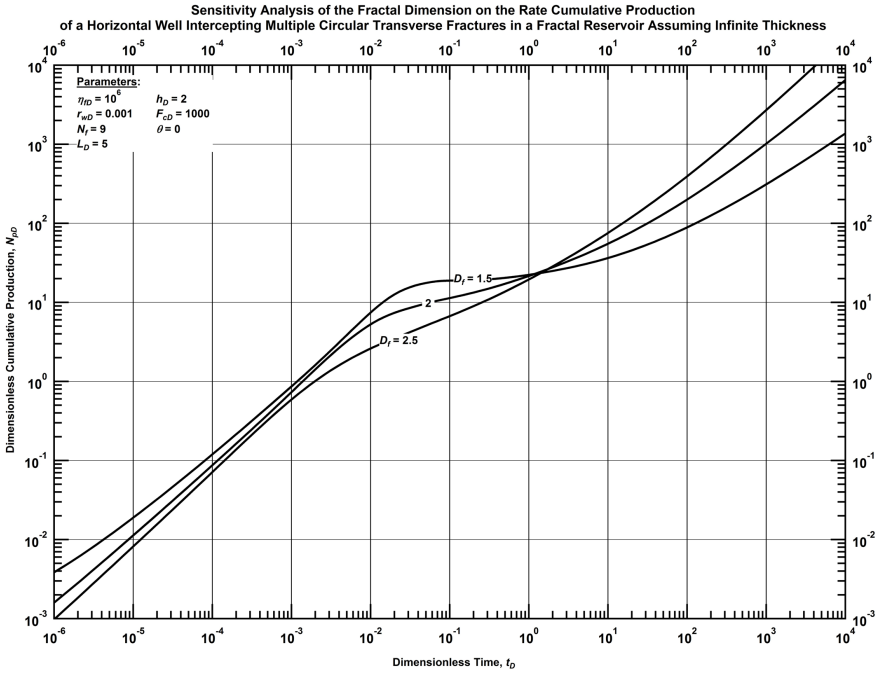

Figure 4.8 — Log-log plot of the dimensionless cumulative production function for a horizontal well intercepting multiple transverse hydraulic fractures with high conductivity in a fractal reservoir for selected values of the fractal dimension (D_f), assuming infinite thickness. (constant-pressure case)

Based on the signatures of the pressure derivatives of the cases presented in **Fig. 4.6**, we summarized the start and the end of their periods of flow in **Table 1**. In these cases, the pressure derivative functions provide constant values during "Period 1," which is characteristic of the radial (fracture) flow. The constant value of the pressure derivative is also lower as the D_f-value increases. The three cases presented in **Fig. 4.6** for "Period 3" yield straight-lines in the pressure derivative function with slope equal to the v-parameter, which is characteristic of the pseudo-fractal flow regime. During "Period 2," the pressure derivative curves show power-law behaviors that correspond to the *LRF* sub-period of flow and are followed by a prolonged transition period (approximately two log-cycles), where this transition period is the result of the interference between hydraulic fractures. For D_f= 2.5, the *LRF* sub-period yields a straight-line with a slope of

3:4, whereas the slope for D_f=2 is slightly below 1 and above 1 (5:4) for D_f=1.5. We consider that the fractional values of the slopes that approach unity (exhibited by the *LRF* sub-periods for D_f =2 and D_f=1.5) are the result of the combined effect of the fractal nature of the reservoir and the finite extent of the hydraulic fractures.

We conclude that horizontal wells intercepting multiple fractures in fractal reservoir with low fractal dimension, D_f (consequently low *v*-values) (1) show shorter fracture flow periods and *LRF* sub-periods and (2) yield steeper straight-lines in the pressure derivative during "Period 2."

The dimensionless flowrate function for D_f=1.5 presented in **Fig. 4.7** shows a disruptive trend within the period of dimensionless time defined by 10^{-1} and 10^{1}. We associate this erratic behavior with the computation of the uniform flux solution using the "Fractal Point Source" function for *v*-values less than 2 (see Appendix H).

Table 4.1 — Definition of flow periods, based on the pressure derivative, for the sensitivity analysis of the fractal dimension (D_f) on the pressure transient performance behavior for a horizontal well intercepting multiple circular transverse hydraulic fractures.

D_f	*v*	Period 1	Period 2	Period 3
2.5	-0.25	$t_D < 2\text{x}10^{-5}$	$2\text{x}10^{-4} < t_D < 4\text{x}10^{-2}$ (LRF)	$2\text{x}10^{2} < t_D$
2.0	0	$t_D < 6\text{x}10^{-4}$	$2\text{x}10^{-3} < t_D < 3\text{x}10^{-2}$ (LRF)	$2\text{x}10^{2} < t_D$
1.5	0.25	$t_D < 2\text{x}10^{-3}$	$5\text{x}10^{-3} < t_D < 2\text{x}10^{-2}$ (LRF)	$2\text{x}10^{2} < t_D$

Sensitivity to the Conductivity Index (θ) — Circular Fractures

Figure 4.9 presents the influence of the conductivity index (θ) on the pressure and pressure transient derivative functions for a horizontal well intercepting multiple circular transverse vertical fractures. Analogous to the sensitivity analysis for the fractal dimension (D_f), we observe an intersection/inflection point of the dimensionless pressure and pressure derivative curves located

at $t_D \approx 3$ and $t_D \approx 0.7$, respectively. Similarly, the constant-pressure solutions also show such intersection points. Considering the rate-transient performance behavior shown in **Fig. 4.10** this feature is located at $t_D \approx 0.5$, whereas for the dimensionless cumulative production shown in **Fig. 4.11** this feature is observed at $t_D \approx 2$, where it is logical that such features would be "delayed" for the cumulative production case considering the nature of a cumulative function.

For dimensionless times (t_D) greater than 3, the systems with higher θ-values (consequently, high v-values) yield larger dimensionless pressure drops. This implies that for dimensionless times greater than 0.5, the systems with higher θ-values yield lower flowrates. These tendencies are opposite for t_D<3 and t_D<0.5 in regard to the pressure and the flowrate, respectively.

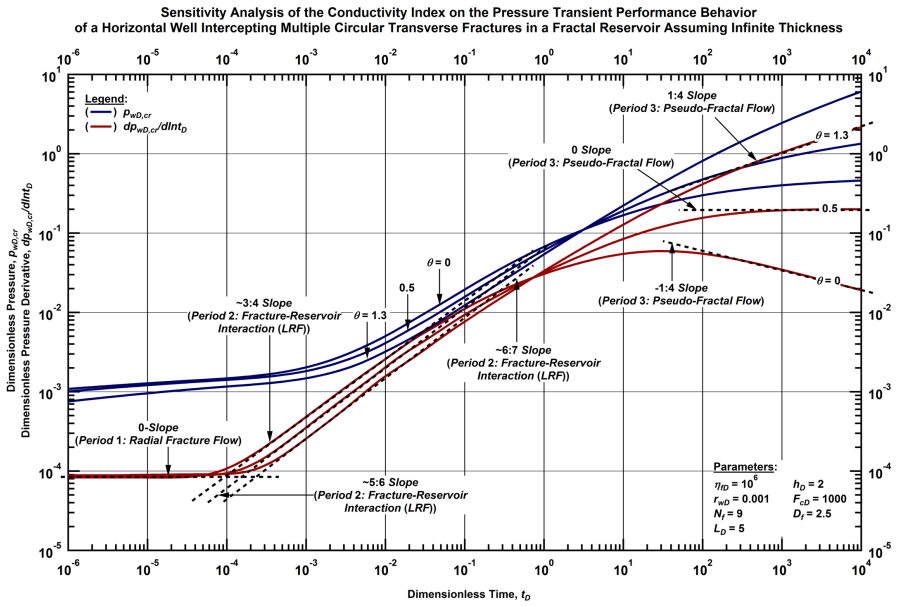

Figure 4.9 — Log-log plot of the dimensionless pressure and dimensionless pressure derivative functions for a horizontal well intercepting multiple transverse hydraulic fractures with high conductivity in a fractal reservoir for selected values of the conductivity index (θ), assuming infinite thickness. (constant-rate case)

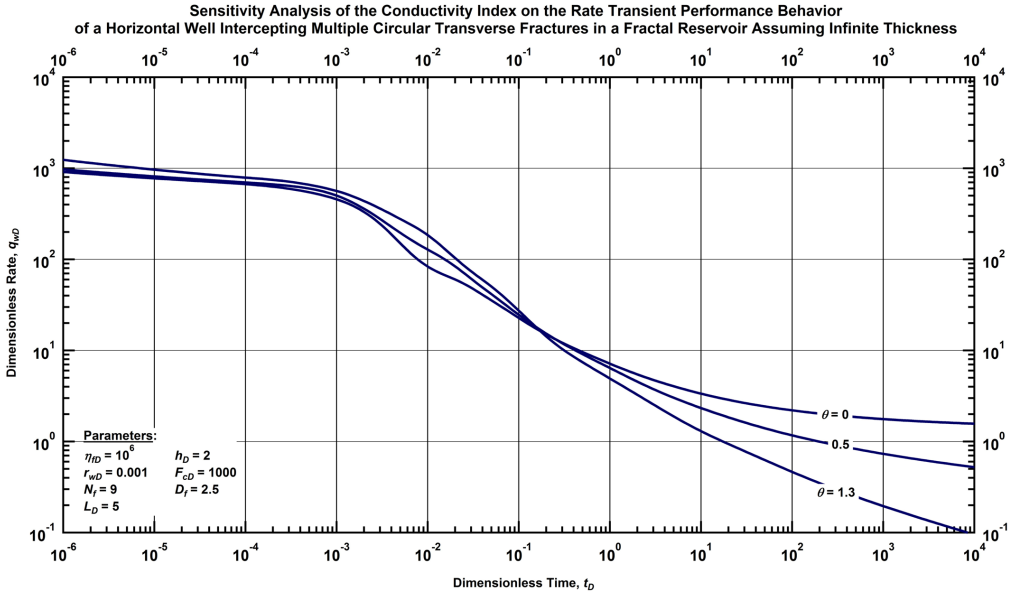

Figure 4.10 — Log-log plot of the dimensionless rate and dimensionless rate derivative functions for a horizontal well intercepting multiple transverse hydraulic fractures with high conductivity in a fractal reservoir for selected values of the conductivity index (θ), assuming infinite thickness. (constant-pressure case)

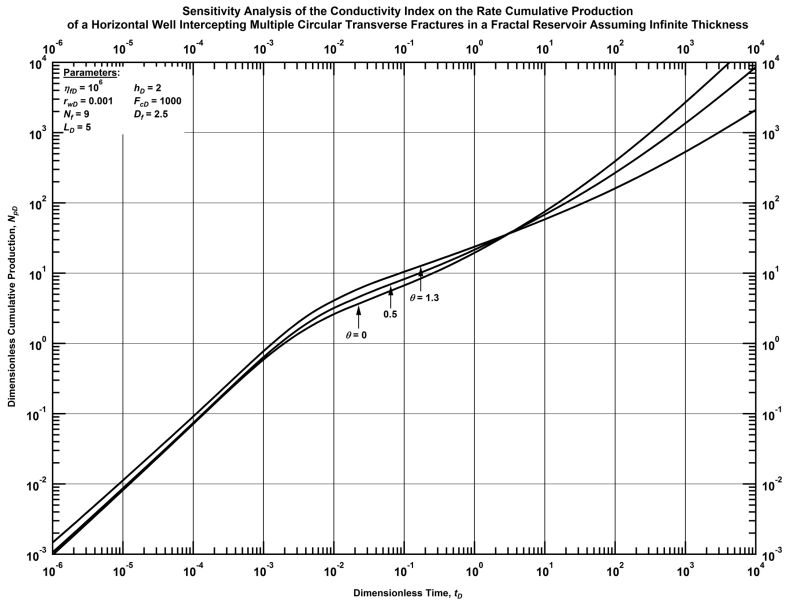

Figure 4.11 — Log-log plot of the dimensionless cumulative production function for a horizontal well intercepting multiple transverse hydraulic fractures with high conductivity in a fractal reservoir for selected values of the conductivity index (θ), assuming infinite thickness. (constant-pressure case)

As in the previous analyses, we have identified the flow periods in **Fig. 4.9**, using the pressure derivative functions and summed them up in **Table 4.2**. In this case, the pressure derivative for all cases collapse into a single trend at early times (depicting radial (fracture) flow). The duration of the fracture flow is longer for higher θ-values (higher v-values). After the fracture flow period, we observe the appearance of the *LRF* sub-period, which yields straight-lines with slopes of 3:4, 4:5, and 6:7 for θ-values of 0, 0.5 and 1.3, respectively. At late times (Period 3), the signatures of the pressure derivative functions yield straight-lines on a log-log scale with slopes equal to the v-parameter. Similar to the sensitivity analyses presented for the fractal dimension (D_f), we identified a transition period between the *LRF* and the pseudo-fractal flow for all of the cases which illustrate pressure interference between the hydraulic fractures.

In general, we note that the conductivity index (θ) has a similar influence on the pressure transient performance behavior in horizontal wells intercepting multiple fractures in a fractal reservoir as the fractal dimension (D_f) — that is, the systems with higher θ-values (consequently lower v-values) (1) show longer fracture flow periods and shorter *LRF* sub-periods and (2) yield steeper straight-lines in the pressure derivative during "Period 2." However, we also observe that the behavioral features caused by the conductivity index (θ) are less dramatic than those caused by the fractal dimension (D_f).

Table 4.2 — Definition of flow periods, based on the pressure derivative, for the sensitivity analysis of the conductivity index (θ) on the pressure transient performance behavior for a horizontal well intercepting multiple circular transverse hydraulic fractures.

θ	v	Period 1	Period 2	Period 3
0	-0.25	$t_D < 2\text{x}10^{-5}$	$2\text{x}10^{-4} < t_D < 4\text{x}10^{-2}$ (LRF)	$2\text{x}10^{2} < t_D$
0.5	0	$t_D < 1\text{x}10^{-4}$	$3\text{x}10^{-4} < t_D < 1\text{x}10^{-2}$ (LRF)	$2\text{x}10^{2} < t_D$
1.3	0.25	$t_D < 2\text{x}10^{-4}$	$5\text{x}10^{-4} < t_D < 8\text{x}10^{-3}$ (LRF)	$2\text{x}10^{2} < t_D$

Sensitivity to the Fractal Dimension (D_f) — Rectangular Hydraulic Fractures

In **Fig. 4.12**, we present the sensitivity analysis of the fractal dimension (D_f) in the dimensionless pressure and dimensionless pressure derivative functions for a horizontal well intercepting multiple (9) rectangular longitudinal hydraulic fractures of high fracture conductivity. Similar to the cases for a horizontal well intercepting multiple circular transverse fractures, we observe an intersection/inflection point of the dimensionless pressure curves located at $t_D \approx 2$ and at $t_D \approx 0.5$ in the dimensionless pressure derivative curves. For $t_D < 2$, the high D_f-values (*i.e.*, low v-values) yield a higher dimensionless pressure drop, which results in lower flowrates (see **Fig. 4.13**). These trends are reversed at t_D-values above the intersection point, *i.e.*, lower pressure drop and higher flowrates for higher D_f-values —consequently, lower v-values — for $t_D > 2$. In the case of the cumulative production (**Fig. 4.14**), we observe three intersection points instead of one: (1) at $t_D \approx 1$ between the D_f-curves of 2 and 2.5, (2) at $t_D \approx 7$ between the D_f-curves of 2.5 and 1.5, and (3) at $t_D \approx 15$ between the D_f-curves of 1.5 and 2.

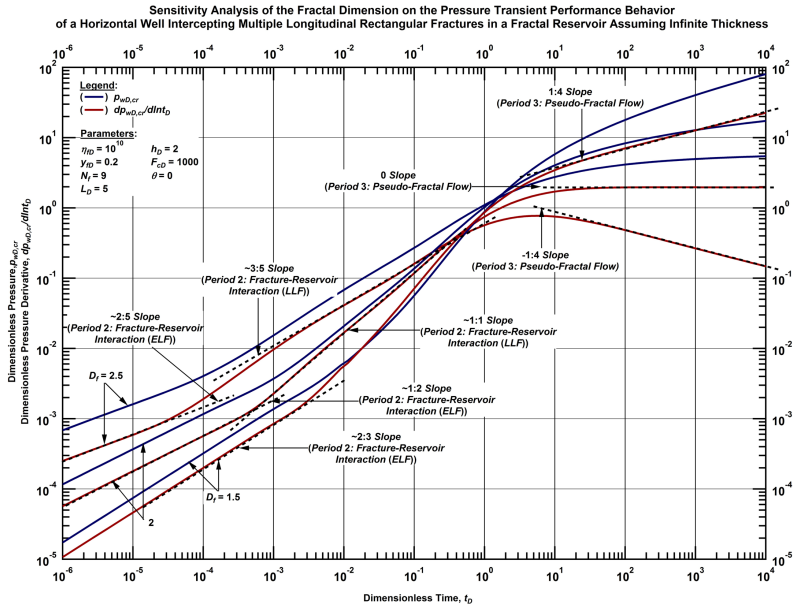

Figure 4.12 — Log-log plot of the dimensionless pressure and dimensionless pressure derivative functions for a horizontal well intercepting multiple longitudinal hydraulic fractures with high conductivity in a fractal reservoir for selected values of the fractal dimension (D_f), assuming infinite thickness. (constant-rate case)

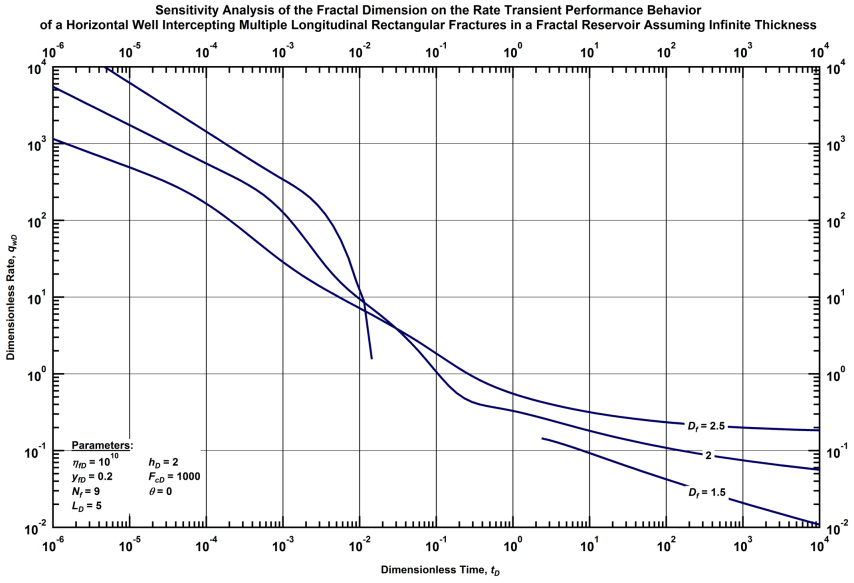

Figure 4.13 — Log-log plot of the dimensionless rate and dimensionless rate derivative functions for a horizontal well intercepting multiple longitudinal hydraulic fractures with high conductivity in a fractal reservoir for selected values of the fractal dimension (D_f), assuming infinite thickness. (constant-pressure case)

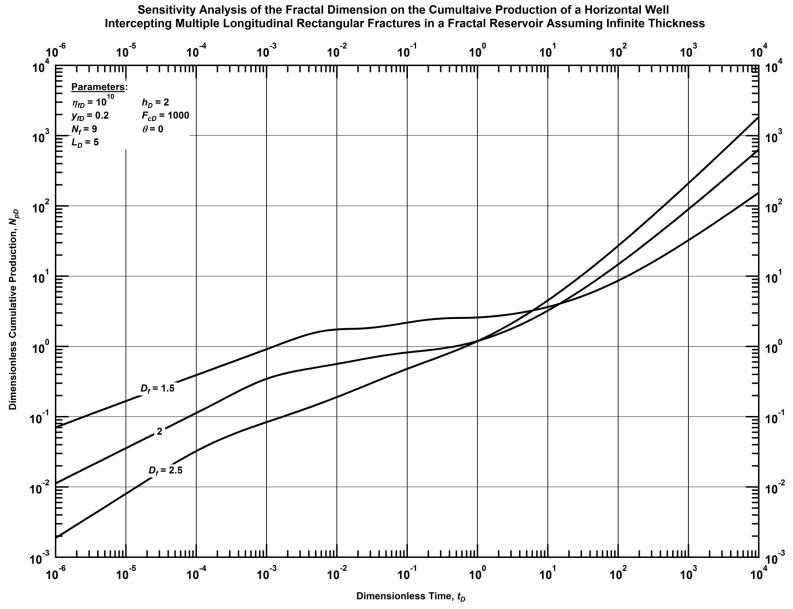

Figure 4.14 — Log-log plot of the dimensionless cumulative production function for a horizontal well intercepting multiple longitudinal hydraulic fractures with high conductivity in a fractal reservoir for selected values of the fractal dimension (D_f), assuming infinite thickness. (constant-pressure case)

In **Table 4.3** we present a summary of the flow periods that we identified in the signatures of the dimensionless pressure derivative functions for the cases presented in **Fig. 4.12**. At late times, the pseudo-fractal flow period behaves in the same manner as in the circular fracture cases — *i.e.*, the dimensionless pressure derivative functions yield straight lines with slopes equal to their corresponding *v*-value in the log-log plot. For the case of "Period 2," for D_f=2.5 we observe two power-law trends with slopes of approximately of 2:5 and 3:5 which correspond to the *ELF* and *LLF* sub-periods. Similarly, during "Period 2," for D_f=2, we observe a half-slope behavior during the *ELF* sub-period and a power-law behavior with slope slightly below 1 during the *LLF* sub-period.

We also observed that, for the case defined by D_f = 1.5, a power-law trend with a slope approximately of 2:3 that corresponds to the *ELF* sub-period is observed. We could not (specifically) identify the LLF sub-period for the D_f =1.5 case — instead, we observed that the dimensionless pressure derivative function is higher than the dimensionless pressure function in the t_D range defined by $0.03<t_D<1$ (which is a somewhat anomalous behavior). Similar to the circular transverse fractures case, this case has an anomalous flowrate function (**Fig. 4.13**) in the t_D range defined by $10^{-2}<t_D<10^2$ - specifically, zero flowrates are observed in this region. The behavior of the flowrate functions in **Fig. 4.13** leads to observation of the "wavy" and "flat" portions observed in the dimensionless cumulative production (**Fig. 4.14**).

Table 4.3 — Definition of flow periods, based on the pressure derivative, for the sensitivity analysis of the fractal dimension (D_f) on the pressure transient performance behavior for a horizontal well intercepting multiple rectangular longitudinal hydraulic fractures.

D_f	v	Period 1	Period 2	Period 3
2.5	-0.25	—	$1x10^{-6}<t_D<2x10^{-5}$ (ELF) $1x10^{-3}<t_D<1x10^{0}$ (LLF)	$2x10^{2}<t_D$
2.0	0	—	$1x10^{-6}<t_D<5x10^{-4}$ (ELF) $1x10^{-6}<t_D<5x10^{-1}$ (LLF)	$2x10^{2}<t_D$
1.5	0.25	—	$1x10^{-6}<t_D<3x10^{-3}$ (ELF)	$2x10^{2}<t_D$

Sensitivity to the Conductivity Index (θ) — Rectangular Fractures

The sensitivity analyses considering variations in the conductivity index (θ) on the pressure and rate-transient performance behaviors are shown in **Figs. 4.15 and 4.16**, respectively. Again, we observed an intersection point for the dimensionless pressure curves at $t_D \approx 1$ and at $t_D \approx 0.2$ in the dimensionless pressure derivative curves (**Fig. 4.15**). However, the dimensionless flowrate (**Fig. 4.16**) and the dimensionless cumulative production (**Fig. 4.17**) do have exhibit "crossovers," but

not a unique intersection point. Although we do not observe a unique intersection point in the rate-transient performance behavior (**Fig. 4.16**) and the dimensionless cumulative production (**Fig. 4.17**), the influence of the conductivity index (θ) is consistent with the circular transverse vertical fractures case. This means that the higher the θ-value, the higher flow dimensionless pressure drop and the lower the dimensionless flowrate at early and inter-mediate times and the trend reverses at late times.

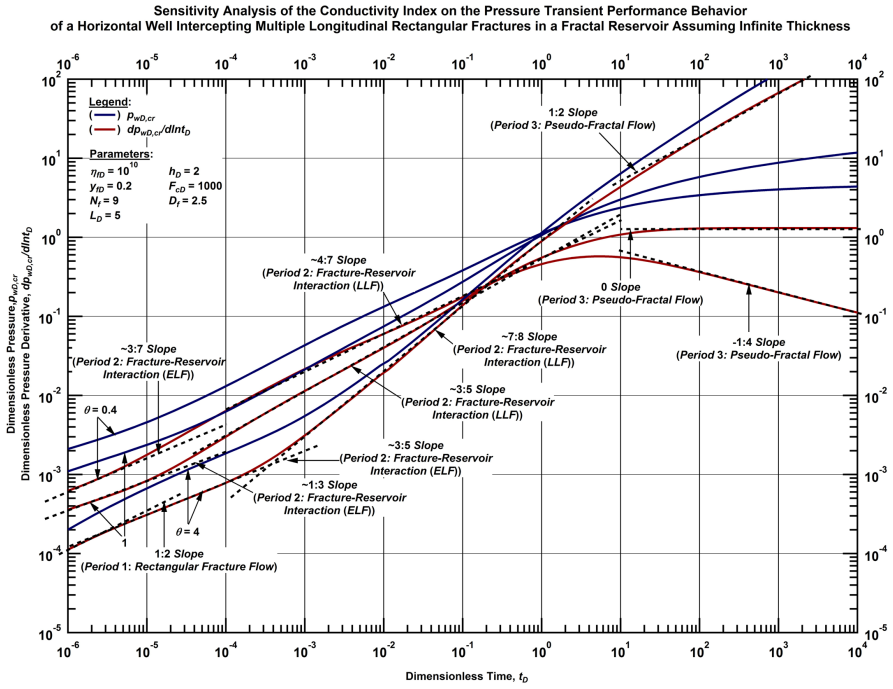

Figure 4.15 — Log-log plot of the dimensionless pressure and dimensionless pressure derivative functions for a horizontal well intercepting multiple longitudinal hydraulic fractures with high conductivity in a fractal reservoir for selected values of the conductivity index (θ), assuming infinite thickness. (constant-rate case)

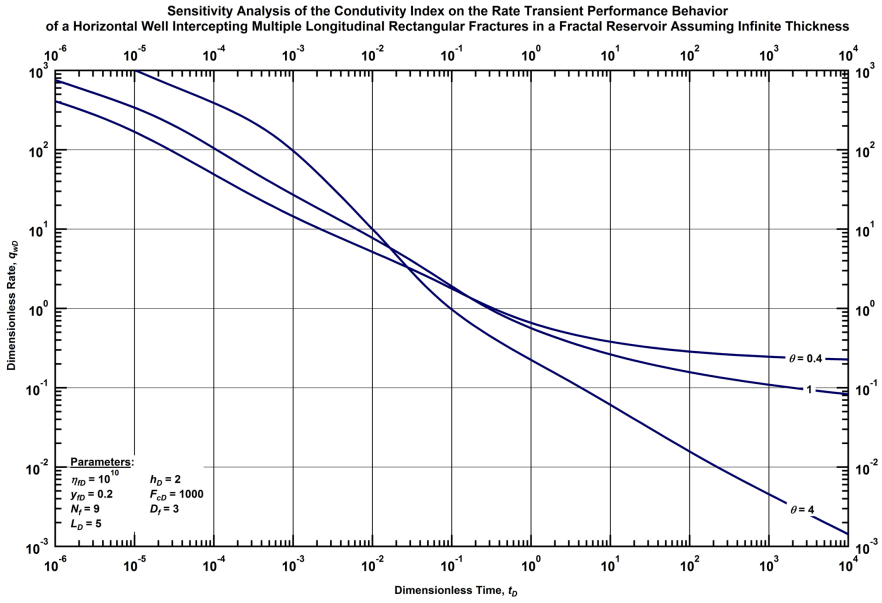

Figure 4.16 — Log-log plot of the dimensionless rate and dimensionless rate derivative functions for a horizontal well intercepting multiple longitudinal hydraulic fractures with high conductivity in a fractal reservoir for selected values of the conductivity index (θ), assuming infinite thickness. (constant-pressure case)

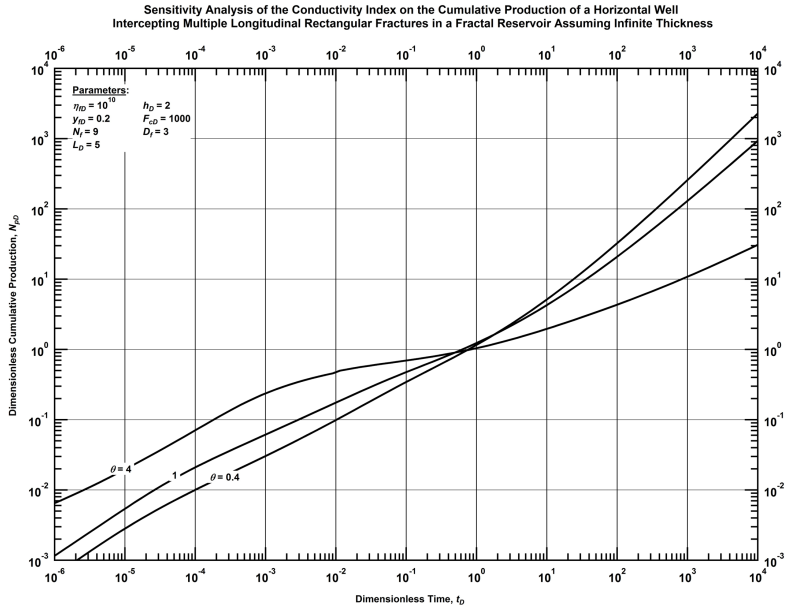

Figure 4.17 — Log-log plot of the dimensionless cumulative production function for a horizontal well intercepting multiple longitudinal hydraulic fractures with high conductivity in a fractal reservoir for selected values of the conductivity index (θ), assuming infinite thickness. (constant-pressure case)

As in the previous analyses, we identified the periods of flow using the pressure derivative function and summarized these results in **Table 4.4**. The *ELF* and the *LLF* sub-periods are evident and exhibit power-law behaviors (*i.e.*, straight-lines) on the log-log plot of the dimensionless pressure derivative functions for all cases (**Fig. 4.15**). The *ELF* sub-periods show straight-lines with slopes of 3:7, 1:3, and 3:5 for θ-values of 0.4, 1 and 4, respectively. For the *LLF* sub-periods, the straight-lines have slopes of 4:7, 3:5 and 7:8, for the values of the conductivity index (θ) of 0.4, 1 and 4.

Table 4.4 — Definition of flow periods, based on the pressure derivative, for the sensitivity analysis of the conductivity index (θ) on the pressure transient performance behavior for a horizontal well intercepting multiple rectangular longitudinal hydraulic fractures.

θ	v	Period 1	Period 2	Period 3
0.4	-0.25	—	$1x10^{-6}<t_D<4x10^{-6}$ (ELF) $5x10^{-4}<t_D<7x10^{-1}$ (LLF)	$2x10^{1}<t_D$
1	0	—	$1x10^{-6}<t_D<1x10^{-5}$ (ELF) $1x10^{-4}<t_D<1x10^{-1}$ (LLF)	$4x10^{1}<t_D$
4	0.5	$3x10^{-6}<t_D$	$3x10^{-6}<t_D<2x10^{-4}$ (ELF) $1x10^{-3}<t_D<1x10^{0}$(LLF)	$10^{2}<t_D$

4.3. Summary

In this chapter, we used the principle of superposition in space to extend the models developed in Chapter III for a horizontal well intercepting a single finite conductivity fracture to the so-called "multi-fractured well" case. We have observed that our solutions based on the "fractal point source" approach yield unexpected behaviors in the pressure and rate-transient performance behaviors at intermediate times when $v\geq 0$. In Appendix H we present analyses of the application of the traditional line/point source approaches for fractal reservoirs and introduce the concept of fractional integrals as an alternative to model the pressure and rate-transient behavior in fractured

wells in fractal reservoirs. We applied the image well method to model impermeable parallel vertical boundaries in a fractal reservoir.

CHAPTER V

PRESSURE AND RATE-TRANSIENT BEHAVIOR OF DOUBLE POROSITY RESERVOIR WITH TRANSIENT INTERPOROSITY TRANSFER WITH FRACTAL MATRIX BLOCKS[3]

In this chapter we present double porosity models considering matrix blocks with fractal geometry and fracture networks with either radial or fractal fracture networks. The recent development of anomalous diffusion models has opened the possibility of adapting double porosity models to estimate reservoir (and related) parameters for unconventional reservoirs. The primary objective of the development of these models is to provide physical explanations for the anomalous diffusion phenomenon.

Traditionally, fractal diffusivity models have been used to model highly heterogenous reservoirs (*e.g.*, NFRs and shale reservoirs). In double porosity systems (fractures and matrix blocks), such models are used to describe the flow of fluids within the network of natural fractures (*e.g.*, Chang *et al.*, 1990, Olarewaju, 1996 and Valdes-Perez, 2013). To the best of our knowledge, no attempt to apply the fractal theory to model the flow from the matrix blocks to the fractures has been made. Given that the porosity of the matrix blocks in shale oil/gas reservoirs is a combination of multiple organic and inorganic porosities, we believe that it is appropriate (in terms of geological evidence) to model the matrix blocks as fractal objects.

---

[3] Reprinted with permission from "Pressure-Transient Behavior of Double Porosity Reservoirs with Transient Interporosity Transfer with Fractal Matrix Blocks " by Valdes-Perez, and Blasingame, T.A., 2018. *SPE Europec featured at* 80th *EAGE Conference and Exhbition Proceedings*, SPE-190841-MS. Copyright [2018] by Society of Petroleum Engineers, Inc.

5.1. Theory of the Double Porosity Models with Transient Interporosity Transfer

The use of double porosity models to depict the pressure-transient behavior of NFRs has been studied since the 1960s. These models idealize reservoirs with multiple porous media (e.g., micro/nano fractures, micro/nano vugs, matrix blocks, etc.) as double porosity reservoirs (fracture network and matrix blocks). The double porosity models can be classified as transient or pseudosteady-state inteporosity transfer models. In this chapter, we will focus only on the transient interporosity transfer condition.

In 1976, de Swaan presented a double porosity analytical model with transient interporosity transfer. For this model, de Swaan established a radial fracture network and considered either slabs or spherical matrix blocks. The transient interporosity transfer was modeled with a convolution integral of the flux from the matrix blocks weighted by the derivative of the pressure in the radial network of fractures with respect to time. The flux of the matrix blocks was determined by solving the diffusivity equation for either linear or spherical systems considering constant-pressure at the matrix-fracture interface (see Appendix E for detailed derivation).

The periods of flow exhibited by the double porosity model with transient interporosity transfer conditions are (see **Fig. 5.1**):

- Period 1 — (fractal fracture network flow): This period exhibits a flat slope (radial flow) in the pressure derivative function that represents that the flow is dominated by the properties of the radial fracture network.

- Period 2 — (interaction between the fractal fracture network and the matrix blocks): This period can be subdivided into three sub-periods: (1) a transition sub-period

dominated by the early interaction of the matrix blocks, (2) a pseudoradial flow, and (3) a transition sub-period, dominated by the closed boundaries of the matrix blocks.

- Period 3 — (single porosity fractal reservoir flow): In this period of flow, the double porosity reservoir has achieved equilibrium and behaves as a single porosity reservoir. However, this period is dominated by the geometry of the fracture

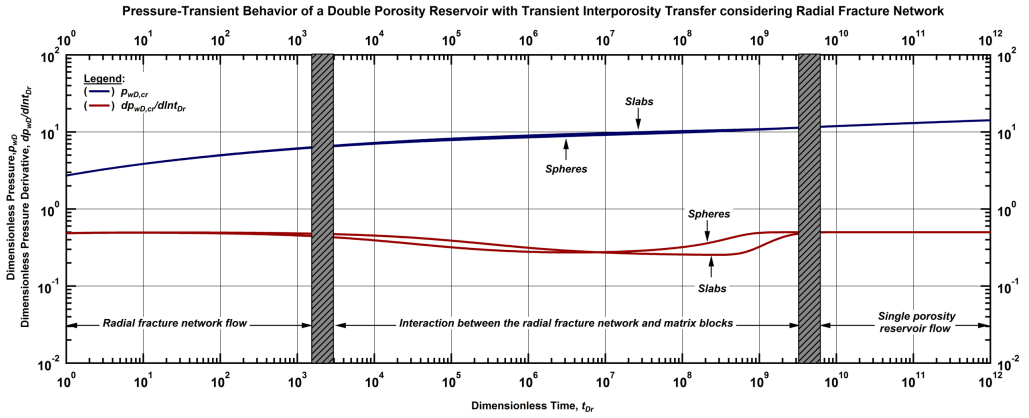

Figure 5.1 — Schematics of the pressure transient performance behavior of a double porosity reservoir considering slab matrix blocks, and spherical matrix blocks.

In 1982, three independent research groups modified de Swaan's model and obtained asymptotic solutions in the real domain to be used for well-test analysis (Cinco-Ley *et al.*, Serra *et al.*, and Streltsova). In this work, we will use the model presented by Cinco-Ley *et al.* (1982) to include the effects of a fractal matrix. A summary of the development of this model is presented in Appendix E.

5.2. Models Assumptions

In this chapter, we present models that consider two porous media: (1) matrix blocks and (2) a fracture network. All the models consider the matrix blocks to be fractal, whereas the fracture

network is considered to be either radial or fractal. The assumptions of the models are summarized in **Table 5.1**.

Table 5.1 — Assumptions used to develop the proposed double porosity reservoir models

Medium	Assumptions
All	● Flow to the wellbore occurs only through the fracture network (radial or fractal). ● Pressure-squared gradients are negligible. ● Uniform initial pressure, p_i ● Single slightly-compressible fluid flow with constant compressibility, c_o, and constant viscosity, μ
Fractal matrix blocks	● Single size of the matrix blocks of D_{fma}-dimension ● Flow obeys modified Darcy's Law for fractal systems of θ_{ma}-conductivity index. This implies that both porosity and permeability varies according to power law functions. Reference matrix porosity, ϕ_{0ma}, and matrix permeability, k_{0ma}, are considered. ● The matrix blocks have constant compressibility, c_{ma}.
Radial fracture network	● Unbounded radial network ● Flow obeys Darcy's Law. ● The radial fracture network has constant properties: compressibility, c_{fb}, permeability, k_{fb}, and porosity, $\phi_{fb.}$
Fractal fracture network	● Unbounded fractal fracture network of D_f-dimension ● Flow obeys modified Darcy's Law for fractal systems of θ-conductivity index with reference fractured bulk porosity, ϕ_{0fb}, and matrix of the fractured bulk, k_{0fb}, are considered. ● The fractal fracture network has constant compressibility, c_{fb}.

5.3. Development of the Models

Fluid Transfer Function considering Fractal Matrix Blocks

The fluid transfer function from fractal matrix blocks to the fracture network, $F(\eta_{maD},h_{maD},t_D)$, is defined by the geometry and properties of the matrix blocks. To derive this function, we have used an analogous procedure to the one presented by de Swaan (1976) for repetitive elements of matrix blocks (see Appendix E for details). We have investigated two scenarios: (1) closed matrix blocks and (2) infinite-acting matrix blocks. For the closed matrix blocks case, this function is defined by:

$$F(\eta_{maD},h_{maD},t_D)=\frac{1}{\sqrt{\eta_{maD}}}\left[\frac{h_{maD}}{2}\right]^{\theta_{ma}/2}L^{-1}\left[\frac{1}{\sqrt{u}}\left[\frac{\Gamma[v_{ma}]\Gamma[1-v_{ma}]I_{v_{ma}-1}[\xi]-2K_{v_{ma}-1}[\xi]}{2K_{v_{ma}}[\xi]+\Gamma[v_{ma}]\Gamma[1-v_{ma}]I_{v_{ma}}[\xi]}\right]\right], \quad (5.1)$$

where $v_{ma}=[1-\beta_{ma}]/[\theta_{ma}+2]$, and:

$$\xi = \frac{2}{\theta_{ma}+2}\left[\frac{h_{maD}}{2}\right]^{[\theta_{ma}+2]/2}\sqrt{\frac{u}{\eta_{maD}}} \quad \text{..... (5.2)}$$

β_{ma} is the spatial dimension of the matrix. It is defined as $\beta_{ma}=D_{fma}-\theta_{ma}-1$. The expression given by Eq. 5.1 applies for $v_{ma} \neq 0$. If $v_{ma} = 0$, the following expression should be used:

$$F(\eta_{maD}, h_{maD}, t_D) = \frac{1}{\sqrt{\eta_{maD}}}\left[\frac{h_{maD}}{2}\right]^{\theta_{ma}/2} L^{-1}\left[\frac{1}{\sqrt{u}}\frac{I_{v_{ma}-1}[\xi]}{I_{v_{ma}}[\xi]}\right] \quad \text{..... (5.3)}$$

Due to the extremely low permeability of the matrix blocks in shale oil/gas reservoirs, we modeled the behavior of the matrix blocks as infinite-acting (fully transient) media. The fluid transfer function for infinite-acting matrix blocks is:

$$F(\eta_{maD}, h_{maD}, t_D) = \frac{1}{\sqrt{\eta_{maD}}}\left[\frac{h_{maD}}{2}\right]^{\theta_{ma}/2} L^{-1}\left[\frac{1}{\sqrt{u}}\frac{K_{v_{ma}-1}[\xi]}{K_{v_{ma}}[\xi]}\right] \quad \text{..... (5.4)}$$

The dimensionless variables for the models presented in this chapter are summarized in **Table 5.2.**

Asymptotic behaviors

As pointed out by Cinco-Ley et al. (1982), the flow from the matrix blocks to the fracture network is linear at early and intermediate times (Periods 1 and 2) regardless of the geometry of the matrix block. During these periods of flow, the behavior of the fluid transfer function for closed and infinite-acting matrix blocks are the same. Therefore, the fluid transfer function *for all cases at early and intermediate times* can be simplified to:

$$F(\eta_{maD}, h_{maD}, t_D) = \frac{1}{\sqrt{\pi \eta_{maD}}} \left[\frac{h_{maD}}{2} \right]^{\theta_{ma}/2} t_D^{-1/2} \quad \text{..... (5.5)}$$

At late times, the fluid transfer function for the infinite-acting matrix blocks case can be simplified to:

$$F(\eta_{maD}, h_{maD}, t_D) = \frac{[\theta_{ma} + 2]^{1-2\nu_{ma}}}{\Gamma[\nu_{ma}] \eta_{maD}^{\nu_{ma}}} \left[\frac{h_{maD}}{2} \right]^{-\beta_{ma}} t_D^{-\nu_{ma}} \quad \text{..... (5.6)}$$

Table 5.2 — Dimensionless variables for the proposed double porosity reservoir models

Dimensionless Variable	Definition for the radial fracture network model	Definition for the double fractal model
Pressure in the fracture network	$p_{rfnD,cr}(r_D, t_{Dr}) = \frac{k_{fb} h [p_i - p_{rfn}(r,t)]}{qB\mu}$	$p_{ffnD,cr}(R_D, t_{Df}) = \frac{aV_s k_{0fb} [p_i - p_{ffn}(R,t)]}{qB\mu r_w^{1-\beta} \phi_{0fb}}$
Pressure in the fractal matrix blocks	$p_{maD,cr}(r_D, t_{Dr}) = \frac{k_{fb} h [p_i - p_{ma}(r,t)]}{qB\mu}$	$p_{maD,cr}(R_D, t_{Df}) = \frac{aV_s k_{0fb} [p_i - p_{ma}(R,t)]}{qB\mu r_w^{1-\beta} \phi_{0fb}}$
Time	$t_{Dr} = \frac{k_{fb}}{[\phi c_t]_t \mu r_w^2} t$	$t_{Df} = \frac{k_{0fb}}{[\phi c_t]_t \mu r_w^{\theta+2}} t$
Radius	$r_D = \frac{r}{r_w}$	$r_D = \frac{r}{r_w}$
Storativity ratio	$\omega = \frac{\phi_{fb} c_{tfb}}{[\phi c_t]_t}$	$\omega = \frac{\phi_{0fb} c_{tfb}}{[\phi c_t]_t}$
Fracture area	$A_{fD} = A_{fma} h_{ma}$	$A_{fD} = A_{fma} h_{ma} r_w^{\theta}$
Hydraulic diffusivity of the fractal matrix blocks	$\eta_{maD} = \frac{k_{0ma} [c\phi_t]_t}{c_{ma} \phi_{0ma} k_{fb} r_w^{\theta_{ma}}}$	$\eta_{maD} = \frac{k_{0ma} [c\phi_t]_t}{c_{ma} \phi_{0ma} k_{fb}}$
Matrix block size	$h_{maD} = \frac{h_{ma}}{r_w}$	$h_{maD} = \frac{h_{ma}}{r_w}$

Double Porosity Model considering Radial Fracture Network and Fractal Matrix Blocks

To model the flow within the radial fracture network, we have considered the diffusivity equation presented by Cinco-Ley *et al*. (1982). This expression in its dimensionless form is given by:

$$\frac{1}{r_D}\frac{\partial}{\partial r_D}\left[r_D\frac{\partial p_{rfnD,cr}}{\partial r_D}\right]=\omega\frac{\partial p_{rnfD,cr}}{\partial t_D}+[1-\omega]\frac{A_{fD}\eta_{maD}}{h_{maD}}\int_0^{t_{Dr}}\frac{\partial p_{rfnD,cr}}{\partial \tau_{Dr}}F(\eta_{maD},h_{maD},t_{Dr}-\tau)d\tau \ldots (5.7)$$

The solution of Eq. 5.1 in the Laplace domain considering constant flow rate at the wellbore and infinite fracture network is given by:

$$\bar{p}_{rfnD,cr}(r_D,u)=\frac{K_0\left[r_D\sqrt{uf(u)}\right]}{u\sqrt{uf(u)}K_1\left[\sqrt{uf(u)}\right]}, \ldots (5.8)$$

where:

$$f(u)=\omega+[1-\omega]\frac{A_{fD}\eta_{maD}}{h_{maD}}\bar{F}(\eta_{maD},h_{maD},u) \ldots (5.9)$$

To obtain the performance of Eq. 5.8 in the real domain, a numerical inversion should be used. Additionally, we have derived asymptotic solutions, evaluated at the wellbore, for the main periods of flow depicted in this model. These solutions are summarized in **Table 5.3**.

Analogy to the Anomalous Diffusion Model

The 2D diffusivity model presented by Raghavan (2012) included the anomalous diffusion effects by using a version of Darcy's Law expressed in terms of a fractional derivative. The definition of the fractional derivative involves a convolution term where the derivative of the pressure with respect to time is weighted by a power-law function of the time. A similar diffusivity model can be obtained from the double porosity model considering a radial fracture network and fractal matrix blocks. Such a model is obtained by neglecting the storativity ratio (ω=0) and considering

the asymptotic behavior for late times of the fluid transfer function for infinite-acting fractal matrix blocks with positive v_{ma}-values (Eq.5.6). The resulting diffusivity equation is:

$$\frac{1}{r_D}\frac{\partial}{\partial r_D}\left[r_D\frac{\partial p_{rfnD,cr}}{\partial r_D}\right]=\frac{\alpha_1}{\Gamma[1-v_{ma}]}\int_0^{t_{Dr}}\frac{\partial p_{rfnD,cr}}{\partial \tau}[t_{Dr}-\tau]^{-v_{ma}}\,d\tau \quad \text{..... (5.10)}$$

where:

$$\alpha_1=\frac{A_{fD}\eta_{maD}^{1-v_{ma}}}{2}\frac{[\theta_{ma}+2]^{1-2v_{ma}}\,\Gamma[1-v_{ma}]}{\Gamma[v_{ma}]}\left[\frac{h_{maD}}{2}\right]^{-\beta_{ma}-1} \quad \text{..... (5.11)}$$

To provide a model that is comparable to the anomalous diffusion model presented by Raghavan (2012a), we have considered a time-dependent inner boundary condition modeled by a power-law function mathematically defined by:

$$\left[r_D\frac{\partial p_{fD}}{\partial r_D}\right]_{r_D=1}=-t_{Dr}^{v_0-v_{ma}}, \quad \text{..... (5.12)}$$

where v_0 is an arbitrary reference exponent. We have assumed a unit value of this parameter.

The line source approximation in the Laplace domain of Eq. 5.10 considering variable flow rate (Eq. 5.12) and infinite radial fracture network is given by:

$$\bar{p}_{rfnD,cr}(r_D,u)=\frac{\Gamma[2-v_{ma}]K_0\left[r_D\sqrt{ug(u)}\right]}{u^{2-v_{ma}}} \quad \text{..... (5.13)}$$

where:

$$g(u)=\alpha_1 u^{v_{ma}-1} \quad \text{..... (5.14)}$$

Table 5.3 — Asymptotic constant-rate solutions in the real domain for the double porosity model considering radial fracture network

	Asymptotic solution
Early times	$p_{wD,cr}(t_{Dr}) = \frac{1}{2}\ln\left[\frac{\exp[\gamma]}{\omega}t_{Dr}\right]$
Intermediate times	$p_{wD,cr}(t_{Dr}) = \frac{1}{4}\ln[t_{Dr}] + \frac{1}{2}\ln\left[\frac{\exp[\gamma/2]}{[1-\omega]}\frac{h_{maD}}{A_{fD}}\left[\left[\frac{h_{maD}}{2}\right]^{\theta_{ma}}\eta_{maD}\right]^{-1/2}\right]$
Late times	$p_{wD,cr}(t_{Dr}) = \frac{1}{2}\ln[\exp[\gamma]t_{Dr}]$ (for closed matrix blocks)
	$p_{wD,cr}(t_{Dr}) = \frac{v_{ma}}{2}\left[\ln[\exp[\gamma]t_{Dr}]\right] - \frac{1}{2}\ln\left[\frac{A_{fD}[\theta_{ma}+2]^{1-2v_{ma}}}{h_{maD}\eta_{maD}^{v_{ma}-1}}\frac{\Gamma[1-v_{ma}]}{\Gamma[v_{ma}]}\left[\frac{2}{h_{maD}}\right]^{[\beta_{ma}+1]/2}\right]$ (for infinite-acting matrix blocks)

Double Porosity Model considering Fractal Fracture Network and Fractal Matrix Blocks (*Double Fractal Model*)

The motivation of the double fractal model is to provide a reservoir model to depict the transient performance behavior of highly heterogeneous multi-porosity systems, such as shale oil and shale gas reservoirs. The objective of this model is to take into account the randomness and heterogeneity of the natural fractures and the matrix blocks.

The presence of natural fractures in shale reservoirs is significantly lower than in carbonate reservoirs. Therefore, the porosity of the natural fractures in shale reservoirs is very small, and the storativity ratio would be negligible. However, it is important to consider the presence of the natural fractures because it has a significant impact in the flow of fluids towards hydraulic fractures and/or the wellbore. To model the flow within the fractal fracture network, we have considered the diffusivity equation presented by Valdes-Perez (2013). Such an equation in its dimensionless form is defined by:

$$\frac{1}{R_D^{D_f-1}}\frac{\partial}{\partial R_D}\left[R_D^{\beta}\frac{\partial p_{ffnD,cr}}{\partial R_D}\right]=\omega\frac{\partial p_{ffnD,cr}}{\partial t_D}+[1-\omega]\frac{A_{fD}\eta_{maD}}{h_{maD}}\int_0^{t_{Df}}\frac{\partial p_{ffnD,cr}}{\partial \tau}F(\eta_{maD},h_{maD},t_{Df}-\tau)d\tau\,.$$

..... (5.15)

The solution of Eq. 5.15 in the Laplace domain considering constant-rate at the wellbore and infinite fracture network is given by:

$$\bar{p}_{ffnD,cr}(R_D,u)=\frac{K_v\left[\frac{2R_D\sqrt{uf(u)}}{\theta+2}\right]}{u\sqrt{uf(u)}K_{v-1}\left[\frac{2\sqrt{uf(u)}}{\theta+2}\right]}\,.$$ ..... (5.16)

where $v = [1-\beta]/[\theta+2]$. The transfer function $f(u)$ has the same shape as the one presented in Eq. 5.9. For this model, we have considered only the behavior of the fluid transfer function of the matrix blocks as infinite-acting (Eq. 5.4) due to their extremely low permeability in shale oil/gas reservoirs.

For systems with negligible storativity ratio and considering the fluid transfer function at intermediate times (Eq. 5.5) the model given by Eq. 15 can be simplified to:

$$\frac{1}{R_D^{D_f-1}}\frac{\partial}{\partial R_D}\left[R_D^{\beta}\frac{\partial p_{ffnD,cr}}{\partial R_D}\right]=\frac{\alpha_0}{\sqrt{\pi}}\int_0^{t_{Df}}\frac{\partial p_{ffnD,cr}}{\partial \tau}[t_{Df}-\tau]^{-1/2}d\tau$$ ..... (5.17)

where:

$$\alpha_0=\frac{A_{fD}\sqrt{\eta_{maD}}}{2}\left[\frac{h_{maD}}{2}\right]^{\theta_{ma}/2-1}$$ ..... (5.18)

A similar model for radial fracture networks and Euclidean matrix blocks was developed by Cinco-Ley *et al*. (1982).

For late times, substituting Eq. 5.6 in Eq. 5.14 and neglecting storativiy ratio, the following model is derived:

$$\frac{1}{R_D^{Df-1}}\frac{\partial}{\partial R_D}\left[R_D^{\beta}\frac{\partial p_{ffnD,cr}}{\partial R_D}\right]=\frac{\alpha_1}{\Gamma[1-v_{ma}]}\int_0^{t_D}\frac{\partial p_{ffnD,cr}}{\partial \tau}[t_{Df}-\tau]^{-v_{ma}}\,d\tau \quad \text{..... (5.19)}$$

Eq. 5. 19 has the same shape as the models assuming the anomalous diffusion phenomena (Camacho-Velazquez *et al*., 2008 and Raghavan, 2012a). This model relates its parameters to the physical properties related to the geology of the matrix blocks. The asymptotic constant-rate solutions in the real domain of Eq. 5.17 and Eq. 5.19 are summarized in **Table 5.4**.

Table 5.4 — Asymptotic constant-rate solutions in the real domain for the double fractal model.

	Asymptotic solution
Early-Intermediate times	$p_{wD,cr}(t_{Df})=\frac{1}{\Gamma[5/4]\sqrt{\alpha_0}}t_{Df}^{1/4}$
Late-Intermediate times	$p_{wD,cr}(t_{Df})=\frac{[\theta+2]^{2v-1}\Gamma[v]}{\alpha_0^{v}\Gamma[1-v]\Gamma[v/2+1]}t_{Df}^{v/2}\quad(v>0)$
Late times	$p_{wD,cr}(t_{Df})=\frac{[\theta+2]^{2v-1}\Gamma[v]}{\alpha_1^{v}\Gamma[1-v]\Gamma[vv_{ma}+1]}t_{Df}^{vv_{ma}}\quad(v>0)$

Constant Pressure Solutions

The rate-transient performance behavior of the models presented in this chapter is obtained using Dunhamel's principle, which relates the constant-rate and constant-pressure solutions in the Laplace domain, as presented in Chapter I.

5.4. Results and Discussion

In this section, we present the sensitivity analyses of the characterizing parameters involved in the models presented in Section 5.3. To perform such analyses, we numerically inverted the solutions in the Laplace domain using the Gaver-Wynn-Rho algorithm implemented in *Mathematica*.

Double Porosity Model considering Radial Fracture Network and Fractal Matrix Blocks

Sensitivity to the D_{fma}-Parameter: Closed Matrix Blocks

Fig. 5.2 exhibits the effect of the fractal dimension of the matrix (D_{fma}) in the pressure transient performance behavior of a double porosity reservoir considering a radial fracture network (Eq. 5.8) and closed matrix blocks (Eq. 1 for $D_{fma} \neq 2$ and Eq. 3 for $D_{fma} = 2$). This plot shows no evident differences among the pressure-transient signatures when the fractal dimension of the matrix (D_{fma}) is varied. However, the influence of the D_{fma} -parameter is clear in the pressure derivative function. For all cases, the pressure derivative function exhibits two radial flows. The first one (fracture network flow) occurs at early times and represents the geometry and the expansion within the radial fracture network. The second radial flow (single porosity reservoir flow) occurs at late times and represents that the radial fracture network and the matrix blocks behave as a single porosity system where the geometry of the fracture network prevails. At intermediate times (interaction between the fracture network and the matrix blocks), we have observed that the interaction between the fracture network and the matrix blocks and the boundary effects of the matrix blocks occur faster when the matrix blocks have higher values of the fractal dimension (keeping unchanged the other parameters). This model can reproduce the behavior of the transfer functions

developed by de Swaan (1976) when the conductivity index of the matrix is zero (*i.e.*, θ_{ma}=0) and D_{fma} =1 for slabs and D_{fma} =3 for spheres.

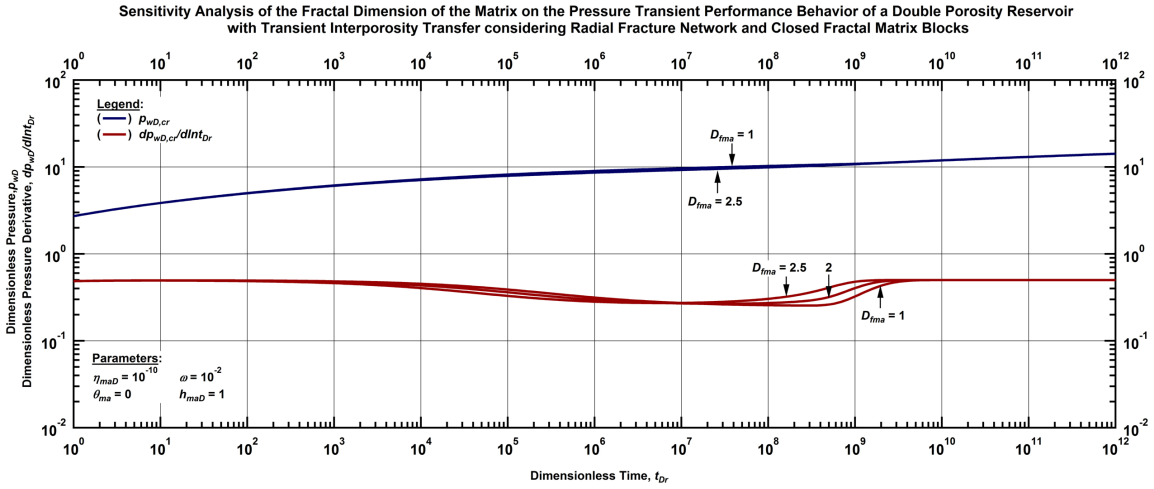

Figure 5.2 — Log-log plot of the pressure-transient and pressure derivative performance behaviors of a double porosity reservoir considering radial fracture network and closed fractal matrix blocks for selected values of the fractal dimension of the matrix (D_{fma}).

Fig. 5.3 shows the rate-transient case for the example presented in **Fig. 5.2**. Based on the rate derivative function in this plot, we observed that is not possible to distinguish the first period of flow (*i.e.*, the radial fracture network flow). However, the acceleration effect of the fractal dimension of the matrix (D_{fma}) is also observed in this plot, *i.e.*, the higher the D_{fma} -value, the sooner the boundary effects of the matrix will appear.

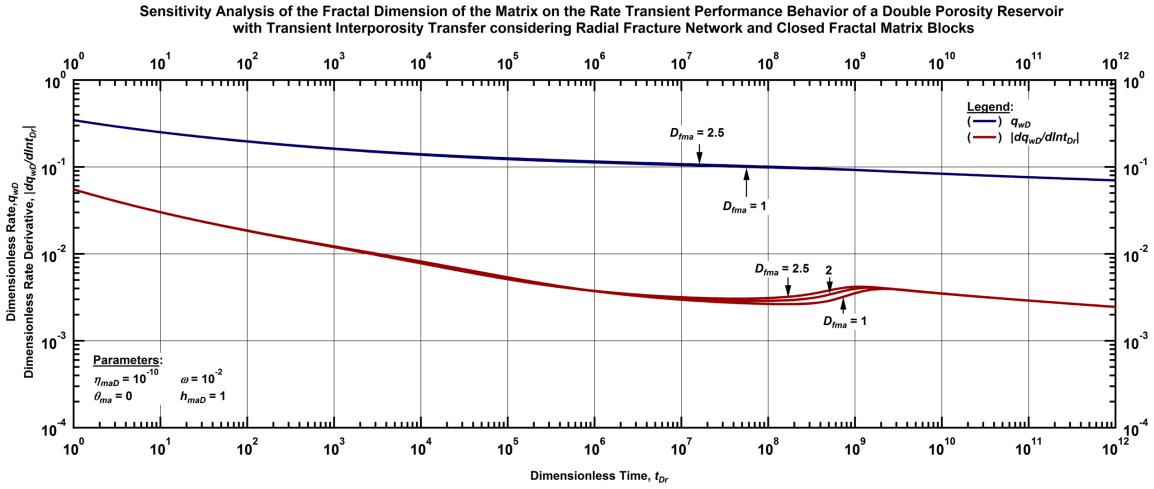

Figure 5.3 — Log-log plot of the rate-transient and rate derivative performance behaviors of a double porosity reservoir considering radial fracture network and closed fractal matrix blocks for selected values of the fractal dimension of the matrix (D_{fma}).

Sensitivity to the θ_{ma}-Parameter: Closed Matrix Blocks

Fig. 5.4 presents the sensitivity analysis of the conductivity index of the matrix (θ_{ma}) in the pressure transient performance behavior for the radial fracture network and closed matrix blocks case (Eq. 5.1 for $\theta_{ma} \neq 1$ and Eq. 3 for $\theta_{ma} = 1$). For the θ_{ma} -parameter instance, we have observed two phenomena: (1) there is a delay in the interaction between the fracture network when the matrix blocks have higher θ_{ma} -values and (2) the boundary effects of the matrix blocks occur at earlier times for high values of the conductivity index of the matrix. High θ_{ma} -values represent that the permeable sites inside the matrix blocks are poorly connected.

Based on **Fig. 5.5**, we concluded that better connected matrix blocks (lower θ_{ma} -values) yield higher flow rates. Similar to the fractal dimension of the matrix case, the boundary effects of the matrix appear at earlier times for high θ_{ma} -values.

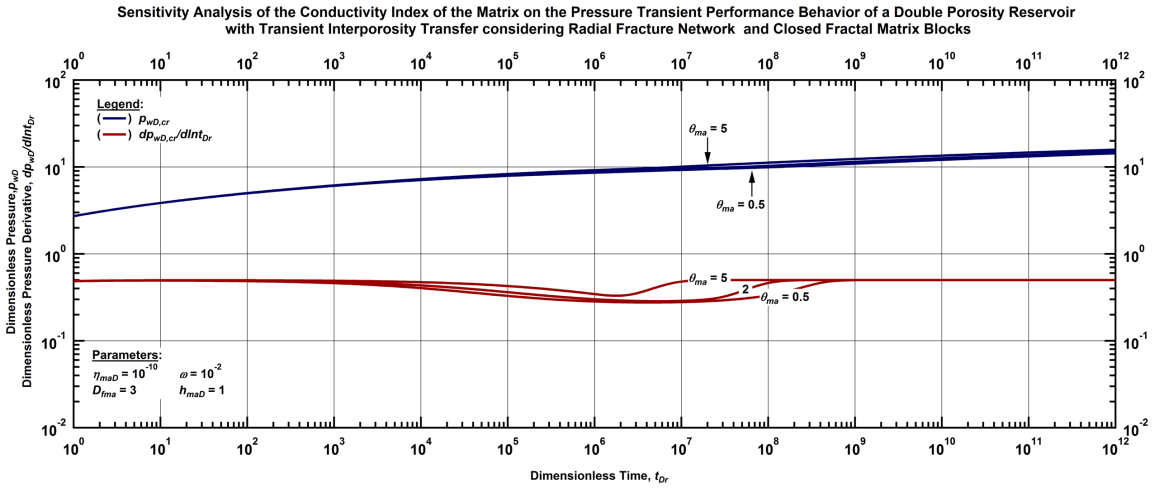

Figure 5.4 — Log-log plot of the pressure-transient and pressure derivative performance behaviors of a double porosity reservoir considering radial fracture network and closed fractal matrix blocks for selected values of the conductivity index of the matrix (θ_{ma}).

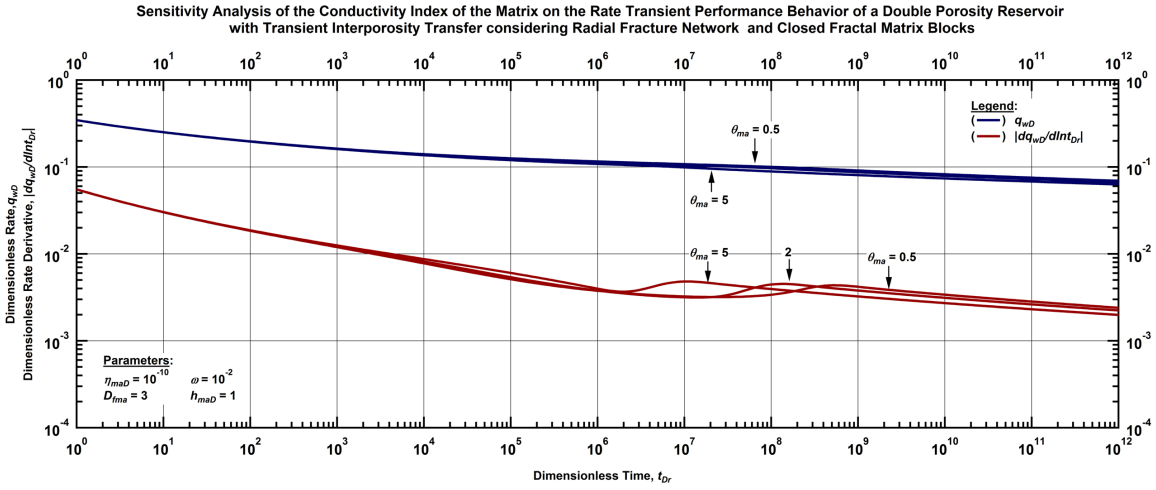

Figure 5.5 — Log-log plot of the rate-transient and rate derivative performance behaviors of a double porosity reservoir considering radial fracture network and closed fractal matrix blocks for selected values of the conductivity index of the matrix (θ_{ma}).

Sensitivity to the D_{fma}-Parameter: Infinite-Acting Matrix Blocks

In **Fig. 5.6**, we present the sensitivity analysis of the fractal dimension of the matrix (D_{fma}) in the pressure transient performance behavior for the radial fracture network considering infinite-acting matrix blocks (Eq. 5.4). This plot shows that fractal matrix blocks with lower D_{fma} -values yield a higher drop of pressure of the double porosity system. The pressure derivative function in this plot exhibits the same behavior as the closed fractal matrix case at early times (fracture network flow) and intermediate times (interaction between the fracture network and the matrix blocks). However at late times, the flow is dominated by the fluid transfer from the matrix to the factures. For D_{fma} -values higher than two, the pressure derivative function yields a negative slope equal to the v_{ma}-parameter. If D_{fma} is lower than two (and higher than one), the pressure derivative function stabilizes to a constant value equal to v_{ma} /2.

The rate-transient performance behavior in **Fig. 5.7** shows that fractal matrix blocks with higher D_{fma} -values yield higher flow rates. In addition, the rate derivative function has a response at early and intermediate times similar to the one observed in the closed matrix blocks case. At late times, the infinite-acting nature of the matrix blocks dominates.

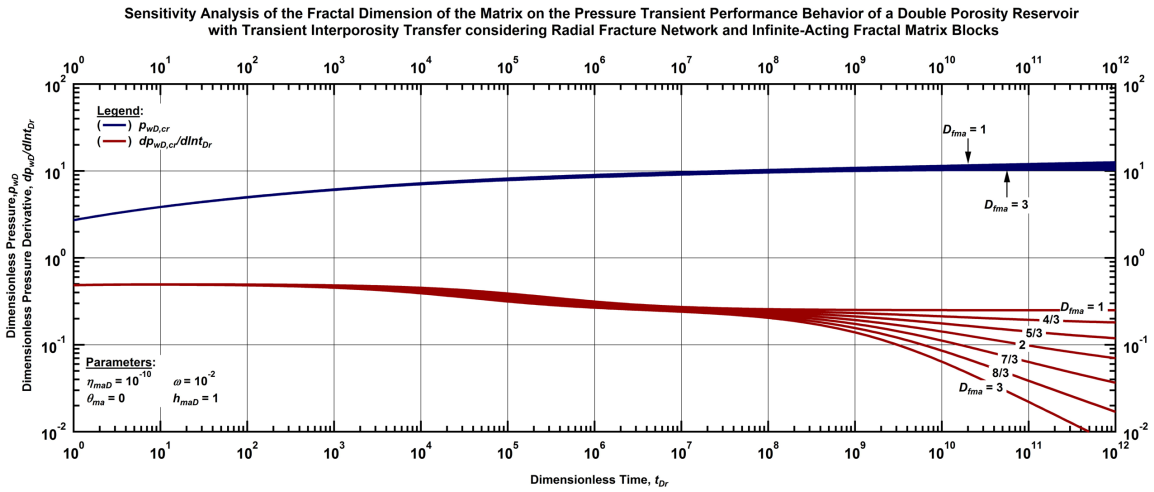

Figure 5.6 — Log-log plot of the pressure-transient and pressure derivative performance behaviors of a double porosity reservoir considering radial fracture network and infinite-acting matrix blocks for selected values of the fractal dimension of the matrix (D_{fma}).

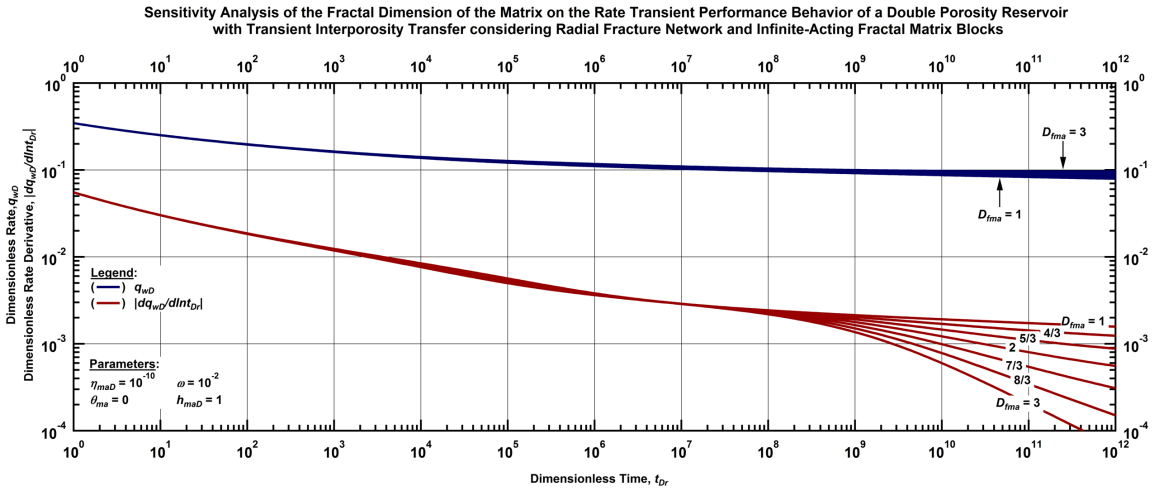

Figure 5.7 — Log-log plot of the rate-transient and rate derivative performance behaviors of a double porosity reservoir considering radial fracture network and infinite-acting fractal matrix blocks for selected values of the fractal dimension of the matrix (D_{fma}).

Sensitivity to the θ_{ma}-Parameter: Infinite-Acting Matrix Blocks

The plot in **Fig. 5.8** presents the sensitivity analysis of the conductivity index of the matrix (θ_{ma}) in the pressure transient performance behavior of a double porosity reservoir considering radial fracture network and infinite-acting matrix blocks. The example shown in this plot considers a small storativity ratio ($\omega=10^{-10}$). Therefore, the flat slope of the pressure derivative function for dimensionless times from 10^0 to 10^7 corresponds to the interaction between the fracture network and the matrix blocks. **Fig. 5.8** shows that better connected permeable sites inside matrix blocks (low θ_{ma} -values) yield a lower drop of pressure. In the rate-transient case, this implies that low θ_{ma} -values yield higher flow-rates (see **Fig. 5.9**).

In **Fig. 5.8**, we observe that poorly connected permeable sites inside matrix blocks (high θ_{ma} -values) accelerate the appearance of the single system behavior period. Similar to the fractal dimension case, the pressure derivative function yields a negative slope equal to the v_{ma}-parameter for θ_{ma} -values lower than one. If θ_{ma} is greater than one, the pressure derivative function stabilizes to a constant value equal to $v_{ma}/2$. Therefore, by increasing the v_{ma} -value to very high values, the pressure derivative function approaches to a constant value of 0.5.

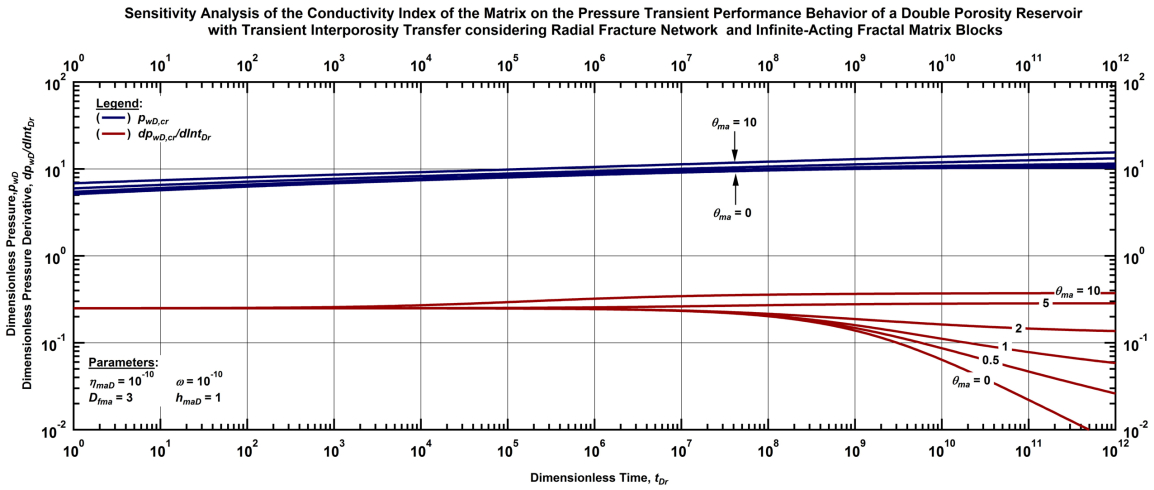

Figure 5.8 — Log-log plot of the pressure-transient and pressure derivative performance behaviors of a double porosity reservoir considering radial fracture network and infinite-acting matrix blocks for selected values of the conductivity index of the matrix (θ_{ma}).

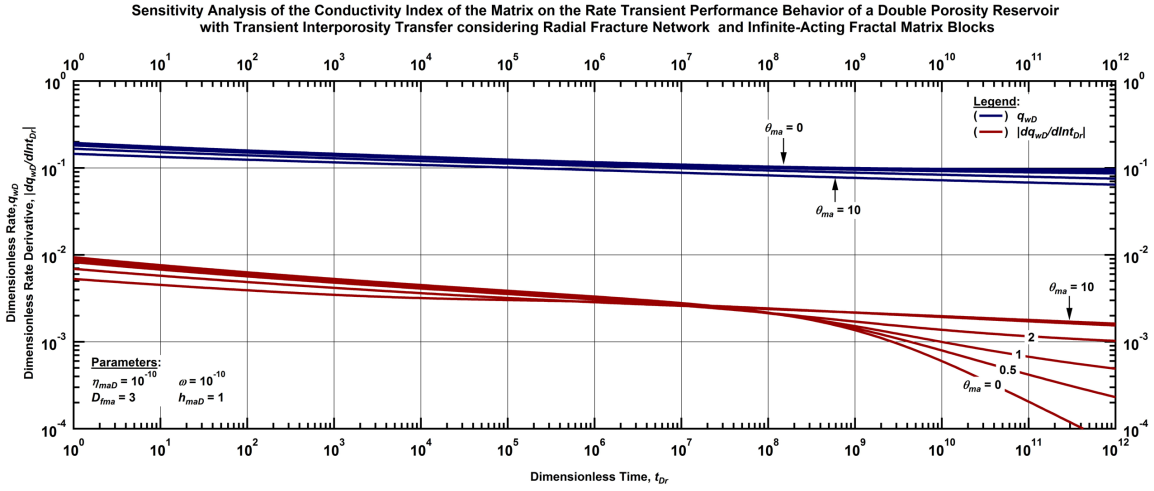

Figure 5.9 — Log-log plot of the rate-transient and rate derivative performance behaviors of a double porosity reservoir considering radial fracture network and infinite-acting fractal matrix blocks for selected values of the conductivity index of the matrix (θ_{ma}).

Wellbore Storage Effects

The wellbore storage effects for all the models presented in this section are incorporated using the standard scheme presented in Chapter I. **Fig. 5.10** and **Fig. 5.11** exhibit the impact of the wellbore storage in the pressure transient behavior presented in **Fig. 5.6** and **Fig. 5.8**, respectively. These plots show that wellbore storage effects can hinder the radial fracture flow when the storativity ratio is relatively high (**Fig. 5.10**) and shorten the transition period between early and intermediate times when the storativity ratio is relatively low (**Fig. 5.11**).

Analogy to the Anomalous Diffusion Model: Sensitivity to the D_{fma}-Parameter

Fig. 5.12 shows the influence of the fractal dimension of the matrix (D_{fma}) in the pressure and pressure derivative functions of the double porosity model considering radial fracture network and infinite-acting fractal matrix blocks, assuming the time-dependent inner boundary condition.

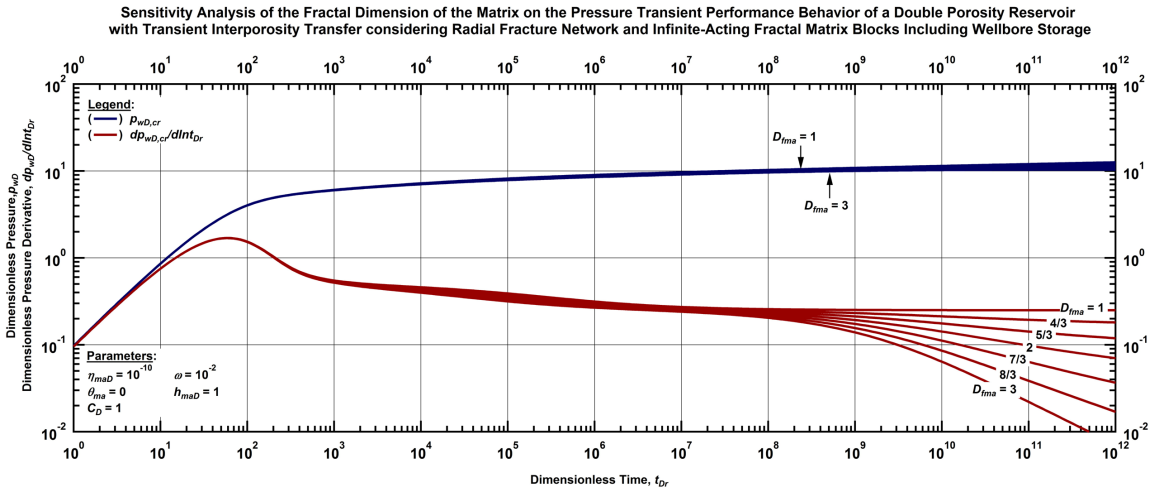

Figure 5.10 — Log-log plot of the pressure-transient and pressure derivative performance behaviors of a double porosity reservoir considering radial fracture network and infinite-acting fractal matrix blocks for selected values of the fractal dimension of the matrix (D_{fma}).

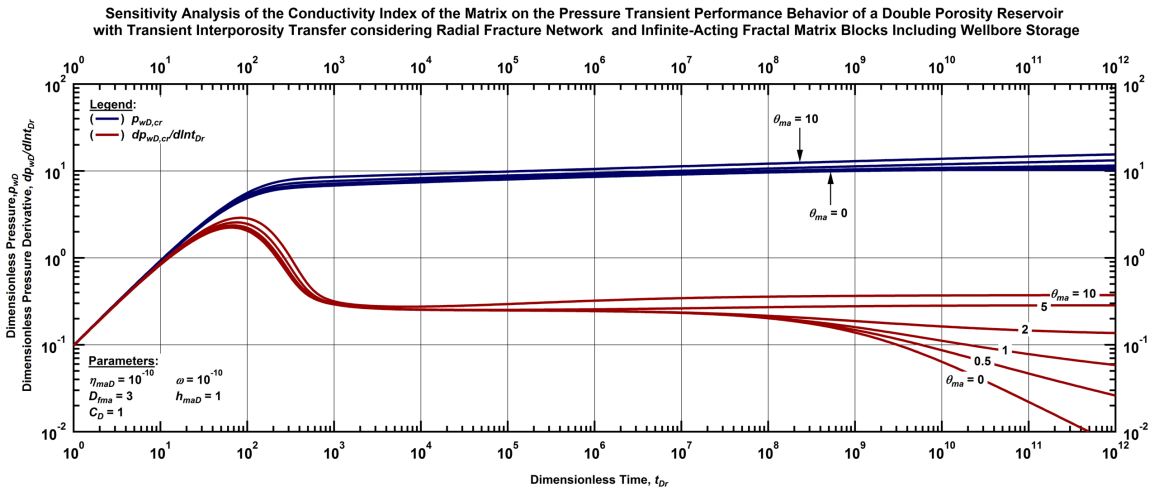

Figure 5.11 — Log-log plot of the pressure-transient and pressure derivative performance behaviors of a double porosity reservoir considering radial fracture network and infinite-acting matrix blocks for selected values of the conductivity index of the matrix (θ_{ma}) considering wellbore storage.

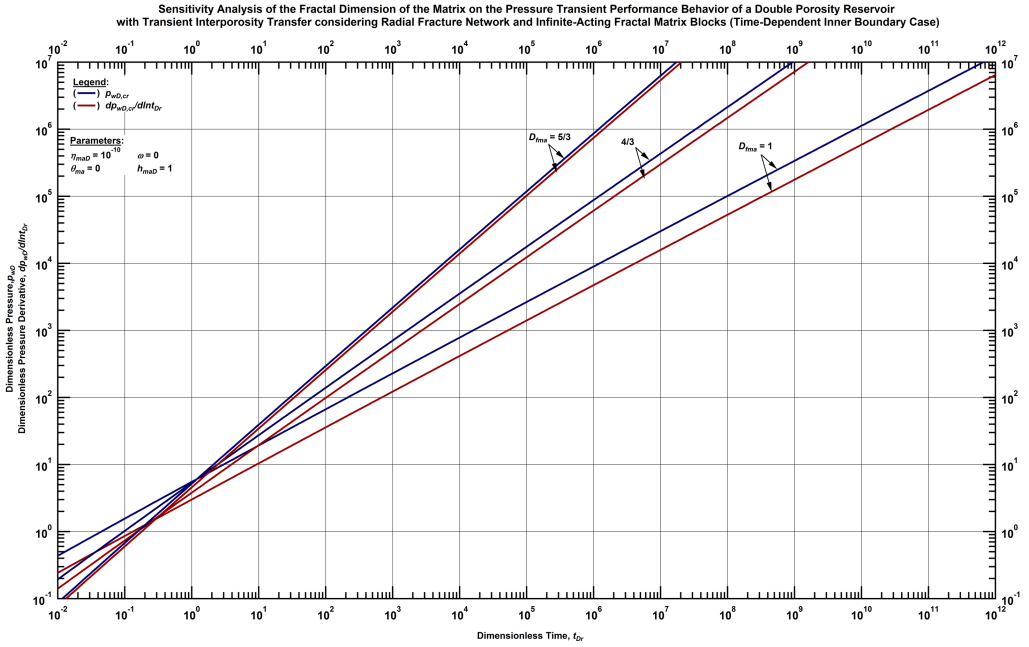

Figure 5.12 — Log-log plot of the pressure-transient and pressure derivative performance behaviors of a double porosity reservoir with time-dependent inner boundary, considering radial fracture network and infinite-acting matrix blocks for selected values of the fractal dimension of the matrix (D_{fma}).

We have observed that none of the cases in **Fig. 5.12** show the characteristic signature of radial flow (0-slope of the pressure derivative function), even though the geometry of the fracture network was assumed to be radial. Instead, the responses of the pressure and pressure derivative functions of this model yield power-law behaviors equal to the exponent of the inner boundary condition as shown by the β-pressure derivative function in **Fig. 5.13**. We conclude that the higher the D_{fma} -parameter (lower vma) the steeper the log-log straight-line.

Fig. 5.14 presents the constant-pressure version for the example presented in **Fig. 5.12**. The rate and rate derivative functions yield power-law behaviors whose slope in the log-log plot is equal to the negative value of slope in the constant-rate case (*i.e.*, v_{ma}-1). This is confirmed by the β-rate derivative (**Fig. 5.15**). We have observed that at dimensionless times greater than 10^{-1}, the fractal matrix blocks with higher D_{fma} -values yield higher flow rates. However, an unrealistic scenario is observed at earlier times ($t_D < 10^{-1}$), where the highest flow-rates are yielded by fractal matrix blocks with lower D_{fma} -values. The reason why this scenario is unrealistic is because high D_{fma} -values represent, basically, more permeable sites within the matrix blocks.

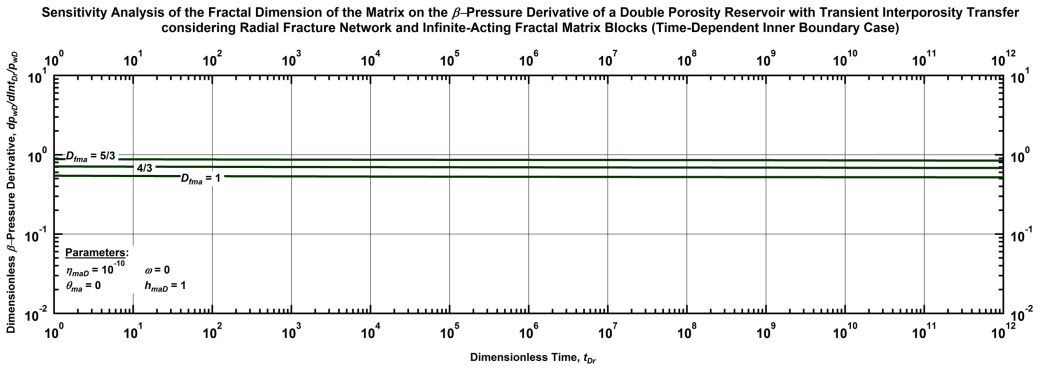

Figure 5.13 — Log-log plot of the β-pressure derivative function of a double porosity reservoir with time-dependent inner boundary, considering radial fracture network and infinite-acting matrix blocks for selected values of the fractal dimension of the matrix (D_{fma}).

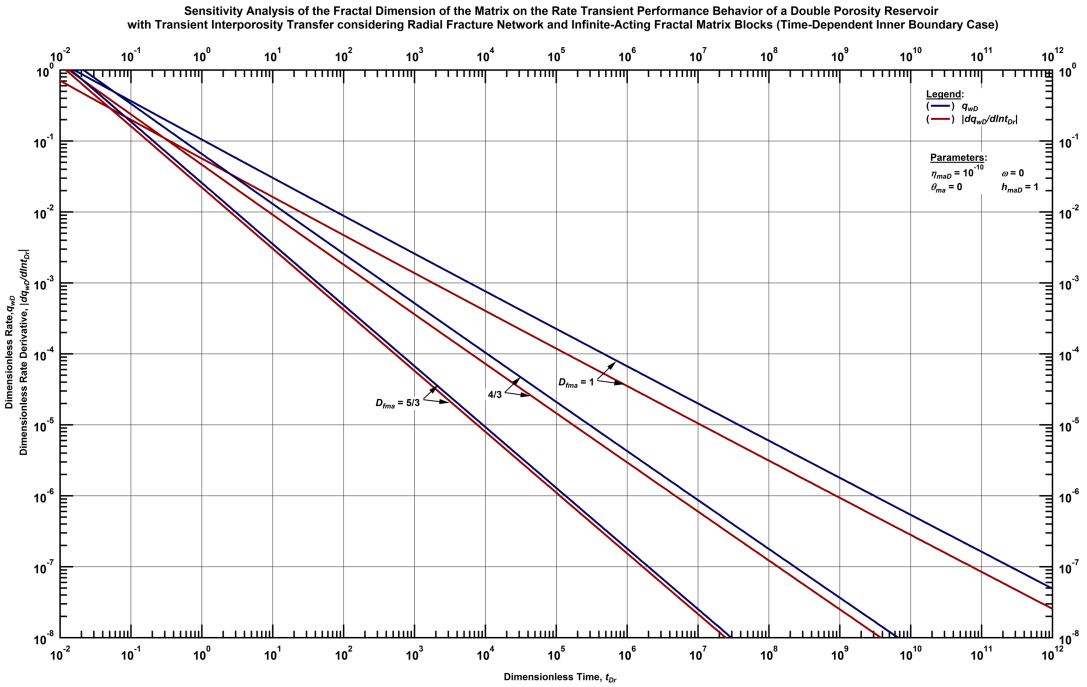

Figure 5.14 — Log-log plot of the rate-transient and rate derivative performance behaviors of a double porosity reservoir with time-dependent inner boundary, considering radial fracture network and infinite-acting matrix blocks for selected values of the fractal dimension of the matrix (D_{fma}).

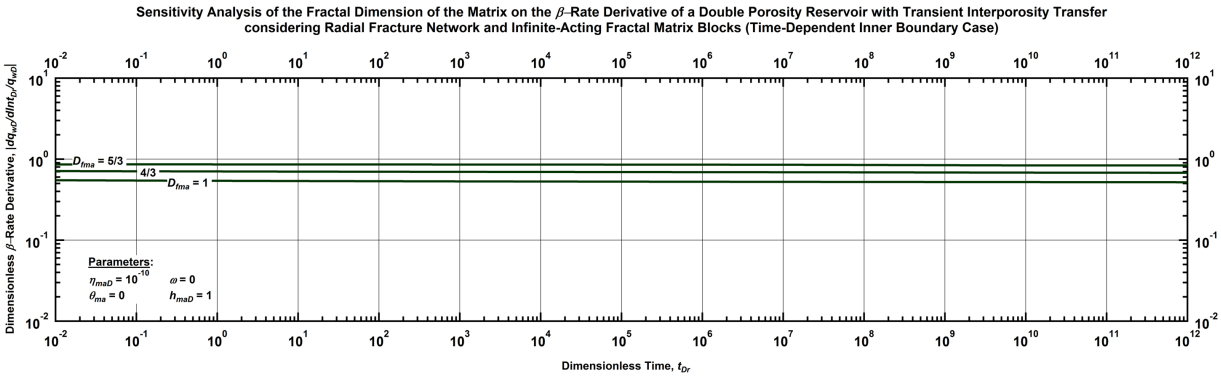

Figure 5.15 — Log-log plot of the β-rate derivative function of a double porosity reservoir with time-dependent inner boundary, considering radial fracture network and infinite-acting matrix blocks for selected values of the fractal dimension of the matrix (D_{fma}).

Analogy to the Anomalous Diffusion Model: Sensitivity to the θ_{ma}-Parameter

In **Fig. 5.16**, we present the sensitivity analysis of the conductivity index of the matrix (θ_{ma}). At late times ($t_D > 10^9$), this plot shows a behavior similar to the one observed for the D_{fma} -parameter, *i.e.*, the signatures of the pressure and pressure derivative functions yield power-law behaviors equal to the exponent of the inner boundary condition (*i.e.*, 1-ν_{ma}). This is confirmed by the β-pressure derivative function presented in **Fig. 5.17**. At early and intermediate times ($t_D < 10^9$), the β-pressure derivative function exhibits a variable behavior for all the cases presented. We concluded that the better connected permeable sites inside the matrix (*i.e.*, lower θ_{ma}- and consequently ν_{ma}-values), the steeper the log-log straight-line of the pressure and pressure derivative functions.

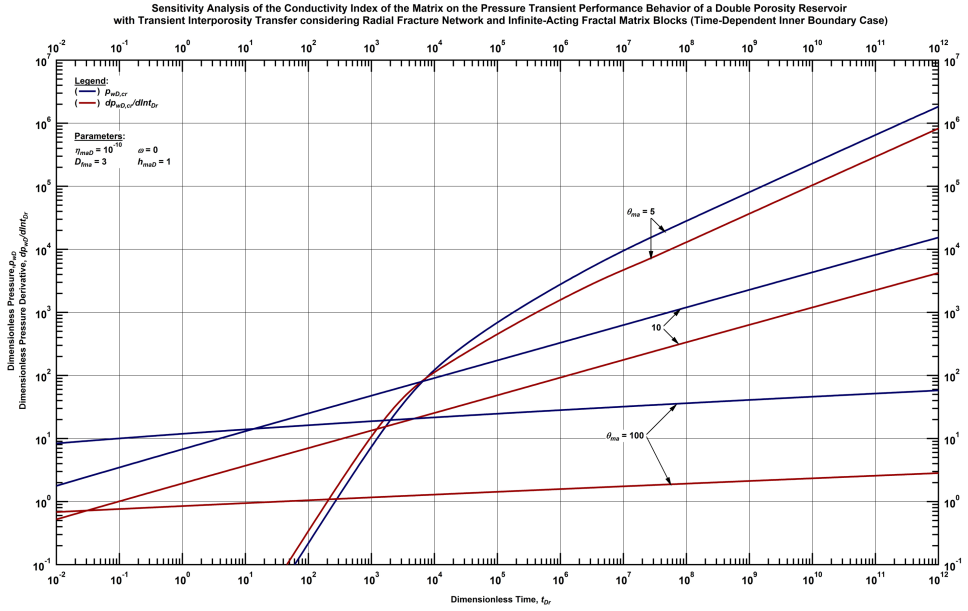

Figure 5.16 — Log-log plot of the pressure-transient and pressure derivative performance behaviors of a double porosity reservoir with time-dependent inner boundary, considering radial fracture network and infinite-acting matrix blocks for selected values of the conductivity index of the matrix (θ_{ma}).

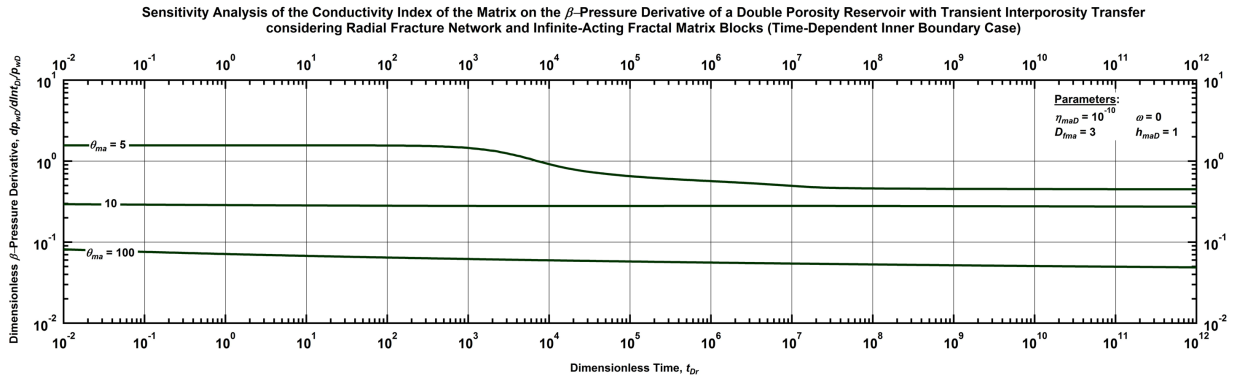

Figure 5.17 — Log-log plot of the β-pressure derivative function of a double porosity reservoir with time-dependent inner boundary, considering radial fracture network and infinite-acting matrix blocks for selected values of the conductivity index of the matrix (θ_{ma}).

Based on **Fig. 5.18**, we conclude that better connected permeable sites inside the matrix blocks (low θ_{ma}-values) yield higher flow rate. Similar to the fractal dimension of the matrix (D_{fma}), the β-rate derivatives presented in **Fig. 5.19** show that rate and rate derivative functions exhibited in **Fig. 5.18** yield power-law behaviors with a slope equal to v_{ma} -1, for θ_{ma} -values equal to 5 (only after $t_D > 10^7$) and 10. The non-constant behavior of the β-rate derivative for θ_{ma} equal to 100 indicates that the rate-transient for this case does not correspond to a power-law behavior.

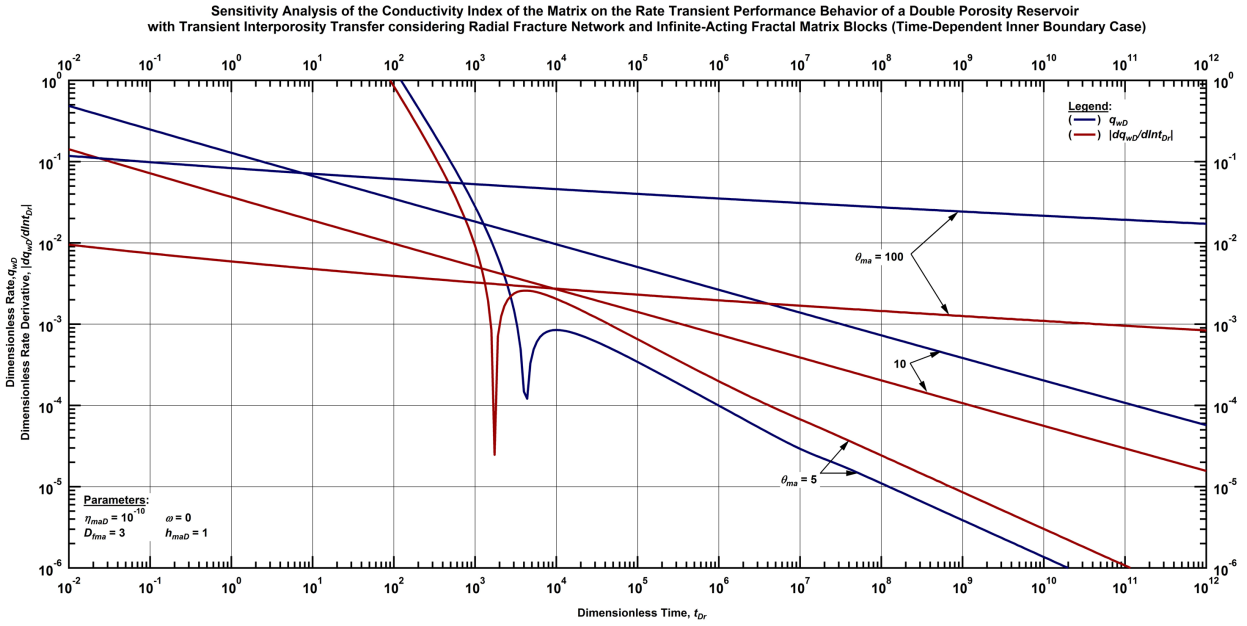

Figure 5.18 — Log-log plot of the rate-transient and rate derivative performance behaviors of a double porosity reservoir with time-dependent inner boundary, considering radial fracture network and infinite-acting matrix blocks for selected values of the conductivity index of the matrix (θ_{ma}).

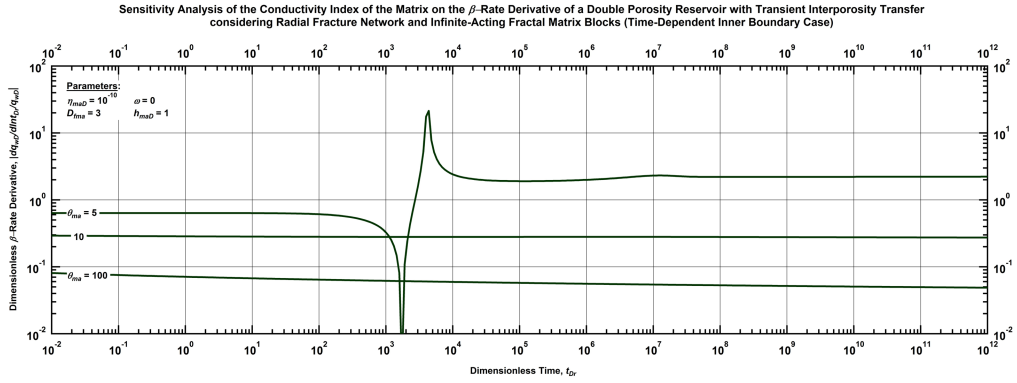

Figure 5.19 — Log-log plot of the β-rate derivative function of a double porosity reservoir with time-dependent inner boundary, considering radial fracture network and infinite-acting matrix blocks for selected values of the conductivity index of the matrix (θ_{ma}).

Given that the scheme to include the wellbore storage effects was developed assuming a constant inner boundary condition, it is not appropriate to use it to models with a variable inner boundary condition.

Double Porosity Model considering Fractal Fracture Network and Infinite-Acting Fractal Matrix Blocks (*Double Fractal Model*)

In general, the most significant parameters in a diffusivity model for a fractal object are the fractal dimension and the conductivity index. The fractal dimension can get values from one to three, whereas the conductivity index can get values higher than zero. Both parameters have a similar influence in the slope of the pressure derivative function. Therefore, we will restrict our sensitivity analyses only to the conductivity indexes (both, fractures and matrix) and consider that the fractal dimension is equal to three for both media.

Sensitivity to the θ-Parameter

Fig. 5.20 presents the sensitivity analysis of the conductivity index of the fracture network (θ) in the pressure transient performance behavior of the double fractal model, considering both cases, with and without wellbore storage effects. **Fig. 5.21** shows the β-pressure derivative of the cases presented in **Fig. 5.20**. In the no-wellbore storage case, we observe that there are two periods of flow separated by a smooth transition period. The first period corresponds to the interaction between the fracture network and the matrix blocks, and the second period corresponds to single system behavior. In both figures, the first period is not observed when the wellbore storage effects are taken into account. This leads to the hypothesis that for practical applications in pressure transient analysis, the only period of flow that could be observed is the single system behavior

period, and the fluid transfer function of the matrix could be reduced to the expression given by Eq. 5.5.

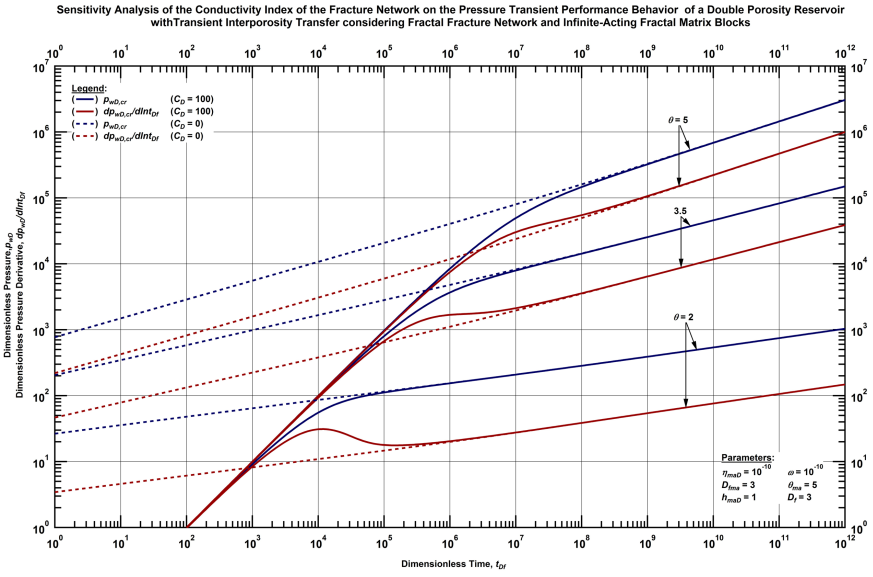

Figure 5.20 — Log-log plot of the pressure-transient and pressure derivative performance behaviors of a double porosity reservoir with time-dependent inner boundary, considering radial fracture network and infinite-acting matrix blocks for selected values of the conductivity index of the fractal fracture network (θ).

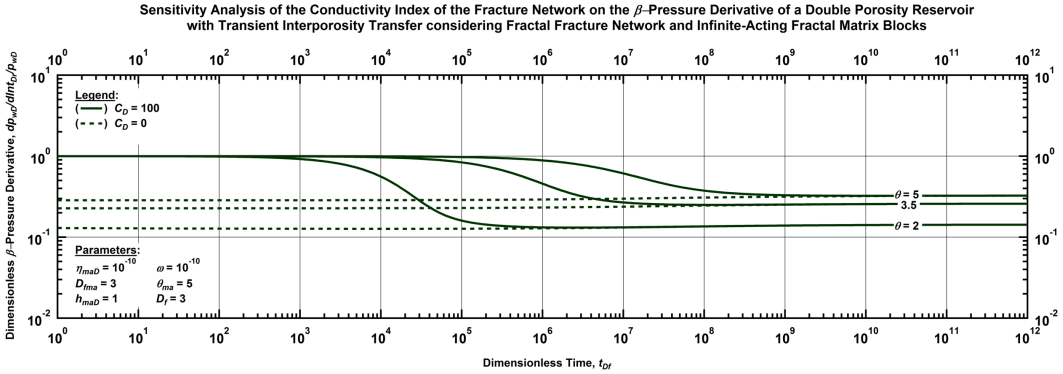

Figure 5.21 — Log-log plot of the β-pressure derivative function of a double porosity reservoir with time-dependent inner boundary, considering radial fracture network and infinite-acting matrix blocks for selected values of the conductivity index of the fractal fracture network (θ).

In **Fig. 5.22**, we observe that a better connected fractal fracture network yield higher flow rates (*i.e.*, the lower the θ-value, the higher flow rate). Given that the standard (constant) wellbore storage effects do not affect the rate transient behavior, it is possible to observe the two periods of flow of the transient behavior of the double fractal reservoir. As in the pressure-transient case, the two periods of flow can be detected in the β-rate derivative presented in **Fig. 5.23**.

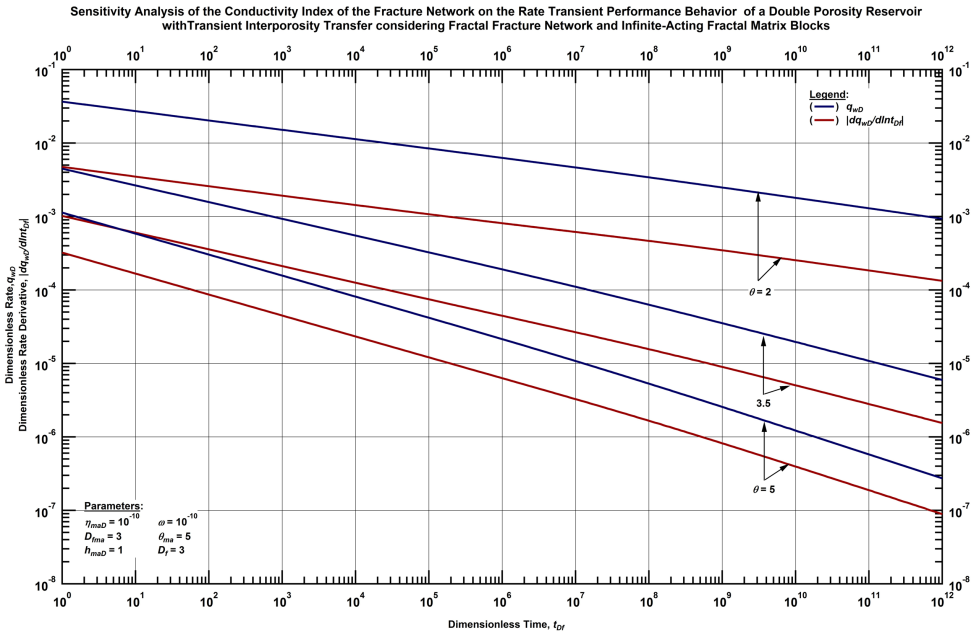

Figure 5.22 — Log-log plot of the rate-transient and rate derivative performance behaviors of a double porosity reservoir considering fractal fracture network and infinite-acting matrix blocks for selected values of the conductivity index of the fractal fracture network (θ).

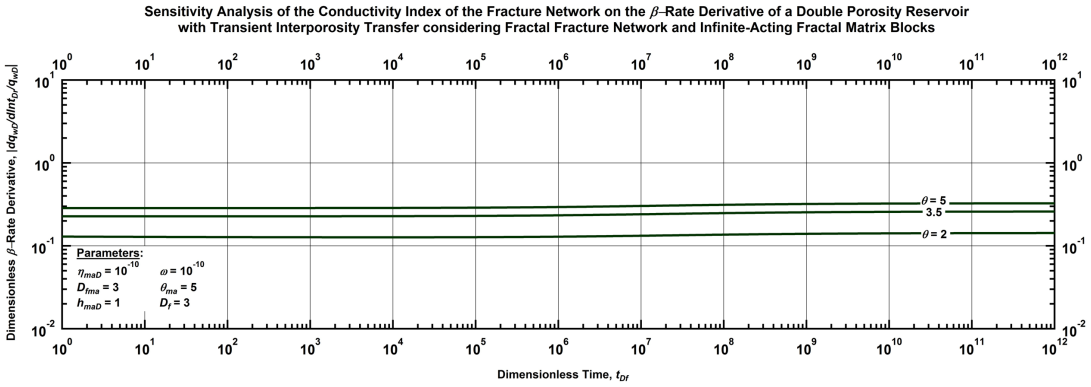

Figure 5.23 — Log-log plot of the β-rate derivative function of a double porosity reservoir considering fractal fracture network and infinite-acting matrix blocks for selected values of the conductivity index of the fractal fracture network (θ).

Sensitivity to the θ_{ma}-Parameter

Fig. 5.24 shows the influence of the conductivity index of the matrix (θ_{ma}) in the pressure transient performance behavior of the double fractal model, considering both cases, with and without wellbore storage effects. **Fig. 5.25** shows the β-pressure derivative of the cases presented in **Fig. 24**. Similar to the case of the conductivity index of the fracture network (θ), we observe that in the no-wellbore storage case two periods of flow are separated by a smooth transition period. In this case, the first period of flow is also hindered by wellbore storage effects. The main difference with the θ-case (**Fig. 5.21**) is that the first period of flow in **Fig. 5.24** is the same for all the θ_{ma} -values. Such a period of flow is shorter, and the appearance of the transition period occurs faster for higher v_{ma}-values (higher θ_{ma}-values). The second period of flow in **Fig. 5.24** yields a straight-line with slope equal to the product $v_{ma}v$. This is confirmed by their β-pressure derivative plot (**Fig. 5.25**).

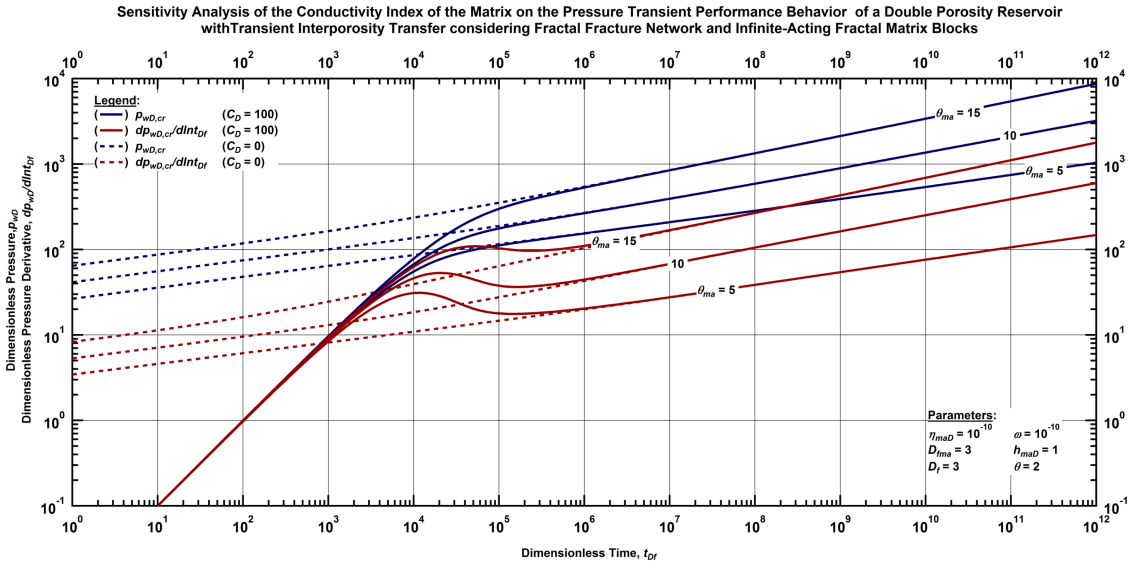

Figure 5.24 — Log-log plot of the pressure-transient and pressure derivative performance behaviors of a double porosity reservoir considering fractal fracture network and infinite-acting matrix blocks for selected values of the conductivity index of the matrix (θ_{ma}).

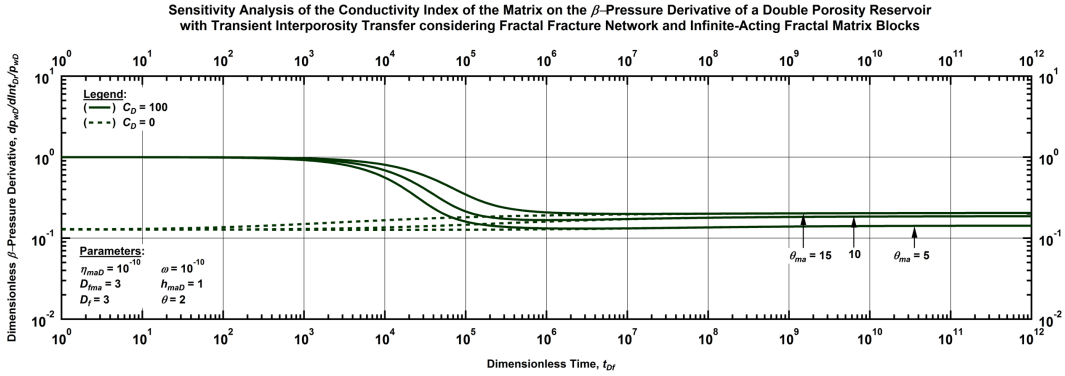

Figure 5.25 — Log-log plot of the β-pressure derivative function of a double porosity reservoir considering fractal fracture network and infinite-acting matrix blocks for selected values of the conductivity index of the matrix (θ_{ma}).

Fig. 5.26 shows that better connected permeable sites inside the fractal matrix blocks yield higher flow rates (*i.e.*, the lower the θ_{ma}-value, the higher flow rate). **Fig. 5.27** shows two periods of flow for each one of the cases presented in **Fig. 5.27**. We observed that the first period of flow corresponds to the interaction between the fracture network and the matrix blocks and it is the same for all the cases. The behavior of the second period is dominated by the θ_{ma}-value, and we have observed that the higher the conductivity index of the matrix, the sooner the second period appears.

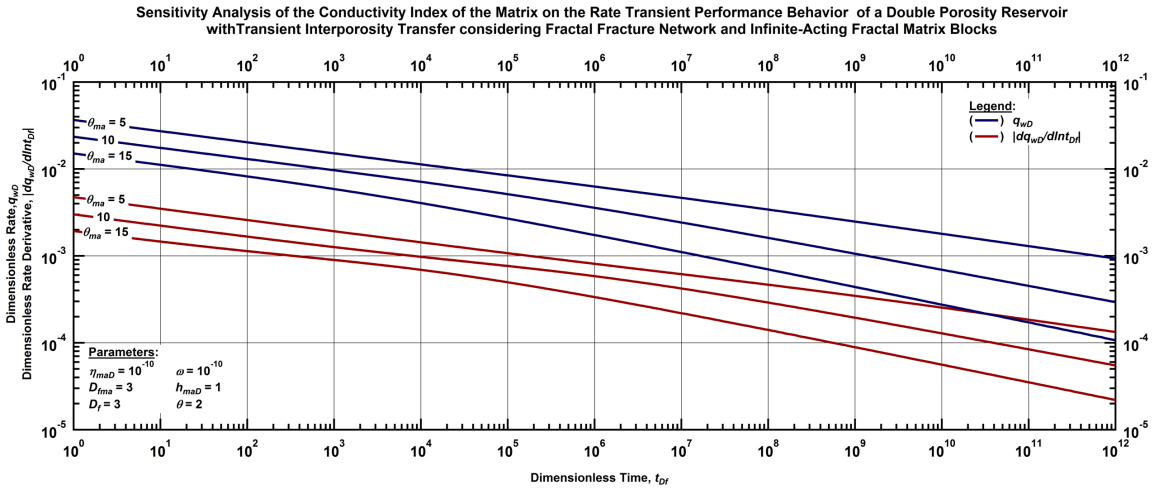

Figure 5.26 — Log-log plot of the rate-transient and rate derivative performance behaviors of a double porosity reservoir considering fractal fracture network and infinite-acting matrix blocks for selected values of the conductivity index of the matrix (θ_{ma}).

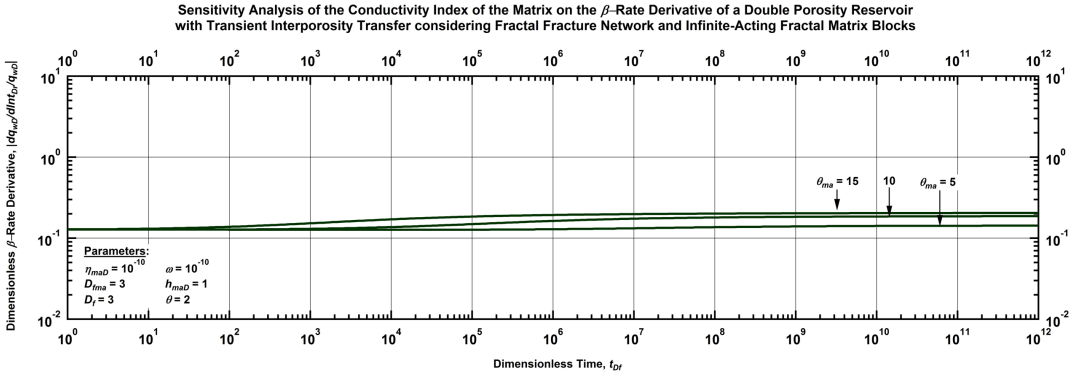

Figure 5.27 — Log-log plot of the β-rate derivative function of a double porosity reservoir considering fractal fracture network and infinite-acting matrix blocks for selected values of the conductivity index of the matrix (θ_{ma}).

5.5. Summary

The purpose of the development of the models presented in this chapter is to provide analytical models for the estimation of parameters of unconventional reservoirs, using pressure and rate transient data.

CHAPTER VI

CONCLUSIONS AND RECOMMENDATIONS

The following conclusions have been derived from this work:

1. We have utilized the fractal geometry theory to develop reservoir models for shale reservoirs. We have extended the existing models for multi-fractured wells to consider the fractal reservoir scenario.

2. Using our new solutions for a horizontal well intercepting a single finite-conductivity, we have found that at early-transient (hydraulic fracture flow) and intermediate-transient times (interaction between the hydraulic fracture and the fractal reservoir), are very sensitive to the fractal parameters of the reservoir. In addition, the influence of the fractal parameters at early and intermediate-transient times is more evident at low values of the dimensionless fracture conductivity.

3. When considering a double porosity reservoir with a fractal fracture network and Euclidean matrix blocks, the presence of a single finite conductivity hydraulic fracture can yield as many as twelve (12) power-law sub-periods of flow as observed in the dimensionless pressure and dimensionless pressure derivative functions as exhibited by our new solutions.

4. We applied the principle of superposition in space to the single finite-conductivity solution to generate the multi-fractured well case, which is a more practical/realistic scenario. Analogous to the case where the horizontal wells are drilled in conventional/homogenous reservoirs, we

found that the transient performance of these types of wells in fractal reservoirs behaves as an equivalent system of a horizontal well intercepting a single fracture.

5. We have studied the impact of the anomalous diffusion phenomenon in the pressure and rate transient performance behaviors and compared these responses to the typical (constant) diffusion cases. We have found that the anomalous diffusion phenomenon shows an additional influence on the pressure and rate responses during early and intermediate-transient times. However; at late times, the anomalous diffusion phenomenon exhibits an overall lower pressure drop for the constant rate solution and consequently, the inclusion of the anomalous diffusion phenomenon results in higher values of flowrate and cumulative production at late-transient times.

6. Our partial results and the mathematical background of the models considering anomalous diffusion made us believe that the fractal reservoir model with typical diffusion is more likely in theory and in practice than the anomalous diffusion case. To provide an explanation to the anomalous diffusion based on the concepts of petroleum reservoir engineering, we developed the double fractal model.

7. We considered that the highly heterogeneous and the low/ultralow nature of the shale reservoirs make appropriate (1) the use of transient interporosity transfer functions and (2) the modeling of the fractal matrix blocks as infinite-acting media. This approach results in a diffusivity equation with the same shape as the so-called anomalous diffusion equation. Therefore, we concluded that the anomalous diffusivity phenomenon in unconventional reservoirs can be related to the fractal geometry and the heterogeneities of the fractal matrix blocks.

8. To model the matrix blocks as fractal objects, we investigated the closed and the infinite-acting matrix blocks scenarios. We found that the fractal dimension of the matrix blocks does not have a significant impact in the signature of the pressure and pressure-transient derivative functions, when the blocks are considered closed (small blocks and/or high hydraulic diffusivity). However, when the matrix blocks behave as "infinite-acting," the pressure- and rate-transient performance behaviors are sensitive to a combined effect of the properties of the fracture network and the matrix blocks at late times.

Based on the results presented in this work, we have defined the following recommendations for future work:

1. In this dissertation, we followed the traditional approaches to superimpose the flow of a reservoir (fractal reservoir) on the plane of the hydraulic fracture. Nonetheless, we have questioned ourselves on the validity of these methods when coupling a fractal and a Euclidean object. The reason is the lack of a physical explanation to observe higher flowrates at early and intermediate times in fractal reservoirs with poorly connected permeable sites (high θ-values) and/or lower fractal dimension (D_f). Therefore, our first recommendation is to explore other alternatives to define the continuity between a hydraulic fracture and a fractal reservoir.

2. Our second recommendation is related to the development of analytical solutions for RTA. In shale reservoirs, the Power-Law/Stretched exponential empirical model is widely used because of its accuracy and flexibility. The shape of this model corresponds to the asymptotic behavior of Fox's functions for small arguments. The solution to the double fractal model can be expressed in terms of this type of function. We believe that the parameters of the double fractal

model can be related to the empirical parameters of the Power-Law/Stretched Exponential model. Consequently, we recommend the development analytical relations between this empirical model and the asymptotic solutions of the double fractal model.

NOMENCLATURE

Field Variables

A_{fma} = Fracture area per unit of matrix volume, L^{-1} [m^{-1}] or [ft^{-1}]

B = Oil formation volume factor, [bbl/STB] or [Rm^3/Sm^3]

c_f = Hydraulic fracture compressibility, $(M/Lt^2)^{-1}$ [Pa^{-1}] or [psi^{-1}]

c_{fb} = Radial fracture network compressibility, $(M/Lt^2)^{-1}$ [Pa^{-1}] or [psi^{-1}]

c_o = Fluid compressibility (oil), $(M/Lt^2)^{-1}$ [Pa^{-1}] or [psi^{-1}]

c_{ma} = Matrix blocks compressibility, $(M/Lt^2)^{-1}$ [Pa^{-1}] or [psi^{-1}]

c_t = Total compressibility, $(M/Lt^2)^{-1}$ [Pa^{-1}] or [psi^{-1}]

c_{tfb} = Total compressibility (natural fractures, radial or fractal), $(M/Lt^2)^{-1}$ [Pa^{-1}] or [psi^{-1}]

c_{tma} = Matrix blocks total compressibility, $(M/Lt^2)^{-1}$ [Pa^{-1}] or [psi^{-1}]

c_{tf} = Hydraulic fracture total compressibility, $(M/Lt^2)^{-1}$ [Pa^{-1}] or [psi^{-1}]

h = Formation thickness, L [m] or [ft]

h_{ma} = Matrix block size, L [m] or [ft]

k = Permeability, L^2 [mD] or [m^2]

k_0 = Reference permeability for a fractal reservoir, L^2 [mD] or [m^2]

k_{0fb} = Reference permeability for a fractal fracture network, L^2 [mD] or [m^2]

k_{0ma} = Reference permeability for the fractal matrix blocks, L^2 [mD] or [m^2]

k_f = Hydraulic fracture permeability, L^2 [mD] or [m^2]

k_{fb} = Radial fracture network permeability, L^2 [mD] or [m^2]

k_{ma} = Matrix permeability, L^2 [mD] or [m^2]

L_r = Reference Length, L [m] or [ft]

p = Pressure, M/Lt^2 [Pa] or [psi]

p_i = Initial reservoir pressure, M/Lt^2 [Pa] or [psi]

p_f = Fracture pressure, M/Lt^2 [Pa] or [psi]

p_{wf} = Wellbore flowing pressure, M/Lt^2 [Pa] or [psi]

$p_{\phi f}$ = Wellbore phase redistribution pressure, M/Lt^2 [Pa] or [psi]

p_{tf} = Tubing flowing pressure at surface, M/Lt^2 [Pa] or [psi]

r = Radial distance, L [m] or [ft]

R = Radial distance (fractal or spherical systems), L [m] or [ft]

r_f = Radius of a circular hydraulic fracture, L [m] or [ft]

r_w = Wellbore radius, L [m] or [ft]

s = Skin factor, dimensionless

q_w = Well Flowrate, L^3/t [m^3/sec] or [ft^3/s]

t = Time, t [sec]

u = Laplace transform variable

w = Fracture width, L [m] or [ft]

x_f = Fracture half length, L [m] or [ft]

Dimensionless Variables

A_{fD} = Dimensionless natural fracture area

A_{ffD} = Dimensionless fractal fracture area

D_f = Fractal dimension of a fractal reservoir

D_{fb} = Fractal dimension of a fractal fracture network

D_{fma} = Fractal dimension of the matrix blocks

C_{fD} = Dimensionless wellbore storage constant

F_{cD} = Dimensionless fracture conductivity

h_D = Dimensionless formation thickness

h_{maD} = Dimensionless matrix block size

N_{pD} = Dimensionless cumulative production

$p_{D,cr}$ = Dimensionless pressure in the reservoir defined for the constant-rate solution

$p_{fD,cr}$ = Dimensionless pressure in the hydraulic fracture defined for the constant-rate solution

$p_{fbD,cr}$ =Dimensionless pressure in the fracture network defined for the constant-rate solution

$p_{ffnD,cr}$ =Dimensionless pressure in the fractal-fracture network for the constant-rate solution

$p_{rfnD,cr}$ =Dimensionless pressure in the radial-fracture network the constant-rate solution

$p_{maD,cr}$ =Dimensionless pressure in the fractal matrix blocks for the constant-rate solution

p_{wD} = Dimensionless wellbore flowing pressure

r_D = Dimensionless radius for a circular system

r_{wD} = Dimensionless radius wellbore

R_D = Dimensionless radius for a spherical or fractal system

q_{wD} = Dimensionless flowrate

S_{int} = Interporosity skin

t_D = Dimensionless time

t_{Dr} = Dimensionless time (dimensionless variables for a radial fracture network)

t_{Df} = Dimensionless time (dimensionless variables for a fractal fracture network)

x_D = Dimensionless linear position in the x-direction

z_D = Dimensionless linear position in the z-direction

v = Grouping parameter of the fractal variables of a fractal fracture network/reservoir.

v_{ma} = Grouping parameter of the fractal variables of the fractal matrix blocks

Greek Symbols

α_0 = Grouping parameter of the properties the fractal matrix block, dimensionless

α_1 = Grouping parameter of the properties the fractal matrix block, dimensionless

α_{Df} = Area of a unit sphere in D_f dimensions

β = Spatial dimension, dimensionless

β_{ma} = Spatial dimension of the fractal fracture network, dimensionless

γ = Anomalous diffusivity exponent as function of fractal parameters, dimensionless

δq_D = Point density fluid withdrawal, dimensionless

θ = Conductivity index, dimensionless

θ_{ma} = Conductivity index of the fractal matrix blocks, dimensionless

η_{fD} = Dimensionless hydraulic diffusivity of the hydraulic fracture, dimensionless

η_{maD} = Dimensionless hydraulic diffusivity of the matrix, dimensionless

μ = Newtonian Viscosity, M/Lt [cp] or [lb_m/ft•s]

ξ = Grouping parameter, dimensionless

ξ_{RD} = Function of R_D, dimensionless

ϕ = Porosity, fraction

ϕ_0 = Reference porosity for a fractal reservoir, fraction

ϕ_{0fb} = Reference porosity for fractal fracture network, fraction

ϕ_f = Hydraulic fracture porosity, fraction

ϕ_{fb} = Natural fracture network porosity, fraction

ϕ_{0ma} = Reference porosity for the fractal matrix blocks, fraction

ϕ_{ma} = Matrix porosity, fraction

ω = Storativity ratio, dimensionless

Mathematical Functions

$E_i(x)$ = Exponential Integral Function

$I_v(x)$ = Modified Bessel Functions of the first kind, *v*-order

$K_v(x)$ = Modified Bessel Functions of the second kind, *v*-order

$\Gamma(x)$ = Gamma function

$\Gamma(a,x)$=Incomplete Gamma function

REFERENCES

Abbaszadeh, M. 1995. Pressure-transients in Reservoirs with Stochastic Fractal Geometry Patterns. Society of Petroleum Engineers. SPE-29615-MS

Acuna, J. A., and Yortsos, Y. C. 1991. Numerical Construction And Flow Simulation In Networks Of Fractures Using Fractal Geometry. SPE Annual Technical Conference and Exhibition, Dallas, Texas. 6-9 October. SPE-22703-MS. https://doi:10.2118/22703-MS

Acuna, J. A., Ershaghi, I., and Yortsos, Y. C. 1995. Practical Application of Fractal Pressure-transient Analysis of Naturally Fractured Reservoirs. *SPE Form Eval*. **10** (03). SPE-24705-PA. https://doi.org/10.2118/24705-PA

Barker, J. A. 1988. A generalized radial flow model for hydraulic tests in fractured rock. *Water Resour. Res.* **24** (10): 1796–1804. 10.1029/WR024i010p01796

Barnsley, M.F. 1988. Fractals Everywhere. Academic Press, Boston.

Beier, R. A. 1994. Pressure-transient Model of a Vertically Fractured Well in a Fractal Reservoir. *SPE Form Eval*. SPE-20582-PA. https://doi:10.2118/20582-PA

Blasingame, T. A., and Poe, B. D. 1993. Semianalytic Solutions for a Well With a Single Finite conductivity Vertical Fracture. SPE Annual Technical Conference and Exhibition, Houston, Texas. 3-6 October. SPE-26424-MS. https://doi.org/10.2118/26424-MS

Brown, M., Ozkan, E., Raghavan, R., and Kazemi, H. 2011. Practical Solutions for Pressure-Transient Responses of Fractured Horizontal Wells in Unconventional Shale Reservoirs. *SPE Res Eval & Eng* **14** (06). SPE-125043-PA. https://doi.org/10.2118/125043-PA

Camacho-Velazquez-Velazquez, R., Fuentes-Cruz, G., and Vasquez-Cruz, M. A. 2008. Decline-Curve Analysis of Fractured Reservoirs With Fractal Geometry. *SPE Res Eval & Eng*. SPE-104009-PA. https://doi:10.2118/104009-PA

Chang, J., and Yortsos, Y. C. 1993. A Note On Pressure-Transient Analysis Of Fractal Reservoirs. Society of Petroleum Engineers. http://doi:10.2118/25296-PA

Chang, J., and Yortsos, Y. C. 1990. Pressure-transient Analysis of Fractal Reservoirs. *SPE Form Eval* **5** (1). SPE-18170-PA. https://doi:10.2118/18170-PA

Chatas, A. T. 1966. Unsteady Spherical Flow in Petroleum Reservoirs. Society of Petroleum Engineers. *SPE J*. **6** (02). SPE-1305-PA. https://doi:10.2118/1305-PA

Chen, C.-C., and Rajagopal, R. 1997. A Multiply-Fractured Horizontal Well in a Rectangular Drainage Region. *SPE J* **2** (04). SPE-37072-PA. https://doi.org/10.2118/37072-PA

Cinco L., H., Samaniego V., F., and Dominguez A., N. 1978. *SPE J* **18** (4). SPE-6014-PA. https://doi:10.2118/6014-PA

Cinco-Ley, H., and Samaniego-V., F. 1981a. Pressure-transient Analysis for Fractured Wells. *J Pet Technol* **33** (09). SPE-7490-PA. https://doi:10.2118/7490-PA

Cinco-Ley, H., and Samaniego-V., F. 1981b. Pressure-transient Analysis: Finite conductivity Fracture Case Versus Damaged Fracture Case. SPE Annual Technical Conference and Exhibition, San Antonio, Texas. 4-7 October. SPE-10179-MS. https://doi.org/10.2118/10179-MS

Cinco-Ley, H., and Samaniego V., F. 1982. Pressure-transient Analysis for Naturally Fractured Reservoirs. SPE Annual Technical Conference and Exhibition, New Orleans, Louisiana. 26-29 September. SPE-11026-MS. https://doi:10.2118/11026-MS

Cinco-Ley, H., Samaniego V., F., and Kucuk, F. 1985. The Pressure-transient Behavior for Naturally Fractured Reservoirs With Multiple Block Size. SPE Annual Technical Conference and Exhibition, Las Vegas, Nevada, 22-26 September. SPE-14168-MS. https://doi:10.2118/14168-MS

Cinco-Ley, H., and Meng, H.-Z. 1988. Pressure-transient Analysis of Wells With Finite conductivity Vertical Fractures in Double Porosity Reservoirs. SPE Annual Technical Conference and Exhibition, Houston, Texas. 2-5 October. SPE-18172-MS. https://doi:10.2118/18172-MS

Cossio, M., Moridis, G., and Blasingame, T. A. 2013. A Semianalytic Solution for Flow in Finite conductivity Vertical Fractures by Use of Fractal Theory. *SPE J.* SPE-153715-PA. https://doi.org/10.2118/153715-PA

De Swaan, A. 1976. Analytic Solutions for Determining Naturally Fractured Reserviors Properties by Well Testing. *SPE J* **16** (3). SPE-5346-PA. https://doi:10.2118/5346-PA

Doe, T. W. 1991. Fractional Dimension Analysis of Constant-Pressure Well Tests. SPE Annual Technical Conference and Exhibition, Dallas, Texas. 6-9 October. SPE-22702-MS. http://10.2118/22702-MS

Flamenco-Lopez, F., and Camacho-Velazquez, R. 2001. Fractal Pressure-transient Behavior of Naturally Fractured Reservoirs. SPE Annual Technical Conference and Exhibition, New Orleans, Louisiana. 30 September – 3 October. SPE-71591-MS. http://doi:10.2118/71591-MS

Flamenco-Lopez, F., and Camacho-Velazquez, R. 2003. Determination of Fractal Parameters of Fracture Networks Using Pressure-Transient Data. *SPE Res Eval & Eng* **6** (01). https://doi:10.2118/82607-PA

Gaver, D.P. Jr. 1965. Observing Stochastic Processes, and approximate transform inversion. *Operations Research*, **14** (3): 444-459

Gringarten, A. C., Ramey, H. J., and Raghavan, R. 1974. Unsteady-State Pressure Distributions Created by a Well With a Single Infinite conductivity Vertical Fracture. *SPE J* **14** (04). SPE-4051-PA. https://doi:10.2118/4051-PA

Houze, O. P., Horne, R. N., and Ramey, H. J. 1988. Pressure-Transient Response of an Infinite conductivity Vertical Fracture in a Reservoir with Double-Porosity Behavior. *SPE Form Eval*.**3** (03). SPE-12778-PA. http://doi:10.2118/12778-PA

Larsen, L., and Hegre, T. M. 1991. Pressure-Transient Behavior of Horizontal Wells With Finite conductivity Vertical Fractures. International Artic Technology Conference. Anchorage, Alaska. 29-31 May. SPE-22076-MS. http://doi:10.2118/22076-MS

Larsen, L., and Hegre, T. M. 1994. Pressure-transient Analysis of Multi-fractured Horizontal Wells. SPE Annual Technical Conference and Exhibition, New Orleans, Louisiana. 25-28 September. SPE-28386-MS. http://doi:10.2118/28389-MS

Lee, S.-T., & Brockenbrough, J. R. 1986. A New Approximate Analytic Solution for Finite conductivity Vertical Fractures. *SPE Form Eval*. **1** (01). SPE-12013-PA. https://doi.org/10.2118/12013-PA

Madelbrot, B. B. 1977. *The Fractal Geometry of Nature*. New York: W.H. Freeman and Company.

MATLAB 2015a. The MathWorks.

Medeiros, F., Ozkan, E., and Kazemi, H. 2008. Productivity and Drainage Area of Fractured Horizontal Wells in Tight Gas Reservoirs. *SPE Res Eval & Eng* **11** (05). SPE-108110-PA. https://doi.org/10.2118/108110-PA

Metzler, R., Glöckle, W.G., and Nonnenmacher, T.F. 1994. Fractional Model Equation for Anomalous Diffusion. *Physica* **A** (211): 13-24. http://doi:10.1016/0378-4371 (94) 90064-7

Miller, F.G. 1962. Theory of Unsteady State Influx of Water in Linear Reservoirs. *J. Inst. Pet*. 48, 467.

O'Shaughnessy, B. and Procaccia, I. 1985. Diffusion in Fractals. *Physical Review*. **A** (32): 3073-3083. https://doi.org/10.1103/PhysRevA.32.3073

Oberhettinger, F. and Badii, L. 1973, *Tables of Laplace Transform*, first edition. Heidelberg, Germany. Srpinger-Verlag.

Olarewaju, J. 1996. Modeling Fractured Reservoirs With Stochastic Fractals. Abu Dhabi International Petroleum Exhibition and Conference, Abu Dhabi, United Arab Emirates. 13-16 October. SPE-36207-MS. https://doi:10.2118/36207-MS

Ortegueira, M., and Machado, J. 2017. Fractional Definite Integral. *Fractal and Fractional*. 1(2). https://doi.org/10.3390/fractalfract1010002

Ozcan, O., Sarak, H., Ozkan, E., & Raghavan, R. S. 2014. A Trilinear Flow Model for a Fractured Horizontal Well in a Fractal Unconventional Reservoir. SPE Annual Technical Conference and Exhibition, Amsterdam, The Netherlands. 27-29 October. SPE-170971-MS. https://doi.org/10.2118/170971-MS

Ozkan, E., and Raghavan, R. 1991. New Solutions for Well-Test-Analysis Problems: Part 1-Analytical Considerations (includes associated papers 28666 and 29213). *SPE Form Eval*. **6** (03). SPE-18615-PA. https://doi.org/10.2118/18615-PA

Ozkan, E., Brown, M. L., Raghavan, R., and Kazemi, H. 2011. Comparison of Fractured-Horizontal-Well Performance in Tight Sand and Shale Reservoirs. *SPE Res Eval & Eng* **14** (02). SPE-121290-PA. https://doi.org/10.2118/121290-PA

Razminia, K. Razminia, A., and Teneiro Machado, J. A. 2014. Analysis of diffusion process in fractured reservoirs using fractional derivative approach. *Communications in Nonlinear Science and Numerical Simulation*. **19** (09). 3161-3170. https://doi.org/10.1016/j.cnsns.2014.01.025

Razminia, K. Razminia, A., and Trujilo, J. J. 2015a. Analysis of radial composite systems based on fractal theory and fractional calculus, *Signal Processing*, 107, 378-388. https://doi.org/10.1016/j.sigpro.2014.05.008

Razminia, K. Razminia, A., and Torres, D. F. M. 2015b. Pressure responses of a vertically hydraulic fractured well in a reservoir with fractal structure, *Applied Mathematics and Computation*, 257, 374-380.

Raghavan, R. S., Chen, C.-C., and Agarwal, B. 1997. An Analysis of Horizontal Wells Intercepted by Multiple Fractures. *SPE J.* **2** (03). SPE-27652-PA. https://doi.org/10.2118/27652-PA

Raghavan, R 2012a. Fractional derivatives: Application to transient flow, *Journal of Petroleum Science and Engineering*, 80, 7-13.

Raghavan, R 2012b. Fractional diffusion: Performance of fractured wells, *Journal of Petroleum Science and Engineering*, 92-93, 167-173.

Raghavan, R. and Chen, C. 2013. Fractional diffusion in rocks produced by horizontal wells with multiple, transverse hydraulic fractures of finite conductivity, *Journal of Petroleum Science and Engineering*, 109, 133-143.

Sahimi, M., and Yortsos, Y. C. 1990. Applications of Fractal Geometry To Porous Media: A Review. SPE-20476-MS.

Serra, K., Reynolds, A. C., and Raghavan, R. 1983. New Pressure-transient Analysis Methods for Naturally Fractured Reservoirs. *J Pet Technol* **35** (12). SPE-10780-PA. http://doi:10.2118/10780-PA

Soliman, M. Y., Hunt, J. L., and El Rabaa, A. M. 1990. Fracturing Aspects of Horizontal Wells. *J Pet Technol* **42** (8). SPE-18542-PA. http://doi:10.2118/18542-PA

Streltsova, T. D. 1983. Well Pressure Behavior of a Naturally Fractured Reservoir. *SPE J.* **23** (05). SPE-10782-PA. http://doi:10.2118/10782-PA

Stehfest, H. (1970). Algorithm 368 – Numerical Inversion of Laplace Transforms. *Communication, ACM* 13 (1): 47-49.

Valdes-Perez, A.R., Pulido, H., Cinco-Ley, H. Galicia-Muñoz, G. 2011. A new bilinear flow model for Naturally Fractured Reservoirs with Transient Interporosity Transfer. 36th Workshop on Geothermal Reservoir Engineering, Stanford, California. January 31st – February, 2nd.

Valdes-Perez Alex. 2013. A new double porosity fractal model for well test analysis with transient interporosity transfer for petroleum and geothermal systems, MSc Dissertation, U. of Stavanger, Norway.

Valdes-Perez, A.R., Larsen, L., and Blasingame, T.A. 2018. Pressure-Transient Behavior of a Horizontal Well with a Finite-Conductivity Fracture within a Fractal Reservoir. SPE Canada Unconventional Resources Conference. Calgary, Canada. 13-14 March. SPE-189814-MS. http://doi.org/10.2118/189814-MS

Valdes-Perez, A.R., and Blasingame, T.A. 2018. Pressure-Transient Behavior of Double Porosity Reservoirs with Transient Interporosity Transfer with Fractal Matrix Blocks. SPE Europec featured at 80th EAGE Conference and Exhibition. Copenhagen, Denmark. 11-14 June. SPE-190841-MS. https://doi.org/10.2118/190841-MS

Valdes-Perez, A.R., Larsen, L., and Blasingame, T.A. 2018. Pressure and Rate Transient Behavior of a Horizontal Well Intercepting Multiple Hydraulic Fractures within a Fractal Reservoir. Unconventional Resources Technology Conference. Houston, Texas. 23-25 July. URTeC-2902854

Valkó, P.P. and Abate, K. 2004. Comparison of Sequence Accelerators for the Gaver Method of Numerical Laplace Transform Inversion. *Computers and Mathematics with Application.* **48** (3-40) pp 629-636.

Van Everdingen, A. F., and Hurst, W. 1949. The Application of the Laplace Transformation to Flow Problems in Reservoirs. Society of Petroleum Engineers. https://doi:10.2118/949305-G

Wolfram Research, Inc. Mathematica 11, 2017. *Wolfram Research, Inc.* Champaign, Illinois.

Wong, D. W., Harrington, A. G., and Cinco-Ley, H. 1986. Application of the Pressure Derivative Function in the Pressure-transient Testing of Fractured Wells. *SPE Form Eval*. **1** (05). SPE-13056-PA. https://doi.org/10.2118/13056-PA

APPENDIX A

PRESSURE-TRANSIENT BEHAVIOR OF HORIZONTAL WELLS WITH FINITE-CONDUCTIVITY VERTICAL FRACTURES

In this Appendix, we present the detailed derivation and the procedure to obtain the solution of the model presented by Larsen *et al*. (1991).

A.1. Development of the Radial Diffusivity Equation for a Circular Transverse Finite Conductivity Fracture

To develop the radial diffusivity equation that describes the flow inside the circular hydraulic fracture, consider the control volume shown in **Fig. A.1**. The control volume is constructed by two concentric horizontal cylinders. The inner and outer cylinders have radii r and $r+\Delta r$, respectively. For this model, the flow occurs in the r- and z-directions (angular flow is neglected).

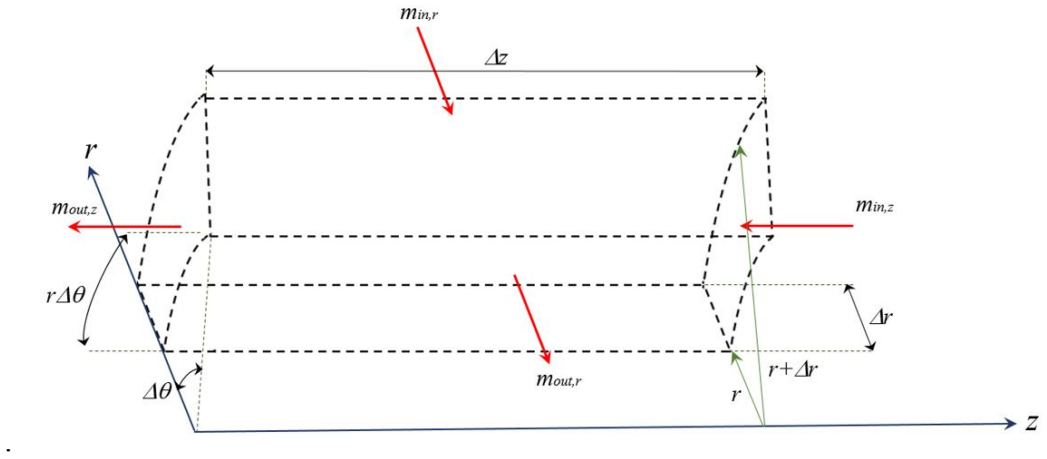

Figure A.1 — Control volume of a circular vertical hydraulic fracture.

The volume of the geometric shape exhibit in **Fig. A.1** is given by:

$$V_c = r\Delta r\Delta\theta\Delta z\,. \quad \text{(A.1)}$$

The incoming mass of a fluid, $m_{in,r}$, throughout the outer cylinder is:

$$m_{in,r} = -\rho v_r[r+\Delta r]\Delta\theta\Delta z\Delta t\,, \quad \text{(A.2)}$$

and the outgoing mass, $m_{out,r}$, throughout the outer cylinder is given by:

$$m_{out,r} = [-\rho v_r + \Delta(\rho v_r)]r\Delta\theta\Delta z\Delta t\,. \quad \text{(A.3)}$$

Analogously, the incoming mass of fluid in the z-direction is:

$$m_{in,z} = -\rho v_z r\Delta r\Delta\theta\Delta z\Delta t\,. \quad \text{(A.4)}$$

and the outgoing mass in the same direction is defined by:

$$m_{out,z} = [-\rho v_z + \Delta(\rho v_z)]r\Delta r\Delta\theta\Delta z\Delta t\,. \quad \text{(A.5)}$$

The cumulative mass of the fluid is determined by:

$$m_c = m_{out,r} + m_{out,z} - [m_{in,r} + m_{in,z}]\,. \quad \text{(A.6)}$$

The following expression results from combining Eqs. A.2 through A.6 and arraying:

$$m_c = \Delta(\rho v_r)r\Delta\theta\Delta z\Delta t + \rho v_r\Delta r\Delta\theta\Delta z\Delta t + \Delta(\rho v_z)r\Delta r\Delta\theta\Delta z\Delta t\,. \quad \text{(A.7)}$$

The mass of fluid at an initial time can be expressed as:

$$m_{t_1} = \phi_f S_f \rho r\Delta r\Delta\theta\Delta z\,. \quad \text{(A.8)}$$

At a final time, the mass of fluid is given by:

$$m_{t_2} = \phi_f S_f \rho r \Delta r \Delta\theta \Delta z + \Delta(\phi_f S_f \rho) r \Delta r \Delta\theta \Delta z \,. \quad \text{(A.9)}$$

The cumulative mass of fluid for the time-dependent case is given by:

$$m_c = m_{t_2} - m_{t_1} \,. \quad \text{(A.10)}$$

Substituting Eq. A.8 and Eq. A.9 in Eq. A.10:

$$m_c = \Delta(\phi_f S_f \rho) r \Delta r \Delta\theta \Delta z \,. \quad \text{(A.11)}$$

Equating Eq. A.7 and Eq. A.11:

$$\Delta(\rho v_r) r \Delta\theta \Delta z \Delta t + \rho v_r \Delta r \Delta\theta \Delta z \Delta t + \Delta(\rho v_z) r \Delta r \Delta\theta \Delta z \Delta t = \Delta(\phi_f S_f \rho) r \Delta r \Delta\theta \Delta z \,. \quad \text{(A.12)}$$

Dividing Eq. A.12 by $V_c \Delta t$, such an equation reduces to:

$$\frac{\Delta(\rho v_r)}{\Delta r} + \frac{\rho v_r}{r} + \frac{\Delta(\rho v_z)}{\Delta z} = \frac{\Delta(\phi_f S_f \rho)}{\Delta t} \,. \quad \text{(A.13)}$$

Taking the limits of Δr, Δt and Δz to zero, Eq. A.13 can be written in its differential form. Such an equation becomes:

$$\frac{\partial(\rho v_r)}{\partial r} + \frac{\rho v_r}{r} + \frac{\partial(\rho v_z)}{\partial z} = \frac{\partial(\phi_f S_f \rho)}{\partial t} \,. \quad \text{(A.14)}$$

To obtain the diffusivity equation for radial flow, the continuity equation defined by Eq. A.14 must be combined with an equation of motion and an equation of state. For this model, Darcy's Law flow will be considered in both *r*- and *z*-directions. For the *r*-direction:

$$v_r = \frac{k_r}{\mu}\frac{\partial p_f}{\partial r}, \quad \text{.....(A.15)}$$

and in the *z*-direction:

$$v_r = \frac{k_z}{\mu}\frac{\partial p_f}{\partial z}. \quad \text{.....(A.16)}$$

Substituting Eq. A.15 and Eq. A.16 in Eq. A.14 and assuming single fluid flow (*i.e.*, *Sf*=1):

$$\frac{\partial}{\partial r}\left[\rho\frac{k_r}{\mu}\frac{\partial p_f}{\partial r}\right]+\frac{\rho}{r}\left[\frac{k_r}{\mu}\frac{\partial p_f}{\partial r}\right]+\frac{\partial}{\partial z}\left[\rho\frac{k_z}{\mu}\frac{\partial p_f}{\partial z}\right]=\frac{\partial(\phi_f\rho)}{\partial t} \quad \text{.....(A.17)}$$

Expanding Eq. A.15 and assuming constant permeability and viscosity, such an equation is rewritten as:

$$\frac{\partial}{\partial r}\left[\rho\frac{k_r}{\mu}\frac{\partial p_f}{\partial r}\right]+\frac{\rho}{r}\left[\frac{k_r}{\mu}\frac{\partial p_f}{\partial r}\right]+\frac{\partial}{\partial z}\left[\rho\frac{k_z}{\mu}\frac{\partial p_f}{\partial z}\right]=\frac{\partial(\phi_f\rho)}{\partial t} \quad \text{.....(A.18)}$$

Expanding Eq. A.15 and assuming constant permeability and viscosity, such an equation is rewritten as:

$$\frac{\partial^2 p_f}{\partial r^2}+\frac{1}{r}\frac{\partial p_f}{\partial r}+\frac{k_z}{k_r}\frac{\partial^2 p_f}{\partial z^2}+\frac{1}{\rho}\frac{\partial\rho}{\partial r}\frac{\partial p_f}{\partial r}+\frac{1}{\rho}\frac{\partial\rho}{\partial z}\frac{k_z}{k_r}\frac{\partial p_f}{\partial z}=\frac{\phi_f\mu}{k_r}\left[\frac{1}{\rho}\frac{\partial\rho}{\partial t}+\frac{1}{\phi_f}\frac{\partial\phi_f}{\partial t}\right] \quad \text{.....(A.19)}$$

To include the effects of a slightly compressible fluid, it is convenient to express some of the derivatives in Eq. A.19 in terms of the change in density of porosity of the hydraulic fracture with respect to pressure. Therefore, using the chain rule:

$$\frac{\partial\rho}{\partial r}=\frac{\partial\rho}{\partial p_f}\frac{\partial p_f}{\partial r}, \quad \text{.....(A.20)}$$

$$\frac{\partial \rho}{\partial z} = \frac{\partial \rho}{\partial p_f}\frac{\partial p_f}{\partial z}, \quad \text{(A.21)}$$

$$\frac{\partial \rho}{\partial t} = \frac{\partial \rho}{\partial p_f}\frac{\partial p_f}{\partial t}, \quad \text{(A.22)}$$

$$\frac{\partial \phi_f}{\partial t} = \frac{\partial \phi_f}{\partial p_f}\frac{\partial p_f}{\partial t} \quad \text{(A.23)}$$

Substituting Eq. A.20 through Eq. A.23 in Eq. A.19 and arraying:

$$\frac{\partial^2 p_f}{\partial r^2} + \frac{1}{r}\frac{\partial p_f}{\partial r} + \frac{k_z}{k_r}\frac{\partial^2 p_f}{\partial z^2} + \frac{1}{\rho}\frac{\partial \rho}{\partial p_f}\left[\left[\frac{\partial p_f}{\partial r}\right]^2 + \frac{k_z}{k_r}\left[\frac{\partial p_f}{\partial z}\right]^2\right] = \frac{\phi_f \mu}{k_r}\left[\frac{1}{\rho}\frac{\partial \rho}{\partial p_f} + \frac{1}{\phi_f}\frac{\partial \phi_f}{\partial p_f}\right]\frac{\partial p_f}{\partial t}. \quad \text{(A.24)}$$

The compressibility of the fluid is defined by:

$$c_o = \frac{1}{\rho}\frac{\partial \rho}{\partial p_f}, \quad \text{(A.25)}$$

and the compressibility of the hydraulic fracture is:

$$c_f = \frac{1}{\phi_f}\frac{\partial \phi_f}{\partial p_f}. \quad \text{(A.26)}$$

Substituting Eqs. A.25 and A.26 in Eq. A.24 and assuming negligible squared pressure gradients, Eq. A.24 becomes:

$$\frac{\partial^2 p_f}{\partial r^2} + \frac{1}{r}\frac{\partial p_f}{\partial r} + \frac{k_z}{k_r}\frac{\partial^2 p_f}{\partial z^2} = \frac{\phi_f \mu c_{tf}}{k_r}\frac{\partial p_f}{\partial t}, \quad \text{(A.27)}$$

where the total compressibility of the fracture is defined by:

$$c_{tf} = c_o + c_f \,. \quad \text{(A.28)}$$

Rewriting Eq. A.27 in the compact form and considering the fracture as an isotropic media (*i.e.*, $k_f = k_r = k_z$):

$$\frac{1}{r}\left[r \frac{\partial p_f}{\partial r} \right] + \frac{\partial^2 p_f}{\partial z^2} = \frac{\phi_f \mu c_{tf}}{k_f} \frac{\partial p_f}{\partial t} \quad \text{(A.29)}$$

To couple the two porous media (the circular hydraulic fracture and the 3D reservoir), the pressure and the flowrate in both media must be the same. Hence, for the pressure:

$$p_f(z = \pm w/2, t) = p(z = \pm w/2, t) \approx p(z = 0, t) \,, \quad \text{(A.30)}$$

and for the flowrate:

$$\left[k_f \frac{\partial p_f}{\partial z} \right]_{z=\pm w/2} \approx \left[k \frac{\partial p}{\partial z} \right]_{z=0} . \quad \text{(A.31)}$$

The second derivative of the pressure in the circular fracture with respect to z can be reduced by taking an averaged pressure in the fracture:

$$\frac{1}{r}\left[r \frac{\partial}{\partial r}\left[\frac{1}{w} \int_{-w/2}^{w/2} p_f \, dz \right] \right] + \frac{1}{w} \int_{-w/2}^{w/2} \frac{\partial^2 p_f}{\partial z^2} dz = \frac{\phi_f \mu c_{tf}}{k_f} \frac{\partial}{\partial t}\left[\frac{1}{w} \int_{-w/2}^{w/2} p_f \, dz \right] . \quad \text{(A.32)}$$

Applying the integral and evaluating the integration limits Eq. A.32 becomes:

$$\frac{1}{r}\left[r \frac{\partial}{\partial r}\left[\frac{1}{w} \int_{-w/2}^{w/2} p_f \, dz \right] \right] + \frac{1}{w}\left[\left[\frac{\partial p_f}{\partial z} \right]_{z=w/2} - \left[\frac{\partial p_f}{\partial z} \right]_{z=-w/2} \right] = \frac{\phi_f \mu c_{tf}}{k_f} \frac{\partial}{\partial t}\left[\frac{1}{w} \int_{-w/2}^{w/2} p_f \, dz \right] . \quad \text{(A.33)}$$

Assuming no significant difference between the averaged pressure in the circular fracture and the pressure and any point of it, *i.e.*:

$$p_f = \frac{1}{w}\int_{-w/2}^{w/2} p_f\, dz, \quad \text{(A.34)}$$

and according to Eq. A.31, Eq. A.33 reduces to:

$$\frac{1}{r}\left[r\frac{\partial p_f}{\partial r}\right] + \frac{2k}{wk_f}\left[\frac{\partial p}{\partial z}\right]_{z=0} = \frac{\phi_f \mu c_{tf}}{k_f}\frac{\partial p_f}{\partial t} \quad \text{(A.35)}$$

Larsen *et al*. (1991) presented solutions considering constant flowrate at the wellbore. Therefore, to generalize the problem, the following dimensionless variables were defined. The dimensionless pressure for the circular fracture is:

$$p_{fD,cr}(r_D, t_D) = \frac{2\pi kh}{qB\mu}[p_i - p_f(r,t)], \quad \text{(A.36)}$$

and for the 3D reservoir case:

$$p_{D,cr}(R_D, t_D) = \frac{2\pi kh}{qB\mu}[p_i - p(R,t)]. \quad \text{(A.37)}$$

The dimensionless time for this model is defined by:

$$t_D = \frac{k}{\phi\mu c_t r_f^2}. \quad \text{(A.38)}$$

The dimensionless (radial) position within the fracture is:

$$r_D = \frac{r}{r_f}. \quad \text{(A.39)}$$

The horizontal position is:

$$z_D = \frac{z}{r_f} \quad \text{(A.40)}$$

Using the chain rule, the derivative of the pressure in the circular fracture with respect to the time can be expressed as:

$$\frac{\partial p_f}{\partial t} = \frac{\partial p_f}{\partial p_{fD,cr}} \frac{\partial p_{fD,cr}}{\partial t_D} \frac{\partial t_D}{\partial t} \quad \text{(A.41)}$$

Then, based on Eq. A.37 and Eq. A.38:

$$\frac{\partial p_f}{\partial t} = -\frac{qB\mu}{2\pi kh} \frac{k}{\phi \mu c_t r_f^2} \frac{\partial p_{fD,cr}}{\partial t_D} \quad \text{(A.42)}$$

Similarly, for the first derivative of the pressure in the circular fracture with respect to *r*:

$$\frac{\partial p_f}{\partial r} = \frac{\partial p_f}{\partial p_{fD,cr}} \frac{\partial p_{fD,cr}}{\partial r_D} \frac{\partial r_D}{\partial r} = -\frac{qB\mu}{2\pi kh} \frac{1}{r_f} \frac{\partial p_{fD,cr}}{\partial r_D} \quad \text{(A.43)}$$

The derivative of pressure in the 3D reservoir with respect to *z* has a similar shape:

$$\frac{\partial p}{\partial z} = \frac{\partial p}{\partial p_{D,cr}} \frac{\partial p_{D,cr}}{\partial z_D} \frac{\partial z_D}{\partial z} = -\frac{qB\mu}{2\pi kh} \frac{1}{r_f} \frac{\partial p_{D,cr}}{\partial z_D} \quad \text{(A.44)}$$

Considering the definition of the dimensionless radius (Eq. A.39) and substituting Eqs. A.41 through A. 44 in Eq. A.35 results in:

$$\frac{1}{r_D}\left[r_D\left[-\frac{qB\mu}{2\pi khr_f}\frac{\partial p_{fD,cr}}{\partial r_D}\right]\right] + \frac{2k}{wk_f}\left[-\frac{qB\mu}{2\pi khr_f}\frac{\partial p_{D,cr}}{\partial z_D}\right]_{z=0} = \frac{\phi_f \mu c_{tf}}{k_f}\left[-\frac{qB\mu}{2\pi kh}\frac{k}{\phi\mu c_t r_f^2}\frac{\partial p_{fD,cr}}{\partial t_D}\right] \quad \text{(A.45)}$$

Eliminating terms, Eq. A.45 reduces to the radial diffusivity equation with a source term in its dimensionless form:

$$\frac{1}{r_D}\left[r_D \frac{\partial p_{fD,cr}}{\partial r_D}\right]+\frac{2}{F_{cD}}\left[\frac{\partial p_{D,cr}}{\partial z_D}\right]_{z_D=0}=\frac{1}{\eta_{fD}}\frac{\partial p_{fD,cr}}{\partial t_D}, \quad \text{.....(A.46)}$$

where the dimensionless hydraulic diffusivity of the radial fracture is defined by:

$$\eta_{fD}=\frac{k_f \phi c_t}{\phi_f c_{tf} k}, \quad \text{.....(A.47)}$$

and the dimensionless fracture conductivity is:

$$F_{cD}=\frac{wk_f}{kr_f}. \quad \text{.....(A.48)}$$

To obtain the general solution of Eq. A.46 it is convenient to eliminate one of the independent variables. This reduction of variables is made by discretizing the circular fracture into segments such that the gradient in the *z*-direction can be approximated by:

$$\left[\frac{\partial p}{\partial z}\right]_{z=0} \approx \frac{\delta q_{r,j} B\mu}{2kr_f^2}, \quad \text{.....(A.49)}$$

where $\delta q_{r,j}$ is the flowrate from the reservoir flowing towards the *j*-segment of the discretized circular fracture. Transforming Eq. A.49 to dimensionless variables:

$$\left[\frac{\partial p_{D,cr}}{\partial z_D}\right]_{z_D=0} \approx -\pi \delta q_{D,j} h_D, \quad \text{.....(A.50)}$$

where the dimensionless reservoir rate in the *j*-segment is defined by:

$$\delta q_{D,j} = \frac{\delta q_{r,j}}{q}, \quad \text{(A.51)}$$

and the dimensionless thickness is:

$$h_D = \frac{h}{r_f}, \quad \text{(A.52)}$$

Substituting Eq. A.50 in Eq.A.46:

$$\frac{1}{r_D}\left[r_D \frac{\partial p_{fD,cr}}{\partial r_D}\right] - \frac{2\pi}{F_{hcD}} \delta q_{D,j} = \frac{1}{\eta_{fD}} \frac{\partial p_{fD,cr}}{\partial t_D}, \quad \text{(A.53)}$$

where F_{hcD} is an alternate parameter to describe the fracture conductivity. It is defined as:

$$F_{hcD} = \frac{F_{cD}}{h_D}. \quad \text{(A.54)}$$

Applying the Laplace transform to Eq. A.53and treating the dimensionless reservoir rate in the j-interval as a function of time:

$$\frac{1}{r_D}\left[r_D \frac{d\bar{p}_{fD,cr}}{dr_D}\right] - \frac{2\pi}{F_{hcD}} \bar{\delta q}_{D,j} = \frac{1}{\eta_{fD}} [u\bar{p}_{fD,cr}(r_D,u) - p_{fD,cr}(r_D, t_D = 0)], \quad \text{(A.55)}$$

For this model, it is assumed that the pressure is initially distributed. In dimensionless variables it is expressed as:

$$p_{fD,cr}(r_D, t_D = 0) = 0. \quad \text{(A.56)}$$

Hence, Eq. A.55 can be rewritten as follows:

$$r_D^2 \frac{d^2 \bar{p}_{fD,cr}}{dr_D^2} + r_D \frac{d\bar{p}_{fD,cr}}{dr_D} - r_D^2 \frac{u}{\eta_{fD}} \bar{p}_{fD,cr} - r_D^2 \frac{2\pi}{F_{hcD}} \delta\bar{q}_{D,j} = 0 \quad \text{.....(A.57)}$$

Eq. A.57 is a non-homogenous partial differential equation. The particular solution to the non-homogeneous part is obtained by removing the derivatives of the dimensionless pressure in the circular fracture. Such a particular solution is given by:

$$\bar{p}_{fD,cr} = \frac{2\pi\eta_{fD}}{uF_{hcD}} \delta\bar{q}_{D,j} \text{ . .....(A.58)}$$

To solve the homogenous part of Eq. A.57 consider the transformation function:

$$\bar{G}(\xi) = \bar{p}_{fD,cr} \text{ , ...(A.59)}$$

and the transformation variable:

$$\xi = r_D \sqrt{\frac{u}{\eta_{fD}}} \text{ , ...(A.60)}$$

Using the chain rule, the derivative of the dimensionless pressure in the fracture in the Laplace domain with respect to the dimensionless radius is:

$$\frac{d\bar{p}_{fD,cr}}{dr_D} = \frac{d\bar{p}_{fD,cr}}{dG(\xi)} \frac{d\bar{G}(\xi)}{d\xi} \frac{d\xi}{dr_D} = \sqrt{\frac{u}{\eta_{fD}}} \frac{d\bar{G}(\xi)}{d\xi} \text{ . .....(A.61)}$$

Applying the second derivative to Eq. A.61 with respect to r_D:

$$\frac{d^2 \bar{p}_{fD,cr}}{dr_D^2} = \frac{u}{\eta_{fD}} \frac{d^2 \bar{G}(\xi)}{d\xi^2} \text{ . .....(A.62)}$$

Taking the homogenous part of Eq. A.57 and substituting Eqs. A. 59 through A. 61:

$$\xi^2 \frac{d^2\overline{G}(\xi)}{d\xi^2} + \xi \frac{d\overline{G}(\xi)}{d\xi} - \xi^2 \overline{G}(\xi) = 0 . \quad \text{.....(A.63)}$$

By inspection, the general solution of Eq. A.63 is given by:

$$\overline{G}(\xi) = A_j K_0(\xi) + B_j I_0(\xi) \quad \text{.....(A.64)}$$

The general solution to Eq. A.57 is given by adding Eq. A.58 and Eq. A.64 and using the definitions given by Eqs. A.59 and A.60:

$$\overline{p}_{fD,cr}(r_D, u) = A_j K_0\left[r_D \sqrt{\frac{u}{\eta_{fD}}} \right] + B_j I_0\left[r_D \sqrt{\frac{u}{\eta_{fD}}} \right] - \frac{2\pi\eta_{fD}}{uF_{hcD}} \delta\overline{q}_{D,j} \quad \text{.....(A.65)}$$

A.2. Development of the Linear Diffusivity Equation for a Rectangular Longitudinal Finite Conductivity Fracture

To develop the diffusivity equation for a linear system with a source to represent the flow within a rectangular fracture, consider the control volume shown in **Fig. A.2**. The control volume is constructed by a rectangular prism whose volume is defined by:

$$V_c = \Delta x \Delta y \Delta z . \quad \text{.....(A.66)}$$

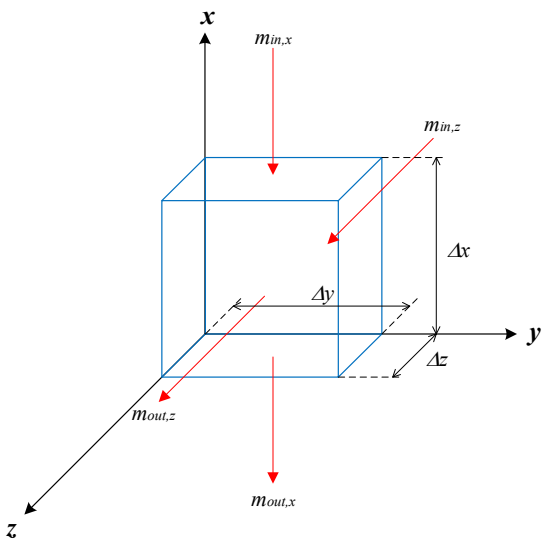

Figure A.2 — Control volume of a rectangular hydraulic fracture.

The incoming mass of fluid, $m_{in,x}$, throughout the rectangular prism through in the x-direction is:

$$m_{in,x} = -\rho v_x \Delta y \Delta z \Delta t \,, \quad \text{(A.67)}$$

and the outgoing mass, $m_{out,x}$, in the same direction is:

$$m_{out,x} = [-\rho v_x + \Delta(\rho v_x)]\Delta y \Delta z \Delta t \,. \quad \text{(A.68)}$$

Analogously, the incoming mass of fluid in the z-direction is:

$$m_{in,z} = -\rho v_z \Delta x \Delta y \Delta t \,, \quad \text{(A.69)}$$

and the outgoing mass is:

$$m_{out,z} = [-\rho v_z + \Delta(\rho v_z)]\Delta x \Delta y \Delta t \,. \quad \text{(A.70)}$$

The cumulative mass of fluid is given by:

$$m_c = m_{out,x} + m_{out,z} - [m_{in,x} + m_{in,z}] = \Delta(\rho v_x)\Delta y\Delta z\Delta t + \Delta(\rho v_z)\Delta x\Delta y\Delta t \,. \quad \text{(A.71)}$$

The mass of fluid at an initial time can be expressed as (considering a single fluid, *i.e.,* S_f=1):

$$m_{t_1} = \phi_f \rho \Delta x\Delta y\Delta z, \quad \text{(A.72)}$$

and at a final time, the mass of the fluid is given by:

$$m_{t_2} = \phi_f \rho \Delta x\Delta y\Delta z + \Delta(\phi_f \rho)\Delta x\Delta y\Delta z \quad \text{(A.73)}$$

Combining Eqs. A.71 through A. 73:

$$m_c = \Delta(\phi_f \rho)\Delta x\Delta y\Delta z \quad \text{(A.74)}$$

Equating Eqs. A.71 and A. 74:

$$\Delta(\rho v_x)\Delta y\Delta z\Delta t + \Delta(\rho v_z)\Delta x\Delta y\Delta t = \Delta(\phi_f \rho)\Delta x\Delta y\Delta z \quad \text{(A.75)}$$

Dividing Eq. A.75 by $\Delta x\Delta y\Delta z\Delta t$:

$$\frac{\Delta(\rho v_x)}{\Delta x} + \frac{\Delta(\rho v_z)}{\Delta z} = \frac{\Delta(\phi_f \rho)}{\Delta t} \,. \quad \text{(A.76)}$$

Taking the limits of Δx, Δz, and Δt to zero, Eq. A.76 results the 2D continuity equation:

$$\frac{\partial(\rho v_x)}{\partial x} + \frac{\partial(\rho v_z)}{\partial z} = \frac{\partial(\phi_f \rho)}{\partial t} \quad \text{(A.77)}$$

Darcy's law for a linear system in *i*-direction is defined by

$$v_i = \frac{k_i}{\mu}\frac{\partial p_f}{\partial i} \,. \quad \text{(A.78)}$$

Substituting Eq. A.78 in Eq. A.77 for x and z directions and assuming (1) isotropic media with constant permeability, k_f, and (2) a fluid with constant viscosity, the following expression is obtained:

$$\frac{k_f}{\mu}\frac{\partial}{\partial x}\left[\rho\frac{\partial p_f}{\partial x}\right]+\frac{k_f}{\mu}\frac{\partial}{\partial z}\left[\rho\frac{\partial p_f}{\partial z}\right]=\frac{\partial(\phi_f\rho)}{\partial t}. \quad \text{(A.79)}$$

Applying the derivatives in Eq. A.79:

$$\frac{\partial^2 p_f}{\partial x^2}+\frac{\partial^2 p_f}{\partial z^2}+\frac{1}{\rho}\frac{\partial\rho}{\partial x}\frac{\partial p_f}{\partial x}+\frac{1}{\rho}\frac{\partial\rho}{\partial z}\frac{\partial p_f}{\partial z}=\frac{\mu}{k_f}\left[\frac{1}{\rho}\frac{\partial\rho}{\partial t}+\frac{1}{\phi_f}\frac{\partial\phi_f}{\partial t}\right] \quad \text{(A.80)}$$

Using the chain rule as in the previous section:

$$\frac{\partial\rho}{\partial x}=\frac{\partial\rho}{\partial p_f}\frac{\partial p_f}{\partial x}, \quad \text{(A.81)}$$

$$\frac{\partial\rho}{\partial z}=\frac{\partial\rho}{\partial p_f}\frac{\partial p_f}{\partial z}, \quad \text{(A.82)}$$

$$\frac{\partial\rho}{\partial t}=\frac{\partial\rho}{\partial p_f}\frac{\partial p_f}{\partial t}, \quad \text{(A.83)}$$

$$\frac{\partial\phi_f}{\partial t}=\frac{\partial\phi_f}{\partial p_f}\frac{\partial p_f}{\partial t} \quad \text{(A.84)}$$

Substituting Eqs. A.81 through A.84 in Eq. A.80:

$$\frac{\partial^2 p_f}{\partial x^2}+\frac{\partial^2 p_f}{\partial z^2}+\frac{1}{\rho}\frac{\partial\rho}{\partial p_f}\frac{\partial p_f}{\partial x}\frac{\partial p_f}{\partial x}+\frac{1}{\rho}\frac{\partial\rho}{\partial p_f}\frac{\partial p_f}{\partial z}\frac{\partial p_f}{\partial z}=\frac{\mu}{k_f}\left[\frac{1}{\rho}\frac{\partial\rho}{\partial p_f}\frac{\partial p_f}{\partial t}+\frac{1}{\phi_f}\frac{\partial\phi_f}{\partial p_f}\frac{\partial p_f}{\partial t}\right]. \quad \text{(A.85)}$$

According to the definition of the compressibility of the fluid (Eq. A.25) and the compressibility of the hydraulic fracture (Eq. A.26), Eq. A.85 can be rewritten as:

$$\frac{\partial^2 p_f}{\partial x^2}+\frac{\partial^2 p_f}{\partial z^2}+c_o\left[\left[\frac{\partial p_f}{\partial x}\right]^2+\left[\frac{\partial p_f}{\partial z}\right]^2\right]=\frac{\phi_f \mu c_{tf}}{k_f}\frac{\partial p_f}{\partial t}. \quad \text{(A.86)}$$

where c_{tf} is the total compressibility and is defined by Eq. A.28. Neglecting the squared-pressure gradient results in the 2D diffusivity equation:

$$\frac{\partial^2 p_f}{\partial x^2}+\frac{\partial^2 p_f}{\partial z^2}=\frac{\phi_f \mu c_{tf}}{k_f}\frac{\partial p_f}{\partial t}. \quad \text{(A.87)}$$

The second derivative of the pressure in the fracture with respect to z in Eq. A.86 should be treated as in section A.1, *i.e.*: the average pressure of the fracture should be taken and the flowrate at the interface between the rectangular fracture and the 3D reservoir should be considered equal (*i.e.* Eq. A.31). After this mathematical treatment, Eq. A.86 becomes:

$$\frac{\partial^2 p_f}{\partial x^2}+\frac{2k}{k_f w}\left[\frac{\partial p}{\partial z}\right]_{z=0}=\frac{\phi_f \mu c_{tf}}{k_f}\frac{\partial p_f}{\partial t}. \quad \text{(A.88)}$$

For this model, the dimensionless variables are analogously defined by Eqs. A. 36 through A.40, but the reference length for the rectangular fracture is the half-length x_f instead of the radius of the fracture r_f. Therefore, Eq. A.88 expressed in dimensionless variables is:

$$\frac{\partial^2 p_{fD,cr}}{\partial x_D^2}+\frac{2}{F_{cD}}\left[\frac{\partial p_{D,cr}}{\partial z_D}\right]_{z_D=0}=\frac{1}{\eta_{fD}}\frac{\partial p_{fD,cr}}{\partial t_D}, \quad \text{(A.89)}$$

where the dimensionless hydraulic diffusivity of the radial fracture is defined by Eq. A.47 and the

dimensionless fracture conductivity for this case is:

$$F_{cD} = \frac{wk_f}{kx_f} \quad \text{(A.90)}$$

To reduce the number of variables in Eq. A.89 and make the process of solving easier, the same procedure depicted in Section A.1should be applied. For this case, the approximation of the gradient of the pressure with respect of z is given by:

$$\left[\frac{\partial p}{\partial z}\right]_{z=0} \approx \frac{\delta q_{r,j} B\mu}{2kx_f^2} \quad \text{(A.91)}$$

Transforming Eq. A.91 to dimensionless variables yields the same shape as Eq. A.50. Substituting such an expression in Eq. A.89:

$$\frac{\partial^2 p_{fD,cr}}{\partial x_D^2} - \frac{2\pi}{F_{hcD}} \delta q_{D,j} = \frac{1}{\eta_{fD}} \frac{\partial p_{fD,cr}}{\partial t_D}. \quad \text{(A.92)}$$

where F_{hcD} is defined exactly as for the circular fracture case (Eq. A.54).

Applying the Laplace transform to Eq. A.92:

$$\frac{d^2 \bar{p}_{fD,cr}}{dx_D^2} - \frac{2\pi}{F_{hcD}} \delta \bar{q}_{D,j} = \frac{1}{\eta_{fD}} [u\bar{p}_{fD,cr} - p_{fD,cr}(x_D, t_D = 0)]. \quad \text{(A.93)}$$

Considering that the initial pressure is uniformly distributed, *i.e.*:

$$p_{fD,cr}(x_D, t_D = 0) = 0, \quad \text{(A.94)}$$

Eq. A.93 is rewritten as:

$$\frac{d^2\bar{p}_{fD,cr}}{dx_D^2} - \frac{2\pi}{F_{hcD}}\delta\bar{q}_{D,j} = \frac{u}{\eta_{fD}}\bar{p}_{fD,cr}. \quad \text{(A.95)}$$

Similar to Eq. A.57, Eq. A.95 is also a non-homogenous partial differential equation. Therefore, Eq. A.95 can be solved following the same procedure used for Eq. A.57. The solution of the non-homogenous part is:

$$\bar{p}_{fD,cr,nh} = -\frac{2\pi\eta_{fD}}{F_{hcD}u}\delta\bar{q}_{D,j} \quad \text{(A.96)}$$

The homogenous part of Eq. A.95 is:

$$\frac{d^2\bar{p}_{fD,cr}}{dx_D^2} - \frac{u}{\eta_{fD}}\bar{p}_{fD,cr} = 0 \quad \text{(A.97)}$$

Eq. A.97 is an ordinary differential equation of second order with constant coefficients. Hence, its solution can be written as:

$$\bar{p}_{fD,cr,h} = A_j \exp\left[-x_D\sqrt{\frac{u}{\eta_{fD}}}\right] + B_j \exp\left[x_D\sqrt{\frac{u}{\eta_{fD}}}\right] \quad \text{(A.98)}$$

The solution of Eq. A.95 is given by adding the solution of the non-homogenous part (Eq. A.96) and the homogenous part (Eq. A.97):

$$\bar{p}_{fD,cr,j}(x_D,u) = A_j \exp\left[-x_D\sqrt{\frac{u}{\eta_{fD}}}\right] + B_j \exp\left[x_D\sqrt{\frac{u}{\eta_{fD}}}\right] - \frac{2\pi\eta_{fD}}{F_{hcD}u}\delta\bar{q}_{D,j}. \quad \text{(A.99)}$$

The value of the constants A_j and B_j depends on the segment of the discretized fracture where the solution is evaluated. These values are determined by solving a system of equations. The

construction of such a system and the procedure to obtain its solution will be addressed in Section A.5

A.3. Development of the Diffusivity Equation for a 3D reservoir (Spherical Flow) and its constant-rate solution

Based on **Fig. A.3**, the control volume for a spherical system is constructed by two concentric spheres, and it is determined by:

$$V_c = R^2 \Delta\theta \Delta\omega \Delta R \sin\theta \quad \text{.....(A.100)}$$

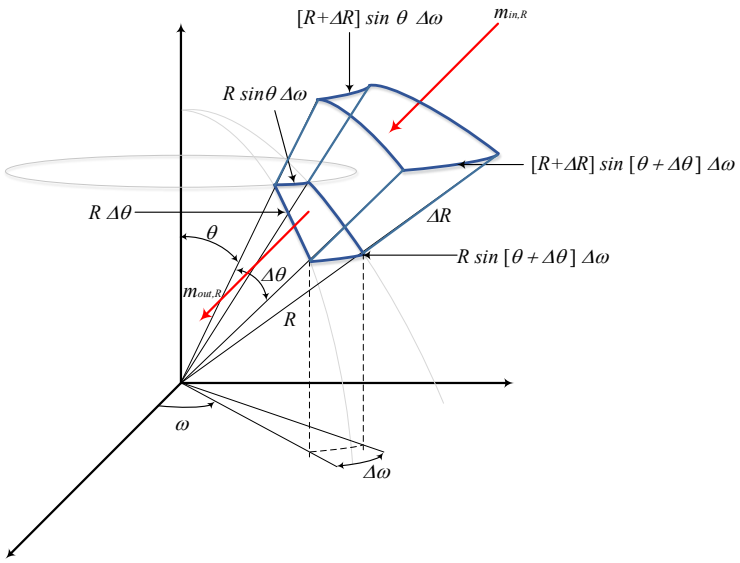

Figure A.3 — Control volume of a 3D reservoir.

The incoming mass of a fluid, $m_{in,R}$, throughout the outer sphere is:

$$m_{in,R} = -\rho v_R [R + \Delta R]^2 \sin\theta \Delta\theta \Delta\omega \Delta t \,, \quad \text{.....(A.101)}$$

and the outgoing mass, $m_{out,r}$, throughout the outer cylinder is given by:

$$m_{out,R} = [-\rho v_R + \Delta(\rho v_R)]R^2 \sin\theta \Delta\theta \Delta\omega \Delta t \quad \text{.....(A.102)}$$

The cumulative mass of the fluid is determined by:

$$m_c = m_{out,R} - m_{in,R} = [-\rho v_R + \Delta(\rho v_R)]R^2 \sin\theta \Delta\theta \Delta\omega \Delta t + \rho v_R [R^2 + 2R\Delta R + \Delta R^2] \sin\theta \Delta\theta \Delta\omega \Delta t \text{, ..(A.103)}$$

and it is reduced to:

$$m_c = \Delta(\rho v_R)R^2 \sin\theta \Delta\theta \Delta\omega \Delta t + [2R + \Delta R]\rho v_R \Delta R \sin\theta \Delta\theta \Delta\omega \Delta t \text{ . .....(A.104)}$$

The mass of a single fluid (S_f= 1) at an initial time can be expressed as:

$$m_{t_1} = \phi\rho R^2 \Delta\theta \Delta\omega \Delta R \sin\theta \text{. .....(A.105)}$$

At a final time, the mass of fluid is given by:

$$m_{t_2} = \phi\rho R^2 \Delta\theta \Delta\omega \Delta R \sin\theta + \Delta(\phi\rho)R^2 \Delta\theta \Delta\omega \Delta R \sin\theta \text{ .....(A.106)}$$

The cumulative mass of fluid for the time-dependent case is given by:

$$m_c = m_{t_2} - m_{t_1} \text{ . .....(A.107)}$$

Substituting Eq. A.105 and Eq. A.106 in Eq. A.107:

$$m_c = \Delta(\phi\rho)R^2 \Delta\theta \Delta\omega \Delta R \sin\theta \quad \text{.....(A.108)}$$

Equating Eq. A.104 and Eq. A.108:

$$\Delta(\rho v_R)R^2 \sin\theta \Delta\theta \Delta\omega \Delta t + [2R + \Delta R]\rho v_R \Delta R \sin\theta \Delta\theta \Delta\omega \Delta t = \Delta(\phi\rho)R^2 \Delta\theta \Delta\omega \Delta R \sin\theta \text{ . .....(A.109)}$$

Dividing Eq. A.109 by $V_c \Delta t$, such an equation reduces to:

$$\frac{\Delta(\rho v_R)}{\Delta R} + \frac{[2R + \Delta R]\rho v_R}{R^2} = \frac{\Delta(\phi\rho)}{\Delta t} \quad \text{(A.110)}$$

Taking the limits of ΔR and Δt to zero, Eq. A.110 can be written in its differential form:

$$\frac{\partial(\rho v_R)}{\partial R} + \frac{2\rho v_R}{R} = \frac{\partial(\phi\rho)}{\partial t} \quad \text{(A.111)}$$

Recall Darcy's law:

$$v_R = \frac{k}{\mu}\frac{\partial p}{\partial R} \quad \text{(A.112)}$$

Substituting Eq. A.112 in Eq. A.111 and applying the derivatives assuming constant permeability and viscosity results in:

$$\frac{\partial^2 p}{\partial R^2} + \frac{1}{\rho}\frac{\partial \rho}{\partial R}\frac{\partial p}{\partial R} + \frac{2}{R}\frac{\partial p}{\partial R} = \frac{\mu}{k\rho}\left[\rho\frac{\partial \phi}{\partial t} + \phi\frac{\partial \rho}{\partial t}\right]. \quad \text{(A.113)}$$

Use the chain rule as in the previous sections to apply the definitions of the compressibility of a fluid (Eq. A.25) and the compressibility of the reservoir which is defined:

$$c = \frac{1}{\phi}\frac{\partial \phi}{\partial p}. \quad \text{(A.114)}$$

As a results of this, Eq. A.113 is rewritten as:

$$\frac{\partial^2 p}{\partial R^2} + \frac{2}{R}\frac{\partial p}{\partial R} = \frac{\phi\mu c_t}{k}\frac{\partial p}{\partial t}. \quad \text{(A.115)}$$

Consider the dimensionless variables defined in section A.1, *i.e.,* the pressure of the 3D reservoir (Eq. A.37), the dimensionless time (Eq. A.38) and the dimensionless radius of the 3D reservoir:

$$R_D = \frac{R}{L_r}, \quad \text{(A.116)}$$

where L_r is the reference length (r_f for the circular fracture case and x_f for the rectangular fracture).

Transforming Eq. A.115 to dimensionless variables results in the following equation results (in the compact form):

$$\frac{1}{R_D^2}\frac{\partial}{\partial R_D}\left[R_D^2\frac{\partial p_D}{\partial R_D}\right] = \frac{\partial p_D}{\partial t_D}. \quad \text{(A.117)}$$

To solve Eq. A.115, consider the following initial and boundary conditions:

$$p_D(R_D, t_D = 0) = 0 \quad \text{(initial condition)}, \quad \text{(A.118)}$$

$$\left[\frac{\partial p_{D,cr}}{\partial R_D}\right]_{R_D = R_{wD}} = -\frac{\delta q_D h_D}{2R_{wD}^2} \quad \text{(inner boundary condition)}, \quad \text{(A.119)}$$

$$\lim_{R_D \to \infty} p_D(R_D, t_D) = 0 \quad \text{(outer boundary condition)} \quad \text{(A.120)}$$

where the dimensionless reservoir rate is defined by:

$$\delta q_D = \frac{\delta q_r}{q} \quad \text{(A.121)}$$

The dimensionless thickness is:

$$h_D = \frac{h}{L_r}, \quad \text{(A.122)}$$

and dimensionless radius of the source is:

$$R_{wD} = \frac{R_w}{L_r}, \quad \text{(A.123)}$$

Consider the transformation:

$$p_D = \frac{b_D}{R_D}, \quad \text{(A.124)}$$

then use the chain rule:

$$\frac{\partial p_D}{\partial t_D} = \frac{1}{R_D}\frac{\partial b_D}{\partial t_D}, \quad \text{(A.125)}$$

and:

$$\frac{\partial p_D}{\partial R_D} = -\frac{b_D}{R_D^2} + \frac{1}{R_D}\frac{\partial b_D}{\partial R_D}. \quad \text{(A.126)}$$

Substituting Eq. A.125 and Eq. A.126 in Eq. A.117:

$$\frac{1}{R_D}\frac{\partial}{\partial R_D}\left[-b_D + R_D\frac{\partial b_D}{\partial R_D}\right] = \frac{\partial b_D}{\partial t_D} \quad \text{(A.127)}$$

Applying the derivative on the left hand side of Eq. A.127 reduces to:

$$\frac{\partial^2 b_D}{\partial R_D^2} = \frac{\partial b_D}{\partial t_D}. \quad \text{(A.128)}$$

Applying the transformation defined in Eq. A.114 in the initial condition (Eq. A.118):

$$b_D(R_D, t_D) = 0. \quad \text{(A.129)}$$

Applying the Laplace transform to Eq. A.128 and considering the initial condition (Eq. A.129), the following equation results in:

$$\frac{d^2\bar{b}_D}{dR_D^2} - u\bar{b}_D = 0. \quad \text{(A.130)}$$

Mathematically, Eq. A.130 has the same shape of Eq. A.97. Hence, the general solution of Eq. A.130 is given by:

$$\bar{b}_D(R_D,u) = C_1 \exp[-R_D\sqrt{u}] + C_2 \exp[R_D\sqrt{u}], \quad \text{(A.131)}$$

or, in terms of the dimensionless pressure, it is given by:

$$\bar{p}_D(R_D,u) = \frac{C_1}{R_D}\exp[-R_D\sqrt{u}] + \frac{C_2}{R_D}\exp[R_D\sqrt{u}], \quad \text{(A.132)}$$

Applying the outer boundary condition (Eq. A.120) to Eq. A.132:

$$\lim_{R_D\to\infty}\bar{p}_D(R_D,u) = C_1 \lim_{R_D\to\infty}\left[\frac{1}{R_D}\exp[-R_D\sqrt{u}]\right] + C_2 \lim_{R_D\to\infty}\left[\frac{1}{R_D}\exp[R_D\sqrt{u}]\right] = 0, \quad \text{(A.133)}$$

It is concluded that C_2 must be zero. Therefore, the bounded solution is:

$$\bar{p}_D(R_D,u) = \frac{C_1}{R_D}\exp[-R_D\sqrt{u}], \quad \text{(A.134)}$$

To apply the inner boundary condition, the derivative of the dimensionless pressure with respect to R_D of Eq. A.134 should be considered:

$$\frac{\partial\bar{p}_D}{\partial R_D} = -C_1\left[\frac{1}{R_D^2} + \frac{\sqrt{u}}{R_D}\right]\exp[-R_D\sqrt{u}]. \quad \text{(A.135)}$$

Evaluating Eq. A.134 in R_{wD} and comparing it with the inner boundary condition (Eq. A.119) expressed in the Laplace domain, it is concluded that:

$$C_1 = \frac{\delta\bar{q}_D h_D}{2[1 + R_{wD}\sqrt{u}]} \exp[R_{wD}\sqrt{u}] \quad \text{(A.136)}$$

Substituting Eq. A.136 in Eq. A.134, the solution for this model is obtained:

$$\bar{p}_D(R_D, u) = \frac{\delta\bar{q}_D h_D}{2R_D[1 + R_{wD}\sqrt{u}]} \exp\left[[R_{wD} - R_D]\sqrt{u}\right], \quad \text{(A.137)}$$

Assuming a point source (*i.e.*, R_{wD}=0), Eq. A.138 reduces to:

$$\bar{p}_D(R_D, u) = \frac{\delta\bar{q}_D h_D}{2R_D} \exp\left[-R_D\sqrt{u}\right] \quad \text{(A.138)}$$

A.4. Constant-Rate Solution for the Model of a Horizontal Well Intercepting a Circular Transverse Finite Conductivity Fracture within a 3D Reservoir

Recall the general solution of the radial flow model of a circular fracture (Eq.A.65):

$$\bar{p}_{fD,cr,j}(r_D, u) = A_j K_0\left[r_D\sqrt{\frac{u}{\eta_{fD}}}\right] + B_j I_0\left[r_D\sqrt{\frac{u}{\eta_{fD}}}\right] - \frac{2\pi\eta_{fD}}{uF_{hcD}}\delta\bar{q}_{D,j}.$$

The last term on the right hand side of the equation represents the "contribution of pressure" due to the flow from the 3D reservoir to the circular fracture. Such a term results from the approximation of the gradient in the *z*-direction.

Fig A.4 shows a schematic example of a circular fracture logarithmically discretized in five segments. Larsen (2016) suggested that a discretization in eleven segments provides accurate

results. However, for the sake of giving an example, five segments will be used. The responses of the dimensionless pressure for each one of the segments in **Fig.A.4** are:

$$\bar{p}_{fD,cr,1}(r_D,u) = A_1 K_0\left[r_D\sqrt{\frac{u}{\eta_{fD}}}\right] + B_1 I_0\left[r_D\sqrt{\frac{u}{\eta_{fD}}}\right] - \frac{2\pi\eta_{fD}}{uF_{hcD}}\delta\bar{q}_{D,1}\ (r_{D0}\leq r_D \leq r_{D1}), \text{.....(A.139)}$$

$$\bar{p}_{fD,cr,2}(r_D,u) = A_2 K_0\left[r_D\sqrt{\frac{u}{\eta_{fD}}}\right] + B_2 I_0\left[r_D\sqrt{\frac{u}{\eta_{fD}}}\right] - \frac{2\pi\eta_{fD}}{uF_{hcD}}\delta\bar{q}_{D,2}\ (r_{D1}\leq r_D \leq r_{D2}), \text{.....(A.140)}$$

$$\bar{p}_{fD,cr,3}(r_D,u) = A_3 K_0\left[r_D\sqrt{\frac{u}{\eta_{fD}}}\right] + B_3 I_0\left[r_D\sqrt{\frac{u}{\eta_{fD}}}\right] - \frac{2\pi\eta_{fD}}{uF_{hcD}}\delta\bar{q}_{D,3}\ (r_{D2}\leq r_D \leq r_{D3}), \text{.....(A.141)}$$

$$\bar{p}_{fD,cr,4}(r_D,u) = A_4 K_0\left[r_D\sqrt{\frac{u}{\eta_{fD}}}\right] + B_4 I_0\left[r_D\sqrt{\frac{u}{\eta_{fD}}}\right] - \frac{2\pi\eta_{fD}}{uF_{hcD}}\delta\bar{q}_{D,4}\ (r_{D3}\leq r_D \leq r_{D4}), \text{.....(A.142)}$$

$$\bar{p}_{fD,cr,5}(r_D,u) = A_5 K_0\left[r_D\sqrt{\frac{u}{\eta_{fD}}}\right] + B_5 I_0\left[r_D\sqrt{\frac{u}{\eta_{fD}}}\right] - \frac{2\pi\eta_{fD}}{uF_{hcD}}\delta\bar{q}_{D,5}\ (r_{D3}\leq r_D \leq r_{D4}). \text{.....(A.143)}$$

This approach leads to fifteen unknowns (in general 3*N* unknowns for *N*-segments of the circular fracture). To set a system of fifteen equations (3*N* in general) four conditions must be considered: (1) boundary conditions of the circular fracture, (2) continuity of pressure at the interfaces of the discretized fracture, (3) continuity of flowrate at the interfaces of the discretized fracture, and (4) pressure continuity between the fracture and the 3D reservoir.

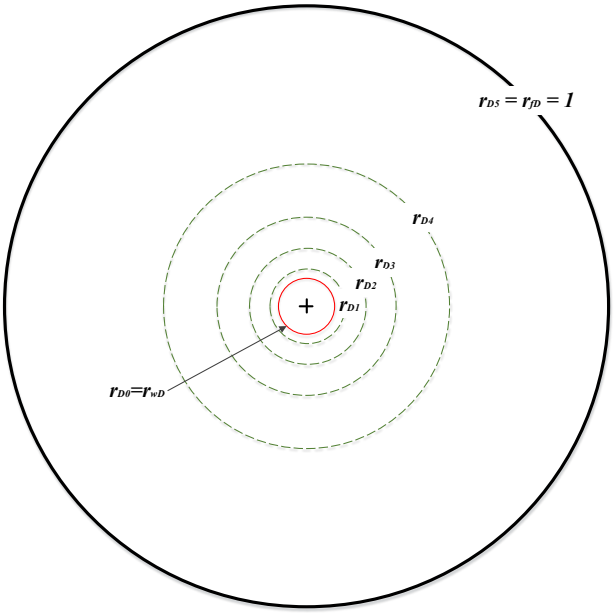

Figure A.4 — Logarithmic discretization of the circular fracture.

1. Boundary conditions of the circular fracture.

It is assumed that the well at the center of the circular fracture is produced at a constant rate and such a fracture is closed. Therefore, the inner boundary condition is defined by:

$$\left[r\frac{\partial p_f}{\partial r}\right]_{r=r_w} = \frac{qB\mu}{2\pi k_f w}, \quad \text{.....(A.144)}$$

and the outer boundary condition is defined by

$$\left[\frac{\partial p_f}{\partial r}\right]_{r=rf} = 0 \quad \text{.....(A.145)}$$

Transforming Eqs. A.144 and A.145 to dimensionless variables, they become:

$$\left[r_D\frac{\partial p_{fD,cr}}{\partial r_D}\right]_{r_D=r_{wD}} = -\frac{1}{F_{hcD}}, \quad \text{.....(A.146)}$$

and:

$$\left[\frac{\partial p_{fD,cr}}{\partial r_D}\right]_{r_D=1}=0, \quad \text{(A.147)}$$

respectively. Given that the inner boundary condition corresponds to the segment defined by r_{D0} and r_{D1}, it must be applied to Eq. A.139. Applying the Laplace transform to Eq. A.146 and then the boundary condition to Eq. A.139, the following expression is derived:

$$\left[r_D\frac{\partial \bar{p}_{fD,cr,1}}{\partial r_D}\right]_{r_D=r_{wD}}=-r_{wD}\sqrt{\frac{u}{\eta_{fD}}}\left[A_1K_1\left[r_{wD}\sqrt{\frac{u}{\eta_{fD}}}\right]-B_1I_1\left[r_{wD}\sqrt{\frac{u}{\eta_{fD}}}\right]\right]=-\frac{1}{F_{hcD}u}. \quad \text{(A.148)}$$

Rewriting Eq. A.148:

$$A_1K_1\left[r_{wD}\sqrt{\frac{u}{\eta_{fD}}}\right]-B_1I_1\left[r_{wD}\sqrt{\frac{u}{\eta_{fD}}}\right]=\frac{\sqrt{\eta_{fD}}}{F_{hcD}r_{wD}u^{3/2}}. \quad \text{(A.149)}$$

Similarly, applying the outer boundary condition to Eq. A.143:

$$A_5K_1\left[\sqrt{\frac{u}{\eta_{fD}}}\right]-B_5I_1\left[\sqrt{\frac{u}{\eta_{fD}}}\right]=0. \quad \text{(A.150)}$$

2. Continuity of pressure at the interfaces of the discretized fracture.

To establish continuity of the pressure along the circular fracture, the pressure must be equal at every interface, *i.e.*,

$$\bar{p}_{fD,cr,j-1}(r_{Dj-1},u)=\bar{p}_{fD,cr,j}(r_{Dj-1},u), \quad \text{(A.151)}$$

for $2\leq j\leq N$. For the segments defined in **Fig. A.4**:

$$A_1 K_0\left[r_{D1}\sqrt{\frac{u}{\eta_{fD}}}\right] + B_1 I_0\left[r_{D1}\sqrt{\frac{u}{\eta_{fD}}}\right] - \frac{2\pi\eta_{fD}}{uF_{hcD}}\delta\bar{q}_{D,1} = A_2 K_0\left[r_{D1}\sqrt{\frac{u}{\eta_{fD}}}\right] + B_2 I_0\left[r_{D1}\sqrt{\frac{u}{\eta_{fD}}}\right] - \frac{2\pi\eta_{fD}}{uF_{hcD}}\delta\bar{q}_{D,2}$$

(r_{D1}-interface), ...(A.152)

$$A_2 K_0\left[r_{D2}\sqrt{\frac{u}{\eta_{fD}}}\right] + B_2 I_0\left[r_{D2}\sqrt{\frac{u}{\eta_{fD}}}\right] - \frac{2\pi\eta_{fD}}{uF_{hcD}}\delta\bar{q}_{D,2} = A_3 K_0\left[r_{D2}\sqrt{\frac{u}{\eta_{fD}}}\right] + B_3 I_0\left[r_{D2}\sqrt{\frac{u}{\eta_{fD}}}\right] - \frac{2\pi\eta_{fD}}{uF_{hcD}}\delta\bar{q}_{D,3}$$

(r_{D2}-interface),.....(A.153)

$$A_3 K_0\left[r_{D3}\sqrt{\frac{u}{\eta_{fD}}}\right] + B_3 I_0\left[r_{D3}\sqrt{\frac{u}{\eta_{fD}}}\right] - \frac{2\pi\eta_{fD}}{uF_{hcD}}\delta\bar{q}_{D,3} = A_4 K_0\left[r_{D3}\sqrt{\frac{u}{\eta_{fD}}}\right] + B_4 I_0\left[r_{D3}\sqrt{\frac{u}{\eta_{fD}}}\right] - \frac{2\pi\eta_{fD}}{uF_{hcD}}\delta\bar{q}_{D,4}$$

(r_{D3}-interface),.....(A.154)

$$A_4 K_0\left[r_{D4}\sqrt{\frac{u}{\eta_{fD}}}\right] + B_4 I_0\left[r_{D4}\sqrt{\frac{u}{\eta_{fD}}}\right] - \frac{2\pi\eta_{fD}}{uF_{hcD}}\delta\bar{q}_{D,4} = A_5 K_0\left[r_{D4}\sqrt{\frac{u}{\eta_{fD}}}\right] + B_5 I_0\left[r_{D4}\sqrt{\frac{u}{\eta_{fD}}}\right] - \frac{2\pi\eta_{fD}}{uF_{hcD}}\delta\bar{q}_{D,5}$$

(r_{D4}-interface).....(A.155)

3. Continuity of flowrate at the interfaces of the discretized fracture.

In addition to the continuity of the pressure, continuity of the flowrate at every interface along the circular fracture must also be considered, *i.e.*,

$$\left[\frac{\partial\bar{p}_{fD,cr,j-1}}{\partial r_D}\right]_{r_D=r_{Dj-1}} = \left[\frac{\partial\bar{p}_{fD,cr,j}}{\partial r_D}\right]_{r_D=r_{Dj-1}},$$ .....(A.156)

for $2\leq j\leq N$. For the segments defined in **Fig. A.4**:

$$A_1 K_1\left[r_{D1}\sqrt{\frac{u}{\eta_{fD}}}\right] - B_1 I_1\left[r_{D1}\sqrt{\frac{u}{\eta_{fD}}}\right] = A_2 K_1\left[r_{D1}\sqrt{\frac{u}{\eta_{fD}}}\right] - B_2 I_1\left[r_{D1}\sqrt{\frac{u}{\eta_{fD}}}\right] \quad (r_{D1}\text{-interface}), \ldots.(A.157)$$

$$A_2 K_1\left[r_{D2}\sqrt{\frac{u}{\eta_{fD}}}\right] - B_2 I_1\left[r_{D2}\sqrt{\frac{u}{\eta_{fD}}}\right] = A_3 K_1\left[r_{D2}\sqrt{\frac{u}{\eta_{fD}}}\right] - B_3 I_1\left[r_{D2}\sqrt{\frac{u}{\eta_{fD}}}\right] \quad (r_{D2}\text{-interface}), \ldots(A.158)$$

$$A_3 K_1\left[r_{D3}\sqrt{\frac{u}{\eta_{fD}}}\right] - B_3 I_1\left[r_{D3}\sqrt{\frac{u}{\eta_{fD}}}\right] = A_4 K_1\left[r_{D3}\sqrt{\frac{u}{\eta_{fD}}}\right] - B_4 I_1\left[r_{D3}\sqrt{\frac{u}{\eta_{fD}}}\right] \quad (r_{D3}\text{-interface}), \ldots(A.159)$$

$$A_1 K_1\left[r_{D1}\sqrt{\frac{u}{\eta_{fD}}}\right] - B_1 I_1\left[r_{D1}\sqrt{\frac{u}{\eta_{fD}}}\right] = A_2 K_1\left[r_{D1}\sqrt{\frac{u}{\eta_{fD}}}\right] - B_2 I_1\left[r_{D1}\sqrt{\frac{u}{\eta_{fD}}}\right] \quad (r_{D4}\text{-interface}). \ldots.(A.160)$$

4. Continuity of pressure between the fracture and the 3D reservoir.

So far, ten out of the fifteen equations needed to obtain the fifteen unknowns in Eqs.A.139 – A.143 have been set up. The remaining five are defined by superposing the pressure of the 3D reservoir on the plane of the circular fracture (see **Fig. A.5**). To show this procedure, consider the "point well" solution obtained in section A.3 (Eq. A.138):

$$\bar{p}_D(R_D,u) = \frac{\delta\bar{q}_D h_D}{2R_D}\exp\left[-R_D\sqrt{u}\right].$$

The superposition of Eq. A.138 over the area of the fracture is given by the double integral over the domain of the angle, θ, and the radius r_D:

$$\bar{p}_{Dcr,j} = \frac{\delta\bar{q}_{D,j} h_D}{2}\int_{r_{D\min}}^{r_{D\max}}\int_{0}^{\theta(r_D)}\frac{r_D}{R_D}\exp\left[-R_D\sqrt{u}\right]d\theta dr_D \cdot \ldots\ldots(A.161)$$

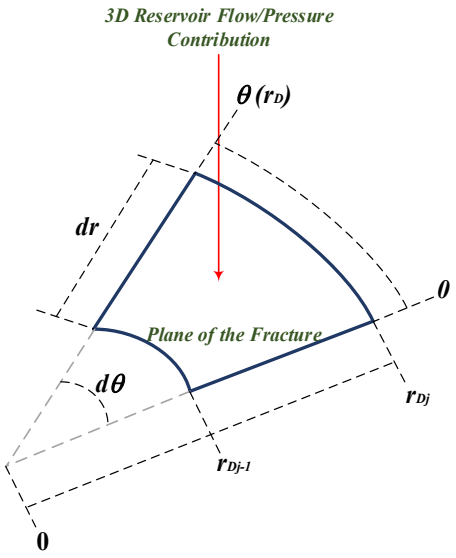

Figure A.5 — Fluid transfer from the 3D reservoir to an infinitesimal section of the circular fracture.

Integrating Eq. A.161 over the domain of θ:

$$\bar{p}_{Dcr,j} = \frac{\delta\bar{q}_{D,j} h_D}{2} \int_{r_{D\min}}^{r_{D\max}} \frac{r_D}{R_D} \theta(r_D) \exp\left[-R_D\sqrt{u}\right] dr_D \quad \text{.....(A.162)}$$

The value of the angle θ depends on the position along the r_D-axis. To obtain a function that relates these two variables, consider an observation point (r^*_{Dj},0,0) in cartesian coordinates. On the other hand, the equation of a circumference with center (h,k) and radius r_{Dj} in the XY-plane is:

$$(x-h)^2 + (y-k)^2 = r_{Dj}^2 \quad \text{.....(A.163)}$$

Taking r^*_D as the center of the circumference, then Eq. A.163 becomes:

$$x^2 - 2xr_{Dj}^* + (r_{Dj}^*)^2 + y^2 = r_{Dj}^2 \quad \text{.....(A.164)}$$

Based on the definition of the radius of a circle in cartesian coordinates:

$$r_D^2 = x^2 + y^2, \quad \text{.....(A.165)}$$

and the projection of the radius on the *x*-axis:

$$x = r_D \cos\theta. \quad \text{.....(A.166)}$$

Substituting Eqs. A.165 and A.166 in Eq. A.164:

$$-2r_{Dj}^* r_D \cos\theta + (r_{Dj}^*)^2 + r_D^2 = r_{Dj}^2. \quad \text{.....(A.167)}$$

Solving Eq. A.167 for θ:

$$\theta = \cos^{-1}\left[\frac{(r_{Dj}^*)^2 - r_{Dj}^2 + r_D^2}{2r_{Dj}^* r_D}\right]. \quad \text{.....(A.168)}$$

Substituting Eq. A.168 in Eq. A.162:

$$\bar{p}_{Dcr,j}(R_D, z_{0D}, u) = \frac{\delta\bar{q}_{D,j} h_D}{2} \int_{r_{D\min}}^{r_{D\max}} \frac{r_D}{R_D} \cos^{-1}\left[\frac{(r_{Dj}^*)^2 - r_{Dj}^2 + r_D^2}{2r_{Dj}^* r_D}\right] \exp\left[-R_D\sqrt{u}\right] dr_D. \quad \text{.....(A.169)}$$

The radius of the spherical reservoir (R_D) is related to the radius of the circular fracture (r_D) as:

$$R_D^2 = r_D^2 + z_{0D}^2, \quad \text{.....(A.170)}$$

where z_{0D} is the observation point along the wellbore.

To provide the remaining expressions to complete the system of equations, the solution of the pressure at the circular fracture should be evaluated at certain r^*_{Dj}-value and equated to an

expression that represents the pressure of the reservoir at the same point. Total pressure acting on a r^*_{Dj} point located at j-segment defined in **Fig. A.5** is determined by:

$$\bar{p}_{Dcr,j}(r^*_{Dj},u)=\frac{h_D}{2}\sum_{i=1}^{5}\delta\bar{q}_{D,j}[G_c(r^*_{Dj},r_{Di},u)-G_c(r^*_{Dj},r_{Di-1},u)] \quad \text{.....(A.171)}$$

where:

$$G_c(r^*_{Dj},r_{Dk},u)=\int_{r_{D\min}}^{r_{D\max}}\frac{r_D}{R_D}\cos^{-1}\left[\frac{(r^*_{Dj})^2-r^2_{Dk}+r^2_D}{2r^*_{Dj}r_D}\right]\exp\left[-R_D\sqrt{u}\right]dr_D \quad \text{.....(A.172)}$$

Larsen *et al*. (1991) used Simpson's rule to perform the integral in Eq. A.172 in their calculations. To perform the integral in Eq. A.172, such an equation must be arranged to consider the relative position of the observation point and the integration limits. This arrangement is shown at the end of this subsection.

It is convenient to define the observation points, r^*_{Dj}, at the midpoint of every segment of the discretized circular fracture (see **Fig. A.6**). At the observation points, the dimensionless pressure of the circular fracture and the dimensionless pressure of the 3D reservoir are equal. Evaluating Eq. A.65 at the generic observation point, r^*_{Dj}, and equating this expression to Eq. A.171 results in:

$$A_jK_0\left[r^*_{Dj}\sqrt{\frac{u}{\eta_{fD}}}\right]+B_jI_0\left[r^*_{Dj}\sqrt{\frac{u}{\eta_{fD}}}\right]-\frac{2\pi\eta_{fD}}{uF_{hcD}}\delta\bar{q}_{D,j}=\frac{h_D}{2}\sum_{i=1}^{5}\delta\bar{q}_{D,i}[G_c(r^*_{Dj},r_{Di},u)-G_c(r^*_{Dj},r_{Di-1},u)] \quad \text{.....(A.173)}$$

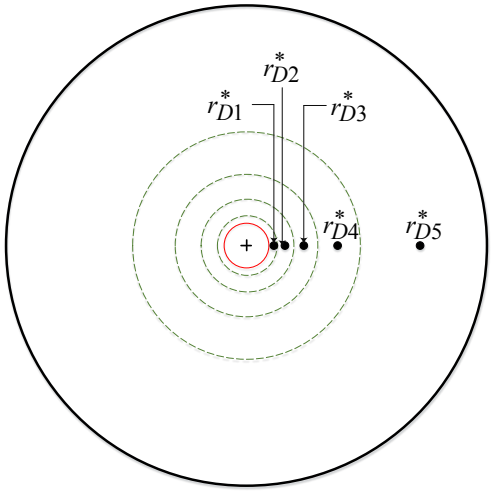

Figure A.6 — Definition of the observation points to define the continuity of pressure between the circular fracture and the 3D reservoir.

Then, the following set of equations should be used for the case presented in **Fig. A.6**:

$$A_1 K_0\left[r^*_{D1}\sqrt{\frac{u}{\eta_{fD}}}\right] + B_1 I_0\left[r^*_{D1}\sqrt{\frac{u}{\eta_{fD}}}\right] - \frac{2\pi\eta_{fD}}{uF_{hcD}}\delta\bar{q}_{D,1} = \frac{h_D}{2}\sum_{i=1}^{5}\delta\bar{q}_{D,i}\left[G_c(r^*_{D1}, r_{Di}, u) - G_c(r^*_{D1}, r_{Di-1}, u)\right] \quad \text{, ...(A.174)}$$

$$A_2 K_0\left[r^*_{D2}\sqrt{\frac{u}{\eta_{fD}}}\right] + B_2 I_0\left[r^*_{D2}\sqrt{\frac{u}{\eta_{fD}}}\right] - \frac{2\pi\eta_{fD}}{uF_{hcD}}\delta\bar{q}_{D,2} = \frac{h_D}{2}\sum_{i=1}^{5}\delta\bar{q}_{D,i}\left[G_c(r^*_{D2}, r_{Di}, u) - G_c(r^*_{D2}, r_{Di-1}, u)\right] \quad \text{, ...(A.175)}$$

$$A_3 K_0\left[r^*_{D3}\sqrt{\frac{u}{\eta_{fD}}}\right] + B_3 I_0\left[r^*_{D3}\sqrt{\frac{u}{\eta_{fD}}}\right] - \frac{2\pi\eta_{fD}}{uF_{hcD}}\delta\bar{q}_{D,3} = \frac{h_D}{2}\sum_{i=1}^{5}\delta\bar{q}_{D,i}\left[G_c(r^*_{D3}, r_{Di}, u) - G_c(r^*_{D3}, r_{Di-1}, u)\right] \quad \text{, ...(A.176)}$$

$$A_4 K_0\left[r_{D1}^*\sqrt{\frac{u}{\eta_{fD}}}\right]+B_4 I_0\left[r_{D4}^*\sqrt{\frac{u}{\eta_{fD}}}\right]-\frac{2\pi\eta_{fD}}{uF_{hcD}}\delta\bar{q}_{D,4}= \frac{h_D}{2}\sum_{i=1}^{5}\delta\bar{q}_{D,i}\left[G_c(r_{D4}^*,r_{Di},u)-G_c(r_{D4}^*,r_{Di-1},u)\right] \quad \text{, ...(A.177)}$$

$$A_5 K_0\left[r_{D5}^*\sqrt{\frac{u}{\eta_{fD}}}\right]+B_5 I_0\left[r_{D5}^*\sqrt{\frac{u}{\eta_{fD}}}\right]-\frac{2\pi\eta_{fD}}{uF_{hcD}}\delta\bar{q}_{D,5}= \frac{h_D}{2}\sum_{i=1}^{5}\delta\bar{q}_{D,i}\left[G_c(r_{D5}^*,r_{Di},u)-G_c(r_{D5}^*,r_{Di-1},u)\right] \quad \text{. .....(A.178)}$$

Considerations for the integration of the G_c-function

Recall Eq. A.172:

$$G_c(r_{Dj}^*,r_{Dk},u)=\int_{r_{D\min}}^{r_{D\max}}\frac{r_D}{R_D}\cos^{-1}\left[\frac{(r_{Dj}^*)^2-r_{Dk}^2+r_D^2}{2r_{Dj}^* r_D}\right]\exp\left[-R_D\sqrt{u}\right]dr_D\,.$$

If the observation point, r^*_{Dj}, in Eq. A.172 is greater than the upper integration limit ($r_{Dk}< r^*_{Dj}$), the integration limits should be adjusted to consider the circumference created by radius r_{Dk} (see **Fig. A.7**). The lower integration limit is redefined as:

$$r_{D\min}=r_{Dj}^*-r_{Dk}\,, \quad \text{.....(A.179)}$$

and the upper integration limit is:

$$r_{D\max}=r_{Dj}^*+r_{Dk}\,. \quad \text{.....(A.180)}$$

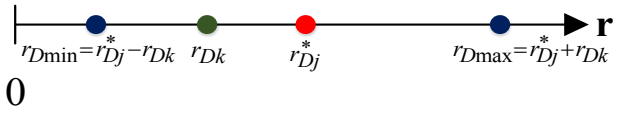

Figure A.7 — Definition of the integration limits for r_D when the observation point, r^*_{Dj}, is greater than the limit r_{Dk}.

If the observation point in Eq. A.172 is lower than the upper integration limit ($r_{Dk} > r^*_{Dj}$), then the lower limit, r_{Dmin}, will be zero and the upper integration limit, r_{Dmax}, is equal to r_{Dk} (see **Fig. A.8**). For this case, there is a "natural lower bound" defined by:

$$r_\alpha = r_{Dk} - r^*_{Dj} \,. \qquad \text{(A.181)}$$

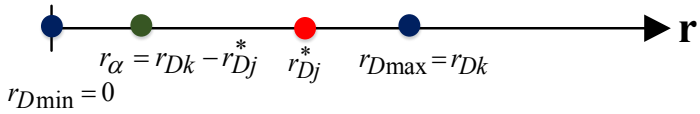

Figure A.8 — Definition of the integration limits for r_D when the observation point, r^*_{Dj}, is lower than the limit r_{Dk}.

The numerical integration when $r_{Dk} > r^*_{Dj}$ causes some difficulties given that the lower integration limit is zero. Therefore, it is convenient to use the "natural lower bound" to split the integral to avoid such difficulties. To do so, it is more convenient to write Eq. A.172 in terms of R_D:

$$G_c(r^*_{Dj}, r_{Dk}, u) = \int_{R_{D\min}}^{R_{D\max}} \cos^{-1}\left[\frac{(r^*_{Dj})^2 - r^2_{Dk} + R^2_D - z^2_{0D}}{2r^*_{Dj}\sqrt{R^2_D - z^2_{0D}}}\right] \exp\left[-R_D\sqrt{u}\right] dR_D \,, \qquad \text{(A.182)}$$

where:

$$R_{D\min} = \sqrt{r^2_{D\min} + z^2_{0D}} \,, \qquad \text{(A.183)}$$

and:

$$R_{D\max} = \sqrt{r_{Dk}^2 + z_{0D}^2} \quad \text{.....(A.184)}$$

Splitting the integral in Eq. A.182 at the "natural lower bound" it becomes:

$$G_c(r_{Dj}^*, r_{Dk}, u) = \int_{R_{D\min}}^{R_{D\alpha}} \cos^{-1}\left[\frac{(r_{Dj}^*)^2 - r_{Dk}^2 + R_D^2 - z_{0D}^2}{2r_{Dj}^*\sqrt{R_D^2 - z_{0D}^2}}\right]\exp\left[-R_D\sqrt{u}\right]dR_D + \int_{R_{D\alpha}}^{R_{D\max}} \cos^{-1}\left[\frac{(r_{Dj}^*)^2 - r_{Dk}^2 + R_D^2 - z_{0D}^2}{2r_{Dj}^*\sqrt{R_D^2 - z_{0D}^2}}\right]\exp\left[-R_D\sqrt{u}\right]dR_D \quad \text{.....(A.185)}$$

where:

$$R_{D\alpha} = \sqrt{(r_{Dk} - r_{Dj}^*)^2 + z_{0D}^2} \quad \text{.....(A.186)}$$

Considering the trigonometric identity:

$$\cos^{-1}(-x) = \pi - \cos^{-1}(x), \quad \text{.....(A.187)}$$

Eq. A. 185 is rewritten as:

$$G_c(r_{Dj}^*, r_{Dk}, u) = \pi\int_{R_{D\min}}^{R_{D\alpha}} \exp\left[-R_D\sqrt{u}\right]dr_D - \int_{R_{D\min}}^{R_{D\alpha}} \cos^{-1}\left[\frac{r_{Dk}^2 + z_{0D}^2 - (r_{Dj}^*)^2 + R_D^2}{2r_{Dj}^*\sqrt{R_D^2 - z_{0D}^2}}\right]\exp\left[-R_D\sqrt{u}\right]dR_D + \int_{R_{D\alpha}}^{R_{D\max}} \cos^{-1}\left[\frac{(r_{Dj}^*)^2 - r_{Dk}^2 + R_D^2 - z_{0D}^2}{2r_{Dj}^*\sqrt{R_D^2 - z_{0D}^2}}\right]\exp\left[-R_D\sqrt{u}\right]dR_D \quad \text{.....(A.188)}$$

Integrating the first term on the right hand side:

$$G_c(r_{Dj}^*, r_{Dk}, u) = \pi[\exp[-R_{D\alpha}\sqrt{u}] - \exp[-R_{D\min}\sqrt{u}]] -$$
$$\int_{R_{D\min}}^{R_{D\alpha}} \cos^{-1}\left[\frac{r_{Dk}^2 + z_{0D}^2 - (r_{Dj}^*)^2 + R_D^2}{2r_{Dj}^*\sqrt{R_D^2 - z_{0D}^2}}\right]\exp\left[-R_D\sqrt{u}\right]dR_D + \quad \text{(A.189)}$$
$$\int_{R_{D\alpha}}^{R_{D\max}} \cos^{-1}\left[\frac{(r_{Dj}^*)^2 - r_{Dk}^2 + R_D^2 - z_{0D}^2}{2r_{Dj}^*\sqrt{R_D^2 - z_{0D}^2}}\right]\exp\left[-R_D\sqrt{u}\right]dR_D$$

Given that the lower limit, r_{Dmin}, is zero and the observation point z_{0D} is also zero, Eq. A.183 reduces to:

$$R_{D\min} = 0, \quad \text{(A.190)}$$

and Eq. A.186 becomes:

$$R_{D\alpha} = r_{Dk} - r_{Dj}^*. \quad \text{(A.191)}$$

Consequently, the integration interval of the integral of the second term in the right hand side of Eq. A.189 is defined over the $[1,\infty)$-interval, which is out of the real domain of the cos^{-1}-function. Therefore, such an integral is equal to zero and Eq. A.189 reduces to:

$$G_c(r_{Dj}^*, r_{Dk}, u) = \pi[\exp[-R_{D\alpha}\sqrt{u}] - \exp[-R_{D\min}\sqrt{u}]] +$$
$$\int_{R_{D\alpha}}^{R_{D\max}} \cos^{-1}\left[\frac{(r_{Dj}^*)^2 - r_{Dk}^2 + R_D^2 - z_{0D}^2}{2r_{Dj}^*\sqrt{R_D^2 - z_{0D}^2}}\right]\exp\left[-R_D\sqrt{u}\right]dR_D \quad \text{(A.192)}$$

A.5. Constant-Rate Solution for the Model of a Horizontal Well Intercepting a Rectangular Longitudinal Finite Conductivity Fracture within a 3D Reservoir

The procedure to develop the constant-rate solution for the rectangular longitudinal fracture case within a 3D reservoir is essentially the same as in the previous section. Therefore, recall the solution developed in section A.2 for a discretized rectangular fracture (Eq. A.99):

$$\bar{p}_{fD,cr,j}(x_D,u) = A_j \exp\left[-x_D\sqrt{\frac{u}{\eta_{fD}}}\right] + B_j \exp\left[x_D\sqrt{\frac{u}{\eta_{fD}}}\right] - \frac{2\pi\eta_{fD}}{F_{hcD}u}\delta\bar{q}_{D,j}.$$

Fig A.9 shows an example of a rectangular fracture logarithmically discretized into three segments. A discretization in thirty segments is recommended. However, for the sake of providing an example, three segments will be used. The dimensionless pressure response of the discretized rectangular fracture shown in **Fig. A.9** is given by the set of equations:

$$\bar{p}_{fD,cr,1}(x_D,u) = A_1 \exp\left[-x_D\sqrt{\frac{u}{\eta_{fD}}}\right] + B_1 \exp\left[x_D\sqrt{\frac{u}{\eta_{fD}}}\right] - \frac{2\pi\eta_{fD}}{F_{hcD}u}\delta\bar{q}_{D,1} \quad (x_{D0}\leq x_D \leq x_{D1}), \text{.....(A.193)}$$

$$\bar{p}_{fD,cr,2}(x_D,u) = A_2 \exp\left[-x_D\sqrt{\frac{u}{\eta_{fD}}}\right] + B_2 \exp\left[x_D\sqrt{\frac{u}{\eta_{fD}}}\right] - \frac{2\pi\eta_{fD}}{F_{hcD}u}\delta\bar{q}_{D,2} \quad (x_{D1}\leq x_D \leq x_{D2}), \text{.....(A.194)}$$

$$\bar{p}_{fD,cr,3}(x_D,u) = A_3 \exp\left[-x_D\sqrt{\frac{u}{\eta_{fD}}}\right] + B_3 \exp\left[x_D\sqrt{\frac{u}{\eta_{fD}}}\right] - \frac{2\pi\eta_{fD}}{F_{hcD}u}\delta\bar{q}_{D,3} \quad (x_{D2}\leq x_D \leq x_{D3}). \text{.....(A.195)}$$

This approach results in a set of nine unknowns (3*N*-unknowns for *N*-segments of the rectangular fracture). To determine the values of the unknowns the procedure shown in section A.4 is also applied for this case.

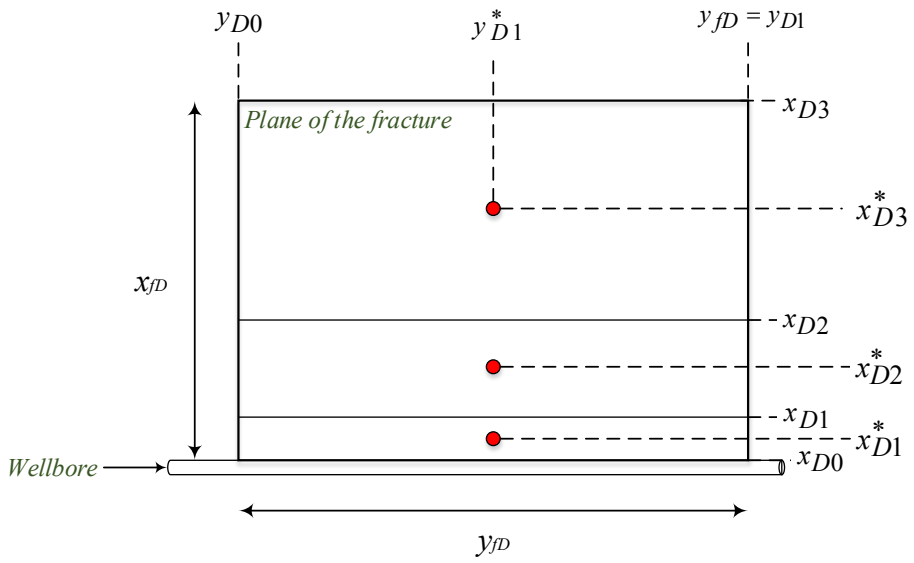

Figure A.9 — Logarithmic discretization of a rectangular fracture and definition of observation points.

1. Boundary conditions of the rectangular fracture.

The inner boundary condition for the well intercepting the rectangular fracture and producing at constant rate is:

$$\left[\frac{\partial p_f}{\partial x}\right]_{x=0} = \frac{qB\mu}{4k_f y_f w}. \quad \text{.....(A.196)}$$

Eq. A.196 expressed in dimensionless variables is:

$$\left[\frac{\partial p_{fD,cr}}{\partial x_D}\right]_{x_D=0} = -\frac{\pi}{2F_{hcD} y_{fD}}, \quad \text{.....(A.197)}$$

where dimensionless horizontal length of the fracture is:

$$y_{fD} = \frac{y_f}{x_f} \quad \text{.....(A.198)}$$

For this model, it is considered a closed hydraulic fracture. Therefore the outer boundary condition is defined by:

$$\left[\frac{\partial p_f}{\partial x}\right]_{x=x_f} = 0, \quad \text{(A.199)}$$

or, expressed in dimensionless variables:

$$\left[\frac{\partial p_{fD,cr}}{\partial x_D}\right]_{x_D=1} = 0 \quad \text{(A.200)}$$

Transforming the inner boundary condition (A.197) to the Laplace domain and then applying it to Eq. A.193 (segment defined by x_{D0} and x_{D1}), this results in the expression:

$$A_1 - B_1 = \frac{\pi\sqrt{\eta_{fD}}}{2F_{hcD}y_{fD}u^{3/2}}. \quad \text{(A.201)}$$

Similarly, applying the outer boundary condition (Eq. A.200) to Eq. A.195:

$$A_3 \exp\left[-\sqrt{\frac{u}{\eta_{fD}}}\right] - B_3 \exp\left[\sqrt{\frac{u}{\eta_{fD}}}\right] = 0. \quad \text{(A.202)}$$

2. Continuity of pressure at the interfaces of the discretized fracture.

The continuity of the pressure for this case is defined by:

$$\bar{p}_{fD,cr,j-1}(x_{Dj-1},u) = \bar{p}_{fD,cr,j}(x_{Dj-1},u), \quad \text{(A.203)}$$

for $2 \leq j \leq N$. For the segments defined in **Fig. A.9**:

$$A_1 \exp\left[-x_{D1}\sqrt{\frac{u}{\eta_{fD}}}\right]+B_1 \exp\left[x_{D1}\sqrt{\frac{u}{\eta_{fD}}}\right]-\frac{2\pi\eta_{fD}}{F_{hcD}u}\delta\overline{q}_{D,1} = A_2 \exp\left[-x_{D1}\sqrt{\frac{u}{\eta_{fD}}}\right]+B_2 \exp\left[x_{D1}\sqrt{\frac{u}{\eta_{fD}}}\right]-\frac{2\pi\eta_{fD}}{F_{hcD}u}\delta\overline{q}_{D,2}$$

(x_{D1}-interface), ...(A.204)

$$A_2 \exp\left[-x_{D2}\sqrt{\frac{u}{\eta_{fD}}}\right]+B_2 \exp\left[x_{D2}\sqrt{\frac{u}{\eta_{fD}}}\right]-\frac{2\pi\eta_{fD}}{F_{hcD}u}\delta\overline{q}_{D,2} = A_3 \exp\left[-x_{D2}\sqrt{\frac{u}{\eta_{fD}}}\right]+B_3 \exp\left[x_{D2}\sqrt{\frac{u}{\eta_{fD}}}\right]-\frac{2\pi\eta_{fD}}{F_{hcD}u}\delta\overline{q}_{D,3}$$

(x_{D2}-interface), ...(A.205)

3. Continuity of flowrate at the interfaces of the discretized fracture.

The continuity of flowrate is defined by:

$$\left[\frac{\partial\overline{p}_{fD,cr,j-1}}{\partial x_D}\right]_{x_D=x_{Dj-1}} = \left[\frac{\partial\overline{p}_{fD,cr,j}}{\partial x_D}\right]_{x_D=x_{Dj-1}}$$

,...(A.206)

for $2 \le j \le N$. For the example given in **Fig. A.9**:

$$-A_1 \exp\left[-x_{D1}\sqrt{\frac{u}{\eta_{fD}}}\right]+B_1 \exp\left[x_{D1}\sqrt{\frac{u}{\eta_{fD}}}\right] = -A_2 \exp\left[-x_{D1}\sqrt{\frac{u}{\eta_{fD}}}\right]+B_2 \exp\left[x_{D1}\sqrt{\frac{u}{\eta_{fD}}}\right]$$

(x_{D1}-interface),...............(A.207)

$$-A_2 \exp\left[-x_{D2}\sqrt{\frac{u}{\eta_{fD}}}\right]+B_2 \exp\left[x_{D2}\sqrt{\frac{u}{\eta_{fD}}}\right] = -A_3 \exp\left[-x_{D2}\sqrt{\frac{u}{\eta_{fD}}}\right]+B_3 \exp\left[x_{D2}\sqrt{\frac{u}{\eta_{fD}}}\right]$$

(x_{D2}-interface),.............(A.208)

4. Continuity of pressure between the fracture and the 3D reservoir.

To provide the remaining expressions to complete the system of equations for this model, consider the superposition of the dimensionless pressure of the 3D reservoir on the plane of the rectangular fracture (analogous to the circular fracture case):

$$\bar{p}_{Dcr,j}(r^*_{Dj},u)=\frac{h_D}{2}\sum_{i=1}^{N}\delta\bar{q}_{D,j}G_R(r^*_{Dj},\theta,u) \quad \text{(A.209)}$$

where:

$$G_R(r^*_{Dj},\theta,u)=\int_{r_D}\int_{\theta}\frac{1}{R_D}\exp[-R_D\sqrt{u}]r_D d\theta dr_D \quad \text{(A.210)}$$

The integral in Eq. A.210 is defined in polar coordinates. To integrate a rectangular surface using polar coordinates consider **Fig. A.10**. Note that a rectangular area can be subdivided into three semicircular areas, each one defined by minimum and maximum radii and an angle.

Given that r_D and θ are defined depending on the observation point (x^*_{Dk}, y^*_{Dk}) and any coordinate (x_{iD}, y_{jD}), it is convenient to use the following notation in terms of function Z_R:

$$G_R(r^*_{Dj},\theta,u)=Z_R(x^*_{Dk},y^*_{Dk},x_{1D},y_{1D},x_{2D},y_{2D},u) \quad \text{(A.211)}$$

Based on **Fig A.10**, observe that the minimum and maximum radii and angle depend on the segment (semicircular area) of the rectangle. Hence, the integrals n Z_R-function can be written as:

$$Z_R(x^*_{Dk}, y^*_{Dk}, x_{1D}, y_{1D}, x_{2D}, y_{2D}, u) = \int_{r_{D1}}^{r_{D2}} \int_{\theta\min,I}^{\theta\max,I} \frac{1}{R_D} \exp[-R_D\sqrt{u}] r_D d\theta dr_D + \int_{r_{D2}}^{r_{D3}} \int_{\theta\min,II}^{\theta\max,II} \frac{1}{R_D} \exp[-R_D\sqrt{u}] r_D d\theta dr_D + \int_{r_{D3}}^{r_{D4}} \int_{\theta\min,III}^{\theta\max,III} \frac{1}{R_D} \exp[-R_D\sqrt{u}] r_D d\theta dr_D \quad \text{.....(A.212)}$$

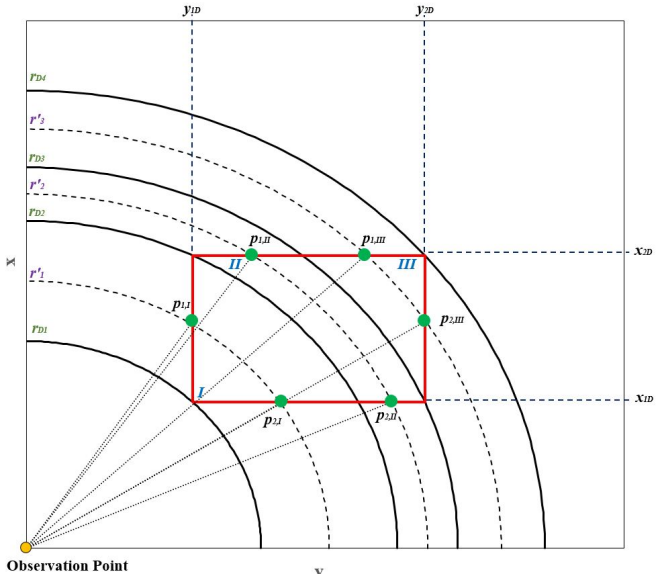

Figure A.10 — Subdivision of a rectangular area into semicircular areas.

Integrating Eq. A.212 with respect to θ:

$$Z_R(x^*_{Dk}, y^*_{Dk}, x_{1D}, y_{1D}, x_{2D}, y_{2D}, u) = \int_{r_{D1}}^{r_{D2}} [\theta\max, I - \theta\min, I] \frac{r_D}{R_D} \exp[-R_D\sqrt{u}] dr_D + \int_{r_{D2}}^{r_{D3}} [\theta\max, II - \theta\min, II] \frac{r_D}{R_D} \exp[-R_D\sqrt{u}] dr_D + , \quad \text{.....(A.213)}$$
$$\int_{r_{D3}}^{r_{D4}} [\theta\max, III - \theta\min, III] \frac{r_D}{R_D} \exp[-R_D\sqrt{u}] dr_D$$

where:

$$\theta_{\min,I} = \sin^{-1}\left[\frac{x_{1D}}{r_D}\right], \quad \text{.....(A.214)}$$

$$\theta_{\max,I} = \cos^{-1}\left[\frac{y_{1D}}{r_D}\right], \quad \text{(A.215)}$$

$$\theta_{\min,II} = \sin^{-1}\left[\frac{x_{1D}}{r_D}\right], \quad \text{(A.216)}$$

$$\theta_{\max,II} = \sin^{-1}\left[\frac{x_{2D}}{r_D}\right], \quad \text{(A.217)}$$

$$\theta_{\min,III} = \cos^{-1}\left[\frac{y_{2D}}{r_D}\right], \quad \text{(A.218)}$$

$$\theta_{\max,III} = \sin^{-1}\left[\frac{x_{2D}}{r_D}\right]. \quad \text{(A.219)}$$

Because of the reference system, angles $\theta_{min,II}$ and $\theta_{max,II}$ are different from the ones reported by Larsen *et al.* (1991). However the expressions yield the same results.

If the observation point is located at the origin, then r_{D1} and $\theta_{min,I}$ (Eq.A.214) become zero, and $\theta_{max,I}$ is $\pi/2$. Consequently, the first integral on the right hand side of Eq. A.213 can be performed analytically. The resulting equation is:

$$Z_R(x^*_{Dk}, y^*_{Dk}, x_{1D}, y_{1D}, x_{2D}, y_{2D}, u) = \frac{\pi}{2\sqrt{u}}\left[\exp[-z_{0D}\sqrt{u}] - \exp\left[-\sqrt{u[r_{D2}^2 - z_{0D}^2]}\right]\right] + \int_{r_{D2}}^{r_{D3}} [\theta\max, II - \theta\min, II]\frac{r_D}{R_D}\exp[-R_D\sqrt{u}]dr_D + \int_{r_{D3}}^{r_{D4}} [\theta\max, III - \theta\min, III]\frac{r_D}{R_D}\exp[-R_D\sqrt{u}]dr_D \quad \text{(A.220)}$$

The observation point (x^*_{Di}, y^*_{Di}) should be selected exactly where the pressure of the 3D reservoir will be evaluated. Such points should correspond to the center point of each segment of the

discretized rectangular fracture (see **Fig. A.8**). To perform the integrals given in Eq. A.220, it is convenient to always translate the observation point to the origin of the coordinate system by resetting the observation point(x^*_{Di}, y^*_{Di}) as the origin (0,0). The translation of the rest of the points are made by rescaling the *x*-axis as

$$x'_{jD} = x_{jD} - x^*_{Di}, \quad \text{(A.221)}$$

and *y*-axis as:

$$y'_{jD} = y_{jD} - y^*_{Di} \quad \text{(A.222)}$$

This translation of axes allows some of the variables of the Z_R-function to drop. It is redefined as:

$$Z_R(x'_{1D}, y'_{1D}, x'_{2D}, y'_{2D}, u) = Z_R(x^*_{Dk}, y^*_{Dk}, x_{1D}, y_{1D}, x_{2D}, y_{2D}, u). \quad \text{(A.223)}$$

After the axes translation, some of the coordinates can become negative. If that is the case, the area (or areas) of the rectangle that relies on the negative section of the translated reference system can be translated again to be considered in the positive section. These cases are summarized and graphically shown in **Table A.1**. For such cases, the Z_R- function should be mathematically treated as follows:

$$Z_R(x'_{1D}, y'_{1D}, x'_{2D}, y'_{2D}, u) = Z_R(0, y'_{1D}, |x'_{1D}|, y'_{2D}, u) + Z_R(0, y'_{1D}, x'_{2D}, y'_{2D}, u) \quad (x'_{1D} < 0 < x'_{2D}), \quad \text{(A.224)}$$

$$Z_R(x'_{1D}, y'_{1D}, x'_{2D}, y'_{2D}, u) = Z_R(x'_{1D}, 0, x'_{2D}, |y'_{1D}|, u) + Z_R(x'_{1D}, 0, x'_{2D}, y'_{2D}, u) \quad (y'_{1D} < 0 < y'_{2D}), \quad \text{(A.225)}$$

$$Z_R(x'_{1D}, y'_{1D}, x'_{2D}, y'_{2D}, u) = Z_R(0,0, x'_{2D}, y'_{2D}, u) + Z_R(0,0, x'_{2D}, |y'_{1D}|, u) + Z_R(0,0, |x'_{1D}|, |y'_{1D}|, u) + Z_R(0,0, |x'_{1D}|, y'_{2D}, u) \quad (x'_{1D} < 0 < x'_{2D} \text{ and } y'_{1D} < 0 < y'_{2D}), \quad \text{...(A.226)}$$

As shown in **Fig. A.9**, the continuity of pressure between the rectangular fracture and the 3D reservoir generates three equations by comparing the dimensionless pressure of the fracture (Eq. A.99) and the superposed dimensionless pressure of the 3D reservoir over each segment of the fracture (Eq. A.209). Both equations should be evaluated at the observation points defined in **Fig. A.9**. These equations are:

$$A_1 \exp\left[-x^*_{D1}\sqrt{\frac{u}{\eta_{fD}}}\right] + B_1 \exp\left[x^*_{D1}\sqrt{\frac{u}{\eta_{fD}}}\right] - \frac{2\pi\eta_{fD}}{F_{hcD}u}\delta\bar{q}_{D,1} = \frac{h_D}{2}\sum_{i=1}^{3}\delta\bar{q}_{D,i} Z_R(x^*_{D1}, y^*_{D1}, x_{D0}, y_{D0}, x_{D1}, y_{D1}, u) \quad \text{,.....(A.227)}$$

$$A_2 \exp\left[-x^*_{D2}\sqrt{\frac{u}{\eta_{fD}}}\right] + B_2 \exp\left[x^*_{D2}\sqrt{\frac{u}{\eta_{fD}}}\right] - \frac{2\pi\eta_{fD}}{F_{hcD}u}\delta\bar{q}_{D,2} = \frac{h_D}{2}\sum_{i=1}^{3}\delta\bar{q}_{D,i} Z_R(x^*_{D2}, y^*_{D1}, x_{D1}, y_{D0}, x_{D2}, y_{D1}, u) \quad \text{,.....(A.228)}$$

$$A_3 \exp\left[-x^*_{D3}\sqrt{\frac{u}{\eta_{fD}}}\right] + B_3 \exp\left[x^*_{D3}\sqrt{\frac{u}{\eta_{fD}}}\right] - \frac{2\pi\eta_{fD}}{F_{hcD}u}\delta\bar{q}_{D,3} = \frac{h_D}{2}\sum_{i=1}^{3}\delta\bar{q}_{D,i} Z_R(x^*_{D3}, y^*_{D1}, x_{D2}, y_{D0}, x_{D3}, y_{D1}, u) \quad \text{. .....(A.229)}$$

In general, for a discretization into *N*-segments:

$$A_j \exp\left[-x^*_{Dj}\sqrt{\frac{u}{\eta_{fD}}}\right] + B_j \exp\left[x^*_{Dj}\sqrt{\frac{u}{\eta_{fD}}}\right] - \frac{2\pi\eta_{fD}}{F_{hcD}u}\bar{\delta q}_{D,j} = \frac{h_D}{2}\sum_{i=1}^{N}\bar{\delta q}_{D,i} Z_R(x^*_{Dj}, y^*_{D1}, x_{Dj-1}, y_{D0}, x_{Dj-1}, y_{D1}, u) \quad \text{.....(A.230)}$$

Table A.1 — Translation of the observation points and rectangular areas.

	Case I	**Case II**	**Case III**
Original set	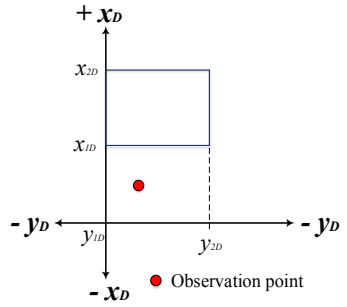	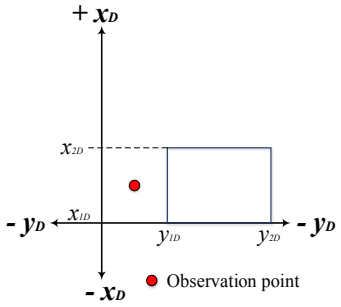	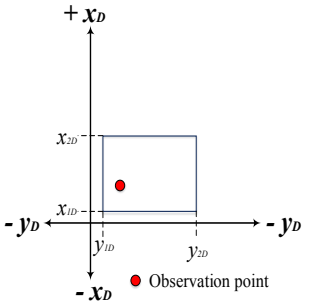
After Translation	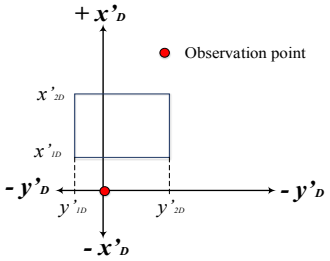	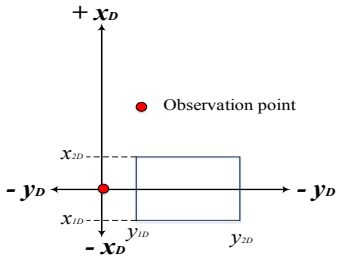	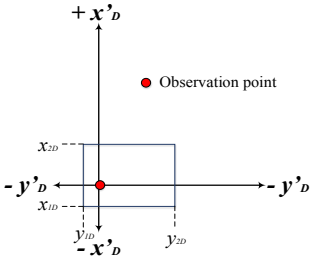
Equivalent geometry due to symmetry	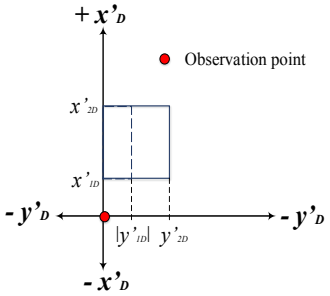	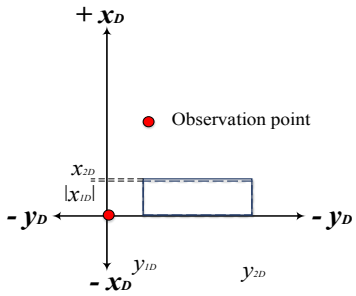	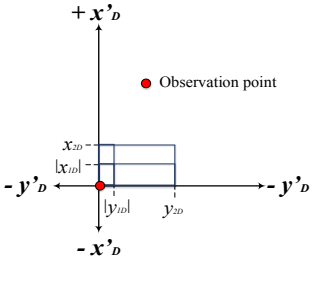

APPENDIX B

PRESSURE-TRANSIENT ANALYSIS OF FRACTAL RESERVOIRS

This Appendix is divided into two sections. In the first section, we show the detailed derivation of the diffusivity equation presented by Chang *et al*. (1990) to depict the pressure-transient behavior of a fractal reservoir. In the second section, we present the constant-rate solution of such a diffusivity equation, assuming an infinite fractal reservoir.

B.1. Development of the Diffusivity Equation for a Fractal Reservoir

Consider that the number of permeable sites contained in a volume with characteristic length R is determined by a power-law:

$$N(R) = \sigma R^{D_f - 1}, \quad \text{(B.1)}$$

where D_f is the fractal dimension of the permeable sites. The sign of the exponent D_f depicts the proportionality between the permeable sites and the volume.

Assuming that all permeable sites in the reservoir have the same volume, V_s, the pore volume of the permeable sites is determined by:

$$PV(R) = V_s N(R). \quad \text{(B.2)}$$

To obtain the porosity of the fractal reservoir, the pore volume must be divided by the volume of the reservoir. Chang *et al.*, (1990) defined the size of the reservoir in terms of a geometry factor, G. However, it is more appropriate to use the generalized definition (Barker, 1988):

$$V_r(R) = \alpha_d R^{d-1} b^{3-d} \Delta R, \quad \text{(B.3)}$$

where d is the Euclidean dimension and α_d is the area of a unit sphere in d dimensions:

$$\alpha_d = \frac{2\pi^{d/2}}{\Gamma[d/2]}, \quad \text{(B.4)}$$

Then, if d=1, the reservoir would have the shape of a rectangular prism with two sides of size b and one of size $2R$. If d=2, the reservoir would have the shape of cylinder of radius R and height b. If d=3, the reservoir would have the shape of sphere of radius R.

Combining Eq. B.2 and Eq. B.3:

$$\phi(R) = \frac{PV}{V_r} = \phi_0 R^{Df-d}, \quad \text{(B.5)}$$

where ϕ_0 is a reference porosity defined by:

$$\phi_0 = \frac{\sigma V_s}{\alpha_d b^{3-d}}. \quad \text{(B.6)}$$

To develop the Darcy's law equation for a fractal system, consider the Hagen-Poiseuille equation to determine the flowrate of a fluid of viscosity μ through a capillary tube of radius r_c and length R:

$$q_u = \frac{\pi r_c^4}{8\mu}\frac{\partial p}{\partial R}. \quad \text{(B.7)}$$

For a system of n_p capillary tubes with the same shape, the total flow rate of the system is given by:

$$q_u = n_p \frac{\pi r_c^4}{8\mu}\frac{\partial p}{\partial R}. \quad \text{(B.8)}$$

An equivalent number of capillary tubes of volume V_c contained in a reservoir volume V_r with pore volume PV is determined by:

$$n_p = \frac{PV}{V_c}, \quad \text{(B.9)}$$

Combining Eqs. B.1, B.2, B.8 and B.9 gives us:

$$q_u = \frac{\sigma R^{D_f - 1} V_s}{V_c} \frac{\pi r_c^4}{8\mu} \frac{\partial p}{\partial R}. \quad \text{(B.10)}$$

Assuming that the volume of the permeable site and the volume of the capillary tube are equal and that the radius of the capillary tube is a power-law function of the characteristic length of the reservoir, R:

$$r_c = \xi R^{-\theta/4}. \quad \text{(B.11)}$$

Substituting Eq. B.11 in Eq. B.10 results in the following expression:

$$q_u = \xi^* \frac{R^{D_f - \theta - 1}}{\mu} \frac{\partial p}{\partial R}, \quad \text{(B.12)}$$

where:

$$\xi^* = \frac{\pi \sigma \xi^4}{8}. \quad \text{(B.13)}$$

On the other hand, consider Darcy's law with variable permeability:

$$q_R = \frac{k(R) A}{\mu} \frac{\partial p}{\partial R}. \quad \text{(B.14)}$$

where A is the area exposed to flow. Based on Eq. B.3, the area exposed to flow can be defined as:

$$A = \alpha_d b^{3-d} . \quad \text{(B.15)}$$

Assuming that the variation of permeability can be represented by a power-law function:

$$k(R) = k_0 R^{\beta}, \quad \text{(B.16)}$$

where k_0 is a reference permeability. Then, substituting Eq. B.15 and Eq. B.16 in Eq. B.14 results in:

$$q_R = R^{\beta} \alpha_d b^{3-d} \frac{k_0}{\mu} \frac{\partial p}{\partial R} \quad \text{(B.17)}$$

Alternatively, using Eq. B.6:

$$q_R = \frac{\sigma V_s}{\phi_0} \frac{R^{\beta} k_0}{\mu} \frac{\partial p}{\partial R} \quad \text{(B.18)}$$

Comparing Eq. B.12 and Eq. B. 17, it is concluded that

$$\xi^* = \frac{\sigma V_s}{\phi_0}, \quad \text{(B.19)}$$

and that index β is related to the distribution of the sites, D_f and the connectivity of them:

$$\beta = D_f - \theta - 1 . \quad \text{(B.20)}$$

To develop the diffusivity equation for a fractal reservoir, consider the incoming mass of fluid, $m_{in,R}$ through an infinitesimal section of the reservoir can be expressed as:

$$m_{in,R} = -\rho q_R \Delta t \cdot \quad \text{(B.21)}$$

Similarly, the outgoing mass of fluid:

$$m_{out,R} = [-\rho q_R + \Delta(\rho q_R)]\Delta t \cdot \quad \text{(B.22)}$$

The cumulative mass of fluid is determined by:

$$m_c = m_{out,R} - m_{in,R} = \Delta(\rho q_R)\Delta t \cdot \quad \text{(B.23)}$$

The mass of a single saturating fluid at an initial time can be expressed as:

$$m_{t_1} = \phi\rho V_r \quad \text{(B.24)}$$

Analogously, at a final time the mass of fluid is:

$$m_{t_2} = \phi\rho V_r + \Delta(\phi\rho)V_r \cdot \quad \text{(B.25)}$$

The cumulative mass of fluid can be also given by:

$$m_c = m_{t_2} - m_{t_1} = \Delta(\phi\rho)V_r \cdot \quad \text{(B.26)}$$

Equating Eq. B.23 and Eq. B.26:

$$\Delta(\rho q_R)\Delta t = \Delta(\phi\rho)V_r \quad \text{(B.27)}$$

Based on Eq. B.3, Eq. B.26 can be rewritten as:

$$\frac{1}{\alpha_d R^{d-1} b^{3-d}} \frac{\Delta(\rho q_R)}{\Delta R} = \frac{\Delta(\phi\rho)}{\Delta t} \cdot \quad \text{(B.28)}$$

Taking the limits of ΔR and Δt to zero, Eq. B.28 takes the differential form:

$$\frac{1}{\alpha_d R^{d-1} b^{3-d}} \frac{\partial(\rho q_R)}{\partial R} = \frac{\partial(\phi\rho)}{\partial t}. \quad \text{(B.29)}$$

Applying the derivative on the right hand side of Eq. B.29 and arraying, it results in:

$$\frac{1}{\alpha_d R^{d-1} b^{3-d}} \frac{1}{\phi} \frac{\partial(\rho q_R)}{\partial R} = \rho\left[\frac{1}{\phi}\frac{\partial\phi}{\partial t} + \frac{1}{\rho}\frac{\partial\rho}{\partial t}\right]. \quad \text{(B.30)}$$

Substituting the definition of the porosity (Eq. B.5) and Darcy's equation in its fractal form (Eq. B.18) in Eq. B.30, such an expression reduces to:

$$\frac{1}{R^{Df-1}} \frac{\partial}{\partial R}\left[\rho \frac{R^{\beta} k_0}{\mu} \frac{\partial p}{\partial R}\right] = \rho\phi_0\left[\frac{1}{\phi}\frac{\partial\phi}{\partial t} + \frac{1}{\rho}\frac{\partial\rho}{\partial t}\right]. \quad \text{(B.31)}$$

Applying the derivative on the left hand side of Eq. B.29 gives the expression:

$$\frac{1}{R^{Df-1}}\left[\frac{\partial}{\partial R}\left[R^{\beta}\frac{\partial p}{\partial R}\right] + \frac{R^{\beta}}{\rho}\frac{\partial p}{\partial R}\frac{\partial\rho}{\partial R}\right] = \frac{\phi_0\mu}{k_0}\left[\frac{1}{\phi}\frac{\partial\phi}{\partial t} + \frac{1}{\rho}\frac{\partial\rho}{\partial t}\right] \quad \text{(B.32)}$$

Using the chain rule similar to the cases shown in Appendix A:

$$\frac{\partial\rho}{\partial R} = \frac{\partial\rho}{\partial p}\frac{\partial p}{\partial R}, \quad \text{(B.33)}$$

$$\frac{\partial\rho}{\partial t} = \frac{\partial\rho}{\partial p}\frac{\partial p}{\partial t}, \quad \text{(B.34)}$$

$$\frac{\partial\phi}{\partial t} = \frac{\partial\phi}{\partial p}\frac{\partial p}{\partial t}. \quad \text{(B.35)}$$

Substituting Eqs. B.33-B.35 in Eq. B.32 results in:

$$\frac{1}{R^{D_f-1}}\left[\frac{\partial}{\partial R}\left[R^{\beta}\frac{\partial p}{\partial R}\right]+\frac{R^{\beta}}{\rho}\frac{\partial \rho}{\partial p}\left[\frac{\partial p}{\partial R}\right]^2\right]=\frac{\phi_0\mu}{k_0}\left[\frac{1}{\phi}\frac{\partial \phi}{\partial p}+\frac{1}{\rho}\frac{\partial \rho}{\partial p}\right]\frac{\partial p}{\partial t}. \quad \text{(B.36)}$$

The compressibility of the fluid can be defined by:

$$c_o=\frac{1}{\rho}\frac{\partial \rho}{\partial p}, \quad \text{(B.37)}$$

and the compressibility of the fractal reservoir as:

$$c=\frac{1}{\phi}\frac{\partial \phi}{\partial p}. \quad \text{(B.38)}$$

Substituting Eqs. B.37 and B.38 in Eq. B.36 and neglecting the squared gradient on the left hand side of the equation, this yields the expression:

$$\frac{1}{R^{D_f-1}}\frac{\partial}{\partial R}\left[R^{\beta}\frac{\partial p}{\partial R}\right]=\frac{\phi_0\mu c_t}{k_0}\frac{\partial p}{\partial t}, \quad \text{(B.39)}$$

where the total compressibility of the fractal reservoir is defined by:

$$c_t=c_o+c \quad \text{(B.40)}$$

For this model, consider the following dimensionless variables: Dimensionless pressure:

$$p_{D,cr}(R_D,t_D)=\frac{\sigma V_s k_0}{qB\mu r_w^{1-\beta}\phi_0}[p_i-p(R,t)], \quad \text{(B.41)}$$

dimensionless time:

$$t_D=\frac{k_0}{\phi_0\mu c_t r_w^{\theta+2}}, \quad \text{(B.42)}$$

and dimensionless position in the fractal reservoir:

$$R_D = \frac{R}{r_w} \quad \text{(B.43)}$$

Using the chain rule, the derivative of the pressure with respect to time is expressed as:

$$\frac{\partial p}{\partial t} = \frac{\partial p_f}{\partial p_{D,cr}} \frac{\partial p_{D,cr}}{\partial t_D} \frac{\partial t_D}{\partial t} = -\frac{qB\mu r_w^{1-\beta}\phi_0}{\sigma V_s k_0} \frac{k_0}{\phi_0 \mu c_t r_w^{\theta+2}} \frac{\partial p_{D,cr}}{\partial t_D} \quad \text{(B.44)}$$

Similarly, for the first derivative of the pressure with respect to R:

$$\frac{\partial p}{\partial R} = \frac{\partial p}{\partial p_{D,cr}} \frac{\partial p_{D,cr}}{\partial R_D} \frac{\partial R_D}{\partial R} = -\frac{qB\mu r_w^{1-\beta}\phi_0}{\sigma V_s k_0} \frac{1}{r_w} \frac{\partial p_{fD,cr}}{\partial r_D} \quad \text{(B.45)}$$

Substituting Eqs. B.43-B.45 in Eq. B.39 gives the diffusivity equation for a fractal reservoir in its dimensionless form:

$$\frac{1}{R_D^{D_f-1}} \frac{\partial}{\partial R_D}\left[R_D^{\beta} \frac{\partial p_{D,cr}}{\partial R_D}\right] = \frac{\partial p_{D,cr}}{\partial t_D} \quad \text{(B.46)}$$

B.2. Constant-Rate Solution for the Fractal Reservoir Model

To solve Eq. B.46, consider the following initial and boundary conditions:

$$p_D(R_D, t_D = 0) = 0 \qquad \text{(initial condition)}, \quad \text{(B.47)}$$

$$\left[R_D^{\beta} \frac{\partial p_{D,cr}}{\partial R_D}\right]_{R_D=1} = -1 \qquad \text{(inner boundary condition)}, \quad \text{(B.48)}$$

$$\lim_{R_D \to \infty} p_D(R_D, t_D) = 0 \qquad \text{(outer boundary condition)} \quad \text{(B.49)}$$

Applying the derivative on the left hand side of Eq. B.46 and arraying, it yields the following equation:

$$R_D^2 \frac{\partial^2 p_{D,cr}}{\partial R_D^2} + \beta R_D \frac{\partial p_{D,cr}}{\partial R_D} - R_D^{\theta+2} \frac{\partial p_{D,cr}}{\partial t_D} = 0 \quad \text{(B.50)}$$

Applying the Laplace transform to Eq. B.50, it becomes:

$$\frac{d^2 \bar{p}_{D,cr}}{dR_D^2} + \frac{\beta}{R_D} \frac{d\bar{p}_{D,cr}}{dR_D} - uR_D^{\theta} \bar{p}_{D,cr} = 0 \quad \text{(B.51)}$$

Consider the transformation function:

$$G(z) = \bar{p}_{D,cr}(R_D, u), \quad \text{(B.52)}$$

and the transformation variable:

$$z = \frac{2\sqrt{u}}{\theta+2} R_D^{[\theta+2]/2} \quad \text{(B.53)}$$

Using the chain rule, the derivative of the dimensionless pressure in the Laplace domain with respect to the dimensionless radius is:

$$\frac{d\bar{p}_{D,cr}}{dR_D} = \frac{d\bar{p}_{D,cr}}{dG(z)} \frac{dG(z)}{dz} \frac{dz}{dR_D} = R_D^{\theta/2} \sqrt{u} \frac{dG(z)}{dz}. \quad \text{(B.54)}$$

Applying the second derivative to Eq. B.52 with respect to R_D:

$$\frac{d^2 \bar{p}_{D,cr}}{dR_D^2} = R_D^{\theta} u \frac{d^2 G(z)}{dz^2} + \frac{\theta}{2} R_D^{[\theta-2]/2} \sqrt{u} \frac{dG(z)}{dz} \quad \text{(B.55)}$$

Substituting Eqs. B.52 and B.53 in Eq. B.49 and arraying, it reduces to the following expression:

$$z^2\frac{d^2G(z)}{dz^2}+[1-2v]z\frac{dG(z)}{dz}-z^2G(z)=0 \text{ (where } v=[1-\beta]/[\theta+2]) \quad \text{(B.56)}$$

Defining a new transformation function:

$$B(z)=\left[\frac{2\sqrt{u}}{\theta+2}\right]^{-v}z^vG(z), \quad \text{(B.57)}$$

the derivative of the function $G(z)$ with respect to z can be expressed as:

$$\frac{dG(z)}{dz}=\left[\frac{2\sqrt{u}}{\theta+2}\right]^{-v}z^v\frac{dB(z)}{dz}+\left[\frac{2\sqrt{u}}{\theta+2}\right]^{-v}vz^{v-1}B(z) \quad \text{(B.58)}$$

Taking the second derivative to Eq. B.56 yields:

$$\frac{d^2G(z)}{dz^2}=\left[\frac{2\sqrt{u}}{\theta+2}\right]^{-v}\left[z^v\frac{d^2B(z)}{dz^2}+vz^{v-1}\frac{dB(z)}{dz}\right]+\left[\frac{2\sqrt{u}}{\theta+2}\right]^{-v}v\left[z^{v-1}\frac{dB(z)}{dz}+[v-1]z^{v-2}B(z)\right]. \quad \text{(B.59)}$$

Substituting Eqs. B.57-B.59 in Eq. B.56 and arraying, it reduces to the following differential equation:

$$z^2\frac{d^2B(z)}{dz^2}+z\frac{dB(z)}{dz}-[v^2+z^2]B(z)=0. \quad \text{(B.60)}$$

By inspection, the general solution to Eq. B.60 is given by:

$$B(z) = C_1 K_v(z) + C_2 I_v(z) \quad \text{(B.61)}$$

Expressing Eq. E.61 in terms of the pressure:

$$\bar{p}_{D,cr}(R_D,u) = R_D^{[1-\beta]/2}\left[C_1 K_v\left[\frac{2\sqrt{u}}{\theta+2}R_D^{[\theta+2]/2}\right] + C_2 I_v\left[\frac{2\sqrt{u}}{\theta+2}R_D^{[\theta+2]/2}\right]\right] \quad \text{(B.62)}$$

Applying the outer boundary condition (Eq.B.49) to Eq. B.62, we can conclude that C_2 must be zero. Then, the bounded solution for this problem is:

$$\bar{p}_{D,cr}(R_D,u) = R_D^{[1-\beta]/2} C_1 K_v\left[\frac{2\sqrt{u}}{\theta+2}R_D^{[\theta+2]/2}\right] \quad \text{(B.63)}$$

The value of the constant C_1 results from applying the inner boundary condition (Eq.B.48 in the Laplace domain) to Eq. B.63. Such a value is:

$$C_1 = \frac{1}{u^{3/2}}\frac{1}{K_{v-1}\left[\frac{2\sqrt{u}}{\theta+2}\right]} \quad \text{(B.64)}$$

The particular solution is obtained by substituting Eq. B.64 in Eq. B.63:

$$\bar{p}_{D,cr}(R_D,u) = \frac{R_D^{[1-\beta]/2}}{u^{3/2}}\frac{K_v\left[\frac{2\sqrt{u}}{\theta+2}R_D^{[\theta+2]/2}\right]}{K_{v-1}\left[\frac{2\sqrt{u}}{\theta+2}\right]} \quad \text{(B.65)}$$

To provide the particular solution in the real domain, consider the "point source" approximation, *i.e.*:

$$K_{v-1}\left[\frac{2\sqrt{u}}{\theta+2}\right]=K_{1-v}\left[\frac{2\sqrt{u}}{\theta+2}\right]\approx\frac{\Gamma[1-v]}{2}\left[\frac{\sqrt{u}}{\theta+2}\right]^{-[1-v]} \quad \text{(for } v>0\text{)} \qquad \text{(B.66)}$$

Substituting Eq. B.66 in Eq. B.65:

$$\bar{p}_{D,cr}(R_D,u)=\frac{2R_D^{[1-\beta]/2}}{[\theta+2]^{1-v}\Gamma[1-v]}u^{-[2+v]/2}K_v\left[\frac{2\sqrt{u}}{\theta+2}R_D^{[\theta+2]/2}\right] \qquad \text{(B.67)}$$

Applying the inverse Laplace transform to Eq. B.67 (Eq. A32 from Barker, 1988):

$$p_{D,cr}(R_D,t_D)=\frac{R_D^{[1-\beta]}}{[\theta+2]\Gamma[1-v]}\Gamma\left[-v,\frac{R_D^{[\theta+2]}}{[\theta+2]^2 t_D}\right] \qquad \text{(B.68)}$$

APPENDIX C

PRESSURE-TRANSIENT BEHAVIOR OF A VERTICALLY FRACTURED WELL IN A FRACTAL RESERVOIR

In this Appendix, we show the detailed derivation of the uniform-flux solution of a vertical well intercepted by a hydraulic fracture in a fractal reservoir (Beier, 1994).

C.1. Uniform-Flux Solution of a Vertically Fractured Well within a Fractal Reservoir

Recall the constant-rate solution for an infinite fractal reservoir (Eq. B.68):

$$p_{D,cr}(R_D,t_D)=\frac{R_D^{[1-\beta]}}{[\theta+2]\Gamma[1-\nu]}\Gamma\left[-\nu,\frac{R_D^{\theta+2}}{[\theta+2]^2 t_D}\right] \text{ (where } \nu=[1-\beta]/[\theta+2]).$$

Consider the redefinition of the dimensionless time:

$$t_{D,Be}=\frac{[\theta+2]^2}{4}\left[\frac{r_w}{x_f}\right]^{\theta+2} t_D, \quad \text{.....(C.1)}$$

and:

$$p_{DBe}(R_D,t_{D,Be})=\frac{[\theta+2]}{4}p_{D,cr}(R_D,t_D) \quad \text{.....(C.2)}$$

Then, Eq.B.66 can be written as:

$$p_{DBe}(R_D,t_{D,Be})=\frac{R_D^{[1-\beta]}}{4\Gamma[1-\nu]}\Gamma\left[-\nu,\frac{R_D^{\theta+2}}{4t_{D,Be}}\right]. \quad \text{.....(C.3)}$$

Based on the definition of the Incomplete Gamma Function, Eq. C.3 can be written as:

$$p_{DBe}(R_D, t_{D,Be}) = \frac{R_D^{[1-\beta]}}{4\Gamma[1-\nu]} \int_{\psi}^{\infty} z^{-\nu-1} \exp[-z] dz \,, \quad \text{(C.4)}$$

where:

$$\psi = \frac{R_D^{\theta+2}}{4 t_{D,Be}} \,. \quad \text{(C.5)}$$

According to the grouping variable z:

$$z = \frac{R_D^{\theta+2}}{4\tau} \,, \quad \text{(C.6)}$$

Eq. C.3 can be rewritten as:

$$p_{DBe}(R_D, t_{D,Be}) = \frac{1}{\Gamma[1-\nu]} \int_{0}^{t_{D,Be}} \frac{1}{[4\tau]^{1-\nu}} \exp\left[-\frac{R_D^{\theta+2}}{4\tau} \right] d\tau \quad \text{(C.7)}$$

To be consistent with the solution presented by Beier (1994), consider the change of variables:

$$d_s = \frac{2D_f}{\theta+2} \,, \quad \text{(C.8)}$$

consequently:

$$1-\nu = \frac{d_s}{2} \quad \text{(C.9)}$$

Using Eq. C.8 and C.9, Eq. C.7 can be written as:

$$p_{DBe}(R_D, t_{D,Be}) = \frac{1}{\Gamma[d_s/2]} \int_{0}^{t_{D,Be}} \frac{1}{[4\tau]^{d_s/2}} \exp\left[-\frac{R_D^{2D_f/d_s}}{4\tau} \right] d\tau \,. \quad \text{(C.10)}$$

Assuming that the "fractal radius" is given by:

$$R_D^{2D_f/d_s} = [x_D - x_{wD}]^{2D_f/d_s} + [y_D - y_{wD}]^{2D_f/d_s}, \quad \text{(C.11)}$$

then, Eq. C.10 is rewritten as:

$$p_{DBe}(R_D, t_{D,Be}) = \frac{1}{\Gamma[d_s/2]} \int_0^{t_{D,Be}} \exp\left[-\frac{[x_D - x_{wD}]^{2D_f/d_s}}{4\tau}\right] \exp\left[-\frac{[y_D - y_{wD}]^{2D_f/d_s}}{4\tau}\right] \frac{d\tau}{[4\tau]^{d_s/2}} \quad . \quad \text{(C.12)}$$

Assuming that y_{wD} is zero and integrating over the domain of the x_D-axis results in:

$$p_{DBe}(x_D, y_D, t_{D,Be}) = \frac{1}{\Gamma[d_s/2]} \int_0^{t_{D,Be}} \exp\left[-\frac{[y_D]^{2D_f/d_s}}{4\tau}\right] \int_{-1}^{1} \exp\left[-\frac{[x_D - x_{wD}]^{2D_f/d_s}}{4\tau}\right] dx_{wD} \frac{d\tau}{[4\tau]^{d_s/2}} \quad \text{(C.13)}$$

To integrate Eq. C.13 over the x_{wD} interval, consider the change of variables:

$$w = \frac{x_D - x_{wD}}{[4\tau]^{d_s/2D_f}}, \quad \text{(C.14)}$$

and consequently:

$$dw = \frac{-dx_{wD}}{[4\tau]^{d_s/2D_f}}. \quad \text{(C.15)}$$

Evaluating at y_D=0 and substituting Eq. C.14 and Eq. C.15 into Eq. C.13, it becomes:

$$p_{DBe}(x_D, t_{D,Be}) = \frac{1}{\Gamma[d_s/2]}$$
$$\int_0^{t_{D,Be}} \int_{w_l}^{w_u} \exp\left[-w^{2D_f/d_s}\right][4\tau]^{-d_s/2}\left[-[4\tau]^{2D_f/d_s}\, dw\right] d\tau \frac{1+x_D}{[4\tau]^{d_s/2D_f}}, \quad \text{(C.16)}$$

where:

$$w_l = \frac{1+x_D}{[4\tau]^{d_s/2D_f}}, \quad \text{(C.17)}$$

and:

$$w_u = \frac{-1+x_D}{[4\tau]^{d_s/2D_f}} \quad \text{(C.18)}$$

Splitting and arraying the inner integral in Eq. C.16 results in:

$$p_{DBe}(x_D, t_{D,Be}) = \frac{1}{\Gamma[d_s/2]}$$
$$\int_0^{t_{D,Be}} [4\tau]^{-\left[\frac{d_s}{2}\right]\left[1-\frac{1}{D_f}\right]} \left[\int_{w_u}^{0} \exp\left[-w^{2D_f/d_s}\right] dw + \int_0^{w_l} \exp\left[-w^{2D_f/d_s}\right]\right] d\tau \quad \text{(C.19)}$$

Using the change of variables:

$$z = w^{2D_f/d_s}. \quad \text{(C.20)}$$

The first integral inside the brackets in Eq. C.19 becomes:

$$\int_{w_u}^{0} \exp\left[-w^{2D_f/d_s}\right] dw = \frac{d_s}{2D_f} \int_0^{z_u} z^{\frac{d_s}{2D_f}-1} \exp[-z]\, dz, \quad \text{(C.21)}$$

where:

$$z_u = \frac{[1-x_D]^{2D_f/d_s}}{4\tau}. \quad \text{(C.22)}$$

According to the definition of the lower incomplete gamma function, Eq. C.21 can be expressed as:

$$\int_{w_u}^{0} \exp\left[-w^{2D_f/d_s}\right] dw = \frac{d_s}{2D_f}\gamma\left[\frac{d_s}{2D_f}, \frac{[1-x_D]^{2D_f/d_s}}{4\tau}\right] \quad \text{(C.23)}$$

Similarly, for the second integral inside the brackets into Eq. C.19:

$$\int_{0}^{w_l} \exp\left[-w^{2D_f/d_s}\right] dw = \frac{d_s}{2D_f}\gamma\left[\frac{d_s}{2D_f}, \frac{[1+x_D]^{2D_f/d_s}}{4\tau}\right] \quad \text{(C.24)}$$

Substituting Eqs. C.23 and C.24 in Eq. C.19:

$$p_{DBe}(x_D, t_{D,Be}) = \frac{4^{\nu}}{\Gamma[d_s/2]}\frac{d_s}{2D_f} \int_{0}^{t_{D,Be}} \tau^{\nu}\left[\gamma\left[\frac{d_s}{2D_f}, \frac{[1-x_D]^{2D_f/d_s}}{4\tau}\right] + \gamma\left[\frac{d_s}{2D_f}, \frac{[1+x_D]^{2D_f/d_s}}{4\tau}\right]\right] d\tau, \quad \text{(C.25)}$$

where:

$$\nu = -\left[\frac{d_s}{2}\right]\left[1-\frac{1}{D_f}\right] \quad \text{(C.26)}$$

Applying the distribution property to the integral on the right hand side of Eq. C.26 results in two definite integrals of the product of a power-law function and a lower incomplete gamma function. The integral for these types of functions is:

$$\int_0^t \tau^a \gamma[b, c\tau^{-1}]d\tau = \frac{t^{a+1}}{a+1}\gamma[b, c\tau^{-1}] - \int_0^t \frac{\tau^{a+1}}{a+1}\frac{\partial\gamma[b, c\tau^{-1}]}{\partial\tau}d\tau \,. \quad \text{(C.27)}$$

The derivative of the lower incomplete gamma function is obtained by using the Leibniz rule:

$$\frac{\partial\gamma[b, c\tau^{-1}]}{\partial\tau} = \frac{\partial}{\partial\tau}\int_0^{c\tau^{-1}} z^{b-1}\exp[-z]dz = -c^b\tau^{-b-1}\exp[-c\tau^{-1}]d\tau \,. \quad \text{(C.28)}$$

Substituting Eq. C.28 into Eq. C.27 and arraying results in:

$$\int_0^t \tau^a \gamma[b, c\tau^{-1}]d\tau = \frac{t^{a+1}}{a+1}\gamma[b, c\tau^{-1}] + \frac{c^b}{a+1}\int_0^t \tau^{a-b}\exp[-c\tau^{-1}]d\tau \,. \quad \text{(C.29)}$$

Using the change of variable:

$$u = c\tau^{-1}, \quad \text{(C.30)}$$

Eq. C.29 becomes:

$$\int_0^t \tau^a \gamma[b, c\tau^{-1}]d\tau = \frac{t^{a+1}}{a+1}\gamma[b, c\tau^{-1}] + \frac{c^{a+1}}{a+1}\int_{c/t}^{\infty} u^{b-a-2}\exp[-u]du \,. \quad \text{(C.31)}$$

Eq. C.32 can be written in terms of the upper incomplete gamma function as:

$$\int_0^t \tau^a \gamma[b, c\tau^{-1}]d\tau = \frac{t^{a+1}}{a+1}\gamma[b, c\tau^{-1}] + \frac{c^{a+1}}{a+1}\Gamma[b-a-1, c\tau^{-1}] \,. \quad \text{(C.33)}$$

Using Eq. C.30 in the first integral on the right hand side of Eq. C.26 results in:

$$\int_0^{t_{DBe}} \tau^\nu \gamma\left[\frac{d_s}{2D_f}, \frac{[1-x_D]^{2D_f/d_s}}{4}\frac{1}{\tau}\right]d\tau = \frac{t_{DBe}^{\nu+1}}{\nu+1}\gamma\left[\frac{d_s}{2D_f}, \frac{[1-x_D]^{2D_f/d_s}}{4t_{DBe}}\right] + \frac{1}{\nu+1}\left[\frac{[1-x_D]^{2D_f/d_s}}{4}\right]^{\nu+1}\Gamma\left[\frac{d_s}{2D_f} - \nu - 1, \frac{[1-x_D]^{2D_f/d_s}}{4t_{DBe}}\right] \,. \quad \text{(C.34)}$$

Similarly, the second integral:

$$\int_0^{t_{DBe}} \tau^{\nu}\gamma\left[\frac{d_s}{2D_f},\frac{[1+x_D]^{2D_f/d_s}}{4}\frac{1}{\tau}\right]d\tau = \frac{t_{DBe}^{\nu+1}}{\nu+1}\gamma\left[\frac{d_s}{2D_f},\frac{[1+x_D]^{2D_f/d_s}}{4t_{DBe}}\right]+ \frac{1}{\nu+1}\left[\frac{[1+x_D]^{2D_f/d_s}}{4}\right]^{\nu+1}\Gamma\left[\frac{d_s}{2D_f}-\nu-1,\frac{[1+x_D]^{2D_f/d_s}}{4t_{DBe}}\right] \quad \text{.....(C.35)}$$

Substituting Eqs. C.32 and C. 33 into Eq. C.25:

$$p_{DBe}(x_D,t_{DBe}) = \frac{4^{\nu}}{\Gamma[d_s/2]}\frac{d_s}{2D_f}\left[\frac{t_{DBe}^{\nu+1}}{\nu+1}\gamma\left[\frac{d_s}{2D_f},\frac{[1-x_D]^{2D_f/d_s}}{4t_{DBe}}\right]+ \frac{1}{\nu+1}\left[\frac{[1-x_D]^{2D_f/d_s}}{4}\right]^{\nu+1}\Gamma\left[\frac{d_s}{2D_f}-\nu-1,\frac{[1-x_D]^{2D_f/d_s}}{4t_{DBe}}\right]+\frac{t_{DBe}^{\nu+1}}{\nu+1}\gamma\left[\frac{d_s}{2D_f},\frac{[1+x_D]^{2D_f/d_s}}{4t_{DBe}}\right]+ \frac{1}{\nu+1}\left[\frac{[1+x_D]^{2D_f/d_s}}{4}\right]^{\nu+1}\Gamma\left[\frac{d_s}{2D_f}-\nu-1,\frac{[1+x_D]^{2D_f/d_s}}{4t_{DBe}}\right]\right] \quad \text{, ...(C.36)}$$

Substituting Eq. C.26 in Eq. C.36 and arraying results in the expression provided by Beier (1994):

$$p_{DBe}(x_D,t_{D,Be}) = C_1\left[\gamma\left[\frac{d_s}{2D_f},\frac{[1-x_D]^{2D_f/d_s}}{4t_{DBe}}\right]+\gamma\left[\frac{d_s}{2D_f},\frac{[1+x_D]^{2D_f/d_s}}{4t_{DBe}}\right]\right]+ C_2\left[[1+x_D]^{C_3}\Gamma\left[\frac{d_s}{2}-1,\frac{[1+x_D]^{2D_f/d_s}}{4t_{DBe}}\right]+[1-x_D]^{C_3}\Gamma\left[\frac{d_s}{2}-1,\frac{[1-x_D]^{2D_f/d_s}}{4t_{DBe}}\right]\right] \quad \text{,.....(C.37)}$$

where:

$$C_1 = \frac{2^{-d_s[1-1/D_f]}}{\Gamma[d_s/2]}\frac{d_s}{2D_f}\frac{t_{DBe}^{1-d_s[1-1/D_f]/2}}{[1-d_s[1-1/D_f]/2]}, \quad \text{.....(C.38)}$$

$$C_2 = \frac{d_s / D_f}{8[1 - d_s[1 - 1/D_f]/2]\Gamma[d_s/2]}, \quad \text{(C.39)}$$

and:

$$C_3 = 2D_f[1 - d_s[1 - 1/D_f]/2]/d_s \cdot \quad \text{(C.40)}$$

APPENDIX D

DERIVATION OF THE MODEL OF A HORIZONTAL WELL INTERCEPTING A SINGLE FINITE CONDUCTIVITY FRACTURE WITHIN A FRACTAL RESERVOIR

In this Appendix, we show the mathematical development of the models of a horizontal well intercepting a single finite conductivity fracture within a fractal reservoir considering either typical or anomalous diffusion.

D.1. Point Source Constant-Rate Solution of the Diffusivity Equation for a Fractal Reservoir with Typical Diffusion

Flow Model and Initial and Boundary Conditions

In this section, we show the procedure to obtain the particular solution of the diffusivity equation for an infinite fractal reservoir producing at a constant rate through a "point well." Consider the diffusivity equation for a fractal object presented by Chang *et al*. (1990):

$$\frac{1}{R^{D_f-1}}\frac{\partial}{\partial R}\left[R^{\beta}\frac{\partial p}{\partial R}\right]=\frac{\phi_0\mu c_t}{k_0}\frac{\partial p}{\partial t}, \quad \text{(D.1)}$$

where β is the spatial dimension and it is defined as $\beta = D_f - \theta - 1$. Assuming that the initial pressure is uniformly distributed along the reservoir, the initial condition is:

$$p(R,t=0)=p_i. \quad \text{(D.2)}$$

Considering constant-rate conditions, the inner boundary condition is:

$$\left[\frac{\partial p}{\partial R}\right]_{R=R_w} = \frac{\delta q_r B\mu}{\alpha_{D_f} b^{3-D_f} R_w^{\beta} k_0}. \quad \text{(D.3)}$$

For an infinite fractal reservoir, the outer boundary condition is defined as:

$$\lim_{R\to\infty} p(R,t) = p_i \quad \text{(D.4)}$$

Transformation to Dimensionless Variables

For the constant-rate case, the dimensionless pressure in the fractal reservoir is defined as:

$$p_{D,cr}(R_D, t_D) = \frac{2\pi k_0 h}{q_w B\mu L_r^{\theta}}[p_i - p(R,t)], \quad \text{(D.5)}$$

where L_r is the reference length. It must be changed for the radius of the fracture, r_f, in the case of the circular fracture or the half-length of the fracture, x_f, for a rectangular fracture. Dimensionless time is defined as:

$$t_D = \frac{k_0}{\phi_0 \mu c_t L_r^{2+\theta}} t \quad \text{(D.6)}$$

The dimensionless position in the fractal reservoir is defined by:

$$R_D = \frac{R}{L_r} \quad \text{(D.7)}$$

Using the chain rule, Eq. D.1 is transformed to dimensionless variables as:

$$\frac{1}{R_D^{D_f-1}} \frac{\partial}{\partial R_D}\left[R_D^{\beta} \frac{\partial p_{D,cr}}{\partial R_D}\right] = \frac{\partial p_{D,cr}}{\partial t_D} \quad \text{(D.8)}$$

Similarly, initial and boundary conditions become:

$$p_{D,cr}(R_D, t_D = 0) = 0 \qquad \text{(initial condition)}, \quad \text{(D.9)}$$

$$\left[\frac{\partial p_{D,cr}}{\partial R_D}\right]_{R_D = R_{wD}} = -\frac{\delta q_D h_D}{2R_{wD}^{\beta}} \qquad \text{(inner boundary condition)}, \quad \text{(D.10)}$$

$$\lim_{R_D \to \infty} p_{D,cr}(R_D, t_D) = 0 \qquad \text{(outer boundary condition)}, \quad \text{(D.11)}$$

The dimensionless parameters involved in Eq. D.10 are defined as follows. Dimensionless fractal reservoir rate:

$$\delta q_D = \frac{4\pi}{\alpha_{D_f}}\left[\frac{b}{L_r}\right]^{Df-3}\frac{\delta q_r}{q_w}. \quad \text{(D.12)}$$

Dimensionless height:

$$h_D = \frac{h}{L_r}. \quad \text{(D.13)}$$

Dimensionless fractal source radius:

$$R_{wD} = \frac{R_w}{L_r} \quad \text{(D.14)}$$

Constant-Rate Solution to the Diffusivity Equation for an Infinite Fractal Reservoir

As shown in Appendix B, the general solution in the Laplace domain of the diffusivity equation for a fractal reservoir is given by:

$$\bar{p}_{D,cr}(R_D, u) = R_D^{[1-\beta]/2}\left[C_1 K_v\left[R_D^{[\theta+2]/2}\frac{2\sqrt{u}}{\theta+2}\right] + C_2 I_v\left[R_D^{[\theta+2]/2}\frac{2\sqrt{u}}{\theta+2}\right]\right], \quad \text{(D.15)}$$

where v is a grouping parameter and it is defined as:

$$v = \frac{1-\beta}{\theta+2} \quad \text{.....(D.16)}$$

Applying the outer boundary condition to Eq. D.15, a bounded solution is obtained:

$$\bar{p}_{D,cr}(R_D,u) = C_1 R_D^{[1-\beta]/2} K_v\left[R_D^{[\theta+2]/2}\,\frac{2\sqrt{u}}{\theta+2}\right] \quad \text{.....(D.17)}$$

Applying the inner boundary condition to Eq. D.17, the value of the constant C_1 is obtained:

$$C_1 = \frac{\delta\bar{q}_D h_D}{2R_{wD}^{D_f/2}\sqrt{u}K_{1-v}\left[R_{wD}^{[\theta+2]/2}\,\frac{2\sqrt{u}}{\theta+2}\right]} \quad \text{.....(D.18)}$$

The particular solution for this model is obtained by substituting Eq. D.18 in Eq. D.17. It is given by:

$$\bar{p}_{D,cr}(R_D,u) = \frac{\delta\bar{q}_D h_D}{2R_{wD}^{D_f/2}}\,\frac{R_D^{[1-\beta]/2}K_v\left[R_D^{[\theta+2]/2}\,\frac{2\sqrt{u}}{\theta+2}\right]}{\sqrt{u}K_{1-v}\left[R_{wD}^{[\theta+2]/2}\,\frac{2\sqrt{u}}{\theta+2}\right]} \quad \text{.....(D.19)}$$

The point source solution is obtained by taking the limit to Eq. D.19 when R_{wD} tends to zero. This implies that the modified Bessel function in the denominator in Eq. D.19 can be approximated to a power-law function:

$$K_{1-v}\left[R_{wD}^{[\theta+2]/2}\,\frac{2\sqrt{u}}{\theta+2}\right] \approx \frac{\Gamma[1-v]}{2}\left[\frac{\theta+2}{R_{wD}^{[\theta+2]/2}\sqrt{u}}\right]^{1-v} \quad \text{.....(D.20)}$$

The following expression results after Substituting Eq. D.20 in Eq. D.19:

$$\bar{p}_{D,cr}(R_D,u)=\frac{\delta\bar{q}_D h_D R_D^{[1-\beta]/2}}{[\theta+2]\Gamma[1-v]}\left[\frac{\theta+2}{\sqrt{u}}\right]^{v} K_v\left[R_D^{[\theta+2]/2}\,\frac{2\sqrt{u}}{\theta+2}\right] \quad \text{.....(D.21)}$$

Extension to Double Porosity Reservoirs (*Valdes-Perez,* 2013)

It is well known that a solution with the shape of Eq. D.21 can be extended to models for double porosity reservoirs if the Laplace parameter u is replaced by $uf(u)$ where $f(u)$ is the interporosity transfer function. Hence, the following expression is obtained:

$$\bar{p}_{D,cr}(R_D,u)=\frac{\delta\bar{q}_D h_D R_D^{[1-\beta]/2}}{[\theta+2]\Gamma[1-v]}\left[\frac{\theta+2}{\sqrt{uf(u)}}\right]^{v} K_v\left[R_D^{[\theta+2]/2}\,\frac{2\sqrt{uf(u)}}{\theta+2}\right]. \quad \text{.....(D.22)}$$

In this model, the interporosity transfer function to be used is:

$$f(u)=\omega+\frac{[1-\omega]A_{fD}\bar{F}(\eta_{maD},h_{maD},u)}{1+\dfrac{h_{maD}^2 S_{\text{int}}}{\eta_{maD}}\bar{F}(\eta_{maD},h_{maD},u)}, \quad \text{.....(D.23)}$$

where the function $F(\eta_{maD},h_{maD},u)$ depends on the shape and properties of the matrix blocks (see Appendix E). The dimensionless hydraulic diffusivity of the matrix is defined as:

$$\eta_{maD}=\frac{k_{ma}[\phi c_t]_t L_r^{\theta}}{k_{fb}\phi_{ma}c_{tma}}. \quad \text{.....(D.24)}$$

The dimensionless size of the matrix blocks is:

$$h_{maD}=\frac{h_{ma}}{L_r}, \quad \text{.....(D.25)}$$

the storativity ratio is:

$$\omega = \frac{\phi_{0fb} c_{tfb}}{\phi_{0fb} c_{tfb} + \phi_{ma} c_{tma}}, \quad \text{(D.26)}$$

and the interporosity skin is:

$$S_{\text{int}} = \frac{k_{ma} l_d}{k_d h_{ma}}. \quad \text{(D.27)}$$

For matrix blocks with the shape of slabs, the transfer function is:

$$\bar{F}(\eta_{maD}, h_{maD}, u) = \frac{1}{h_{maD}} \sqrt{\frac{\eta_{maD}}{u}} \tanh\left[\frac{h_{maD}}{2} \sqrt{\frac{u}{\eta_{maD}}}\right], \quad \text{(D.28)}$$

whereas for matrix blocks with the shape of spheres, the transfer function is:

$$\bar{F}(\eta_{maD}, h_{maD}, u) = \frac{1}{h_{maD}} \sqrt{\frac{\eta_{maD}}{u}} \left[\coth\left[\frac{h_{maD}}{2} \sqrt{\frac{u}{\eta_{maD}}}\right] - \frac{2}{h_{maD}} \sqrt{\frac{\eta_{maD}}{u}}\right] \quad \text{(D.29)}$$

D.2. Point Source Constant-Rate Solution of the Diffusivity Equation for a Fractal Reservoir with Anomalous Diffusion

The diffusivity equation for fractal reservoir with anomalous diffusion expressed in dimensionless variables was presented by Camacho-Velazquez *et al.* (2008). The model is given by:

$$\frac{1}{R_D^{D_f - 1}} \frac{\partial}{\partial R_D} \left[R_D^{\beta} \frac{\partial p_{D,cr}}{\partial R_D}\right] = \frac{\partial^{\gamma} p_{D,cr}}{\partial t_D^{\gamma}}. \quad \text{(D.30)}$$

Where γ is the fractional derivative order and it is a function of the conductivity index. Such a function is defined as:

$$\gamma = \frac{2}{2+\theta} \quad \text{(D.31)}$$

The time fraction derivative of order γ in Eq. D.30 is defined as:

$$\frac{\partial^{\gamma} p_{D,cr}}{\partial t_D^{\gamma}} = \frac{1}{\Gamma[1-\gamma]} \frac{\partial}{\partial t_D} \int_0^{t_D} [t_D - \tau]^{-\gamma} p_{D,cr}(R_D, \tau) d\tau \quad \text{(D.32)}$$

Analogous to the case presented in the previous section, the initial and boundary condition for Eq. D.22 are defined by Eq. D.9 though D.11. The procedure to solve Eq. D.30 is similar to the one shown in Appendix B and in section D.1. Then, applying the Laplace transform to Eq. D.30:

$$\frac{1}{R_D^{D_f - 1}} \frac{\partial}{\partial R_D} \left[R_D^{\beta} \frac{\partial \bar{p}_{D,cr}}{\partial R_D} \right] = u^{\gamma} \bar{p}_{D,cr} \quad \text{(D.33)}$$

To find the general solution for this case, the transformation variable to be used is:

$$z = \frac{2}{\theta+2} \left[u^{\gamma} R_D^{[\theta+2]} \right]^{1/2} \quad \text{(D.34)}$$

Using the transformation variable defined in Eq. D.34 and the procedure shown in Appendix B, the general solution for this model is given by:

$$\bar{p}_{D,cr}(R_D, u) = R_D^{[1-\beta]/2} \left[C_1 K_v \left[R_D^{[\theta+2]/2} \frac{2u^{\gamma/2}}{\theta+2} \right] + C_2 I_v \left[R_D^{[\theta+2]/2} \frac{2u^{\gamma/2}}{\theta+2} \right] \right], \quad \text{(D.35)}$$

Applying the outer boundary condition, the resulting bounded solution is:

$$\bar{p}_{D,cr}(R_D, u) = C_1 R_D^{[1-\beta]/2} K_v \left[R_D^{[\theta+2]/2} \frac{2u^{\gamma/2}}{\theta+2} \right], \quad \text{(D.36)}$$

The value of the constant C_1 is obtained by applying the inner boundary condition to Eq. D.36:

$$C_1 = \frac{\delta \overline{q}_D h_D}{2R_{wD}^{D_f/2} u^{\gamma/2} K_{1-v}\left[R_{wD}^{[\theta+2]/2}\,\frac{2u^{\gamma/2}}{\theta+2}\right]} \quad \text{.....(D.37)}$$

Then, the particular solution for this model is:

$$\overline{p}_{D,cr}(R_D,u) = \frac{\delta \overline{q}_D h_D R_D^{[1-\beta]/2}}{2R_{wD}^{D_f/2} u^{\gamma/2}} \frac{K_v\left[R_D^{[\theta+2]/2}\,\frac{2u^{\gamma/2}}{\theta+2}\right]}{K_{1-v}\left[R_{wD}^{[\theta+2]/2}\,\frac{2u^{\gamma/2}}{\theta+2}\right]} \quad \text{.....(D.38)}$$

For this case, the point source solution is given by:

$$\overline{p}_{D,cr}(R_D,u) = \frac{\delta \overline{q}_D h_D R_D^{[1-\beta]/2}}{[\theta+2]\Gamma[1-v]}\left[\frac{\theta+2}{u^{\gamma/2}}\right]^v K_v\left[R_D^{[\theta+2]/2}\,\frac{2u^{\gamma/2}}{\theta+2}\right] \quad \text{.....(D.39)}$$

To consider double porosity conditions, Eq. D.22 should be used considering the following transfer function, $f(u)$:

$$f(u) = \omega u^{\gamma-1} + \frac{[1-\omega]A_{fD}\overline{F}(\eta_{maD},h_{maD},u)}{1+\frac{h_{maD}^2 S_{\text{int}}}{\eta_{maD}}\overline{F}(\eta_{maD},h_{maD},u)} \quad \text{.....(D.40)}$$

D.3. Constant-Rate Solution for the Model of a Horizontal Well Intercepting a Circular Transverse Finite Conductivity Fracture within a Fractal Reservoir

This model considers radial flow within a hydraulic fracture as previously presented by Larsen *et al.* (1991). The flow within the circular fracture obeys the diffusivity equation developed in Appendix C and given by:

$$\frac{1}{r}\frac{\partial}{\partial r}\left[r\frac{\partial p_f}{\partial r}\right]+\frac{2k}{wk_f}\left[\frac{\partial p}{\partial z}\right]_{z=0}=\frac{\phi_f \mu c_{tf}}{k_f}\frac{\partial p_f}{\partial t}. \quad \text{(D.41)}$$

Considering that the initial pressure is uniformly distributed along the hydraulic fracture, the initial condition is:

$$p_f(r,t=0)=p_i. \quad \text{(D.42)}$$

For a well intercepting a hydraulic fracture producing at a constant rate, the inner boundary condition is:

$$\left[r\frac{\partial p_f}{\partial r}\right]_{r=r_w}=\frac{q_w B\mu}{2\pi k_f w} \quad \text{(D.43)}$$

For an closed hydraulic fracture, the outer boundary condition is defined as:

$$\left[\frac{\partial p_f}{\partial r}\right]_{r=r_f}=0 \quad \text{(D.44)}$$

Similar to the reservoir model shown in section D.1, the dimensionless pressure in the circular hydraulic fracture is defined as:

$$p_{fD,cr}(r_D,t_D)=\frac{2\pi k_0 h}{q_w B\mu r_f^{\theta}}[p_i-p_f(r,t)], \quad \text{(D.45)}$$

Dimensionless time is defined by Eq. D.6 and the dimensionless radius of the circular hydraulic fracture is:

$$r_D=\frac{r}{r_f}, \quad \text{(D.46)}$$

and the dimensionless position in the *z*-direction is:

$$z_D = \frac{z}{r_f}, \quad \text{(D.47)}$$

Transforming Eq. D.41 to dimensionless variables, it becomes:

$$\frac{1}{r_D}\frac{\partial}{\partial r_D}\left[r_D \frac{\partial p_{fD,cr}}{\partial r_D}\right] + \frac{2}{F_{cD}}\left[\frac{\partial p_{D,cr}}{\partial z_D}\right]_{z_D=0} = \frac{1}{\eta_{fD}}\frac{\partial p_{fD,cr}}{\partial t_D}, \quad \text{(D.48)}$$

where dimensionless fracture conductivity is:

$$F_{cD} = \frac{k_f w}{k r_f}, \quad \text{(D.49)}$$

and the dimensionless fractal hydraulic diffusivity of the circular fracture is:

$$\eta_{fD} = \frac{\phi_0 c_t k_f r_f^{\theta}}{\phi_f c_{tf} k_0}. \quad \text{(D.50)}$$

Similarly, initial and boundary conditions become:

$$p_{fD,cr}(r_D, t_D = 0) = 0 \qquad \text{(initial condition)}, \quad \text{(D.51)}$$

$$\left[r_D \frac{\partial p_{fD,cr}}{\partial r_D}\right]_{r_D = r_{wD}} = -\frac{1}{F_{fhcD}} \qquad \text{(inner boundary condition)}, \quad \text{(D.52)}$$

$$\left[\frac{\partial p_{fD,cr}}{\partial r_D}\right]_{r_D = 1} = 0 \qquad \text{(outer boundary condition)}, \quad \text{(D.53)}$$

where dimensionless fracture fractal conductivity is:

$$F_{fhcD} = \frac{k_f w r_f^{\theta}}{kh}, \quad \text{(D.54)}$$

Analogous to the approach made by Larsen *et al.* (1991), the circular fracture should be discretized into sufficiently small segments so the pressure gradient in Eq. D.48 can be approximated as:

$$\left[\frac{\partial p_{D,cr}}{\partial z_D}\right]_{z_D=0} \approx -\pi \delta q_{Dj} h_D . \quad \text{(D.55)}$$

Then, Eq. D.48 becomes:

$$\frac{1}{r_D}\frac{\partial}{\partial r_D}\left[r_D \frac{\partial p_{fD,cr}}{\partial r_D}\right] - \frac{2\pi h_D}{F_{cD}} \delta q_{Dj} = \frac{1}{\eta_{fD}} \frac{\partial p_{fD,cr}}{\partial t_D} . \quad \text{(D.56)}$$

Following the procedure presented in Appendix A, the general solution to Eq. D.56 in the Laplace domain of a *j*-segment of the discretized circular hydraulic fracture is:

$$\bar{p}_{fD,cr} = A_j K_0\left[r_D \sqrt{\frac{u}{\eta_{fD}}}\right] + B_j I_0\left[r_D \sqrt{\frac{u}{\eta_{fD}}}\right] - \frac{2\pi h_D \eta_{fD}}{u F_{cD}} \delta \bar{q}_{Dj} . \quad \text{(D.57)}$$

This discretization generates a system of equations with 3*N* unknowns. Therefore, it is necessary to define 3*N* equations to solve such a system.

Two out of the 3*N* equations of the system are obtained by applying the boundary conditions to the corresponding segment. The first equation is defined by applying the inner boundary condition to segment one. The resulting expression is:

$$A_1 K_1\left[r_{wD} \sqrt{\frac{u}{\eta_{fD}}}\right] - B_1 I_1\left[r_{wD} \sqrt{\frac{u}{\eta_{fD}}}\right] = \frac{\sqrt{\eta_{fD}}}{F_{fhcD} r_{wD} u^{3/2}} . \quad \text{(D.58)}$$

The second equation is obtained by applying the outer boundary condition to segment *N*. The resulting equation is:

$$A_N K_1\left[r_D\sqrt{\frac{u}{\eta_{fD}}}\right]-B_N I_1\left[r_D\sqrt{\frac{u}{\eta_{fD}}}\right]=0 \quad \text{.....(D.59)}$$

N-1 equations are defined by establishing pressure continuity between each one of the segments. This is obtained by equating the pressure of a segment *j* with the pressure of the adjacent segment *j*-1, both evaluated at the interface *j*-1:

$$\begin{aligned} A_{j-1}K_0\left[r_{Dj-1}\sqrt{\frac{u}{\eta_{fD}}}\right]+B_{j-1}I_0\left[r_{Dj-1}\sqrt{\frac{u}{\eta_{fD}}}\right]-\frac{2\pi h_D\eta_{fD}}{uF_{cD}}\delta\bar{q}_{Dj-1} = \\ A_jK_0\left[r_{Dj}\sqrt{\frac{u}{\eta_{fD}}}\right]+B_jI_0\left[r_{Dj}\sqrt{\frac{u}{\eta_{fD}}}\right]-\frac{2\pi h_D\eta_{fD}}{uF_{cD}}\delta\bar{q}_{Dj} \end{aligned} \quad \text{.....(D.60)}$$

Similarly, *N*-1 more equations are defined by establishing rate continuity between each one of the segments. Then, for this case:

$$A_{j-1}K_1\left[r_{Dj-1}\sqrt{\frac{u}{\eta_{fD}}}\right]-B_{j-1}I_1\left[r_{Dj-1}\sqrt{\frac{u}{\eta_{fD}}}\right]=A_{j-1}K_1\left[r_{Dj-1}\sqrt{\frac{u}{\eta_{fD}}}\right]-B_jI_1\left[r_{Dj-1}\sqrt{\frac{u}{\eta_{fD}}}\right] \quad \text{.....(D.61)}$$

To complete the system of equations, it is necessary to establish pressure continuity between the segments of the circular fracture and the fractal reservoir. First, the flow from the fractal reservoir to the circular fracture must be integrated over the area of the circular segment:

$$\bar{p}_{D,cr}(R_D,u)=\frac{\delta\bar{q}_D h_D}{[\theta+2]\Gamma[1-\nu]}G_F(r^*_{Dj},r_{Di},u) \quad \text{.....(D.62)}$$

Then, defining the observations points at the midpoint of each one of the *N*-segments of the discretized fracture, the dimensionless pressure of the circular fracture and dimensionless pressure of the fractal reservoir should be equated. The following expression is obtained:

$$A_j K_0\left[r_{Dj}\sqrt{\frac{u}{\eta_{fD}}}\right]+B_j I_0\left[r_{Dj}\sqrt{\frac{u}{\eta_{fD}}}\right]-\frac{2\pi h_D \eta_{fD}}{uF_{cD}}\delta\bar{q}_{Dj}= \frac{h_D}{[\theta+2]\Gamma[1-\nu]}\sum_{i=1}^{N}\delta\bar{q}_{Di}[G_F(r^*_{Dj},r_{Di-1},u)-G_F(r^*_{Dj},r_{Di-1},u)] \quad \ldots(D.63)$$

The function G_F for a fractal reservoir with <u>typical diffusion</u> is:

$$G_F(r^*_{Dj},r_{Di},u)=\left[\frac{\theta+2}{\sqrt{u}}\right]^{\nu}\int_{r_D}\frac{r_D}{R_D^{[\beta-1]/2}}\cos^{-1}\left[\frac{(r^*_{Dj})^2-r_{Dj}^2+r_D}{2r^*_{Dj}r_D}\right]K_\nu\left[R_D^{[\theta+2]/2}\frac{2\sqrt{u}}{\theta+2}\right]dr_D \quad \ldots\ldots\ldots\ldots(D.64)$$

For a fractal reservoir with <u>anomalous diffusion</u> is:

$$G_F(r^*_{Dj},r_{Di},u)=\left[\frac{\theta+2}{u^{\gamma/2}}\right]^{\nu}\int_{r_D}\frac{r_D}{R_D^{[\beta-1]/2}}\cos^{-1}\left[\frac{(r^*_{Dj})^2-r_{Dj}^2+r_D}{2r^*_{Dj}r_D}\right]K_\nu\left[R_D^{[\theta+2]/2}\frac{2u^{\gamma/2}}{\theta+2}\right]dr_D \ldots\ldots\ldots(D.65)$$

For double porosity reservoirs:

$$G_F(r^*_{Dj},r_{Di},u)=\left[\frac{\theta+2}{\sqrt{uf(u)}}\right]^{\nu}\int_{r_D}\frac{r_D}{R_D^{[\beta-1]/2}}\cos^{-1}\left[\frac{(r^*_{Dj})^2-r_{Dj}^2+r_D}{2r^*_{Dj}r_D}\right]K_\nu\left[R_D^{[\theta+2]/2}\frac{2\sqrt{uf(u)}}{\theta+2}\right]dr_D \ldots.(D.66)$$

For all cases:

$$R_D=\sqrt{r_D^2+z_{0D}^2} \quad \ldots\ldots\ldots\ldots(D.67)$$

Similar to the model developed by Larsen *et al.* (1991), the integrals involved in Eq. D.64 through D.66 must be performed numerically. For this case, we have used the adaptative quadrature

method (*MATLAB*'s *integral*-function). Besides, the cases when the observation point is greater or less than the upper integration limit should also be taken into account. Therefore, if the observation point is greater than the upper integration limit, the following expression for a fractal reservoir with typical diffusion should be used:

$$G_F(r_{Dj}^*, r_{Di}, u) = \left[\frac{\theta+2}{\sqrt{u}}\right]^v \int_{r_{Dj}^*-r_{Dk}}^{r_{Dj}^*+r_{Dk}} \frac{r_D}{R_D^{[\beta-1]/2}} \cos^{-1}\left[\frac{(r_{Dj}^*)^2 - r_{Dj}^2 + r_D}{2r_{Dj}^* r_D}\right] K_v\left[R_D^{[\theta+2]/2}\,\frac{2\sqrt{u}}{\theta+2}\right] dr_D \quad \text{....(D.68)}$$

For a fractal reservoir with anomalous diffusion:

$$G_F(r_{Dj}^*, r_{Di}, u) = \left[\frac{\theta+2}{u^{\gamma/2}}\right]^v \int_{r_{Dj}^*-r_{Dk}}^{r_{Dj}^*+r_{Dk}} \frac{r_D}{R_D^{[\beta-1]/2}} \cos^{-1}\left[\frac{(r_{Dj}^*)^2 - r_{Dj}^2 + r_D}{2r_{Dj}^* r_D}\right] K_v\left[R_D^{[\theta+2]/2}\,\frac{2u^{\gamma/2}}{\theta+2}\right] dr_D \quad \text{...(D.69)}$$

For double porosity reservoirs:

$$G_F(r_{Dj}^*, r_{Di}, u) = \left[\frac{\theta+2}{\sqrt{uf(u)}}\right]^v \int_{r_{Dj}^*-r_{Dk}}^{r_{Dj}^*+r_{Dk}} \frac{r_D}{R_D^{[\beta-1]/2}} \cos^{-1}\left[\frac{(r_{Dj}^*)^2 - r_{Dj}^2 + r_D}{2r_{Dj}^* r_D}\right] K_v\left[R_D^{[\theta+2]/2}\,\frac{2\sqrt{uf(u)}}{\theta+2}\right] dr_D \quad \text{.....(D.70)}$$

If the observation point is smaller than the upper integration limit, the following expression for a fractal reservoir with typical diffusion should be used:

$$G_F(r_{Dj}^*, r_{Di}, u) = \left[\frac{\theta+2}{\sqrt{u}}\right]^v \pi \int_{R_{D\min}}^{R_{Dmid}} R_D^{[3-\beta]/2} K_v\left[R_D^{[\theta+2]/2}\,\frac{2\sqrt{u}}{\theta+2}\right] dR_D + \left[\frac{\theta+2}{\sqrt{u}}\right]^v \int_{R_{Dmid}}^{R_{D\max}} R_D^{[3-\beta]/2} \cos^{-1}\left[\frac{(r_{Dj}^*)^2 - r_{Dj}^2 + R_D^2 - z_{0D}^2}{2r_{Dj}^* \sqrt{R_D^2 - z_{0D}^2}}\right] K_v\left[R_D^{[\theta+2]/2}\,\frac{2\sqrt{u}}{\theta+2}\right] dR_D \quad \text{....(D.71)}$$

For a fractal reservoir with anomalous diffusion:

$$G_F(r_{Dj}^*, r_{Di}, u) = \left[\frac{\theta+2}{u^{\gamma/2}}\right]^v \pi \int_{R_{D\min}}^{R_{Dmid}} R_D^{[3-\beta]/2} K_v\left[R_D^{[\theta+2]/2}\,\frac{2u^{\gamma/2}}{\theta+2}\right] dR_D + \left[\frac{\theta+2}{u^{\gamma/2}}\right]^v \int_{R_{Dmid}}^{R_{D\max}} R_D^{[3-\beta]/2} \cos^{-1}\left[\frac{(r_{Dj}^*)^2 - r_{Dj}^2 + R_D^2 - z_{0D}^2}{2r_{Dj}^* \sqrt{R_D^2 - z_{0D}^2}}\right] K_v\left[R_D^{[\theta+2]/2}\,\frac{2u^{\gamma/2}}{\theta+2}\right] dR_D \quad \text{.(D.72)}$$

For double porosity reservoirs:

$$G_F(r_{Dj}^*, r_{Di}, u) = \left[\frac{\theta+2}{\sqrt{uf(u)}}\right]^v \pi \int_{R_{D\min}}^{R_{Dmid}} R_D^{[3-\beta]/2} K_v\left[R_D^{[\theta+2]/2}\,\frac{2\sqrt{uf(u)}}{\theta+2}\right] dR_D + \left[\frac{\theta+2}{\sqrt{uf(u)}}\right]^v \int_{R_{Dmid}}^{R_{D\max}} R_D^{[3-\beta]/2} \cos^{-1}\left[\frac{(r_{Dj}^*)^2 - r_{Dj}^2 + R_D^2 - z_{0D}^2}{2r_{Dj}^* \sqrt{R_D^2 - z_{0D}^2}}\right] K_v\left[R_D^{[\theta+2]/2}\,\frac{2\sqrt{uf(u)}}{\theta+2}\right] dR_D \quad \text{...(D.73)}$$

Where:

$$R_{D\min} = \sqrt{r_{D\min}^2 + z_{0D}^2}\,, \quad \text{.....(D.74)}$$

$$R_{Dmid} = \sqrt{[r_{Dk} - r_{Dj}^*]^2 + z_{0D}^2}\,, \quad \text{.....(D.75)}$$

and:

$$R_{D\max} = \sqrt{r_{Dk}^2 + z_{0D}^2}\,. \quad \text{.....(D.76)}$$

D.4. Constant-Rate Solution for the Model of a Horizontal Well Intercepting a Circular Transverse Finite Conductivity Fracture within a Fractal Reservoir

The flow within the rectangular fracture is governed by the diffusivity equation for linear flow with a source term. It is given by:

$$\frac{\partial^2 p_f}{\partial x^2}+\frac{2k}{k_f w}\left[\frac{\partial p}{\partial z}\right]_{z=0}=\frac{\phi_f \mu c_{tf}}{k_f}\frac{\partial p_f}{\partial t}. \quad \text{.....(D.77)}$$

Analogous to the circular fracture case, the initial and boundary conditions for the present case are:

$$p_f(x,t=0)=p_i \qquad \text{(initial condition), ...(D.78)}$$

$$\left[\frac{\partial p_f}{\partial x}\right]_{x=0}=\frac{q_w B\mu}{4k_f y_f w} \qquad \text{(inner boundary condition), ...(D.79)}$$

$$\left[\frac{\partial p_f}{\partial x}\right]_{x=x_f}=0 \qquad \text{(outer boundary condition). .....(D.80)}$$

For the rectangular hydraulic fracture case, the dimensionless pressure in the fracture is:

$$p_{fD,cr}(x_D,t_D)=\frac{2\pi k_0 h}{q_w B\mu x_f^{\theta}}[p_i-p_f(x,t)]. \quad \text{.....(D.81)}$$

The dimensionless time is defined by Eq. D.6 and the dimensionless position in the *x*-direction is:

$$x_D=\frac{x}{x_f} \quad \text{.....(D.82)}$$

The dimensionless position in the *z*-direction is:

$$z_D=\frac{z}{x_f} \quad \text{.....(D.83)}$$

Transforming Eq. D.77 to dimensionless variables, it becomes:

$$\frac{\partial^2 p_{fD,cr}}{\partial x_D^2}+\frac{2}{F_{cD}}\left[\frac{\partial p_{D,cr}}{\partial z_D}\right]_{z_D=0}=\frac{1}{\eta_{fD}}\frac{\partial p_{fD,cr}}{\partial t_D}, \quad \text{(D.84)}$$

where dimensionless fracture conductivity is:

$$F_{cD}=\frac{k_f w}{k x_f}, \quad \text{(D.85)}$$

and the dimensionless fractal hydraulic diffusivity of the rectangular fracture is:

$$\eta_{fD}=\frac{\phi_0 c_t k_f x_f^{\theta}}{\phi_f c_{tf} k_0}. \quad \text{(D.86)}$$

Similarly, initial and boundary conditions become:

$$p_{fD,cr}(x_D, t_D=0)=0 \qquad \text{(initial condition)}, \quad \text{(D.87)}$$

$$\left[\frac{\partial p_{fD,cr}}{\partial x_D}\right]_{r_D=r_{wD}}=-\frac{\pi}{2F_{fhcD}y_{fD}} \qquad \text{(inner boundary condition)}, \quad \text{(D.88)}$$

$$\left[\frac{\partial p_{fD,cr}}{\partial x_D}\right]_{x_D=1}=0 \qquad \text{(outer boundary condition)}. \quad \text{(D.89)}$$

Where the dimensionless fracture fractal conductivity is:

$$F_{fhcD}=\frac{k_f w x_f^{\theta}}{kh}, \quad \text{(D.90)}$$

and the dimensionless fracture length along the wellbore is:

$$y_{fD} = \frac{y_f}{x_f}, \quad \text{(D.91)}$$

For this case, the discretization of the rectangular fracture into sufficiently small segments permits the approximation of the pressure gradient in Eq. D.84 by using Eq. D.55. Consequently, Eq. D.84 becomes:

$$\frac{\partial^2 p_{fD,cr}}{\partial x_D^2} - \frac{2\pi h_D}{F_{cD}} \delta q_{Dj} = \frac{1}{\eta_{fD}} \frac{\partial p_{fD,cr}}{\partial t_D}. \quad \text{(D.92)}$$

Following the procedure presented in Appendix A, the general solution to Eq. D.92 in the Laplace domain of a *j*-segment of the discretized rectangular hydraulic fracture is:

$$\bar{p}_{fD,cr} = A_j \exp\left[-x_D \sqrt{\frac{u}{\eta_{fD}}}\right] + B_j \exp\left[x_D \sqrt{\frac{u}{\eta_{fD}}}\right] - \frac{2\pi h_D \eta_{fD}}{u F_{cD}} \delta \bar{q}_{Dj}. \quad \text{(D.93)}$$

Analogous to the circular fracture case, the first equation to establish the system of *3N* equations results from applying the inner boundary condition to segment one. The resulting expression is:

$$A_1 - B_1 = \frac{\pi \sqrt{\eta_{fD}}}{2 F_{fhcD} y_{fD} u^{3/2}} \quad \text{(D.94)}$$

The second equation is obtained by applying the outer boundary condition to segment *N*. The resulting equation is:

$$A_N \exp\left[-\sqrt{\frac{u}{\eta_{fD}}}\right] - B_N \exp\left[\sqrt{\frac{u}{\eta_{fD}}}\right] = 0. \quad \text{(D.95)}$$

The pressure continuity between each one of the segments is obtained by equating the pressure of a segment *j* with the pressure of the adjacent segment *j*-1, both evaluated at the interface *j*-1:

$$A_{j-1}\exp\left[-x_{Dj-1}\sqrt{\frac{u}{\eta_{fD}}}\right]+B_{j-1}\exp\left[x_{Dj-1}\sqrt{\frac{u}{\eta_{fD}}}\right]-\frac{2\pi h_D\eta_{fD}}{uF_{cD}}\delta\bar{q}_{Dj-1}= A_j\exp\left[-x_{Dj-1}\sqrt{\frac{u}{\eta_{fD}}}\right]+B_j\exp\left[x_{Dj-1}\sqrt{\frac{u}{\eta_{fD}}}\right]-\frac{2\pi h_D\eta_{fD}}{uF_{cD}}\delta\bar{q}_{Dj} \quad \text{.....(D.96)}$$

Similarly, the rate continuity between each one of the segments is defined by:

$$-A_{j-1}\exp\left[-x_{Dj-1}\sqrt{\frac{u}{\eta_{fD}}}\right]+B_{j-1}I_1\left[x_{Dj-1}\sqrt{\frac{u}{\eta_{fD}}}\right]= -A_j\exp\left[x_{Dj-1}\sqrt{\frac{u}{\eta_{fD}}}\right]-B_j\exp\left[r_{Dj-1}\sqrt{\frac{u}{\eta_{fD}}}\right] \quad \text{.....(D.97)}$$

The pressure continuity between each one of the segments of the hydraulic fracture and the fractal reservoir is obtained by equating the pressure of a segment *j* with the pressure of the fractal reservoir, superimposed over the area of the segment *j*:

$$A_j\exp\left[-x_D^*\sqrt{\frac{u}{\eta_{fD}}}\right]+B_j\exp\left[x_D^*\sqrt{\frac{u}{\eta_{fD}}}\right]-\frac{2\pi h_D\eta_{fD}}{uF_{cD}}\delta\bar{q}_{Dj}=\frac{h_D}{[\theta+2]\Gamma[1-v]} \quad \text{.....(D.98)}$$

$$\sum_{i=1}^{N}\delta\bar{q}_{Di}[Z_F(x_{Dj}^*,y_{Dj}^*,x_{Dj-1},y_{Dj-1},x_{Dj},y_{Dj},u)+Z_F(x_{Dj}^*,y_{Dj}^*,-x_{Dj},y_{Dj-1},-x_{Dj-1},y_{Dj},u)]$$

The function Z_F for a fractal reservoir with typical diffusion is:

$$Z_F(x^*_{Dk}, y^*_{Dk}, x_{1D}, y_{1D}, x_{2D}, y_{2D}, u) =$$

$$\left[\frac{\theta+2}{\sqrt{u}}\right]^v \int_{r_{D1}}^{r_{D2}} \frac{r_D[\vartheta_{\max,I} - \vartheta_{\min,I}]}{R_D^{[\beta-1]/2}} K_v\left[R_D^{[\theta+2]/2}\ \frac{2\sqrt{u}}{\theta+2}\right] dr_D +$$

$$\left[\frac{\theta+2}{\sqrt{u}}\right]^v \int_{r_{D2}}^{r_{D3}} \frac{r_D[\vartheta_{\max,II} - \vartheta_{\min,II}]}{R_D^{[\beta-1]/2}} K_v\left[R_D^{[\theta+2]/2}\ \frac{2\sqrt{u}}{\theta+2}\right] dr_D + \quad \text{.....(D.99)}$$

$$\left[\frac{\theta+2}{\sqrt{u}}\right]^v \int_{r_{D3}}^{r_{D4}} \frac{r_D[\vartheta_{\max,III} - \vartheta_{\min,III}]}{R_D^{[\beta-1]/2}} K_v\left[R_D^{[\theta+2]/2}\ \frac{2\sqrt{u}}{\theta+2}\right] dr_D$$

For a fractal reservoir with <u>anomalous diffusion</u>, the function is:

$$Z_F(x^*_{Dk}, y^*_{Dk}, x_{1D}, y_{1D}, x_{2D}, y_{2D}, u) =$$

$$\left[\frac{\theta+2}{u^{\gamma/2}}\right]^v \int_{r_{D1}}^{r_{D2}} \frac{r_D[\vartheta_{\max,I} - \vartheta_{\min,I}]}{R_D^{[\beta-1]/2}} K_v\left[R_D^{[\theta+2]/2}\ \frac{2u^{\gamma/2}}{\theta+2}\right] dr_D +$$

$$\left[\frac{\theta+2}{u^{\gamma/2}}\right]^v \int_{r_{D2}}^{r_{D3}} \frac{r_D[\vartheta_{\max,II} - \vartheta_{\min,II}]}{R_D^{[\beta-1]/2}} K_v\left[R_D^{[\theta+2]/2}\ \frac{2u^{\gamma/2}}{\theta+2}\right] dr_D + \quad \text{.....(D.100)}$$

$$\left[\frac{\theta+2}{u^{\gamma/2}}\right]^v \int_{r_{D3}}^{r_{D4}} \frac{r_D[\vartheta_{\max,III} - \vartheta_{\min,III}]}{R_D^{[\beta-1]/2}} K_v\left[R_D^{[\theta+2]/2}\ \frac{2u^{\gamma/2}}{\theta+2}\right] dr_D$$

For double porosity reservoirs:

$$Z_F(x^*_{Dk}, y^*_{Dk}, x_{1D}, y_{1D}, x_{2D}, y_{2D}, u) =$$

$$\left[\frac{\theta+2}{\sqrt{uf(u)}}\right]^v \int_{r_{D1}}^{r_{D2}} \frac{r_D[\vartheta_{\max,I} - \vartheta_{\min,I}]}{R_D^{[\beta-1]/2}} K_v\left[R_D^{[\theta+2]/2}\ \frac{2\sqrt{uf(u)}}{\theta+2}\right] dr_D +$$

$$\left[\frac{\theta+2}{\sqrt{uf(u)}}\right]^v \int_{r_{D2}}^{r_{D3}} \frac{r_D[\vartheta_{\max,II} - \vartheta_{\min,II}]}{R_D^{[\beta-1]/2}} K_v\left[R_D^{[\theta+2]/2}\ \frac{2\sqrt{uf(u)}}{\theta+2}\right] dr_D + \quad \text{....(D.101)}$$

$$\left[\frac{\theta+2}{\sqrt{uf(u)}}\right]^v \int_{r_{D3}}^{r_{D4}} \frac{r_D[\vartheta_{\max,III} - \vartheta_{\min,III}]}{R_D^{[\beta-1]/2}} K_v\left[R_D^{[\theta+2]/2}\ \frac{2\sqrt{uf(u)}}{\theta+2}\right] dr_D$$

For all cases:

$$\vartheta_{\min,I} = \sin^{-1}\left[\frac{y_{1D}}{r_D}\right], \quad \text{(D.102)}$$

$$\vartheta_{\max,I} = \cos^{-1}\left[\frac{x_{1D}}{r_D}\right], \quad \text{(D.103)}$$

$$\vartheta_{\min,II} = \cos^{-1}\left[\frac{x_{2D}}{r_D}\right], \quad \text{(D.104)}$$

$$\vartheta_{\max,II} = \cos^{-1}\left[\frac{x_{1D}}{r_D}\right], \quad \text{(D.105)}$$

$$\vartheta_{\min,III} = \cos^{-1}\left[\frac{x_{2D}}{r_D}\right], \quad \text{(D.106)}$$

$$\vartheta_{\max,III} = \sin^{-1}\left[\frac{y_{2D}}{r_D}\right], \quad \text{(D.107)}$$

and:

$$r_{D1} = \sqrt{x_{1D}^2 + y_{1D}^2}, \quad \text{(D.108)}$$

$$r_{D2} = \sqrt{x_{2D}^2 + y_{1D}^2}, \quad \text{(D.109)}$$

$$r_{D3} = \sqrt{x_{1D}^2 + y_{2D}^2}, \quad \text{(D.110)}$$

$$r_{D4} = \sqrt{x_{2D}^2 + y_{2D}^2}, \quad \text{(D.111)}$$

The same considerations of symmetry and change of variables shown in Appendix A for the calculation of Z_R must be made for Z_F.

APPENDIX E

TRANSIENT INTERPOROSITY TRANSFER FUNCTIONS

In this Appendix, we present the derivation of the classic transient interporosity transfer functions developed by de Swaan (1976) and their application in the double porosity flow model presented by Cinco-Ley *et al*. (1982). In addition, we show the development of the transient interporosity transfer function considering fractal matrix blocks and the derivation of the asymptotic solution of the double fractal model.

E.1. Transient Interporosity Transfer Functions (de Swaan, 1976)

Development of the transfer interporosity function considering slab matrix blocks

The diffusivity equation for the linear flow occurring in slab matrix blocks as shown in **Fig. E.1** is given by:

$$\frac{\partial^2 p_{ma}}{\partial z^2} = \frac{1}{\eta_{ma}} \frac{\partial p_{ma}}{\partial t}, \quad \text{.....(E.1)}$$

Where the hydraulic diffusivity of the matrix is defined by:

$$\eta_{ma} = \frac{k_{ma}}{\phi_{ma} \mu c_{tma}}. \quad \text{.....(E.2)}$$

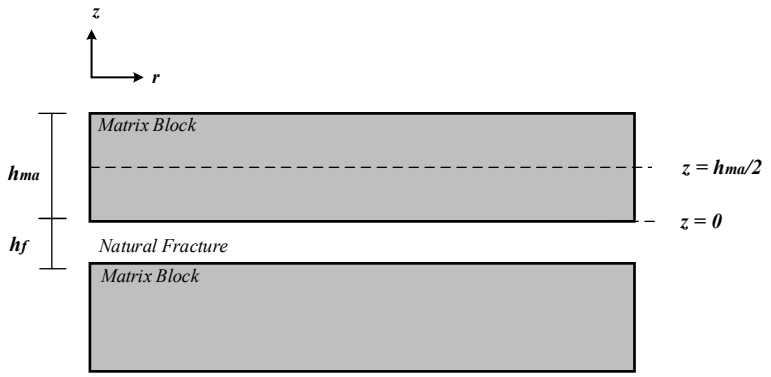

Figure E.1 — Schematics of a Naturally Fractured Reservoir with slab matrix blocks and horizontal fractures.

The matrix blocks are assumed to have uniformly distributed initial pressure, p_i. Hence the initial condition for Eq E.1 is given by:

$$p_{ma}(z, t=0) = p_i \quad \text{(E.3)}$$

The interface between the matrix blocks and the natural fractures is assumed to be unrestricted (*i.e.*, without interporosity skin). Therefore, the inner boundary condition is:

$$p_{ma}(z=0, t) = p_f(r, t) \quad \text{(E.4)}$$

Since the matrix blocks are assumed to be closed systems, the outer boundary condition for Eq. 1 is:

$$\left[\frac{\partial p_{ma}}{\partial z}\right]_{z=h_{ma}/2} = 0 \quad \text{(E.5)}$$

To solve Eq. E.1 in the Laplace domain, it is more convenient to express it in terms of a normalized drop of pressure. For this case, the normalized drop of pressure is defined as:

$$\Delta p_{ma}(z,t) = \frac{p_i - p_{ma}(z,t)}{p_i - p_f(r,t)} \quad \text{(E.6)}$$

Using the chain rule, Eq. E.1 is rewritten as:

$$\frac{\partial^2 \Delta p_{ma}}{\partial z^2} = \frac{1}{\eta_{ma}} \frac{\partial \Delta p_{ma}}{\partial t}, \quad \text{(E.7)}$$

and the initial and boundary conditions become:

$$\Delta p_{ma}(z, t=0) = 0 \qquad \text{(initial condition)}, \quad \text{(E.8)}$$

$$\Delta p_{ma}(z=0, t) = 1 \qquad \text{(inner boundary condition)}, \quad \text{(E.9)}$$

$$\left[\frac{\partial \Delta p_{ma}}{\partial z}\right]_{z=h_{ma}/2} = 0 \qquad \text{(outer boundary condition)}. \quad \text{(E.10)}$$

Applying the Laplace transform to Eq. E.7 and according to the initial condition, the following differential equation is obtained:

$$\frac{d^2 \Delta \bar{p}_{ma}}{dz^2} - \frac{u}{\eta_{ma}} \Delta \bar{p}_{ma} = 0. \quad \text{(E.11)}$$

By inspection, the general solution of Eq. E.11 can be given by a linear combination of hyperbolic sines and hyperbolic cosines. Therefore, for this problem the general solution is:

$$\Delta \bar{p}_{ma}(z,u) = C_1 \sinh\left[z\sqrt{\frac{u}{\eta_{ma}}}\right] + C_2 \cosh\left[z\sqrt{\frac{u}{\eta_{ma}}}\right]. \quad \text{(E.12)}$$

Applying the outer boundary condition to the general solution, the following expression results in:

$$\left[\frac{d\Delta \bar{p}_{ma}(z,u)}{dz}\right]_{z=h_{ma}/2} = C_1 \cosh\left[\frac{h_{ma}}{2}\sqrt{\frac{u}{\eta_{ma}}}\right] + C_2 \sinh\left[\frac{h_{ma}}{2}\sqrt{\frac{u}{\eta_{ma}}}\right] = 0. \quad \text{(E.13)}$$

From Eq. E.13, it is concluded that the constant C_1 is:

$$C_1 = -C_2 \tanh\left[\frac{h_{ma}}{2}\sqrt{\frac{u}{\eta_{ma}}}\right] \quad \text{(E.14)}$$

Substituting Eq. E.14 in Eq. E.12, a bounded solution for this problem is:

$$\Delta\bar{p}_{ma}(z,u) = -C_2 \tanh\left[\frac{h_{ma}}{2}\sqrt{\frac{u}{\eta_{ma}}}\right]\sinh\left[z\sqrt{\frac{u}{\eta_{ma}}}\right] + C_2 \cosh\left[z\sqrt{\frac{u}{\eta_{ma}}}\right] \quad \text{(E.15)}$$

Applying the inner boundary condition to Eq. 15, it is concluded that the constant C_2 is:

$$\Delta\bar{p}_{ma}(z=0,u) = C_2 = \frac{1}{u} \quad \text{(E.16)}$$

The particular solution for this problem is obtained by substituting C_2 in Eq. E.15:

$$\Delta\bar{p}_{ma}(z,u) = -\frac{1}{u}\tanh\left[\frac{h_{ma}}{2}\sqrt{\frac{u}{\eta_{ma}}}\right]\sinh\left[z\sqrt{\frac{u}{\eta_{ma}}}\right] + \frac{1}{u}\cosh\left[z\sqrt{\frac{u}{\eta_{ma}}}\right] \quad \text{(E.17)}$$

The derivative of the pressure with respect to z evaluated in zero is required to estimate the flow rate transferred from the matrix to the fractures. Based on Eq. E.17, such a derivative is:

$$\left[\frac{d\Delta\bar{p}_{ma}(z,u)}{dz}\right]_{z=0} = -\frac{1}{\sqrt{u\eta_{ma}}}\tanh\left[\frac{h_{ma}}{2}\sqrt{\frac{u}{\eta_{ma}}}\right] \quad \text{(E.18)}$$

Applying the inverse Laplace transform to Eq. E.18 (Eq.8.51 from Oberhettinger et *al.* (1973), p.294) the following expression is obtained:

$$\left[\frac{d\Delta p_{ma}(z,t)}{dz}\right]_{z=0} = -\frac{2}{h_{ma}}\theta_2\left[0\middle|\frac{4\eta_{ma}}{h_{ma}^2}t\right] = -\frac{4}{h_{ma}}\sum_{n=0}^{\infty}\exp\left[-\frac{4\pi^2[2n+1]^2\eta_{ma}}{h_{ma}^2}t\right] \quad \text{(E.19)}$$

Under the transient regime, the flow rate per unit of fracture volume from the matrix blocks to the fractures surrounding the matrix blocks can be expressed using the convolution integral. The convolution is defined as:

$$q = -\frac{2}{A_{ma} h_f} \int_0^t \frac{\partial \Delta p_f}{\partial \tau} q_{uma}(t-\tau) d\tau \quad \text{(E.20)}$$

where q_{uma} is the fluid transfer rate from the matrix blocks to the fracture. Based on Darcy's Law, the fluid transfer rate from the matrix blocks to the fracture is:

$$q_{uma} = -\frac{k_{ma} A_{ma}}{\mu} \left[\frac{d\Delta p_{ma}}{dz} \right]_{z=0} . \quad \text{(E.21)}$$

Substituting Eq. E.19 and Eq. E. 21 in Eq. E.20:

$$q = \frac{8 k_{ma}}{h_f h_{ma} \mu} \int_0^t \frac{\partial \Delta p_f}{\partial \tau} \sum_{n=0}^{\infty} \exp\left[-\frac{4\pi^2 [2n+1]^2 \eta_{ma} [t-\tau]}{h_{ma}^2} \right] d\tau \quad \text{(E.22)}$$

Development of the transfer interporosity function considering spherical matrix blocks

For this case, consider an array as the one shown in **Fig. E.2**. The diffusivity equation for a system with the shape of a sphere is given by:

$$\frac{\partial^2 p_{ma}}{\partial R^2} + \frac{2}{R} \frac{\partial p_{ma}}{\partial R} = \frac{1}{\eta_{ma}} \frac{\partial p_{ma}}{\partial t}, \quad \text{(E.23)}$$

where hydraulic diffusivity of the matrix, η_{ma} is defined exactly as for the case of slab matrix blocks (Eq. E.2). The initial and the boundary conditions for this case are the same as in the previous section, *i.e.*:

$$p_{ma}(R, t=0) = p_i \quad \text{(initial condition),} \quad \text{(E.24)}$$

$$\left[\frac{\partial p_{ma}}{\partial R}\right]_{R=0} = 0 \quad \text{(inner boundary condition),} \quad \text{(E.25)}$$

$$p_{ma}(R = R_{ma}, t) = p_f(r, t) \quad \text{(outer boundary condition).} \quad \text{(E.26)}$$

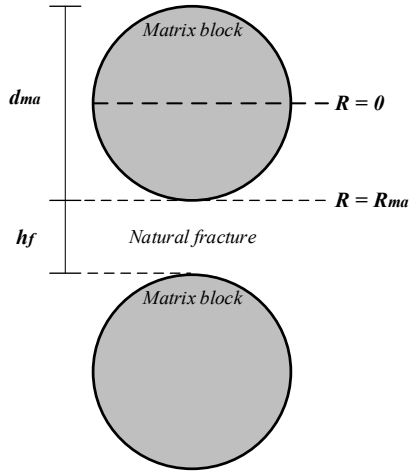

Figure E.2 — Schematics of a Naturally Fractured Reservoir with spherical matrix blocks and horizontal fractures.

Analogous to the previous subsection, the normalized drop of pressure for this case is:

$$\Delta p_{ma}(R, t) = \frac{p_i - p_{ma}(R, t)}{p_i - p_f(r, t)}. \quad \text{(E.27)}$$

Consequently, Eq. E.23 is rewritten as:

$$\frac{\partial^2 \Delta p_{ma}}{\partial R^2} + \frac{2}{R}\frac{\partial \Delta p_{ma}}{\partial R} = \frac{1}{\eta_{ma}}\frac{\partial \Delta p_{ma}}{\partial t} \quad \text{(E.28)}$$

and, the initial and boundary conditions become:

$$\Delta p_{ma}(R, t=0) = 0 \quad \text{(initial condition),} \quad \text{(E.29)}$$

$$\Delta p_{ma}(R = R_{ma}, t) = 1 \quad \text{(inner boundary condition),} \quad \text{(E.30)}$$

$$\left[\frac{\partial \Delta p_{ma}}{\partial R}\right]_{R=0} = 0 \quad \text{(outer boundary condition).} \quad \text{(E.31)}$$

As shown in Appendix A, the transformation defined by:

$$\Delta p_{ma}(R,t) = \frac{b(R,t)}{R} \quad \text{(E.32)}$$

facilitates the procedure to find a solution to an equation with the shape as of Eq. E.28. Applying such a transformation, Eq. E.28 becomes:

$$\frac{\partial^2 b}{\partial R^2} = \frac{1}{\eta_{ma}}\frac{\partial b}{\partial t}. \quad \text{(E.33)}$$

Since Eq. E.33 has exactly the same shape as Eq. E.7, its general solution in the Laplace domain is:

$$\bar{b}(R,u) = C_1 \sinh\left[R\sqrt{\frac{u}{\eta_{ma}}}\right] + C_2 \cosh\left[R\sqrt{\frac{u}{\eta_{ma}}}\right] \quad \text{(E.34)}$$

In terms of the drop of pressure in the matrix (Eq. E.32):

$$\Delta\bar{p}_{ma}(R,u) = \frac{C_1}{R}\sinh\left[R\sqrt{\frac{u}{\eta_{ma}}}\right] + \frac{C_2}{R}\cosh\left[R\sqrt{\frac{u}{\eta_{ma}}}\right] \quad \text{(E.35)}$$

Applying the outer boundary condition, it is concluded that the constant C_2 is zero. Therefore, the bounded solution for this problem is:

$$\Delta\bar{p}_{ma}(R,u) = \frac{C_1}{R}\sinh\left[R\sqrt{\frac{u}{\eta_{ma}}}\right] \quad \text{(E.36)}$$

Applying the inner boundary condition, the value of the constant C_1 is obtained. It is given by:

$$C_1 = \frac{R_{ma}}{u} \frac{1}{\sinh\left[R_{ma}\sqrt{\frac{u}{\eta_{ma}}}\right]}. \quad \text{(E.37)}$$

Substituting Eq. E.37 in Eq. E.36, the particular solution for this problem is:

$$\Delta\bar{p}_{ma}(R,u) = \frac{R_{ma}}{\sinh\left[R_{ma}\sqrt{\frac{u}{\eta_{ma}}}\right]} \frac{1}{u} \frac{\sinh\left[R\sqrt{\frac{u}{\eta_{ma}}}\right]}{R} \quad \text{(E.38)}$$

The derivative of Eq. E.38 with respect of the radius R and evaluated in R_{ma} is:

$$\left[\frac{d\Delta\bar{p}_{ma}(R,u)}{dR}\right]_{R=R_{ma}} = -\frac{1}{R_{ma}u} + \frac{1}{\sqrt{\eta_{ma}u}} \coth\left[R_{ma}\sqrt{\frac{u}{\eta_{ma}}}\right]. \quad \text{(E.39)}$$

The Inverse Laplace Transform of Eq. E.39 is (Eq. 8.52, Oberhettinger *et al.*, 1973, p. 294):

$$\left[\frac{d\Delta p_{ma}(R,t)}{dR}\right]_{R=R_{ma}} = \frac{1}{R_{ma}}\left[-1+\theta_3\left[0\middle|\frac{\eta_{ma}}{R_{ma}^2}t\right]\right] = \frac{2}{R_{ma}}\sum_{n=1}^{\infty}\exp\left[-\frac{\pi^2 n^2 \eta_{ma}}{R_{ma}^2}t\right]. \quad \text{(E.40)}$$

E.2. Double Porosity Model with Transient Interporosity Transfer

Constant-rate solution (*Cinco-Ley et al.,* 1982)

The flow in a radial fracture network considered by Cinco-Ley *et al*. (1982) is modeled by:

$$\frac{1}{r}\frac{\partial}{\partial r}\left[r\frac{\partial p_f}{\partial r}\right] = \frac{\phi_{fb}\mu c_{tfb}}{k_{fb}}\frac{\partial p_f}{\partial t} + \frac{\mu}{k_{fb}}q^*, \quad \text{(E.41)}$$

where q^* is the fluid transfer from the matrix to the fracture network per unit of bulk volume. As shown by de Swaan (1976), it can be modeled by the convolution integral:

$$q^* = \int_0^t \frac{\partial p_f}{\partial \tau} q^*_{uma}(t-\tau)d\tau \,, \quad \text{(E.42)}$$

where:

$$q^*_{uma} = \frac{A_{fb} k_{ma}}{\mu} [\nabla p_{ma}]_{sur} \quad \text{(E.43)}$$

Substituting Eq. E.42 and Eq. E.43 in Eq. E.41:

$$\frac{1}{r}\frac{\partial}{\partial r}\left[r \frac{\partial p_f}{\partial r} \right] = \frac{\phi_{fb}\mu c_{tfb}}{k_{fb}} \frac{\partial p_f}{\partial t} + \frac{k_{ma} A_{fb}}{k_{fb}} \int_0^t \frac{\partial p_f}{\partial \tau} [\nabla p_{ma}]_{sur}(t-\tau)d\tau \,. \quad \text{(E.44)}$$

The initial and boundary conditions for this model are:

$$p_f(r, t=0) = p_i \qquad \text{(initial condition),} \quad \text{(E.45)}$$

$$\left[r \frac{\partial p_f}{\partial r} \right]_{r=r_w} = \frac{2\pi k_{fb} h}{B\mu} \qquad \text{(inner boundary condition),} \quad \text{(E.46)}$$

$$\lim_{r\to\infty} p_f(r,t) = p_i \qquad \text{(outer boundary condition)} \quad \text{(E.47)}$$

The dimensionless variables defined for this model are summarized in **Table E.1**.

Table E.1 — Dimensionless variables for the Cinco-Ley *et al.* (1982) model.

Dimensionless Variable	Definition
Pressure in the fracture network	$p_{fD,cr}(r_D,t_D)=\frac{k_{fb}h}{qB\mu}[p_i-p_f(r,t)]$
Pressure in the matrix blocks	$p_{maD,cr}(r_D,t_D)=\frac{k_{fb}h}{qB\mu}[p_i-p_{ma}(r,t)]$
Time	$t_D=\frac{k_{fb}}{[\phi c_t]_t\,\mu r_w^2}t$
Radius	$r_D=\frac{r}{r_w}$
Storativity ratio	$\omega=\frac{\phi_{fb}c_{tfb}}{[\phi c_t]_t}$
Fracture area	$A_{fD}=A_{fma}h_{ma}$

Eq. E.44 expressed in dimensionless form is:

$$\frac{1}{r_D}\frac{\partial}{\partial r_D}\left[r_D\frac{\partial p_{fD,cr}}{\partial r_D}\right]=\omega\frac{\partial p_{fD,cr}}{\partial t_D}+[1-\omega]\frac{A_{fD}\eta_{maD}}{h_{maD}}\int_0^{t_D}\frac{\partial p_{fD,cr}}{\partial\tau}F(\eta_{maD},h_{maD},t_D-\tau)d\tau\,, \quad \text{(E.48)}$$

where:

$$F(\eta_{maD},h_{maD},t_D-\tau)=[\nabla p_{maD,cr}]_{z_D=surface} \quad \text{(E.49)}$$

The initial and boundary conditions in dimensionless variables become:

$$p_{fD}(r_D,t_D=0)=0 \qquad \text{(initial condition),} \quad \text{(E.50)}$$

$$\left[r_D\frac{\partial p_{fD}}{\partial r_D}\right]_{r_D=1}=-1 \qquad \text{(inner boundary condition),} \quad \text{(E.51)}$$

$$\lim_{r_D\to\infty}p_{fD}(r_D,t_D)=0 \qquad \text{(outer boundary condition)} \quad \text{(E.52)}$$

Applying the Laplace transform to Eq. E.48 and arraying it can be written as:

$$\frac{1}{r_D}\frac{d}{dr_D}\left[r_D\frac{d\bar{p}_{fD,cr}}{dr_D}\right]-f(u)u\bar{p}_{fD,cr}=0 \quad \text{(E.53)}$$

Considering the boundary conditions for this model, the particular solution of Eq. E.53 is:

$$\bar{p}_{fD,cr}(r_D,u)=\frac{K_0\left[r_D\sqrt{uf(u)}\right]}{u\sqrt{uf(u)}K_1\left[\sqrt{uf(u)}\right]}. \quad \text{(E.54)}$$

where $f(u)$ is the interporosity transfer function. Such a function depends on the properties of the matrix blocks (geometry and petrophysical properties) and the interporosity transfer regime. For unrestricted flow (without interporosity skin), it is defined as:

$$f(u)=\omega+[1-\omega]\frac{A_{fD}\eta_{maD}}{h_{maD}}\bar{F}(\eta_{maD},h_{maD},u), \quad \text{(E.55)}$$

For the classic cases (slab and spheres matrix blocks) presented by Cinco-Ley *et al.*, (1982) the functions are:

$$f(u)=\omega+[1-\omega]\frac{A_{fD}}{h_{maD}}\sqrt{\frac{\eta_{maD}}{u}}\tanh\left[\frac{h_{maD}}{2}\sqrt{\frac{u}{\eta_{maD}}}\right], \quad \text{(E.56)}$$

for slabs, and:

$$f(u)=\omega+[1-\omega]\frac{A_{fD}}{h_{maD}}\sqrt{\frac{\eta_{maD}}{u}}\left[\coth\left[\frac{h_{maD}}{2}\sqrt{\frac{u}{\eta_{maD}}}\right]-\frac{2}{h_{maD}}\sqrt{\frac{\eta_{maD}}{u}}\right], \quad \text{(E.57)}$$

for spheres.

Solution considering time-depend inner boundary condition

For this model, we have considered the diffusivity equation given defined by Eq. E.48 and the same initial and outer boundary conditions as in the previous section (*i.e.,* Eq. 50 and Eq. E.52). For the inner boundary condition, we have assumed a power-law time dependent pressure gradient around the wellbore, *i.e.*,:

$$\left[r_D \frac{\partial p_{fD}}{\partial r_D}\right]_{r_D=1} = -t_D^{v_0 - v} \qquad \text{(inner boundary condition),} \qquad \text{(E.58)}$$

Where v_0 is an arbitrary reference exponent. We have considered a unit value of this parameter.

Applying the outer boundary condition, the bounded solution of Eq. E.48 in the Laplace domain is:

$$\bar{p}_{fD,cr}(r_D,u) = C_1 K_0\left[r_D\sqrt{uf(u)}\right] . \qquad \text{(E.59)}$$

Applying the inner boundary condition, the value of the constant C_1 is obtained:

$$C_1 = \frac{\Gamma[2-v]}{u^{2-v}\sqrt{uf(u)}K_1\left[\sqrt{uf(u)}\right]} . \qquad \text{(E.60)}$$

Hence, the particular solution for this problem is:

$$\bar{p}_{fD,cr}(r_D,u) = \frac{\Gamma[2-v]K_0\left[r_D\sqrt{uf(u)}\right]}{u^{2-v}\sqrt{uf(u)}K_1\left[\sqrt{uf(u)}\right]} . \qquad \text{(E.61)}$$

Taking the line source approximation, Eq. E.61 reduces to:

$$\bar{p}_{fD,cr}(r_D,u)=\frac{\Gamma[2-v]K_0\left[r_D\sqrt{uf(u)}\right]}{u^{2-v}}. \quad \text{(E.62)}$$

E.3. Transient Interporosity Transfer Function Considering Fractal Matrix Blocks

Development of the transfer interporosity function considering closed fractal matrix blocks

If matrix blocks with fractal geometry are considered (see **Fig. E.3**), the model developed by Chang *et al.*, (1990) for fractal fracture networks can be extended to fractal matrix blocks. For this case, consider the diffusivity equation for a fractal matrix block:

$$\frac{1}{R^{D_{fma}-1}}\frac{\partial}{\partial R}\left[R^{\beta_{ma}}\frac{\partial p_{ma}}{\partial R}\right]=\frac{1}{\eta_{ma}}\frac{\partial p_{ma}}{\partial t}. \quad \text{(E.63)}$$

where η_{ma} is the geometry hydraulic diffusivity of the matrix, exactly defined as for the cases of slab and sphere matrix blocks. D_{fma} is the fractal dimension of the matrix block and β_{ma} is the spatial dimension of the matrix, defined as $\beta_{ma}=D_{fma}-\theta_{ma}-1$.

Analogous to the cases shown in Section E.1 of this Appendix, the initial and the boundary conditions for this problem are:

$$p_{ma}(R,t=0)=p_i \qquad \text{(initial condition),} \quad \text{(E.64)}$$

$$p_{ma}(R=R_0,t)=p_f(r,t) \qquad \text{(inner boundary condition),} \quad \text{(E.65)}$$

$$\left[\frac{\partial p_{ma}}{\partial R}\right]_{R=h_{ma}/2}=0 \qquad \text{(outer boundary condition).} \quad \text{(E.66)}$$

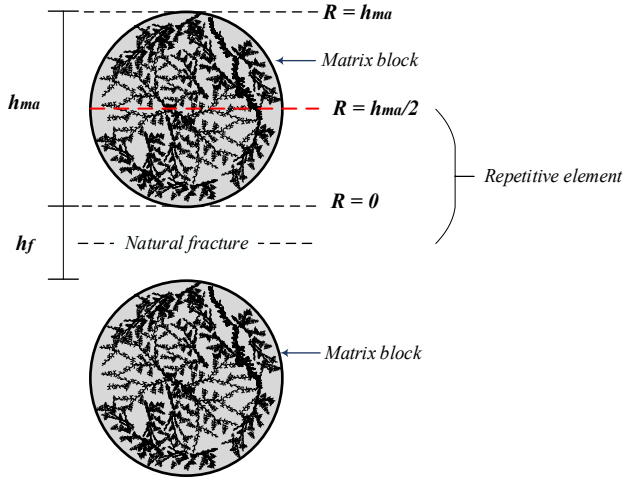

Figure E.3 — Schematics of a Naturally Fractured Reservoir with fractal matrix blocks.

For this model, the dimensionless pressure in the matrix is:

$$p_{maD,cp}(R_D,t_D)=\frac{p_i-p_{ma}(R,t)}{p_i-p_f(r,t)} \quad \text{(E.67)}$$

The dimensionless time is defined as:

$$t_D=\frac{k_{fb}}{[\phi c_t]_t \mu r_w^2}=\frac{\eta_f}{r_w^2}t, \quad \text{(E.68)}$$

and the dimensionless position in the fractal matrix block is:

$$R_D=\frac{R}{r_w} \quad \text{(E.69)}$$

Applying the definitions of the dimensionless variables, Eq. E.63 becomes:

$$\frac{1}{R_D^{D_{fma}-1}}\frac{\partial}{\partial R_D}\left[R_D^{\beta_{ma}}\frac{\partial p_{maD,cp}}{\partial R_D}\right]=\frac{1}{\eta_{maD}}\frac{\partial p_{maD,cp}}{\partial t_D}, \quad \text{(E.70)}$$

where the dimensionless hydraulic anomalous diffusivity is defined as:

$$\eta_{maD} = \frac{\eta_{ma}}{\eta_f r_w^{\theta_{ma}}} \quad \text{(E.71)}$$

The initial and boundary conditions in dimensionless variables become:

$$p_{maD,cp}(R_D, t_D = 0) = 0 \qquad \text{(initial condition),} \quad \text{(E.72)}$$

$$\left[\frac{\partial p_{maD,cp}}{\partial R_D}\right]_{R_D = R_{0D}} = 0 \qquad \text{(inner boundary condition),} \quad \text{(E.73)}$$

$$p_{maD,cp}(R_D = h_{maD}/2, t_D) = 1 \qquad \text{(outer boundary condition).} \quad \text{(E.74)}$$

As shown in Appendix B, the general solution to Eq. E.70 in the Laplace domain is:

$$\bar{p}_{maD,cp}(R_D, u) = R_D^{[1-\beta_{ma}]/2}\left[C_1 K_{v_{ma}}\left[\xi_{R_D}\right] + C_2 I_{v_{ma}}\left[\xi_{R_D}\right]\right], \quad \text{(E.75)}$$

where:

$$v_{ma} = \frac{1-\beta_{ma}}{\theta_{ma}+2}, \quad \text{(E.76)}$$

and:

$$\xi_{R_D} = R_D^{[\theta_{ma}+2]/2}\,\frac{2}{\theta_{ma}+2}\sqrt{\frac{u}{\eta_{maD}}}. \quad \text{(E.77)}$$

Applying inner boundary condition, the resulting bounded solution is:

$$\bar{p}_{maD,cp}(R_D, u) = C_2 R_D^{[1-\beta_{ma}]/2}\left[\frac{I_{v_{ma}-1}\left[\xi_0\right]}{K_{v_{ma}-1}\left[\xi_0\right]} K_{v_{ma}}\left[\xi_{R_D}\right] + I_{v_{ma}}\left[\xi_{R_D}\right]\right], \quad \text{(E.78)}$$

where:

$$\xi_0 = \lim_{R_D \to R_{0D}} \xi_{R_D} \quad \text{(E.79)}$$

Given that R_{0D} is located at zero, the following approximation can be used:

$$\frac{I_{v_{ma}-1}[\xi_0]}{K_{v_{ma}-1}[\xi_0]} = \frac{2}{\Gamma[v_{ma}]\Gamma[1-v_{ma}]}. \quad \text{(E.80)}$$

Then, Eq. E.78 becomes:

$$\bar{p}_{maD,cp}(R_D,u) = R_D^{[1-\beta_{ma}]/2} C_2 \left[\frac{2}{\Gamma[v_{ma}]\Gamma[1-v_{ma}]} K_{v_{ma}}\left[\xi_{R_D}\right] + I_{v_{ma}}\left[\xi_{R_D}\right] \right]. \quad \text{(E.81)}$$

Applying outer boundary condition, the particular solution for this problem is obtained:

$$\bar{p}_{maD,cp}(R_D,u) = \frac{1}{u}\left[\frac{2R_D}{h_{maD}}\right]^{[1-\beta_{ma}]/2} \left[\frac{2K_{v_{ma}}\left[\xi_{R_D}\right] + \Gamma[v_{ma}]\Gamma[1-v_{ma}]I_{v_{ma}}\left[\xi_{R_D}\right]}{2K_{v_{ma}}[\xi] + \Gamma[v_{ma}]\Gamma[1-v_{ma}]I_{v_{ma}}[\xi]} \right], \quad \text{(E.82)}$$

where:

$$\xi = \left[\frac{h_{maD}}{2}\right]^{[\theta_{ma}+2]/2} \frac{2}{\theta_{ma}+2}\sqrt{\frac{u}{\eta_{maD}}}. \quad \text{(E.83)}$$

Taking the derivative to Eq. E.83 with respect of R_D:

$$\frac{\partial \bar{p}_{maD,cp}}{\partial R_D} = \frac{R_D^{\theta_{ma}/2}}{\sqrt{u\eta_{maD}}}\left[\frac{2R_D}{h_{maD}}\right]^{[1-\beta_{ma}]/2} \left[\frac{\Gamma[v_{ma}]\Gamma[1-v_{ma}]I_{v_{ma}-1}\left[\xi_{R_D}\right] - 2K_{v_{ma}-1}\left[\xi_{R_D}\right]}{2K_{v_{ma}}\left[\xi\right] + \Gamma[v_{ma}]\Gamma[1-v_{ma}]I_{v_{ma}}\left[\xi\right]} \right]. \quad \text{(E.84)}$$

Evaluating at the interface, Eq. E.84 can be expressed in terms of the function $F(\eta_{maD}, h_{maD}, t_D)$:

$$F(\eta_{maD}, h_{maD}, t_D) = \sqrt{\frac{1}{\eta_{maD}}\left[\frac{h_{maD}}{2}\right]^{\theta_{ma}}}\, L^{-1}\left[\frac{1}{\sqrt{u}}\left[\frac{\Gamma[v_{ma}]\Gamma[1-v_{ma}]I_{v_{ma}-1}[\xi] - 2K_{v_{ma}-1}[\xi]}{2K_{v_{ma}}[\xi] + \Gamma[v_{ma}]\Gamma[1-v_{ma}]I_{v_{ma}}[\xi]}\right]\right] \quad \text{(E.85)}$$

Development of the transfer interporosity function considering infinite-acting fractal matrix blocks

To model infinite-acting matrix blocks, we considered matrix blocks of infinite length. Therefore, we solved Eq. E.70 using the following initial and boundary conditions:

$$p_{maD,cp}(R_D, t_D = 0) = 0 \qquad \text{(initial condition)}, \quad \text{(E.86)}$$

$$p_{maD,cp}(R_D = h_{maD}/2, t_D) = 1 \qquad \text{(inner boundary condition)}, \quad \text{(E.87)}$$

$$\lim_{R_D \to \infty} p_{maD,cp}(R_D, t_D) = 0 \qquad \text{(outer boundary condition)}. \quad \text{(E.88)}$$

Applying the boundary conditions to the general solution (Eq. E.75) the particular solution is:

$$\bar{p}_{maD,cp}(R_D, u) = \left[\frac{2R_D}{h_{maD}}\right]^{[1-\beta_{ma}]/2} \frac{K_{v_{ma}}\left[\xi R_D\right]}{uK_{v_{ma}}[\xi]} \quad \text{(E.89)}$$

where ξ is given by Eq. E.83. Taking the derivative to Eq. E. 89 the following equation is derived:

$$\frac{\partial \bar{p}_{maD,cp}}{\partial R_D} = -R_D^{\theta_{ma}/2} \frac{1}{\sqrt{u\eta_{maD}}}\left[\frac{2R_D}{h_{maD}}\right]^{[1-\beta_{ma}]/2} \frac{K_{v_{ma}-1}\left[\xi R_D\right]}{K_{v_{ma}}[\xi]} \quad \text{(E.90)}$$

Evaluating at the interface:

$$\left[\frac{\partial \bar{p}_{maD,cp}}{\partial R_D}\right]_{R_D = h_{maD}/2} = -\left[\frac{h_{maD}}{2}\right]^{\theta_{ma}/2} \frac{1}{\sqrt{u\eta_{maD}}} \frac{K_{v_{ma}-1}[\xi]}{K_{v_{ma}}[\xi]} \quad \text{(E.91)}$$

At early and intermediate times (large values of the Laplace parameter u), the Modified Bessel function of second order ($K_v(x)$) can be approximated as:

$$K_v(x) \approx \sqrt{\frac{\pi}{2x}} e^{-x} \quad \text{(E.92)}$$

Hence, at early and intermediate times Eq. E.91 can be written in terms of Eq. E.49 as:

$$\bar{F}(\eta_{maD}, h_{maD}, u) = \left[\frac{h_{maD}}{2}\right]^{\theta_{ma}/2} \frac{1}{\sqrt{u\eta_{maD}}} \quad \text{(E.93)}$$

Applying the inverse Laplace transform to Eq. E.93:

$$F(\eta_{maD}, h_{maD}, t_D) = \frac{1}{\sqrt{\pi\eta_{maD}}}\left[\frac{h_{maD}}{2}\right]^{\theta_{ma}/2} t_D^{-1/2} \quad \text{(E.94)}$$

Eq. E.94 applies for both closed and infinite-acting matrix blocks.

At late times (small values of the Laplace parameter u), the Modified Bessel function of second order ($K_v(x)$) can be approximated as:

$$K_v(x) \approx \frac{\Gamma[v]}{2}\left[\frac{z}{2}\right]^{-v} \quad \text{(E.95)}$$

Taking the approximation given by Eq. E.95, Eq. E.91 is reduced to (in terms of Eq. E.49):

$$\bar{F}(\eta_{maD}, h_{maD}, u) = \left[\frac{h_{maD}}{2}\right]^{\theta_{ma}/2} \frac{1}{\sqrt{u\eta_{maD}}} \frac{\Gamma[1-v_{ma}]}{\Gamma[v_{ma}]}\left[\frac{\xi}{2}\right]^{2v_{ma}-1} \quad \text{(E.96)}$$

Applying the inverse Laplace transform to Eq. E. 96:

$$F(\eta_{maD}, h_{maD}, t_D) = \frac{[\theta_{ma}+2]^{1-2\nu_{ma}}}{\Gamma[\nu_{ma}]\eta_{maD}^{\nu_{ma}}}\left[\frac{h_{maD}}{2}\right]^{-\beta_{ma}} t_D^{-\nu_{ma}} \quad \text{(E.97)}$$

E.4. Asymptotic Solutions of the Double Porosity Model with Transient Interporosity Transfer considering Fractal Matrix Blocks

To develop the asymptotic solutions of the constant-rate case of this model, consider the line-source approximation of Eq. E.54 and evaluate such an expression at wellbore (*i.e.*, r_D=1). The resulting equation is:

$$\bar{p}_{wD,cr}(u) = \frac{K_0\left[\sqrt{uf(u)}\right]}{u} \quad \text{(E.98)}$$

Additionally, the Modified Bessel function in Eq. 98 for small arguments can be approximated using Eq. 9.6.8 from Abramowitz *et al*. (1970). Therefore, the resulting expression is:

$$\bar{p}_{wD,cr}(u) = -\frac{1}{2u}\left[\ln[u] + \ln[f(u)]\right] \quad \text{(E.99)}$$

To obtain the asymptotic constant-pressure solutions for this model, consider the approximation (Earlougher, 1977):

$$p_{wD,cr}(t_D) \approx \frac{1}{q_{wD}(t_D)} \quad \text{(E.100)}$$

Closed Matrix Blocks

For this case, the interporosity transfer function defined by Eq. E. 85 should be considered. At early times, such a function approximates to the value of the storativity ratio (*i.e.*, $f(u)=\omega$). Therefore, the asymptotic constant-rate solution in the Laplace domain at early times is:

$$\bar{p}_{wD,cr}(u) = -\frac{1}{2u}\left[\ln[u] + \ln[\omega]\right]. \quad \text{(E.101)}$$

Applying the inverse Laplace transform to Eq. E.101 results in:

$$p_{wD,cr}(t_D) = \frac{1}{2}\ln[t_D] + \frac{1}{2}\ln\left[\frac{\exp[\gamma]}{\omega}\right]. \quad \text{(E.102)}$$

Hence, using the relation given by Eq. E.100 we obtain:

$$q_{wD}(t_D) = \frac{2}{\ln[t_D] + \ln\left[\frac{\exp[\gamma]}{\omega}\right]}, \quad \text{(E.103)}$$

where γ is Euler's constant (0.57721…). As pointed out by Cinco-Ley *et al*. (1982), the flow from the matrix blocks to the fracture network is linear at early and intermediate times regardless the geometry of the matrix block. For these periods of flow, the function $F(\eta_{maD}, h_{maD}, t_D)$ takes asymptotic behavior given by Eq. E.94 and the interporosity transfer function is approximated as:

$$f(u) \approx [1-\omega]\frac{A_{fD}}{h_{maD}}\sqrt{\left[\frac{h_{maD}}{2}\right]^{\theta_{ma}}\frac{\eta_{maD}}{u}} \quad \text{(E.104)}$$

Substituting Eq. 104 in Eq. E.99 and arraying it results in:

$$\bar{p}_{wD,cr}(u) = -\frac{1}{4u}\left[\ln[u] + 2\ln\left[[1-\omega]\frac{A_{fD}}{h_{maD}}\sqrt{\left[\frac{h_{maD}}{2}\right]^{\theta_{ma}}\eta_{maD}}\right]\right]. \quad \text{(E.105)}$$

Applying inverse Laplace transform to Eq. E.105, it results:

$$p_{wD,cr}(t_D) = \frac{1}{4}\ln[t_D] + \frac{1}{2}\ln\left[\frac{\exp[\gamma/2]}{[1-\omega]}\frac{h_{maD}}{A_{fD}}\left[\left[\frac{h_{maD}}{2}\right]^{\theta_{ma}}\eta_{maD}\right]^{-1/2}\right]. \quad \text{(E.106)}$$

Consequently, the constant-pressure asymptotic solution for this case is:

$$q_{wD}(t_D) = \frac{2}{\frac{\ln[t_D]}{2} + \ln\left[\frac{\exp[\gamma/2]}{[1-\omega]}\frac{h_{maD}}{A_{fD}}\left[\left[\frac{h_{maD}}{2}\right]^{\theta_{ma}}\eta_{maD}\right]^{-1/2}\right]} \quad \text{(E.107)}$$

At late times, the behavior of the interporosity transfer function approaches one (*i.e.*, $f(u)=1$). Substituting such a value in Eq. E.94 and applying inverse Laplace transform, the asymptotic constant-rate solution is:

$$p_{wD,cr}(t_D) = \frac{1}{2}[\ln[t_D] + \gamma] \quad \text{(E.108)}$$

where γ is Euler's constant (0.57721…). Similar to the previous cases, the constant-pressure solution is:

$$q_{wD}(t_D) = \frac{2}{\ln[t_D] + \gamma}. \quad \text{(E.109)}$$

Infinite-Acting Matrix Blocks

The flow behavior of the matrix blocks assuming either closed or infinite-acting conditions is the same at early and intermediate times (*i.e.*, before the outer boundary condition of the matrix blocks are reached). Therefore, the asymptotic solutions developed for closed matrix blocks, for early and intermediate times (constant-rate and constant-pressure cases), also apply for the infinite-acting matrix blocks. The asymptotic constant-rate solution in the Laplace domain for $v_{ma} > 0$ is obtained by plugging Eq. E.97 in the interporosity transfer function (Eq. E.55). Substituting the resulting equation in Eq. E.99, gives us:

$$\bar{p}_{wD,cr}(u) = -\frac{1}{2u}\left[v_{ma} \ln[u] + \ln\left[\frac{A_{fD}[\theta_{ma}+2]^{1-2v_{ma}}}{h_{maD}\eta_{maD}^{v_{ma}-1}} \frac{\Gamma[1-v_{ma}]}{\Gamma[v_{ma}]} \left[\frac{2}{h_{maD}}\right]^{[\beta_{ma}+1]/2} \right] \right] \quad \text{(E.110)}$$

(γ is Euler's constant). The expression in Eq. E. 110 in the real domain is given by:

$$p_{wD,cr}(t_D) = \frac{v_{ma}}{2}\ln[t_D] + \frac{v_{ma}}{2}\gamma - \frac{1}{2}\ln\left[\frac{A_{fD}[\theta_{ma}+2]^{1-2v_{ma}}}{h_{maD}\eta_{maD}^{v_{ma}-1}} \frac{\Gamma[1-v_{ma}]}{\Gamma[v_{ma}]} \left[\frac{2}{h_{maD}}\right]^{[\beta_{ma}+1]/2} \right] \quad \text{(E.111)}$$

Applying the relation defined by Eq. E.100, the constant-pressure solution is:

$$q_{wD}(t_D) = \frac{1}{\frac{v_{ma}}{2}\ln[t_D] + \frac{v_{ma}}{2}\gamma - \frac{1}{2}\ln\left[\frac{A_{fD}[\theta_{ma}+2]^{1-2v_{ma}}}{h_{maD}\eta_{maD}^{v_{ma}-1}} \frac{\Gamma[1-v_{ma}]}{\Gamma[v_{ma}]} \left[\frac{2}{h_{maD}}\right]^{[\beta_{ma}+1]/2} \right]} \quad \text{(E.112)}$$

E.5. Asymptotic Solutions of the Double Fractal Model

Pressure –Transient Solutions

Consider the constant-rate solution of the diffusivity equation to model the flow within the infinite fractal fracture network of a double porosity reservoir:

$$\bar{p}_{wD,cr}(u) = \frac{K_v\left[\frac{2\sqrt{uf(u)}}{\theta+2}\right]}{u\sqrt{uf(u)}K_{1-v}\left[\frac{2\sqrt{uf(u)}}{\theta+2}\right]} \quad \text{(E.113)}$$

Using the approximation given in Eq. E.92, at early-intermediate times, Eq. E.113 reduces to:

$$\bar{p}_{wD,cr}(u) = \frac{1}{u\sqrt{uf(u)}} \quad \text{(E.114)}$$

The asymptotic behavior of the function $F(\eta_{maD}, h_{maD}, t_D)$ at early-intermediate times is given by Eq. E. 93. Substituting such an expression in the interporosity transfer function (Eq. E.55) and neglecting the storativity ratio ($\omega = 0$) derives the following expression:

$$f(u) = \alpha_0 u^{1/2}, \quad \text{(E.115)}$$

where:

$$\alpha_0 = \frac{A_{fD}\sqrt{\eta_{maD}}}{2}\left[\frac{h_{maD}}{2}\right]^{\theta_{ma}/2-1} \quad \text{(E.116)}$$

Substituting Eq. E.115 in Eq. E.114:

$$\bar{p}_{wD,cr}(u) = \frac{u^{-5/4}}{\sqrt{\alpha_0}} \quad \text{(E.117)}$$

Applying the inverse Laplace transform to Eq. E.116 the asymptotic solution in the real domain at early-intermediate times is:

$$p_{wD,cr}(t_{Df}) = \frac{t_{Df}^{1/4}}{\Gamma[5/4]\sqrt{\alpha_0}} \quad \text{(E.118)}$$

At late-intermediate and late times, the Modified Bessel function of second kind can be approximated using Eq. E. 95. Applying such an approximation in Eq. E. 113 results in:

$$\bar{p}_{wD,cr}(u) = \frac{\Gamma[v]}{[\theta+2]^{1-2v}\Gamma[1-v]}\frac{[uf(u)]^{-v}}{u}. \quad \text{(E.119)}$$

The following expression results from substituting Eq. E.115 in Eq. E.119:

$$\bar{p}_{wD,cr}(u) = \frac{[\theta+2]^{2v-1}\Gamma[v]}{\alpha_0^v \Gamma[1-v]} u^{-[v/2+1]}. \quad \text{(E.120)}$$

Applying the inverse Laplace transform to Eq. E.120 the asymptotic solution in the real domain at late-intermediate times is:

$$p_{wD,cr}(t_{Df}) = \frac{[\theta+2]^{2v-1}\Gamma[v]}{\alpha_0^v \Gamma[1-v]\Gamma[v/2+1]} t_{Df}^{v/2} \quad \text{(E.121)}$$

The asymptotic behavior of the function $F(\eta_{maD}, h_{maD}, t_D)$ at late times is given by Eq. E. 97. Substituting such an expression in the interporosity transfer function (Eq. E.55) and neglecting the storativity ratio ($\omega = 0$) derives in the following expression:

$$f(u) = \alpha_1 u^{v_{ma}/2}, \quad \text{(E.122)}$$

where:

$$\alpha_1 = \frac{A_{fD}\eta_{maD}^{1-v_{ma}}}{2} \frac{[\theta_{ma}+2]^{1-2v_{ma}}\Gamma[1-v_{ma}]}{\Gamma[v_{ma}]} \left[\frac{h_{maD}}{2}\right]^{-\beta_{ma}-1}. \quad \text{(E.123)}$$

Substituting Eq. E.122 in Eq. E.119:

$$\bar{p}_{wD,cr}(u) = \frac{[\theta+2]^{2v-1}\Gamma[v]}{\alpha_1^v \Gamma[1-v]} u^{-[vv_{ma}+1]}. \quad \text{(E.124)}$$

Applying the inverse Laplace transform to Eq. E.124 the asymptotic solution in the real domain at late times is:

$$p_{wD,cr}(t_{Df}) = \frac{[\theta+2]^{2v-1}\Gamma[v]}{\alpha_1^{v}\Gamma[1-v]\Gamma[vv_{ma}+1]} t_{Df}^{vv_{ma}} \quad \text{..... (E.125)}$$

APPENDIX F

ANOMALOUS DIFFUSIVITY MODEL CONSIDERING TIME-DEPENDENT DARCY'S LAW

In this Appendix, we present the derivation of the model presented by Raghavan (2012a) for a cylindrical reservoir. Consider the conservation equation in cartesian coordinates:

$$\frac{\partial q_x}{\partial x}+\frac{\partial q_y}{\partial y}+\frac{\partial q_z}{\partial z}=\phi c_t\frac{\partial p}{\partial t} \quad \text{(F.1)}$$

This model considers a time-dependent version of Darcy's Law, which applies that the flux is not local in time and space for a Continuous Time Random Walk. For this case, Darcy's Law is defined as (Eq. 2.10 from Raghavan, 2012a):

$$q=-\frac{k_l A}{\mu}\frac{\partial^{\alpha-1}}{\partial t^{\alpha-1}}[\nabla p]=-\frac{k_l A}{\mu}\frac{1}{\Gamma[\alpha]}\int_0^t (t-\tau)^{\alpha-1}\frac{d\nabla p}{dt}d\tau. \quad \text{(F.2)}$$

Applying the Laplace transform to Eq. F.2 results in:

$$\bar{q}_i=-\frac{k_l A}{\mu}u^{1-\alpha}\nabla\bar{p}, \quad \text{(F.3)}$$

where i defines the directions x, y or z. Applying the Laplace transform to Eq. F.1 results in

$$\frac{\partial \bar{q}_x}{\partial x}+\frac{\partial \bar{q}_y}{\partial y}+\frac{\partial \bar{q}_z}{\partial z}=\phi c_t[u\bar{p}-p(t=0)]. \quad \text{(F.4)}$$

Substituting and arraying Eq. F.3 in Eq. F.4 gives us:

$$\frac{\partial}{\partial x}\left[-\frac{k_l A}{\mu}\nabla\bar{p}\right]+\frac{\partial}{\partial y}\left[-\frac{k_l A}{\mu}\nabla\bar{p}\right]+\frac{\partial}{\partial z}\left[-\frac{k_l A}{\mu}\nabla\bar{p}\right]=\phi c_t u^{\alpha-1}[u\bar{p}-p(t=0)]. \quad \text{(F.5)}$$

Applying the inverse Laplace transform to Eq. F.5 yields:

$$\frac{\partial}{\partial x}\left[-\frac{k_l A}{\mu}\nabla p\right]+\frac{\partial}{\partial y}\left[-\frac{k_l A}{\mu}\nabla p\right]+\frac{\partial}{\partial z}\left[-\frac{k_l A}{\mu}\nabla p\right]=\phi c_t \frac{\partial^\alpha p}{\partial t^\alpha} \quad \text{(F.6)}$$

The expression inside the brackets is the classic version of Darcy's Law:

$$q_l = -\frac{k_l A}{\mu}\nabla p. \quad \text{(F.7)}$$

Transforming Eq. F.6 to cylindrical coordinates results in:

$$\frac{1}{r}\frac{\partial}{\partial r}\left[r\frac{\partial p}{\partial r}\right]=\frac{\phi\mu c_t}{k_r}\frac{\partial^\alpha p}{\partial t^\alpha}. \quad \text{(F.8)}$$

For a cylindrical system (considering only the radial coordinate), Eq. F.2 is expressed as:

$$q = -\frac{2\pi k_r h}{\mu}\frac{\partial^{\alpha-1}}{\partial t^{\alpha-1}}\left[r\frac{\partial p}{\partial r}\right]. \quad \text{(F.9)}$$

Applying the Laplace transform to Eq. F.9 and solving for the product of the radius and the gradient of the pressure results in:

$$\left[r\frac{d\bar{p}}{dr}\right] = -\frac{\bar{q}\mu}{2\pi k_r h}u^{1-\alpha}. \quad \text{(F.10)}$$

The initial condition to solve Eq. F.8 is:

$$p(r, t=0) = p_i. \quad \text{(F.11)}$$

Assuming constant flow rate at the wellbore, q, the inner boundary condition is (based on Eq. F.9):

$$\left[r \frac{\partial \Delta p}{\partial r} \right]_{r=r_w} = - \frac{q\mu}{2\pi k_r h \Gamma[2-\alpha]} t^{1-\alpha} . \quad \text{(F.12)}$$

The outer boundary condition assumes an infinite cylindrical reservoir, given by:

$$\lim_{r \to \infty} p(r,t) = p_i . \quad \text{(F.13)}$$

Defining the drop of pressure as:

$$\Delta p(r,t) = p_i - p(r,t), \quad \text{(F.14)}$$

Eq. F.8 becomes:

$$\frac{1}{r} \frac{\partial}{\partial r} \left[r \frac{\partial \Delta p}{\partial r} \right] = \frac{\phi \mu c_t}{k_r} \frac{\partial^\alpha \Delta p}{\partial t^\alpha} \quad \text{(F.15)}$$

Similarly, the initial and boundary conditions in terms of the drop of pressure are:

$$\Delta p(r, t=0) = 0 \qquad \text{(initial condition)}, \quad \text{(F.16)}$$

$$\left[r \frac{\partial \Delta p}{\partial r} \right]_{r=r_w} = - \frac{q\mu}{2\pi k_r h \Gamma[2-\alpha]} t^{1-\alpha} \quad \text{(inner boundary condition)}, \quad \text{(F.17)}$$

$$\lim_{r \to \infty} \Delta p(r,t) = 0 \qquad \text{(outer boundary condition)}. \quad \text{(F.18)}$$

Applying the Laplace transform to Eq. F.15 and substituting the initial condition gives us:

$$\frac{d^2 \Delta \bar{p}}{dr^2} + \frac{1}{r} \frac{d \Delta \bar{p}}{dr} - \frac{\phi \mu c_t}{k_r} u^\alpha \Delta \bar{p} = 0 , \quad \text{(F.19)}$$

multiplying Eq. F.19 by r^2:

$$r^2 \frac{d^2\Delta\bar{p}}{dr^2} + r\frac{d\Delta\bar{p}}{dr} - r^2 u^{\alpha} \frac{\phi\mu c_t}{k_r}\Delta\bar{p} = 0, \quad \text{(F.20)}$$

and defining the transformation variable z as:

$$z = ru^{\alpha/2}\sqrt{\frac{\phi\mu c_t}{k_r}} \quad \text{(F.21)}$$

Then, using the chain rule the first derivative of the drop of pressure with respect to *r* is:

$$\frac{d\Delta\bar{p}}{dr} = \frac{d\Delta\bar{p}}{dz}\frac{dz}{dr} = u^{\alpha/2}\sqrt{\frac{\phi\mu c_t}{k_r}}\frac{d\Delta\bar{p}}{dz} \quad \text{(F.22)}$$

Similarly, the second derivative of Eq. F.22 is:

$$\frac{d^2\Delta\bar{p}}{dr^2} = u^{\alpha/2}\sqrt{\frac{\phi\mu c_t}{k_r}}\frac{d}{dr}\left[\frac{d\Delta\bar{p}}{dz}\right]\frac{dz}{dr} = u^{\alpha}\frac{\phi\mu c_t}{k_r}\frac{d^2\Delta\bar{p}}{dz^2} \quad \text{(F.23)}$$

Substituting Eq. F.22 and Eq. F.23 in Eq. F.20 results in:

$$r^2 u^{\alpha}\frac{\phi\mu c_t}{k_r}\frac{d^2\Delta\bar{p}}{dz^2} + ru^{\alpha/2}\sqrt{\frac{\phi\mu c_t}{k_r}}\frac{d\Delta\bar{p}}{dz} - r^2 u^{\alpha}\frac{\phi\mu c_t}{k_r}\Delta\bar{p} = 0 \quad \text{(F.24)}$$

Then, using the definition given by Eq. F.21, Eq. F.24 is rewritten as:

$$z^2\frac{d^2\Delta p}{dz^2} + z\frac{d\Delta p}{dz} - z^2\Delta\bar{p} = 0\,. \quad \text{(F.25)}$$

By inspection, the general solution to Eq. F.25 is:

$$\Delta\bar{p} = AK_0\left[ru^{\alpha/2}\sqrt{\frac{\phi\mu c_t}{k_r}}\right] + BI_0\left[ru^{\alpha/2}\sqrt{\frac{\phi\mu c_t}{k_r}}\right] \quad \text{(F.26)}$$

Applying outer boundary condition (infinite reservoir) to Eq. F.26, the bounded solution is:

$$\Delta\bar{p} = AK_0\left[ru^{\alpha/2}\sqrt{\frac{\phi\mu c_t}{k_r}}\right] \quad \text{(F.27)}$$

The derivative of the drop of pressure with respect to r is:

$$\frac{d\Delta\bar{p}}{dr} = -Au^{\alpha/2}\sqrt{\frac{\phi\mu c_t}{k_r}}K_1\left[ru^{\alpha/2}\sqrt{\frac{\phi\mu c_t}{k_r}}\right] \quad \text{(F.28)}$$

Then, applying the inner boundary condition to Eq. F.26 gives us:

$$\left[r\frac{d\Delta\bar{p}}{dr}\right]_{r=r_w} = -Ar_w u^{\alpha/2}\sqrt{\frac{\phi\mu c_t}{k_r}}K_1\left[r_w u^{\alpha/2}\sqrt{\frac{\phi\mu c_t}{k_r}}\right] = -\frac{q\mu}{2\pi k_r h u^{2-\alpha}} \quad \text{(F.29)}$$

Solving for A:

$$A = \frac{q\mu}{2\pi k_r h u^{2-\alpha} r_w u^{\alpha/2}\sqrt{\frac{\phi\mu c_t}{k_r}}K_1\left[r_w u^{\alpha/2}\sqrt{\frac{\phi\mu c_t}{k_r}}\right]} \quad \text{(F.30)}$$

Hence, the particular solution for this problem is:

$$\Delta\bar{p} = \frac{q\mu K_0\left[ru^{\alpha/2}\sqrt{\frac{\phi\mu c_t}{k_r}}\right]}{2\pi k_r h u^{2-\alpha} r_w u^{\alpha/2}\sqrt{\frac{\phi\mu c_t}{k_r}}K_1\left[r_w u^{\alpha/2}\sqrt{\frac{\phi\mu c_t}{k_r}}\right]} \quad \text{(F.31)}$$

For small arguments, the Modified Bessel Function $K_1(x)$ is approximated as:

$$K_1\left[r_w u^{\alpha/2}\sqrt{\frac{\phi\mu c_t}{k_r}}\right] \approx \frac{1}{r_w u^{\alpha/2}}\sqrt{\frac{k_r}{\phi\mu c_t}}. \quad \text{(F.32)}$$

Then, Eq. F.31 reduces to:

$$\Delta\bar{p} = \frac{q\mu}{2\pi k_r h} \frac{K_0\left[ru^{\alpha/2}\sqrt{\frac{\phi\mu c_t}{k_r}}\right]}{u^{2-\alpha}} \quad \text{(F.33)}$$

Eq. F.33 is equivalent to the line-source solution (Eq. 4.10 in Raghavan, 2012a).

APPENDIX G

SENSITIVITY ANALYSES OF PRESSURE AND RATE TRANSIENT BEHAVIORS OF HORIZONTAL WELLS INTERCEPTING MULTIPLE FRACTURES

G.1. Horizontal well intercepting N_f fractures in a Fractal Reservoir with Infinite Thickness

Circular Transverse Fractures — High Conductivity

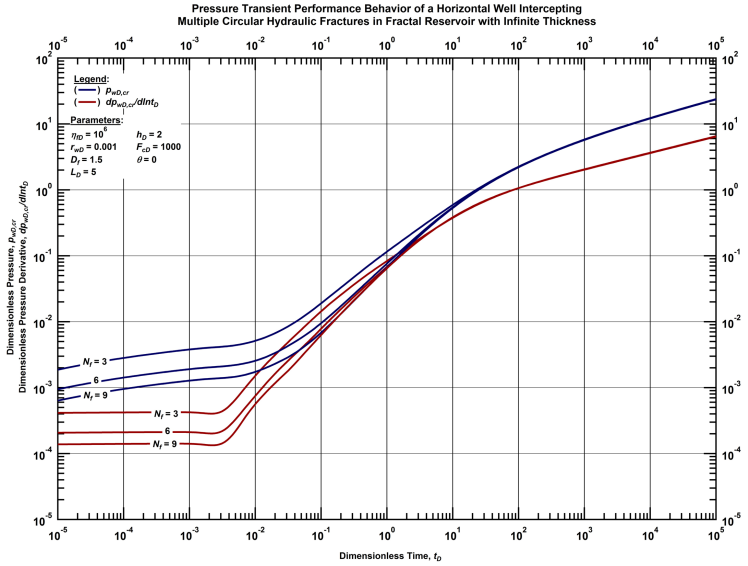

Figure G.1 — Log-log plot of the dimensionless pressure and dimensionless pressure derivative functions for a horizontal well intercepting N_f circular transverse hydraulic fractures with high conductivity in a fractal reservoir of infinite thickness with fixed fractal dimension (D_f=1.5) and conductivity index (θ=0) (constant-rate case).

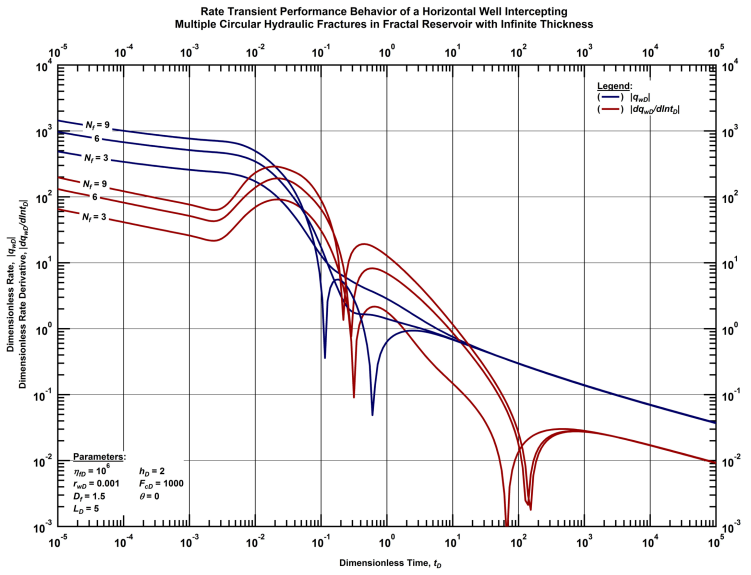

Figure G.2 — Log-log plot of the dimensionless rate and dimensionless rate derivative functions for a horizontal well intercepting N_f circular transverse hydraulic fractures with high conductivity in a fractal reservoir of infinite thickness with fixed fractal dimension (D_f=1.5) and conductivity index (θ=0) (constant-pressure case).

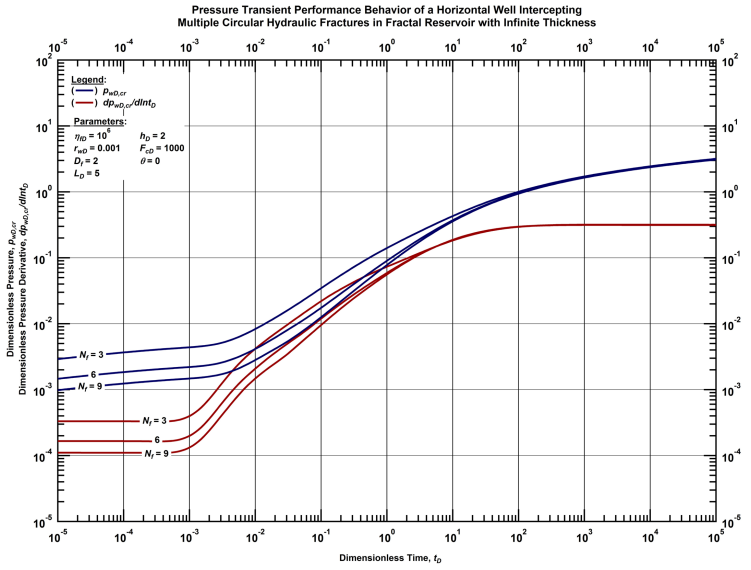

Figure G.3 — Log-log plot of the dimensionless pressure and dimensionless pressure derivative functions for a horizontal well intercepting N_f circular transverse hydraulic fractures with high conductivity in a fractal reservoir of infinite thickness with fixed fractal dimension (D_f=2) and conductivity index (θ=0) (constant-rate case).

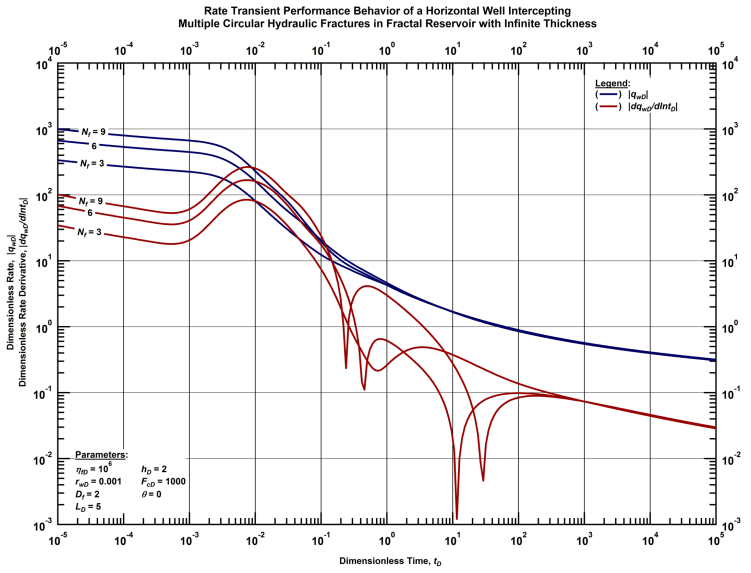

Figure G.4 — Log-log plot of the dimensionless rate and dimensionless rate derivative functions for a horizontal well intercepting N_f circular transverse hydraulic fractures with high conductivity in a fractal reservoir of infinite thickness with fixed fractal dimension (D_f=2) and conductivity index (θ=0) (constant- pressure case).

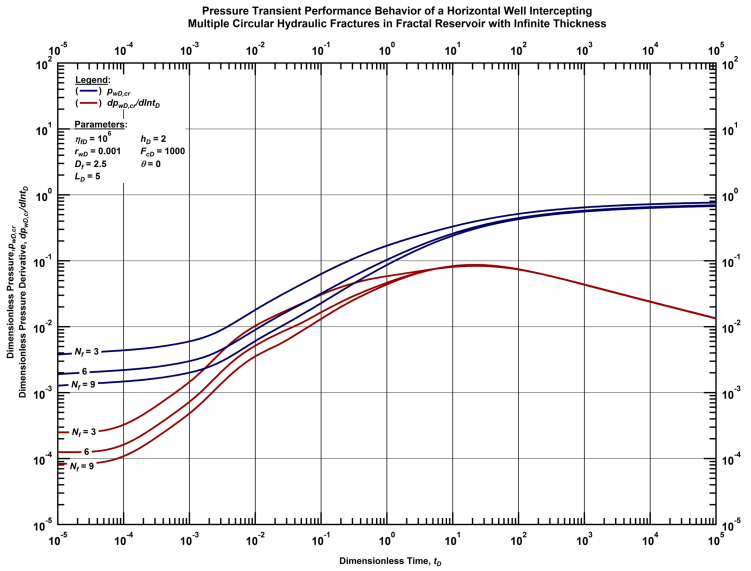

Figure G.5 — Log-log plot of the dimensionless pressure and dimensionless pressure derivative functions for a horizontal well intercepting N_f circular transverse hydraulic fractures with high conductivity in a fractal reservoir of infinite thickness with fixed fractal dimension (D_f=2.5) and conductivity index (θ=0) (constant-rate case).

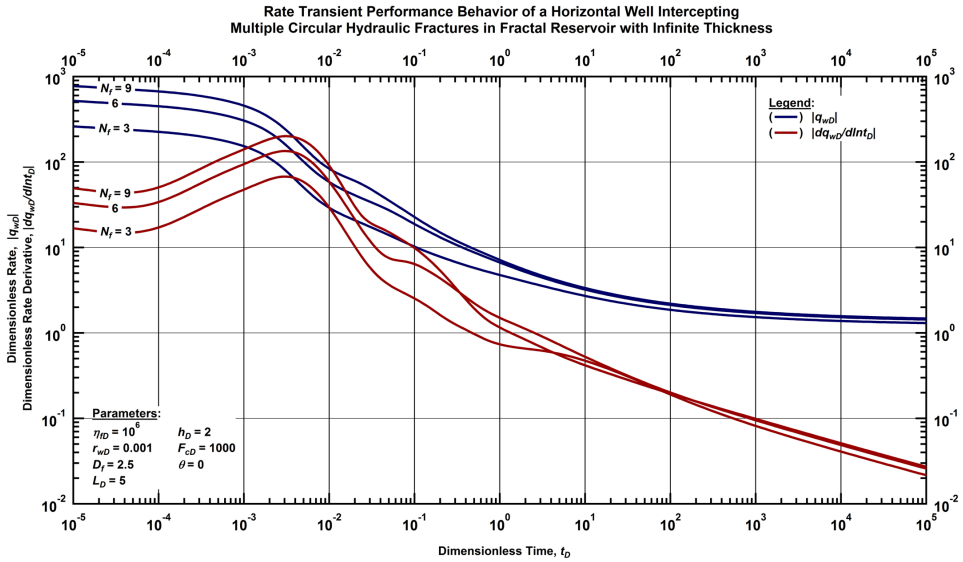

Figure G.6 — Log-log plot of the dimensionless rate and dimensionless rate derivative functions for a horizontal well intercepting N_f circular transverse hydraulic fractures with high conductivity in a fractal reservoir of infinite thickness with fixed fractal dimension (D_f=2.5) and conductivity index (θ=0) (constant-pressure case).

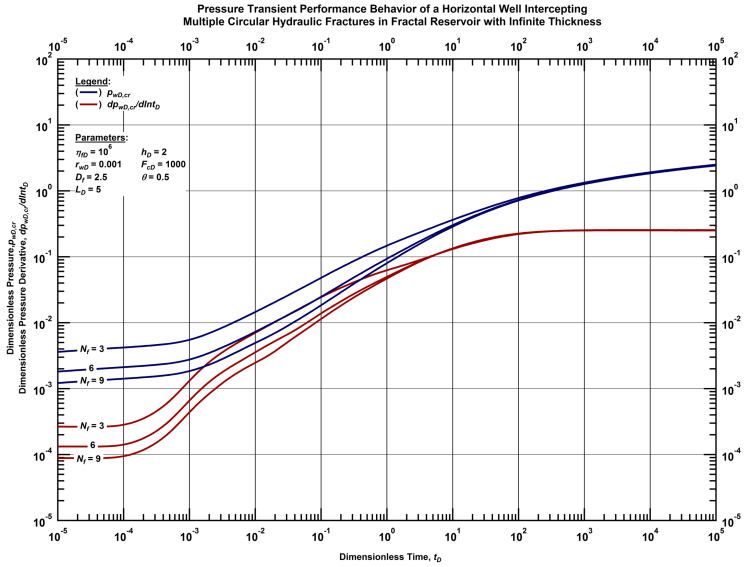

Figure G.7 — Log-log plot of the dimensionless pressure and dimensionless pressure derivative functions for a horizontal well intercepting N_f circular transverse hydraulic fractures with high conductivity in a fractal reservoir of infinite thickness with fixed fractal dimension (D_f=2.5) and conductivity index (θ=0.5) (constant-rate case).

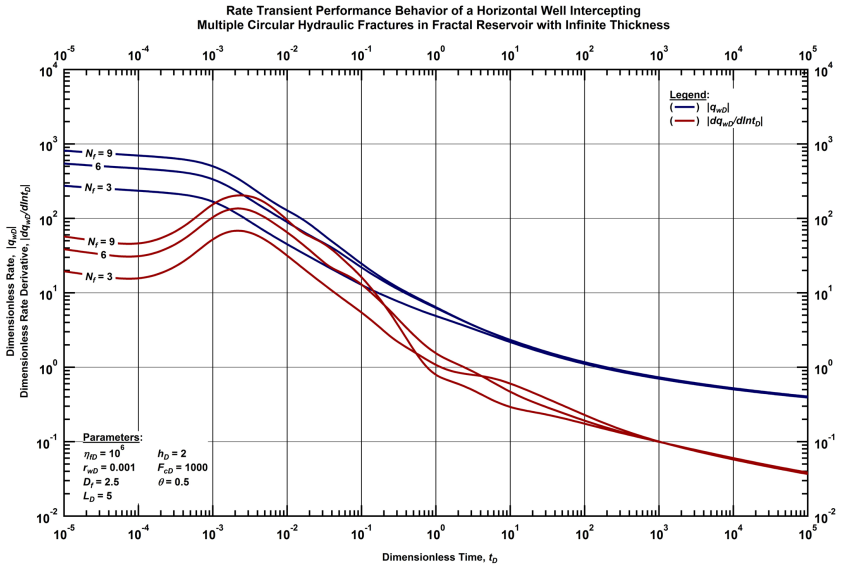

Figure G.8 — Log-log plot of the dimensionless rate and dimensionless rate derivative functions for a horizontal well intercepting N_f circular transverse hydraulic fractures with high conductivity in a fractal reservoir of infinite thickness with fixed fractal dimension (D_f=2.5) and conductivity index (θ=0.5) (constant-pressure case).

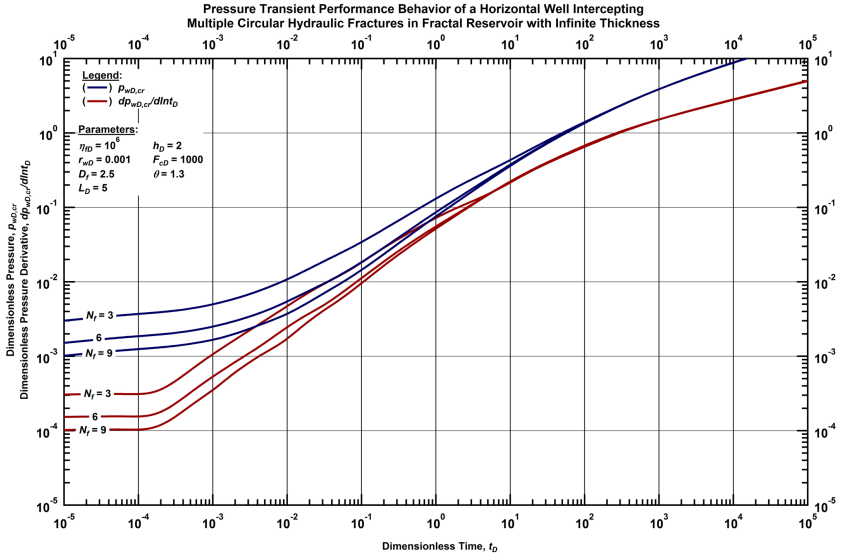

Figure G.9 — Log-log plot of the dimensionless pressure and dimensionless pressure derivative functions for a horizontal well intercepting N_f circular transverse hydraulic fractures with high conductivity in a fractal reservoir of infinite thickness with fixed fractal dimension (D_f=2.5) and conductivity index (θ=1.3) (constant-rate case).

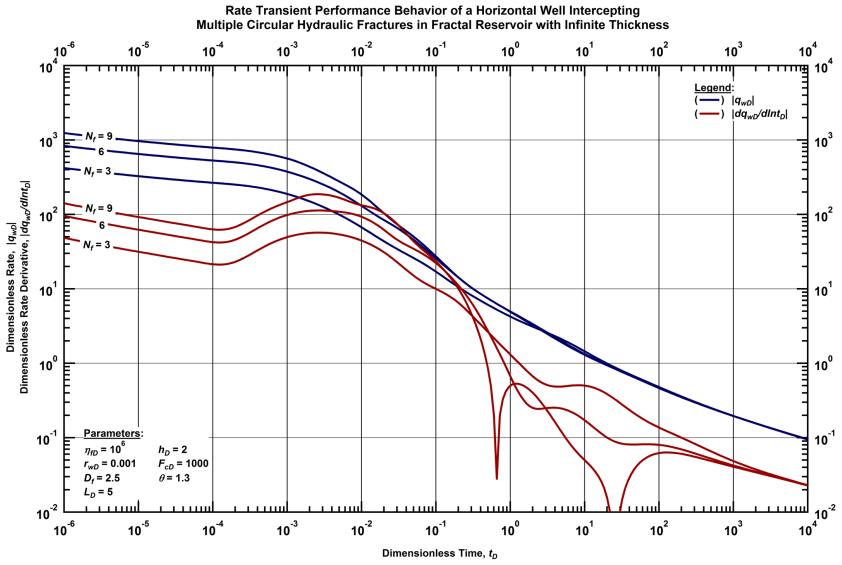

Figure G.10 — Log-log plot of the dimensionless rate and dimensionless rate derivative functions for a horizontal well intercepting N_f circular transverse hydraulic fractures with high conductivity in a fractal reservoir of infinite thickness with fixed fractal dimension (D_f=2.5) and conductivity index (θ=1.3) (constant-pressure case).

Circular Transverse Fractures — Intermediate Conductivity

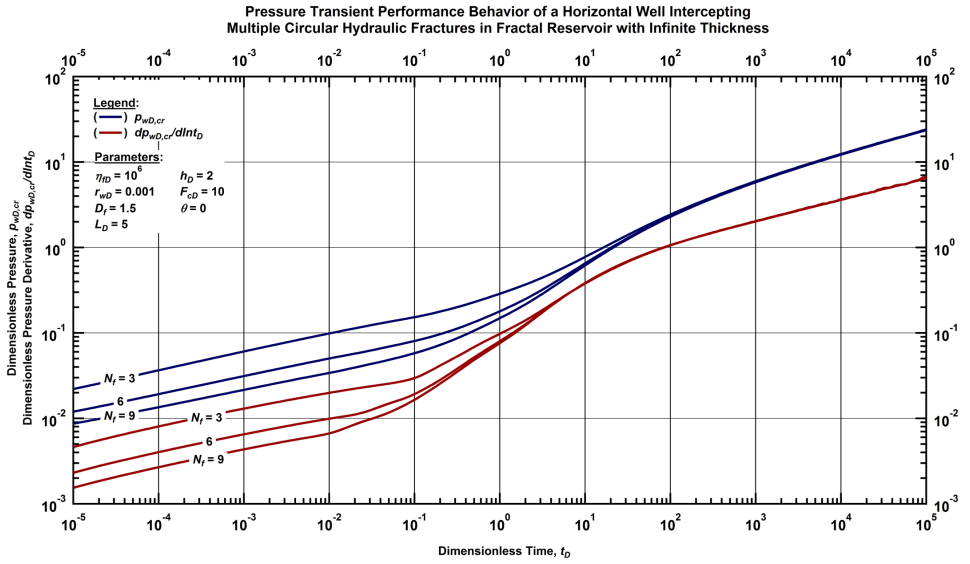

Figure G.11 — Log-log plot of the dimensionless pressure and dimensionless pressure derivative functions for a horizontal well intercepting N_f circular transverse hydraulic fractures with intermediate conductivity in a fractal reservoir of infinite thickness with fixed fractal dimension (D_f=1.5) and conductivity index (θ=0) (constant-rate case).

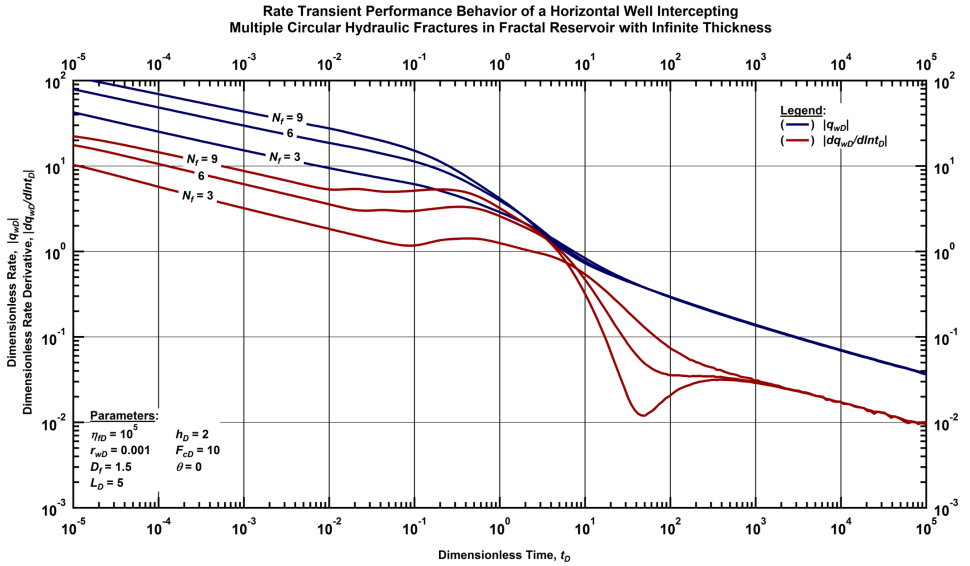

Figure G.12 — Log-log plot of the dimensionless rate and dimensionless rate derivative functions for a horizontal well intercepting N_f circular transverse hydraulic fractures with intermediate conductivity in a fractal reservoir of infinite thickness with fixed fractal dimension (D_f=1.5) and conductivity index (θ=0) (constant-pressure case).

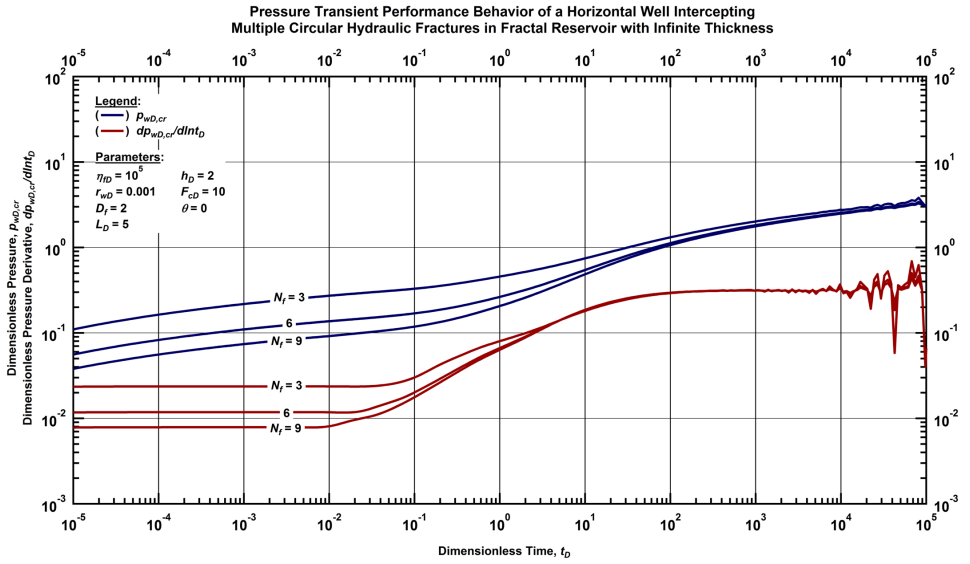

Figure G.13 — Log-log plot of the dimensionless pressure and dimensionless pressure derivative functions for a horizontal well intercepting N_f circular transverse hydraulic fractures with intermediate conductivity in a fractal reservoir of infinite thickness with fixed fractal dimension (D_f=2) and conductivity index (θ=0) (constant-rate case).

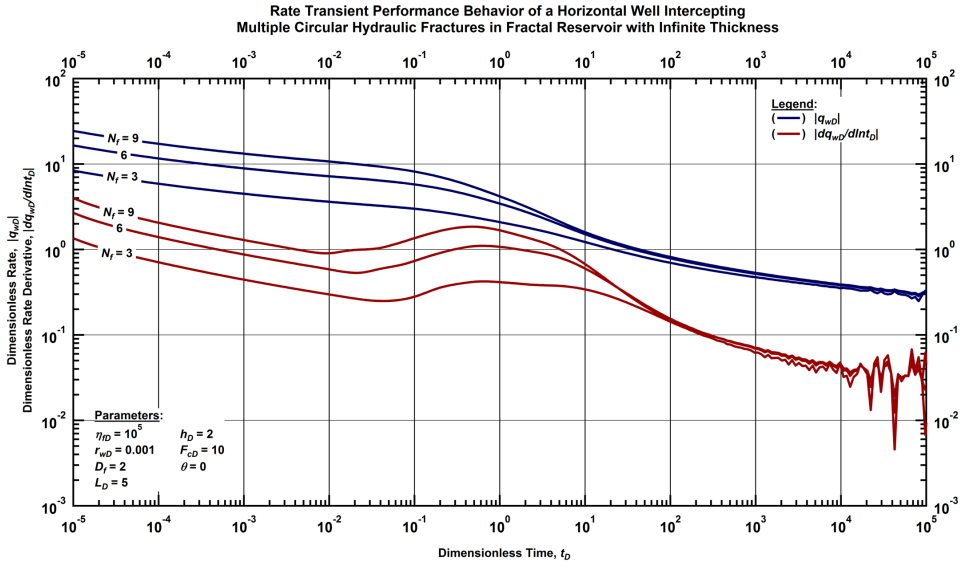

Figure G.14 — Log-log plot of the dimensionless rate and dimensionless rate derivative functions for a horizontal well intercepting N_f circular transverse hydraulic fractures with intermediate conductivity in a fractal reservoir of infinite thickness with fixed fractal dimension (D_f=2) and conductivity index (θ=0) (constant-pressure case).

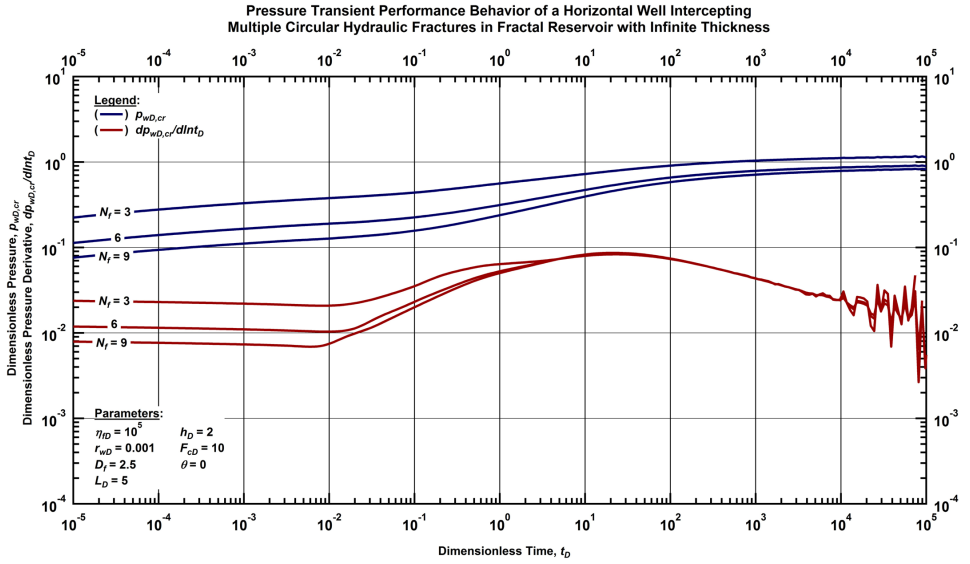

Figure G.15 — Log-log plot of the dimensionless pressure and dimensionless pressure derivative functions for a horizontal well intercepting N_f circular transverse hydraulic fractures with intermediate conductivity in a fractal reservoir of infinite thickness with fixed fractal dimension (D_f=2.5) and conductivity index (θ=0) (constant-rate case).

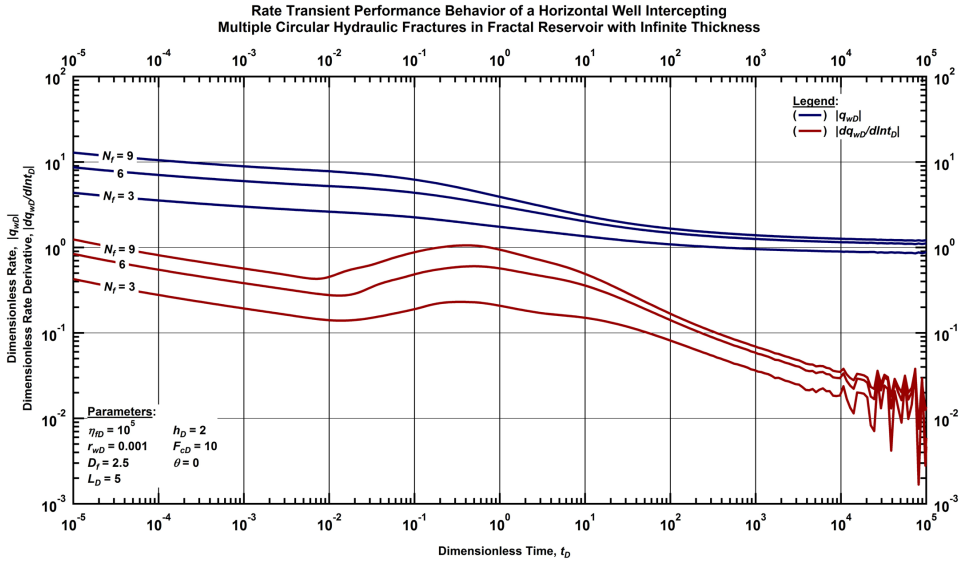

Figure G.16 — Log-log plot of the dimensionless rate and dimensionless rate derivative functions for a horizontal well intercepting N_f circular transverse hydraulic fractures with intermediate conductivity in a fractal reservoir of infinite thickness with fixed fractal dimension (D_f=2.5) and conductivity index (θ=0) (constant-pressure case).

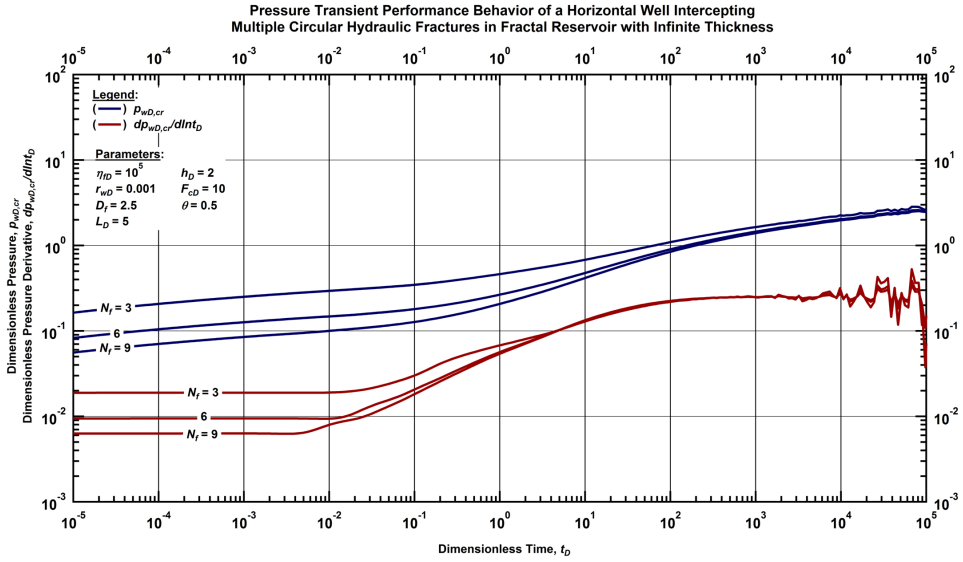

Figure G.17 — Log-log plot of the dimensionless pressure and dimensionless pressure derivative functions for a horizontal well intercepting N_f circular transverse hydraulic fractures with intermediate conductivity in a fractal reservoir of infinite thickness with fixed fractal dimension (D_f=2.5) and conductivity index (θ=0.5) (constant-rate case).

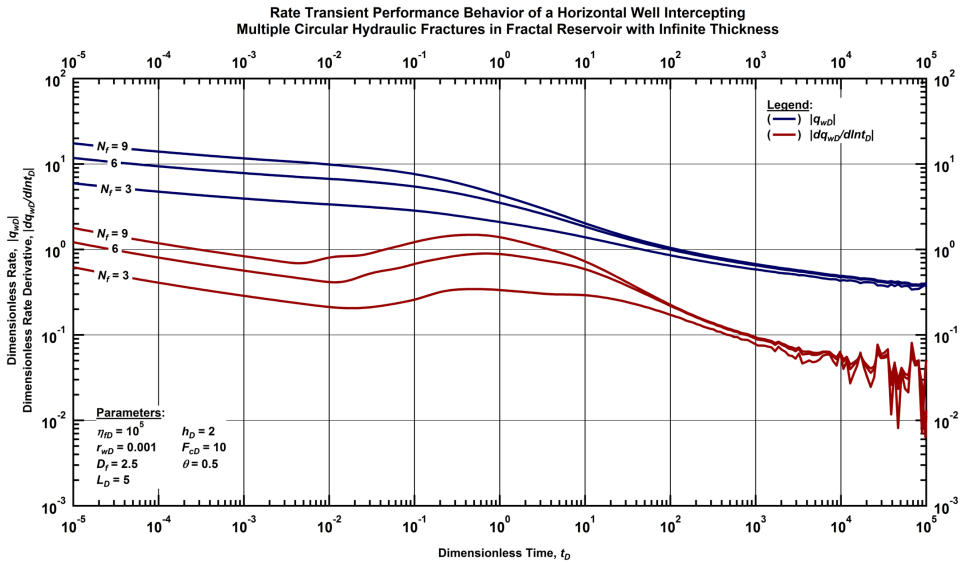

Figure G.18 — Log-log plot of the dimensionless rate and dimensionless rate derivative functions for a horizontal well intercepting N_f circular transverse hydraulic fractures with intermediate conductivity in a fractal reservoir of infinite thickness with fixed fractal dimension (D_f=2.5) and conductivity index (θ=0.5) (constant-pressure case).

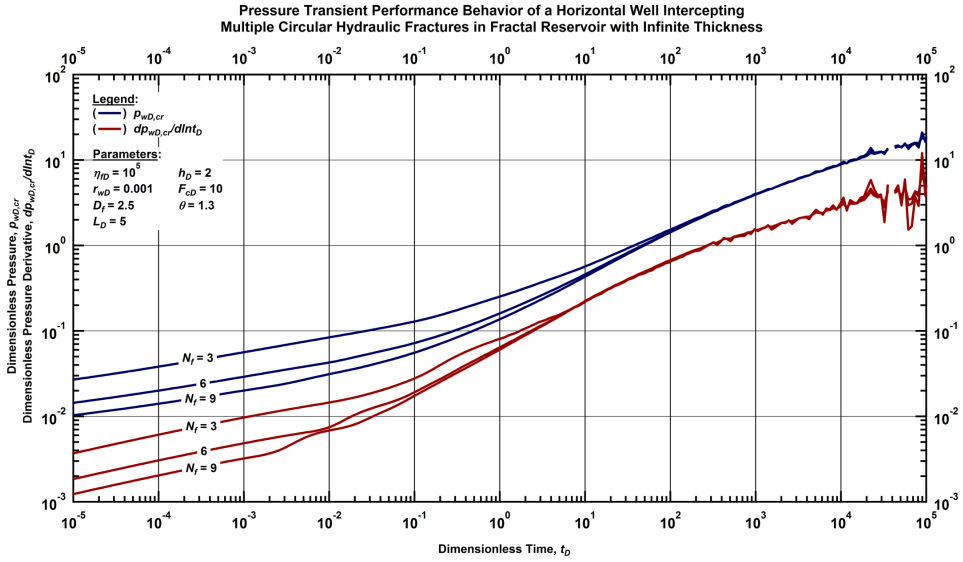

Figure G.19 — Log-log plot of the dimensionless pressure and dimensionless pressure derivative functions for a horizontal well intercepting N_f circular transverse hydraulic fractures with intermediate conductivity in a fractal reservoir of infinite thickness with fixed fractal dimension (D_f=2.5) and conductivity index (θ=1.3) (constant-rate case).

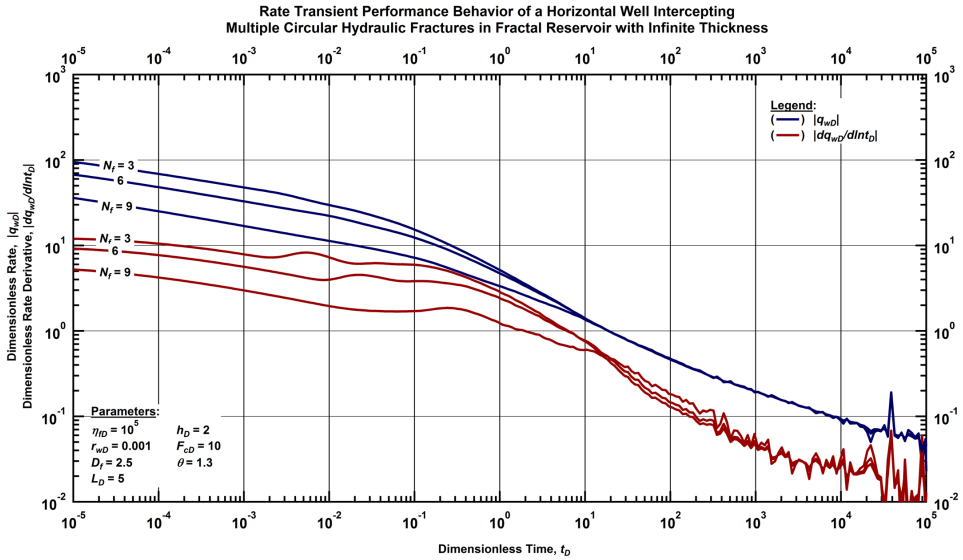

Figure G.20 — Log-log plot of the dimensionless rate and dimensionless rate derivative functions for a horizontal well intercepting N_f circular transverse hydraulic fractures with intermediate conductivity in a fractal reservoir of infinite thickness with fixed fractal dimension (D_f=2.5) and conductivity index (θ=1.3) (constant-pressure case).

Circular Transverse Fractures — Low Conductivity

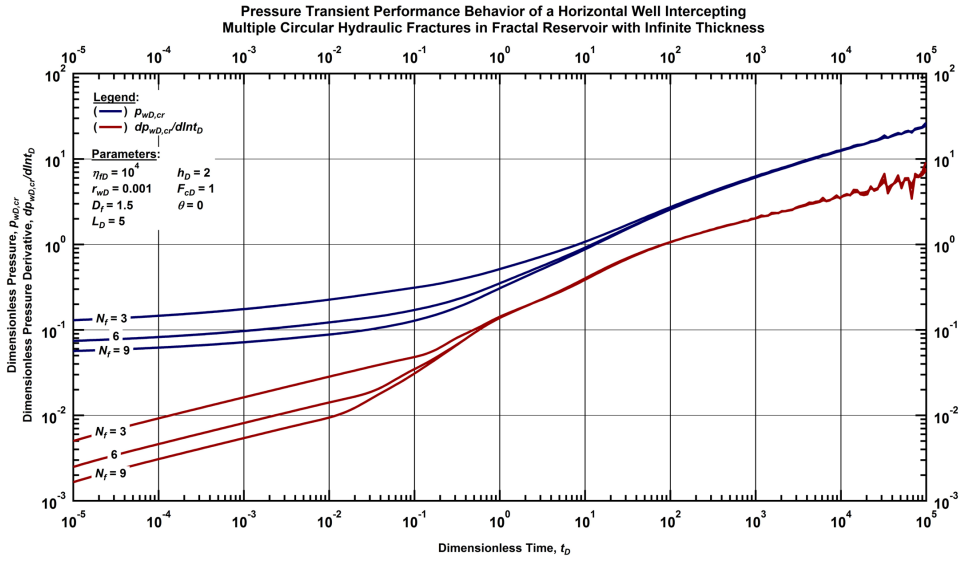

Figure G.21 — Log-log plot of the dimensionless pressure and dimensionless pressure derivative functions for a horizontal well intercepting N_f circular transverse hydraulic fractures with low conductivity in a fractal reservoir of infinite thickness with fixed fractal dimension (D_f=1.5) and conductivity index (θ=0) (constant-rate case).

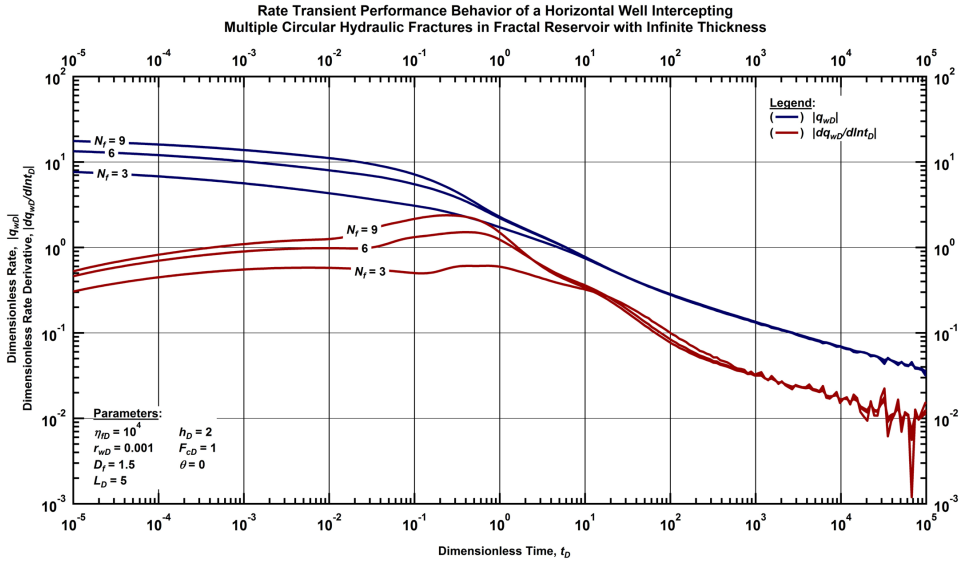

Figure G.22 — Log-log plot of the dimensionless rate and dimensionless rate derivative functions for a horizontal well intercepting N_f circular transverse hydraulic fractures with low conductivity in a fractal reservoir of infinite thickness with fixed fractal dimension (D_f=1.5) and conductivity index (θ=0) (constant-pressure case).

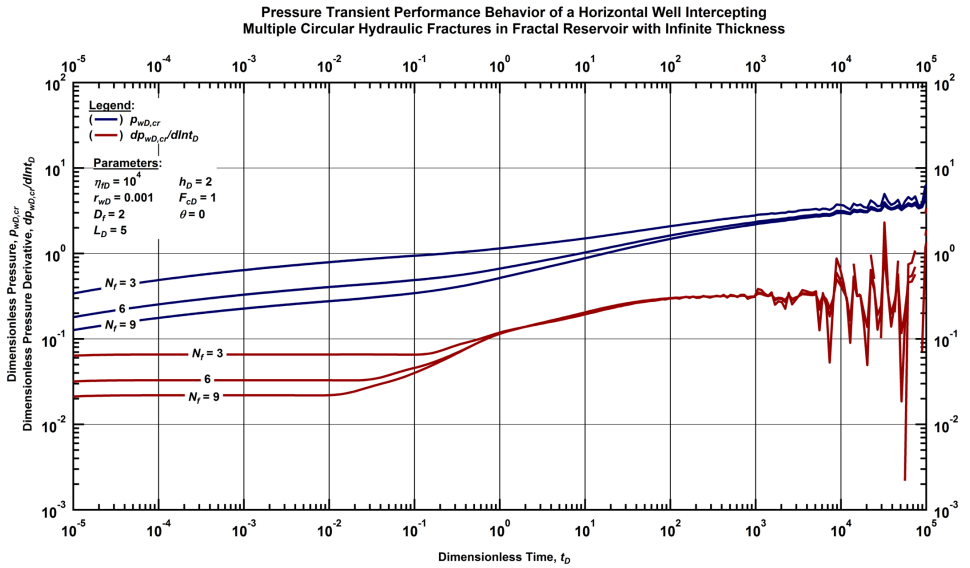

Figure G.23 — Log-log plot of the dimensionless pressure and dimensionless pressure derivative functions for a horizontal well intercepting N_f circular transverse hydraulic fractures with low conductivity in a fractal reservoir of infinite thickness with fixed fractal dimension (D_f=2) and conductivity index (θ=0) (constant-rate case).

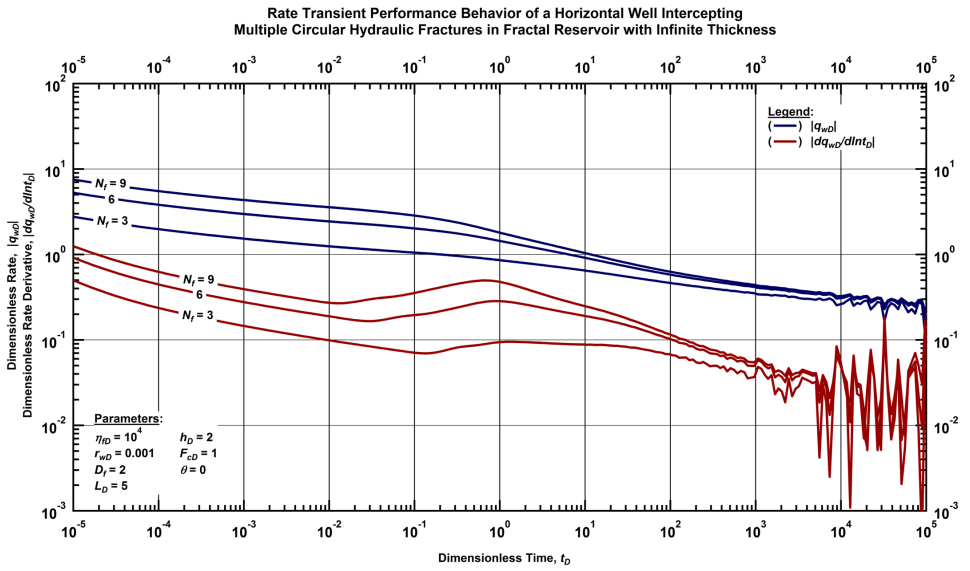

Figure G.24 — Log-log plot of the dimensionless rate and dimensionless rate derivative functions for a horizontal well intercepting N_f circular transverse hydraulic fractures with low conductivity in a fractal reservoir of infinite thickness with fixed fractal dimension (D_f=2) and conductivity index (θ=0) (constant- pressure case).

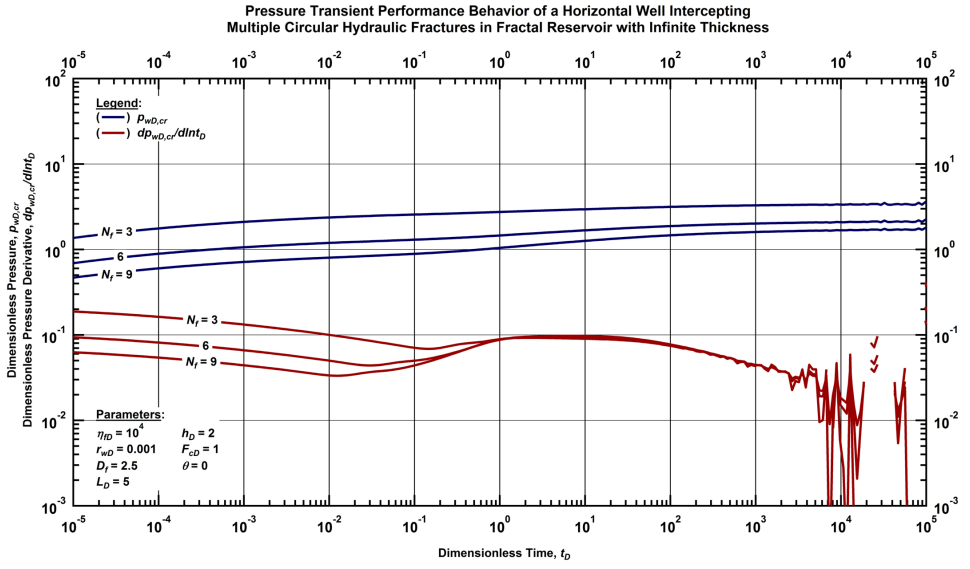

Figure G.25 — Log-log plot of the dimensionless pressure and dimensionless pressure derivative functions for a horizontal well intercepting N_f circular transverse hydraulic fractures with low conductivity in a fractal reservoir of infinite thickness with fixed fractal dimension (D_f=2.5) and conductivity index (θ=0) (constant-rate case).

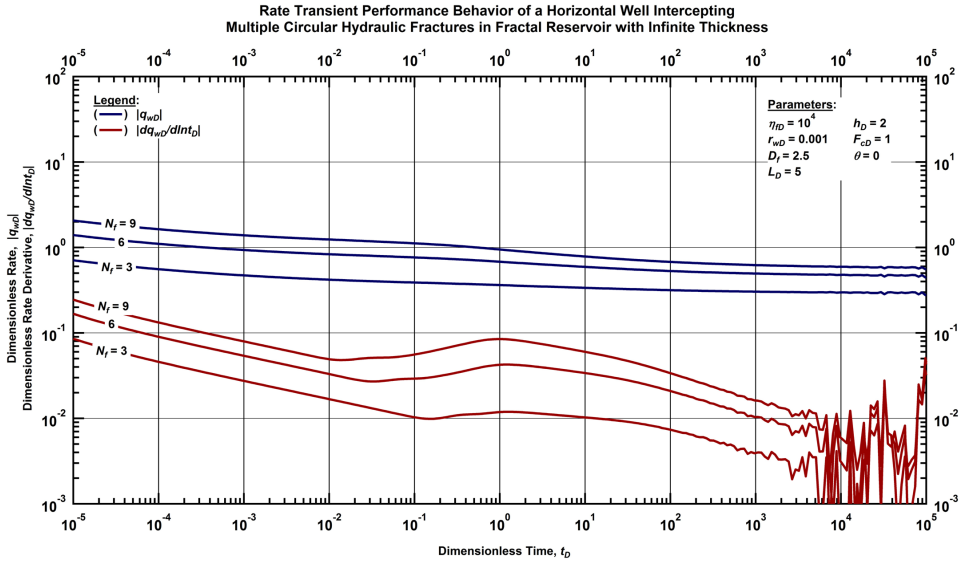

Figure G.26 — Log-log plot of the dimensionless rate and dimensionless rate derivative functions for a horizontal well intercepting N_f circular transverse hydraulic fractures with low conductivity in a fractal reservoir of infinite thickness with fixed fractal dimension (D_f=2.5) and conductivity index (θ=0) (constant-pressure case).

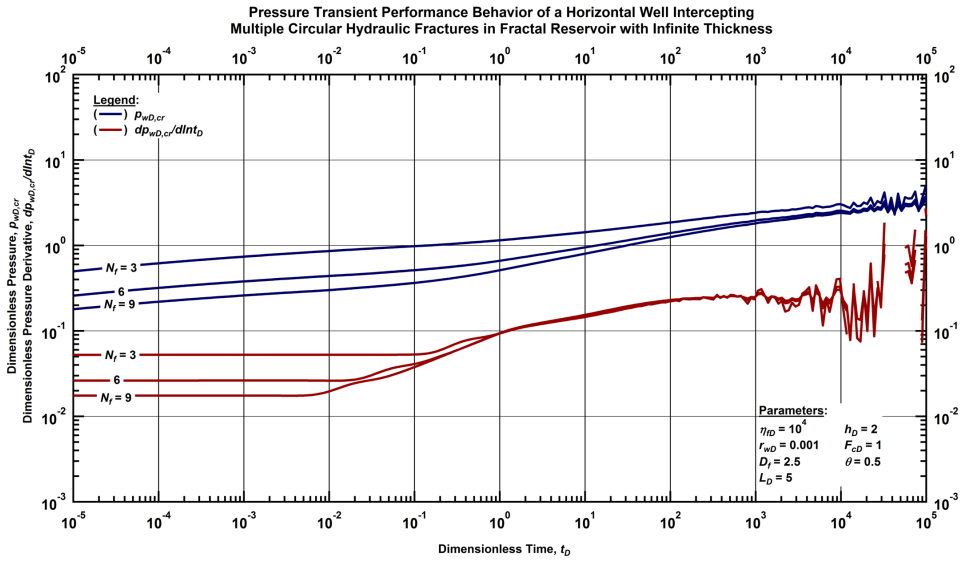

Figure G.27 — Log-log plot of the dimensionless pressure and dimensionless pressure derivative functions for a horizontal well intercepting N_f circular transverse hydraulic fractures with low conductivity in a fractal reservoir of infinite thickness with fixed fractal dimension (D_f=2.5) and conductivity index (θ=0.5) (constant-rate case).

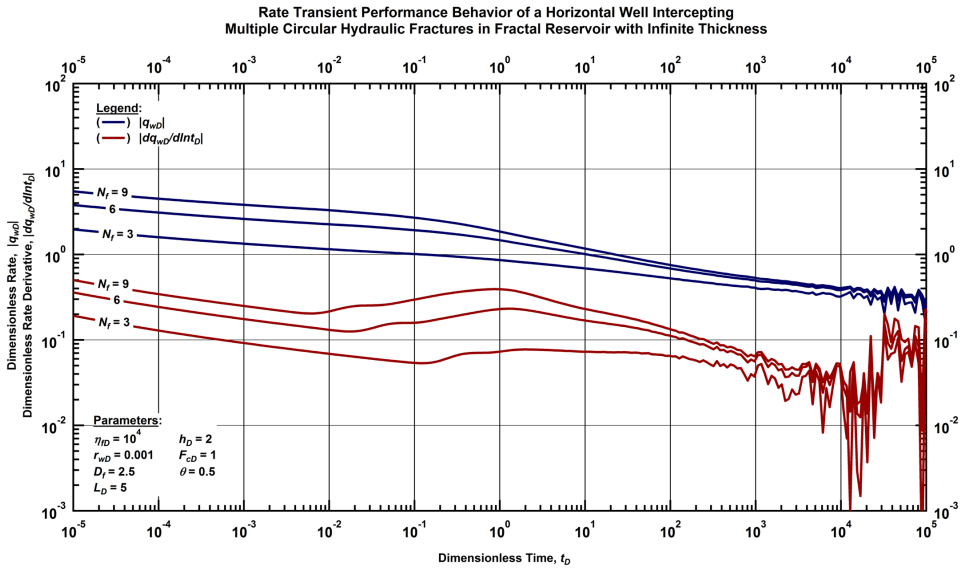

Figure G.28 — Log-log plot of the dimensionless rate and dimensionless rate derivative functions for a horizontal well intercepting N_f circular transverse hydraulic fractures with low conductivity in a fractal reservoir of infinite thickness with fixed fractal dimension (D_f=2.5) and conductivity index (θ=0.5) (constant-pressure case).

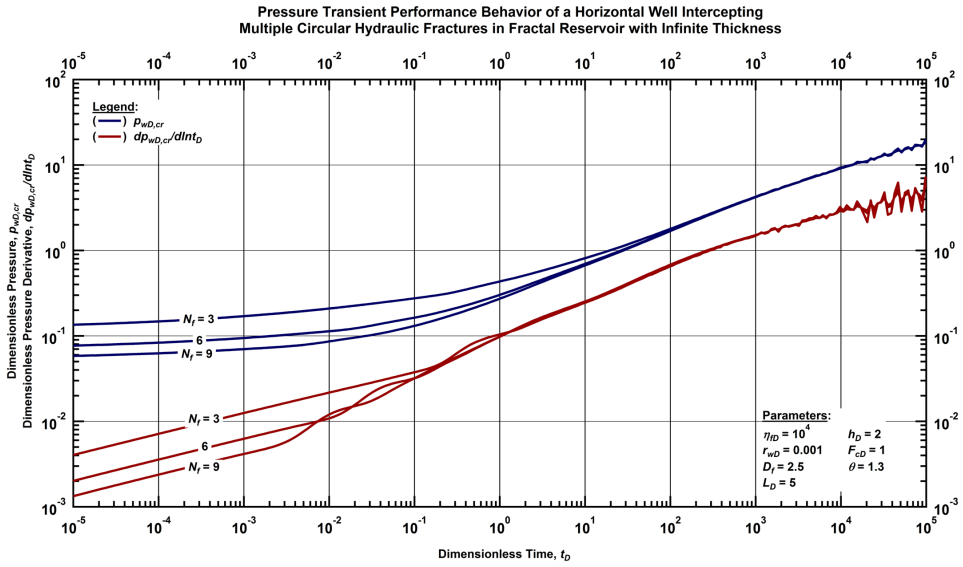

Figure G.29 — Log-log plot of the dimensionless pressure and dimensionless pressure derivative functions for a horizontal well intercepting N_f circular transverse hydraulic fractures with low conductivity in a fractal reservoir of infinite thickness with fixed fractal dimension (D_f=2.5) and conductivity index (θ=1.3) (constant-rate case).

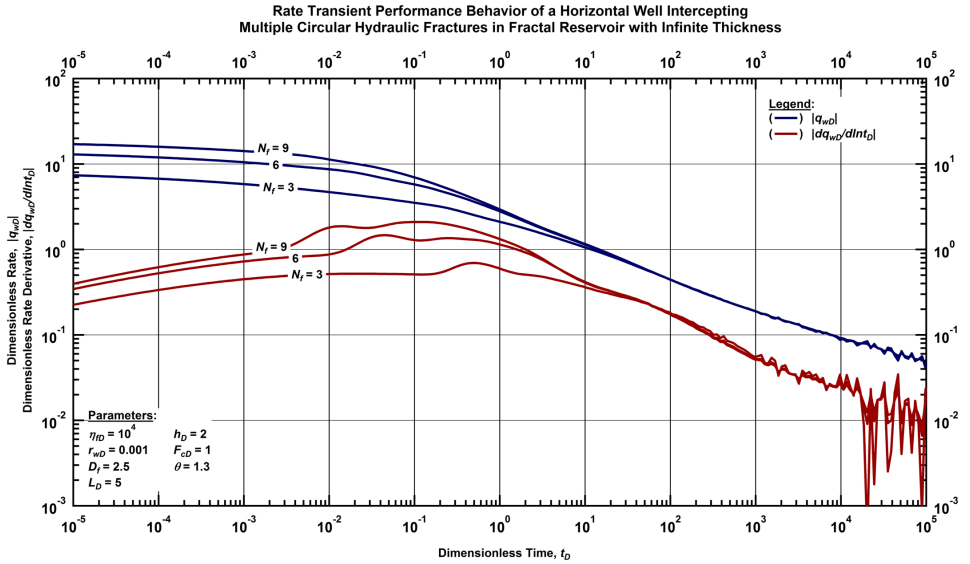

Figure G.30 — Log-log plot of the dimensionless rate and dimensionless rate derivative functions for a horizontal well intercepting N_f circular transverse hydraulic fractures with low conductivity in a fractal reservoir of infinite thickness with fixed fractal dimension (D_f=2.5) and conductivity index (θ=1.3) (constant-pressure case).

Rectangular Transverse Fractures — High Conductivity

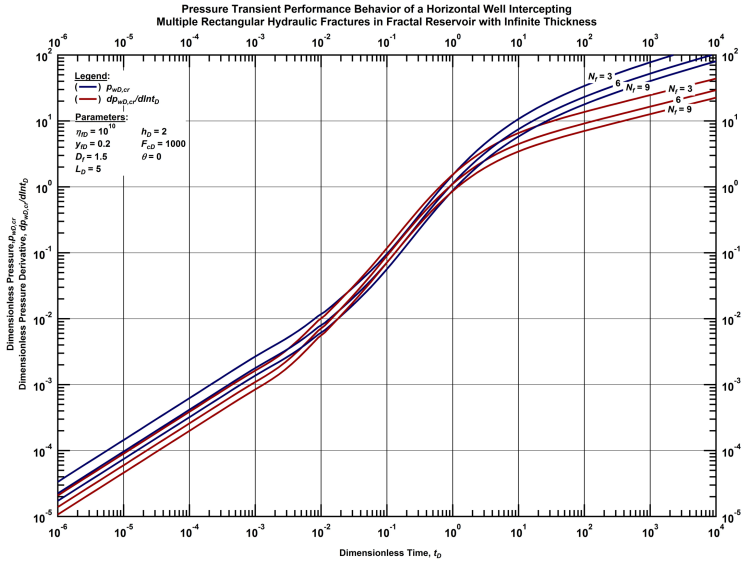

Figure G.31 — Log-log plot of the dimensionless pressure and dimensionless pressure derivative functions for a horizontal well intercepting N_f rectangular longitudinal hydraulic fractures with high conductivity in a fractal reservoir of infinite thickness with fixed fractal dimension (D_f=1.5) and conductivity index (θ=0) (constant-rate case).

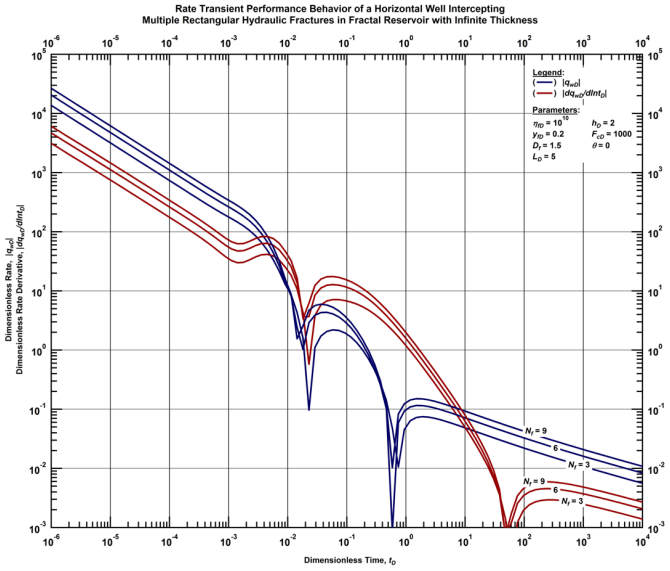

Figure G.32 — Log-log plot of the dimensionless rate and dimensionless rate derivative functions for a horizontal well intercepting N_f rectangular longitudinal hydraulic fractures with high conductivity in a fractal reservoir of infinite thickness with fixed fractal dimension (D_f=1.5) and conductivity index (θ=0) (constant-pressure case).

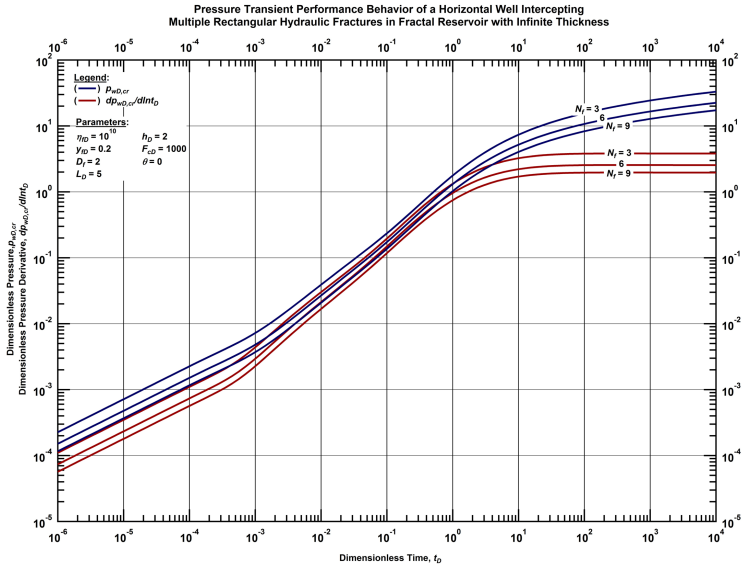

Figure G.33 — Log-log plot of the dimensionless pressure and dimensionless pressure derivative functions for a horizontal well intercepting N_f rectangular longitudinal hydraulic fractures with high conductivity in a fractal reservoir of infinite thickness with fixed fractal dimension (D_f=2) and conductivity index (θ=0) (constant-rate case).

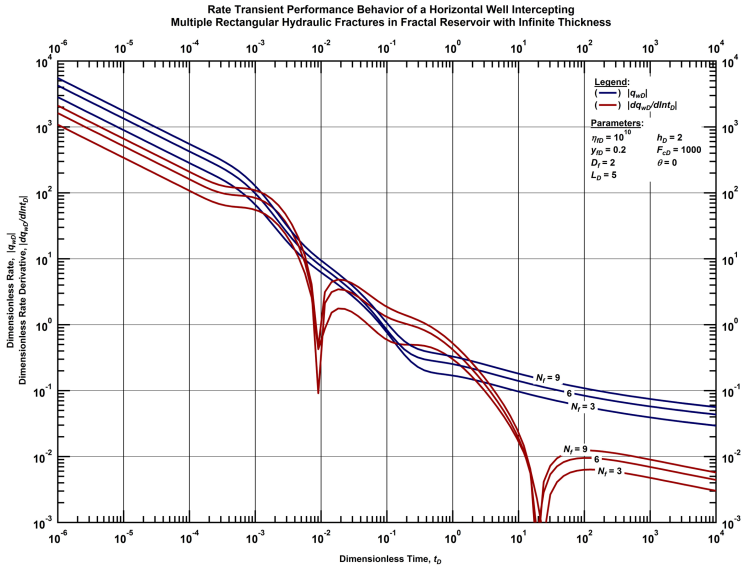

Figure G.34 — Log-log plot of the dimensionless rate and dimensionless rate derivative functions for a horizontal well intercepting N_f rectangular longitudinal hydraulic fractures with high conductivity in a fractal reservoir of infinite thickness with fixed fractal dimension (D_f=2) and conductivity index (θ=0) (constant- pressure case).

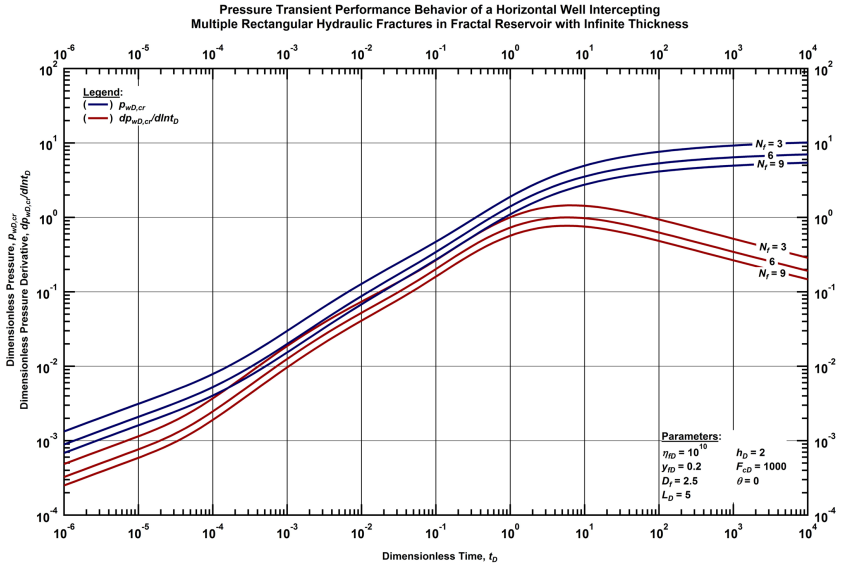

Figure G.35 — Log-log plot of the dimensionless pressure and dimensionless pressure derivative functions for a horizontal well intercepting N_f rectangular longitudinal hydraulic fractures with high conductivity in a fractal reservoir of infinite thickness with fixed fractal dimension (D_f=2.5) and conductivity index (θ=0) (constant-rate case).

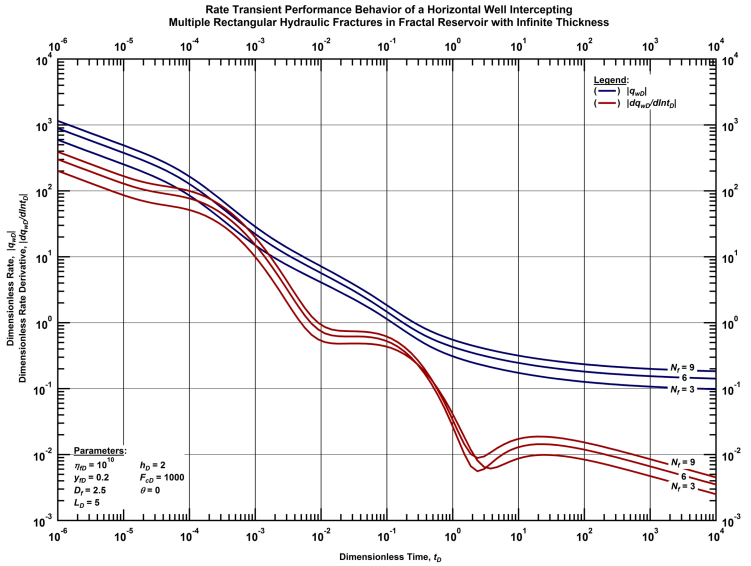

Figure G.36 — Log-log plot of the dimensionless rate and dimensionless rate derivative functions for a horizontal well intercepting N_f rectangular longitudinal hydraulic fractures with high conductivity in a fractal reservoir of infinite thickness with fixed fractal dimension (D_f=2.5) and conductivity index (θ=0) (constant-pressure case).

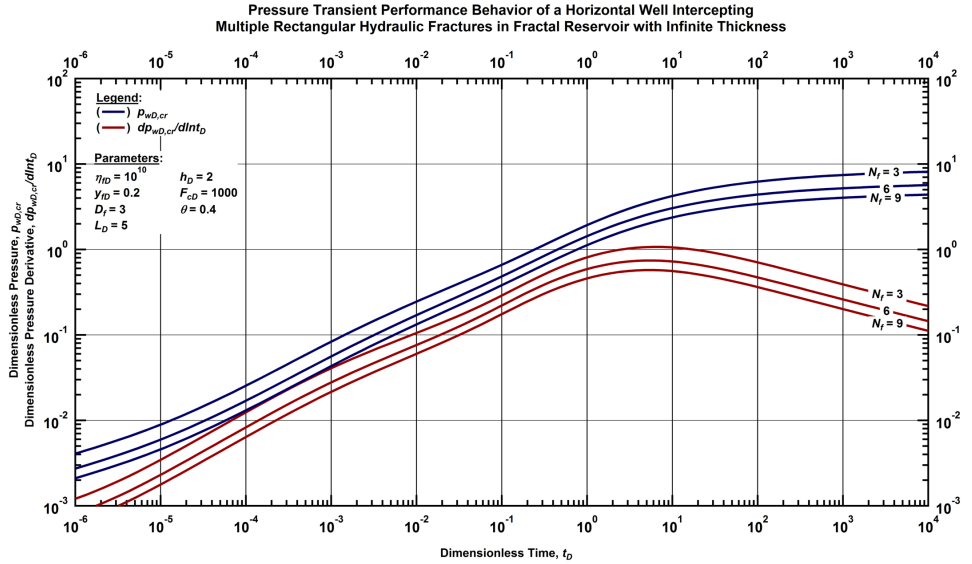

Figure G.37 — Log-log plot of the dimensionless pressure and dimensionless pressure derivative functions for a horizontal well intercepting N_f rectangular longitudinal hydraulic fractures with high conductivity in a fractal reservoir of infinite thickness with fixed fractal dimension (D_f=3) and conductivity index (θ=0.4) (constant-rate case).

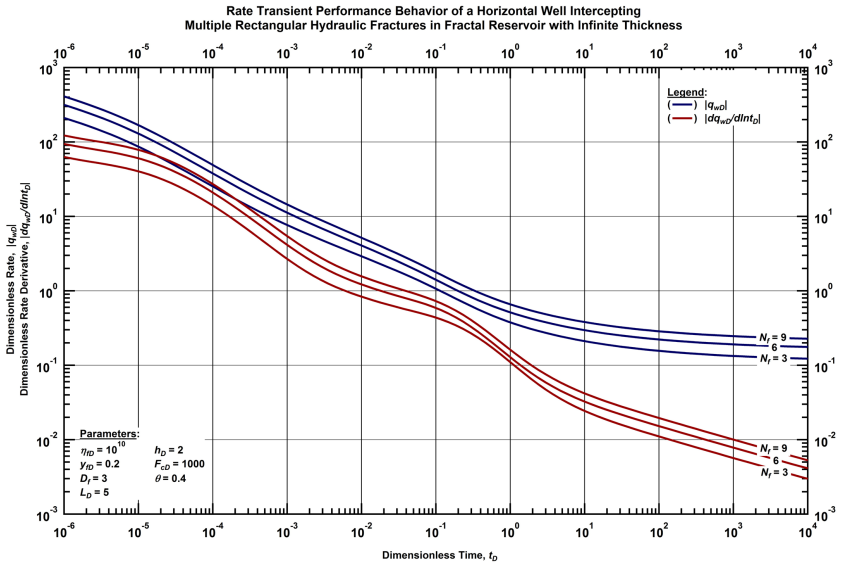

Figure G.38 — Log-log plot of the dimensionless rate and dimensionless rate derivative functions for a horizontal well intercepting N_f rectangular longitudinal hydraulic fractures with high conductivity in a fractal reservoir of infinite thickness with fixed fractal dimension (D_f=3) and conductivity index (θ=0.4) (constant-pressure case).

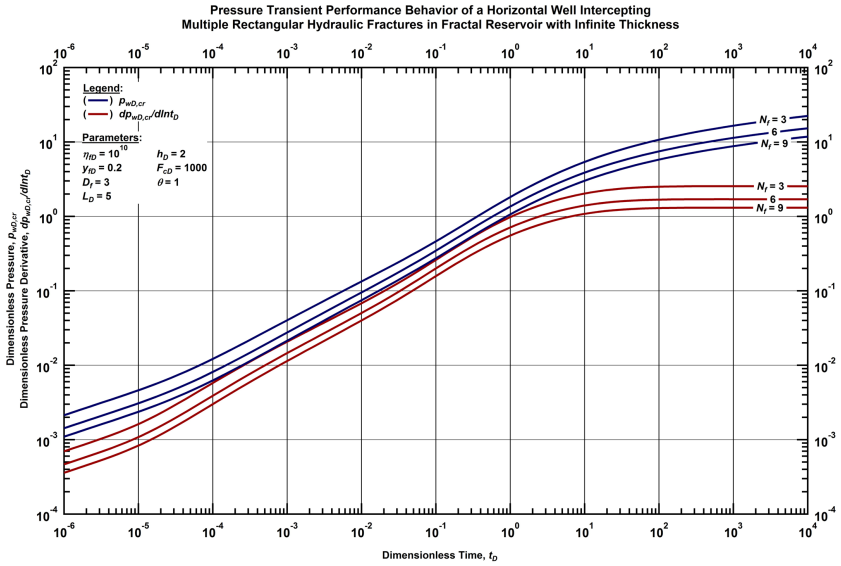

Figure G.39 — Log-log plot of the dimensionless pressure and dimensionless pressure derivative functions for a horizontal well intercepting N_f rectangular longitudinal hydraulic fractures with high conductivity in a fractal reservoir of infinite thickness with fixed fractal dimension (D_f=3) and conductivity index (θ=1) (constant-rate case).

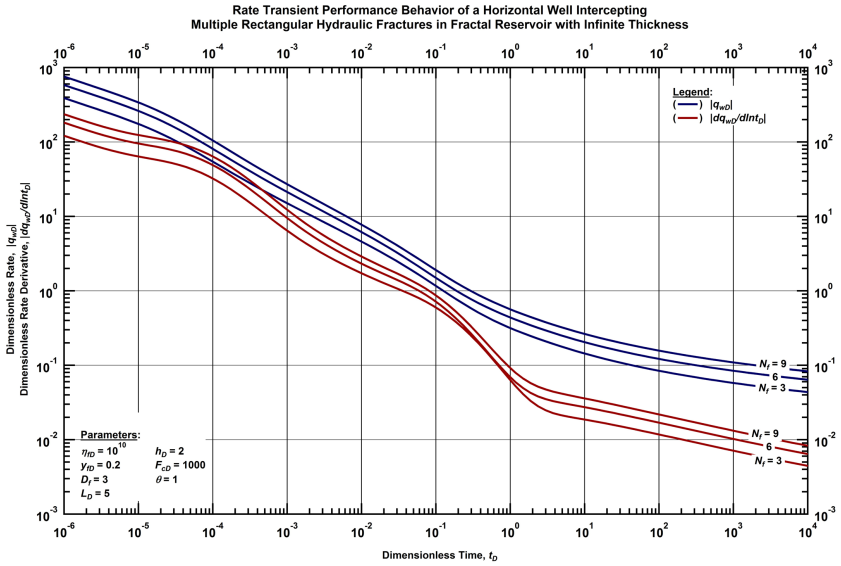

Figure G.40 — Log-log plot of the dimensionless rate and dimensionless rate derivative functions for a horizontal well intercepting N_f rectangular longitudinal hydraulic fractures with high conductivity in a fractal reservoir of infinite thickness with fixed fractal dimension (D_f=3) and conductivity index (θ=1) (constant- pressure case).

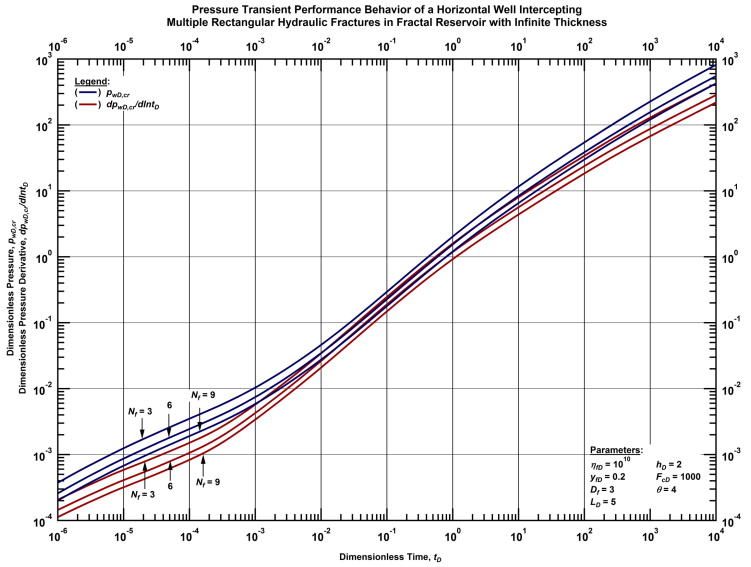

Figure G.41 — Log-log plot of the dimensionless pressure and dimensionless pressure derivative functions for a horizontal well intercepting N_f rectangular longitudinal hydraulic fractures with high conductivity in a fractal reservoir of infinite thickness with fixed fractal dimension (D_f=3) and conductivity index (θ=4) (constant-rate case).

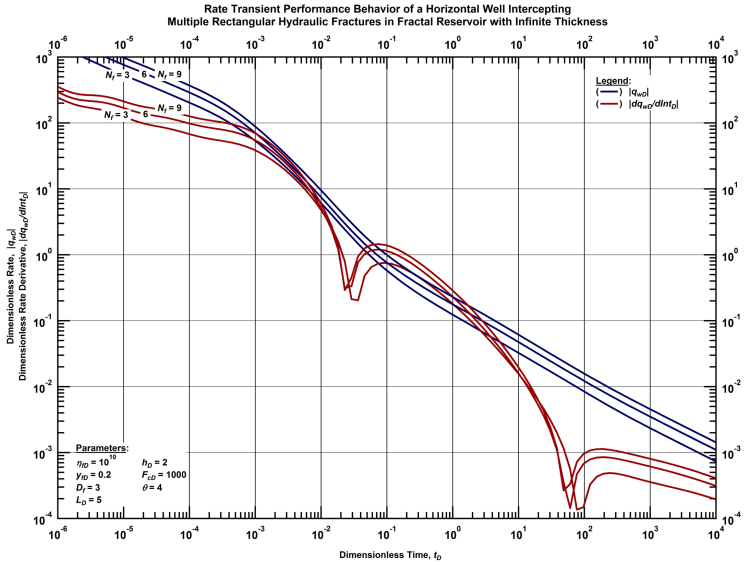

Figure G.42 — Log-log plot of the dimensionless rate and dimensionless rate derivative functions for a horizontal well intercepting N_f rectangular longitudinal hydraulic fractures with high conductivity in a fractal reservoir of infinite thickness with fixed fractal dimension (D_f=3) and conductivity index (θ=4) (constant- pressure case).

Rectangular Transverse Fractures — Intermediate Conductivity

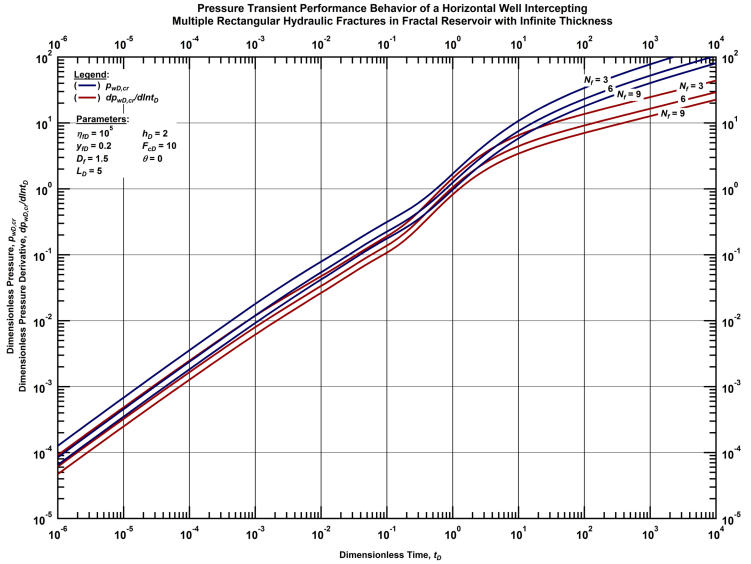

Figure G.43 — Log-log plot of the dimensionless pressure and dimensionless pressure derivative functions for a horizontal well intercepting N_f rectangular longitudinal hydraulic fractures with intermediate conductivity in a fractal reservoir of infinite thickness with fixed fractal dimension (D_f=1.5) and conductivity index (θ=0) (constant-rate case).

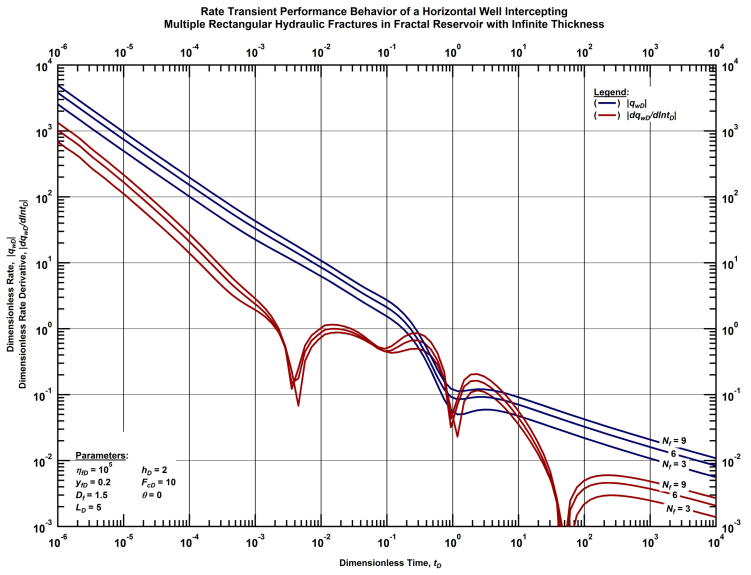

Figure G.44 — Log-log plot of the dimensionless rate and dimensionless rate derivative functions for a horizontal well intercepting N_f rectangular longitudinal hydraulic fractures with intermediate conductivity in a fractal reservoir of infinite thickness with fixed fractal dimension (D_f=1.5) and conductivity index (θ=0) (constant-pressure case).

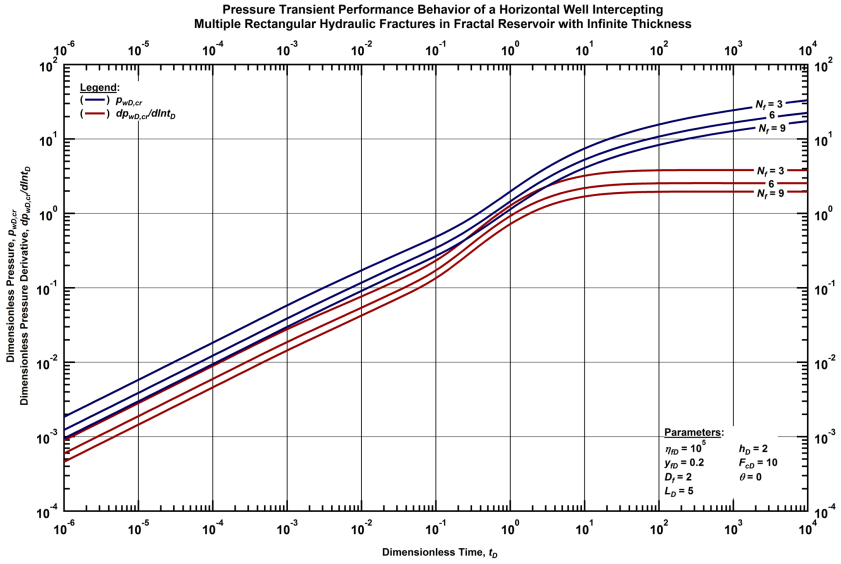

Figure G.45 — Log-log plot of the dimensionless pressure and dimensionless pressure derivative functions for a horizontal well intercepting N_f rectangular longitudinal hydraulic fractures with intermediate conductivity in a fractal reservoir of infinite thickness with fixed fractal dimension (D_f=2) and conductivity index (θ=0) (constant-rate case).

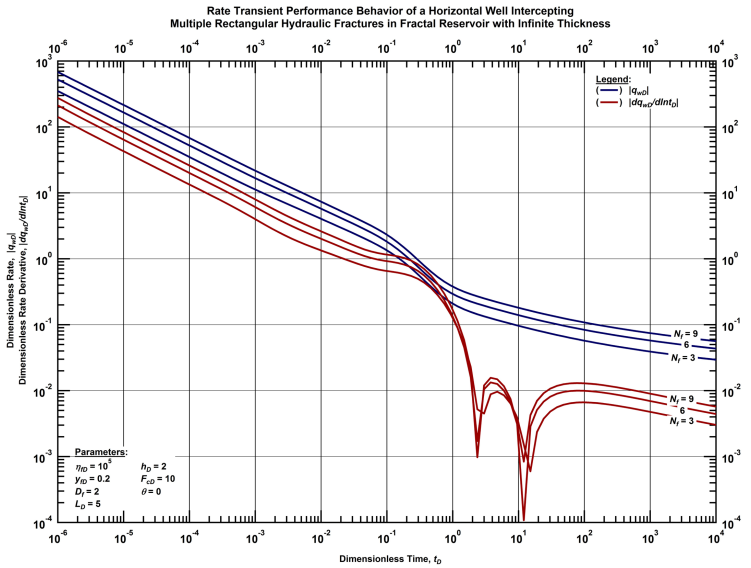

Figure G.46 — Log-log plot of the dimensionless rate and dimensionless rate derivative functions for a horizontal well intercepting N_f rectangular longitudinal hydraulic fractures with intermediate conductivity in a fractal reservoir of infinite thickness with fixed fractal dimension (D_f=2) and conductivity index (θ=0) (constant-pressure case).

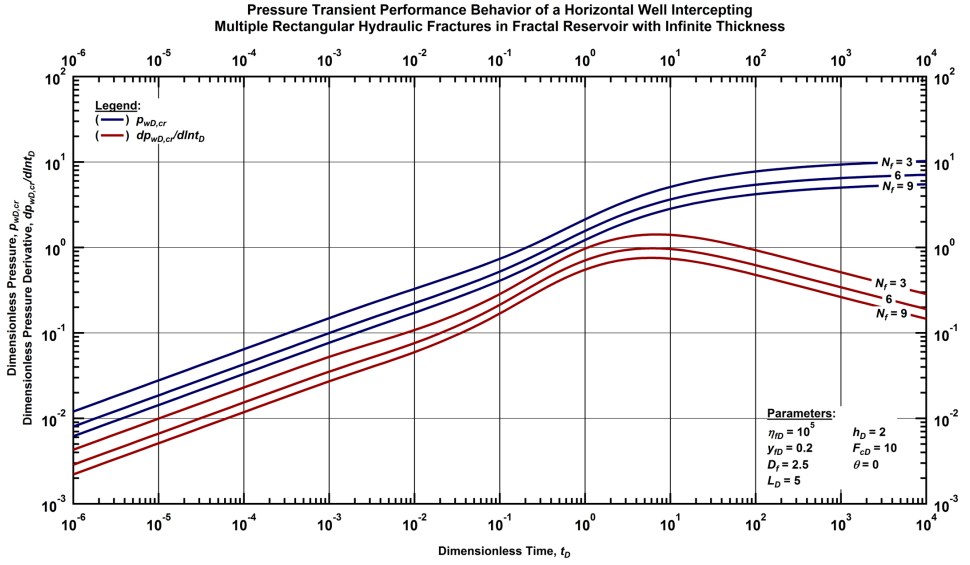

Figure G.47 — Log-log plot of the dimensionless pressure and dimensionless pressure derivative functions for a horizontal well intercepting N_f rectangular longitudinal hydraulic fractures with intermediate conductivity in a fractal reservoir of infinite thickness with fixed fractal dimension (D_f=2.5) and conductivity index (θ=0) (constant-rate case).

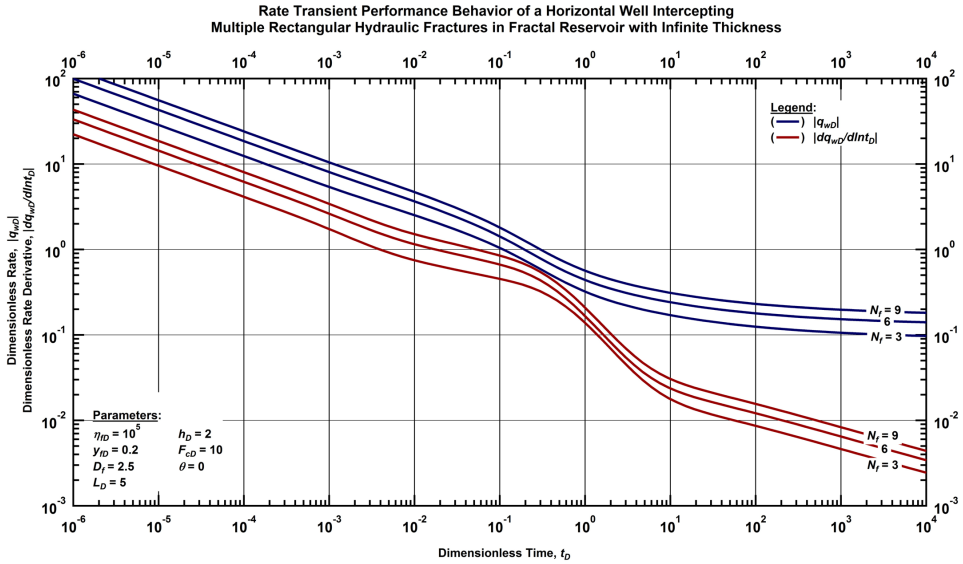

Figure G.48 — Log-log plot of the dimensionless rate and dimensionless rate derivative functions for a horizontal well intercepting N_f rectangular longitudinal hydraulic fractures with intermediate conductivity in a fractal reservoir of infinite thickness with fixed fractal dimension (D_f=2.5) and conductivity index (θ=0) (constant-pressure case).

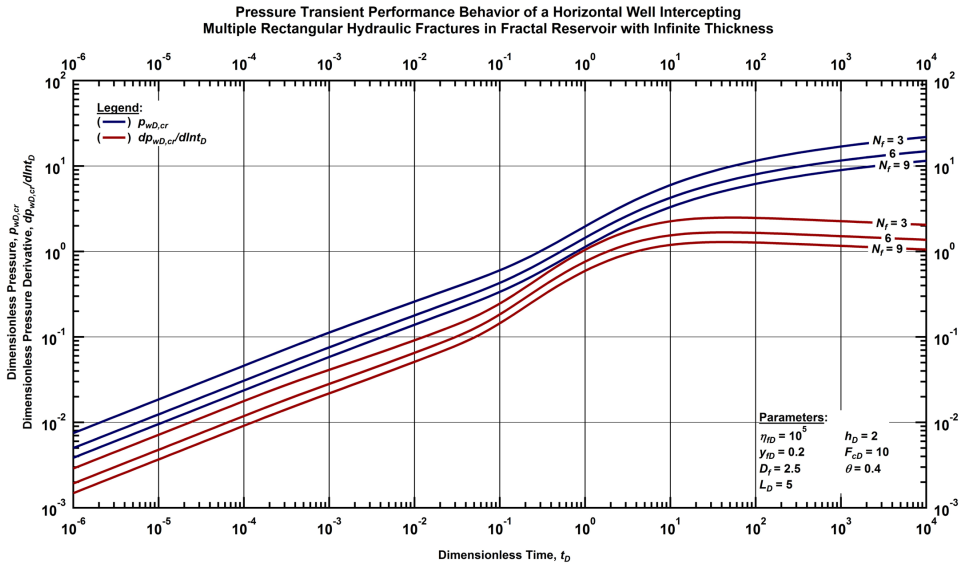

Figure G.49 — Log-log plot of the dimensionless pressure and dimensionless pressure derivative functions for a horizontal well intercepting N_f rectangular longitudinal hydraulic fractures with intermediate conductivity in a fractal reservoir of infinite thickness with fixed fractal dimension (D_f=2.5) and conductivity index (θ=0.4) (constant-rate case).

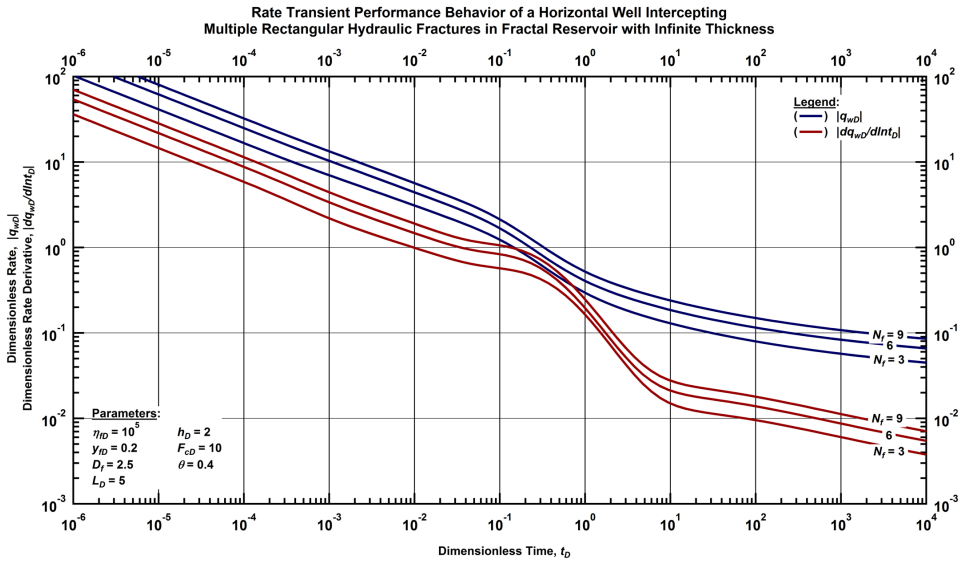

Figure G.50 — Log-log plot of the dimensionless rate and dimensionless rate derivative functions for a horizontal well intercepting N_f rectangular longitudinal hydraulic fractures with intermediate conductivity in a fractal reservoir of infinite thickness with fixed fractal dimension (D_f=2.5) and conductivity index (θ=0.4) (constant-pressure case).

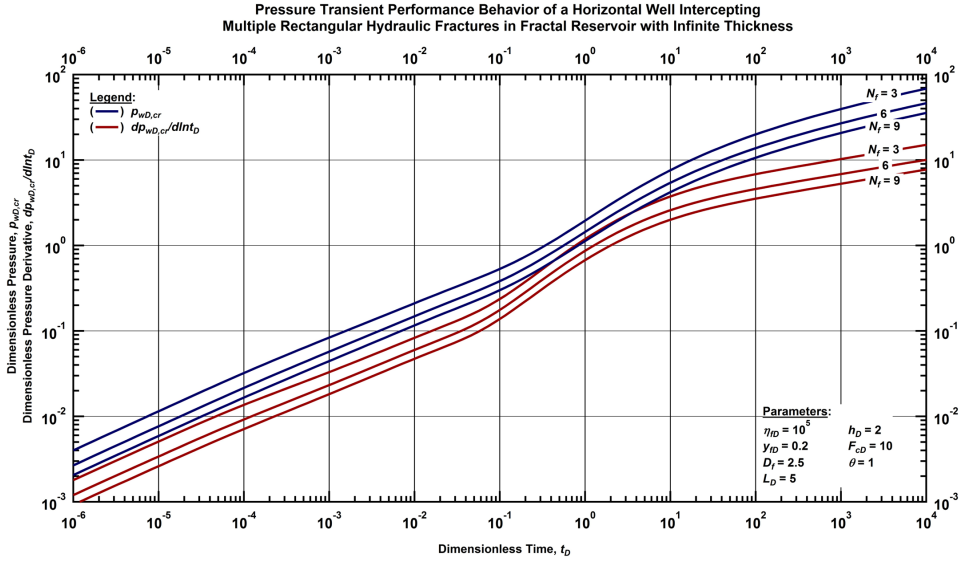

Figure G.51 — Log-log plot of the dimensionless pressure and dimensionless pressure derivative functions for a horizontal well intercepting N_f rectangular longitudinal hydraulic fractures with intermediate conductivity in a fractal reservoir of infinite thickness with fixed fractal dimension (D_f=2.5) and conductivity index (θ=1) (constant-rate case).

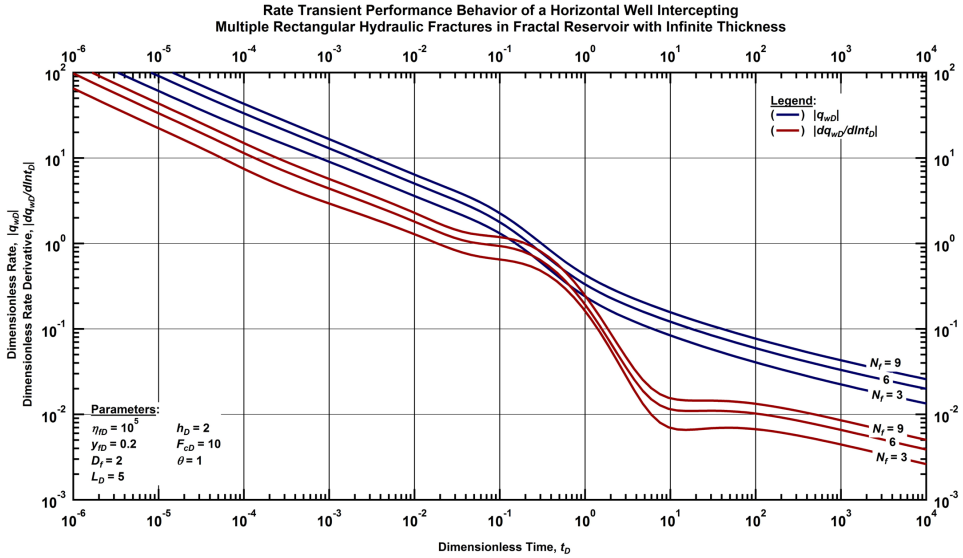

Figure G.52 — Log-log plot of the dimensionless rate and dimensionless rate derivative functions for a horizontal well intercepting N_f rectangular longitudinal hydraulic fractures with intermediate conductivity in a fractal reservoir of infinite thickness with fixed fractal dimension (D_f=2.5) and conductivity index (θ=1) (constant-pressure case).

Rectangular Transverse Fractures — Low Conductivity

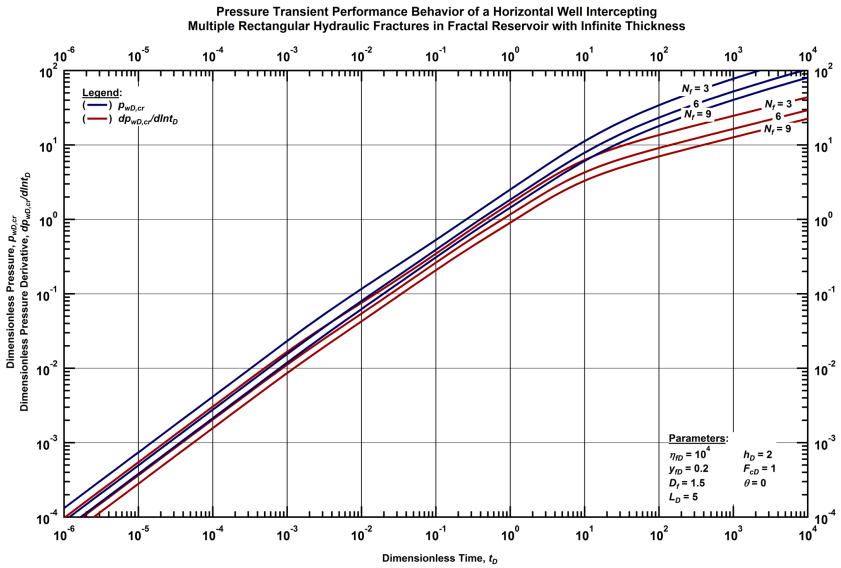

Figure G.53 — Log-log plot of the dimensionless pressure and dimensionless pressure derivative functions for a horizontal well intercepting N_f rectangular longitudinal hydraulic fractures with low conductivity in a fractal reservoir of infinite thickness with fixed fractal dimension (D_f=1.5) and conductivity index (θ=0) (constant-rate case).

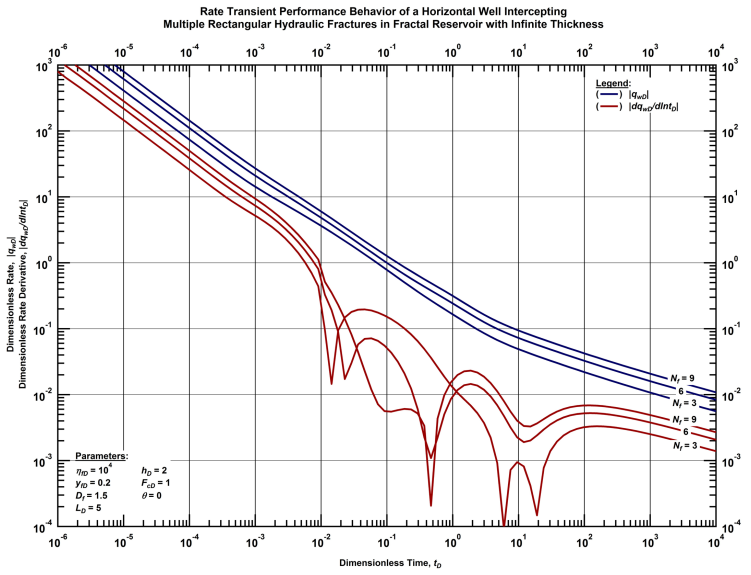

Figure G.54 — Log-log plot of the dimensionless rate and dimensionless rate derivative functions for a horizontal well intercepting N_f rectangular longitudinal hydraulic fractures with low conductivity in a fractal reservoir of infinite thickness with fixed fractal dimension (D_f=1.5) and conductivity index (θ=0) (constant-pressure case).

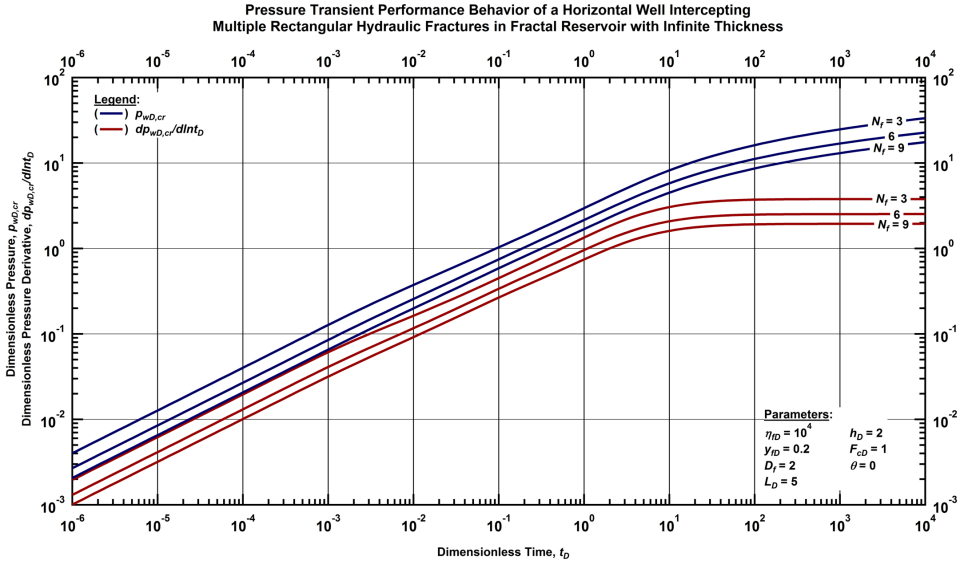

Figure G.55 — Log-log plot of the dimensionless pressure and dimensionless pressure derivative functions for a horizontal well intercepting N_f rectangular longitudinal hydraulic fractures with low conductivity in a fractal reservoir of infinite thickness with fixed fractal dimension (D_f=2) and conductivity index (θ=0) (constant-rate case).

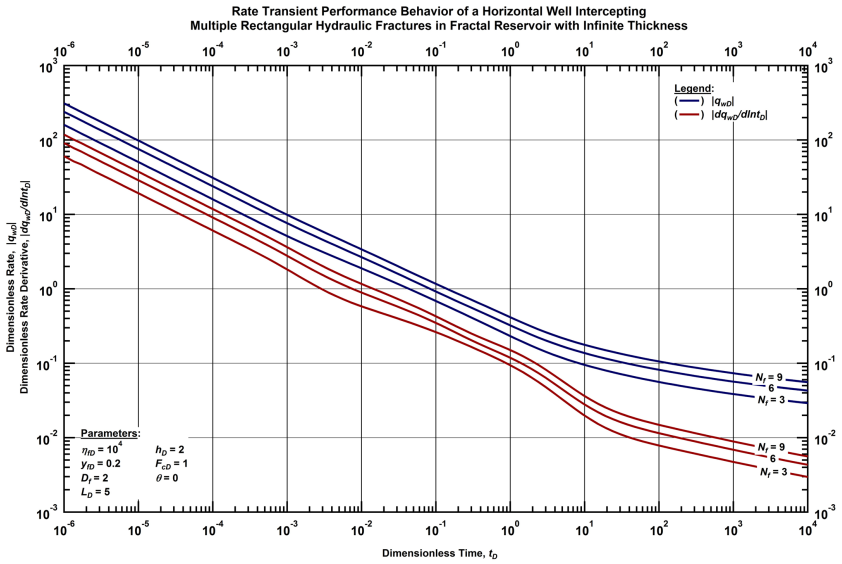

Figure G.56 — Log-log plot of the dimensionless rate and dimensionless rate derivative functions for a horizontal well intercepting N_f rectangular longitudinal hydraulic fractures with low conductivity in a fractal reservoir of infinite thickness with fixed fractal dimension (D_f=2) and conductivity index (θ=0) (constant- pressure case).

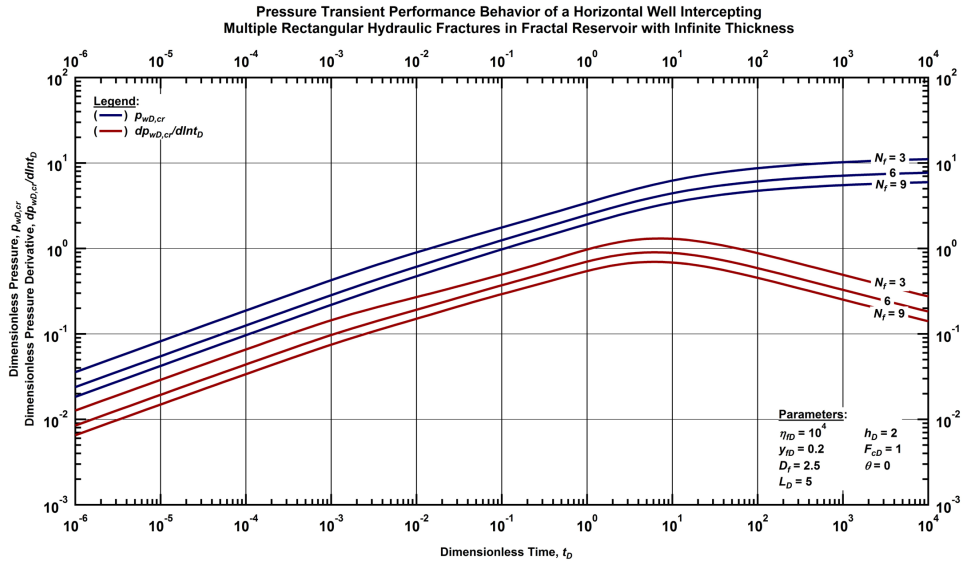

Figure G.57 — Log-log plot of the dimensionless pressure and dimensionless pressure derivative functions for a horizontal well intercepting N_f rectangular longitudinal hydraulic fractures with low conductivity in a fractal reservoir of infinite thickness with fixed fractal dimension (D_f=2.5) and conductivity index (θ=0) (constant-rate case).

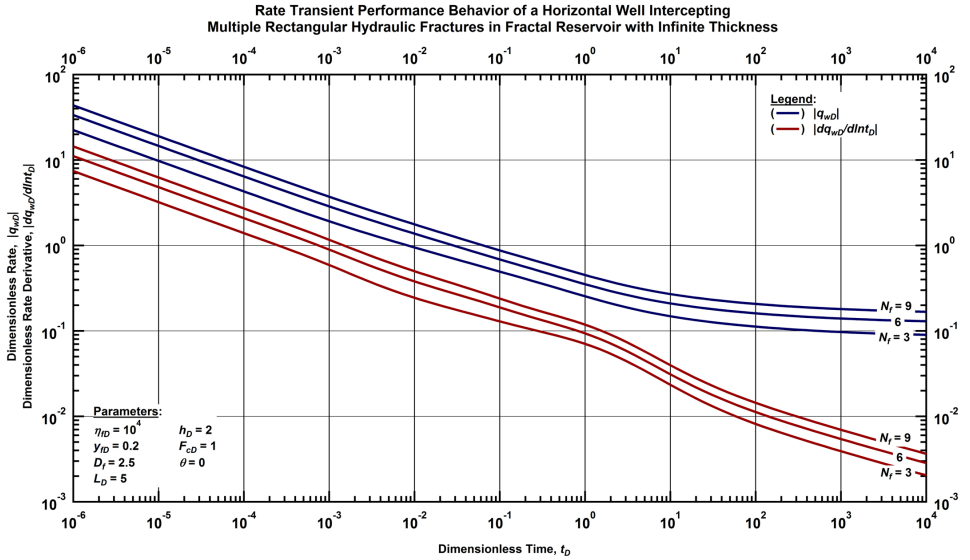

Figure G.58 — Log-log plot of the dimensionless rate and dimensionless rate derivative functions for a horizontal well intercepting N_f rectangular longitudinal hydraulic fractures with low conductivity in a fractal reservoir of infinite thickness with fixed fractal dimension (D_f=2.5) and conductivity index (θ=0) (constant-pressure case).

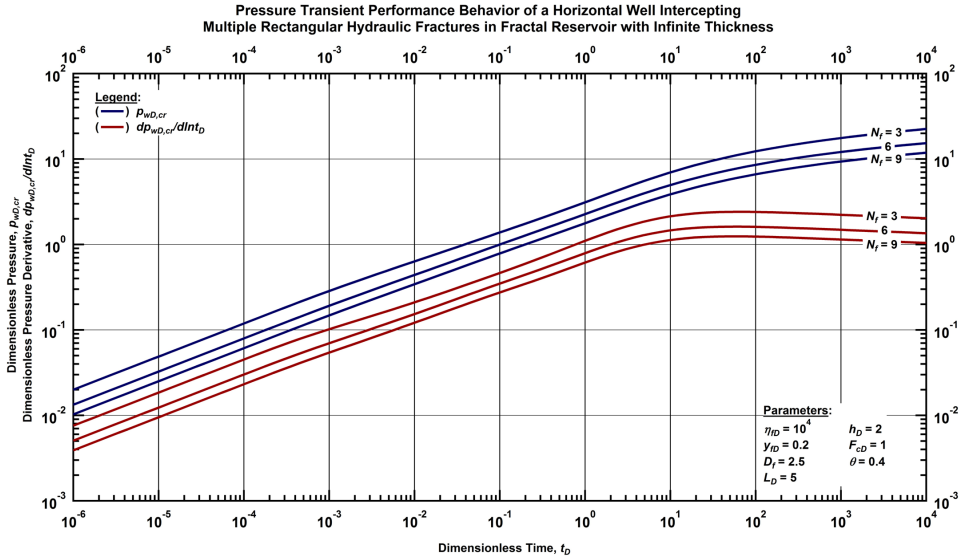

Figure G.59 — Log-log plot of the dimensionless pressure and dimensionless pressure derivative functions for a horizontal well intercepting N_f rectangular longitudinal hydraulic fractures with low conductivity in a fractal reservoir of infinite thickness with fixed fractal dimension (D_f=2.5) and conductivity index (θ=0.4) (constant-rate case).

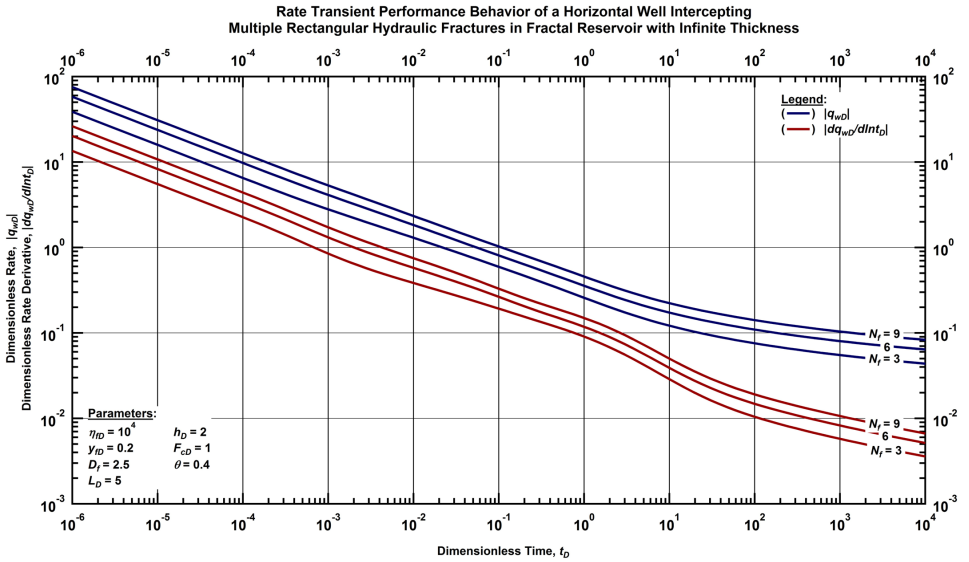

Figure G.60 — Log-log plot of the dimensionless rate and dimensionless rate derivative functions for a horizontal well intercepting N_f rectangular longitudinal hydraulic fractures with low conductivity in a fractal reservoir of infinite thickness with fixed fractal dimension (D_f=2.5) and conductivity index (θ=0.4) (constant-pressure case).

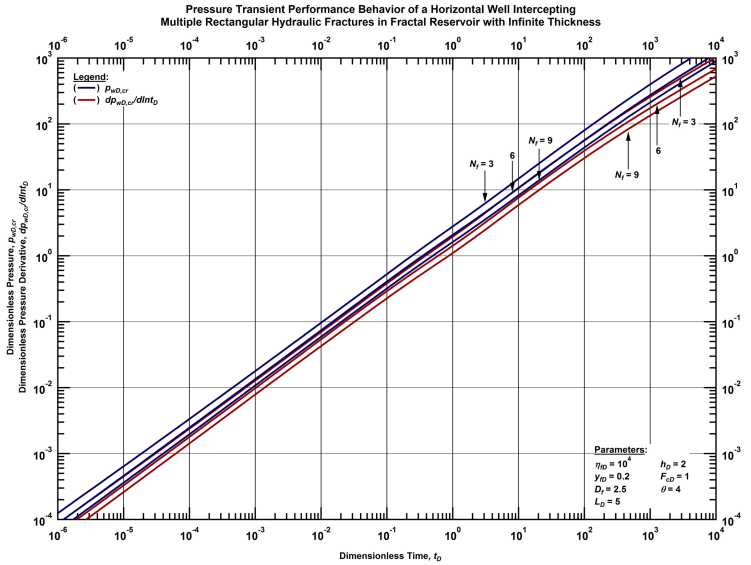

Figure G.61 — Log-log plot of the dimensionless pressure and dimensionless pressure derivative functions for a horizontal well intercepting N_f rectangular longitudinal hydraulic fractures with low conductivity in a fractal reservoir of infinite thickness with fixed fractal dimension (D_f=2.5) and conductivity index (θ=4) (constant-rate case).

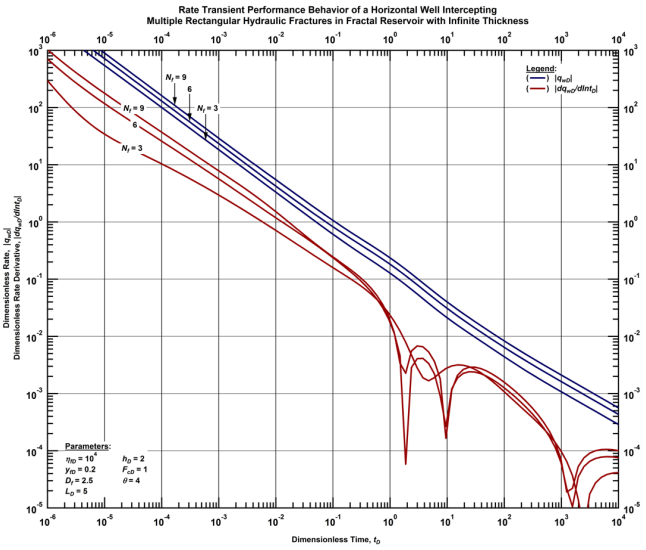

Figure G.62 — Log-log plot of the dimensionless rate and dimensionless rate derivative functions for a horizontal well intercepting N_f rectangular longitudinal hydraulic fractures with low conductivity in a fractal reservoir of infinite thickness with fixed fractal dimension (D_f=2.5) and conductivity index (θ=4) (constant-pressure case).

G.2. Horizontal well intercepting N_f fractures in a Fractal Reservoir with Finite Thickness

Circular Transverse Fractures — High Conductivity

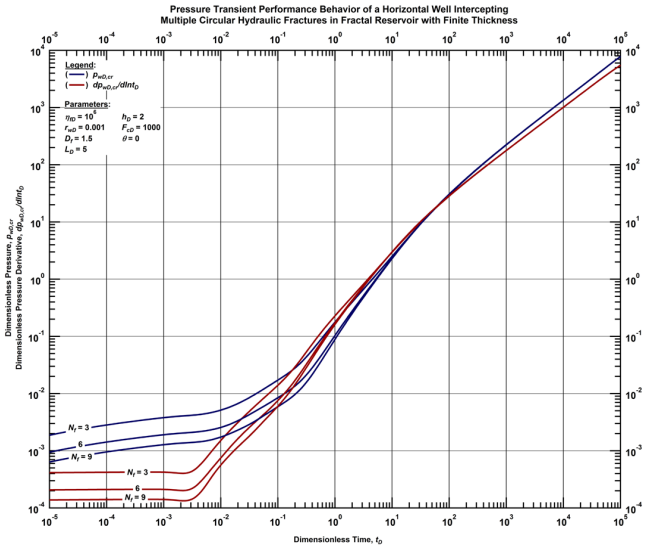

Figure G.63 — Log-log plot of the dimensionless pressure and dimensionless pressure derivative functions for a horizontal well intercepting N_f circular transverse hydraulic fractures with high conductivity in a fractal reservoir of finite thickness with fixed fractal dimension (D_f=1.5) and conductivity index (θ=0) (constant-rate case).

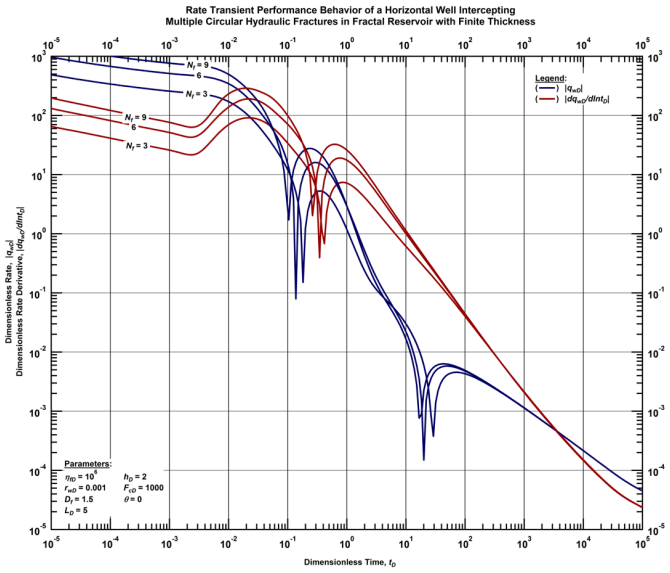

Figure G.64 — Log-log plot of the dimensionless rate and dimensionless rate derivative functions for a horizontal well intercepting N_f circular transverse hydraulic fractures with high conductivity in a fractal reservoir of finite thickness with fixed fractal dimension (D_f=1.5) and conductivity index (θ=0) (constant-pressure case).

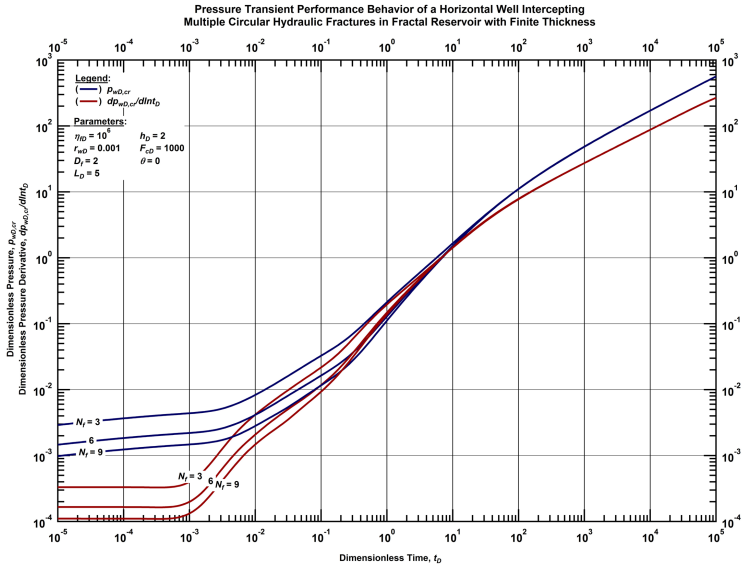

Figure G.65 — Log-log plot of the dimensionless pressure and dimensionless pressure derivative functions for a horizontal well intercepting N_f circular transverse hydraulic fractures with high conductivity in a fractal reservoir of finite thickness with fixed fractal dimension (D_f=2) and conductivity index (θ=0) (constant-rate case).

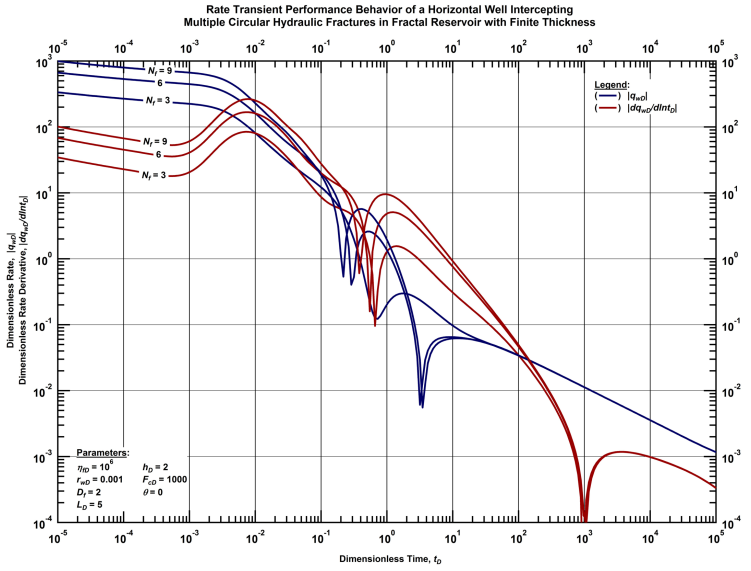

Figure G.66 — Log-log plot of the dimensionless rate and dimensionless rate derivative functions for a horizontal well intercepting N_f circular transverse hydraulic fractures with high conductivity in a fractal reservoir of finite thickness with fixed fractal dimension (D_f=2) and conductivity index (θ=0) (constant- pressure case).

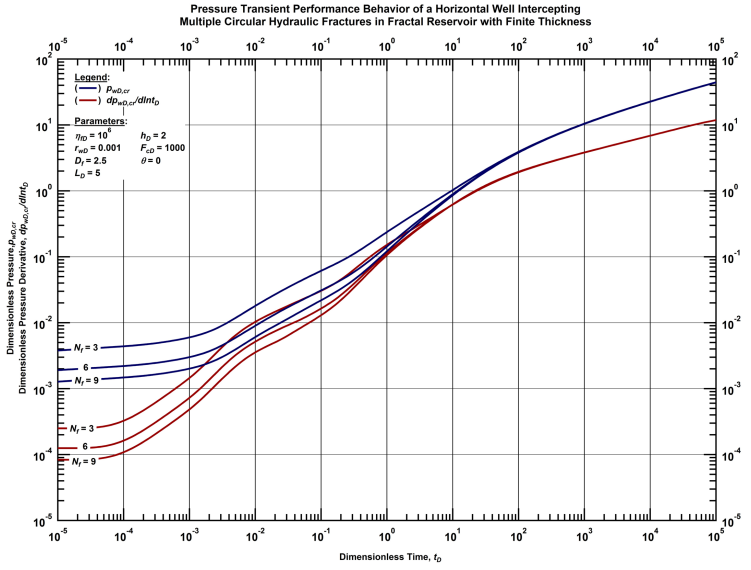

Figure G.67 — Log-log plot of the dimensionless pressure and dimensionless pressure derivative functions for a horizontal well intercepting N_f circular transverse hydraulic fractures with high conductivity in a fractal reservoir of finite thickness with fixed fractal dimension (D_f=2.5) and conductivity index (θ=0) (constant-rate case).

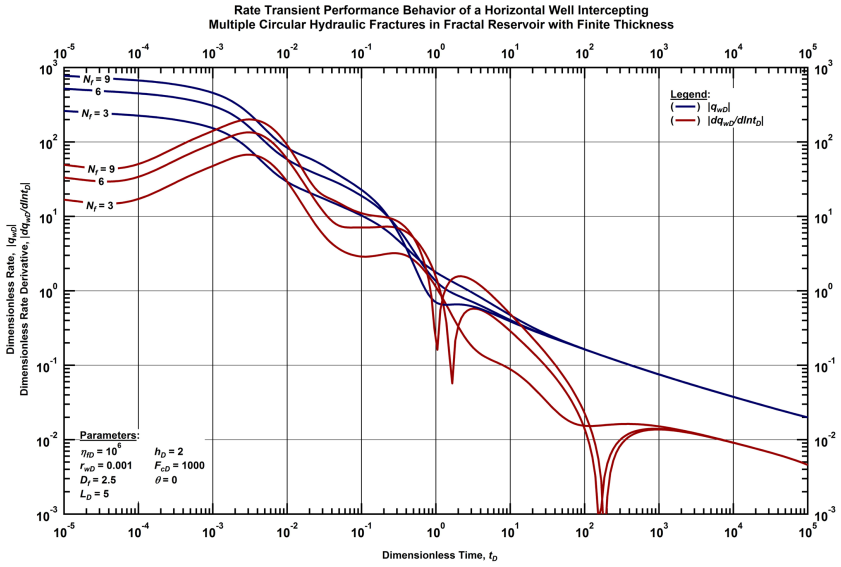

Figure G.68 — Log-log plot of the dimensionless rate and dimensionless rate derivative functions for a horizontal well intercepting N_f circular transverse hydraulic fractures with high conductivity in a fractal reservoir of finite thickness with fixed fractal dimension (D_f=2.5) and conductivity index (θ=0) (constant-pressure case).

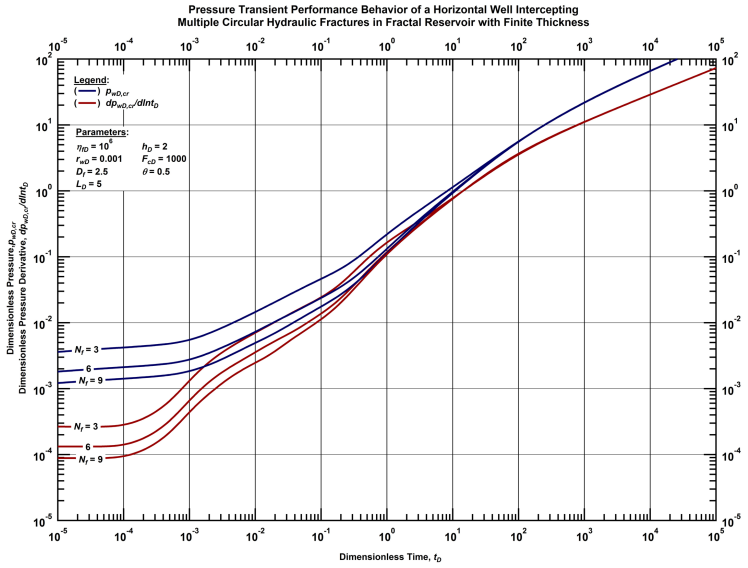

Figure G.69 — Log-log plot of the dimensionless pressure and dimensionless pressure derivative functions for a horizontal well intercepting N_f circular transverse hydraulic fractures with high conductivity in a fractal reservoir of finite thickness with fixed fractal dimension (D_f=2.5) and conductivity index (θ=0.5) (constant-rate case).

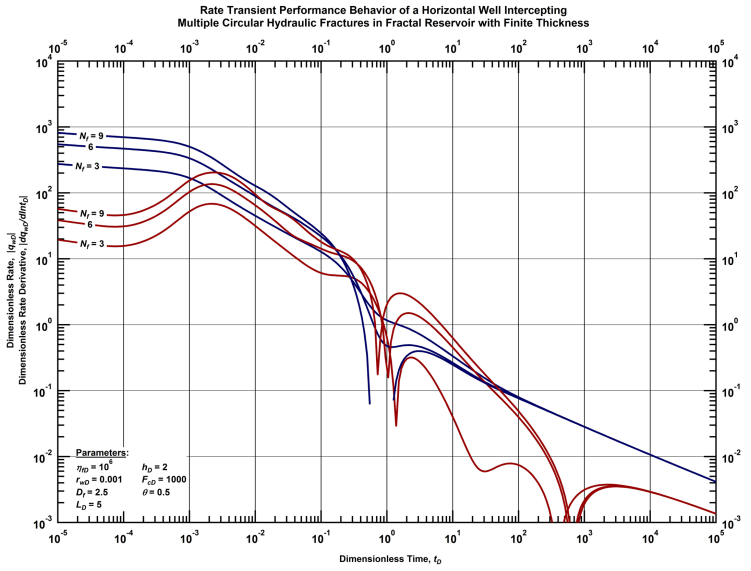

Figure G.70 — Log-log plot of the dimensionless rate and dimensionless rate derivative functions for a horizontal well intercepting N_f circular transverse hydraulic fractures with high conductivity in a fractal reservoir of finite thickness with fixed fractal dimension (D_f=2.5) and conductivity index (θ=0.5) (constant-pressure case).

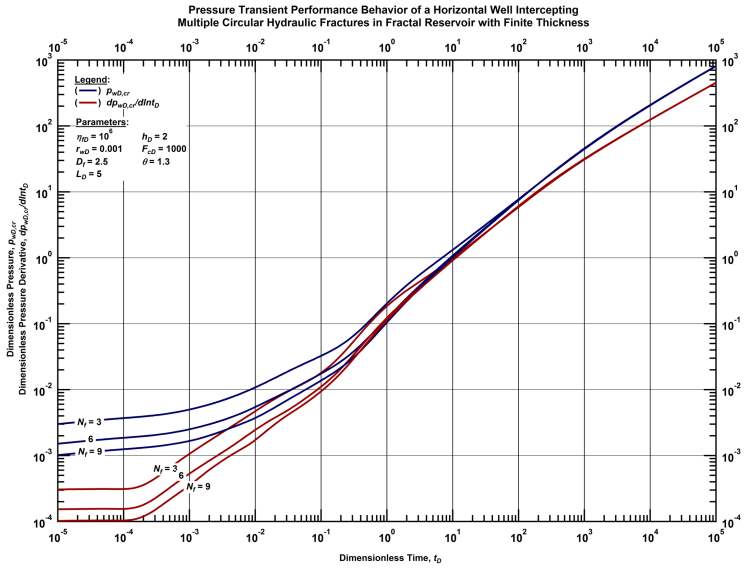

Figure G.71 — Log-log plot of the dimensionless pressure and dimensionless pressure derivative functions for a horizontal well intercepting N_f circular transverse hydraulic fractures with high conductivity in a fractal reservoir of finite thickness with fixed fractal dimension (D_f=2.5) and conductivity index (θ=1.3) (constant-rate case).

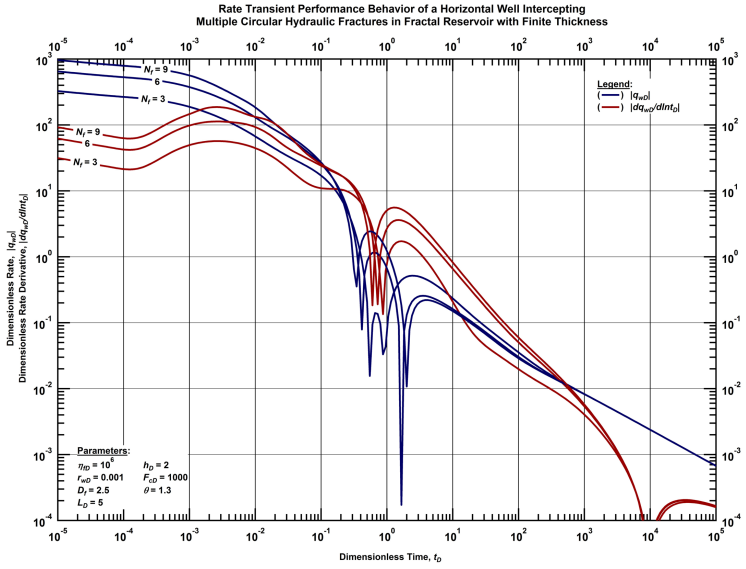

Figure G.72 — Log-log plot of the dimensionless rate and dimensionless rate derivative functions for a horizontal well intercepting N_f circular transverse hydraulic fractures with high conductivity in a fractal reservoir of finite thickness with fixed fractal dimension (D_f=2.5) and conductivity index (θ=1.3) (constant-pressure case).

Circular Transverse Fractures — Intermediate Conductivity

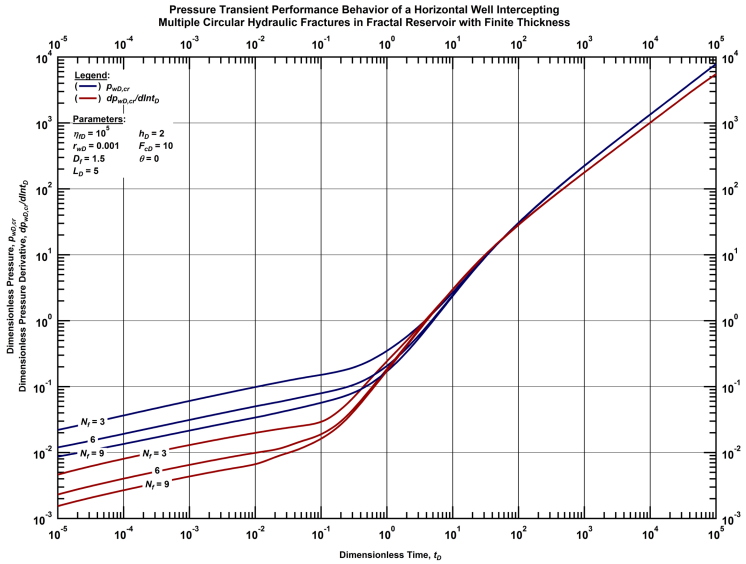

Figure G.73 — Log-log plot of the dimensionless pressure and dimensionless pressure derivative functions for a horizontal well intercepting N_f circular transverse hydraulic fractures with intermediate conductivity in a fractal reservoir of finite thickness with fixed fractal dimension (D_f=1.5) and conductivity index (θ=0) (constant-rate case).

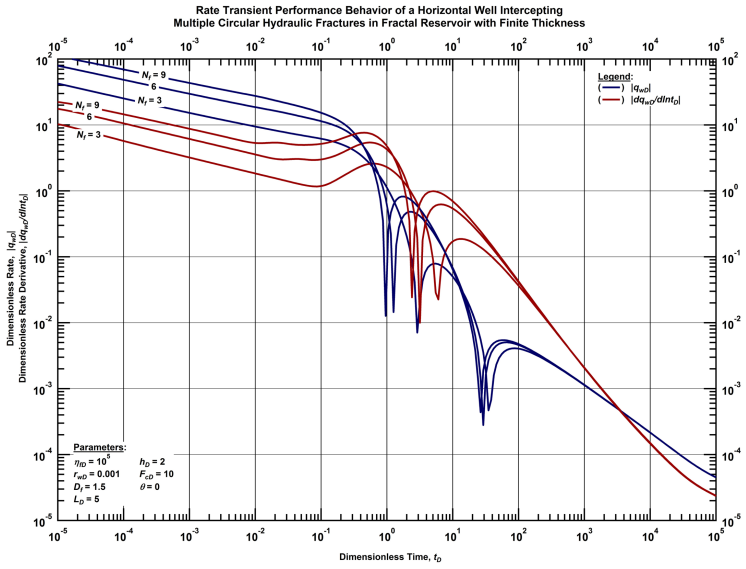

Figure G.74 — Log-log plot of the dimensionless rate and dimensionless rate derivative functions for a horizontal well intercepting N_f circular transverse hydraulic fractures with intermediate conductivity in a fractal reservoir of finite thickness with fixed fractal dimension (D_f=1.5) and conductivity index (θ=0) (constant-pressure case).

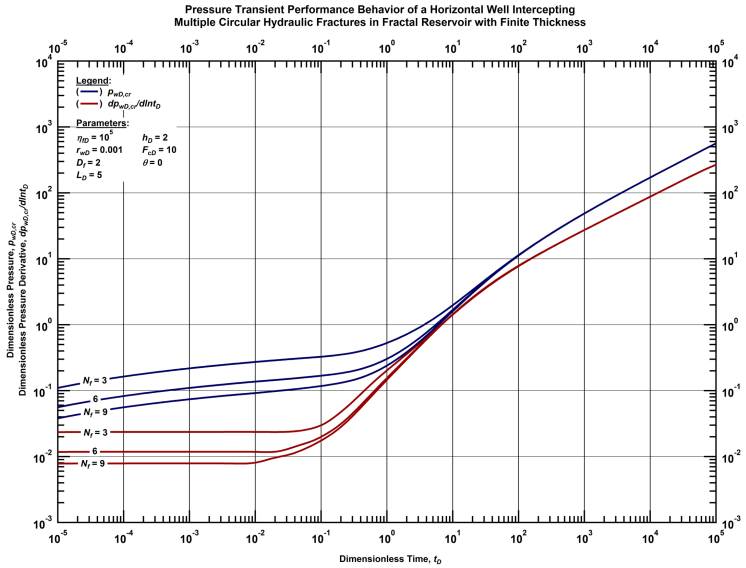

Figure G.75— Log-log plot of the dimensionless pressure and dimensionless pressure derivative functions for a horizontal well intercepting N_f circular transverse hydraulic fractures with intermediate conductivity in a fractal reservoir of finite thickness with fixed fractal dimension (D_f=2) and conductivity index (θ=0) (constant-rate case).

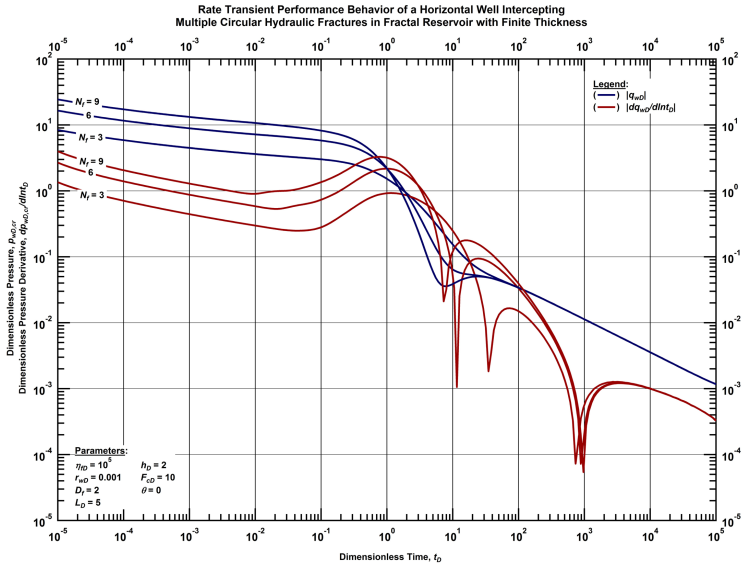

Figure G.76 — Log-log plot of the dimensionless rate and dimensionless rate derivative functions for a horizontal well intercepting N_f circular transverse hydraulic fractures with intermediate conductivity in a fractal reservoir of finite thickness with fixed fractal dimension (D_f=2) and conductivity index (θ=0) (constant-pressure case).

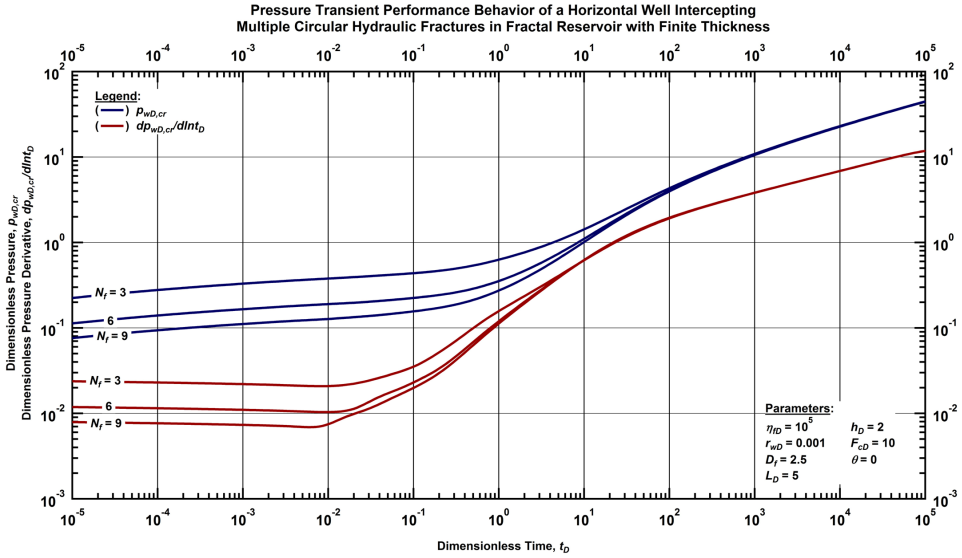

Figure G.77 — Log-log plot of the dimensionless pressure and dimensionless pressure derivative functions for a horizontal well intercepting N_f circular transverse hydraulic fractures with intermediate conductivity in a fractal reservoir of finite thickness with fixed fractal dimension (D_f=2.5) and conductivity index (θ=0) (constant-rate case).

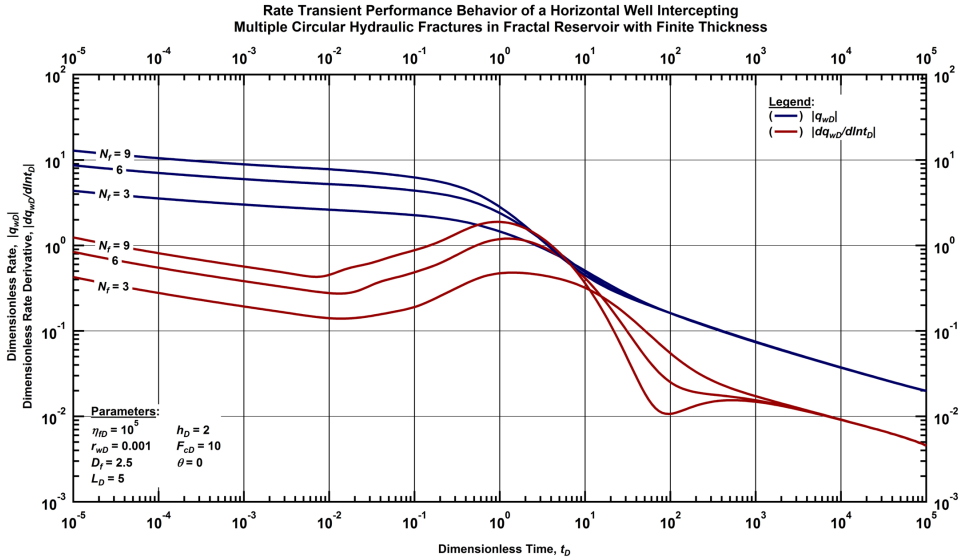

Figure G.78 — Log-log plot of the dimensionless rate and dimensionless rate derivative functions for a horizontal well intercepting N_f circular transverse hydraulic fractures with intermediate conductivity in a fractal reservoir of finite thickness with fixed fractal dimension (D_f=2.5) and conductivity index (θ=0) (constant-pressure case).

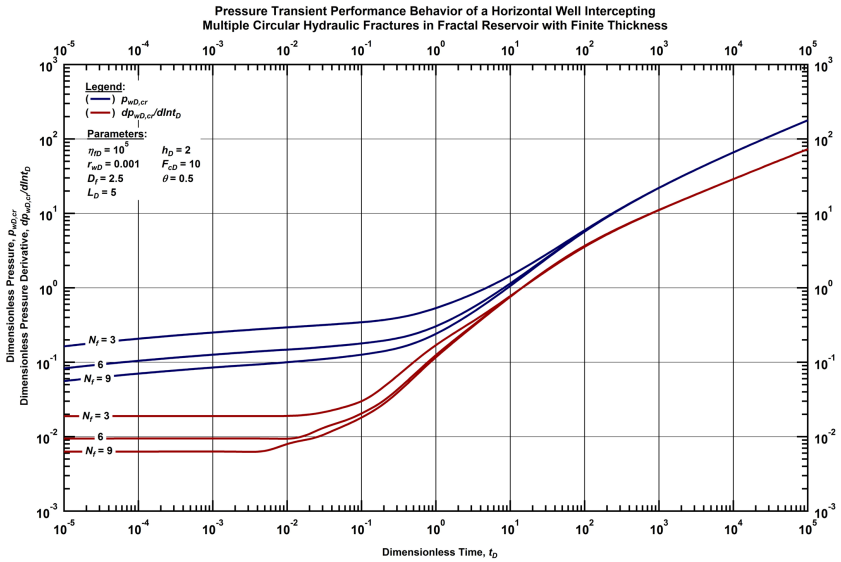

Figure G.79 — Log-log plot of the dimensionless pressure and dimensionless pressure derivative functions for a horizontal well intercepting N_f circular transverse hydraulic fractures with intermediate conductivity in a fractal reservoir of finite thickness with fixed fractal dimension (D_f=2.5) and conductivity index (θ=0.5) (constant-rate case).

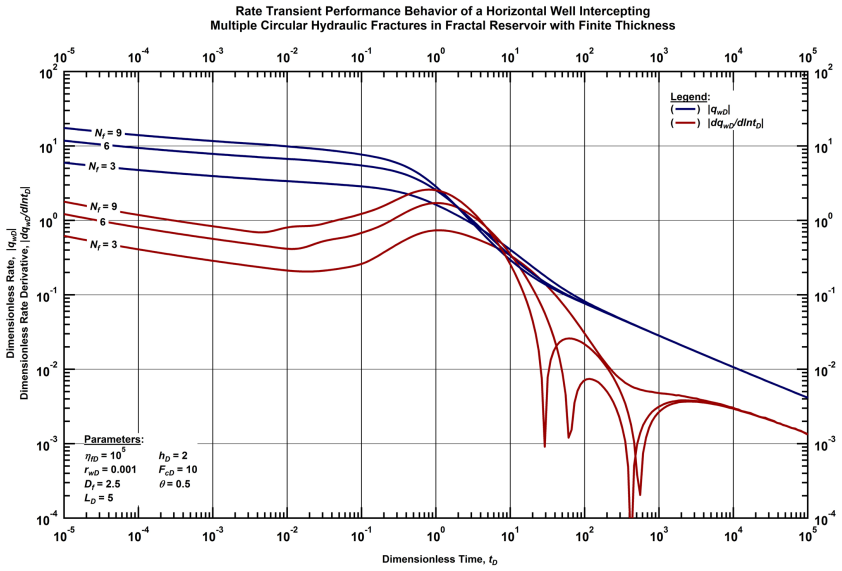

Figure G.80 — Log-log plot of the dimensionless rate and dimensionless rate derivative functions for a horizontal well intercepting N_f circular transverse hydraulic fractures with intermediate conductivity in a fractal reservoir of finite thickness with fixed fractal dimension (D_f=2.5) and conductivity index (θ=0.5) (constant-pressure case).

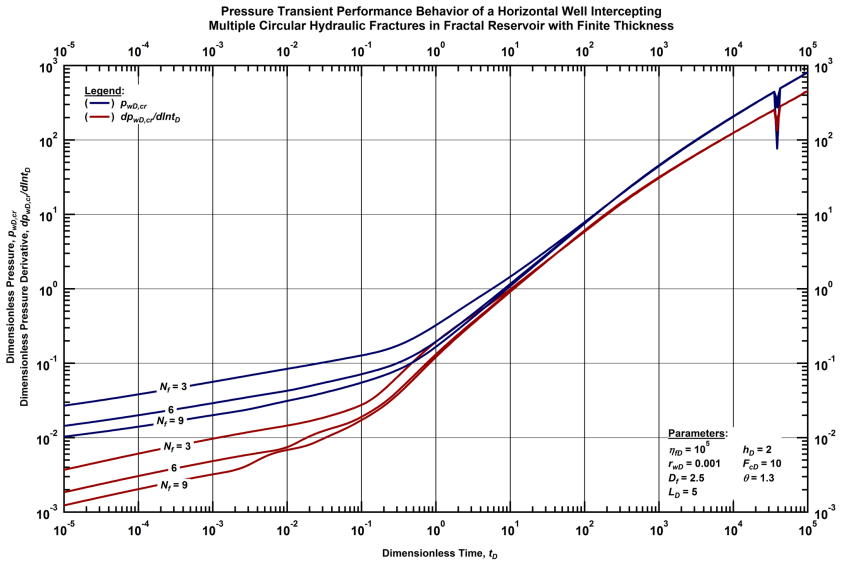

Figure G.81 — Log-log plot of the dimensionless pressure and dimensionless pressure derivative functions for a horizontal well intercepting N_f circular transverse hydraulic fractures with intermediate conductivity in a fractal reservoir of finite thickness with fixed fractal dimension (D_f=2.5) and conductivity index (θ=1.3) (constant-rate case).

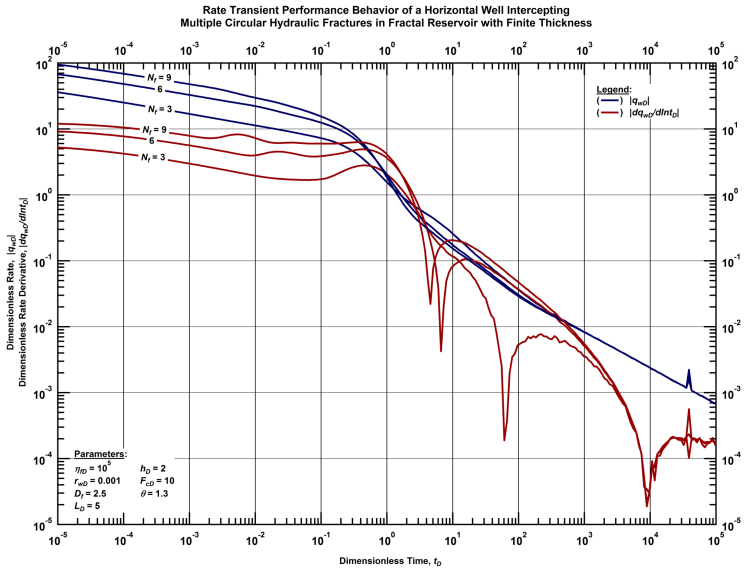

Figure G.82— Log-log plot of the dimensionless rate and dimensionless rate derivative functions for a horizontal well intercepting N_f circular transverse hydraulic fractures with intermediate conductivity in a fractal reservoir of finite thickness with fixed fractal dimension (D_f=2.5) and conductivity index (θ=1.3) (constant- pressure case).

Circular Transverse Fractures — Low Conductivity

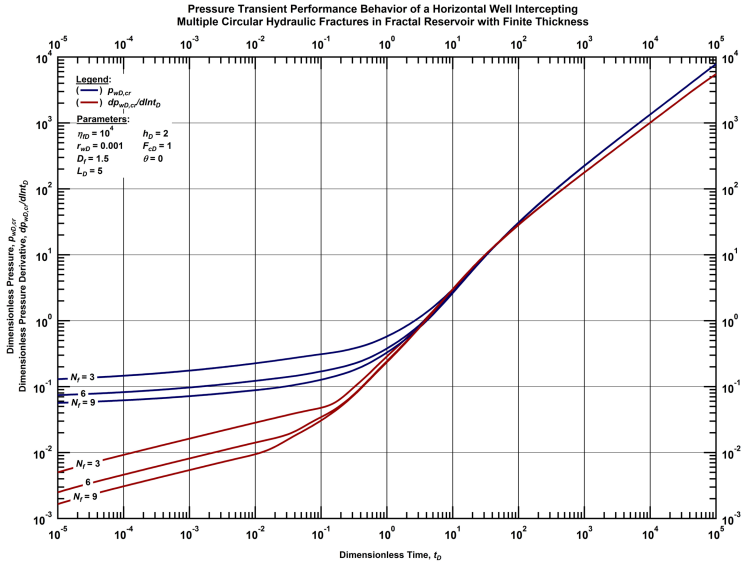

Figure G.83— Log-log plot of the dimensionless pressure and dimensionless pressure derivative functions for a horizontal well intercepting N_f circular transverse hydraulic fractures with low conductivity in a fractal reservoir of finite thickness with fixed fractal dimension (D_f=1.5) and conductivity index (θ=0) (constant-rate case).

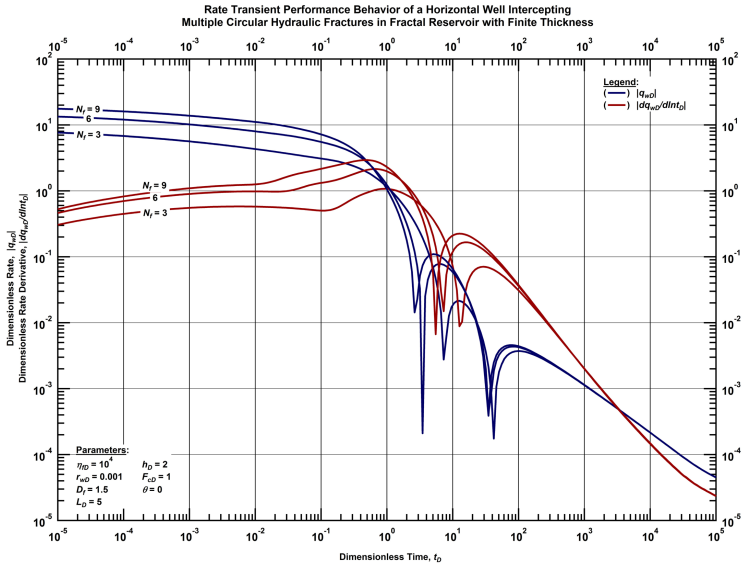

Figure G.84 — Log-log plot of the dimensionless rate and dimensionless rate derivative functions for a horizontal well intercepting N_f circular transverse hydraulic fractures with low conductivity in a fractal reservoir of finite thickness with fixed fractal dimension (D_f=1.5) and conductivity index (θ=0) (constant- pressure case).

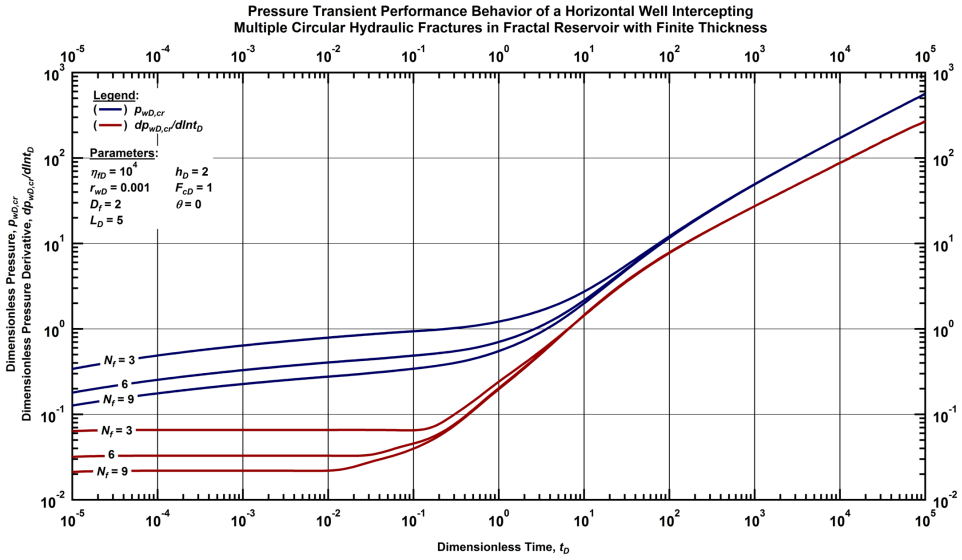

Figure G.85 — Log-log plot of the dimensionless pressure and dimensionless pressure derivative functions for a horizontal well intercepting N_f circular transverse hydraulic fractures with low conductivity in a fractal reservoir of finite thickness with fixed fractal dimension (D_f=2) and conductivity index (θ=0) (constant-rate case).

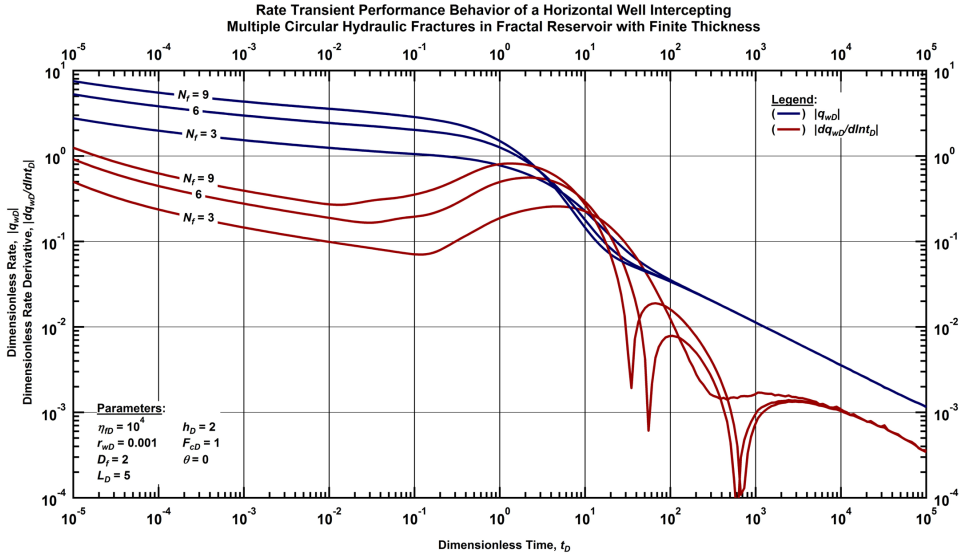

Figure G.86 — Log-log plot of the dimensionless rate and dimensionless rate derivative functions for a horizontal well intercepting N_f circular transverse hydraulic fractures with low conductivity in a fractal reservoir of finite thickness with fixed fractal dimension (D_f=2) and conductivity index (θ=0) (constant- pressure case).

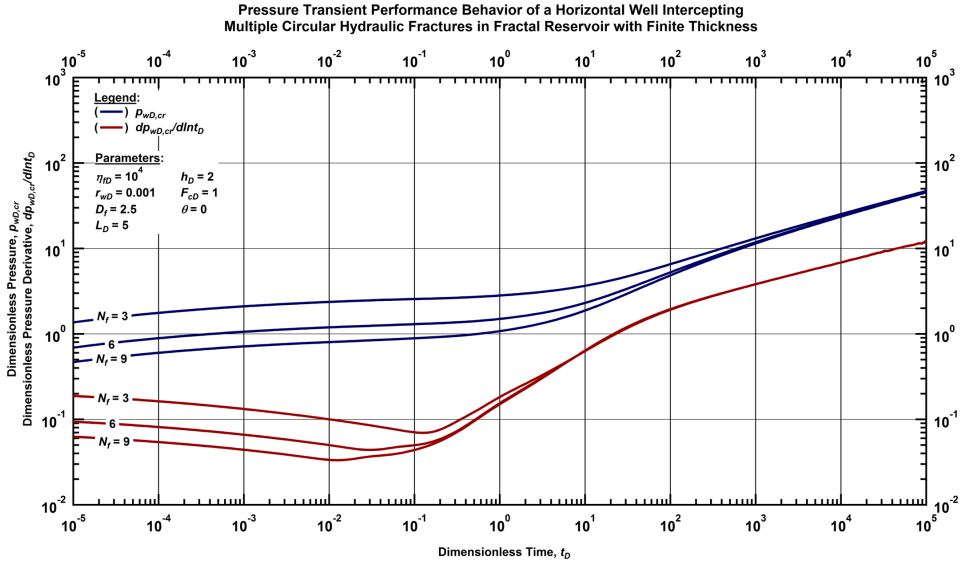

Figure G.87 — Log-log plot of the dimensionless pressure and dimensionless pressure derivative functions for a horizontal well intercepting N_f circular transverse hydraulic fractures with low conductivity in a fractal reservoir of finite thickness with fixed fractal dimension (D_f=2.5) and conductivity index (θ=0) (constant-rate case).

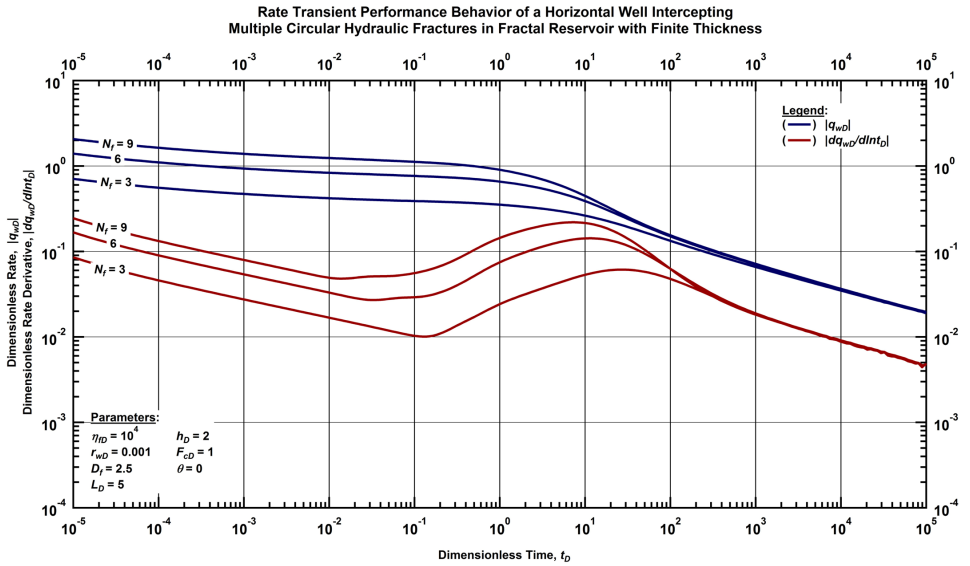

Figure G.88 — Log-log plot of the dimensionless rate and dimensionless rate derivative functions for a horizontal well intercepting N_f circular transverse hydraulic fractures with low conductivity in a fractal reservoir of finite thickness with fixed fractal dimension (D_f=2.5) and conductivity index (θ=0) (constant-pressure case).

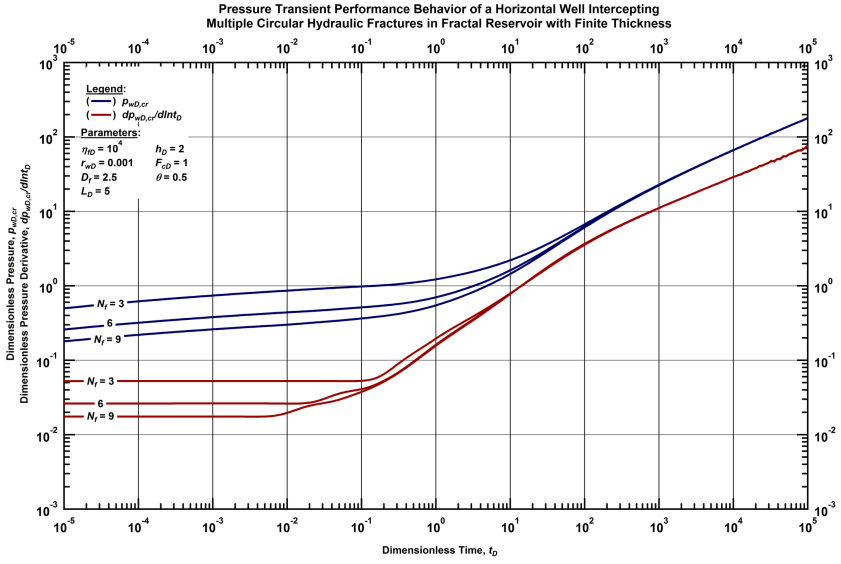

Figure G.89 — Log-log plot of the dimensionless pressure and dimensionless pressure derivative functions for a horizontal well intercepting N_f circular transverse hydraulic fractures with low conductivity in a fractal reservoir of finite thickness with fixed fractal dimension (D_f=2.5) and conductivity index (θ=0.5) (constant-rate case).

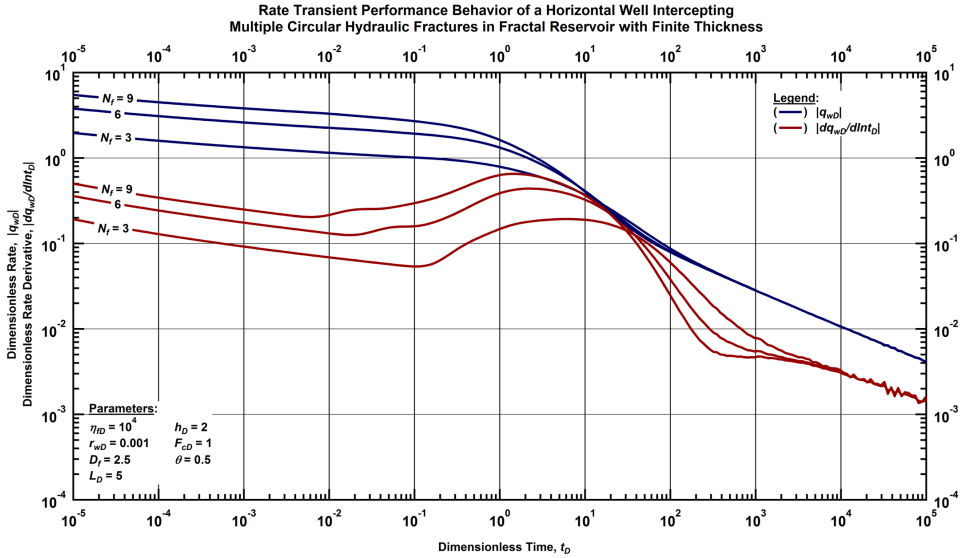

Figure G.90 — Log-log plot of the dimensionless rate and dimensionless rate derivative functions for a horizontal well intercepting N_f circular transverse hydraulic fractures with low conductivity in a fractal reservoir of finite thickness with fixed fractal dimension (D_f=2.5) and conductivity index (θ=0.5) (constant-pressure case).

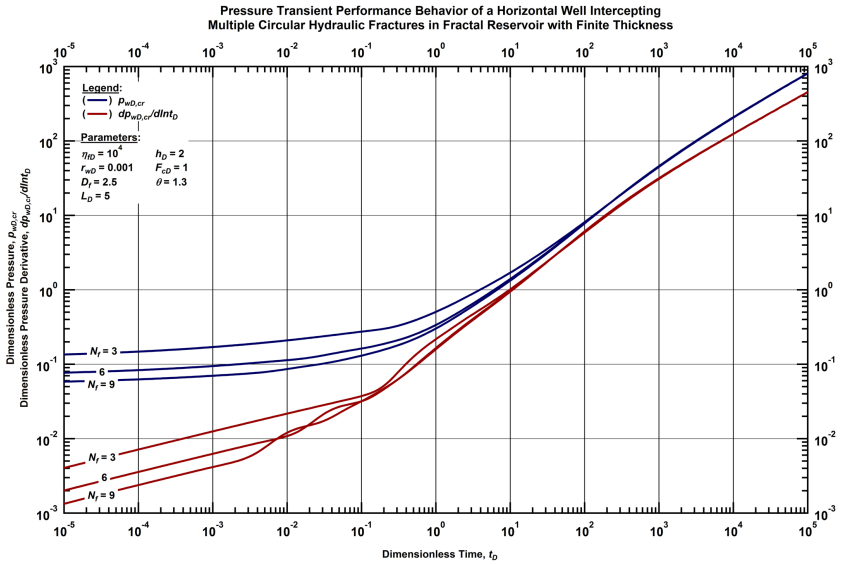

Figure G.91 — Log-log plot of the dimensionless pressure and dimensionless pressure derivative functions for a horizontal well intercepting N_f circular transverse hydraulic fractures with low conductivity in a fractal reservoir of finite thickness with fixed fractal dimension (D_f=2.5) and conductivity index (θ=1.3) (constant-rate case).

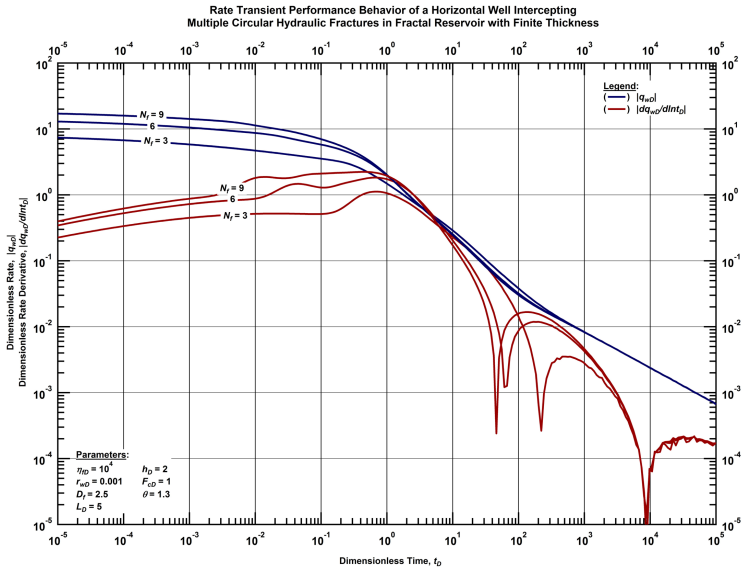

Figure G.92 — Log-log plot of the dimensionless rate and dimensionless rate derivative functions for a horizontal well intercepting N_f circular transverse hydraulic fractures with low conductivity in a fractal reservoir of finite thickness with fixed fractal dimension (D_f=2.5) and conductivity index (θ=1.3) (constant-pressure case).

Rectangular Longitudinal Fractures — High Conductivity

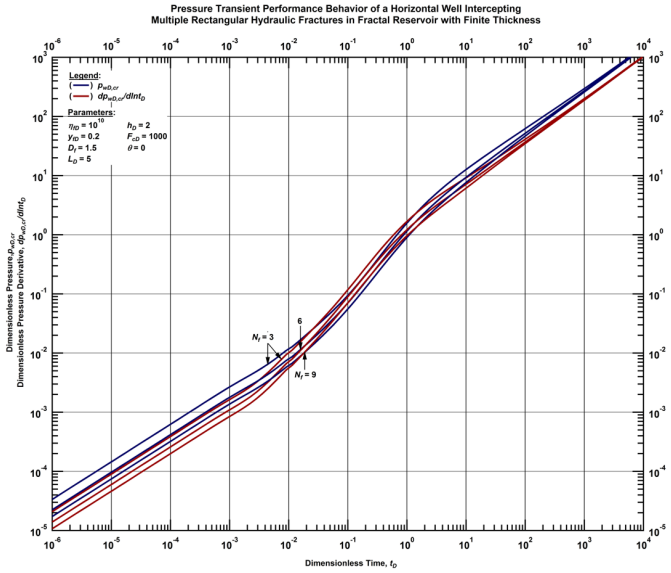

Figure G.93 — Log-log plot of the dimensionless pressure and dimensionless pressure derivative functions for a horizontal well intercepting N_f rectangular longitudinal hydraulic fractures with high conductivity in a fractal reservoir of finite thickness with fixed fractal dimension (D_f=1.5) and conductivity index (θ=0) (constant-rate case).

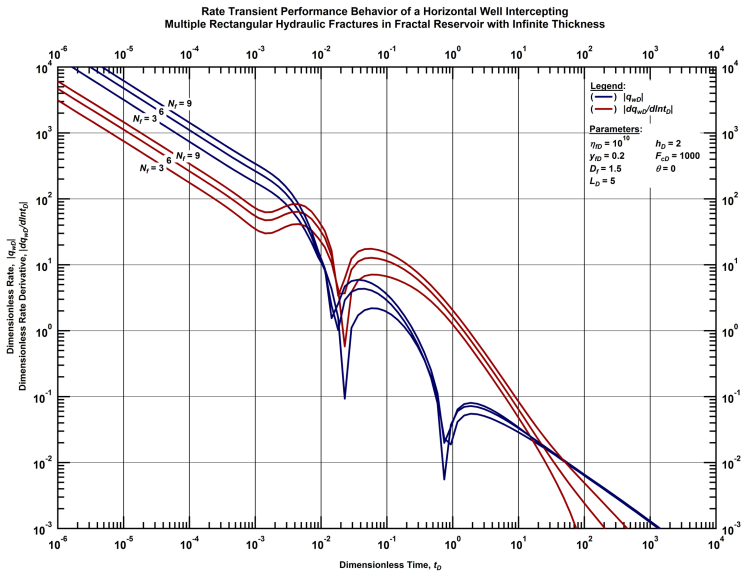

Figure G.94 — Log-log plot of the dimensionless rate and dimensionless rate derivative functions for a horizontal well intercepting N_f rectangular longitudinal hydraulic fractures with high conductivity in a fractal reservoir of finite thickness with fixed fractal dimension (D_f=1.5) and conductivity index (θ=0) (constant-pressure case).

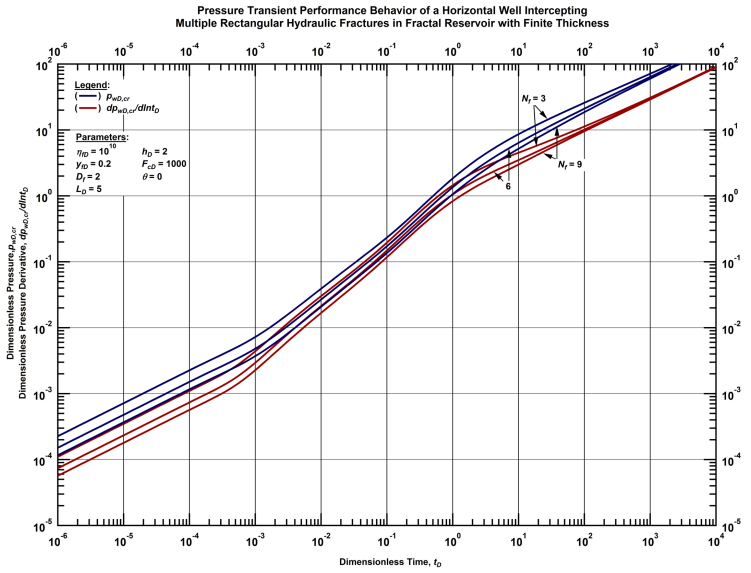

Figure G.95 — Log-log plot of the dimensionless pressure and dimensionless pressure derivative functions for a horizontal well intercepting N_f rectangular longitudinal hydraulic fractures with high conductivity in a fractal reservoir of finite thickness with fixed fractal dimension (D_f=2) and conductivity index (θ=0) (constant-rate case).

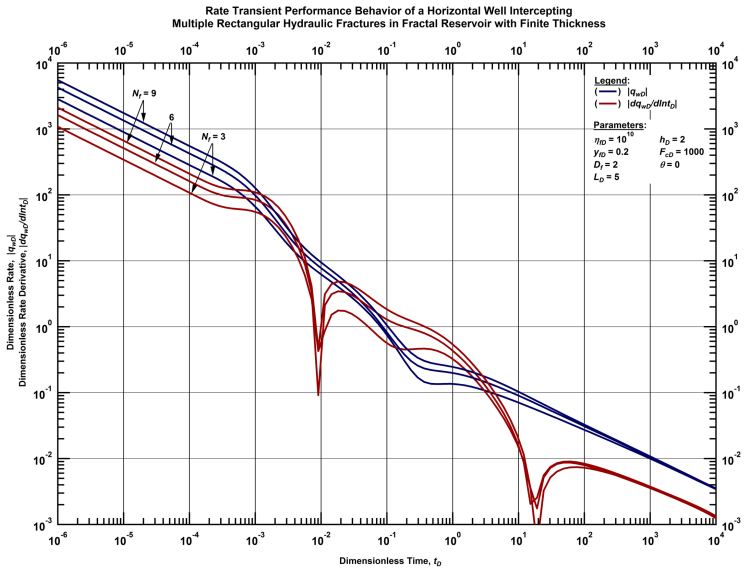

Figure G.96 — Log-log plot of the dimensionless rate and dimensionless rate derivative functions for a horizontal well intercepting N_f rectangular longitudinal hydraulic fractures with high conductivity in a fractal reservoir of finite thickness with fixed fractal dimension (D_f=2) and conductivity index (θ=0) (constant- pressure case).

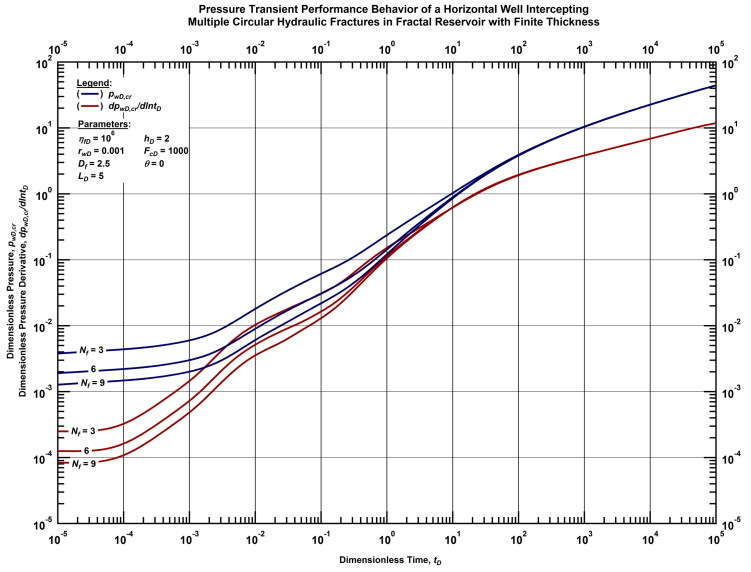

Figure G.97 — Log-log plot of the dimensionless pressure and dimensionless pressure derivative functions for a horizontal well intercepting N_f rectangular longitudinal hydraulic fractures with high conductivity in a fractal reservoir of finite thickness with fixed fractal dimension (D_f=2.5) and conductivity index (θ=0) (constant-rate case).

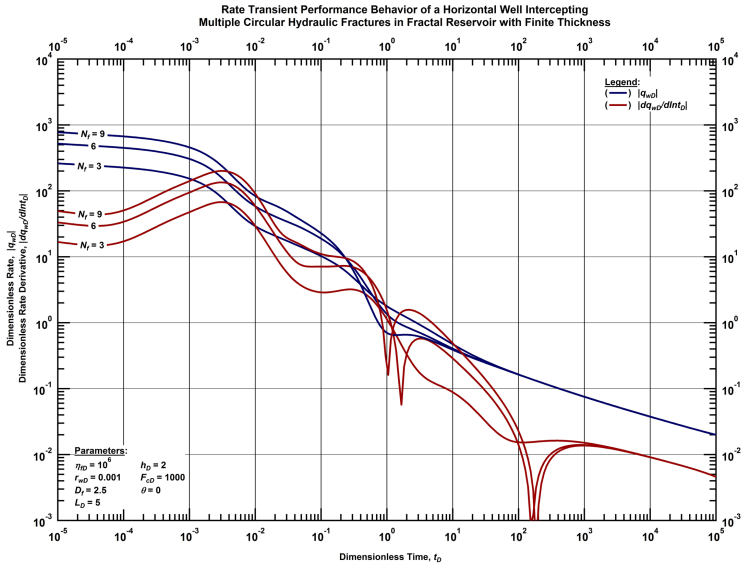

Figure G.98 — Log-log plot of the dimensionless rate and dimensionless rate derivative functions for a horizontal well intercepting N_f rectangular longitudinal hydraulic fractures with high conductivity in a fractal reservoir of finite thickness with fixed fractal dimension (D_f=2.5) and conductivity index (θ=0) (constant-pressure case).

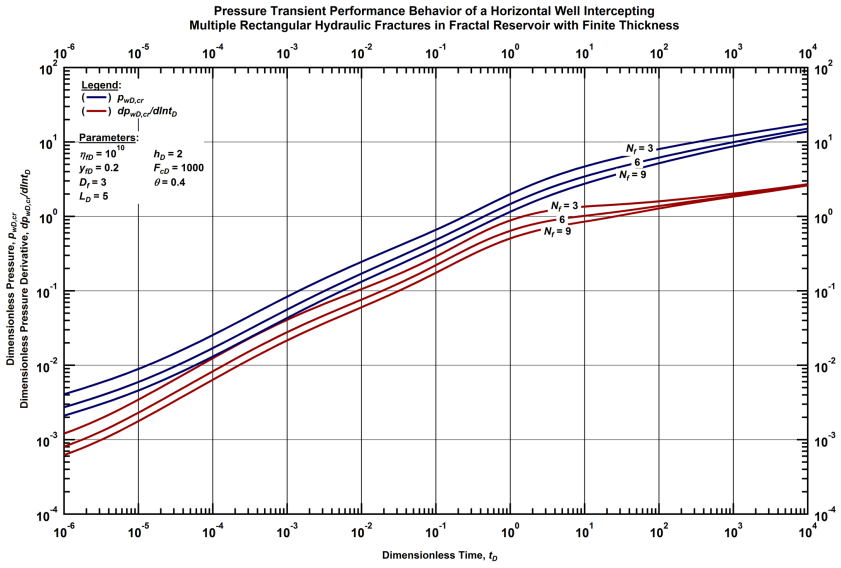

Figure G.99 — Log-log plot of the dimensionless pressure and dimensionless pressure derivative functions for a horizontal well intercepting N_f rectangular longitudinal hydraulic fractures with high conductivity in a fractal reservoir of finite thickness with fixed fractal dimension (D_f=3) and conductivity index (θ=0.4) (constant-rate case).

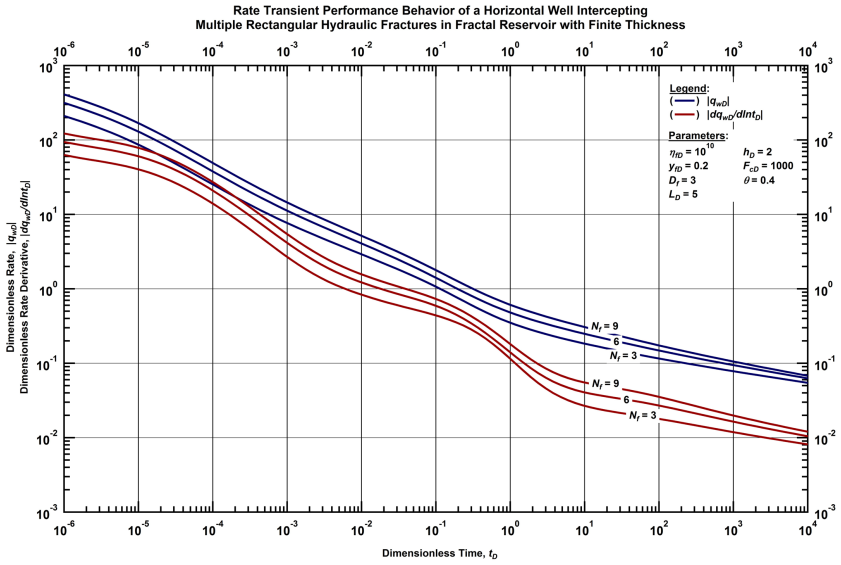

Figure G.100 — Log-log plot of the dimensionless rate and dimensionless rate derivative functions for a horizontal well intercepting N_f rectangular longitudinal hydraulic fractures with high conductivity in a fractal reservoir of finite thickness with fixed fractal dimension (D_f=3) and conductivity index (θ=0.4) (constant-pressure case).

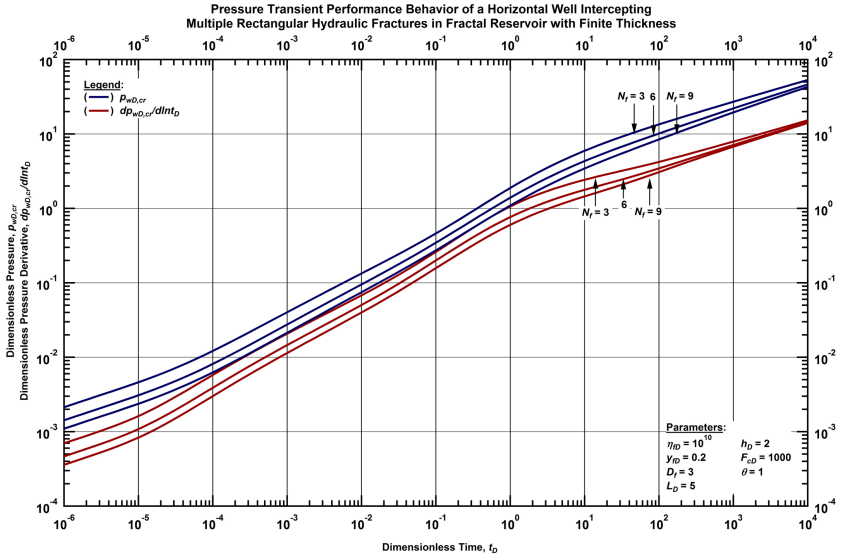

Figure G.101 — Log-log plot of the dimensionless pressure and dimensionless pressure derivative functions for a horizontal well intercepting N_f rectangular longitudinal hydraulic fractures with high conductivity in a fractal reservoir of finite thickness with fixed fractal dimension (D_f=3) and conductivity index (θ=1) (constant-rate case).

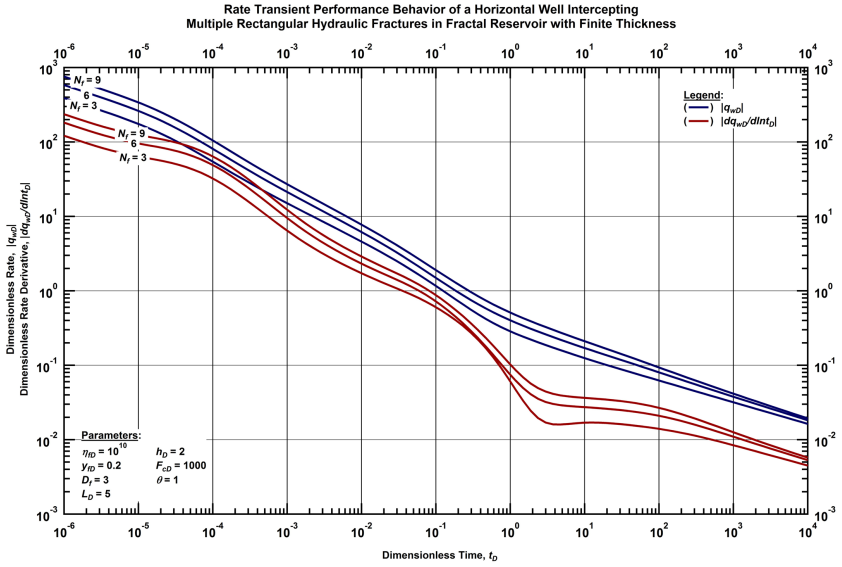

Figure G.102 — Log-log plot of the dimensionless rate and dimensionless rate derivative functions for a horizontal well intercepting N_f rectangular longitudinal hydraulic fractures with high conductivity in a fractal reservoir of finite thickness with fixed fractal dimension (D_f=3) and conductivity index (θ=1) (constant- pressure case).

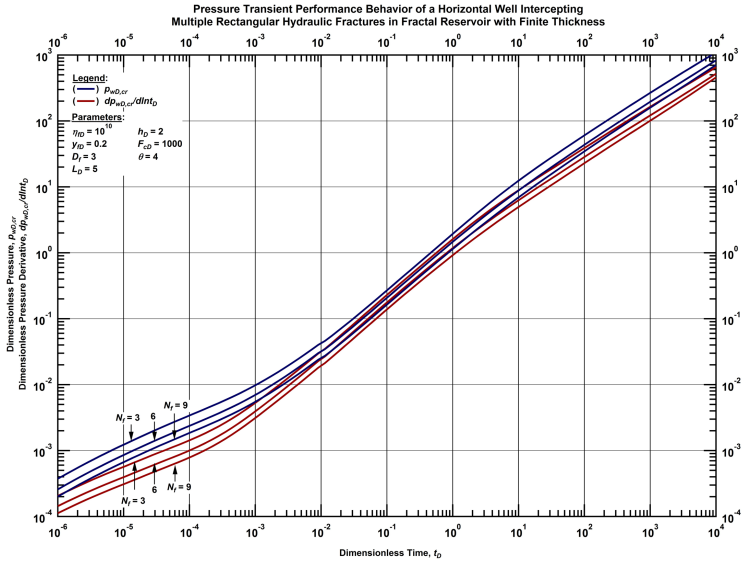

Figure G.103 — Log-log plot of the dimensionless pressure and dimensionless pressure derivative functions for a horizontal well intercepting N_f rectangular longitudinal hydraulic fractures with high conductivity in a fractal reservoir of finite thickness with fixed fractal dimension (D_f=3) and conductivity index (θ=4) (constant-rate case).

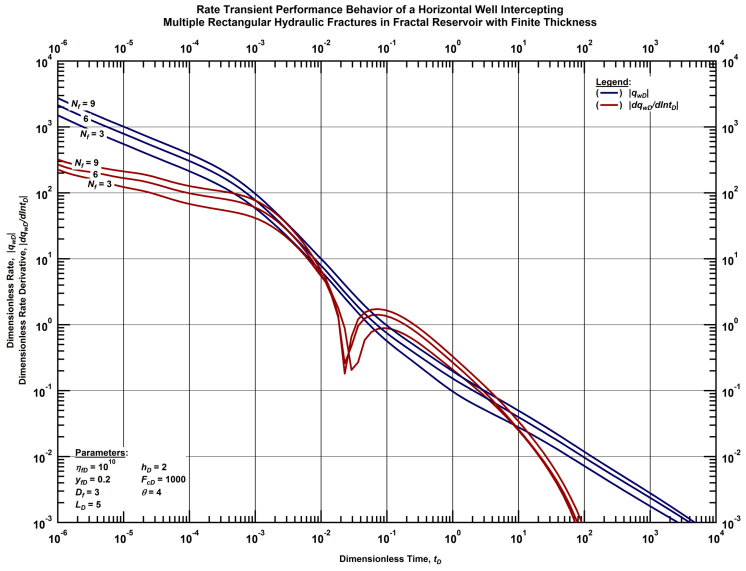

Figure G.104 — Log-log plot of the dimensionless rate and dimensionless rate derivative functions for a horizontal well intercepting N_f rectangular longitudinal hydraulic fractures with high conductivity in a fractal reservoir of finite thickness with fixed fractal dimension (D_f=3) and conductivity index (θ=4) (constant- pressure case).

Rectangular Longitudinal Fractures — Intermediate Conductivity

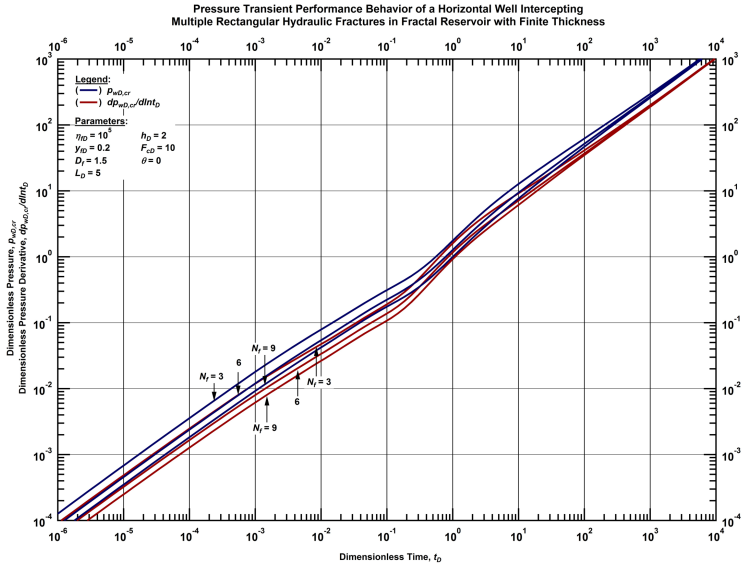

Figure G.105 — Log-log plot of the dimensionless pressure and dimensionless pressure derivative functions for a horizontal well intercepting N_f rectangular longitudinal hydraulic fractures with intermediate conductivity in a fractal reservoir of finite thickness with fixed fractal dimension (D_f=1.5) and conductivity index (θ=0) (constant-rate case).

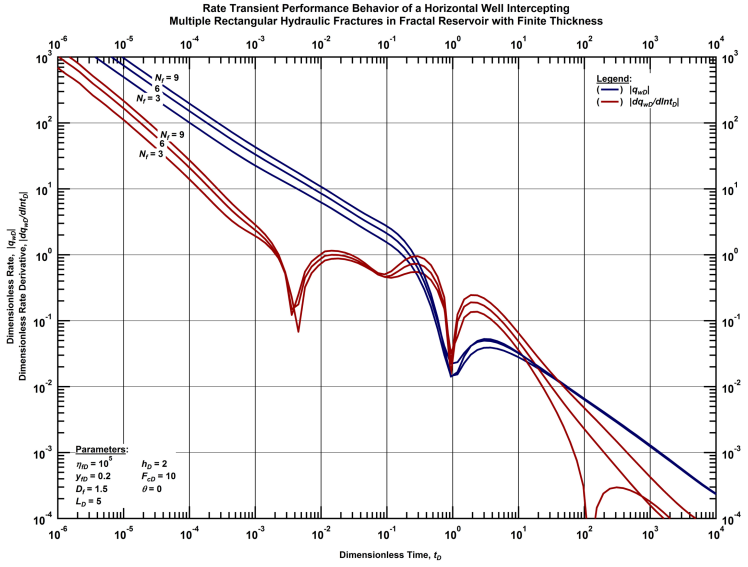

Figure G.106— Log-log plot of the dimensionless rate and dimensionless rate derivative functions for a horizontal well intercepting N_f rectangular longitudinal hydraulic fractures with intermediate conductivity in a fractal reservoir of finite thickness with fixed fractal dimension (D_f=1.5) and conductivity index (θ=0) (constant-pressure case).

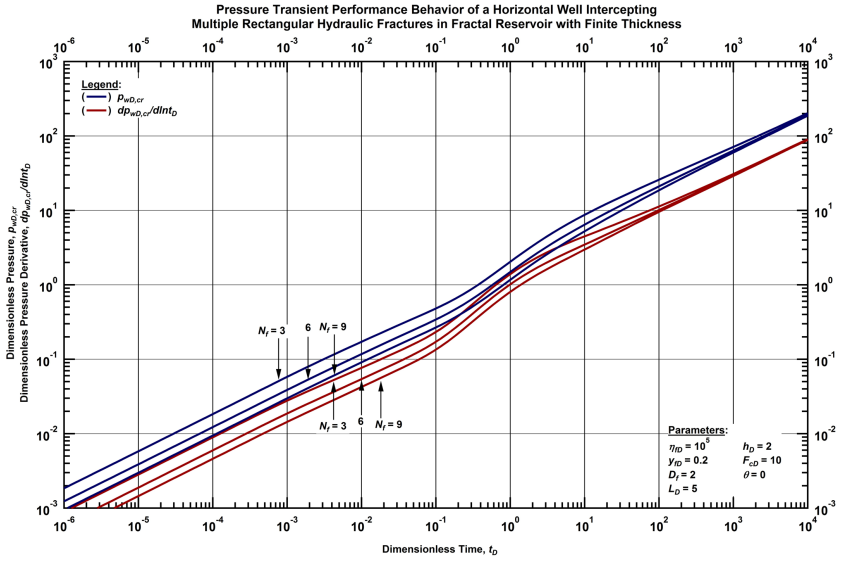

Figure G.107— Log-log plot of the dimensionless pressure and dimensionless pressure derivative functions for a horizontal well intercepting N_f rectangular longitudinal hydraulic fractures with intermediate conductivity in a fractal reservoir of finite thickness with fixed fractal dimension (D_f=2) and conductivity index (θ=0) (constant-rate case).

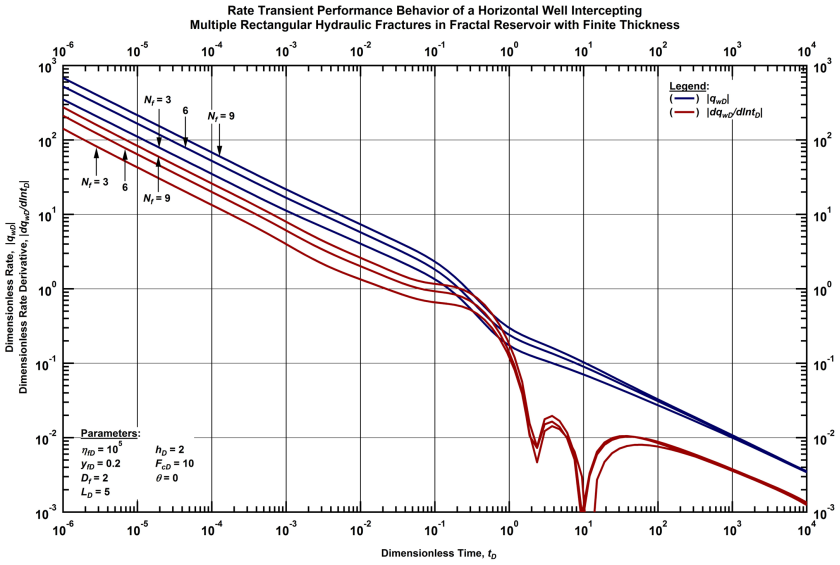

Figure G.108— Log-log plot of the dimensionless rate and dimensionless rate derivative functions for a horizontal well intercepting N_f rectangular longitudinal hydraulic fractures with intermediate conductivity in a fractal reservoir of finite thickness with fixed fractal dimension (D_f=2) and conductivity index (θ=0) (constant-pressure case).

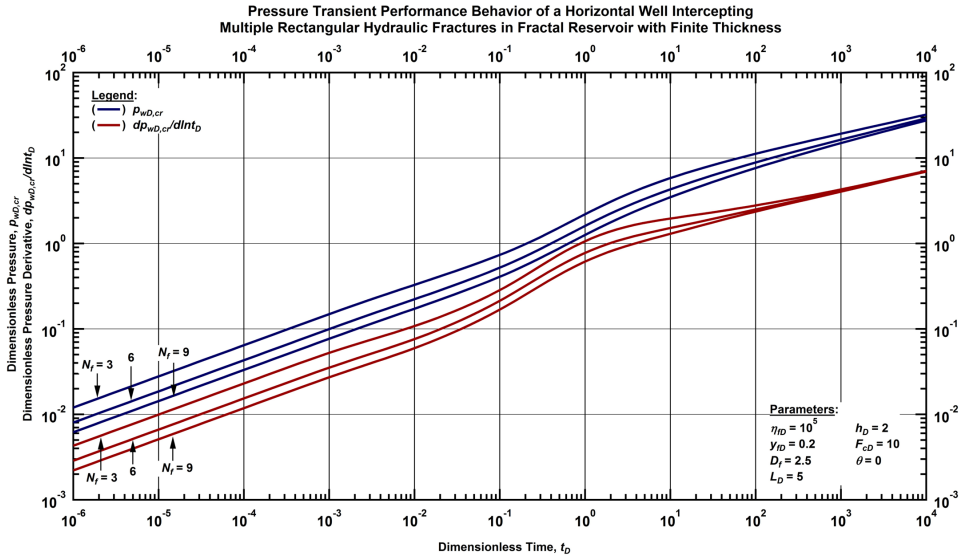

Figure G.109— Log-log plot of the dimensionless pressure and dimensionless pressure derivative functions for a horizontal well intercepting N_f rectangular longitudinal hydraulic fractures with intermediate conductivity in a fractal reservoir of finite thickness with fixed fractal dimension (D_f=2.5) and conductivity index (θ=0) (constant-rate case).

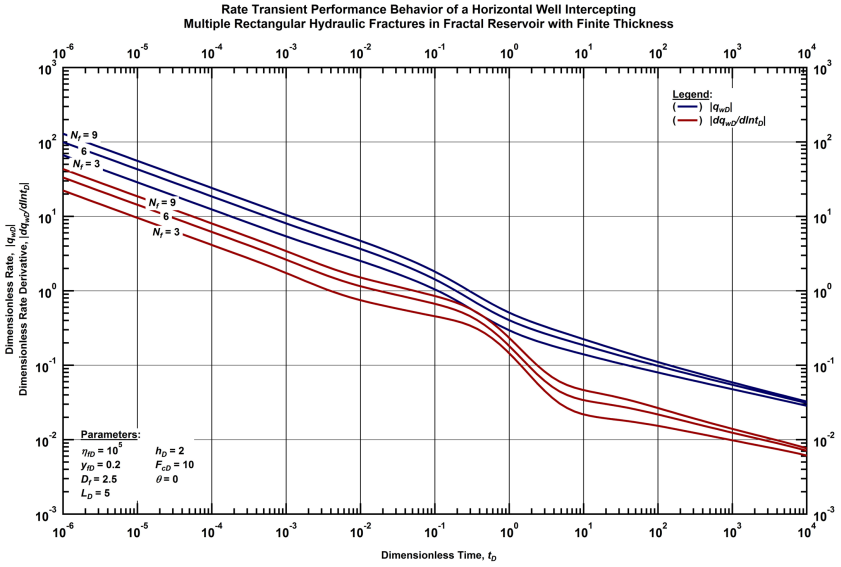

Figure G.110— Log-log plot of the dimensionless rate and dimensionless rate derivative functions for a horizontal well intercepting N_f rectangular longitudinal hydraulic fractures with intermediate conductivity in a fractal reservoir of finite thickness with fixed fractal dimension (D_f=2.5) and conductivity index (θ=0) (constant-pressure case).

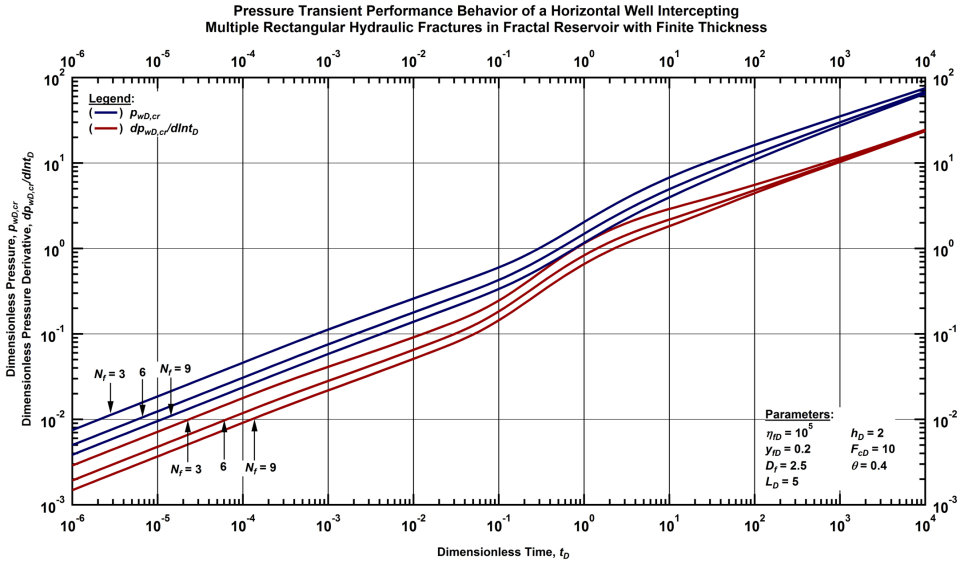

Figure G.111— Log-log plot of the dimensionless pressure and dimensionless pressure derivative functions for a horizontal well intercepting N_f rectangular longitudinal hydraulic fractures with intermediate conductivity in a fractal reservoir of finite thickness with fixed fractal dimension (D_f=2.5) and conductivity index (θ=0.4) (constant-rate case).

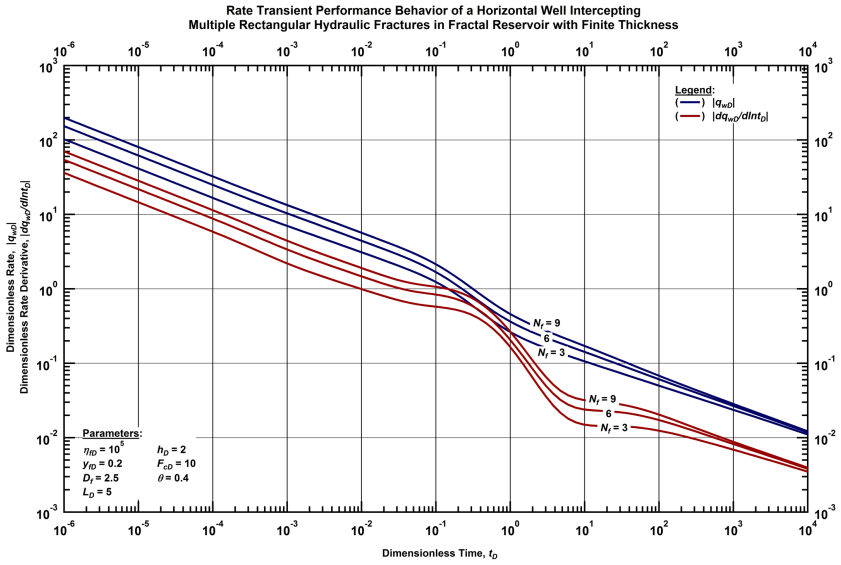

Figure G.112— Log-log plot of the dimensionless rate and dimensionless rate derivative functions for a horizontal well intercepting N_f rectangular longitudinal hydraulic fractures with intermediate conductivity in a fractal reservoir of finite thickness with fixed fractal dimension (D_f=2.5) and conductivity index (θ=0.4) (constant-pressure case).

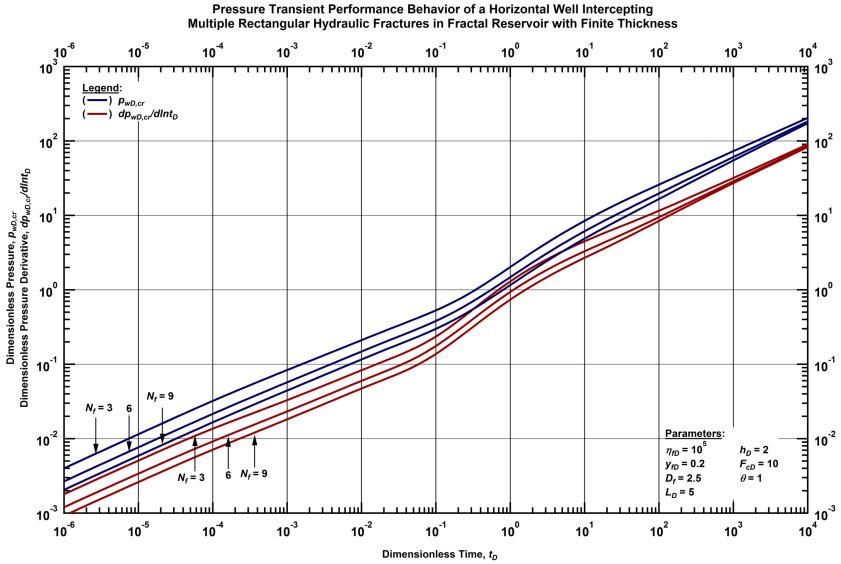

Figure G.113— Log-log plot of the dimensionless pressure and dimensionless pressure derivative functions for a horizontal well intercepting N_f rectangular longitudinal hydraulic fractures with intermediate conductivity in a fractal reservoir of finite thickness with fixed fractal dimension (D_f=2.5) and conductivity index (θ=1) (constant-rate case).

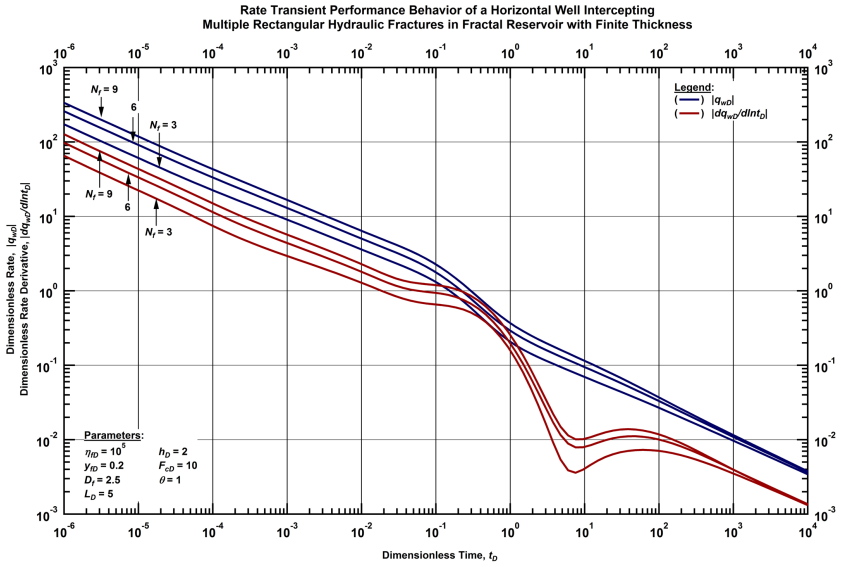

Figure G.114— Log-log plot of the dimensionless rate and dimensionless rate derivative functions for a horizontal well intercepting N_f rectangular longitudinal hydraulic fractures with intermediate conductivity in a fractal reservoir of finite thickness with fixed fractal dimension (D_f=2.5) and conductivity index (θ=1) (constant-pressure case).

Rectangular Longitudinal Fractures — Low Conductivity

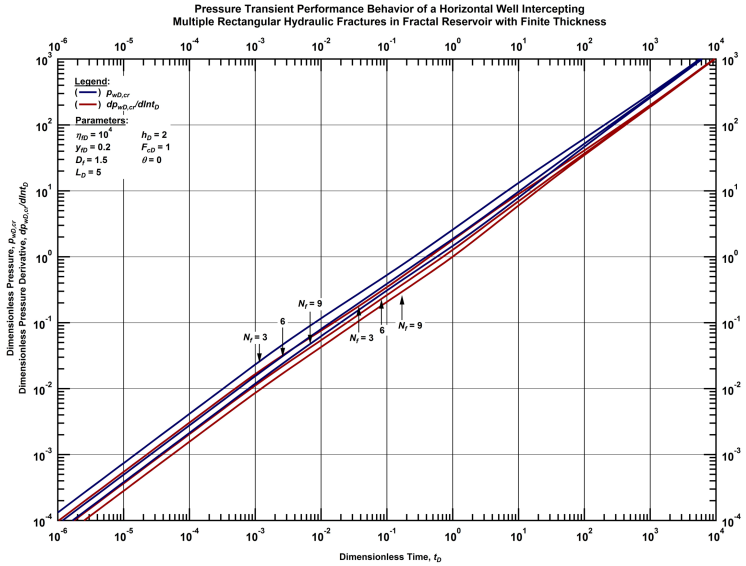

Figure G.115— Log-log plot of the dimensionless pressure and dimensionless pressure derivative functions for a horizontal well intercepting N_f rectangular longitudinal hydraulic fractures with low conductivity in a fractal reservoir of finite thickness with fixed fractal dimension (D_f=1.5) and conductivity index (θ=0) (constant-rate case).

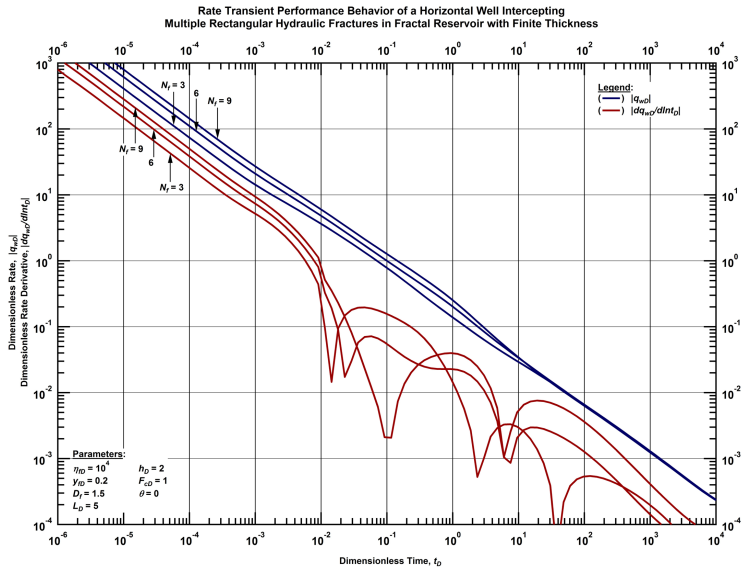

Figure G.116— Log-log plot of the dimensionless rate and dimensionless rate derivative functions for a horizontal well intercepting N_f rectangular longitudinal hydraulic fractures with low conductivity in a fractal reservoir of finite thickness with fixed fractal dimension (D_f=1.5) and conductivity index (θ=0) (constant- pressure case).

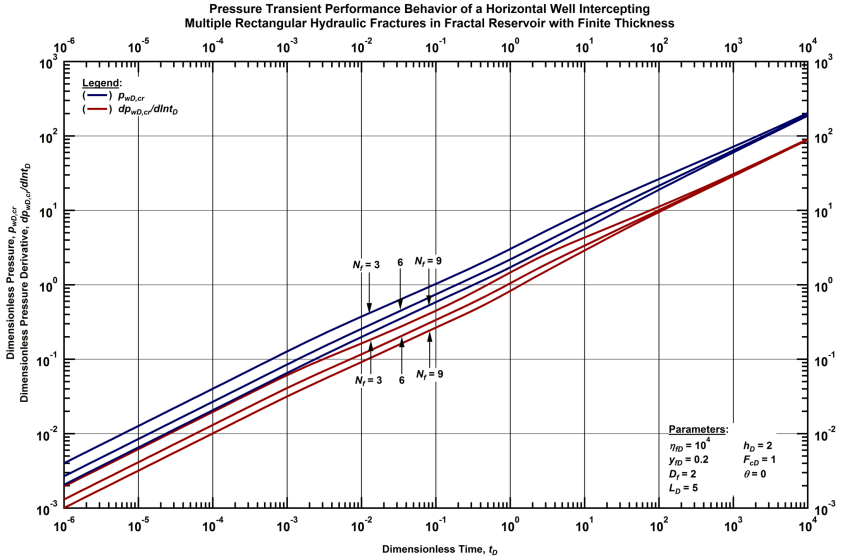

Figure G.117— Log-log plot of the dimensionless pressure and dimensionless pressure derivative functions for a horizontal well intercepting N_f rectangular longitudinal hydraulic fractures with low conductivity in a fractal reservoir of finite thickness with fixed fractal dimension (D_f=2) and conductivity index (θ=0) (constant-rate case).

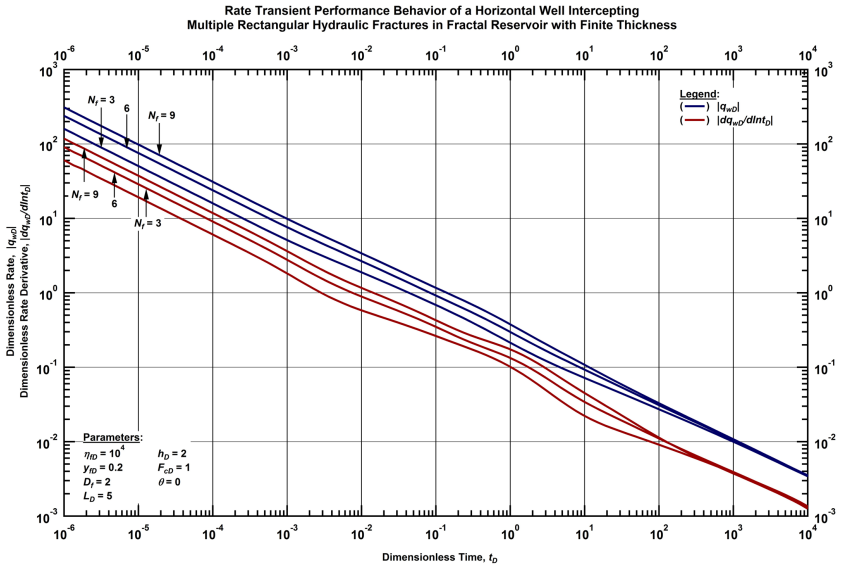

Figure G.118— Log-log plot of the dimensionless rate and dimensionless rate derivative functions for a horizontal well intercepting N_f rectangular longitudinal hydraulic fractures with low conductivity in a fractal reservoir of finite thickness with fixed fractal dimension (D_f=2) and conductivity index (θ=0) (constant- pressure case).

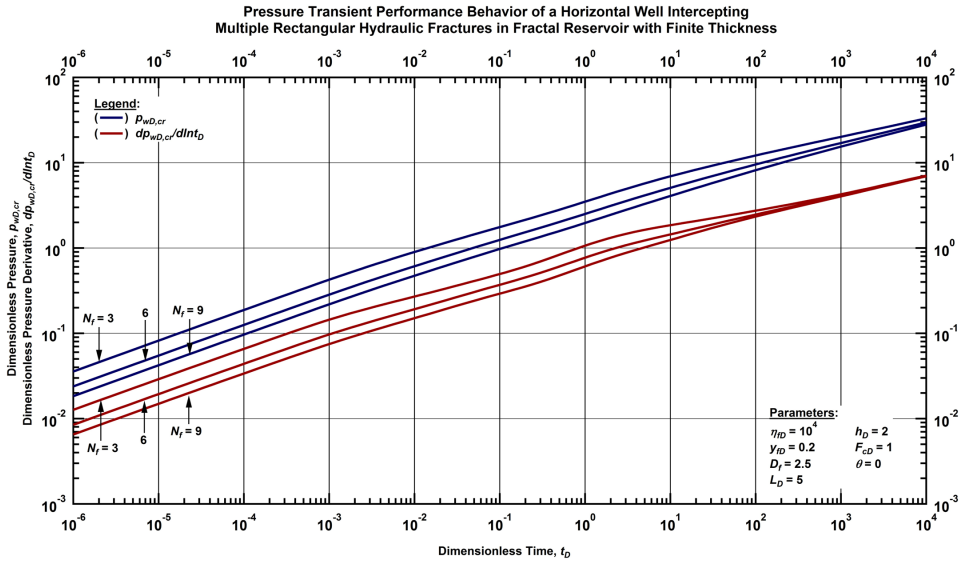

Figure G.119— Log-log plot of the dimensionless pressure and dimensionless pressure derivative functions for a horizontal well intercepting N_f rectangular longitudinal hydraulic fractures with low conductivity in a fractal reservoir of finite thickness with fixed fractal dimension (D_f=2.5) and conductivity index (θ=0) (constant-rate case).

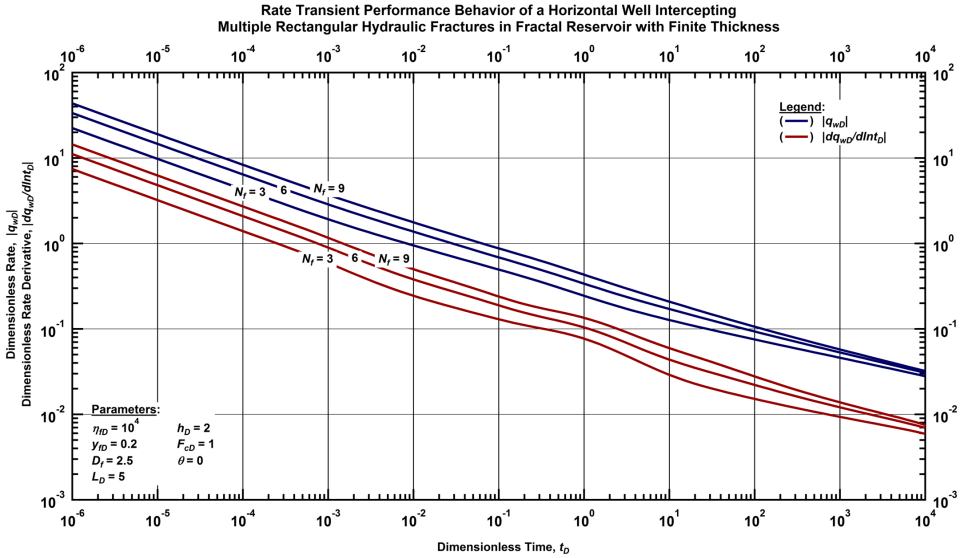

Figure G.120— Log-log plot of the dimensionless rate and dimensionless rate derivative functions for a horizontal well intercepting N_f rectangular longitudinal hydraulic fractures with low conductivity in a fractal reservoir of finite thickness with fixed fractal dimension (D_f=2.5) and conductivity index (θ=0) (constant-pressure case).

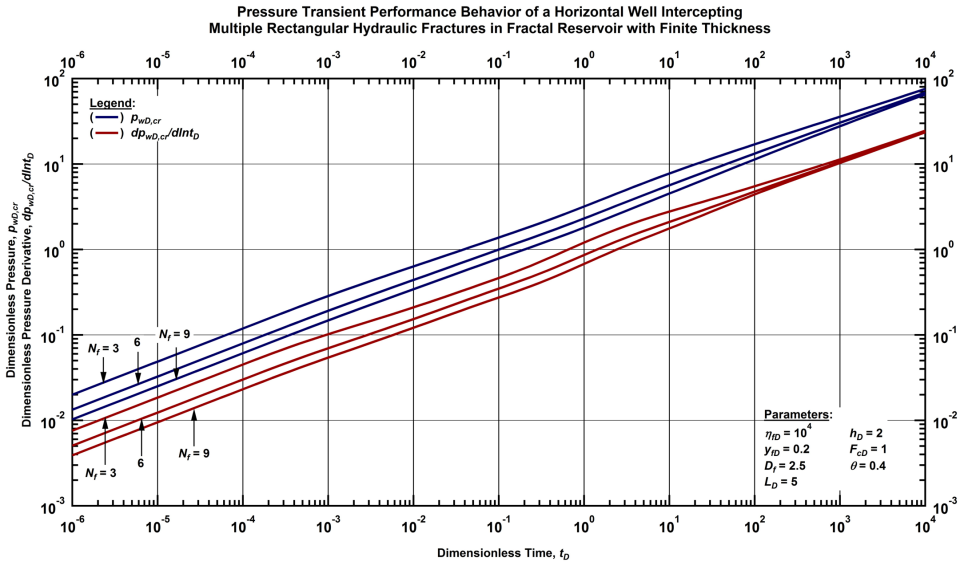

Figure G.121— Log-log plot of the dimensionless pressure and dimensionless pressure derivative functions for a horizontal well intercepting N_f rectangular longitudinal hydraulic fractures with low conductivity in a fractal reservoir of finite thickness with fixed fractal dimension (D_f=2.5) and conductivity index (θ=0.4) (constant-rate case).

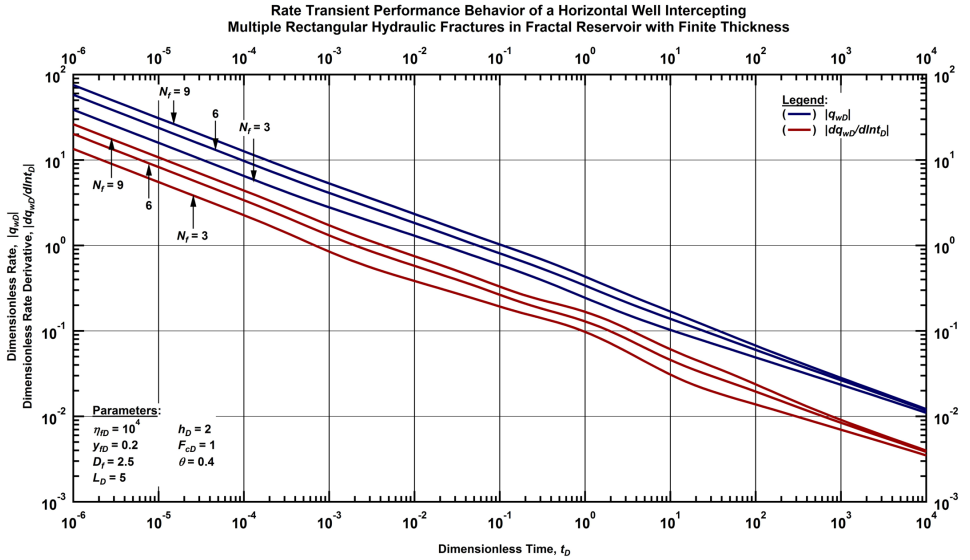

Figure G.122— Log-log plot of the dimensionless rate and dimensionless rate derivative functions for a horizontal well intercepting N_f rectangular longitudinal hydraulic fractures with low conductivity in a fractal reservoir of finite thickness with fixed fractal dimension (D_f=2.5) and conductivity index (θ=0.4) (constant-pressure case).

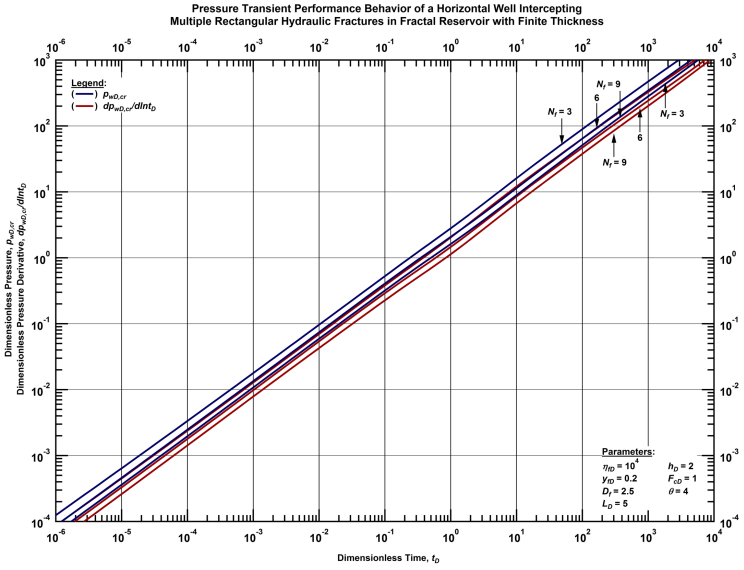

Figure G.123— Log-log plot of the dimensionless pressure and dimensionless pressure derivative functions for a horizontal well intercepting N_f rectangular longitudinal hydraulic fractures with low conductivity in a fractal reservoir of finite thickness with fixed fractal dimension (D_f=2.5) and conductivity index (θ=4) (constant-rate case).

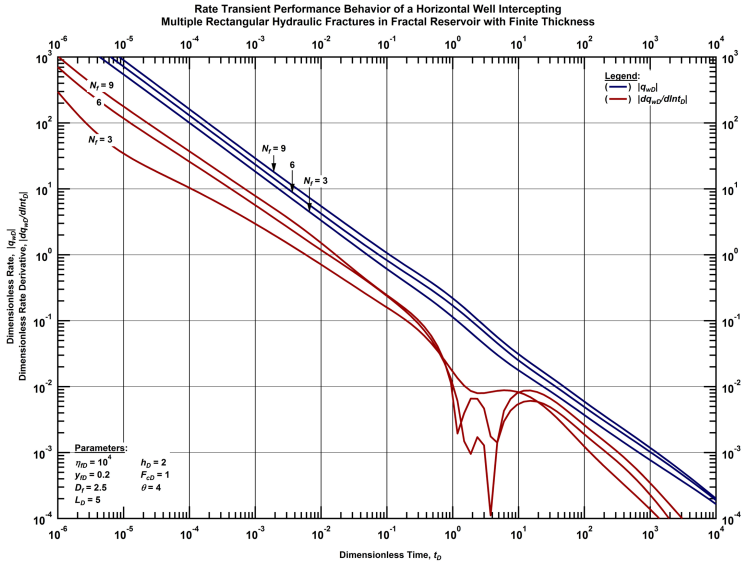

Figure G.124— Log-log plot of the dimensionless rate and dimensionless rate derivative functions for a horizontal well intercepting N_f rectangular longitudinal hydraulic fractures with low conductivity in a fractal reservoir of finite thickness with fixed fractal dimension (D_f=2.5) and conductivity index (θ=4) (constant-pressure case).

APPENDIX H

THE USE OF FRACTIONAL INTEGRALS TO MODEL THE TRANSIENT PERFORMANCE BEHAVIOR OF WELLS INTERCEPTING HYDRAULIC FRACTURES[4]

H.1. Wells Intercepting Hydraulic Fractures in Euclidean Reservoirs: Classic Models

The finite conductivity fracture models are based on the discretization of the hydraulic fracture, which defines a system of equations. The "coupling" between the hydraulic fracture and the reservoir is made by the use of the uniform flux solution of a hydraulic fracture, which implies the superposition of the reservoir (line/point source) solution. Gringarten *et al.* (1974) presented the uniform flux solution for a vertical well intercepting a rectangular fracture within a 2*D* (cylindrical) reservoir (schematics in **Fig. H.1**). The authors developed the solution by assuming that y_D=y_{wD}=0 and superimposing the line source solution over the lateral extent of the hydraulic fracture (-x_{fD}, x_{fD}), *i.e.*:

$$p_{D,cr}(x_D, x_{wD}, y_D, y_{wD}, t_D) = \frac{1}{4}\int_{-1}^{1} E_1\left[\frac{[x_D - x_{wD}]^2}{4t_D}\right] dx_{wD} \quad \text{.....(H.1)}$$

which results in the following expression:

[4] Parts of this Appendix are reprinted with permission from "Pressure and Rate Transient Behavior of a Horizontal Well Intercepting Multiple Hydraulic Fractures within a Fractal Reservoir " by Valdes-Perez, A. R., Larsen, L., and Blasingame, T.A., 2018. *Unconventional Resources Technology Conference* (*URTeC*) *Proceedings*, URTeC-2902854. Copyright [2018] by Society of Petroleum Engineers, Inc.

$$p_{D,cr}(x_D,t_D)=\frac{\sqrt{\pi t_D}}{2}\left[erf\left[\frac{1+x_D}{2\sqrt{t_D}}\right]+erf\left[\frac{1+x_D}{2\sqrt{t_D}}\right]\right]+\frac{1+x_D}{4}E_1\left[\frac{[1+x_D]^2}{4t_D}\right]+\frac{1-x_D}{4}E_1\left[\frac{[1-x_D]^2}{4t_D}\right]\text{.....(H.2)}$$

Evaluating Eq. H.2 at the wellbore (*i.e.*, x_D=0) and taking the logarithmic derivative gives us:

$$\frac{dp_{wD,cr}(t_D)}{d\ln t_D}=\frac{\sqrt{\pi t_D}}{2}erf\left[\frac{1}{2\sqrt{t_D}}\right]\text{.....(H.3)}$$

Fig. H.2 shows the pressure data for a uniform flux fracture published by Gringarten *et al.* (1974) and the pressure derivative function calculated with Eq. H.3. At early times, it exhibits the characteristic formation-linear flow (half-slope in the pressure derivative) followed by the pseudo-radial flow (flat slope in the pressure derivative).

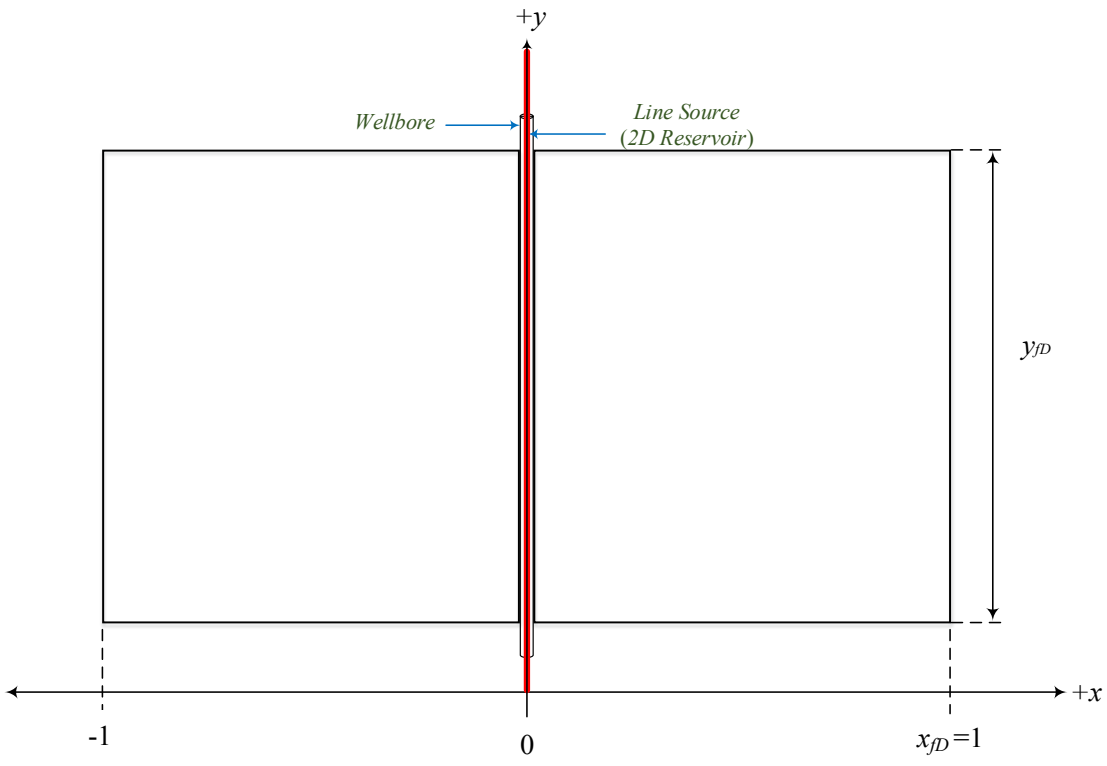

Figure H.1 — Schematic of the uniform flux fracture solution using the line source function.

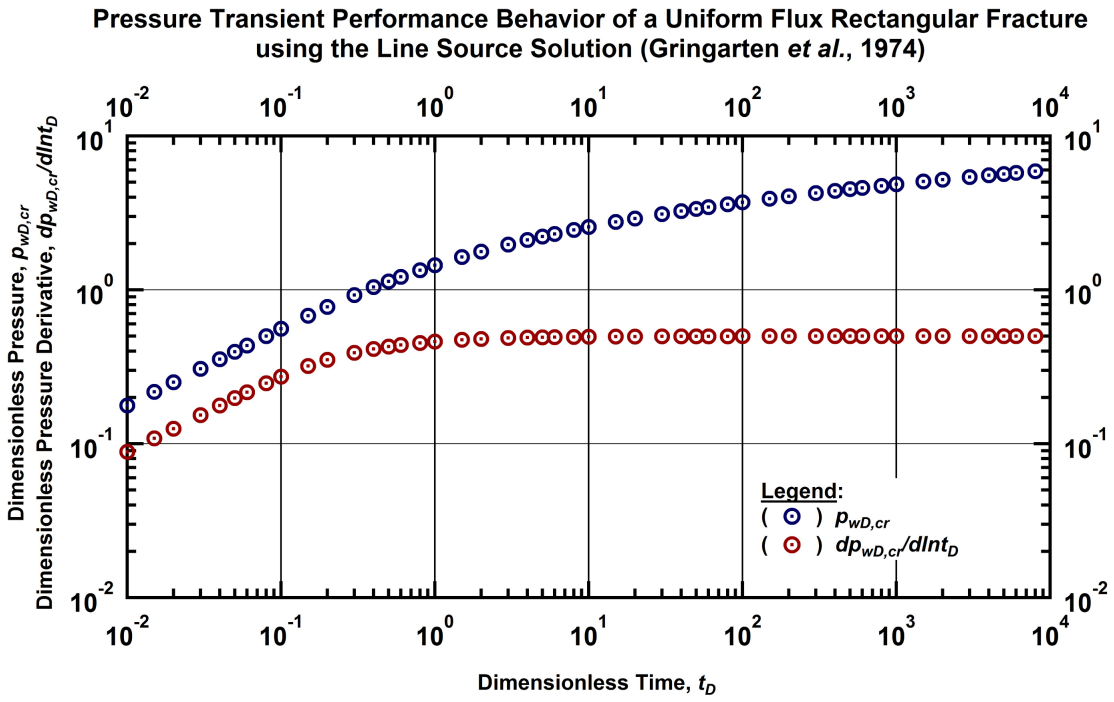

Figure H.2 — Log-log plot of the pressure and pressure derivative functions of the uniform flux fracture solution using the line source.

In 1991, Larsen *et al.* used the point source solution in the Laplace domain to develop the model of a horizontal well intercepting a finite conductivity rectangular fracture within a 3*D* (spherical) reservoir. **Fig. H.3** shows a schematic of this system defined for a vertical (instead of a horizontal) well. The authors applied a double integral in polar coordinates to superimpose the point source solution in the Laplace domain over the surface of the segments of the rectangular fracture. In cartesian coordinates, this expression is given by:

$$\bar{p}_{D,cr}(x_D, x_{wD}, y_D, y_{wD}, u) = \frac{1}{2u} \int_{-1}^{1} \int_{0}^{y_{fD}} \frac{1}{\sqrt{[x_D - x_{wD}]^2 + [y_D - y_{wD}]^2}} \exp\left[-\sqrt{u}\sqrt{[x_D - x_{wD}]^2 + [y_D - y_{wD}]^2}\right] dy_{wD} dx_{wD} \quad \text{.....(H.4)}$$

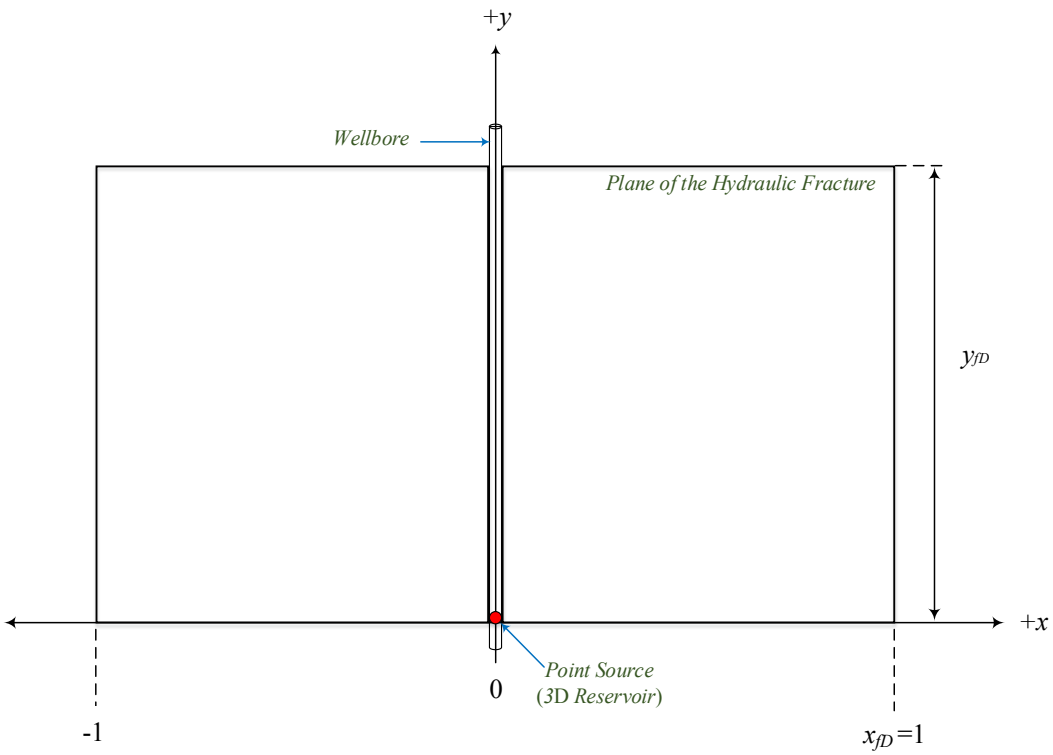

Figure H.3 — Schematics of the uniform flux fracture solution using the point source function.

In their Appendix B, Larsen *et al*. (1991) showed that the uniform flux solution of a hydraulic fracture within a 3*D* (spherical) reservoir (Eq. H.4) converges to the 2*D* (cylindrical) reservoir case if the longitudinal extension of the fracture (y_{fD}) goes to infinity. Utilizing *MATLAB*'s *integral2*-function to numerically integrate Eq. H.4 and subsequently applying the Stehfest algorithm, we generated the pressure and pressure derivative functions of this model for increasing y_{fD}-values. Then, we compared these results to the data presented by Gringarten *et al.* (1974). We present such a comparison in **Fig. H.4**. We observed that the use of the double integral approach in the point source reproduces the formation linear flow at early times and the characteristic negative half slope for spherical systems at late times. The pressure transient behavior of this type of system is similar to the one observed in partially penetrated wells. This solution can also reproduce the pseudoradial flow if the y_{fD}-value is sufficiently high.

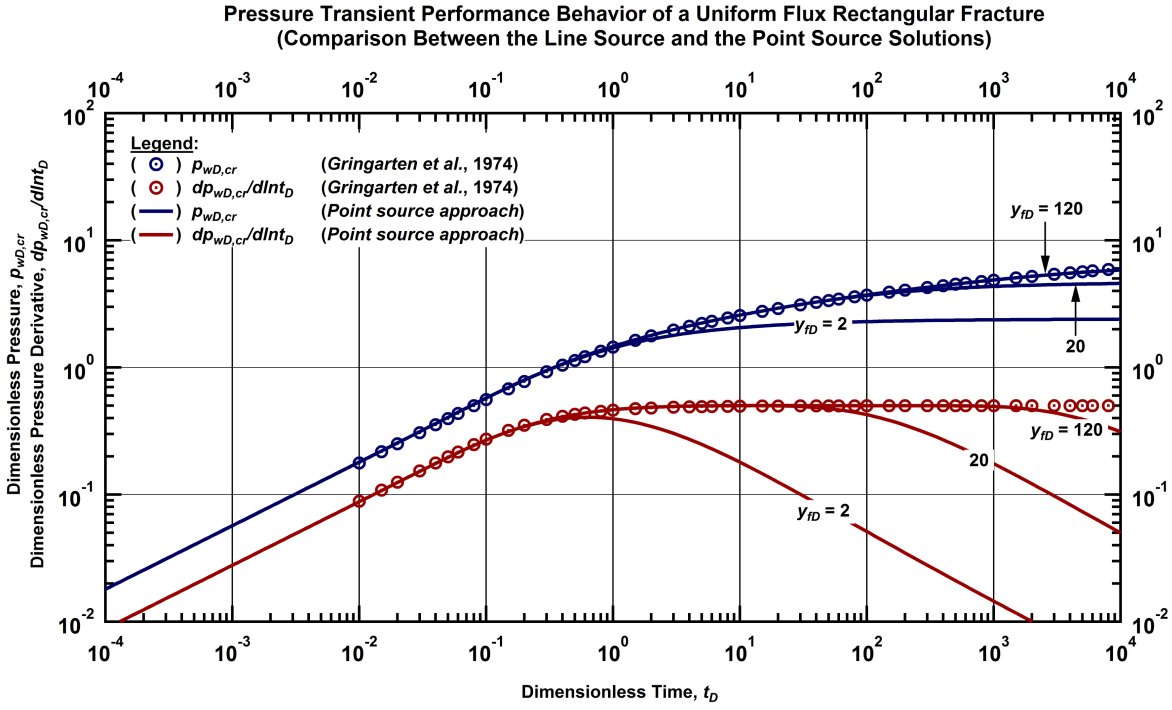

Figure H.4 — Convergence of the uniform flux fracture model using the point source solution (Larsen *et al.*, 1991) to the uniform flux fracture model using the line source solution (Gringarten *et al.*, 1974)

Based on the line source solution, Cinco-Ley *et al.* (1978) developed the finite conductivity fracture model considering a rectangular fracture. Depending on the characteristics (parameters) of the fracture, this model can exhibit the linear fracture flow at early times, the bilinear and formation linear flows at intermediate times, and the pseudoradial flow at late times. **Fig. H.5** shows the pressure data published by the authors. We estimated the pressure derivate data using *MATLAB*'s *spline*- function. Given that the point source function can reproduce the results of the uniform flux fracture using the line source function if one of the axes goes to infinity, the finite conductivity model developed by Larsen *et al.* (1991) should converge to the model presented by Cinco-Ley *et al.* (1978) at long longitudinal extensions of the hydraulic fracture (y_{fD}).

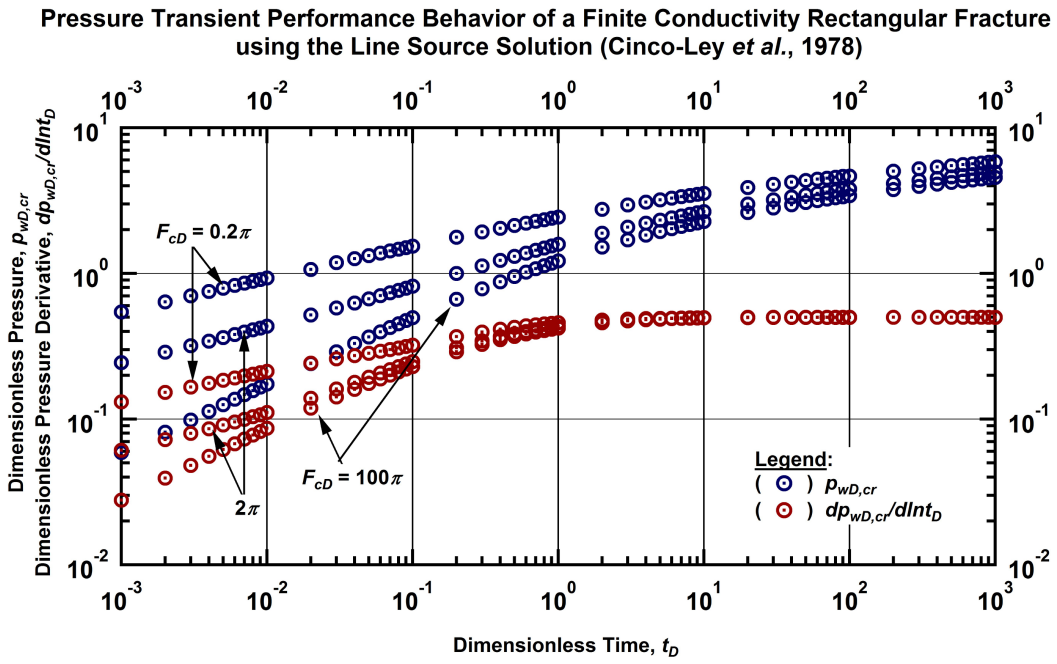

Figure H.5 — Log-log plot of the pressure and pressure derivative functions of the finite conductivity fracture solution using the line source.

To test our hypothesis, we have used the input data (dimensionless fracture conductivity and dimensionless hydraulic diffusivity) provided by Cinco-Ley *et al*. (1978) in the model developed by Larsen *et al* (1991) to compare the results of both models. We noted that to compare the results of these models, the pressure ($p_{wD,L}$) and pressure derivative signatures generated with the Larsen *et al.* model should be rescaled as follows:

$$p_{wD,cr} = \left[\frac{2y_{fD}}{h_D}\right] p_{wD,L}, \quad \text{.....(H.5)}$$

where h_D is the dimensionless formation thickness. We tested both scenarios for a short longitudinal fracture (y_{fD}=2) and for a long longitudinal fracture (y_{fD}=80). Subsequently, we compared these results to the data provided by Cinco-Ley *et al*. (1978). The results are shown in

Fig. H.6. Based on these results, we came to the following conclusions: (1) for high y_{fD}-values, the model proposed by Larsen *et al.* (1991) converges to the model presented by Cinco-Ley *et al.* (1978), and (2) the pressure and pressure derivative functions at early and intermediate times (t_D<10^{-1}) are sensitive only to the F_{cD}- and η_{fD}-parameters, regardless of the longitudinal length of the hydraulic fracture (y_{fD}) and the source solution related to the geometry of the reservoir (line source for a cylindrical reservoir or point source for a spherical reservoir).

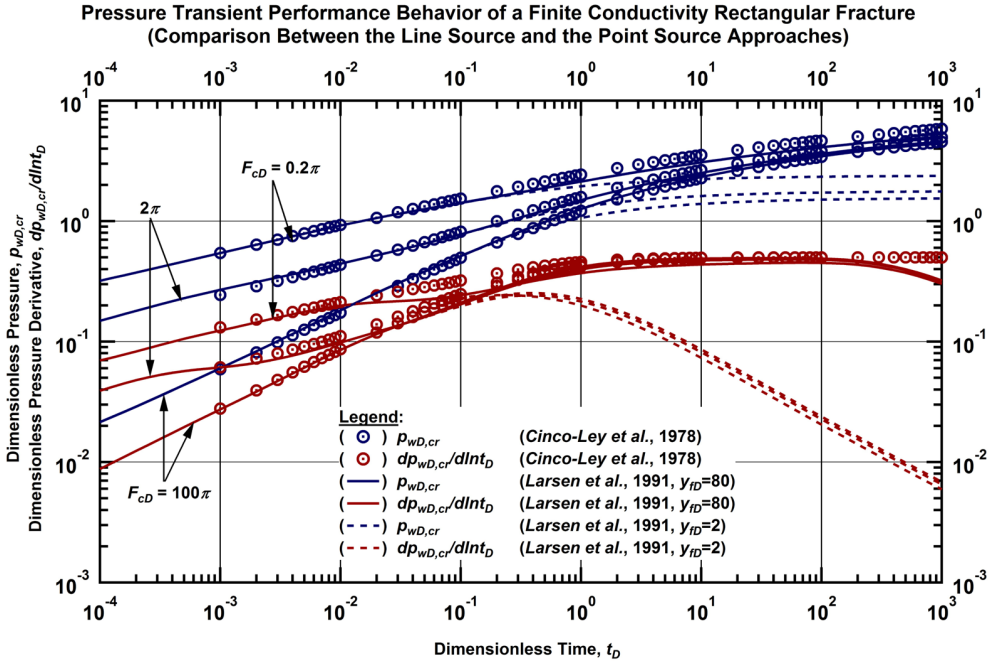

Figure H.6 — Convergence of the finite conductivity fracture model using the point source solution (Larsen *et al.*, 1991) to the finite conductivity fracture model using the line source solution (Cinco-Ley *et al.*, 1978)

H.2. Extension of the Line/Point Source approaches to Fractal Reservoirs

We have observed that our solutions based on the "fractal point" source approach yield erratic behaviors in the pressure and rate transient performance behaviors at intermediate times when v≥0. Beier (1994) redefined the parameters of the fractal reservoir model presented by Chang *et al.*

(1990) and presented the infinite conductivity and uniform flux rectangular fracture solutions using a "fractal line" approach. We have observed that the use of this approach can produce unstable pressure and rate behaviors when $v<0$. These erratic behaviors are related to the treatment of the fractal source function. Beier (1994) used a "line-source" approach (single integral), which involves the superposition of the fractal source along the extent of the rectangular fracture; whereas, we have applied a "point source" approximation (double integral), which implies the superposition of the fractal source over the entire surface of the fracture. We recognize that none of these approaches are appropriate for a fractal reservoir.

The main convergence requirement of the fractal reservoir model establishes that this model should converge to the Euclidean reservoir models (Chang *et al.*, 1990) when (1) $D_f=3$ and $\theta=0$ ($v=-0.5$) for the spherical reservoir model (Chatas, 1966), (2) $D_f=2$ and $\theta=0$ ($v=0$) for the cylindrical reservoir model (van Everdingen *et al.*, 1949), and (3) $D_f=1$ and $\theta=0$ ($v=0.5$) for the linear reservoir model (Miller, 1962). Therefore, the models of wells intercepting hydraulic fractures in fractal reservoirs should be able to reproduce all the Euclidean scenarios. For a well intercepting a finite conductivity rectangular fracture within a fractal reservoir, the model should be able to reproduce the results presented by Cinco-Ley *et al*. (1978) when $D_f=2$ and $\theta=0$ and the ones presented by Larsen *et al.* (1991) when $D_f=3$ and $\theta=0$. Although the model for a rectangular fracture presented in Chapter III fulfills the requirement for the Larsen *et al.* model, it fails to reproduce the results presented by Cinco-Ley *et al.* (1978). Similarly, the infinite conductivity fracture model presented by Beier (1994) fails to converge to the model presented by Larsen *et al.* (1991) (considering a high conductivity fracture).

In Section H.1, we showed that the double integral used for the point source solution (spherical homogeneous reservoir, *i.e.*, D_f=3 and θ=0) and the single integral used for the line source solution (cylindrical homogeneous reservoir, *i.e.*, D_f=2 and θ=0) provide exactly the same pressure and pressure derivative performance behavior at early and intermediate times of a well intercepting a hydraulic fracture. In short, the transient behavior for a fractured well is unaffected by the geometry of the reservoir (fractal dimension, D_f) at early and intermediate times. These results are contradictory to the analyses presented in Chapters III and IV and the ones presented by Beier (1994). Hence, we have concluded that the use of the traditional line/point source approaches for fractal reservoirs is inappropriate. The use of the traditional schemes to model hydraulic fractures in fractal reservoirs can cause the "over-interpretation" of transient data by the introduction of phenomena unlikely to be distinguished in the macro-scale of a reservoir (*e.g.* anomalous diffusion parameters).

H.3. Fractional Integration to Model the Transient Performance Behavior of a Well Intercepting a Rectangular Hydraulic Fracture within a Fractal Reservoir

The traditional schemes to model the transient behavior of a well intercepting a hydraulic fracture in a homogeneous reservoir consist in the "coupling" of two Euclidean objects: the reservoir (cylinder or sphere) and the fracture (rectangular or circular). This process involves the integration of a function over a domain in a "linear" axis or axes. Because a fractal reservoir is an irregular object, it is inappropriate to use the same schemes because the axes are not necessarily linear for all cases. To overcome this problem, we propose the use of fractional integrals. Ortigueira *et al.* (2017) defined the superposition of a function over a rectangular region defined by $(a_1,b_1)x(a_2,b_2)$, utilizing the fractional integrals, as follows:

$$I_{lr}^{\alpha} f(a_1,b_1,a_2,b_2) = \int_{a_1}^{b_1}\int_{a_2}^{b_2} f(x_1,x_2)dx_1^{\alpha_1}dx_2^{\alpha_2} \quad \text{.....(H.6)}$$

The use of Eq. H.6 implies a rescaling of the axes of a given system using power-law functions. For a fractal reservoir, we consider that this is the most appropriate procedure to couple the irregular (fractal) geometry of the reservoir to the Euclidean shape of the hydraulic fracture. For this work, we have considered the case where $\alpha_1=\alpha_2$.

To show the application of the concept defined in Eq. H.6 in the transient performance behavior of a fractured well in a fractal reservoir, consider the fractal source solution in the Laplace domain developed in Appendix D:

$$\bar{p}_{fD,cr}(R_D,u) = \frac{h_D^{D_f-2}}{[\theta+2]^{1-\nu}\Gamma[1-\nu]} u^{-[\nu+2]/2} R_D^{[1-\beta]/2} K_\nu\left[R_D^{[\theta+2]/2}\frac{2\sqrt{u}}{\theta+2}\right] \quad \text{.....(H.7)}$$

Similar to Beier (1994), we defined the fractal radius as:

$$R_D^{\theta+2} = [x'_D - x'_{wD}]^{\theta+2} + [y'_D - y'_{wD}]^{\theta+2} \quad \text{.....(H.8)}$$

In this development, it is important to point out that the variables x'_D, x'_{wD}, y'_D, and y'_{wD} do not correspond to the classic cartesian (linear) axes. This is the main difference to Beier's conceptualization. To provide an equivalent expression in cartesian (linear) axes (x_{wD}, y_{wD}), we considered the following transformations:

$$[x'_D - x'_{wD}] = [x_D - x_{wD}]^{2/\beta} \quad \text{,.....(H.9)}$$

and,

$$[y'_D - y'_{wD}] = [y_D - y_{wD}]^{2/\beta} \quad \text{.....(H.10)}$$

After combining Eqs. H.7 to H.10, the fractal source solution becomes:

$$\bar{p}_{fD,cr}(x_D, x_{wD}, y_D, y_{wD}, u) = \frac{h_D^{D_f-2}}{[\theta+2]^{1-v}\Gamma[1-v]} u^{-[v+2]/2} \left[[x_D - x_{wD}]^{2\xi} + [y_D - y_{wD}]^{2\xi} \right]^{v/2} K_v \left[\left[[x_D - x_{wD}]^{2\xi} + [y_D - y_{wD}]^{2\xi} \right]^{1/2} \frac{2\sqrt{u}}{\theta+2} \right] \quad \text{, ...(H.11)}$$

where $\xi=[\theta+2]/\beta$. In this work, we use a "fractal point" approach (*i.e.*, a double integral) to superimpose the solution of the fractal reservoir (Eq. H.12) over the surface of the hydraulic fracture. The fracture is defined in the domain (-1,1) in the x_{wD}-axis and $(0,y_{fD})$ in the y_{wD}-axis. Therefore, the uniform-flux fracture solution, is defined by:

$$\bar{p}_{fD,cr}(x_D, x_{wD}, y_D, y_{wD}, u) = \frac{h_D^{D_f-2}}{[\theta+2]^{1-v}\Gamma[1-v]} u^{-[v+2]/2} \int_{-1}^{1} \left[\int_{0}^{y_{fD}} \psi^v K_v \left[\psi \frac{2\sqrt{u}}{\theta+2} \right] dy_{wD} \right] dx_{wD} \quad \text{, ...(H.12)}$$

where:

$$\psi = \sqrt{[x_D - x_{wD}]^{2\xi} + [y_D - y_{wD}]^{2\xi}} \quad \text{.....(H.13)}$$

We could not obtain an analytical solution to the general case of the integral defined in Eq. H.12. The results presented in this Appendix were developed using numerical integration (*MATLAB*'s *integral2*-function).

Convergence to the Classic Uniform-Flux Fracture Models

According to the convergence requirements defined in Section H.2 (taken from Chang *et al.*, 1990), the solution given by Eq. H.12 must converge to the uniform-flux fracture solution proposed

by Gringarten *et al.* (1974) for D_f=2 and θ=0, and to the point source solution used by Larsen *et al.* (1991) for D_f=3 and θ=0. In **Fig. H.7**, we present the convergence of the model for the first case (Gringarten *et al.*, 1974), and the convergence to the second case (Larsen *et al.*, 1991) is presented in **Fig. H.8**. We considered a unit thickness (h_D=1) for both scenarios, whereas the longitudinal length of the fracture (y_{fD}) is 1 for the first scenario and 2 for the second. We observed that the results generated with Eq. H.12 provide excellent matches to the pressure, pressure derivative, and β-pressure derivative data from Gringarten *et al.* (1974) and a perfect match to the results generated using the point source solution proposed by Larsen *et al.* (1991). The convergence to the *Larsen et al.* model can be analytically derived by substituting the fractal parameters D_f=3 and θ=0 in Eq. H.12 and it will collapse to the point source approach (Eq. H.4).

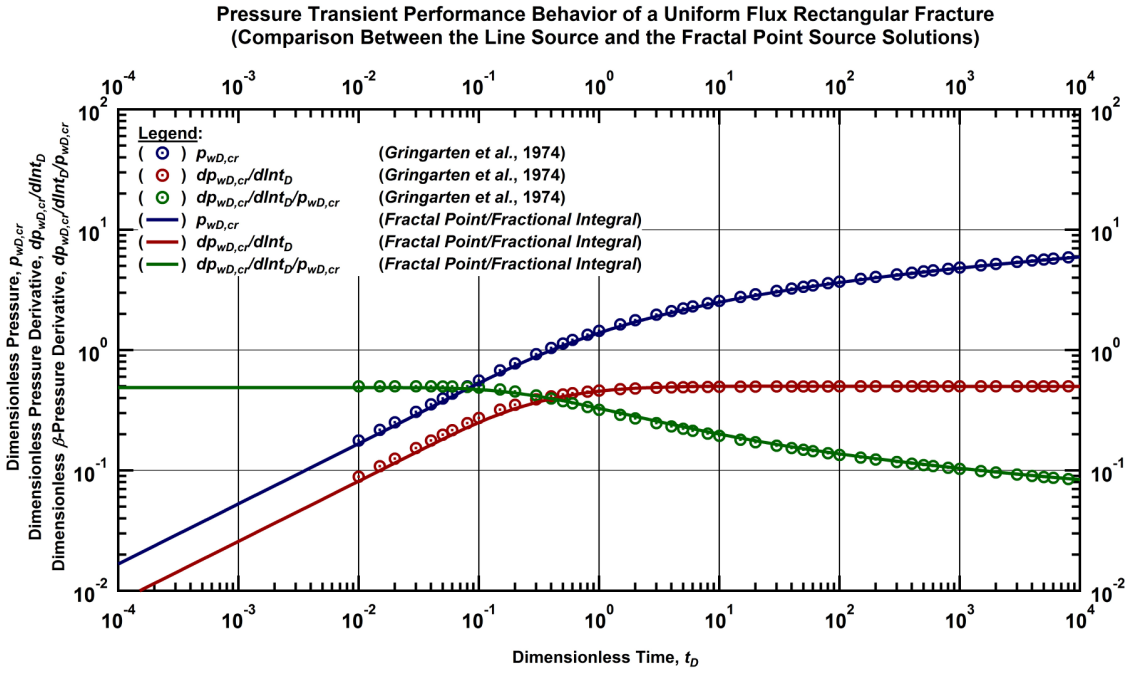

Figure H.7 — Convergence of the uniform flux fracture model within a fractal reservoir using the fractional integral solution to the uniform flux fracture model in a cylindrical reservoir (Gringarten *et al.*, 1974)

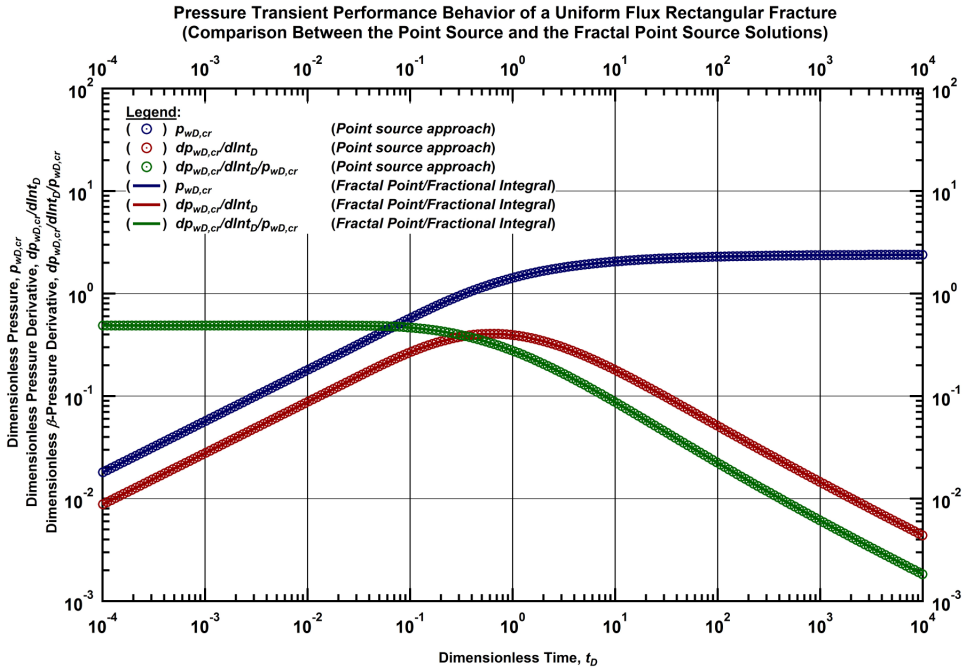

Figure H.8 — Convergence of the uniform flux fracture model within a fractal reservoir using the fractional integral solution to the uniform flux fracture model in a spherical reservoir (Larsen *et al.*, 1991)

Influence of the Fractal Parameters — Fractal Dimension (D_f)

As presented in **Fig. H.9**, the fractal dimension of the reservoir (D_f) does not have influence in the slope of the pressure and pressure derivative functions at early times ($t_D<4x10^{-2}$). All the cases presented in **Fig. H.9** show the characteristic formation linear flow at early times, followed by the pseudo-fractal flow at late times (the slope of the pressure derivative is equal to v). This is confirmed by the β-pressure derivatives presented in **Fig. H.10**. We observed that our proposed solution (Eq. H.12) produces a slight offset towards the right of the plot as the fractal dimension (D_f) decreases. Such an offset is more evident for $D_f< 2$ ($v>0$). This offset is also presented in the rate and rate derivative functions (**Fig. H.11**) and causes slightly higher flowrates at early times, for lower D_f-values.

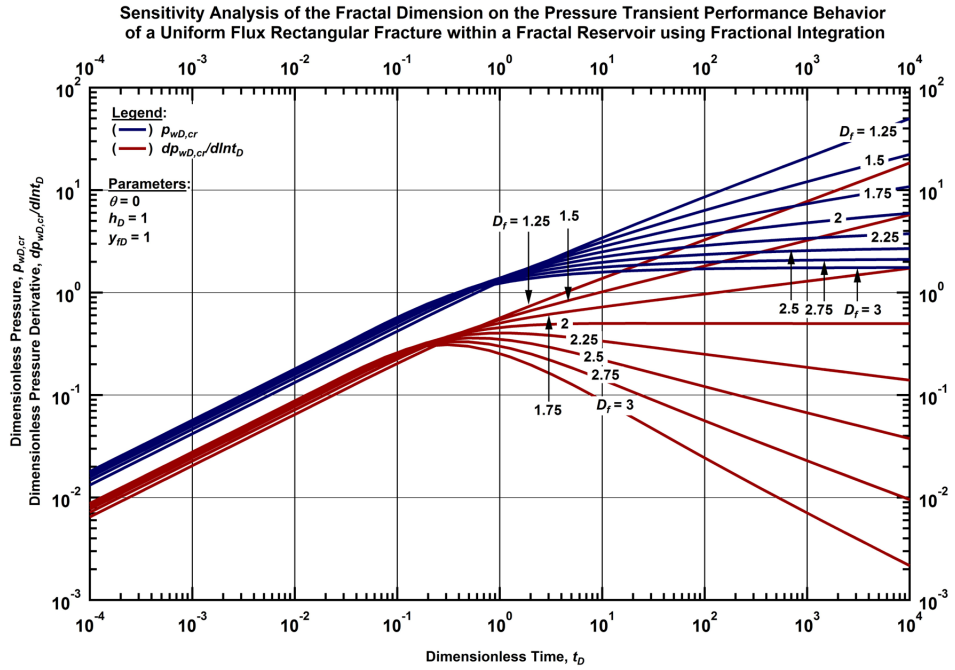

Figure H.9 — Influence of the fractal dimension (D_f) in the pressure and pressure derivative functions of a uniform flux fracture within a fractal reservoir (fractional integral approach).

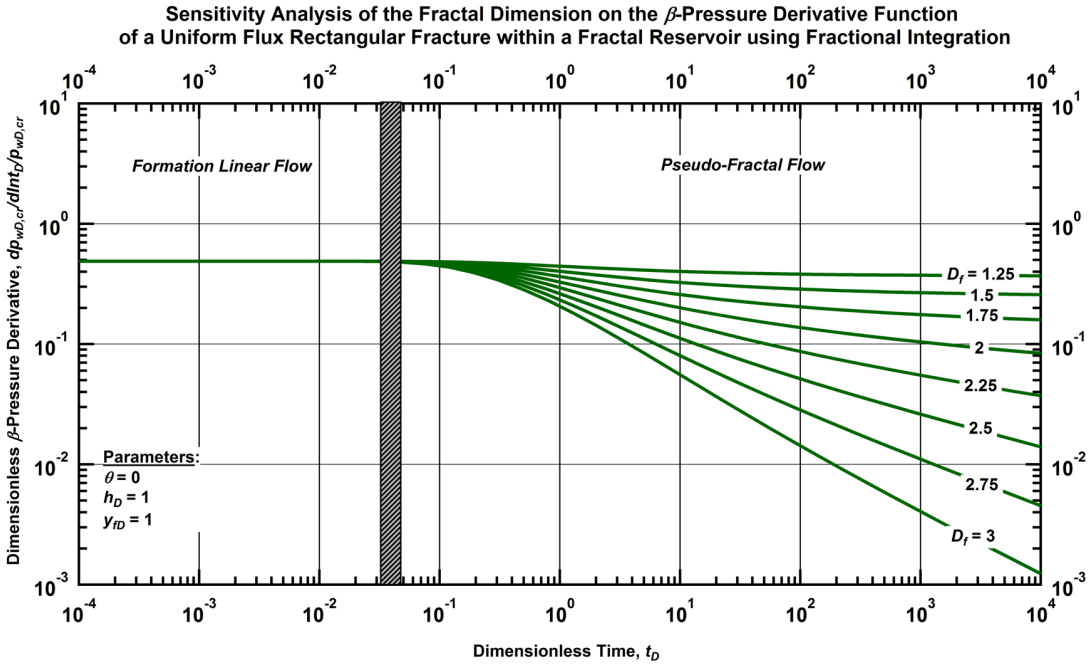

Figure H.10 — Influence of the fractal dimension (D_f) in the β- pressure derivative functions of a uniform flux fracture within a fractal reservoir (fractional integral approach).

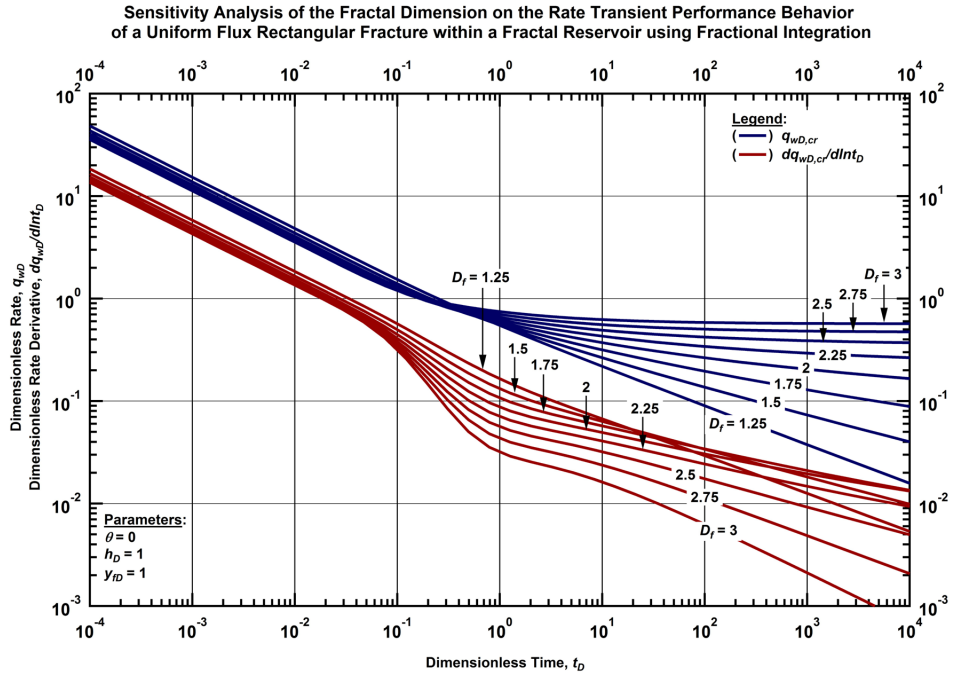

Figure H.11 — Influence of the fractal dimension (D_f) in the rate and rate derivative functions of a uniform flux fracture within a fractal reservoir (fractional integral approach).

Influence of the Fractal Parameters — Conductivity Index (θ)

We present the impact of the conductivity index (θ) in the pressure and pressure derivative signatures in **Fig. H.12**. This parameter describes the connectivity between the permeable sites. Low θ-values represent better connected permeable sites within a fractal system (reservoir). We observed that this parameter does have an impact on the performance behavior of the pressure and pressure derivative (slope) at early and late times. Based on analytical approximations and confirmation with the β-pressure derivative (**Fig. H.13**), we concluded that at early times (early fractal formation flow), the slope of the pressure and pressure derivative functions is equal to $[\theta+2]^{-1}$, whereas at late times (pseudo-fractal flow) the slope of the pressure derivative is equal to v. The relevance of this model is its potential use to directly determine the fractal reservoir

parameters without the use of trial and error methods (*e.g.* Flamenco-Lopez *et al.*, 2003). The conductivity index θ can be estimated from the slope at early times. Once the θ-value is obtained, it would also allow the straight calculation of the fractal dimension (D_f) from the slope of the pressure derivative function (v) if the test is long enough to observe the pseudo-fractal flow.

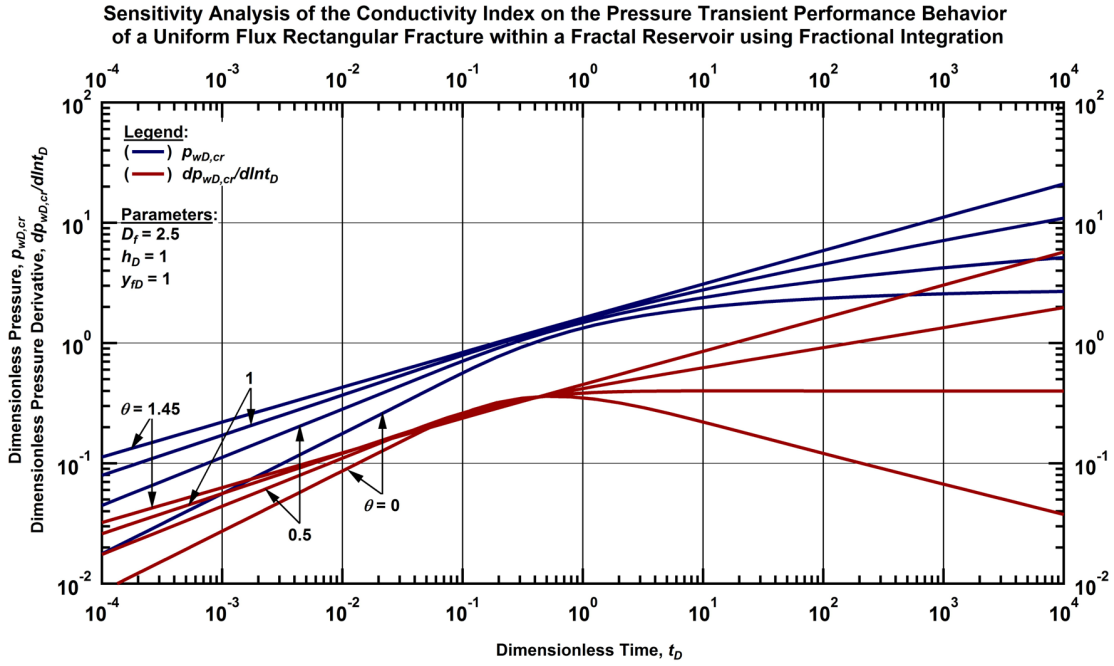

Figure H.12 — Influence of the conductivity index (θ) in the pressure and pressure derivative functions of a uniform flux fracture within a fractal reservoir (fractional integral approach).

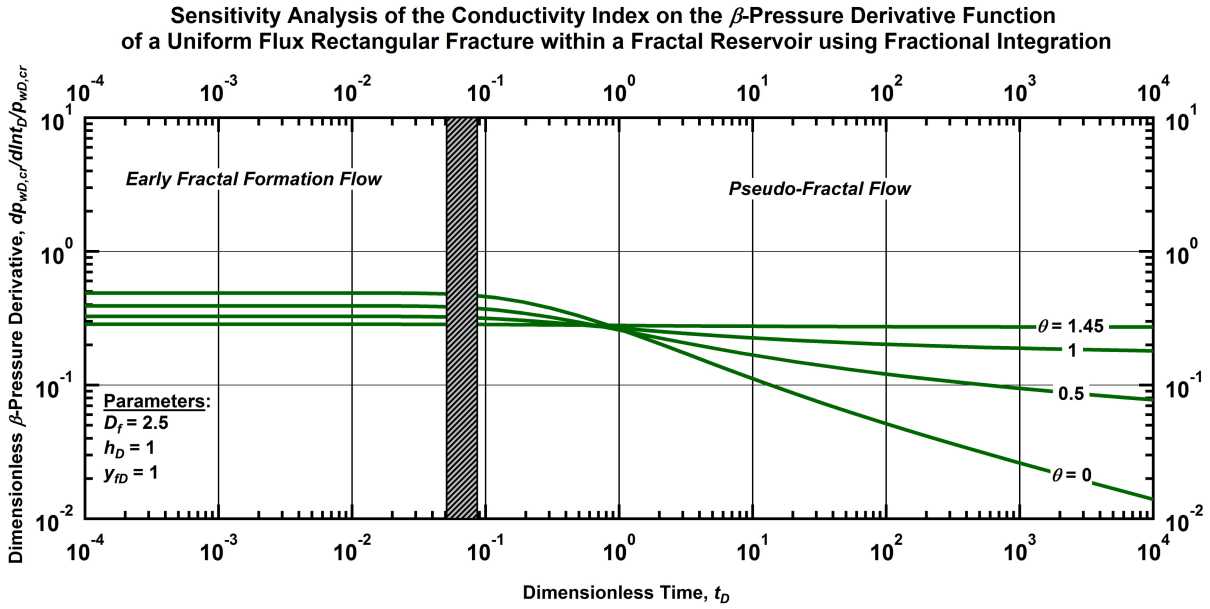

Figure H.13 — Influence of the conductivity index (θ) in the β- pressure derivative functions of a uniform flux fracture within a fractal reservoir (fractional integral approach).

In **Fig. H.14**, we present the constant-pressure solution ("mirror" images) of the cases presented in **Fig. H.12**. This plot shows that the variation of the θ-parameter is consistent to the physics, *i.e.*, better connected permeable sites in the fractal reservoir (low θ-values), yielding higher flowrates during the entire test. These results are contradictory to the ones generated by using the traditional point source/double integral approach and presented in Chapters III and IV, where the flowrate signatures showed that the better connected systems yielded higher flowrates only at late times.

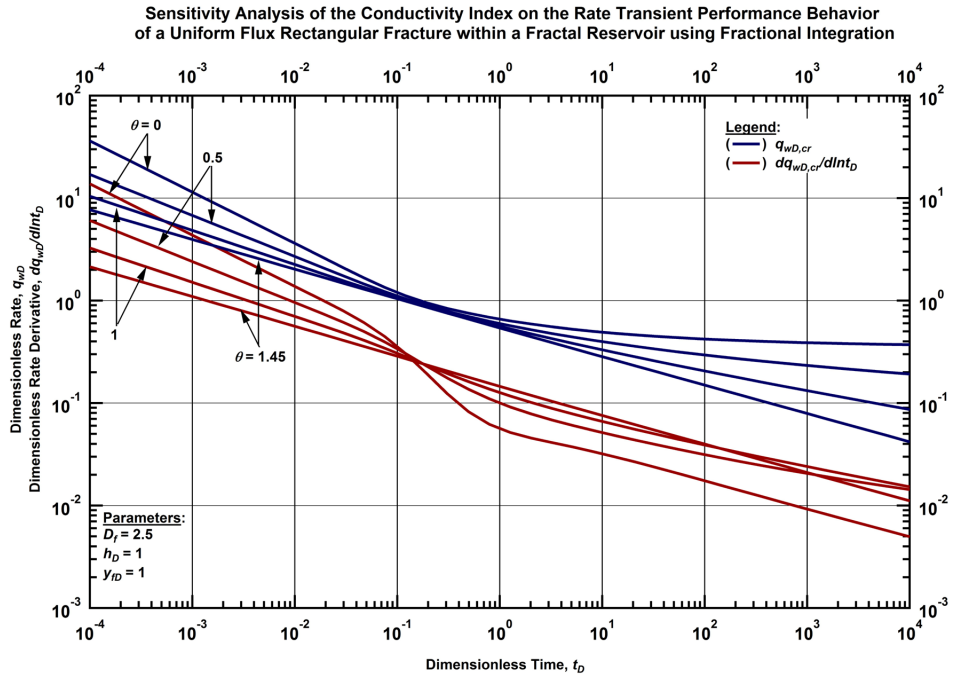

Figure H.14 — Influence of the conductivity index (θ) in the rate and rate derivative functions of a uniform flux fracture within a fractal reservoir (fractional integral approach).

Relation to the Anomalous Diffusion Model

We noted that the shape of the signatures presented in **Fig. H.12** are very similar to ones generated using the anomalous diffusion model presented by Camacho-Velazquez *et al.* (2008) (**Fig. 2.8**). Although their model is for unfractured wells (the model of a uniform flux fracture within a fractal reservoir with anomalous diffusion was presented by Razminia *et al.* 2015b, who used a traditional single/integer integral), we consider that these models are comparable given the use of fractional calculus, *i.e.*, the fractional derivative to model the anomalous diffusion in fractal reservoirs and the fractional integral used to model the fractured well in fractal reservoirs with typical diffusion. We present a comparison of these models in **Fig. H.15** (the input parameters for the uniform-flux fracture model are the same from **Fig. H.12**). We confirmed that the shape of the signatures of

these models are very similar, particularly at early times where the signatures of the β-pressure derivative function from both models overlap (see **Fig. H.16**).

Given that the anomalous diffusion models are entirely based on mechanical statistics and lacks any geological basis, we consider that the fractional integral approach is a more appropriate treatment to reproduce signatures as the one shown in **Fig. H.15**.

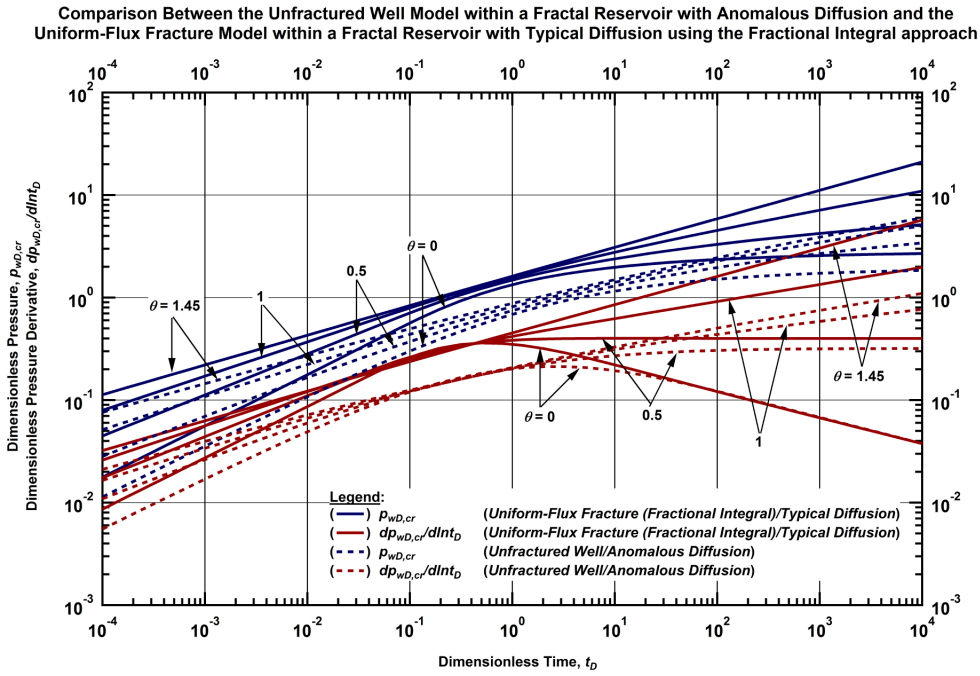

Figure H.15 — Comparison of the pressure and pressure derivative functions between the uniform-flux fracture model using the fractional integral and the anomalous diffusion model for an unfractured well within a fractal reservoir (Camacho-Velazquez *et al.*, 2008).

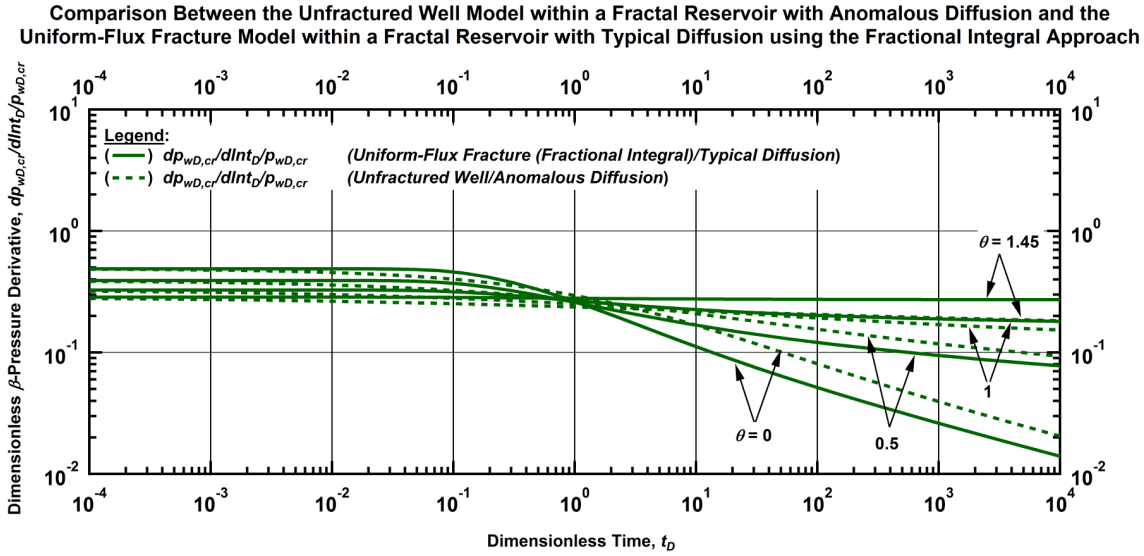

Figure H.16 — Comparison of the β-pressure derivative functions between the uniform-flux fracture model using the fractional integral and the anomalous diffusion model for an unfractured well within a fractal reservoir (Camacho-Velazquez *et al.*, 2008).

Application of the Fractional Integral Uniform Flux Fractures in 2*D* (*Cylindrical*) *Reservoirs*

In Section H.1, we presented the influence of the longitudinal length of the fracture in the point source solution (**Fig. H.4**). We observed that long longitudinal fractures can create two subperiods of flow at late-times: (1) pseudoradial and (2) spherical flow. As an exercise, we performed the same analysis using the double integral approach in the line source solution (see **Fig. H.17**). Although the solution at late times shows the expected pseudoradial flow for all cases, the results show also that at high y_{fD}-values, the characteristic half-slopes at early times (formation linear flow) of the pressure and pressure derivative functions collapse in an unitary slope with no physical significance.

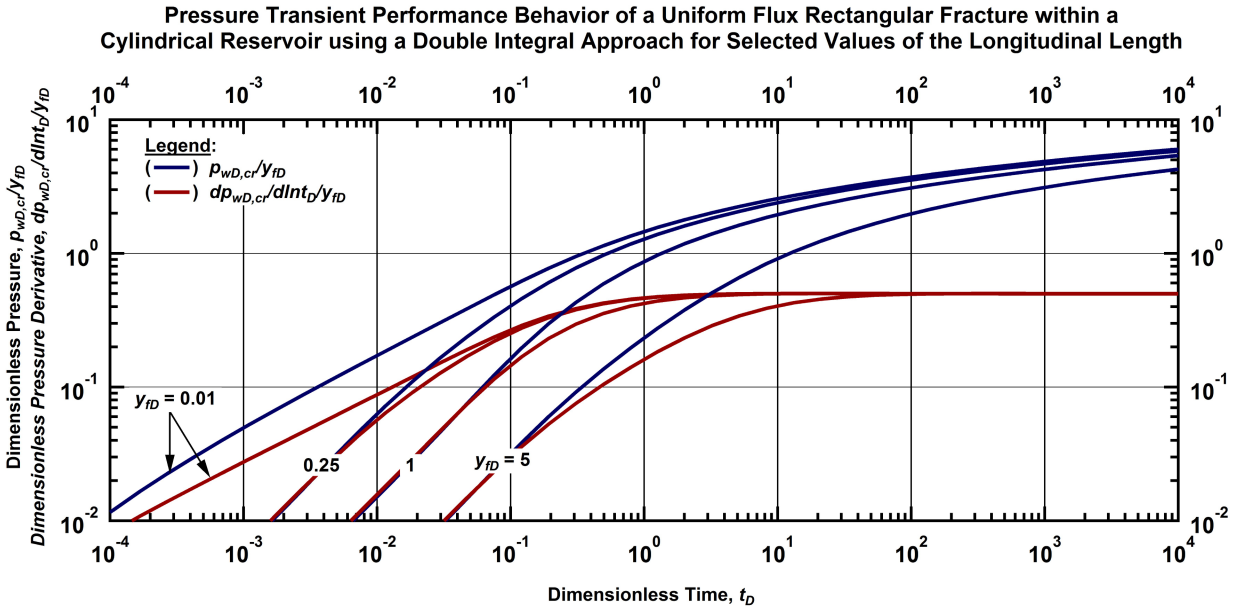

Figure H.17 — Transient performance behavior of the pressure and pressure derivative functions of the uniform flux fracture model using the line source solution and applying the traditional double integer integral approach.

We investigated the possibility of applying the fractional integration in the line source solution (D_f=2 and θ=0 in Eq. H.12) to perform a similar analysis to the ones presented in **Figs. H.4 and. H.17**. We present such an analysis in **Fig. H.18**. For y_{fD}-values different than one, we observed that the fractional integration approach can reproduce the following sequence of three periods of flow: (1) linear, (2) bilinear, and (3) pseudoradial flows. This sequence is the same as the one observed in low conductivity fractures. Given that the fractional integral approach does not consider the flow inside the fracture, the linear and bilinear flows reproduced with the fractional integral approach correspond to the formation linear flow and a "formation bilinear" flow. In a sense, the "formation bilinear flow" can be conceptualized as the reservoir portion of the classic trilinear flow model proposed by Lee *et al.* (1986).

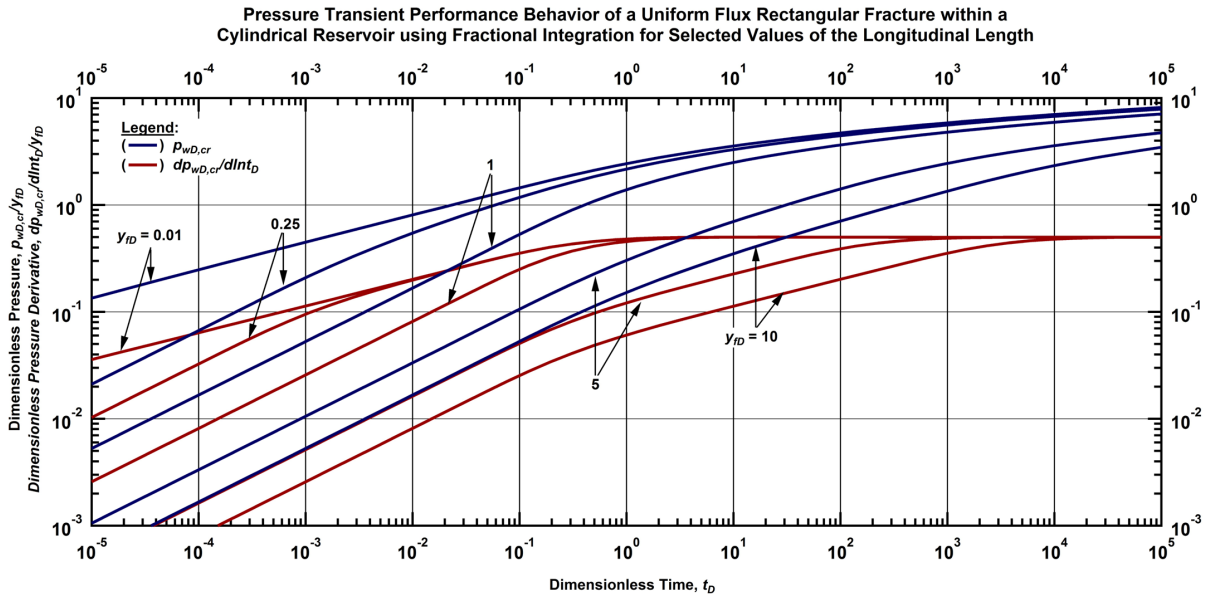

Figure H.18 — Transient performance behavior of the pressure and pressure derivative functions of the uniform flux fracture model using the line source solution and applying the fractional integral approach.

Convergence to the Classic Finite Conductivity Models for Rectangular Fractures

The finite conductivity model for a rectangular fracture in a fractal reservoir presented in Chapter III was developed using a "point source" approach (*i.e.*, double integral). This model can reproduce the results presented by Larsen *et al.* (1991), when the fractal parameters converge to the Euclidean limit of a sphere (*i.e.*, D_f=3 and θ=0). Consequently, it can also reproduce the results presented by Cinco-Ley *et al*. (1978) for high y_{fD}-values, similar to the results presented in Section H.1 (**Fig. H.6**). However, this convergence criterion is weak for a fractal model, which should achieve the convergence based on the fractal properties (D_f=2 and θ=0, for the Cinco-Ley *et al.* model). Therefore, we implemented the fractional derivative approach in scheme of the finite conductivity model presented in Chapter III.

In **Fig. H.19**, we present the convergence of the finite conductivity fracture in a fractal model using the fractional integral approach to the model proposed by Larsen *et al.* (1991). We present three cases: (1) low (F_{cD} =0.2π and η_{fD}=10^3), (2) intermediate (F_{cD} =π and η_{fD}=10^4), and high (F_{cD} =100π and η_{fD}=10^8) conductivity fractures. We observed that the match of these models is perfect for all these cases.

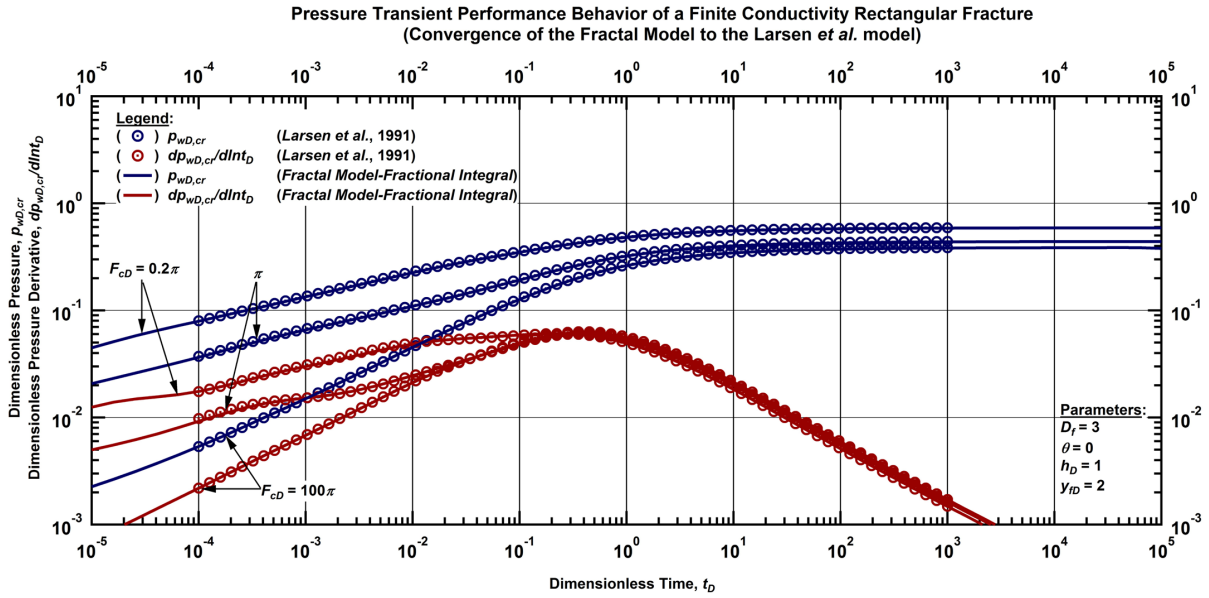

Figure H.19 — Convergence of the finite conductivity fracture model fractal reservoir using the fractional integral solution to the finite conductivity fracture model in a spherical reservoir (Larsen *et al.*, 1991)

Similarly in **Fig. H.20**, we show the convergence of the fractal model using the fractional integral approach to the Cinco-Ley *et al.* model, using the data provided in the original publication. We observed that the pressure ($p_{wD,F}$) and pressure derivative signatures of the generated by the fractal model using the fractional integral approach model are similar (in terms of the shapes of the curves) to the ones presented by Cinco-Ley *et al.* (1978). We found that these models match by rescaling the fractal model as follows:

$$p_{wD,cr} = c_1 \left[\frac{2y_{fD}}{h_D} \right] p_{wD,F}, \quad \text{.....(H.14)}$$

and

$$t_D = c_2 t_{D,F}, \quad \text{.....(H.15)}$$

where $t_{D,F}$ is the dimensionless time of the fractal model and c_1 and c_2 are adjusting factors. We determined these factors by trial and error. For the low conductivity fracture the factors are c_1=1.325 and c_2=0.08, for the intermediate conductivity fracture the factors are c_1=1.085 and c_2=0.16, and for the high conductivity fracture the factors are c_1=1 and c_2=5. We present the normalized models in **Fig. H.21**, where we observed excellent matches for the three cases at early and intermediate times. At late times (pseudofractal/pseudoradial flow), the proposed solution shows numerical instability for the high conductivity case.

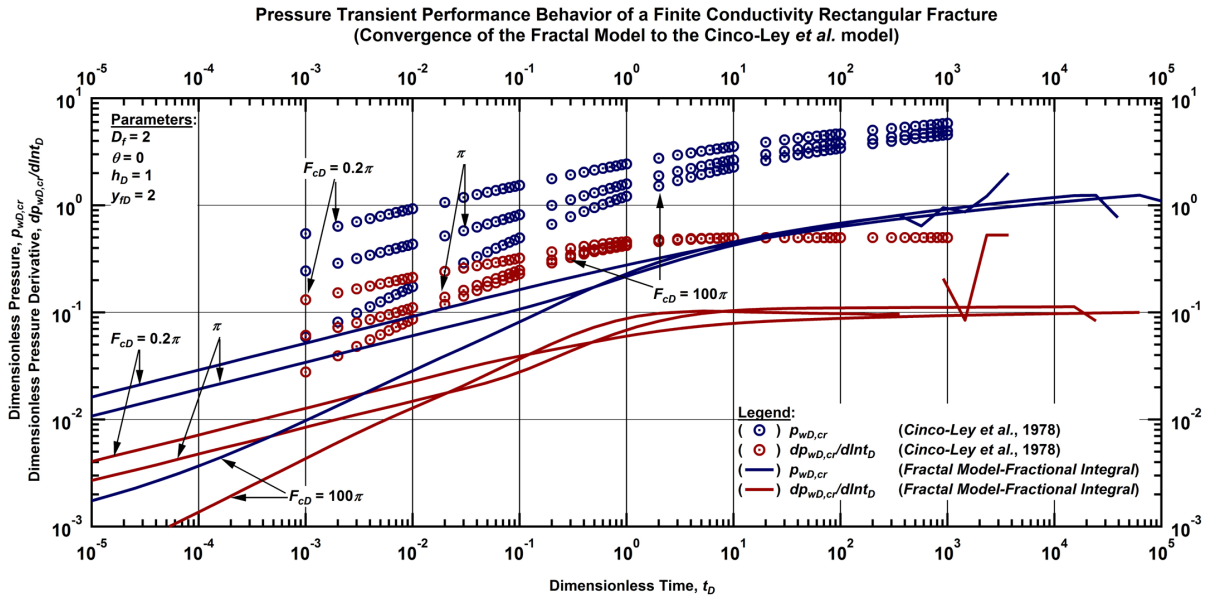

Figure H.20 — Convergence of the finite conductivity fracture model fractal reservoir using the fractional integral solution to the finite conductivity fracture model in a cylindrical reservoir (Cinco-Ley *et al.*, 1978)

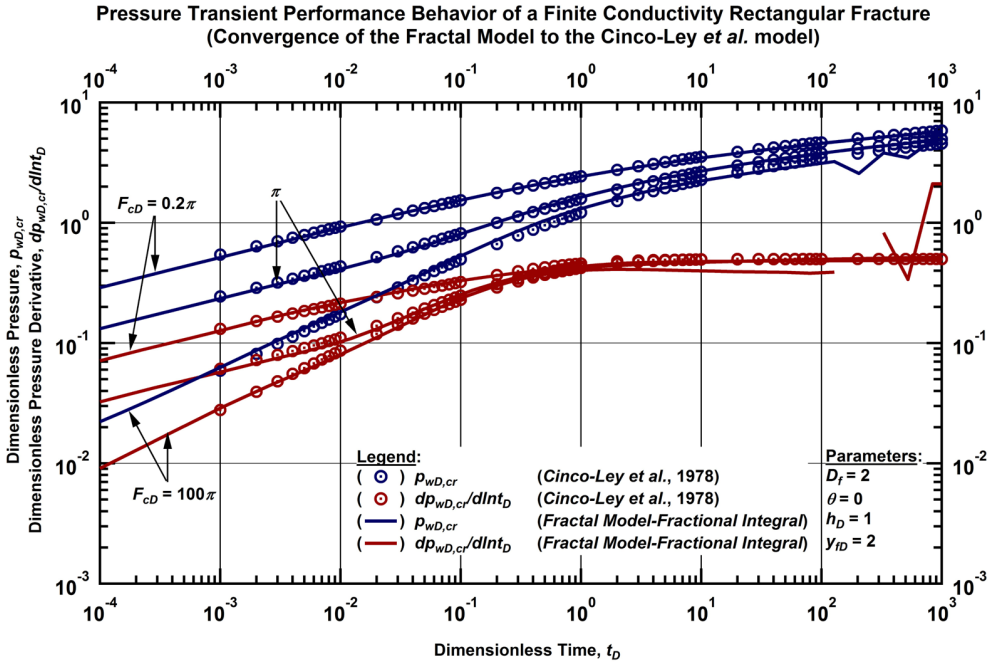

Figure H.21 — Convergence of the finite conductivity fracture model fractal reservoir using adjusting parameters and the fractional integral solution to the finite conductivity fracture model in a cylindrical reservoir (Cinco-Ley *et al.*, 1978)

The discussion should be focused now on the development of analytical functions to determine the adjusting parameters c_1 and c_2. In their literature review, Ortigueira *et al*. (2017) pointed out that there is not a generalized definition for the concept of the fractional integral, *e.g.*, some fractional integrals which involve a convolution scheme have the gamma function of the order of the integral as an integration coefficient. Although we obtained good results using the definition given by Eq. H.6, we believe that the adjusting parameters c_1 and c_2 could be related to an integration coefficient of the fractional integral.

H.4. Mathematical Development of the Fractional Integral Approach

Consider the solution for a fractal reservoir in terms of Green's functions (Chang *et al.*, 1993):

$$p_{D,cr}(R_D, R_{wD}, t_D) = -\alpha \int_0^{t_D} \tau^{D_f/[\theta+2]} \exp\left[-\frac{R_D{}^{\theta+2}}{[\theta+2]^2 \tau}\right] d\tau \,, \quad \text{(H.16)}$$

where α is a constant. The solution given by Eq. H.16 is general and applicable for $D_f \leq 3$, which includes the three Euclidean dimensions. Intuitively, Eq. H.16 can be restricted to consider only one direction as follows:

$$p_{D,cr}(x'_D, x'_{wD}, t_D) = -\alpha \int_0^{t_D} \tau^{D_{fx'}/[\theta_x+2]} \exp\left[-\frac{[x'_D - x'_{wD}]^{\theta_x+2}}{[\theta_x+2]^2 \tau}\right] d\tau \,. \quad \text{(H.17)}$$

where $0 < D_{fx} \leq 1$ and $\theta_x \geq 0$. It is important to point out that the x'_D-axis corresponds to the traditional (1*D*-linear) axis only if $D_{fx}=1$ and $\theta_x=0$. Similarly for the y'_D, and the z'_D axes, the solutions are:

$$p_{D,cr}(y'_D, y'_{wD}, t_D) = -\alpha \int_0^{t_D} \tau^{D_{fy'}/[\theta_y+2]} \exp\left[-\frac{[y'_D - y'_{wD}]^{\theta_y+2}}{[\theta_y+2]^2 \tau}\right] d\tau \,, \quad \text{(H.18)}$$

and:

$$p_{D,cr}(z'_D, z'_{wD}, t_D) = -\alpha \int_0^{t_D} \tau^{D_{fz'}/[\theta_z+2]} \exp\left[-\frac{[z'_D - z'_{wD}]^{\theta_z+2}}{[\theta_z+2]^2 \tau}\right] d\tau \,, \quad \text{(H.19)}$$

Analogous to Gringarten *et al.* (1973), we used the Newman's method to combine Eqs. H.17-H.19 to provide a "3*D*" solution:

$$p_{D,cr}(x'_D, x'_{wD}, y'_D, y'_{wD}, z'_D, z'_{wD}\, t_D) = -\alpha \int_0^{t_D} \tau^{\frac{D_{fx'}}{\theta_x+2}+\frac{D_{fy'}}{\theta_y+2}+\frac{D_{fz'}}{\theta_z+2}} \exp\left[-\frac{[x'_D - x'_{wD}]^{\theta_x+2}}{[\theta_x+2]^2\tau}\right] \exp\left[-\frac{[y'_D - y'_{wD}]^{\theta_y+2}}{[\theta_y+2]^2\tau}\right] \exp\left[-\frac{[z'_D - z'_{wD}]^{\theta_z+2}}{[\theta_z+2]^2\tau}\right] d\tau \quad \text{.....(H.20)}$$

Assuming that the connectivity between permeable sites is the same in all directions (*i.e.*, $\theta=\theta_x=\theta_y=\theta_z$), Eq. H.20 reduces to

$$p_{D,cr}(x'_D, x'_{wD}, y'_D, y'_{wD}, z'_D, z'_{wD}\, t_D) = -\alpha \int_0^{t_D} \tau^{D_f/[\theta+2]} \exp\left[-\frac{[x'_D - x'_{wD}]^{\theta+2} + [y'_D - y'_{wD}]^{\theta+2} + [z'_D - z'_{wD}]^{\theta+2}}{[\theta+2]^2\tau}\right] d\tau, \quad \text{.....(H.21)}$$

where the fractal dimension D_f is given by:

$$D_f = D_{fx} + D_{fy} + D_{fz}. \quad \text{.....(H.22)}$$

Comparing Eq. H.16 and H.21, we can concluded that:

$$R_D{}^{\theta+2} = [x'_D - x'_{wD}]^{\theta+2} + [y'_D - y'_{wD}]^{\theta+2} + [z'_D - z'_{wD}]^{\theta+2} \quad \text{.....(H.23)}$$

Given that the modeling of a hydraulic fracture is a planar (2*D*) structure defined in cartesian coordinates, it is fair to neglect the last term in Eq. H.23 (*i.e.*, $z'_D=z'_{wD}$). Additionally, the axes x'_D and y'_D can be rescaled using a power law function. Assuming that the superposition of the fractal reservoir on the 2*D* hydraulic fracture occurs equally in both directions, we related the 2*D* cartesian coordinates to the coordinates of the fractal reservoir as (here, only for the *x*-axis):

$$[x_D - x_{wD}] = [x'_D - x'_{wD}]^{[D_f-1]/2} \quad \text{.....(H.24)}$$

The exponent $[D_f\text{-}1]/2$ depicts the exposure of the fractal reservoir to the 2D hydraulic fracture. The expression given by Eq. H.24 is applicable for perfectly connected systems (θ=0). We found that the general case of Eq. H.24 is given by:

$$[x_D - x_{wD}] = [x'_D - x'_{wD}]^{\beta/2} \quad \text{.....(H.24)}$$

For β>0. Eq. H.25 introduces the use of the spatial dimension β, which (in a sense) provides an "effective geometry" of the reservoir.